alternate space shuttle concepts study

MSC-03810

FINAL REPORT (B-1)

Part II Technical Summary

Volume II ORBITER DEFINITION

CONTRACT: NAS 9-11160
DRL: M010
LINE ITEM: 11

B35-43RP-12
6 JULY 1971

GRUMMAN
BOEING
AEROJET
AVCO
DASSAULT
DORNIER
EASTERN AIRLINES
GENERAL ELECTRIC
NORTHROP

FOREWORD

This document is one of a series prepared in accordance with Contract NAS 9-11160, Study of Alternate Space Shuttle Concepts. Listed below are the final documents required by Data Line Items Nos. 11 through 15 of the contract. Those listed under B & P Documents were developed under the Grumman/Boeing Bid and Proposal effort in anticipation of proposals for a Space Shuttle System industry competition. The letter to the right of each document title is a unique volume identifier which appears in the upper right hand corner of the corresponding document cover.

CONTRACT DOCUMENTS

Executive Summary	
Technical Summary	
Volume I Shuttle Definition	A
Volume II Orbiter Definition →	B-1
Volume II Orbiter Definition	B-2
Volume II Orbiter Definition	B-3
Volume II Orbiter Definition	B-4
Volume III Booster Definition	C-1
Volume III Booster Definition	C-2
Engineering and Development Plan	
Volume I Shuttle System	D
Volume II Orbiter Vehicle	E-1
Volume II Orbiter Vehicle	E-2
Volume III Booster Vehicle	F-1
Volume III Booster Vehicle	F-2
Operations Plan	G
Program Cost and Schedule Estimates Plan	H
Detail Mass Properties Report	
Volume I Orbiter/Booster Mass Properties	S
Volume II Orbiter Weight Substantiation	T-1
Volume II Orbiter Weight Substantiation	T-2
Volume III Booster Weight Substantiation	U-1
Volume III Booster Weight Substantiation	U-2

B & P DOCUMENTS

Program Management Plan	J	Logistics and Maintenance Plan	N
Manufacturing Plan	K	Quality Assurance Plan	P
Integrated Test Plan	L	Reliability and Maintainability Plan	Q
Facilities Plan	M	Safety Plan	R

INTRODUCTION

ALTERNATE SPACE SHUTTLE CONCEPT STUDY

The study of Alternate Space Shuttle Concepts (ASSC) was initiated on July 6, 1970, in parallel with studies of the fully reusable two-stage-to-orbit earth orbital shuttle.

The ASSC study was conducted jointly by the Grumman Aerospace Corporation, the Boeing Company, and their associates. To assure consistency of results, Grumman and Boeing worked closely together in all areas. In general, Grumman concentrated on overall study management, orbiter design, analysis of mated configurations, and development test planning. Boeing concentrated on booster design, ground operations, and maintenance planning. The other team associates and their major areas of participation are shown in the accompanying figure.

The initial phase of the study was directed toward definition and comparison of promising alternatives to the fully reusable concept including stage-and-one-half, expendable first stages, and variants of the two-stage reusable system. This culminated in a configuration recommendation at the study mid-term point to pursue an External LH_2 Tank Orbiter/Heat Sink Booster configuration. The remainder of the study was devoted to generation of detailed design, operational, and cost data for the selected candidate such that meaningful comparisons with internal tanked orbiter/TPS booster configurations could be made.

During subsequent effort, both two and three-engined orbiters embodying the External Hydrogen Tank/Heat Sink Booster concept were compared to a representative internal hydrogen tank configuration. Results were reviewed by NASA in March and April, 1971. As an outgrowth of these reviews, Grumman/Boeing were authorized to emphasize study of a Three-Engined External Hydrogen Tank Orbiter/Heat Sink Booster utilizing 415K sea level thrust engines. It is this configuration, designated H-33, which forms the basis for the technical, cost, and programmatic documentation submitted in fulfillment of the ASSC contract.

As part of the contract effort, a detailed design and cost comparison was made between the H-33 and a conventional internal LH_2 tank orbiter/TPS booster designated G-3. Results of this comparison show the H-33 to be significantly lighter, simpler, and less costly than its internal tank counterpart. Gross liftoff weight is reduced by 30%, and wetted area is reduced by 16% and 30% on orbiter and booster, respectively. The highlights of the H-33 configuration and its operational characteristics are summarized on the following pages.

H-33 LAUNCH CONFIGURATION

- OLOW 1,101,260 LB
- BLOW 2,824,000 LB
- GLOW 3,925,260 LB
- V_{STAGE} 7000 FPS

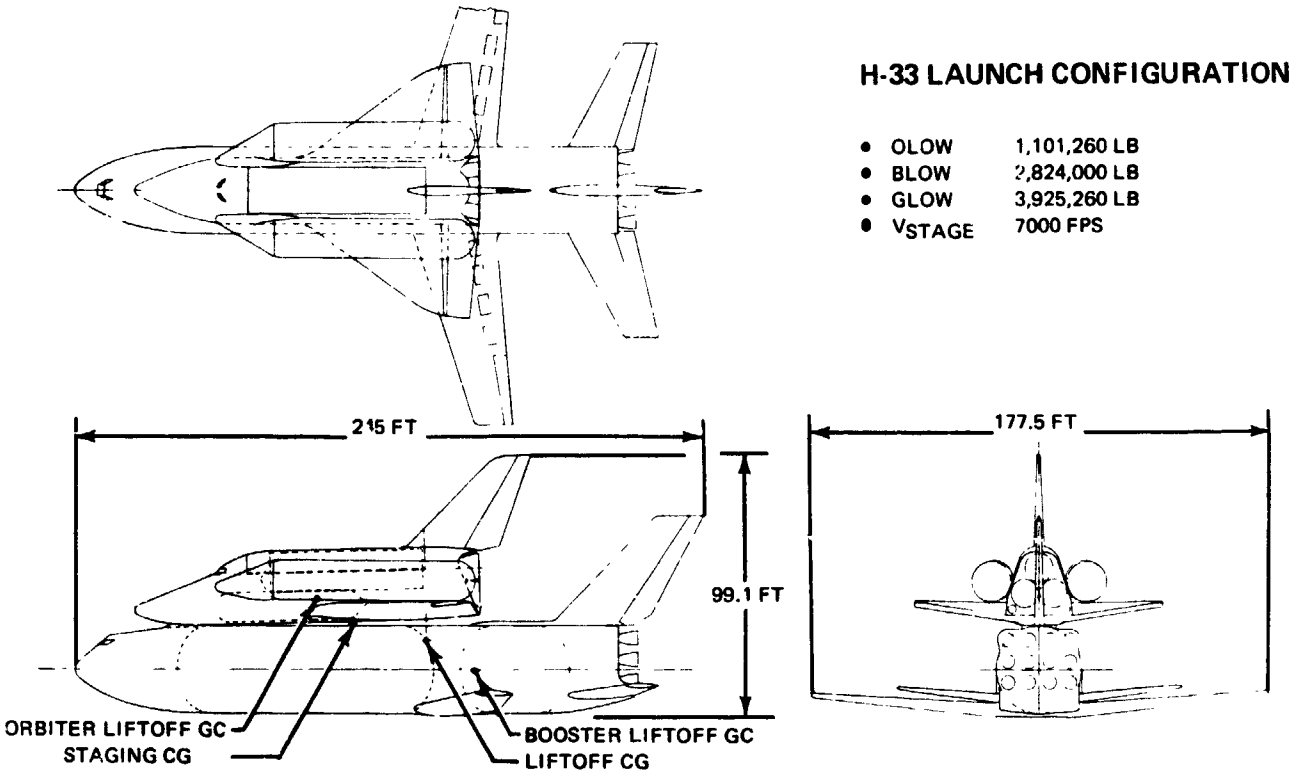

The H-33 Orbiter and Booster are mated in a belly-to-back configuration via two centerline attach/separation points which span the booster LH_2 tank. Lateral mounting stability is provided by aft-mounted outboard pressure pads. Two hydraulically actuated mechanical linkages, recessed in the booster body to minimize the booster-orbiter air gap, provide positive separation at staging. A forward fairing between the vehicles significantly reduces interference heating.

Common 415,000 lb thrust (SL) engines are installed in orbiter and booster, which employ 3 and 12 engines, respectively. The engines are throttleable to 50% and gimbal to provide control during launch and insertion. The air breathing propulsion systems (ABPS) comprise the currently available JTF-22A-4 in both orbiter (4) and booster (8).

The more modest size and lower gross liftoff weight (GLOW) of the configuration is a product of the external LH_2 tank orbiter design concept:

- The external LH_2 tanks permit high orbiter delta-V coupled with low core vehicle size and weight
- The improved orbiter structural efficiency causes the mated vehicle weight to optimize at a low staging velocity (7000 fps)
- The low staging velocity results in a low (227 n mi) booster flyback range, reduces booster size, and permits 100% Heat Sink Booster construction

H-33 ORBITER CONFIGURATION

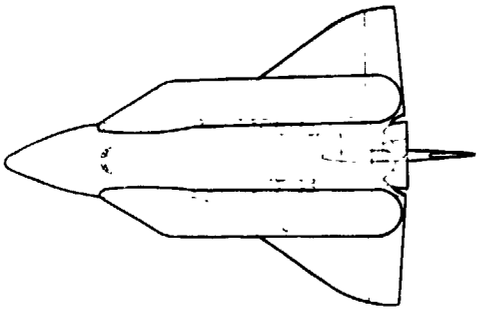

PAYLOAD UP DN (POLAR)	40,000 LB
INJECTION WEIGHT (W/O TANKS)	268,660 LB
INJECTION WEIGHT (W/TANKS)	292,260 LB
LANDED WEIGHT	241,172 LB
MAIN PROPELLANT	809,000 LB
LIFTOFF WEIGHT	1,101,260 LB
MAIN ENGINES, 3 @ T_{VAC}	477,000 LB
T/W	1.30

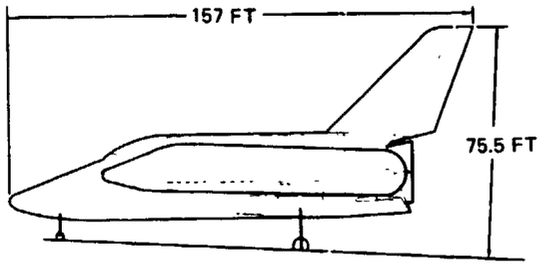

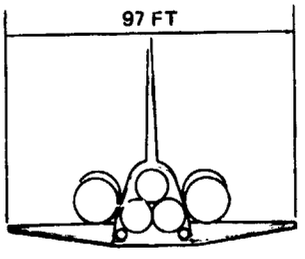

The H-33 Orbiter is a compact delta wing/centerline fin configuration carrying main propulsion LH_2 in two side-mounted jettisonable tanks. Tank nose fairings reduce drag and interference heating during launch. The rocket propulsion installation comprises: three 477,000 lb vacuum thrust engines (415K SL) for insertion; two 15,000 lb thrust RL-10 engines for on-orbit/de-orbit maneuvers; and thirty 1000 lb thrust ACPS engines for fail-op/fail safe attitude control during orbital operations and reentry.

Aerodynamic control is provided by full span elevons and a segmented split rudder which is flared ±30 deg for supersonic directional stability and for drag modulation (lower segment only) during landing. The vehicle meets the 1100 n mi cross-range requirement and is stable over the flight regime. Configuration design characteristics are:

- Constant body cross-section over 16 ft diameter x 65 ft long payload bay
- Payload bay position yields small in/out cg shift (0.7% body length)
- Air breather installation comprises two pairs of deployable JTF-22A-4 off-the-shelf engines; in/out cg shift 0.5% body length; removal yields two 5 x 10 x 13.75 ft compartments for alternate use
- Non-integral twin 11 ft D x 60 ft L oxidizer tanks are simply supported and removable for repair and refurbishment via the nose section manufacturing break
- 990 cu ft crew compartment houses four man crew plus EC/LSS, avionics and EPS. Direct access to payload bay via airlock.
- Thermal protection uses standoff insulated panels except for carbon/carbon on nose, leading edges, and elevon trailing edge
- Landing system comprises dual wheel nose and main gear plus twin 30 ft D drag chutes. Gear rotates aft for deployment; aero blowdown provides second-tier backup

GRUMMAN
BOEING

EXTERNAL TANK GENERAL ARRANGEMENT

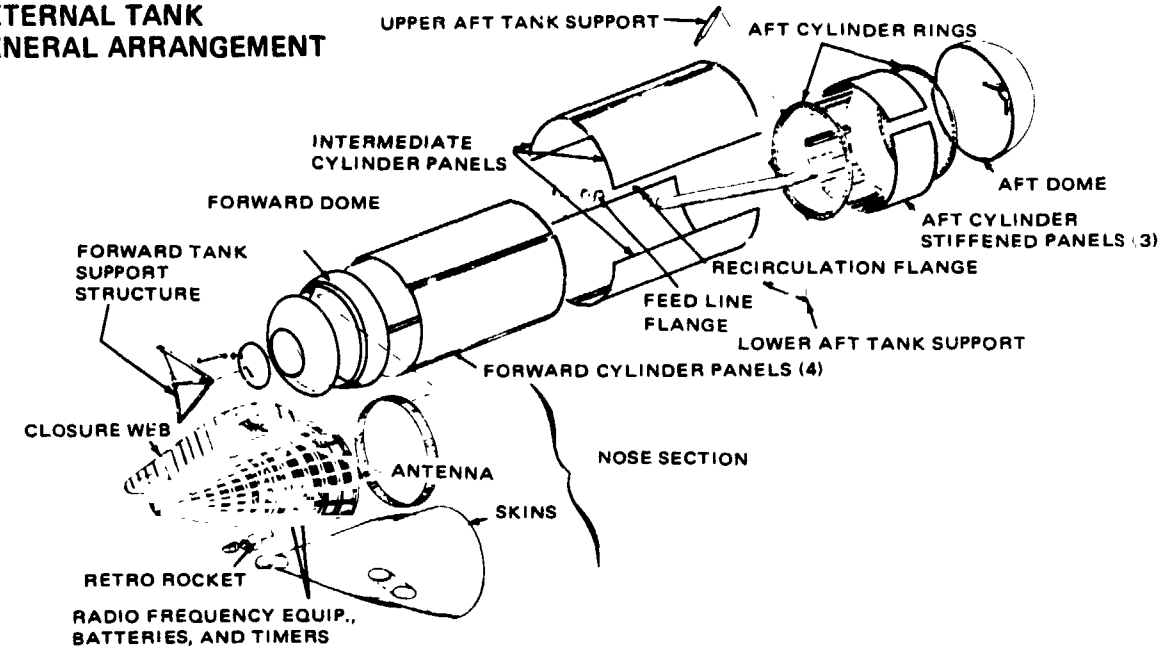

Each external tank is a 14.8 ft D cylinder with simple conical/hemispherical forward/aft end domes. LOA is 102 ft including the 17.6 ft aluminum allow sheet-frame-stringer nose fairing. The tank shell is a welded monocoque structure of 2219 aluminum alloy sheet, 0.057-in. thick between weld lands. LH_2 capacity each tank is 59,394 lb; dry weight is 10,349 lb/tank.

A 0.75-in. thick external layer of spray-on NOPCO BX250A foam provides cryogenic insulation. Spray-on Pirex 250 ablator, 0.1-in. thick, protects the tank inboard surface against interference heating. Nose fairing and strut thermal protection is afforded by an Avcoat 5026-39 ablative cover.

Attach struts are located at the forward and aft ends of the tank. Separation is effected by release of three marman-type clamps via triply redundant explosive bolts plus initiation of two pyrotechnic actuators, which thrust the tanks laterally with a total impulse of 1460 lb-sec/tank. All hardware is retained (no "shrapnel").

The redundant receiver decoders, timing circuits, and batteries used to initiate the tank de-orbit burn are located in the nose fairing together with the 10,000 lb thrust de-orbit SRM. A burn time of 7 sec imparts 200 fps de-orbit delta-V to the tank. Key points of this design approach are:

- Existing technology applicable: aluminum/LH_2 compatibility plus use of S-II spray-on foam insulation and ablator
- Simple fabrication: untapered cylinder, simple end caps, no integral webs
- Decoupled development from basic orbiter structure
- Volume growth potential with minimum impact
- Fracture mechanics/flaw growth issue avoided
- Reusable cryogenic insulation development issue avoided
- Post-flight LH_2 tank purging and inspection eliminated

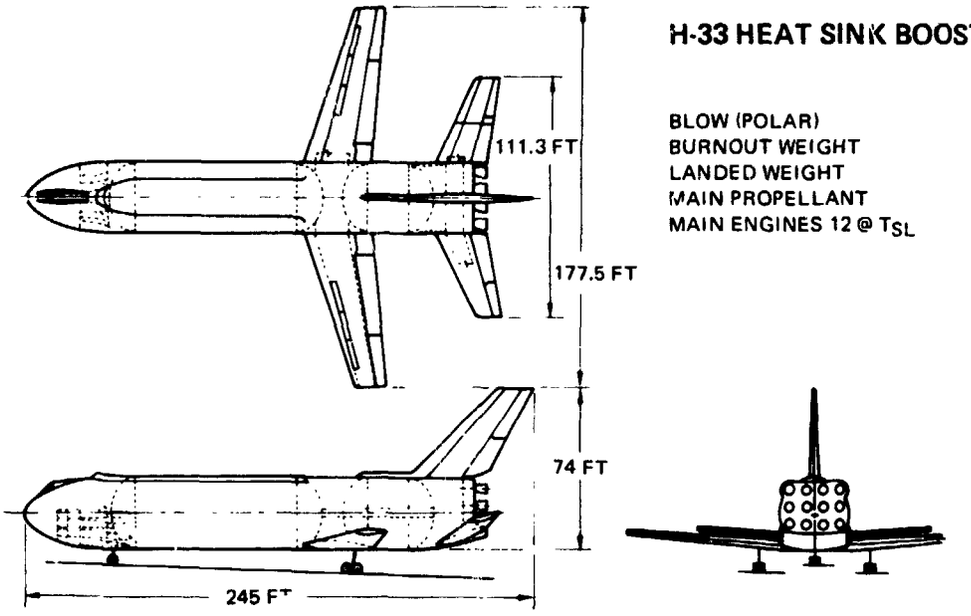

H-33 HEAT SINK BOOSTER

BLOW (POLAR)	2,824,000 LB
BURNOUT WEIGHT	575,000 LB
LANDED WEIGHT	520,000 LB
MAIN PROPELLANT	2,249,000 LB
MAIN ENGINES 12 @ T_{SL}	415,000 LB

FIG 9 1 1 H 33 HEAT SINK BOOSTER CONFIGURATION (MODEL 979 124)

The H-33 booster is a conventional straight wing configuration powered by twelve 415 K lb SL thrust rocket engines plus eight air breathers for flyback. The 218 ft long x 33 ft diameter body contains a two-man crew compartment, buried air breathers with deployable inlets and recessing exit doors, primary propulsion tankage and engines, and the accessories/consumables required for its 60 minute mission.

Booster design employs 100% heat sink structure. The LH_2 tank is a 2219 aluminum alloy cylindrical shell with integral internal waffle stiffening and 70% elliptical end domes. Internally bonded PPO foam maintains initial LH_2 tank temperatures at -220°F and -100°F on heads and cylinder, respectively. The 2219 aluminum alloy LO_2 tank incorporates internal "T" stiffeners and anti-slosh baffles. Its aft location reduces fuselage structural weight, eliminates geysering, minimizes Pogo susceptibility, and accommodates straight-through passage of the wing carrythrough structure.

The wing and all-moving stabilizer are conventional two-spar aluminum alloy structure with titanium leading edges and control surfaces. Haynes 188 structure sustains plume impingement heating on the fin leading edge at orbiter separation. Flight attitude control utilizes boost engine gimballing during launch, 34 ACPS thrusters during coast and entry, and activation of control surfaces for flyback. Significant design characteristics are:

- 100% heat sink construction eliminates TPS panel development and refurbishment. Smooth surfaces minimize slot/protuberance heating
- Saturn technology and tooling are directly applicable to tank design
- LH_2 leaks are readily detectable (visible frost ring)
- Air breather: booster accommodates JTF-22A-4 or the B-1 engine. Development status, commonality, and availability dictates JTF-22A-4
- Aerodynamic configuration: stable/controllable through flight regime; accommodates 30 kt cross wind at landing

MISSION PROFILE, CONFIGURATION H-33

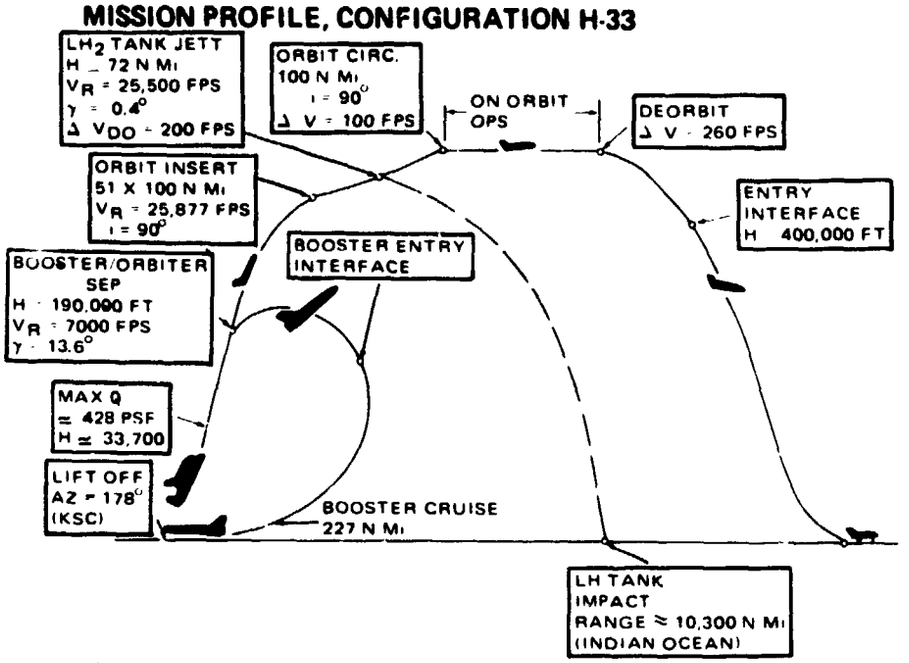

A typical mission profile for the H-33 configuration is shown above. Significant events are summarized below, using values representative of a polar launch.

- Vehicle liftoff is accomplished vertically with an initial T/W ratio of 1.27. Vehicle GLOW is 3.93 M lb
- Maximum dynamic pressure (q) of 428 psf is encountered at an altitude/velocity of 33,700 ft/1051 fps, 76.2 sec after liftoff
- Separation occurs 181.4 sec after liftoff at an altitude/velocity of 190,000 ft/7,000 fps. Flight path angle and q are 13.6 deg and 18.4 psf, respectively
- Booster entry/flyback includes coast to 235,000 ft apogee, trim to 60 deg entry alpha, initiation of 90 deg bank at q max (111 psf), start transition at 30,000 ft (wings level) and start 227 n mi flyback at 16,000 ft. Maximum normal load factor is 3.5 g; approach/landing speeds are 161/155 kt, respectively
- Orbiter insertion into a 51 x 100 n mi orbit requires a burn time of 275.5 sec with an initial T/W of 1.3. Insertion velocity is 25,877 fps
- External tank jettison occurs 20 min after orbiter burnout at an altitude/velocity of 72 n mi/25,500 fps. Tanks are separated at an orbiter attitude of 30 deg nose up; 20 sec later ignition of the de-orbit SRM's is initiated via rf link; impact is 10,300 n mi downrange at 30 deg South Lat/90 deg East longitude (Indian Ocean)
- Orbiter entry is initiated with a 130 sec burn oriented 0 deg to the local horizontal. Entry alpha is 27 deg. The vehicle is controlled to thermal boundaries down to 1/2 circular velocity with subsequent control to a latitude/longitude target. Maximum q/normal load factor are 260 psf and 1.28 g, respectively. Full aero surface control is initiated at M = 4; approach/touchdown speeds are 240/180 kt, respectively.

EXTERNAL TANK ENTRY DISPERSIONS

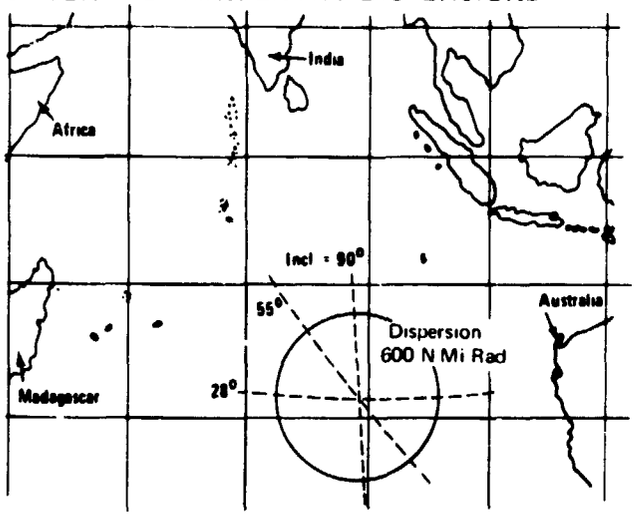

Impact areas and dispersions predicted for the baseline external hydrogen tank disposal system are shown above for KSC launches. The impact zone for KSC reference missions is confined to a single region in the South Indian Ocean, approximately 1500 n mi west of Australia. Impact for polar and retrograde launches from WTR occurs in the Pacific ocean at 60 deg S latitude, north of the Antarctic land mass.

No attitude control system is required on the tank. Dispersion analyses considering variations in orbiter alignment, tank cg location, attitude, and separation/de-orbit system hardware characteristics show an in plane error of 6.5 deg in the de-orbit velocity vector. Resulting impact dispersions of surviving particles for a tumbling tank with a breakup altitude of 300,000 ft are ± 600 n mi downrange, ± 18 n mi crossrange.

Predicted ship traffic densities for 1980 indicate that four ships, out of a possible 29,000 at sea, will be in the approximately 40,000 sq mi elliptical impact area. For any mission, the resulting probability of any one particle impacting a ship is less than 1×10^{-7}. Summarizing the characteristics of the disposal system:

- External LH_2 tank materials and design approach encourage tank breakup and fragment burnup during entry
- Selected impact regions are remote from high density shipping lanes
- Impact dispersions are acceptable without active tank attitude control

GROUND OPERATIONS

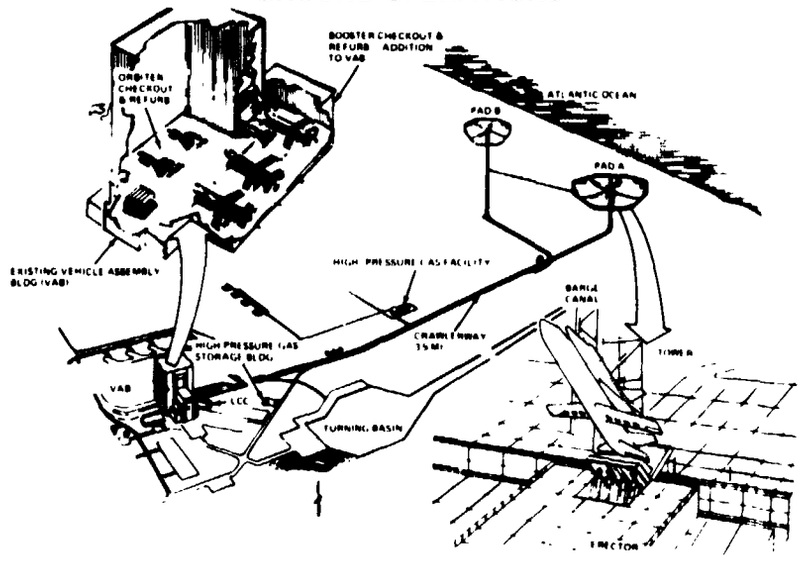

Orbiter and booster are initially barged from the Michoud assembly area with wings and tail surfaces disassembled. Final assembly is accomplished in the vertical assembly building (VAB) at KSC. Subsequent ground operations encompass all maintenance, checkout, mating, and launch operations required on booster, orbiter, and payload from touchdown through launch of the next mission. The ground operations concept is directed toward eventual achievement of "airline type" operating practices utilizing onboard checkout/monitoring provisions. Key events in the operations cycle are:

- Subsystem and system checkout takes place in the VAB. Subsystem tasks comprise visual inspection, scheduled/unscheduled maintenance, and hardware functional checks. System verification of orbiter and booster will be performed to ensure preservation of interface compatibility. Orbiter system testing will be preceded by mating of external LH_2 tanks

- Vehicle mating will be accomplished in a horizontal attitude by positioning the orbiter on the booster via a two-point suspension two-crane operation. Mating and interface verification will be followed by payload installation

- Transfer to the pad will be accomplished by a 747-type tug, which tows the shuttle on the booster landing gear to the pad and positions it on the integral holddown/erector. The holddown clamps are secured to the booster, and the vehicle erected to the launch position

- Final checkout and launch comprises propellant loading, crew and passenger boarding, final status checks by onboard avionics, system pressurization, and switch to internal power. Booster main engines are ignited; upon verification of thrust buildup, the holddown arms are released for liftoff

H-33 ALTERNATE MISSION CAPABILITY (VEHICLES SIZED FOR 40K PAYLOAD TO POLAR ORBIT)

MISSION	OMS DELTA-V REQUIRED* (FPS)		PAYLOAD CAPABILITY (K LB)
	NOMINAL	ABORT **	
POLAR - 90 DEG	810	795	40
RESUPPLY - 55 DEG	1690	720	26.2
DUE EAST -28.5 DEG	1190	695	65.7

* ORBITER CARRIES MAXIMUM OF MISSION OR ABORT OMS DELTA-V

** INCLUDES 120 FPS FOR ENTRY ACPS MANEUVERING

Shuttle requirements specify the following orbiter payload capability for the three reference missions:

- Polar 100 n mi Orbit: 40 K lb up and down (no ABPS)
- 55° Inclination 270 n mi Orbit: 25 K lb up and down (with ABPS)
- Due East 100 n mi Orbit: 65 K lb up, 40 K lb down (no ABPS)

Also required is orbiter once-around abort capability in the event of an inoperative main engine at separation. The abort is accomplished by operating the remaining engine(s) at emergency power in conjunction with a parallel on-orbit maneuvering system (OMS) burn during insertion, followed by a passive entry and return to site.

The capability afforded by the three-engined H-33 configuration in meeting both payload and abort requirements is shown in the above table, which summarizes payload capacity and OMS nominal and abort delta-V requirements for the three reference missions. The following characteristics are noted:

- H-33 provides a close payload match for all three reference missions. The vehicle is sized by the polar mission 40 K lb payload requirement. As indicated in the above table, the payload capability for the remaining reference missions corresponds closely to the requirements
- H-33 OMS propellant quantity is not penalized by abort requirements. This is a consequence of the three-engined installation, which reduces the OMS abort requirement for the engine-out case below the OMS delta-V required by the nominal missions

TRADE STUDY SUMMARY

ENGINEERING		MANUFACTURING	12
• STRUCTURES/TPS	20	GRND OPERATIONS	3
• G&C/AERO/THERMO	21	TEST	2
• PROPULSION	8		
• AVIONICS/ELECTRICAL	5	TOTAL - 82	
• ECLSS/CREW ACCOMM	7		
• PAYLOAD INTEGR/SAFETY	3		
• VEH OPTIMIZATION (V STAGE)	1		

Eighty-two major tradeoff studies have been performed in support of the External LH_2 Tank Orbiter/ Heat Sink Booster system definition, including 65 in engineering, 12 in manufacturing, and 5 in operations and test. While they are by no means an exhaustive collection of studies, they have served to provide a reasonable degree of system optimization and maturity, particularly with respect to vehicle design characteristics, where the greatest emphasis has been placed.

Certain significant factors have not as yet been subjected to tradeoffs, but have been accepted as groundrules: these include the payload and mission performance requirements, the operational program schedule and traffic model, the use of KSC as the launch site, and the approach to transonic/supersonic flight test prior to FMOF.

Of the total number of tradeoff studies tabulated above, 58 have been formally published prior to completion of the study. The remainder are documented in the ASSC final reports.

SYSTEM SUMMARY COMPARISON - POLAR MISSION

	H-33: 3 ENG EXT TK		G-3:2 ENG INT TK		G-3 VS H-33 : DELTAS	
	ORB.	BOOST.	ORB.	BOOST.	ORB.	BOOST.
WEIGHTS, LB						
● GLOW	3,925,260		5,240,920		1,315,360	
● OLOW/BLOW	1,101,260	2,824,000	938,280	4,302,640	-162,980	1,478,640
● INJECTION PROP	809,000	2,249,000	632,275	3,348,470	-176,725	1,099,470
● DRY WT: STAGE	197,238	494,870	220,135	798,448	22,897	303,578
TANKS (2)	20,698	-	-	-	-	-
TOTAL	712,806		1,018,583		305,777	
DIMENSIONS						
● LGTH OVERALL, FT	157	245	173	296	16	51
● SPAN, FT	97	177.5	101.7	221.3	4.7	43.8
● WETTED AREA, FT^2	17,930	33,794	21,350	47,767	3,420	13,973
PROPULSION						
● PRIMARY: NO. ENG/ THRUST	3/477 K (VAC)	12/415 K (SL)	2/632 K (VAC)	13/550 K (SL)	-	-
● AIR BREATHERS	JTF-22A-4(4)	JTF-22A-4(8)	JTF-22A-4(4) (2 W/AB)	B-1 (10)		
PERFORMANCE						
● STAGING VELOCITY, FPS	7,000		9,750		2,750	
● ORB. IDEAL DELTA-V, FPS	19,600	-	16,538	-	-3,062	-
● FLYBACK RANGE, NM		227	-	368		141

The purpose and intent of the ASSC study has been to define and develop a promising alternative to the fully reusable internal tank orbiter/TPS booster configuration, to a depth which permits meaningful comparison of design concepts. The study has culminated in a detailed definition of the H-33 External Tank Orbiter/Heat Sink Booster configuration, which has been compared on technical, operational, and cost bases to its counterpart, the internal tank orbiter/TPS booster G-3 configuration.

The above table lists major characteristics of each vehicle in sufficient detail to contrast key differences. Weight and performance values shown reflect the polar mission, which sized both vehicles. The comparison clearly identifies the advantages of the Three-Engined External Tank Orbiter configuration:

- Higher Orbiter Delta-V: H-33 provides 3,000 fps more insertion delta-V at an all-up (tanks included) dry weight 2200 lb less than G-3. This characteristic results in system weight optimization at a reduced staging velocity, which benefits booster design as cited below

- Lower Staging Velocity: The H-33 7000 fps staging velocity is 2750 fps less than that of G-3. The resultant reduction in boost propellant and flyback range yields a smaller (delta gross weight 1.48 M lb) booster and permits full exploitation of the heat sink approach to booster design. Booster TPS panel design, development, and operational refurbishment are thereby avoided

- Reduced Dry Weight: H-33 is 306,000 lb (30%) less than G-3 in all-up dry weight, with an attendant decrease in overall dimensions and wetted area as tabulated above. This characteristic eases handling and erection requirements as well as inspection and refurbishment of vehicle outer surfaces

- Lower GLOW: H-33 gross liftoff weight is 1.32 M lb (25%) less than G-3. Substantially less boost/injection propellant (922 K lb) is required; liftoff is accomplished with twelve 415 K lb thrust engines as opposed to thirteen 550 K lb thrust engines

As the above summary indicates, application of the external LH_2 tank approach to shuttle design results in orbiter and booster configurations which are smaller, lighter, simpler, and hence less costly than their internal tank counterparts.

* * *

The foregoing introduction has provided a brief description of the Grumman/Boeing External LH_2 Tank Orbiter/Heat Sink Booster Shuttle configuration, its operational characteristics and its capability. The following page contains a Study Volume Guide, which identifies the final documents submitted in fulfillment of the ASSC contract.

Also listed are additional documents developed under the Grumman/Boeing Bid and Proposal effort currently underway in anticipation of proposals for a Space Shuttle System industry competition. These documents represent an interim stage in the Bid and Proposal preparation effort, and as such, are submitted at this time for NASA's information only.

ASSC STUDY VOLUME GUIDE

A. ASSC Contract Documentation	Vol I.D	Grumman Doc. No.	NASA Doc. No.
1) Final Report			
Part I Executive Summary		B35-43RP-11	MSC-03809
Part II Technical Summary		B35-43RP-12	MSC-03810
Vol. I Shuttle Definition	A		
Vol. II Orbiter Definition	B		
Vol. III Booster Definition	C		
Part III Engineering and Development Plan		B35-43RP-13	MSC-03811
Vol. I Shuttle System	D		
Vol. II Orbiter Vehicle	E		
Vol. III Booster Vehicle	F		
Part III Operation Plan	G	B35-43RP-14	MSC-03812
Part III Program Cost and Schedule Plan	H	B35-43RP-15	MSC-03813
2) Detail Mass Properties Report		B35-43RP-16	MSC-03814
Vol. I Orbiter/Booster Mass Properties	S		
Vol. II Orbiter Weight Substantiation	T		
Vol. III Booster Weigh Substantiation	U		
B. Shuttle Bid and Proposal* Documentation			
1) Program Management Plan	J	552-43RP-1	
2) Manufacturing Plan	K	552-43RP-2	
3) Integrated Test Plan	L	552-43RP-3	
4) Facilities Plan	M	552-43RP-4	
5) Logistics and Maintenance Plan	N	552-43RP-5	
6) Quality Assurance Plan	P	552-43RP-6	
7) Reliability and Maintainability Plan	Q	552-43RP-7	
8) Safety Plan	R	552-43RP-8	

* Submitted for NASA's information only; not for dissemination as part of ASSC Study "data dump" to industry.

CONTENTS
(BOOK B-1)

Section			Page
	ALPHABETICAL SUBJECT INDEX		xxxi
8	ORBITER DEFINITION		8.1-1
	8.1	Introduction	8.1-1
	8.2	Configuration	8.2-1
		8.2.1 Summary	8.2-1
	8.3	Characteristics	8.3-1
		8.3.1 H-33 Physical Characteristics	8.3.1-1
		8.3.2 Orbiter Mass Properties	8.3.2-1
		8.3.3 Aerodynamic Characteristics	8.3.3-1
		8.3.4 Performance	8.3.4-1
		8.3.5 Thermal Environment	8.3.5-1
		8.3.6 Loads and Dynamics	8.3.6-1

ILLUSTRATIONS
(BOOK B-1)

Figure		Page
8.2-1	H-33 Orbiter General Arrangement	8.2-7
8.2-2	H-33 Potential Packaging Arrangement	8.2-9
8.2-3	H-33 Orbiter Inboard Profile	8.2-13
8.2-4	H-33 External Tank Orbiter Major Structural Assembly Breakdown	8.2-18
8.2-5	External Tanks	8.2-19
8.3.3-1	H-33 Mach ~ α Envelope	8.3.3-21
8.3.3-2	Hypersonic Longitudinal Performance Characteristics, Trimmed	8.3.3-22
8.3.3-3	H-33 Orbiter Post Entry Aerodynamic Characteristics Summary	8.3.3-23
8.3.3-4	G-3G Orbiter Post Entry Aerodynamic Characteristics Summary	8.3.3-24
8.3.3-5	H-33 Hypersonic Longitudinal Stability and Control	8.3.3-25
8.3.3-6	G-3G Hypersonic Longitudinal Stability and Control	8.3.3-26
8.3.3-7	Variation of H-33 Lift-Drag Ratio with Mach No.	8.3.3-27
8.3.3-8	Hypersonic Lateral-Directional Stability, Body Axis	8.3.3-28
8.3.3-9	H-33 Hypersonic Aileron Effectiveness, Body Axis	8.3.3-29
8.3.3-10	Aerodynamic Trade-offs, Hypersonic Directional Stability	8.3.3-30
8.3.3-11	H-33 Hypersonic Longitudinal Dynamic Derivatives	8.3.3-31
8.3.3-12	H-33 Hypersonic Lateral-Directional Dynamic Derivatives	8.3.3-32
8.3.3-13	H-33 Orbiter Trimmed Lift Characteristics	8.3.3-33
8.3.3-14	H-33 Orbiter Trimmed Drag Polars	8.3.3-35
8.3.3-15	H-33 Orbiter Longitudinal Characteristics	8.3.3-37
8.3.3-16	H-33 Orbiter Longitudinal Aerodynamic Characteristics, Mach = 0.2	8.3.3-39
8.3.3-17	H-33 Orbiter Longitudinal Aerodynamic Characteristics, Mach = 0.6	8.3.3-41

ILLUSTRATIONS (Cont)

Figure		Page
8.3.3-18	H-33 Orbiter Longitudinal Aerodynamic Characteristics, Mach = 0.8	8.3.3-43
8.3.3-19	H-33 Orbiter Longitudinal Aerodynamic Characteristics, Mach = 0.9	8.3.3-45
8.3.3-20	H-33 Orbiter Longitudinal Aerodynamic Characteristics, Mach = 1.3	8.3.3-47
8.3.3-21	H-33 Orbiter Longitudinal Aerodynamic Characteristics, Mach = 1.5	8.3.3-49
8.3.3-22	H-33 Orbiter Longitudinal Aerodynamic Characteristics, Mach = 2.0	8.3.3-51
8.3.3-23	H-33 Orbiter Longitudinal Aerodynamic Characteristics, Mach = 2.48	8.3.3-53
8.3.3-24	H-33 Orbiter Longitudinal Aerodynamic Characteristics, Mach = 3.0	8.3.3-55
8.3.3-25	H-33 Orbiter Longitudinal Aerodynamic Characteristics, Mach = 3.9	8.3.3-57
8.3.3-26	H-33 Elevator Effectiveness	8.3.3-59
8.3.3-27	H-33 Orbiter Zero Lift Drag versus Mach Number	8.3.3-60
8.3.3-28	H-33 Orbiter Estimated Static Directional Stability vs. Mach Number	8.3.3-61
8.3.3-29	H-33 Orbiter Estimated Lateral Stability Variation With Mach Number	8.3.3-62
8.3.3-30	H-33 Orbiter Estimated Side Force Variation With Mach Number	8.3.3-63
8.3.3-31	Correlation of Test Data With Estimation Techniques G-3A Orbiter	8.3.3-64
8.3.3-32a	H-33 Orbiter Estimated Lateral-Directional Characteristics With Flared Rudder Deployed	8.3.3-65
8.3.3-32b	H-33 Orbiter Estimated Lateral-Directional Characteristics With Flared Rudder Deployed	8.3.3-66
8.3.3-33	H-33 Orbiter Estimated Rudder Effectiveness	8.3.3-67
8.3.3-34	H-33 Aileron Effectiveness	8.3.3-68
8.3.3-35	H-33 Aileron Effectiveness	8.3.3-69
8.3.3-36	H-33 Aileron Effectiveness	8.3.3-70
8.3.3-37	H-33 Pitching Derivatives	8.3.3-71
8.3.3-38	H-33 Acceleration Derivatives	8.3.3-72
8.3.3-39	H-33 Roll Dynamic Derivatives	8.3.3-73

ILLUSTRATIONS (Cont)

Figure		Page
8.3.3-40	H-33 Yaw Dynamic Derivatives.	8.3.3-74
8.3.3-41	H-33 Incremental Subsonic Longitudinal Characteristics Due To Ground Proximity	8.3.3-75
8.3.3-42	H-33 Incremental Subsonic Drag Coefficient Due To Ground Proximity.	8.3.3-76
8.3.3-43	H-33 Subsonic Longitudinal Speedbrake Increments.	8.3 3-77
8.3.3-44	H-33 Orbiter Design Trajectory	8.3.3-78
8.3.3-45	H-33 Orbiter Longitudinal Speed Stability and Trim Requirement	8.3.3-79
8.3.3-46	H-33 Orbiter Longitudinal Control Power	8.3.3-80
8.3.3-47	H-33 Orbiter Longitudinal Short Period Dynamic Characteristics During Entry and Cruise	8.3.3-81
8.3.3-48	H-33 Orbiter Longitudinal Short Period Dynamic Characteristics During Approach and Landing.	8.3.3-82
8.3.3-49	H-33 Orbiter Longitudinal Control Lift Loss Requirement in Approach	8.3.3-83
8.3.3-50	H-33 Orbiter Dutch Roll Mode Characteristics.	8.3.3-84
8.3.3-51	H-33 Orbiter Roll Rate Response to Step Aileron Input	8.3.3-85
8.3.3-52	H-33 Orbiter Basic Vehicle Response to Ramp Vertical Gust	8.3.3-86
8.3.3-53	H-33 Orbiter Basic Vehicle Response to Ramp Side Gust	8.3.3-87
8.3.3-54	Basic Vehicle Response to Miscoordinated Roll Control Input at Hypersonic Entry Flight ($\alpha_e = -5^o$)	8.3.3-88
8.3.3-55	Effect of ARI on Bare Airframe Dynamics.	8.3.3-89
8.3.3-56	Dynamic Response of Orbiter with SAS to Roll Rate Command ($\dot{\Phi}_V = 6.3^o$/sec)	8.3.3-90
8.3.3-57	Dynamic Response of Orbiter with Z-DAP to Bank Angle Command ($\Phi_V = 45^o$)	8.3.3-91
8.3.3-58	Dynamic Response of Orbiter with Z-DAP to Roll Rate Command ($\dot{\Phi}_V = 5^o$/sec).	8.3.3-92
8.3.3-59	Dynamic Response of Orbiter with X-DAP to Bank Angle Command ($\Phi_V = 45^o$)	8.3.3-93
8.3.3-60	Dynamic Response of Orbiter with X-DAP to Roll Rate Command ($\dot{\Phi}_V = 5^o$/sec).	8.3.3-94
8.3.3-61	Dynamic Response of Orbiter with Aero/ACPS Control System to Bank Angle Command ($\Phi_V = 45^o$)	8.3.3-95

ILLUSTRATIONS (Cont)

Figure		Page
8.3.3-62	Dynamic Response of Orbiter with Aero/ACPS Control System to Roll Rate Command ($\dot{\Phi}_V = 5^o$/sec)	8.3.3-97
8.3.4-1	Shuttle Position Relative to Target Coelliptic Rendezvous Curvilinear Coordinates	8.3.4-6
8.3.4-2	Shuttle Position Relative to Target, Modified Coelliptic Rendezvous Curvilinear Coordinates	8.3.4-10
8.3.4-3	Shuttle Position Relative to Target, Stable Orbit Rendezvous, Non-Cooperative Target	8.3.4-12
8.3.4-4	Delta-V Penalties for Re-Orbit and Orbital Rendezvous Maneuvers	8.3.4-14
8.3.4-5	Stationkeeping Boundaries	8.3.4-16
8.3.4-6	Downrange and Cross Range Capability for Different Angles-of-Attack	8.3.4-22
8.3.4-7	Crossrange Required	8.3.4-24
8.3.4-8	Entry Flight Path Angle Tradeoff	8.3.4-25
8.3.4-9	Maximum Crossrange and Time of Flight vs Downrange and Angle-of-Attack	8.3.4-26
8.3.4-10	Maximum Centerline Temperature and Total Heat vs Angle-of-Attack	8.3.4-28
8.3.4-11	Thermal Boundaries to Maintain Centerline Aft of 20-Ft Station Below 1800^{o}F	8.3.4-29
8.3.4-12	Baseline Entry	8.3.4-31
8.3.4-13	Entry Trajectory Time History	8.3.4-32
8.3.4-14	Maximum Crossrange and Downrange vs 100-Ft Station Temperature (T_{UB}) and Applied Acceleration (G_A)	8.3.4-33
8.3.4-15	Entry With Angle-of-Attack Modulation, 100 n mi Polar Orbit	8.3.4-35
8.3.4-16	ACPS/Aero-Trim Attitude Control Logic	8.3.4-36
8.3.4-17	ACPS Jet Thruster Firing Command Schematic for the Upper-Half Phase Plane	8.3.4-38
8.3.4-18	Parabolic Switch Line Adjustment Variables ("Coast", "FSHRT") Effectiveness	8.3.4-39
8.3.4-19	Total ACPS Propellant - High Cross Range Entry Effect of Jet Thruster Size and Number	8.3.4-41
8.3.4-20	ACPS Control Accelerations per Axis for Selected Jet Thruster Size and Number	8.3.4-42

Figure		Page
8.3.4-21	Total ACPS Propellant - High Crossrange Orbiter Effect of Lateral CG Offset and Directional Aerodynamic Stability	8.3.4-48
8.3.4-22	Pitch Trim System Jet On-Time Integral Compensation	8.3.4-52
8.3.4-23	3σ $\Delta\alpha$ and $\Delta\beta$ Errors During Entry Using Carousel IV Platform.	8.3.4-52
8.3.4-24	Response to 2-In. Lateral CG Offset, No Aero Trim	8.3.4-53
8.3.4-25	Response to 2-In. Lateral CG Offset, Aero Trim Active.	8.3.4-55
8.3.4-26	G3 30° Aerodynamic Entry Autopilot Block Diagram	8.3.4-57
8.3.4-27	Paths of Dominant Roots for 30° Equilibrium Entry.	8.3.4-58
8.3.4-28	G-3A Aerodynamic Entry Autopilot	8.3.4-61
8.3.4-29	G-3A Aerodynamic Entry Autopilot	8.3.4-63
8.3.4-30	H-33 Orbiter Terminal Footprint.	8.3.4-65
8.3.4-31	Spiral Slide Descent Trajectories to Initiation of Final Approach (Side View)	8.3.4-66
8.3.4-32	Orbiter Ground Track in Spiral Glide Descent Polar View	8.3.4-67
8.3.4-33	H-33 Final Approach Profile.	8.3.4-69
8.3.4-34	Glide Path Control	8.3.4-71
8.3.4-35	H-33 Orbiter Operational Climb Performance	8.3.4-72
8.3.4-36	H-33 Touchdown V locity and Landing Distance Over 50-Ft Obstacle	8.3.4-73
8.3.4-37	H-33 Approach and Go-Around Profile	8.3.4-74
8.3.4-38	H-33 Orbiter Ferry Package Takeoff Distances	8.3.4-78
8.3.4-39	H-33 Orbiter Ferry Package Second Segment Takeoff Climb Gradients	8.3.4-79
8.3.4-40	H-33 Orbiter Ferry Package, V_{MU} - Minimum Nosewheel Unstick Speed, V_{LOF} - Liftoff Speed	8.3.4-80
8.3.4-41	H-33 Cruise Performance	8.3.4-81
8.3.4-42	H-33 Orbiter Ferry Package Time, Fuel, and Distance in Climb from Sea Level to Best Cruise Altitude	8.3.4-82

ILLUSTRATIONS (Cont)

Figure		Page
8.3.4-43	H-33 Orbiter Ferry Package Best Climb Speed	8.3.4-83
8.3.4-44	H-33 Flight Envelope, Intermediate Power	8.3.4-84
8.3.4-45	H-33 Orbiter Ferry Package Minimum Loiter Fuel Flows and Corresponding Velocities	8.3.4-85
8.3.4-46	H-33 Orbiter Ferry Package Ferry Range	8.3.4-86
8.3.4-47	H-33 Ferry Mission Summary	8.3.4-87
8.3.5-1	Ice/Frost Formation Probability	8.3.5-3
8.3.5-2	Probable Ice/Frost Buildup	8.3.5-5
8.3.5-3	Liquid Oxygen Tank Purge	8.3.5-6
8.3.5-4	Liquid Oxygen Tank Heated Purge	8.3.5-8
8.3.5-5	H-33 Ascent Trajectory	8.3.5-9
8.3.5-6	Tank Configurations After Phase Change Paint Test in LRC Hypersonic Wind Tunnel	8.3.5-11
8.3.5-7	Maximum Ratio of Heat Transfer to Orbiter With Flow Disturbed and Undisturbed by Tanks	8.3.5-12
8.3.5-8	Measured Heating Rates to H-33 Contoured External LH_2 Tanks	8.3.5-13
8.3.5-9	Measured Ascent Heating	8.3.5-14
8.3.5-10	Maximum Vehicle Temperatures During Ascent	8.3.5-15
8.3.5-11	External LH_2 Tank Ablator Foam Samples	8.3.5-17
8.3.5-12	Complex Rocket Exhaust; Booster Flow Field	8.3.5-19
8.3.5-13	Plume Impingement Test Model	8.3.5-20
8.3.5-14	Flat Plate Heat Transfer Rate Distribution On Nozzle Centerline Plane	8.3.5-21
8.3.5-15	Flat Plate Heat Transfer Distribution On Body Centerline Plane	8.3.5-22
8.3.5-16	Fin Heat Transfer Rate Distribution on Leading Edge and Side (Two Engines Firing)	8.3.5-23
8.3.5-17	Orbital Average Heat Flux, Earth Oriented	8.3.5-27
8.3.5-18	Orbital Average Heat Flux, Solar Inertial	8.3.5-29
8.3.5-19	On-Orbit Temperatures, ^{o}F, Fuselage Station 900	8.3.5-31
8.3.5-20	H-33 Temperature Time History on Windward Centerline	8.3.5-33
8.3.5-21	Maximum Vehicle Temperatures During Reentry - Windward, = 0.8	8.3.5-34

Figure		Page
8.3.5-22	Maximum Vehicle Temperatures During Reentry - Lee Surfaces $\alpha = 27^{o}$, $\epsilon = 0.8$	8.3.5-35
8.3.5-23	1800°F Windward Surface Temperature Boundaries	8.3.5-37
8.3.5-24	H-33 Design Reentry Trajectory, $\alpha = 27^{o}$	8.3.5-38
8.3.5-25	Ascent Transition Criteria	8.3.5-42
8.3.5-26	Reentry Transition Criteria	8.3.5-43
8.3.5-27	Sensitivity of Reentry Maximum Temperature On The Windward Centerline To Methods and Criteria, $\alpha = 27^{o}$	8.3.5-27
8.3.5-28	Leeside Heating on Simple Shapes	8.3.5-46
8.3.5-29	Leeside Heat Transfer Coefficients At Model Stations With Equal Cross-Sectional Areas and Running Length Reynolds Numbers	8.3.5-47
8.3.5-30	Heating on Leeside of Delta Wing Orbiters	8.3.5-48
8.3.5-31	Purged HPI Insulation Scheme	8.3.5-51
8.3.5-32	OMS Purge Bag	8.3.5-52
8.3.5-33	MLT Thermal Performance, $T_C = 40^{o}R$	8.3.5-53
8.3.5-34	MLT - Thermal Performance, $T_C = 170^{o}R$	8.3.5-54
8.3.5-35	Schematic of Dewar Tension Membrane	8.3.5-58
8.3.6-1	H-33 Baseline and Alternate Interstage Arrangement	8.3.6-3
8.3.6-2	Mated H-3T External Hydrogen Tank Orbiter/Heat Sink Booster	8.3.6-4
8.3.6-3	H-3T Orbiter Configuration	8.3.6-6
8.3.6-4	Ground Wind Profiles	8.3.6-11
8.3.6-5	Synthetic Wind Profile Corresponding to Maximum Aerodynamic Loading at 28,000 Ft. Altitude	8.3.6-12
8.3.6-6	H-3T Orbiter Geometry and Sign Convention	8.3.6-17
8.3.6-7	H-3T Interstage Reactions for Design Ground Winds	8.3.6-19
8.3.6-8	H-3T Orbiter Fuselage Distributed Limit Loads, Launch Loads with Ground Winds	8.3.6-20
8.3.6-9	H-3T Orbiter Fuselage Distributed Limit Loads, Max $q\alpha$ Condition	8.3.6-22
8.3.6-10	H-3T Orbiter Fuselage Distributed Limit Loads, Max $q\beta$ Longitudinal Loads	8.3.6-24
8.3.6-11	H-3T Orbiter Fuselage Distributed Limit Loads, Max $q\beta$ Yaw Plane Loads	8.3.6-25

ILLUSTRATIONS (Cont)

Figure		Page
8.3.6-12	H-3T Orbiter Fuselage Distributed Limit Loads, Initial 3.0G Condition.	8.3.6-26
8.3.6-13	H-3T Orbiter Fuselage Distributed Limit Loads, End Boost Condition	8.3.6-27
8.3.6-14	H-3T Orbiter Fuselage Distributed Limit Loads, Orbiter Ignition Emergency Power	8.3.6-28
8.3.6-15	H-3T Orbiter Fuselage Distributed Limit Loads, Orbiter 2.5G Pullout	8.3.6-29
8.3.6-16	H-3T Orbiter Fuselage Distributed Limit Loads, Landing Loads.	8.3.6-31
8.3.6-17	H-3T Orbiter Fuselage Distributed Limit Loads, Landing Loads (2 Point Level, Spin Up)	8.3.6-32
8.3.6-18	H-3T Orbiter Fuselage Distributed Limit Loads, Landing Loads.	8.3.6-33
8.3.6-19	Preliminary H-33 External Tank Limit Loads Axisymmetric Tank	8.3.6-35
8.3.6-20	Preliminary H-3T External Tank Limit Loads	8.3.6-37
8.3.6-21	H-3T Orbiter Fuselage Applied Loads, Symmetrical End Boost Condition	8.3.6-43
8.3.6-22	H-3T Orbiter Fuselage Applied Loads, Symmetrical Orbiter Engine Thrusting Emergency Power Level (EPL)	8.3.6-47
8.3.6-23	H-3T Orbiter Fuselage Applied Loads, Symmetrical Max q α (+) Wind	8.3.6-51
8.3.6-24	H-3T Orbiter Fuselage Applied Loads, Antisymmetric Max q β	8.3.6-55
8.3.6-25	Structural Analysis Flow	8.3.6-63
8.3.6-26	H-3T Orbiter Dynamic Degree of Freedom Math Model (Symmetric)	8.3.6-77
8.3.6-27	H-3T Booster Dynamic Degree of Freedom Math Model (symmetric)	8.3.6-80
8.3.6-28	Noise Contours and Spectra For Air-Breathing Engines at Maximum Static Thrust.	8.3.6-91
8.3.6-29	Near Field Noise Contours For Air-Breathing Engines at Maximum Static Thrust.	8.3.6-93
8.3.6-30	Data Flow for Shuttle Thermal Stress Analysis	8.3.6-95
8.3.6-31	Integrated Design and Analysis System	8.3.6-97

TABLES
(BOOK B-1)

Table		Page
8.1-1	Contract SOW/Final Report Correlation	8.1-3
8.1-2	Index of Associate Contractor Technical Support	8.1-5
8.2-1	H-33/G-3G Comparisons	8.2-3
8.2-2	Orbiter Delta-U And Propellant Requirements	8.2-5
8.3.2-1	40K Payload South Polar Launch Mission	8.3.2-2
8.3.2-2	Mission Performance Summary	8.3.2-4
8.3.3-1	Orbiter Wind Tunnel Summary	8.3.3-2
8.3.3-2	H-33 Reference Data	8.3.3-9
8.3.3-3	H-33 Orbiter Longitudinal Dynamic Stability Characters	8.3.3-12
8.3.3-4	Lateral Directional Static Trim	8.3.3-13
8.3.3-5	H-33 Orbiter Lateral Directional Dynamic Stability Characteristics	8.3.3-14
8.3.3-6	Summary of Aerodynamic Trade Studies	8.3.3-19
8.3.4-1	OMS Tank Loading Requirement, Space Station Resupply Mission	8.3.4-4
8.3.4-2	Initial Phase of Rendezvous - Trajectory Parameters	8.3.4-7
8.3.4-3	Rendezvous Performance CSM, SXT and VHF with 300 n mi Acquisition Range	8.3.4-9
8.3.4-4	Navigation Performance - Uncooperative Target	8.3.4-13
8.3.4-5	Stationkeeping Delta-V Requirements Per Orbit	8.3.4-17
8.3.4-6	Orbiter Idealized Two-Jet Coast Phase Limit Cycle Propellant Rate	
8.3.4-7	H-33 Orbiter Two-Jet Minimum Impulse Body Axes Rate Change Increment	8.3.4-18
8.3.4-8	ACPS Jet Thruster Sizing Entry Trajectory Control with Guidance/Control Interfraction, High Cross-Range Orbiter	8.3.4-43
8.3.4-9	Entry Trajectory Control, Targeting and ACPS Propellants with 1000 lb ACPS Thrusters Guidance/Control Interaction, High Cross-Range Orbiter	8.3.4-45
8.3.4-10	Entry Trajectory Control, Targeting and ACPS Propellants with 1000 lb Thrusters; Effect of Lateral CG Offset and Lateral Aerodynamic Stability; Guidance/Control Interaction High Cross-Range Orbiter	8.3.4-49

TABLES (Cont)

Table		Page
8.3.4-11	H-33 Orbiter Approach and Landing Profile	8.3.4-75
8.3.4-12	H-33 Orbiter Takeoff Procedures	8.3.4-77
8.3.5-1	Summary of Analytical Aerodynamic Heating Methods.	8.3.5-39
8.3.5-2	Comparison of Results for Spalding - CHI Method	8.3.5-41
8.3.5-3	Purged HPI Insulation System	8.3.5-56
8.3.5-4	Dewar Insulation Parameters & Performance	8.3.5-57
8.3.6-1	Comparison of H-3T and H-33 Physical Characteristics . . .	8.3.6-1
8.3.6-2	H-3T Orbiter Weight Summary.	8.3.6-7
8.3.6-4	H-3T Orbiter Fuselage Weight Distribution (Sheet 1 of 2) . . .	8.3.6-9
8.3.6-4	H-3T Orbiter Fuselage Weight Distribution (Sheet 2 of 2) . . .	8.3.6-10
8.3.6-5	Summary of Applied Limit Loads & Load Factors of the H-3T Orbiter	8.3.6-13
8.3.6-6	Summary of Applied Limit Loads for Exposed Wind and Vertical Tail	8.3.6-16
8.3.6-7	Design Loads and Temperatures for H-3T Main Propellant Tanks	8.3.6-59
8.3.6-8	H-3T Orbiter Structural Math Model Representation	8.3.6-67
8.3.6-9	H-3T Orbiter Weights Model Mass Distribution	8.3.6-68
8.3.6-10	H-3T Orbiter Airload/Applied Loads Model Definition	8.3.6-69
8.3.6-11	Symmetric H-3T Orbiter Dynamic Mathematical Model (LH Side)	8.3.6-76
8.3.6-12	H-3T Dynamic Booster Mathematical Model - Symmetric Degrees of Freedom (LH Side)	8.3.6-79
8.3.6-13	H-3T Combined Orbiter & Booster Free-Free Natural Frequencies	8.3.6-81
8.3.6-14	Engine-Generated Low Frequency Thrust Oscillation Limits (Per Engine)	8.3.6-84
8.3.6-15	H-3T - Maximum Accelerations (g) Due to Engine Unsteady Excitation - Combined Vehicle	8.3.6-85
8.3.6-16	H-3T - Maximum Internal Loads Due to Engine Unsteady Excitation - Orbiter	8.3.6-88
8.3.6-17	Orbiter External Acoustic Environment	8.3.6-89

CONTENTS
(BOOK B-2)

Section		Page
8.4	Structural Subsystems	8.4.1-1
8.4.1	Design Criteria Materials and Failure Control	8.4.1-1
8.4.2	Fuselage Structure	8.4.2-1
8.4.3	Aero Surfaces	8.4.3-1
8.4.4	External Liquid Hydrogen Tanks	8.4.4-1
8.4.5	Composite Applications	8.4.5-1
8.4.6	Thermal Protection	8.4.6-1
8.4.7	Crew Station/Equipment and Passenger Accommodations	8.4.7-1/2
8.4.8	Flight Control Mechanical Equipment	8.4.8-1
8.4.9	Recovery Subsystem	8.4.9-1
8.5	Propulsion Subsystem	8.5.1-1
8.5.1	Main Propulsion Subsystem	8.5.1-1
8.5.2	Air Breathing Propulsion System (ABPS)	8.5.2-1
8.5.3	Orbit Maneuvering System	8.5.3-1
8.5.4	Attitude Control Propulsion System	8.5.4-1
8.6	Avionics Subsystem	8.6-1
8.6.1	Overview	8.6.1-1
8.6.2	Guidance and Navigation Subsystem	8.6.2-1
8.6.3	Flight Control Subsystem	8.6.3-1
8.6.4	Data Management Subsystem	8.6.4-1
8.6.5	Instrumentation Subsystem	8.6.5-1
8.6.6	Telecommunications and Air Traffic Control Subsystem	8.6.6-1
8.6.7	Displays and Controls Subsystem	8.6.7-1
8.6.8	Avionics Subsystem Design	8.6.8-1

CONTENTS (Cont)

Section		Page
8.7	Power Subsystem	8.7.1-1
	8.7.1 Power Generation Subsystem	8.7.1-1
	8.7.2 Electrical Power Distribution Subsystem	8.7.2-1
	8.7.3 Hydraulic System	8.7.3-1
8.8	Environmental Control Life Support Subsystem	8.8-1
	8.8.1 Atmosphere Revitalization Section	8.8-6
	8.8.2 Heat Transport/Heat Rejection Section	8.8-7
	8.8.3 Atmosphere Supply and Composition Control Section	8.8-23
	8.8.4 Water Management Section	8.8-25
	8.8.5 Waste Management Section	8.8-26

ILLUSTRATIONS
(BOOK B-2)

Figure		Page
8.4.1-1	Fracture Control Plan	8.4.1-31
8.4.1-2	Idealized Hoop Tension Fatigure Loading for Main Propulsion System	8.4.1-36
8.4.1-3	Typical Pressure History of Two Points on Main Hydrogen Tank for H-32 Orbiter	8.4.1-37
3.4.1-4	Typical Pressure History of Two Points on Main Oxygen Tank for H-32 Orbiter	8.4.1-38
8.4.1-5	Typical Temperature History of Two Points on Main Propellant Tank Wall for H-32 Orbiter.	8.4.1-39
8.4.1-6	Critical Surface Flaws in 2219-T87 Plate Subjected to -423° Proof Test at Yield Stress	8.4.1-40
8.4.1-7	Allowable Initial Surface Flaws	8.4.1-41
8.4.1-8	Allowable Initial Surface Flaws	8.4.1-42
8.4.1-9	Surface Flaw Stress Intensity	8.4.1-44
8.4.2-1	H-33 External Tank Orbiter Major Structural Assembly Breakdown	8.4.2-2
8.4.2-2	H-33 Orbiter Structural Arrangement	8.4.2-9
8.4.2-3	H-33 Orbiter Structural Arrangement	8.4.2-11
8.4.2-4	H-33 Nose Module	8.4.2-14
8.4.2-5	Nose Gear & Interstage Arrangement	8.4.2-16
8.4.2-6	H-33 FWD & AFT Mid Module	8.4.2-17
8.4.2-7	Orbiter Cabin Structure (H-3), 4-Man Configuration	8.4.2-20
8.4.2-8	Typical Window	8.4.2-23
8.4.2-9	Payload Compartment Envelope	8.4.2-24
8.4.2-10	Cargo Bay Door	8.4.2-26
8.4.2-11	Payload Attachment Arrangement	8.4.2-27
8.4.2-12	ABPS Support Configurations	8.4.2-31
8.4.2-13	H-33 AFT Module	8.4.2-35
8.4.2-14	Injection LO_2 Tank	8.4.2-38
8.4.2-15	OMS Liquid Hydrogen Tank	8.4.2-42
8.4.2-16	ABPS JP-4 Tanks	8.4.2-45

ILLUSTRATIONS (Cont)

Figure		Page
8.4.3-1	H-33 Wing Structural Arrangement	8.4.3-3
8.4.3-2	Strength and Stiffness of Corrugated Skin Panels	8.4.3-5
8.4.3-3	Fin Structural Arrangement	8.4.3-9
8.4.5-1	H-33 Orbiter Composite Applications	8.4.5-2
8.4.5-2	Specific Compression Strength of Materials with Fastener-Filler Holes at Temperature	8.4.5-3
8.4.5-3	Longeron-Intermediate Frame Intersection	8.4.5-6
8.4.5-4	Comparative Optimum Stresses for Advanced Composite and Metal Tubes	8.4.5-8
8.4.5-5	Comparative Tube Weights	8.4.5-8
8.4.5-6	Boron-Epoxy Tube	8.4.5-9
8.4.5-7	Boron-Polyimide-Reinforced Titanium Tube	8.4.5-11
8.4.6-1	Maximum Vehicle Temperatures During Reentry - Lee Surfaces, α = 270, ϵ - 0.8	8.4.6-3
8.4.6-2	Maximum Vehicle Temperatures During Reentry - Windward Surface, = 0.8	8.4.6-4
8.4.6-3	Maximum Vehicle Temperatures During Ascent	8.4.6-5
8.4.6-4	Orbiter Windward C/L Equilibrium Temperature History	8.4.6-6
8.4.6-5	H-33 General Arrangement, Thermal Protection System	8.4.6-7
8.4.6-6	Orbiter TPS Unit Weights	8.4.6-10
8.4.6-7	Typical Metallic Panel Design	8.4.6-17
8.4.6-8	Metal Panel Seal Detail	8.4.6-19
8.4.6-9	Coated Columbia Panel	8.4.6-21
8.4.6-10	Typical External Insulation Panel	8.4.6-22
8.4.6-11	Typical Joint - E1 to E1	8.4.6-23
8.4.6-12	Carbon/Carbon Nose Cone	8.4.6-25
8.4.6-13	Wing Carbon/Carbon Leading Edge	8.4.6-27
8.4.6-14	Microquartz (ρ = 3.5 PCF) Thermal Conductivity Vs Pressure and Mean Temperature	8.4.6-37 8.4.6-37
8.4.6-15	Metallic TPS Transient Temperatures, Typical AFT Fuselage	8.4.6-38
8.4.6-16	Metallic TPS Transient Temperatures, Typical Wing Windward	8.4.6-39

Figure		Page
8.4.6-17	E4 Thermal Conductivity	8.4.6-41
8.4.6-18	Extendible Nozzle Total Program Cost Difference	8.4.6-42
8.4.6-19	Carbon/Carbon Wing Leading Edge Temperature Distribution	8.4.6-44
8.4.6-20	Base Heatshield General Arrangement	8.4.6-46
8.4.7-1	Four-Man Baseline Cabin	8.4.7-3
8.4.7-2	Alternate Four-Man Cabin	8.4.7-5
8.4.7-3	14-Man Cabin Layout Configuration	8.4.7-7
8.4.7-4	Flight Deck Geometry	8.4.7-11
8.4.7-5	View of Runway One Mile	8.4.7-15
8.4.7-6	View of Runway at Cat. II Condition	8.4.7-16
8.4.7-7	View of Runway at Touchdown with Maximum Nose Attitude	8.4.7-17
8.4.7-8	Interchangeability of Standard Crew Seat with Stanley Type Ejection Seat	8.4.7-19
8.4.7-9	Ingress/Egress Paths for Normal & Emergency Conditions	8.4.7-23
8.4.8-1	Flight Control Mechanical Actuation Arrangement	8.4.8-2
8.4.8-2	Orbiter Hydraulic Schematic	8.4.8-3
8.4.8-3	Flight Control Mechanical Equipment, Elevon Drive Functional Schematic	8.4.8-7
8.4.8-4	Flight Control Mechanical Equipment, Rudder/ Speedbrake Drive Functional Schematic	8.4.8-9
8.4.8-5	TVC Actuator Installation	8.4.8-11
8.4.8-6	SST Secondary Actuator	8.4.8-21
8.4.9-1	Recovery System Arrangement	8.4.9-2
8.4.9-2	Nose Gear Arrangement	8.4.9-3
8.4.9-3	Main Landing Gear Arrangement	8.4.9-4
8.4.9-4	Wheel Brake Heat-Sink Material Comparison	8.4.9-6
8.4.9-5	Trade-Off Landing Distance Vs Deceleration Devices	8.4.9-8
8.5.1-1	External Tank Orbiter Main Propulsion Feed System	8.5.1-2
8.5.1-2	H-33 Orbiter Main Propulsion	8.5.1-3

ILLUSTRATIONS (Cont)

Figure		Page
8.5.1-3	GH_2 Pressurization Study H-33	8.5.1-10
8.5.1-4	GO_2 Pressurization Study H-33	8.5.1-11
8.5.1-5	GO_2 Pressurization Study H-33	8.5.1-13
8.5.1-6	Propellant Feed Sep Main Lox Tank	8.5.1-15
8.5.1-7	External Tank LH_2 Disconnect	8.5.1-17
8.5.1-8	Fuel Propellant Management System	8.5.1-19
8.5.1-9	Propellant Management System	8.5.1-19
8.5.1-10	Lox Natural Recirculation System	8.5.1-25
8.5.1-11	LH_2 Recirculation System with External Recirculation Lines	8.5.1-25
8.5.2-1	H-33 Operational Landing, Four-Engine Installation	8.5.2-7
8.5.2-2	H-33 Operational Landing, (4) JTF22A-4	8.5.2-8
8.5.2-3	H-33 Self-Ferry	8.5.2-9
8.5.2-4	Air Breathing Propulsion Subsystem	8.5.2-10
8.5.2-5	JTF22A-4 Engine	8.5.2-11
8.5.2-6	Orbiter Air Breathing Propulsion/JP Fuel Subsystem	8.5.2-13
8.5.2-7	Deployable Engine Installation	8.5.2-15
8.5.3-1	OMS Schematic	8.5.3-3
8.5.3-2	OMS Liquid Hydrogen Tank	8.5.3-10
8.5.3-3	OMS Autogenous Pressurization System Operation Characteristics	8.5.3-11
8.5.3-4	Thermodynamic Processes for Autogenous Pressurants	8.5.3-12
8.5.3-5	Cost Effectiveness of Alternative OMS/ACPS Configurations	8.5.3-19
8.5.3.6	Thermodynamic Vent and Heat Exchange Schematic	8.5.3-24
8.5.4-1	ACPS Thruster Locations	8.5.4-3
8.5.4-2	ACPS Component Arrangement	8.5.4-4
8.5.4-3	Reaction Control System Orbiter Schematic	8.5.4-7
8.5.4-4	ACPS Weight Sensitivity	8.5.4-9
8.5.4-5	ACPS Subsystem Performance Maps	8.5.4-10

Figure		Page
8.5.4-6	ACPS Weight Trending with Thruster Chamber Pressure and Accumulator Max/Min Pressure Ratio	8.5.4-11
8.6.1-1	Integrated Avionics Functional Configuration Diagram	8.6.1-5
8.6.1-2	Integrated Avionics Functional Configuration Diagram	8.6.1-7
8.6.2-1	Guidance and Navigation System	8.6.2-10
8.6.2-2	Functional Description of Redundant IMU Data Logic and Soft Failure Detection	8.6.2-17
8.6.3-1	Flight Control Electronics	8.6.3-11
8.6.3-2	Flight Control Sensors and Crew Input Control	8.6.3-16
8.6.4-1	Shuttle Computer Complex	8.6.4-6
8.6.4-2	Interconnection Diagram	8.6.4-9
8.6.4-3	Typical Racu Configuration	8.6.4-11
8.6.5-1	Instrumentation Subsystem Block Diagram	8.6.5-3
8.6.5-2	Typical Signal Conditioning Module for Strain Gage Transducers	8.6.5-5
8.6.5-3	Development Flight Instrumentation	8.6.5-17
8.6.6-1	Orbiter Communication Subsystem Block Diagram	8.6.6-5
8.6.6-2	Orbiter Antenna Locations	8.6.6.16
8.6.7-1	Displays and Controls	8.6.7-4
8.6.7-2	Display and Control Subsystem Panel Configuration	8.6.7-5
8.6.7-3	Typical Display Formats	8.6.7-7
8.6.7-4	Data Entry Display Keyboard	8.6.7-10
8.6.7-5	D&C Crew Station Mockup	8.6.7-15
8.6.7-6	CRT Displays Simulator	8.6.7-17
8.6.8-1	Module & Rack	8.6.8-3
8.6.8-2	Distribution Center	8.6.8-5
8.6.8-3	Electronic Integration	8.6.8-6
8.6.8-4	Typical Equipment Layout	8.6.8-7
8.7.1-1	SSU Orbiter Electrical Power Profile	8.7.1-4
8.7.1-2	Power Generation Subsystem	8.7.1-8

Figure		Page
8.7.1-3	Power Generation Subsystem	8.7.1-9
8.7.1-4	Fuel Cell Block Diagram	8.7.1-12
8.7.1-5	Auxiliary Power Unit Block Diagram	8.7.1-14
8.7.2-1	Electrical Power Distribution Subsystem	8.7.2-5
8.7.2-2	Typical SMPC Power Conditioner Designs	8.7.2-11
8.7.2-3	Load Distribution Center Characteristics	8.7.2-12
8.7.3-1	Orbiter Hydraulic Schematic	8.7.3-3
8.7.3-2	Hydraulic Equipment Arrangement	8.7.3-5
8.8-1	Environmental Control and Life Support Subsystem Schematic	8.8-3
8.8-2	Typical Coldplate/Coldrail Installation	8.8-10
8.8-3	Heat Transport/Heat Rejection On-Orbit Thermal Balance	8.8-11
8.8-4	Radiator Design Characteristics	8.8-14
8.8-5	Orbital Average Incident Heat Flux for Radiators on Cargo Bay Doors (Gravity Gradient Mode)	8.8-15
8.8-6	Locating Radiators on Outer Surfaces of Vehicle	8.8-21

TABLES
(BOOK B-2)

Table		Page
8.4.1-1	Orbiter - Factors of Safety	8.4.1-3
8.4.1-2	Material Selection - Baseline	8.4.1-5
8.4.1-3	Preliminary Design Mechanical Properties (Tensile Ultimate - F_{tu})	8.4.1-19
8.4.1-4	Preliminary Design Mechanical Properties (Tensile Yield Strength - F_{ty})	8.4.1-21
8.4.1-5	Preliminary Design Mechanical Properties (Compressive Yield Strength - F_{cy})	8.4.1-23
8.4.1-6	Preliminary Design Mechanical Properties (Modulus of Elasticity - E)	8.4.1-25
8.4.1-7	Composite Materials - Preliminary Design Properties at Room Temperature	8.4.1-27
8.4.1-8	Composite Materials - Preliminary Design Properties at Elevated Temperatures	8.4.1-28
8.4.1-9	Summary of Material Trade Studies.	8.4.1-30
8.4.1-10	NDE Plan - Main Propellant Tanks	8.4.1-47
8.4.1-11	NDE Equipment Capability.	8.4.1-48
8.4.1-12	Mechanical Properties of 2219-T87 Al Alloy at Cryogenic Temperature.	8.4.1-50
8.4.2-1	Fuselage Structural Summary	8.4.2-3
8.4.2-2	Internal Tank Structural Summary	8.4.2-7
8.4.2-3	Summary of Fuselage Trade Studies	8.4.2-46
8.4.2-4	Summary of Combined Vehicle Trade Studies	8.4.2-48
8.4.3-1	Aero Surfaces Structural Summary	8.4.3-2
8.4.3-2	Summary of Aero Surfaces Trade Studies	8.4.3-11
8.4.5-1	Typical Properties of Boron-Aluminum (unidirectional Al 45-50 Volume Percent, 4.0 MIL Boron	8.4.5-4
8.4.6	Thermal Protection.	8.4.6-1
8.4.6-1	Design Conditions for TPS Panels	8.4.6-29
8.4.6-2	Summary of TPS Panel Point Designs.	8.4.6-31
8.4.6-3	Summary of Metallic TPS Panel Design	8.4.6-32

TABLES (Cont)

Table		Page
8.4.7-1	Summary of Crew Station and Passenger Accommodation Trade Studies	8.4.7-5
8.4.8-1	Flight Control Equipment Data	8.4.8-5
8.4.8-2	Rudder Segment Usage	8.4.8-5
8.4.8-3	Elevon Actuator Schemes	8.4.8-15
8.4.9-1	Recovery System Alternate Modes of Operation	8.4.9-7
8.4.9-2	Summary of Landing Gear Trade Studies	8.4.9-9
8.5.1-1	Orbiter Main Engine Design Requirements	8.5.1-6
8.5.1-2	H-33 Main Propellant Allotment	8.5.1-23
8.5.1-3	Fluid Temperatures During LO_2 Recirculation	8.5.1-26
8.5.1-4	Main Propulsion Trade Study Summary Chart	8.5.1-34
8.5.2-1	Summary Requirements (Sheet 1 of 3)	8.5.2-3
8.5.2-2	Orbiter Air Breathing Engine Candidates	8.5.2-6
8.5.3-1	OMS Alternate Configuration Summary	8.5.3-15
8.5.3-2	Description of Alternative OMS Concepts	8.5.3-16
8.5.3-3	System Weight and Cost Deltas for Alternative OMS Engine Configurations	8.5.3-18
8.5.3-4	Preliminary OMS Storage System Delta to Revised Purge Bag Design	8.5.3-20
8.5.3-5	Candidate Fail Safe OMS Tankage Concepts	8.5.3-22
8.5.4-1	ACPS Control Requirements	8.5.4-5
8.5.4-2	ACPS System Performance	8.5.4-13/14
8.5.4-3	ACPS System Weights	8.5.4-15
8.6.1-1	Low Cost Avionics Alternatives Studies	8.6.1-2
8.6.1-2	Low Cost Avionics System Requirements	8.6.1-4
8.6.1-3	Summary of Avionics Trade Studies	8.6.1-14
8.6.2-1	IMU Requirements	8.6.2-5
8.6.2-2	Rendezvous Navigation Sensor Requirements	8.6.2-6
8.6.2-3	Rendezvous Navigation Performance	8.6.2-6
8.6.2-4	Insertion Requirements	8.6.2-7
8.6.2-5	Navigation Limits	8.6.2-8
8.6.2-6	Entry Requirements at Transition	8.6.2-8
8.6.2-7	Guidance, Navigation and Control - Major Equipment List	8.6.2-11

TABLES (Cont)

Table		Page
8.6.2-8	IMU Configuration Comparison	8.6.2-13
8.6.2-9	3 Sigma State Vector Errors at End of Entry Phase (Altitude = 70K Ft	8.6.2-14
8.6.2-10	Candidate Shuttle IMU Physical Characteristics Summary	8.6.2-15
8.6.2-11	Candidate Shuttle IMU Performance Characteristics	8.6.2-16
8.6.3-1	Flight Control Subsystem	8.6.3-2
8.6.3-2	FCS Characteristics/Data	8.6.3-4
8.6.4-1	Data Management Subsystem Requirements	8.6.4-3
8.6.4-2	Main Memory Sizing (32-Bit words)	8.4.6-4
8.6.6-1	Space Shuttle Communication RF Link Characteristics and RF Interfaces	8.6.6-2
8.6.6-2	Communications Subsystem Major Component List	8.6.6-6
8.6.6-3	Antenna Performance Characteristics and Radome Types	8.6.6-14
8.6.7-1	Lighting Summary	8.6.7-18
8.7.1-1	Electrical Load Summary (Peak/Avg) (Power in Watts)	8.7.1-5
8.7.1-2	Electrical and Hydraulic Load Summary (Peak/Avg)	8.7.1-6
8.7.2-1	Electrical Power Type/Level/Location/Time Summary (Power in Watts)	8.7.2-3
8.7.3-1	Orbiter Hydraulic-Power Profile	8.7.3-6
8.8-1	Estimate Range for Design Reference Mission Thermal Loads	8.8-9

CONTENTS
(BOOK B-3)

Section			Page
8.9	External Tanks		8.9.1-1
	8.9.1	General Description	8.9.1-1
	8.9.2	Advantages of External Tank Configuration	8.9.2-1
	8.9.3	Selection of Baseline Tank Disposal Mode	8.9.3-1
	8.9.4	Tank Impact Zones	8.9.4-1
	8.9.5	Tank Structures	8.9.5-1
	3.9.6	External Tank Design Loads	8.9.6-1
	8.9.7	Design Criteria, Materials, and Fracture Control	8.9.7-1
	8.9.8	Tank Foam Insulation	8.9.8-1
	8.9.9	Tank Ablators: Interference Heating and Nose Cone	8.9.9-1
	8.9.10	Tank Propulsion	8.9.10-1
	8.9.11	Tank Separation	8.9.11-1
	8.9.12	Jettison System Requirements	8.9.12-1
	8.9.13	Tank Jettison Errors	8.9.13-1
	8.9.14	Intact Tank Entry Dispersions	8.9.14-1
	8.9.15	Tank Breakup Analysis	8.9.15-1
	8.9.16	Tank Fragment Analysis	8.9.16-1
	8.9.17	Tank Fragment Impact Dispersions	8.9.17-1
	8.9.18	Tank Mass Properties	8.9.18-1
	8.9.19	Tank Manufacturing	8.9.19-1
	8.9.20	Abort Considerations	8.9.20-1
	8.9.21	Future Trade Studies	8.9.21-1
8.10	Self-Ferry Provisions		8.10.1-1
	8.10.1	Performance	8.10.1-1
	8.10.2	Ferry Kit	8.10.2-1

CONTENTS (Cont)

Section			Page
8.11	Payload Integration and Docking		8.11-1
8.12	G-3 Configuration		8.12-1
8.13	Reliability, Maintainability, Quality and Safety		8.13.1-1
	8.13.1	Reliability and Maintainability	8.13.1-1
	8.13.2	Quality Assurance	8.13.2-1
	8.13.3	System Safety	8.13.3-1
8.14	Major Study Summaries		8.14.1-1
	8.14.1	Integral vs. Removable Floating Tank Trade Study	8.14.1-1
	8.14.2	Wing Study	8.14.2-1
	8.14.3	ACPS-Aero Control Entry Trade Studies	8.14.3-1
	8.14.4	Active vs. Passive Propellant Utilization Trade	8.14.4-1
	8.14.5	Active vs. Passive Propellant Management Trade	8.14.5-1
	8.14.6	Fixed Nozzle Comparison	8.14.6-1
	8.14.7	Reliability Evaluation of Proposed External Tank Separation Concepts	8.14.7-1
	8.14.8	Non-Destructive Evaluation Trade Study Summary	8.14.8-1
	8.14.9	Ice/Frost Formation on External LH_2 Tanks	8.14.9-1
	8.14.10	Propellant Allotment	8.14.10-1
	8.14.11	Low Cost Avionics Baseline	8.14.11-1
	8.14.12	Autogenous Pressurization System for the H-33 Orbiter Main Propulsion Tanks	8.14.12-1
	8.14.13	Propellant Pre-Conditioning Analysis	8.14.13-1
	8.14.14	Main Propulsion Subsystem Parametric Optimization	8.14.14-1
	8.14.15	Mixture Ratio Study on H-33 Orbiter (B35-150MO-63)	8.14.15-1
	8.14.16	OMS Engine Redundancy Selection (H-33 Configuration)	8.14.16-1
	8.14.17	Reliability Evaluation of Proposed External Tank Separation Concepts	8.14.17-1
	8.14.18	Redundancy Requirements for H-33 Orbiter Main Propulsion Subsystem (MPS)	8.14.18-1

CONTENTS (Cont)

Section		Page
8.14.19	Main Rocket Engine Reliability/Maintainability Analysis	8.14.19-1
8.14.20	Main Rocket Engine Sensitivity Analysis	8.14.20-1
8.14.21	Main Rocket Engine Overhaul Policy	8.14.21-1
8.14.22	TPS Task Time Analysis	8.14.22-1
8.14.23	Hot vs TPS Protected Fin Structure	8.14.23-1

APPENDICES

Preliminary Design Drawings, Orbiter and Booster — Book B-4

ILLUSTRATIONS
(BOOK B-3)

Figure		Page
8.9.1-1	Orbiter General Arrangement	8.9.1-3
8.9.1-2	External Tank Jettison Sequence	8.9.1-7
8.9.1-3	External Tanks	8.9.1-8
8.9.1-4	External Tank Interference Heating Ablator	8.9.1-9
8.9.3-1	Available Tank Impact Area - ETR Launch	8.9.3-2
8.9.4-1	1980 Projected Overall Worldwide Merchant and Fishing Ship Distribution	8.9.4-2
8.9.4-2	Tank Impact Areas - Typical Missions WTR Launches	8.9.4-3
8.9.5-1	External LH_2 Tank	8.9.5-3
8.9.8-1	Ice/Frost Formation Probability	8.9.8-3
8.9.8-2	Probable Ice/Frost Buildup	8.9.8-4
8.9.9-1	H-33 Ascent Trajectory	8.9.9-3
8.9.9-2	Tank Configurations After Phase Change Paint Test In LRC Hypersonic Wind Tunnel	8.9.9-4
8.9.9-3	Maximum Ratio of Heat Transfer to Orbiter with Flow Disturbed & Undisturbed by Tanks	8.9.9-5
8.9.9-4	Measured Heating Rated to H-33 Contoured External LH_2 Tanks	8.9.9-6
8.9.9-5	Measured Ascent Heating	8.9.9-7
8.9.9-6	Maximum Vehicle Temperatures During Ascent	8.9.9-8
8.9.9-7	External LH_2 Tank Ablator Foam Samples.	8.9.9-9
8.9.10-1	Propellant Feed System Main LH_2 Tank.	8.9.10-2
8.9.10-2	External Tank LH_2 Disconnect	8.9.10-3
8.9.10-3	External Tank Deorbit Motor	8.9.10-5
8.9.11-1	Forward Structural Attachment	8.9.11-3
8.9.11-2	Aft Structural Attachment	8.9.11-4
8.9.11-3	Propulsion, De-orbit, Release Details	8.9.11-5
8.9.11-4	Orbiter Closures'.	8.9.11-6
8.9.11-5	Tank Separation and Deorbit System Schematic	8.9.11-7
8.9.11-6	Candidate Tank Separation 5 Strut Arrangement	8.9.11-13

ILLUSTRATIONS (Cont)

Figure		Page
8.9.11-7	Candidate Alternate Tank Separation (Wing Mount)	8.9.11-15
8.9.11-8	Candidate Tank Separation-Parallel Links (Dornier Systems)	8.9.11-16
8.9.12-1	Crew Visibility of External Tank Jettison	8.9.12-3
8.9.12-2	Sensitivity of Downrange to Deorbit Delta-V	8.9.12-5
8.9.12-3	Sensitivity of Downrange to Delta-V Pointing Angle	8.9.12-7
8.9.12-4	Impact Point Prediction	8.9.12-8
8.9.13-1	External Tank Separation Plane Turn Rate	8.9.13-2
8.9.13-2	External Tank Separation Time Distance History	8.9.13-3
8.9.13-3	Tank-Orbiter Clearance Boundary	8.9.13-5
8.9.13-4	Measurement of Separation Force Errors	8.9.13-7
8.9.13-5	Separation Monitoring System Block Diagram	8.9.13-8
8.9.14-1	Effect Of Tank Pitch Rate On Down Range Distance	8.9.14-3
8.9.15-1	Intact External Tank Skin Temperatures and Heating Rates During Reentry	8.9.15-2
8.9.15-2	Tank Breakup	8.9.15-3
8.9.15-3	Weight Penalty for Delaying Tank Breakup	8.9.15-5
8.9.16-1	Fragment Heating During Entry	8.9.16-3
8.9.19-1	Drop Tank Manufacturing Flow	8.9.19-3
8.10.2-1	H-33 Orbiter Ferry Kit	8.10.2-2
8.11-1	Payload Tie Down Mechanism Concept	8.11-2
8.11-2	Payload Attachment Arrangement	8.11-4
8.11-3	Payload/C.G. Envelope	8.11-5
8.11-4	Payload Support/Development	8.11-6
8.11-5	Universal Docking System Applications	8.11-7
8.11-6	Payload Support Pallet	8.11-8
8.12-1	G-3G General Arrangement	8.12-3
8.12-2	G-3G Inboard Profile	8.12-7
8.12-3	G-3G Structural Arrangement	8.12-17
8.12-4	G-3G Orbiter Structural Arrangement	8.12-19
8.12-5	Internal Tank Orbiter Main Propulsion Feed System	8.12-22
8.12-6	G-3G Orbiter Main Propulsion	8.12-23

ILLUSTRATIONS (Cont)

Figure		Page
8.13.1-1	Shuttle Operational Redundancy Selector.	8.13.1-11
8.14.2-1	Wing Carry-Through Concept Study.	8.14.2-3
8.14.6-1	Baseline Configuration = 150 Extendible Nozzle Scooped Back Vehicle Heat Shield	8.14.6-2
8.14.6-2	120 Expansion Ratio Extendable Nozzle Scooped Back Heat Shield	8.14.6-3
8.14.6-3	90 Expansion Ratio (95% Bell) Fixed Nozzle Scooped Back Heat Shield.	8.14.6-4
8.14.7-1	Extendable Nozzle Total Program Cost Difference	8.14.7-4
8.14.8-1	Study Plan: Development of Shuttle Nondestructive Evaluation (NDE) System	8.14.8-2
8.14.9-1	Vehicle Penalty as a Function of Insulation Thickness H-Configuration	8.14.9-2
8.14.9-2	Thermal Model.	8.14.9-4
8.14.9-3	Tank Heat Transfer	8.14.9-5
8.14.9-4	Temperature Probability	8.14.9-7
8.14.9-5	Ice/Frost Formation Probability	8.14.9-8
8.14.9-6	Maximum Frost Formation	8.14.9-11
8.14.9-7	Rainfall Probability.	8.14.9-12
8.14.9-8	Ice Formation Rates	8.14.9-13
8.14.9-9	Probable Ice/Frost Build-up	8.14.9-15
8.14.11-1	Integrated Avionics Functional Configuration	8.14.11-5
8.14.12-1	Active Vent	8.11.12-2
8.14.12-2	Regulator	8.14.12-2
8.14.12-3	Fixed Passive Orifice.	8.14.12-2
8.14.12-4	Active Fixed Orifice (Pressure or Time Actuated)	8.14.12-3
8.14.12-5	Dual Level Continuous Flow System (Pressure Or Time Actuated)	8.14.12-3
8.14.12-6	Dual Level Continuous Flow System with Dual GO_2 Heat Heat Exchangers (Pressure or Time Actuated)	8.14.12-3
8.14.20-1	Maintenance Manhours As a Function of Reliability & Maintainability Improvement	8.14.20-2
8.14.21-1	Planned Main Engine Removal Schedule, Orbiter.	8.14.21-3
8.14.23-1	H-33 Orbiter Fin - Basic Geometry.	8.14.23-2
8.14.23-2	Ultimate Shear, Torque, and Bending Moment - Max q	8.14.23-3

TABLES
(BOOK B-3)

Table		Page
8.9.3-1	Disposal Mode Comparison	8.9.3-4
8.9.4-1	Tank Jettison - WTR Missions	8.9.4-4
8.9.7-1	Cryogenic Tankage	8.9.7-3
8.9.13-1	Tank Jettison and De-Orbit Parameters	8.9.13-9
8.9.13-2	Tank Separation and De-Orbit Error	8.9.13-10
8.9.14-1	De-Orbit Errors	8.9.14-1
8.9.17-1	Effect of Ballistic Coefficient Variations	8.9.17-1
8.9.17-2	Effect of Breakup Altitude Uncertainty	8.9.17-2
8.9.17-3	Effect of Lift on Fragment Range	8.9.17-2
8.9.18-1	Tank Mass Properties, External Tank (LH_2) (115,571 lbs Hydrogen/Aircraft)	8.9.18-3
8.12-1	40K Pound Payload/South Polar Launch Mission	8.12-14
8.12-2	G-3G Main Propellant Allotment	8.12-27
8.13.1-1	Reliability/Maintainability Trade Study Summary Chart	8.13.1-13
8.13.1-2	Maintainability Features of H33 Configuration	8.13.1-23
8.13.2-1	Summary of Nondestructive Evaluation Studies	8.13.2-8
8.13.3-1	Safety Assessment Summary H33 vs G3G	8.13.3-2
8.13.3-2	Hazards Common to Both Orbiter Configurations	8.13.3-6
8.13.3-3	Radiative Booster/Internal Tank Orbiter Hazards	8.13.3-14
8.13.3-4	Heat Sink Booster/External Tank Orbiter Hazards	8.13.3-16
8.13.3-5	Class 2 Risks: Further Study Required to Determine Final Solutions	8.13.3-19
8.13.3-6	Special Studies and Trades: Safety	8.13.3-21
8.13.3-7	Corrective Measures/Compensating Provisions	8.13.3-28
8.14.1-1	C2F Orbiter Relative Weights for Various Tank Arrangements	8.14.1-4
8.14.4-1	Candidate Comparison	8.14.4-3
8.14.6-1	Fuselage and Heat Shield Weight Savings	8.14.6-7
8.14.6-2	Results of Fixed Nozzle Comparison	8.14.6-7
8.14.8-1	Space Shuttle Material/Defect Characteristics and NDE Requirements	8.14.8-3

TABLES (Cont.)

Table		Page
8.14.8-2	Summary of Several Non-Destructive Evaluation Techniques to be used on Space Shuttle Vehicle	8.14.8-7
8.14.12-1	Concepts Studied	8.14.12-1
8.14.1-1	Alternative Avionic Definition Matrix	8.14.11-2
8.14.11-2	Total Cost Comparison	8.14.11-3
8.14.11-3	Low Cost Avionics System Comparison	8.14.11-4
8.14.13-1	Comparison of Engine Pressure Drop Data	8.14.13-2
8.14.13-2	Fluid Temperatures During LOX Recirculation	8.14.13-3
8.14.18-1	H-33 Orbiter MPS - Failure Modes Analysis	8.14.18-2
8.14.23-1	Hot vs TPS Protected Fin Structure Weight Summary	8.14.23-1

ALPHABETICAL SUBJECT INDEX

Subject		Section No.
Abort		5.0
Aerodynamic Characteristics	- Launch Vehicle	6.2
	- Orbiter	8.3.3
	- Booster	9.3.3
Aero Surface Structure	- Orbiter	8.4.3
	- Booster	9.4.2
Avionics	- Orbiter	8.6
	- Booster	9.5
Commonality	- Booster/Orbiter	3.3
Crew and Passenger Provisions	- Orbiter	8.4.2
	- Booster	9.4.5
Design Criteria		8.4.1
Docking		8.11
Environment Control/Life Support	- Orbiter	8.8
	- Booster	9.7
External Tanks	- Orbiter	8.9
Flight Control Actuation	- Orbiter	8.4.8
	- Booster	9.4.6
Fuselage Structure	- Orbiter	8.4.2
	- Booster	9.4.1
Interfaces	- Launch System	3.4
Interfaces	- Payload	8.11
Landing Gear/Recover	- Orbiter	8.4.9
	- Booster	9.4.8
Loads and Dynamics	- Orbiter	8.3.6
	- Booster	9.3.5

Subject		Section No.
Mass Properties	- Launch Vehicle	6.1
	- Orbiter	8.3.2
	- Booster	9.3.2
Materials	- Orbiter	8.4.1, 8.4.5
	- Booster	9.3.6
Payload Integration		8.11
Performance	- Mission	4.0
	- Launch Vehicle	6.3
	- Orbiter	8.3.4
	- Booster	9.3.3
Physical Characteristics	- Launch Vehicle	3.1
	- Orbiter	8.3.1
	- Booster	9.3.1
Quality Assurance		8.13.2
Reliability/Maintainability		8.13.1
Requirements		2.0
Safety	- Orbiter	8.13.3
	- Booster	9.9
Self Ferry	- Orbiter	8.10,8.3.4.4, 8.5.2
	- Booster	9.3.3.13
Separation	- Booster/Orbiter	6.3.2, 9.4.8
Separation	- Orbiter Tanks	8.9
Sizing Rationale		3.2
Structural Analyses	- Orbiter	8.4.1, 8.4.5
	- Booster	9.3.7

Subject		Section No.
Structures	- Orbiter	8.4
	- Booster	9.4
Tanks	- Orbiter	8.4.2, 8.9
	- Booster	9.4.3
Thermal Environment	- Orbiter	8.3.5
	- Booster	9.3.4

Section 8

ORBITER DEFINITION

8.1 INTRODUCTION

This is the Technical Summary of the Alternate Space Shuttle Concepts (ASSC) Final Report. It covers the engineering studies of the vehicle concepts that have been performed since the Mid-Term Report. As directed by NASA, these studies have emphasized the H-33 External Hydrogen Orbiter/Heat Sink Booster Concept. Sufficient continuing studies of the G-3 Internal Hydrogen Tank Orbiter/Conventional Booster Concept were conducted to enable a technical, cost, and schedule comparison between concepts: this comparison is summarized in the Executive Summary of this Report.

Volume I describes the major characteristics of both vehicle concepts, their nominal and abort mission capabilities, and the detailed performance of the mated or launch vehicles. The other elements of the H-33 Shuttle System are defined in the Operations Plan, Facilities Plan and other plans that accompany this report. At the end of Volume I are brief summaries of several of the major system studies that led to the selection of the concept described.

Volume II (this Volume) and Volume III define the H-33 Orbiter and Booster, respectively, their major characteristics, performance, and subsystems. The majority of the data presented defines the H-33. However, much of the data is applicable to both the H-33 and the G-3 vehicles, particularly in the subsystems. Where specific differences exist between these concepts, they are adequately described to allow comparison. It will be noted that in some instances the substantiating analyses described herein are based on earlier versions of the H-33 and G-3. This tends to occur in study areas of longer duration, such as detailed loads, dynamics and structural analyses. In these cases, their applicability to the current vehicle designs is described.

At the end of Volumes II and III are brief summaries of several of the major studies that supported the vehicle concept selections. Layout drawings that support this report are in Appendix A. The detail mass properties and estimating rationale are described in the final mass properties report. The correlation between the ASSC contract Statement of Work and the sections of this report is shown in Table 8.1-1. Table 8.1-2 is an index of the locations of the contributions of the associate contractors.

TABLE 8.1-1 CONTRACT SOW/FINAL REPORT CORRELATION (Sheet 1 of 2)

Initial SOW Paragraph	Final Report - Technical Summary Paragraph - Volume I and II
5.1	2.0
5.2	4.0
5.3	N.A.
5.3.1	8.14, 9.11, 7.0, 3.4
5.3.2	(Operations Plan)
5.3.3	6.3, 8.3.3, 8.3.4, 8.3.5, 8.3.6 9.3.3, 9.3.4, 9.3.5
5.3.4	8.11
5.3.5	5.0
5.3.6	(Task Deleted)
5.3.7	8.13.1, 8.13.2
5.3.8	8.13.1
5.3.9	8.3.4.4, 8.10, 9.3.3.13
5.3.10	8.13.3, 9.9
5.4	N.A.
5.4.1	8.2, 8.3, 9.2, 9.3,
5.4.1.1	8.3.6, 8.4, 9.3.7, 9.4
5.4.1.2	8.4.1, 9.3.6
5.4.1.3	8.3.5, 9.3.4, 9.4.4
5.4.2	N.A.
5.4.2.1	8.5, 9.5
5.4.2.2	8.4.8, 8.4.9, 9.4.6, 9.4.7, 9.4.8
5.4.2.3	8.4.9, 9.4.7
5.4.2.4	8.11
5.4.2.5	8.4.7, 9.4.5
5.4.2.6	3.4
5.4.2.7	8.4.8, 8,5.1, 8.6.3, 9.4.6, 9.5.1, 9.6.3

TABLE 8.1-1 CONTRACT SOW/FINAL REPORT CORRELATION (Sheet 2 of 2)

Initial SOW Paragraph	Final Report - Technical Summary Paragraph - Volumes I and II
5.5	(IR&D Reports)
5.6	(Cost and Schedule Plan)
5.7	(Executive Summary)
5.8	N.A.
Delta SOW Task	
I	6.3, 8.3.3, 8.3.4, 8.3.5
II	8.9
III	4.0, 5.0, 8.13.3
IV	8.9
V	5.0
VI	Boeing D164-10059-1 through -5
VII	Boeing D164-10058-1
VIII	Boeing D164-10057-1

TABLE 8.1-2 INDEX OF ASSOCIATE CONTRACTOR TECHNICAL SUPPORT

Associate	Subject	Tech. Summary Para.
Aerojet	• Cryogenic Tankage	8.4.2.5
AVCO	• Thermal Protection Materials	8.4.6.2.2 8.4.6.3.2
Dassault	• Thermal Protection Materials	8.4.6.2.2
Dornier	• Flight Controls	8.3.3.4.9
	• Base Heating	8.3.5.5.4
	• Surface Oxidation	8.4.1.2.3
	• ABPS Deployment	8.4.2.3.1
	• External Tank Deployment	8.9.11, 8.9.20
Eastern Airlines	• Operations	(Operations Plan)
	• Maintenance	8.13.1.1.1, 8.13.1.4.1
General Electric	• Avionics	8.6
Northrop	• Aerodynamic Analyses and Test Support	6.2
	• Entry Analyses	8.3.4
	• Vertical Fin Design	8.4.3.3

8.2 CONFIGURATION

8.2.1 SUMMARY

The emphasis of this volume is on the H-33 external LH_2 tank orbiter. This concept evolved from 29 different configurations established at the onset of the study. The H-33, simple and relatively small, matched by a low staging velocity heat sink booster, has opened the door to a low cost, readily developed, flexible shuttle. For comparison purposes, the internal hydrogen tank G-3G orbiter is also briefly described below and in subsection 8.12. Both H-33 and G-3G orbiters are designed to meet the following major system requirements:

- Low total program cost for 100 missions/orbiter
- 1100 n mi nominal cross range (providing return to launch from a once around polar orbit)
- 15 ft diameter x 60 ft long payload
- Delivered payloads
  - 40,000 lb to 100 n mi polar orbit (no ABPS)
  - 25,000 lb to 270 n mi, 55 deg orbit (with ABPS)
  - 65,000 lb to 100 n mi, 28.5 deg orbit (no ABPS)
- Landing Payload
  - 40,000 lb - no ABPS
  - 25,000 lb - with ABPS
- Zero to maximum cargo capability with minimum cg excursions
- Docking through the payload
- Pressure cabin sized for four crew members and provided with an airlock

- Self ferry capability - with ferry kit
- Intact abort
  - Post staging; once around trajectory with one engine out
- OMS tanks sized for 2000 fps in 55 deg orbit configuration
- ICD - SSE bell type engines
- Subsonic go-around, with ABPS, tropic day.
  - Approach condition, one engine out from 1000 ft above landing site
  - Landing condition, all engines operating from 200 ft above landing site
- Orbiter ascent performance computed using nominal Isp, main tanks sized for minimum Isp performance
- 1% characteristic velocity flight performance reserve in main tanks
- Visibility - high performance aircraft standards coupled with low weather minima
- Unpowered landing capability with ABPS removed
- JP type fuel for ABPS

For both the internal and external tank orbiter, the majority of subsystems are the same in principle - propulsion, flight controls avionics, ECS, landing gears, etc. It is in the area of packaging, the internal arrangement of the major items, that the differences appear. But even here the main configuration drivers result in similar aerodynamic configurations for G-3G and H-33, once the external tanks have separated. These main drivers are combinations of the requirements listed above, together with th more important configuration tradeoffs summarized in the Shuttle Definition volume, subsection 7.0 and the Orbiter Definition volume, subsection 8.14.

Before passing to a description of the H-33, the major features of the two orbiter/booster combinations are compared in Table 8.2-1.

TABLE 8.2-1 H-33/G-3G COMPARISONS
(Sheet 1 of 2)

	H-33	G-3G
Governing Mission - azimuth	90^{o} (Polar)	
Mission Payload up and down, lb	40,000/40,000 (No ABPS)	
Orbiter		
Dry Weight (incl external tanks), lb	220,838	220,135
Injection Weight (incl external tanks), lb	292,260	306,005
Main Stage Propellant, lb	809,000	632,275
Liftoff Weight, lb	1,101,260	938,280
Mass Fraction	.776	.772
Ideal Velocity, fps	19,600	16,538
Main Engines Vac Thrust, lb	3/477,000	2/632,000
T/Wo	1.30	1.35
Cross Range Capabilities, n mi	1,100	1,100
Hypersonic L/D	1.56	1.53
Landing Weight, lb	241,172	264,190
L/D Approach Configuration	7.2	6.7
ABPS	JTF-22A(4)	JTF-22A(4) (2 w/after burners)
Booster		
Burnout Weight, lb	574,280	951,750
Main Stage Propellant, lb	2,249,000	3,348,470
Liftoff Weight, lb	2,824,000	4,302,640
Gross Liftoff Weight, lb	3,925,260	5,240,920
Mass Fraction	.7964	.776
Staging Velocity, fps	7,000	9,750
Main Engines SL Thrust, lb	12/415,000	13/550,000
T/Wo	1.27	1.36
Fly Home Range, n mi	227	368

TABLE 8.2-1 H-33/G-3G COMPARISONS (Cont)
(Sheet 2 of 2)

	H-33	G-3G
Landing Weight, lb	520,330	832,708
ABPS	F101/F12B3(8)	F101/F12B3 (10)
Total Dry Weight Orbiter & Booster	692,108	1,018,583

Table 8.2-1 clearly shows the technical strength of the total H-33 concept. Relative to the conventional internal LH_2 tank approach, the key feature of the H-33 is the low staging velocity. Because of its inherently better mass fraction, the orbiter provides the increased ideal velocity for a modest weight delta; it remains smaller, simpler and safer. The booster exploits the low staging velocity with a low cost, simple, 100% heat sink structure and a much reduced fly-home range. The natural outcome is a simpler, smaller, lower cost booster with better mass fraction. In its simplest form the GLOW and total dry weight figures tell the whole story.

At various points in this technical summary, reference is made to the H-32/H-3T external LH_2 tank orbiter. This is a two engined orbiter with a staging velocity of about 8500 fps that preceded H-33 and is the basis for much of the structural development and virtually all of the dynamic modelling, loads analysis and aerodynamic and thermodynamic testing completed at this time and discussed herein. Since the bulk of this technical summary is written as applicable to the H-33, is is necessary to understand the difference between these two external tank configurations. A comparison of the H-33 and the H-3T is given in subsection 8.3.6.

8.2.2 H-33 EXTERNAL TANK ORBITER

The external LH_2 tank orbiter avoids the task of bringing the large, empty, potentially dangerous LH_2 tanks home. Typically, these tanks alone represent half the stowed volume that the fuselage wraps around; excluding them causes the fuselage to shrink, the wing and vertical tail follow suit, likewise the TPS, the ABPS, the landing gear, etc. As a result of this relative reduction of inert weight, the mass fraction of the H-33 type of orbiter

C.2

is highly favorable, and in minimizing cost and GLOW, the optimum staging velocity is found to be low, the orbiter shouldering a large share of the task of accelerating the payload to orbital velocity. By installing three main rocket engines onto the orbiter rather than two, the problems of abort to orbit from a low V_{stage} are minimized. The three-engined external LH_2 tank orbiter therefore has an optimum V_{stage} of about 7000 ft/sec, which has the major advantage of combining with a fully heat sink booster, the simplest and lowest cost booster.

This subsection presents a description of the H-33 orbiter in terms of external and internal configuration and subsystem locations. Summary tables of weight, payload capabilities, ascent, on-orbit, reentry, fly-home and ferry performance are also provided.

8.2.2.1 External Configuration

The 40,000 lb payload (w/o ABPS) polar mission proved to be the size-governing mission and therefore established the orbiter delta-V and propellant requirements as shown in Table 8.2-2.

TABLE 8.2-2 ORBITER DELTA-V AND PROPELLANT REQUIREMENTS

100 n mi Polar Orbit	
Liftoff Weight, lb	1,101,260
Ideal Delta-V, fps	19,600
Staging Velocity, fps	7,000
Thrust/Weight Ratio	1.30
Ascent Propellant, lb	809,000
Payload Up/Down, lb	40,000/40,000

The H-33 orbiter (Fig. 8.2-1) is a delta wing vehicle with an overall length of 157 ft, a span of 97 ft and an overall height of 75.5 ft. The biggest elements, the relative positions of which dominate the configuration, are the external LH_2 tanks, the payload bay and the internal LO_2 tanks.

Of these, the design of the external tank involves many issues, see subsection 8.9, but does not have a major impact as to orbiter shape. The relative positions of the payload bay and the main LO_2 tanks constitute the most significant packaging decision of the H-33; the arrangement, chosen after much deliberation, has the following advantages:

- The main portion of the body is of constant cross-section providing room for easy installation and replacement of the twin floating main LO_2 tanks, which are cylindrical in shape
- The load paths from the back of the main tanks to the orbiter/booster interstage thrust fitting and the orbiter engines are short and stiff
- The orbiter cg in the fully fuelled condition is located at 52 1/2% of the body length ensuring a near neutral stability arrangement for the mated body while not imposing excessive stability on the orbiter alone
- The orbiter cg excursion during orbiter main stage burn is limited to about 12 1/2% of the body length
- The geometric center of the payload bay is 85 in. forward of the most aft landing cg
- A large diameter compact space, just forward of the payload bay, is available for a wide variety of pressure cabin options.
- The wing has a highly acceptable carrythrough structure of generous chordwise extent with four main wing beams integrated with four major body frames, and a continuous bottom skin.

Before settling on this arrangement, two other payload bay/main LO_2 tank relationships were explored in considerable depth, see Fig. 8.2-2:

FOLDOUT FRAME 1

B/8.2

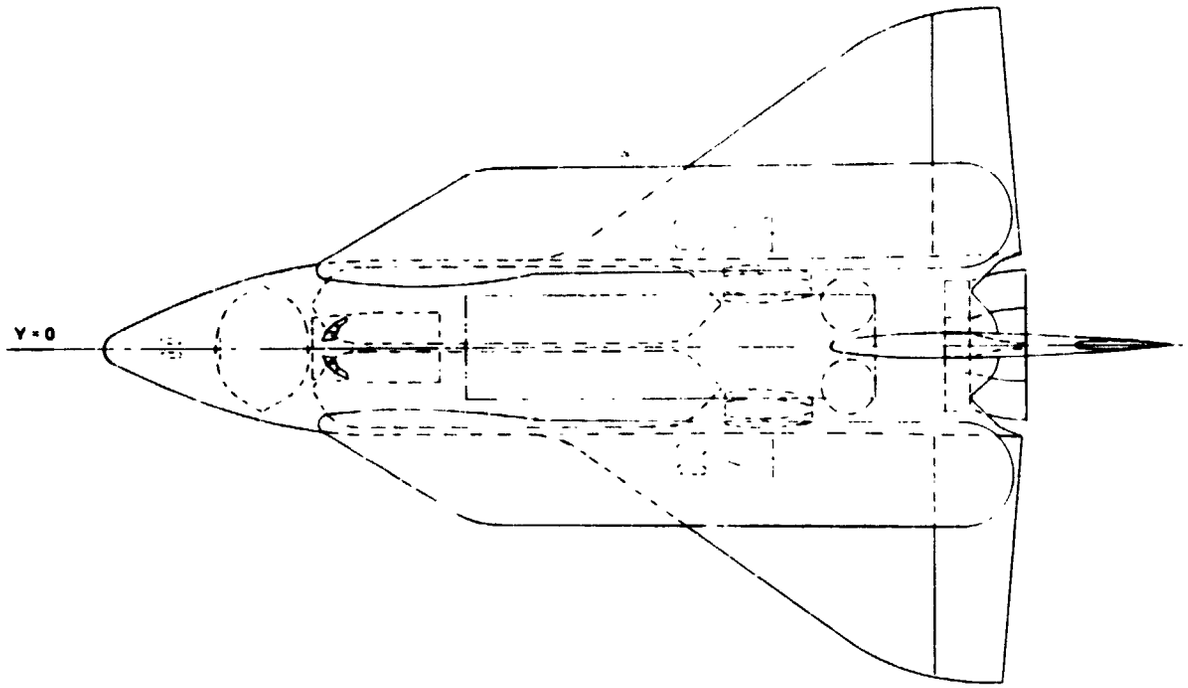

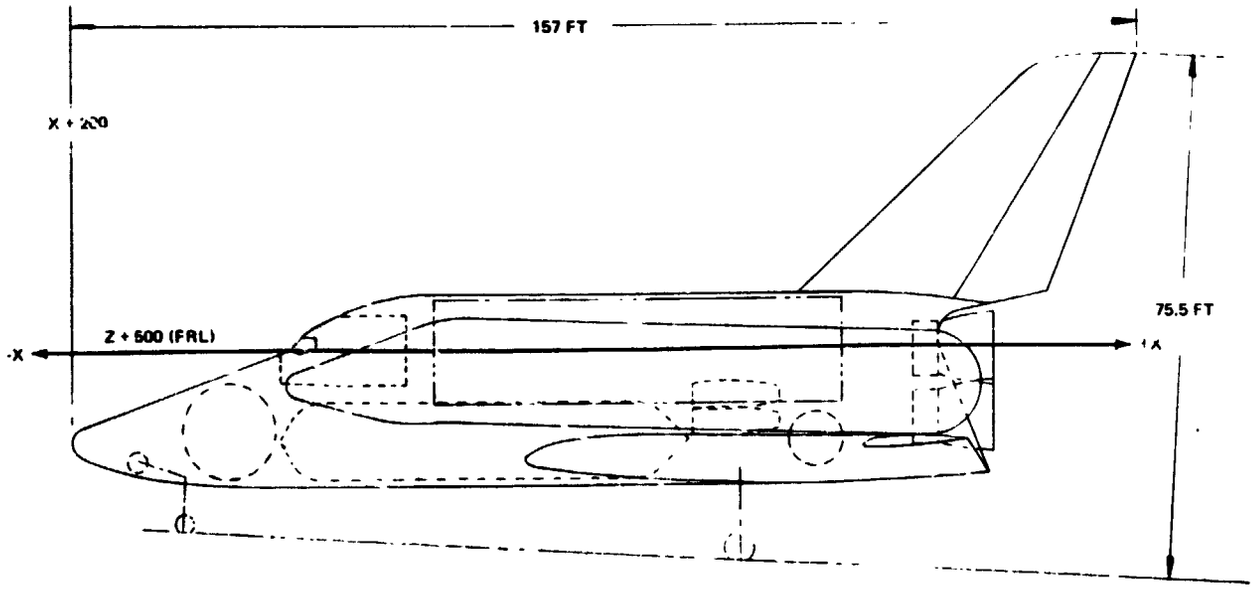

FOLDOUT FRAME 2

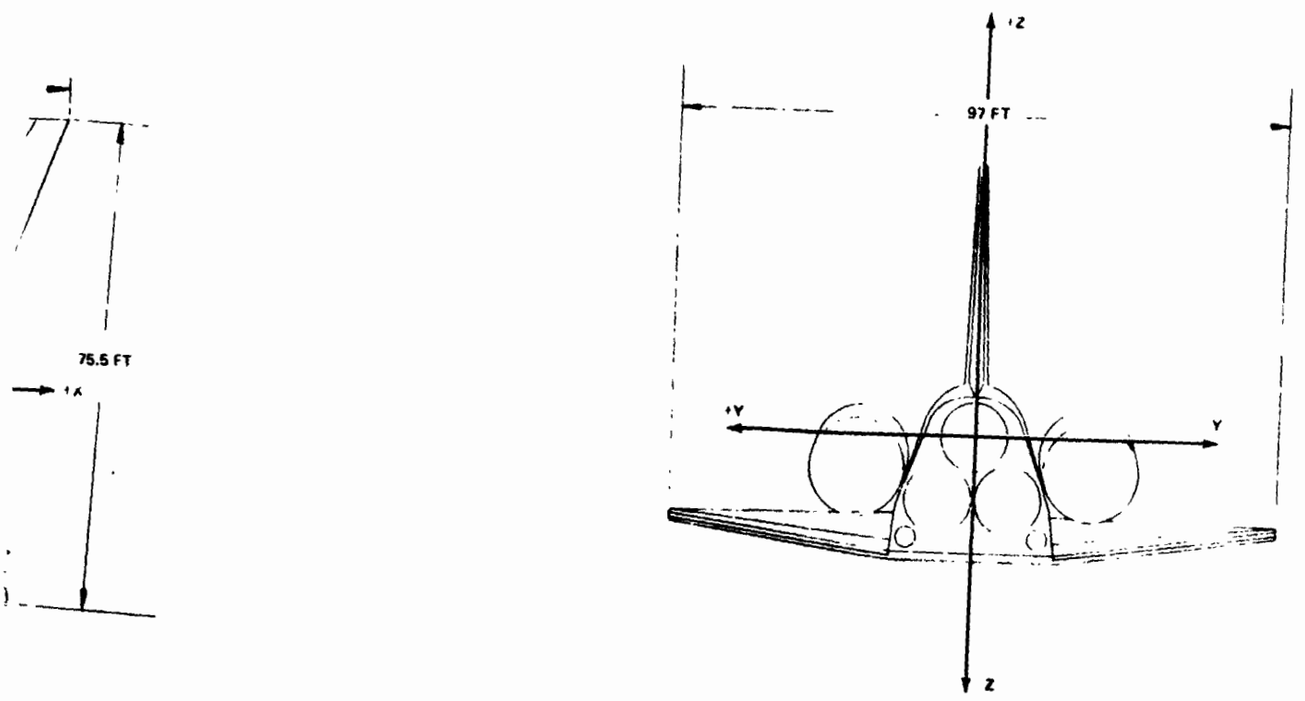

Fig. 8.2-1 H-33 Orbiter General Arrangement

GRUMMAN
BOEING

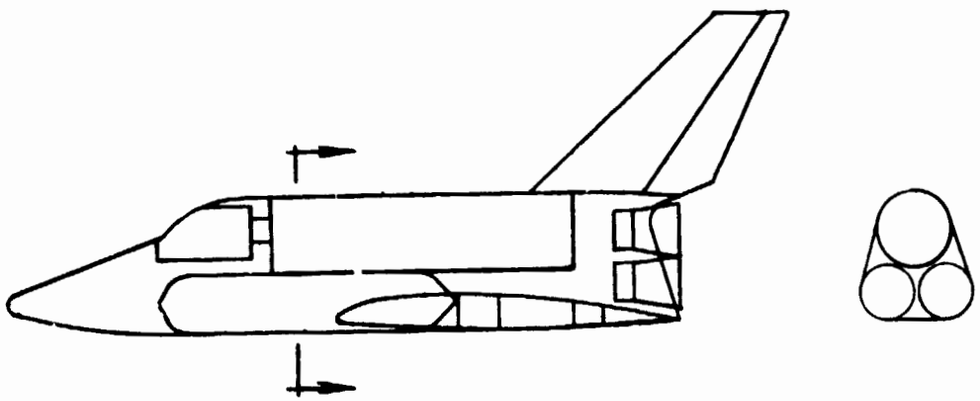

SELECTED ARRANGEMENT

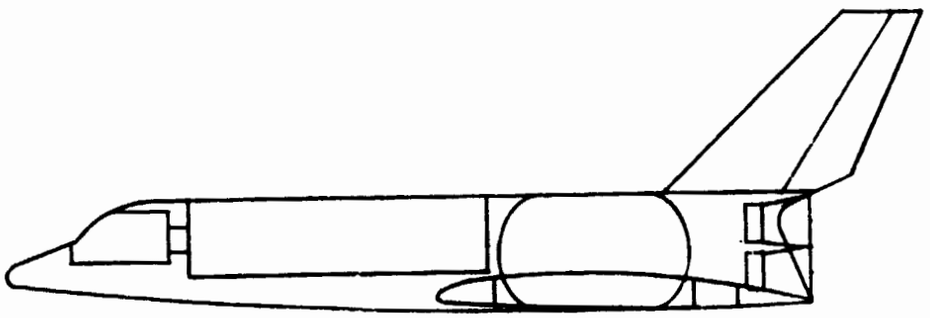

ALTERNATE #1

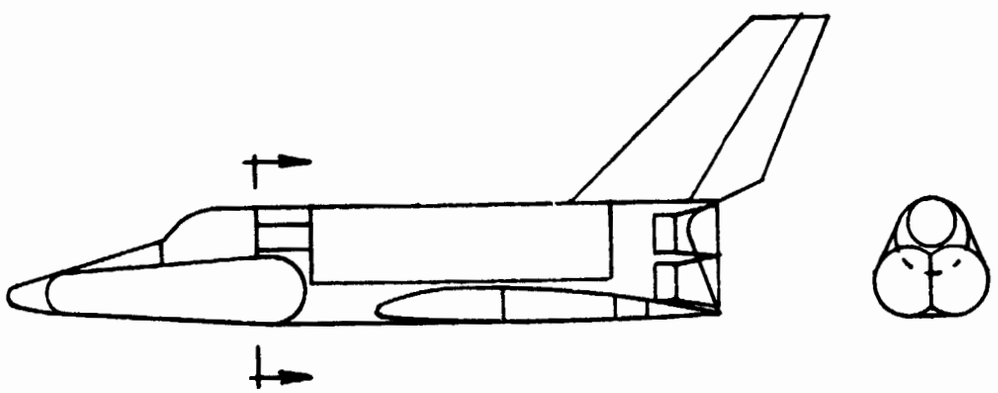

ALTERNATE #2

Fig. 8.2.1-2 H-33 Potential Packaging Arrangements

- Alternate 1, Main LO_2 tank aft - This had the attraction of a higher fineness ratio than the selected design, the body structure was compact with major load paths kept very short and the wing carrythrough structure, though interrupted, was practical. The center of the payload bay was, however, too far forward of the empty aircraft cg and the resultant cg shift with variations of return payload proved excessive. A canard was proposed to handle the problem, but weight and complexity were prohibitive.

- Alternate 2, Main LO_2 tank forward - This also had a high fineness and avoided the excessive cg travel problem. The body structure was not compact, load paths were long, but the wing carrythrough was good. This design was then a serious contender. A considerable effort was made to explore the relative advantages of this and the selected design, involving basic fuselage shell weight, tank weight and complexity, vertical fin weight, TPS weight, propulsion system weight, drag, premature separation stability levels, structural dynamics and overall design flexibility. It was concluded that the advantage lay with the selected design on the score of both weight and the "ilities."

The basic relationship of the main LO_2 tanks and payload bay having been settled, the development of the external shape follows. The shape of the forward section contributes heavily toward determining the maximum hypersonic L/D and the neutral trim angle of attack as well as over-the-nose visibility. Provision is made for 20 deg over-the-nose visibility (refer to paragraph 8.4.7 for further discussion). The forebody planform, chine shaping and camber have been adjusted to provide trim and stability margins throughout the reentry and aerodynamic flight phases. The triangular array of main engines at the rear of the body, lines up naturally with the mid-section packaging of the two LO_2 tanks and payload bay. The sides of the constant section center body provide suitable flat surfaces on which to position the external tanks with a minimum of fairing.

The external tanks shape and position reflects the results of aero/thermodynamic wind tunnel testing and analytical studies conducted to reduce the drag and interference heating effects during launch.

The modified delta wing has a 55 deg leading edge sweep, a faired wing tip and blended leading edge to fuselage fillet to reduce wing-body interaction during reentry. The 2900 sq ft exposed area wing has a Grumman developed airfoil section of 9 1/2% thickness with the maximum thickness at 35% chord at the root and 30% chord at the tip. The sections at the exposed root and tip vary linearly along constant element lines from a root incidence of 2° to a tip incidence of -3°. The 40% line in the wing reference plane has a dihedral angle of +5°. Full span segmented elevons provide pitch and roll control over the entire flight regime.

A single 855 sq ft vertical fin and split rudder provide high and low speed directional stability and yaw control. Both upper and lower rudder segments are split apart vertically at high speed to augment directional stability and improve rudder power. At low speeds the upper elements are closed and function as a rudder with the lower one serving as a speed brake for velocity modulation during unpowered descent.

Figure 8.2-3 presents an inboard profile of the baseline external hydrogen tank orbiter. Major subsystem elements are shown throughout as appropriate.

8.2.2.2 Internal Arrangement

The basic fuselage is divided into forward, mid and aft sections. The forward section extends from the nose to station + X 568 and contains the OMS LH_2 tank, the landing gear nose wheel and the forward orbiter/booster interstage fitting. This section is detachable at its aft end and provides for removal, maintenance or replacement of the main propellant LO_2 tanks and the OMS LH_2 tank.

Locating the OMS LH_2 tank, rather than the LO_2 tank, in the forward section is dictated by a comparison of the inert weights involved in the tankage and support structure and the propellant losses due to venting and chilldown of the lines. Whichever fluid is located aft must be loaded into two tanks because of the lesser fuselage volume available. The LO_2 volume being the smaller, therefore requires less tank weight to contain it, and being the heavier mass, and located close to the orbiter/booster interstage drag fitting, requires less structural weight to support it. Reducing the length of line run for the LO_2 also reduces the propellant losses for venting and chilldown. The least total inert weight penalty results from the forward location of the OMS LH_2 tank.

FOLDOUT FRAME 1

B/8.2

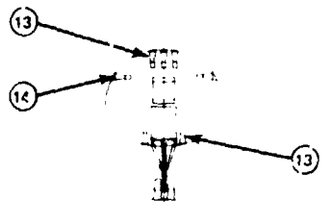

SECTION A-A

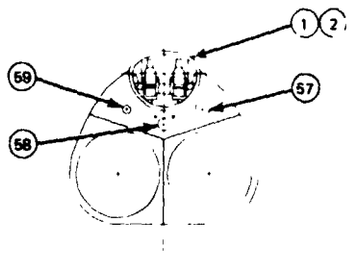

SECTION B-B

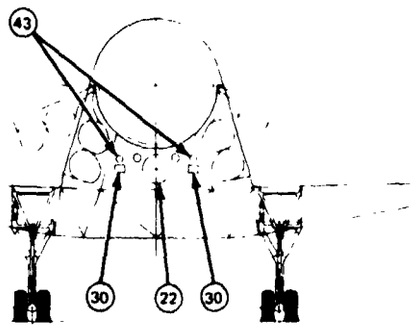

SECTION C-C

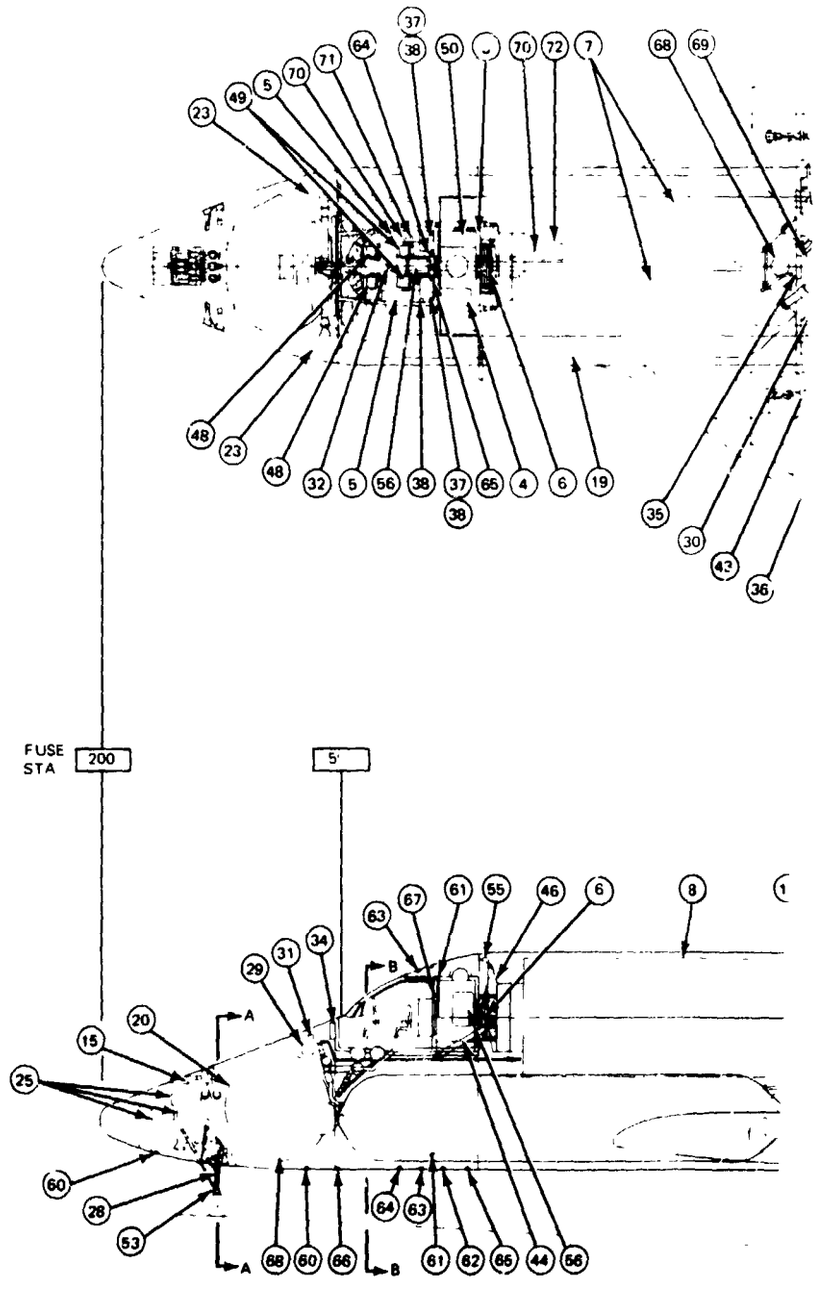

B-240X

FOLDOUT FRAME 2

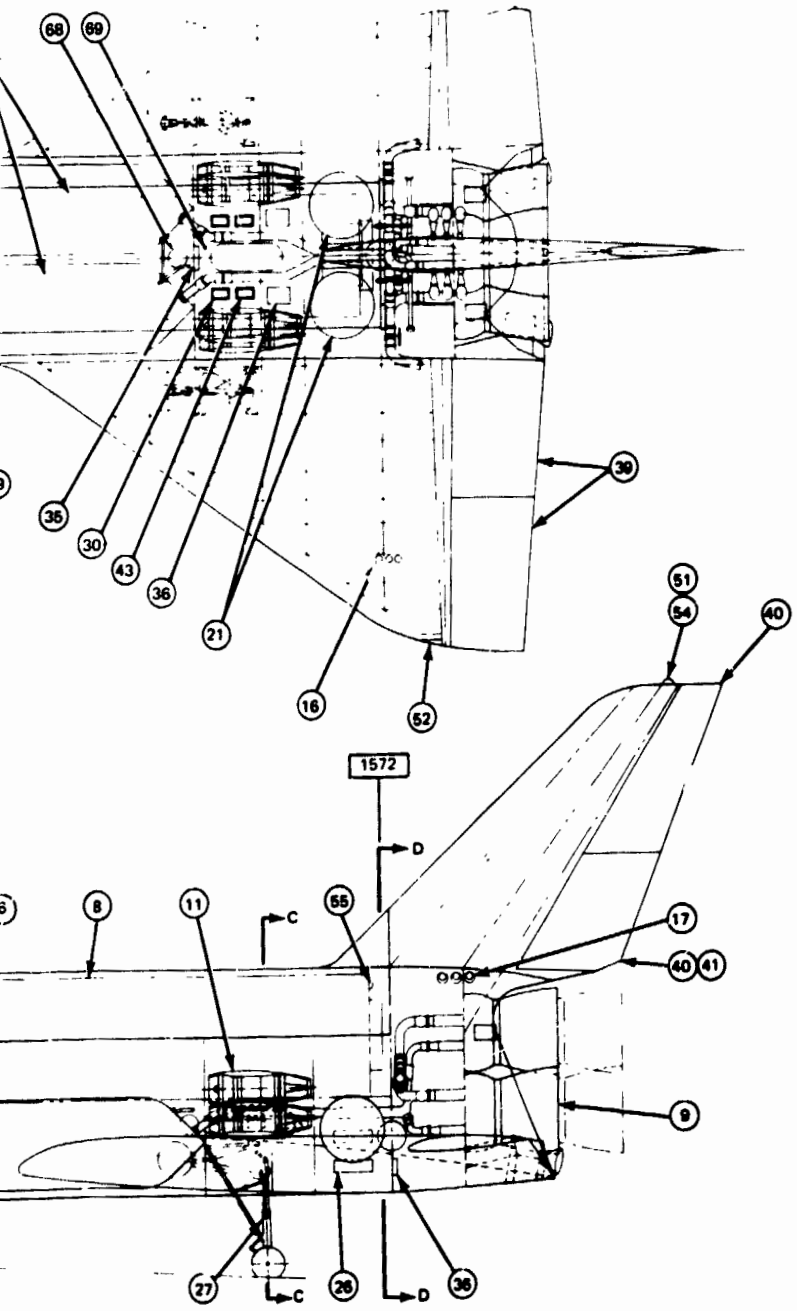

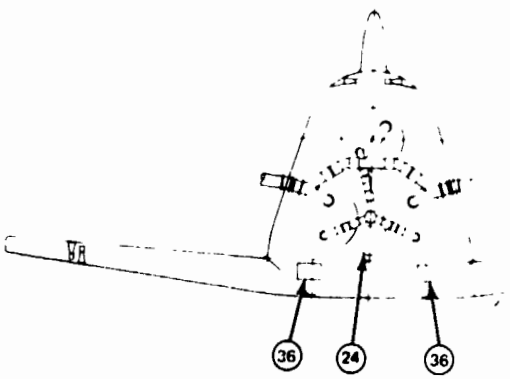

SECTION D-D

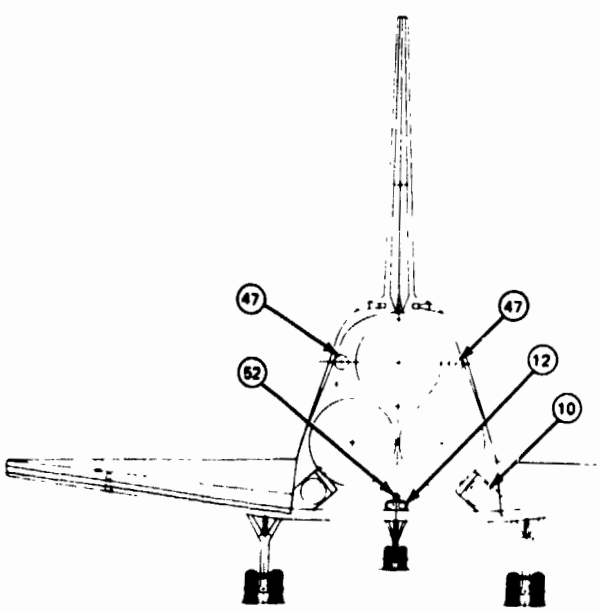

FOLDOUT FRAME 3

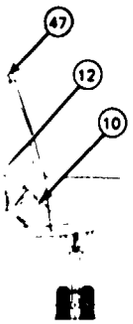

CREW PROVISIONS

1. 2 MAN CREW COMPARTMENT
2. 2 MAN PASSENGER COMPARTMENT
3. AIRLOCK COMPARTMENT
4. GALLEY AREA
6. FLEXIBLE IVA TUNNEL
48. CREW SEATS (2)
49. PASSENGER SEATS (2)
51. ANTI COLLISION LIGHT (1)
52. POSITION LIGHTS (3)
53. LANDING TAXI LIGHT (1)
54. TRACKING LIGHT (1)
55. Ddocking LIGHT (1)
72. MAIN PASSENGER INGRESS/EGRESS
56. CREW INGRESS/EGRESS HATCHES

PROPULSION

9. MAIN PROP. ENGINES (3)
10. OMS ENGINES (2)
11. AIR BREATHING ENGINES (4)
12. ACPS THRUSTERS - AFT FIRING (2)
13. ACPS THRUSTERS - FWD PITCH (5)
14. ACPS THRUSTERS - FWD YAW (4)
15. ACPS THRUSTERS - FWD FIRING (3)
16. ACPS THRUSTERS - AFT PITCH/ROLL (10)
17. ACPS THRUSTERS - AFT YAW (6)
19. ACPS THRUSTERS - LO_2 TANK (2)
20. OMS INTEGRATED LH_2 TANK (1)
21. OMS INTEGRATED LO_2 TANK (2)
22. AIR BREATHING ENGINE JP-4 TANK (1)
23. ACPS H_2 ACCUMULATOR (2)
24. ACPS O_2 ACCUMULATOR
25. ACPS H_2 CONDITIONING MODULE (3)
26. ACPS O_2 CONDITIONING MODULE (3)
68. He PRESSURANT TANK (2)

AVIONICS

5. ELECTRONICS COMPARTMENT
32. DATA MANAGEMENT COMPUTER COMPLEX (4)
37. LM OPTICAL RENDEZVOUS SYSTEM (2)
38. FOUR GIMBAL IMU (3)
60. K_U - BAND SCANNING BEAM ANT. (3)
61. S-BAND COMM. ANT (4)
62. C-BAND ALT. ANT. (6)
63. L-BAND ATC ANT. (2)
64. TACAN ANT. (2)
65. VHF ATC ANT. (2)
66. ORBITER/BOOSTER COMM ANT (2)
67. VHF TDRS ANT. (2)

ENVIRONMENTAL CONTROL

7. PAYLOAD DOORS WITH SPACE RADIATORS
50. WASTE MANAGEMENT SYSTEM
57. N_2 TANK (2)
58. EMERG. O_2 TANK
59. WATER TANK (2)

MISCELLANEOUS

8. PAYLOAD MODULE
69. ELECT. UMBILICAL
70. AIR COND. UMBILICAL
71. ECS/LSS UMBILICAL

MECHANICAL SYSTEM & LANDING GEAR

27. MAIN LANDING GEAR
28. NOSE GEAR
43. HYD. RESERVOIRS (4)
44. PAYLOAD DEPLOYMENT ACTUATOR
46. DOCKING RING ~ HINGED BASE
47. DRAG CHUTE (2)

ELECTRICAL POWER

29. P.G.S. FUEL CELL POWER (2)
30. P.G.S. AUX. POWER UNIT (4)
31. BATTERY (2)
34. FWD MAIN ELECT. DISTRIB. ASSEM
35. AFT MAIN ELECT. DISTRIB. ASSEM
36. LOCAL ELECT DISTRIB. ASSEM (4)

FLIGHT CONTROLS

39. ELEVONS
40. SPLIT RUDDER
41. SPLIT RUDDER/SPEED BRAKE

Fig. 8.2-3 H-33 Orbiter Inboard Profile

GRUMMAN
BOEING

A sloping bulkhead forward of the OMS LH_2 tank provides structural support for the nose gear and the forward orbiter/booster interstage attachment. This permits the efficient use of common load paths and also minimizes structural weight.

The mid section extends from station + X 568 and to station + X 1572 and encompasses the crew compartment, cargo bay, main LO_2 tanks, ABPS compartment, OMS LO_2 tanks, the aft orbiter/booster interstage fitting and the wing carrythrough structure. The forward and aft cargo bay bulkheads provide for the structural support of the external LH_2 tanks.

The mid section is designed around the 16 ft diameter by 65 ft long cargo bay and the two floating main LO_2 tanks. The cargo bay provides for the 15 ft diameter x 60 ft long payload and its deployment mechanism, with adequate clearance for the payload during deployment. With the external LH_2 tanks jettisoned, the payload bay doors can be opened to expose the full length of the payload clear to the Z = 500 water line. On the pad, with the LH_2 tanks assembled, each door can be opened through about 80 deg to allow installation of, and access to the payload. A four-man cabin is located forward of the cargo bay and includes an airlock and a payload/docking viewing dome, which is exposed when the payload doors are open. The cabin provides adequate storage for ECS, LSS, EPS and avionics equipment, waste management and food preparation facilities to handle the maximum 14 man passenger requirements and EVA, PLSS storage facilities. Behind the airlock is a bellows tunnel that connects to an androgynous docking ring which in turn is part of the extension mechanism. This arrangement permits direct docking of the orbiter to an orbiting vehicle through the extended bellows or the attachment of a cargo module to the bellows/docking ring and deployment of the cargo module for docking at its aft end (refer to subsection 8.11).

ECS radiators are installed on the inside of the cargo doors and are exposed upon achieving the mission orbit. They remain exposed throughout the mission until just prior to initiation of the reentry phase of the mission (refer to paragraph 8. 8. 2).

The two main LO_2 tanks, located in the mid section, are floating and supported in a manner to isolate them from the primary fuselage structural loads. The forward end sustains load in the Y-Z plane while the aft apex carries loads in all planes. The drag

support for each ascent LO_2 tank is a titanium/boron composite strut from the tank to the aft interstage fitting on the fuselage centerline. This provides a short, light weight, stiff load path for this large mass and minimizes the effects of the launch and ascent dynamics.

Compartments for the airbreathing propulsion system (ABPS) are located on either side of the fuselage mid section, above the wing. Two cruise engines are mounted in each compartment and deployed as a unit to minimize the weight of such items as the deployment mechanism, doors and fuel feed lines from the single JP fuel tank. The deployable system results in less orbiter scar weight than a fixed installation and locating the engines close to the landing cg, reduces the cg excursion, caused by cruise engines flown or not flown, to about 3/4% of body length. This is within the subsonic trim capability.

The aft section extends from station + X1572 to station + X 1820 and contains the main and auxiliary rocket engines and the vertical tail support structure. The 14 in. diameter external LH_2 feedline interfaces with the orbiter in this section.

The grouping and positioning of the main rocket engines, is dictated by:

- Boattailing of the back end around the top of the fuselage to minimize base drag
- Locating the RL-10 engines low, as discussed in a following paragraph
- Adequate clearance between the engines at all times

Considering cg travel during normal three engine burn and the one engine out case, and with 2 deg overtravel for control purposes, the required maximum angular travel of a gimbal is 15° total. A 6 inch minimum clearance exists between engines at all times. The engines are not gimballed when retracted.

The location of the two RL-10 orbit maneuvering system engines is prompted by their proximity to exisiting primary structure and their remoteness from the vertical tail which minimizes impingement of the RL-10 plume on the rudder. Some thermal protection of the two lower main engine nozzles is necessary to protect them from RL-10 engine plume impingement in the event of parallel burning during abort to orbit. This protection incurs an estimated weight penalty of 100 lb. As an alternative, consideration was given to mounting the RL-10's at the base of the fin, with their nozzle exits aligned with the exits of the main engines extended nozzles. The extra primary structure required, the loss of boattailing and the interruption of airflow at the inboard end of the rudder led

to discarding this approach. These engines are fixed in position with their thrust axes aligned with the on orbit mid-burn cg position. The RCS provides any necessary corrective torques. For an abort-to-once-around case, with the main and orbit maneuvering engines burning in parallel, the main engines will provide the thrust vector control necessary to maintain the desired orbiter attitude.

The volume between the cargo bay and the engines is occupied by the propellant feed lines.

The only deployable antennas are the scanning beams for landing, which are mounted on the nose gear doors. Where necessary, high temperature dielectric windows will be provided in the TPS and structure.

In general, the 30 RCS thrusters are positioned to give maximum moment about the cg for pitch, yaw and roll maneuvers, and to keep plume impingement onto the external LH_2 tanks to a minimum. The thrusters are mounted on exisiting primary structure. Doors are provided at nozzle exits to maintain continuity of the air passage lines and to prevent the entrance of hot reentry gasses.

The major subassemblies comprising the orbiter assembly (Fig. 8.2-4) have been chosen to decouple the higher risk development items from the more straightforward state-of-the-art components. This permits the parallel design, fabrication and testing of the separate subassemblies and minimizes the program impact resulting from the occurrence of specific development problems. Thus, should the development of elements such as the floating main LOX tanks, engines, TPS materials, or LH_2 insulation be delayed. the design and fabrication of the airframe would continue unhindered. Selection of the subassemblies also considers that each module structure is complete and self-supporting to minimize handling difficulties, that the module structural interfaces are readily accessible and mechanically simple, and that service maintenance, major component replacement and orbiter refurbishment requirements are accommodated.

8.2.2.3 External LH_2 Tank

Fig. 8.2.-5 shows the general arrangement of the external LH_2 tank. The tank shape and position reflects the results of aero/thermodynamic wind tunnel testing and analytical

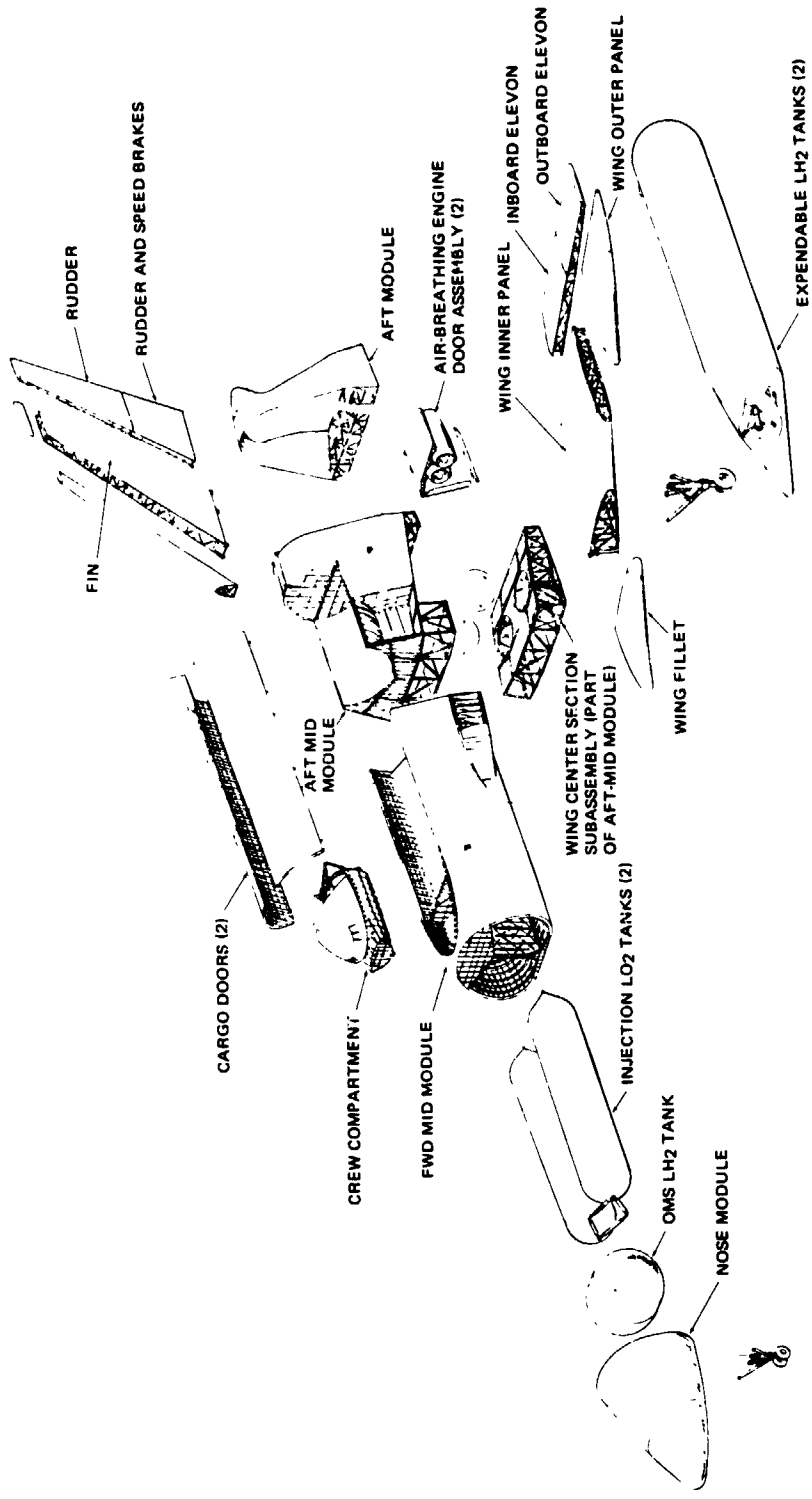

Fig. 8.2-4 H-33 External Tank Orbiter Major Structural Assembly Breakdown

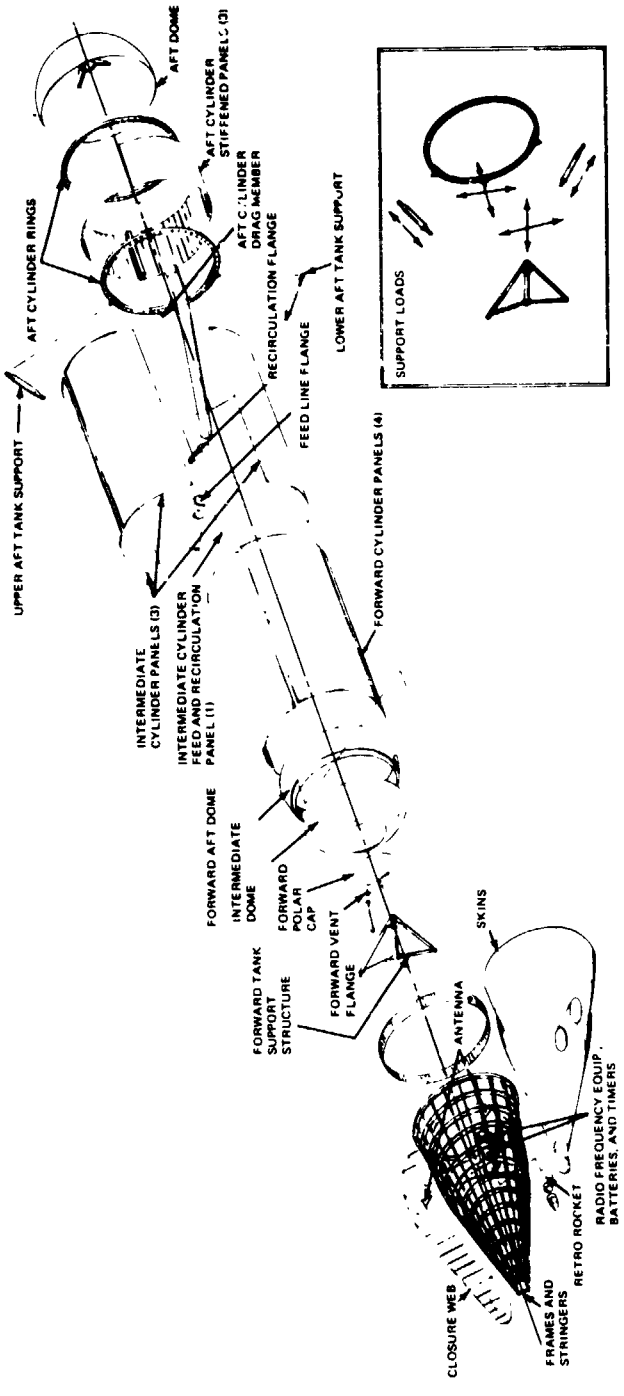
AFT DOME
AFT CYLINDER STIFFENED PANELS (3)
AFT CYLINDER DRAG MEMBER
AFT CYLINDER RINGS
RECIRCULATION FLANGE
LOWER AFT TANK SUPPORT
FEED LINE FLANGE
UPPER AFT TANK SUPPORT
SUPPORT LOADS
FORWARD CYLINDER PANELS (4)
INTERMEDIATE CYLINDER PANELS (3)
INTERMEDIATE CYLINDER FEED AND RECIRCULATION PANEL (1)
FORWARD AFT DOME
INTERMEDIATE DOME
FORWARD POLAR CAP
FORWARD VENT FLANGE
FORWARD TANK SUPPORT STRUCTURE
SKINS
ANTENNA
RADIO FREQUENCY EQUIP., BATTERIES, AND TIMERS
RETRO ROCKET
FRAMES AND STRINGERS
CLOSURE WEB

studies conducted to reduce the drag and interference heating effects during launch. Positioning the tank aft along the orbiter fuselage, ensures that the tank nose cone lies inside the orbiter bow shock envelope. Sloping the nose cone in towards the fuselage leads to a reduction in vehicle drag compared to conical nose tanks and minimizes the interference heating between the tank and orbiter fuselage and wing.

At the front of the tank is a 6 in diameter vent/pressurization line, and at the rear, a 14 in diameter fuel feed line and a 3 in diameter engine cooling flow recirculation line. Electrical interconnections are also at the rear of the tank.

The tank is mounted to the vehicle by a drag and side load attachment towards the aft end of the tank, together with sway braces. The forward attachment is a single point on the apex of the tank end closure cone with struts to the orbiter providing lateral restraint.

Thermal protection of the assembly is provided by molded ablators bonded to the nose fairing, rear supports and rear interconnections. Foam, to minimize boil off and icing, covers the outside of the tank, and an overcoat of spray-on ablative is added to those areas between tank and orbiter subjected to interference heating.

Separation of the tanks from the orbiter, during orbiter coast phase, is pyrotechnically actuated, the movement being normal to the fuselage sides. After the external tanks have been moved to a safe distance, tank de-orbit is commanded by a crew member firing the retro rockets.

All aspects of the external LH_2 tanks are discussed in greater detail in subsection 8.9.

8.2.2.4 Characteristics Summary

Presented here are brief tabular summaries of the H-33 orbiter performance characteristics and weights.

- Weights
  - Liftoff weight, lb 1,101,260
  - Injection weight, lb 292,260

- Landed weight, lb 241,172
- Dry weight (including external tanks, lb) 220,838

- Alternate Payload Capability

Inclination, deg.	Altitude, n mi	Payload Up, k lbs	Payload Down, k lbs
28.5	100	65.7	40
55*	270	26.2	25
90	100	40	40
*With ABPS Installed			

- Ascent
  - Staging velocity, fps 7,000
  - Time of staging, sec 181.3
  - Staging altitude, ft 190,000
  - Dynamic pressure at staging, psf 18.4
  - Initial thrust/weight 1.30
  - Maximum thrust/weight 3.00
  - Rel flight path angle, deg 13.6
  - Total ideal delta-V to 51 x 100 n mi, fps 19,600

- Nominal Delta-V budget,

	Polar	55°	28.5°
- Transfer and rendezvous	100	640	100
- Terminal rendezvous stationkeeping, docking, separation, return phasing		350	350
- Orbit keeping	240	0	240

• Nominal Delta-V budget, (Continued)	Polar	55°	28.5°
- De-orbit	260	450	260
- Reserve	50	50	50
- Total	650	1490	1000
• Entry			
- Angle of attack, deg	27		
- Trimmed C_L (Theor wing)	.42		
- Trimmed L/D	1.56		
- Elevon angle of trim, deg	+3.2		
- Hypersonic W/SC_L, psf	119.5		
- Longitudinal aerodynamic center	0.689 l_b		
- Directional aerodynamic center	0.36 l_b		
- Maximum normal load factor, g	1.5		
• Subsonic			
- Maximum trimmed L/D	7.2		
- Angle of attack at L/D max, deg	8.6		
- Longitudinal aerodynamic center	.68 l_b		
- Directional aerodynamic center	.75 l_b		
- Approach speed, kt	240		
- Touchdown speed, kt	180		
- Touchdown angle of attack, deg	11.4		
- Dry runway length, ft	4850		
- FAA wet runway length, ft	9300		
- Landing parachute diameter, ft	30		

- Ferry

- Takeoff weight, lb	264,820
- Takeoff balanced field length (FAA), ft	7,200 (SL Std Day)
- Second segment - climb gradient, %	8 (SL Std Day)
- Optimum specific range (all engines, average)	.0112
- Optimum average cruise altitude (all engines), ft	19,200
- Optimum average cruise altitude (engine out), ft	15,000
- Mission range (all engines) n mi	300
- Mission time (all engines), hr	1.04
- Nominal fuel reserves	20 minute hold plus missed approach and go-around

8.3 CHARACTERISTICS

8.3.1 H-33 PHYSICAL CHARACTERISTICS

- Vehicle Geometry
  - Total projected planform area ..... 6,060ft^2
  - Total wetted area ..... 17,930ft^2
  - Total length 157ft
  - Total width 97ft
  - Total height (gear up) 61.25ft
- Body Geometry
  - Projected planform area ..... 3,120ft^2
  - Wetted area ..... 10,345ft^2
  - Mold line volume ..... 58,400ft^3
  - Length 135ft
  - Width 25ft
  - Height 27.5ft
  - Base area ..... 461ft^2
  - Max. cross-sectional area ..... 530ft^2
- Wing Geometry
  - Theoretical area ..... 4,840ft^2
  - Projected planform area (exposed) ..... 2,900ft^2
  - Wetted area ..... 5,940ft^2
  - Span (to theoretical tip parallel to fuselage) 94.5ft
  - Aspect ratio 1.846
  - Dihedral angle (at 40% chord line) ..... 5°
  - Leading edge sweep ..... 55°
  - Quarter chord sweep ..... 46.32°
  - Trailing edge sweep ..... -5°

- Incidence angle (body root/tip) ..... 2°/-3°
- Taper ratio (theoretical tip chord/chord at ℄) ..... .178
- Root chord (at ℄) 86.96ft
- Fuselage chord 67.98ft
- Tip chord 15.48ft
- Mean aero. chord (ref. area/exp. area) 59.5ft/47.2ft
- Airfoil section at fuselage side (cambered sec.) ..... t/c=9.5%
- Airfoil section at tip (cambered sec.) ..... t/c=9.5%

• Vertical Tail Geometry

- Number of vertical tails 1
- Side elevation area ..... 855ft^2
- Wetted area ..... 1,727ft^2
- Span (true) 33.75ft
- Aspect ratio 1.33
- Leading edge sweep ..... 47°
- Quarter chord sweep ..... 42.13°
- Trailing edge sweep ..... 21.85°
- Root chord 36.66ft
- Tip chord 14.0ft
- Mean aerodynamic chord (true) 27ft
- Airfoil section at root ..... NACA 64A010
- Airfoil section at tip ..... NACA 64A010
- Taper ratio ..... .38

• Rudder

- Area (to hinge line) ..... 292ft^2
- Root chord 12.76ft
- Tip chord 4.92ft
- Span 34.75ft
- Hinge sweep ..... 32°

- Elevons
  - Total area (to hinge line) ..... 820ft^2
  - Root chord 13.6ft
  - Tip chord 10.0ft
  - Span (each) 34.75ft
  - Hinge sweep ..... 0^o

8.3.2 ORBITER MASS PROPERTIES

An orbiter weight summary for the baseline external tank orbiter is presented in Table 8.3.2.-1. The presentation format is the mission weight summary form required by MIL 30310A. The weights shown are based upon the polar mission.

A summary of the characteristics for the orbiter is shown in subsection 8.3.1. The orbiter is capable of making the payload requirements of all the candidate missions as shown in Table 8.3.2-2.

Complete discussion of mass properties is included in the Detailed Mass Properties Report B35-43RP-16.

TABLE 8.3.2-1 40K PAYLOAD/SOUTH POLAR LAUNCH MISSION
(Sheet 1 of 2)

MISSION WEIGHT SUMMARY (IN POUNDS)							
Code	System	A	B	C	D	E	F
1	Wing Group	19120					
2	Tail Group	6227					
3	Body Group	43590					
4	Induced Envir. Protection	36722					
5	Landing, Recovery, Docking	10313					
6	Propulsion-Ascent	38414					
7	Propulsion-Cruise	1129					
8	Propulsion-Auxiliary	9753					
9	Prime Power	1549					
10	Elect. Conver. & Distr	1907					
11	Hydra Conver & Distr	3042					
12	Surface Controls	2263					
13	Avionics	3395					
14	Environmental Control	1944					
15	Personnel Provisions	478					
16	Range Safety and Abort						
17	Ballast						
18	Growth/Uncertainty	17392					
19							
	Subtotal (Dry Weight)	197238	197238	197238	197238	197238	197238
20	Personnel		458	458	458	458	458
21	Cargo		40000	40000	40000	40000	40000
22	Ordnance						
23	Residual Fluids		3104	3104	3104	3104	3104
24	External Tanks					23600	23600
	Subtotal (Inert Weight)		240800	240800	240800	264400	264400

TABLE 8.3.2-1 40K PAYLOAD/SOUTH POLAR LAUNCH MISSION
(Sheet 2 of 2)

MISSION WEIGHT SUMMARY (IN POUNDS)							
Code	System	A	B	C	D	E	F
25	Reserve Fluids		372	372	5796	5796	5796
26	In Flight Losses				7425	7425	7425
27	Propellant-Ascent						809000
28	Propellant-Cruise						
29	Propellant-Maneuv/ACS				14639	14639	14639
30							
	Total (Gross Weight) Lb.	197238	241172	241172	268660	292260	1101260

Designations:

Events		Current Weight
A	Dry	197238
B	Landed	241172
C	Max. Cruise	241172
D	Injection W/O External Tanks	268660
E	Injection With External Tanks	292260
F	Lift-Off	1101260

TABLE 8.3.2-2 MISSION PERFORMANCE SUMMARY

Parameter	External Tank Orbiter		
	Polar	Due East	Resupply
Orbit Inclination, deg	90	28.5	55
Orbit Altitude, n mi	100	100	270
Payload, K lb Up	40000	65660	26154
Payload, K lb Down	40000	40000	25000
OLOW, K lb	1101260	1136700	1123600
BLOW, K lb	2824000	2830000	2828000
GLOW, K lb	3925260	3966700	3951600
Ideal Velocity, fps, Orbiter	19600	18383	18815
Boost	12023	11813	11883
Staging Velocity, fps, Orbiter	25877	24478	24962
Boost	7000	6775	6855

8.3.3 AERODYNAMIC CHARACTERISTICS

8.3.3.1 Aerodynamic Configuration

The aerodynamic configurations of the H-33 and G-3G Orbiters, shown in Fig. 8.2-1 and 8.12-1, have evolved from a series of continuing analytic studies augmented by approximately 500 hr of wind tunnel testing. This testing over the Mach range from 0.2 to 10 is summarized in the Table 8.3.3-1.

Both configurations are "balanced" designs that have been developed to possess inherent static and dynamic stability over the entire reentry flight path. As can be seen in Fig. 8.3.3-1, which depicts the stability and trim boundaries for the H-33 design, this goal has been achieved with the single exception that a static directional instability exists at hypersonic speed. Sufficient dihedral is provided to ensure positive dynamic stability over the complete operational envelope. Significant geometric characteristics for both the H-33 and G-3G Orbiters are presented in Subsections 8.3.1 and 8.12.4.

For both vehicles a wing leading-edge sweep angle of 55 deg's. has been selected, based on a compromise that minimizes wing weight without incurring excessive leading edge temperatures. After selection of the leading edge sweep, other geometry such as area, twist, camber and thickness, as well as fuselage lines have been tailored to provide required low-speed performance, stability throughout the flight envelope (minimum static margin = 1% body length) and hypersonic trimmability over an angle of attack range from 20 to 50 deg's. Directional stability (C_{n_β}) is provided by a single centerline vertical tail sized to satisfy subsonic requirements. At supersonic speeds the 35% chord rudder is flared ± 30 deg's. to maintain strong positive levels of C_{n_β}. In addition the flared rudder provides a positive pitching moment which provides additional trim capability to maintain low dynamic pressures during the supersonic flight phase.

Pitch and roll control are provided by full span elevons (13.6% of planform area). The elevons have a zero sweep hinge line to minimize adverse yaw during rolling maneuvers.

After transistion directional control is provided by the 35% chord rudder. The rudder in addition to being flared is also split (in the profile view) so that the lower half may be modulated during the landing phase as a speed brake. By using only the lower half, longitudinal trim changes in this mode will be minimal. The upper half will be unflared during landing and acts as a conventional rudder.

TABLE 8.3.3-1 ORBITER WIND TUNNEL SUMMARY

Test		Mach No.	Hours	Facility	Test Objectives
Subsonic	S-0603, 0610	~0.2	198	GAC 7' x 10' LSWT	Verification of Long. and Lat. - Directional Stability and Control, In and Out of Ground Effect
Trans/Supersonic	S-0607 0608 0609	~0.6 to 2.5	252	GAC 26" TWT GAC 15" SSWT Ames 6' x 6' Supersonic	Assessment of Drag, Stability and Control Characteristics
Hypersonic	S-0604	10	64	GAC 36" HSWT	Verification of Hypersonic Estimates of L/D, Stability and Control Characteristics

A summary of primary aerodynamic characteristics are presented in Fig. 8.3.3-1 through 8.3.3- and a detailed development of the complete longitudinal and lateral-directional aerodynamic characteristics is presented in the sections that follow.

8.3.3.2 Entry Characteristics

The estimated H-33/G-3G Orbiter characteristics presented in this section reflect the cumulative design and analysis experience successfully borne out in the course of three Grumman M=10 Orbiter Wind Tunnel Test Series. All final estimates reflect baseline Crumman Aerospace Corporation - High Speed Aerodynamic Prediction Program (GAC-HAPP) computer results augmented by specific data correlations to account for imbedded flow field and interference effects not recognized by contemporary computer prediction techniques. These corrections, primarily affecting longitudinal trim, elevon

control effectiveness, and lateral stability, have been quantitatively identified in the course of almost continuous GAC-HAPP program upgrading and data correlation dating back to 1964. These correlations embrace configuration types extending from reentry capsules and intermediate L/D lifting-body configurations to contemporary delta wing candidate shuttle configurations.

8.3.3.2.1 Longitudinal

Orbiter longitudinal stability and control characteristics appear in Fig. 8.3.3-5 and 8.3.3-6. A near optimum design compromise between the extremes of excessive subsonic-supersonic stability and insufficient hypersonic stable trim capability accounting for forward and aft cg contingencies has been achieved at virtually no penalty in wing sizing beyond that dictated by low-speed landing performance requirements. The inherent stability exhibited by both configurations precludes significant down elevon/aileron operation at high α and provides ample margin against high speed pitchup. A reserve of positive longitudinal stability also extends to α below the minimum α_{DES} = 20 deg to insure unqualified availability of the entire 20 deg. $\leq\alpha\leq$ 50 deg design envelope. Only modest down elevon is required to trim to the minimum design α, a factor favoring low aileron adverse yaw and minimal aero-thermal interference heating.

Estimated variation of H-33 Orbiter L/Dmax and L/D @ α = 20 deg with Mach no. is depicted in Fig. 8.3.3-7. The relatively small variation of L/D with Mach No. indicates the best speed for terminal transition to low-angle-of-attack flight will not be dictated by performance and can be selected to minimize stability and control problems.

8.3.3.2.2 Lateral Directional

Lateral-Directional stability and control characteristics are presented in Fig. 8.3.3-8 and 8.3.3-9. The indicated body-axis static directional instability is an inevitable outgrowth of orbiter design weight minimization efforts. Adequate positive dihedral effect is available, however, to ensure positive lateral-directional dynamic stability, i.e., $C_{n_\beta DYN}>0$, over the design α range.

Predictable design alternatives for further improving basic orbiter static and dynamic lateral-directional characteristics have been explored at Grumman and are discussed in Subsection 8.3.3.2.3

Aileron control characterisitcs for the H-33 Orbiter appear in Fig. 8.3.3-9. Ample roll control power is indicated throughout the α range. Adverse yaw has been minimized by avoiding an aft-swept hinge line and excessive down-elevon longitudinal trim deflections. Reduced levels of adverse yaw offer improved roll-bank coordination and effective lateral trim capability. Further optimization of the aileron control system and detailed configuration refinement for improved lateral-directional stability appear feasible within system weight constraints.

8.3.3.2.3 Supporting Aerodynamic Studies - Orbiter Lateral-Directional Stability

Alternative design options for providing orbiter bare-airframe static directional stability throughout the entire reentry flight envelope have been explored at Grumman pending a definitive outcome of engineering trade studies covering the weight, cost, and safety implications inherent in competing aerodynamic and artificial stability augmentation systems. Significant improvements in orbiter directional stability can be achieved at α = 20 deg with toed-in tip fins, in conjunction with flared rudders; however, our studies indicate severe weight penalties for this approach. This can be inferred from the large 945 sq ft tip fins, each, which would be required to stabilize the H-33 configuration. (See Fig. 8.3.3-10.) Additional low-speed and transonic problems are also introduced with a tip fin arrangement of these proportions and, for this reason, this alternative has not been incorporated.

Fuselage forebody shaping also has a substantial influence on orbiter directional stability, a configuration design approach that was investigated analytically and experimentally at Grumman. Based on these studies a moderately hard chine - high fineness ratio forebody of 6-ft increased length would result in the improved C_{n_β} level depicted in Fig. 8.3.3-10. Grumman test results, however, also substantiated predictions that this type of fuselage forebody design results in severe longitudinal trim problems requiring an additional 900 sq ft of exposed wing area or, alternatively, a very forward cg or an extremely aft wing location. The forward-cg/extremely-aft-wing solutions, however, are illusory and result in excessive low-speed stability and loss in trimmed lift-curve-slope (increased landing attitude, and low subsonic trimmed L/D. In the final analysis it appears that fuselage shaping to achieve substantial improvements in directional stability is not consistent with optimum overall orbiter design.

The most attractive aerodynamic alternative to artificial stability augmentation during reentry appears to be a fixed or deployable ventral(s) configuration operating within the orbiter primary shock envelope. Analytic projections based on Grumman test data indicate a 100 ft^2 ventral will provide positive body axis static directional stability for the H-33 Orbiter throughout the entire α range, 20 deg to 60 deg, as shown in Fig. 8.3.3-10.

8.3.3.2.4 Damping Derivatives

The primary hypersonic rate derivatives appear in Fig. 8.3.3-11 and 8.3.3-12. The acceleration derivatives $C_{L_{\dot{\alpha}}}$ and $C_{m_{\dot{\alpha}}}$ were taken to be zero because of the absence of significant hypersonic downwash lag or apparent mass effects. The side force rate derivatives C_{y_r} and C_{y_p} were also assumed zero since their effect on the high-speed lateral-directional motion is negligible.

8.3.3.3 Post Entry Characteristics

8.3.3.3.1 Longitudinal

The H-33 trimmed static longitudinal characteristics are presented as a function of Mach number in Fig. 8.3.3-13 and 8.3.3-14. The longitudinal derivatives (Fig. 8.3.3-15) were estimated using the methods of Reference 1, Subsection 8.3.3.5, and available wind tunnel data from a similar configuration. The test data and theoretical estimates also shown in Fig. 8.3.3-15 show excellent agreement. The single exception is the wave drag estimate, which proved to be somewhatc conservative. For the H-33 the wave drag was taken directly from tunnel data for a similar configuration.

The untrimmed lift, drag, and pitching moment curves, Fig. 8.3.3-16 through 8.3.3-25, were developed using the estimated static derivatives (alpha = 0) and wind tunnel data variations with angle of attack. The change in lift and pitching moment due to elevon deflection at alpha = 0 (Fig. 8.3.3-26) was estimated by adjusting test data for appropriate differences in moment arm and wing geometry. The zero lift pitching moment and angle of attack were taken directly from test data.

The untrimmed drag polars were calculated by means of a component buildup. Subsonically, profile drag was calculated at zero lift using appropriate factors for supervelocity and pressure drag at a full-scale Reynold's number of 2.0×10^6/ft. Base drag from wind

tunnel results was adjusted (upward) to account for the differences between test and flight Reynolds numbers. To account for roughness, protuberances, and other manufacturing irregularities the subsonic drag was then increased 10%. To this value the wind tunnel variation of wave drag with Mach number was added to produce the variation of C_{D_o} vs Mach number presented in Fig. 8 3.3-27. The variation of both the base drag and profile drag with angle of attack was derived from tunnel data.

Drag due to lift calculated for subsonic speeds was assumed equal to C_L^2/π A. This assumption was also used to extract the profile drag variation with angle of attack. Supersonic drag due to lift was assumed equal to $C_L^2/C_{L\alpha}$. Trim drag due to elevon deflection was extracted directly from tunnel data.

The trimmed longitudinal characteristics were developed by graphically trimming the resulting data in Fig. 8.3.3-16 through 8.3.3-25.

8.3.3.3.2 Lateral-Directional Characteristics

a Stability

Estimated lateral-directional characteristics of the H-33 Orbiter as a function of Mach number are depicted in Fig. 8.3.3-28 through 8.3.3-30. The values presented for zero degrees angle of attack were obtained by means of the methods outlined in Reference 1 Subsection 8.3.3.5, suitably modified to provide correlation with wind tunnel test data (References 2 through 5, Subsection 8.3.3.5). The degree of correlation between estimates and wind tunnel test data for the generally similar G-3A orbiter configuration presented in Fig. 8.3.3-31 give confidence in the use of these methods for the H-33 Orbiter configuration. The variation of H-33 lateral-directional parameters with angle of attack was obtained from trends exhibited by the aforementioned G-3A orbiter wind tunnel test data. Lateral-directional characteristics with flared rudder deployed are depicted in Fig. 8.3.3-32. The incremental effects of flared rudder utilized in generating Fig. 8.3.3-32 were obtained by modification of wind tunnel test data presented in Reference 5, Subsection 8.3.3.5, to conform to H-33 Orbiter geometry.

b. Control

Rudder effectiveness for both conventional full-span and flared-full-span rudder deflections is depicted in Fig. 8.3.3-33. Values for conventional full-span rudder effectiveness were obtained by modification of wind tunnel test result for the similar G-3A rudder configuration (References 2-4, Subsection 8.3.3.5), to account for differences in vehicle geometry. Flared rudder effectiveness in the supersonic speed regime was obtained by utilizing both two-dimensional supersonic theory and wind tunnel test results on the undeflected flared rudder (Reference 5, Subsection 8.3.3.5).

H-33 Orbiter aileron effectiveness as a function of Mach number is presented in Fig. 8.3.3-34 through 8.3.3-36. The data presented were obtained from wind tunnel test results on the G-3A configuration, (References 2 and 3, Subsection 8.3.3.5) modified to account for differences in vehicle geometry.

8.3.3.3.3 Dampin Derivatives

Longitudinal and lateral-directional damping derivatives were estimated using the methods presented in Datcom and are based on the H-33 static aerodynamic characteristics presented in this report. Extrapolations were used to provide coverage for those regions were general methods are inadequate or unavailable.

The longitudinal pitching and acceleration derivatives are presented in Fig. 8.3.3-37 and 8.3.3-38.

The rolling and yawing derivatives are presented in Fig. 8.3.3-39 and 8.3.3-40.

8.3.3.3.4 Ground Effects

Fig. 8.3.3-41 and 8.3.3-42 present the incremental longitudinal aerodynamic characteristics due to ground proximity. These effects are based on wind tunnel results obtained during GWTT 290.

8.3.3.3.5 Speedbrake Effects

The low-speed longitudinal effects of 30 deg split-rudder implementation for speed brakes are presented in Fig. 8.3.3-43. These data are based on results obtained during GWTT 290 for a full-span rudder. Presently it is envisioned to use only the lower portion of the rudder as a speedbrake, the exact split being determined by the incremental drag and hinge moment requirements.

8.3.3.3.6 Landing Gear Drag

The landing gear drag of the H-33 design was derived through analysis of the wind tunnel test data contained in Reference 9, Subsection 8.3.3.5.

These data are associated with a delta wing booster design having a similar landing gear installation as the Grumman H-33 design.

The landing gear drag area at the lift coefficient corresponding to L/D_{max} is 53 sq ft.

8.3.3.3.7 Engine Nacelle Drag

The air-breathing propulsion system drag for the Grumman H-33 design is based on two, twin-pod-mounted JTF22A4 engines located at fuselage station 1370. The installation of these engine nacelles were analyzed during GWTT 290. The engines and pylon mounting resulted in an incremental drag area of 2.5 sq. ft.

8.3.3.4 Flying Qualities Analysis

The bare-airframe orbiter flying qualities have been evaluated along the design trajectory shown in Fig. 8.3.3-44. Significant flight maneuvers during the entry, the dynamic pressure, angle of attack, flight path angle, and specific points on the trajectory used for this analysis are shown.

At altitudes of 300,000 ft and above the dynamic pressures are extremely low, and the vehicle is flown via the ACPS control system. Reference 6, Subsection 8.3.3.5, shows that the aerodynamic control power at dynamic pressures of 20 lb/sq ft can be comparable to the ACPS control power level. Thus, points studied began at an altitude of 255,000 ft and a dynamic pressure of about 18 lb/sq ft.

From this point a constant α = 27 deg trajectory is flown hypersonically to transition. The transition from hypersonic to conventional flight, beginning at Mach 4, is accomplished by gradually reducing angle of attack from 27 deg to 6 deg with a corresponding change in glide slope from near zero to -10 deg at Mach 2. From Mach 2 to Mach .75 an approximately constant angle of attack is maintained. The flight path angle becomes steeper through the low supersonic region until at Mach .75, it is again -10 deg and the altitude is approximately 35,000 ft. From this point a constant equivalent air speed of 240 kt is maintained to an

altitude of 2,000 ft. where the landing gear and speed brakes are deployed in preparation for landing.

The basic mass, inertia, and reference data used are presented in Table 8.3.3-2, and the aerodynamic data is described in Subsections 8.3.3.1, 8.3.3.2 and 8.3.3.3.

TABLE 8.3.3-2 H-33 REFERENCE DATA

Weight	240,000 lb
Body Axis Roll Inertia, I_{xx}	1,899,703 slug ft^2
Body Axis Pitch Inertia, I_{yy}	10,656,866 slug ft^2
Body Axis Yaw Inertia, I_{zz}	10,248,059 slug ft^2
Product of Inertia, I_{xz}	380,782 slug ft^2
Fwd cg Location at FS 1265 (65.7% ℓ_{ref} from nose)	
Aft cg Location at FS 1285 (66.9% ℓ_{ref} from nose)	
Reference Area, S_w = 4840 ft^2	
Reference Length, ℓ_{ref} = 135 ft	
Reference Span, b_{ref} = 94.5 ft	

8.3.3.4.1 Longitudinal Static Stability and Control

The basic vehicle static stability, control power, and flight path stability are described in Subsection 8.3.3.1 and 8.3.4.3.2. Two additional areas also considered are speed stability and the variation of trim elevator setting with Mach number. Speed stability about trim along the trajectory is shown in Fig. 8.3.3-45. The speed stability as shown is defined in the conventional manner; i.e., the parameter $d\delta_e/dv$ defines the ability of the vehicle to return to trim speed after being disturbed, during a constant altitude flight. The results indicate that essentially neutral speed stability occurs at the aft cg limit. Fig. 8.3.3-45 also presents the variation of trim elevon deflection with Mach number for the cg limits.

During the transition to conventional flight between Mach 4 and Mach 2 the trim elevator setting is opposite to the normal motion fo pitch-down maneuver. This is due

primarily to the relative variation with Mach number of the vehicle stability and control effectiveness. Initially a nose over maneuver (reducing angle of attack) requires a trailing edge down or positive deflection of the elevator. As the speed decreases, however, an increasing nose down moment results which requires trailing edge up elevator to reduce the rate of nose over motion. This tucking tendency continues to approximately Mach 2. From Mach 2 to Mach .75, as the pilot attempts hold a constant angle of attack, he will sense a pitch-up tendency resulting in a control stick forward motion. The impact of these effects on pilot opinion must be evaluated critically in future simulation, since the duration of the occurrence must be considered.

In Fig. 8.3.3.46, the maximum longitudinal control power is shown along with the structural g limits, and the trim g's along the design trajectory. Adequate control over the entire g-envelope of the vehicle is assured by increasing the elevon deflection from -30 deg. (low speed limit) to -10 deg at about Mach 2.0.

8.3.3.4.2 Longitudinal Dynamic Stability

The longitudinal short period dynamics of the basic vehicle is compared with suggested criteria from Reference 7, Subsection 8.3.3.5, in Fig. 8.3.3-47. The results indicate that at the most aft cg the basic vehicle longitudinal response easily satisfies level 2 rating and is very close to level 1 throughout the entry trajectory. This corresponds to acceptable or satisfactory pilot ratings. Longitudinal pitch response for the forward cg location will improve these results.

The vehicle dynamic stability in approach is compared with the corresponding criteria from Reference 7, Subsection 8.3.3.5 in Fig. 8.3.3-48. Three specific conditions were evaluated; the dead-stick approach with a speed of 240 knots and a flight path angle of -12,2 deg, a high-speed power approach with a speed of 218 knots and a flight path angle of -3 deg, and the third is a conventional power-on approach with a speed of 180 kt and a flight path angle of -3 deg. The results in Fig. 8.3.3-48 point out that all three conditions are somewhat sluggish in pitch during the approach. This area will also be evaluated on the simulator prior to addition of any augmentation which should readily alleviate the condition.

The short period damping ratio along the entry trajectory is shown in Table 8.3.3-3 along with the phugoid dynamics. The short period damping is compared with the level 2 requirement of Reference 7, Subsection 8.3.3.5. The comparison points out that below 70,000 ft altitude and Mach 2.0, the basic vehicle has acceptable pitch damping; above this altitude augmentation will be necessary.

The phugoid mode is stable throughout the trajectory and thus satisfies the requirement of Reference 7, Subsection 8.3.3.5. Fig. 8.3.3-49 compares the lift loss versus pitch control power requirements for the H-33 Orbiter at the three approach flight conditions. The comparison points out that for small control perturbations about trim the requirement is satisfied. Maximum control throw, however, cannot be practically compared, since it falls out of the range of the requirements.

8.3.3.4.3 Drag Modulation

The ability of the vehicle to maintain the approach velocity and glide slope in the presence of wind disturbances of up to 40 kt is crucial in the high-energy deadstick approach. In Fig. 8.3.4-34 of Subsection 8.3.4.3.2 the speed brake is shown to be adequately sized to satisfy this criteria.

8.3.3.4.4 Lateral-Directional Static Stability and Control

The basic vehicle lateral directional static stability, aileron, and rudder effectiveness are discussed in Subsections 8.3.3.1, 8.3.3.2, and 8.3.3.3. The lateral directional trim capability of the H-33 Orbiter is presented in Table 8.3.3-4, which shows the rudder and aileron deflections required to trim at several critical flight conditions.

8.3.3.4.5 Lateral Directional Dynamic Stability

Figure 8.3.3-50 presents the dutch roll characteristics of the basic airframe in terms of frequency and damping, and compares them with the requirements defined in Reference 7, Subsection 8.3.3.5. The results show that the vehicle basic damping is expectedly low in the hypersonic, high-angle flight regime. The requirement of Reference 7, Subsection 8.3.3.5, is satisfied in the conventional flight range (Mach $\leq$ 2.0).

TABLE 8.3.3-3 H-33 ORBITER LONGITUDINAL DYNAMIC STABILITY CHARACTERISTICS

Category *1	Case No.	h, ft	M	$\omega_{n_{sp}}$, rps	ζ_{SP} *2	nz/α g/rad	ω_{nph}, rps	ζ_{ph}	T_2, 1/2 *3 - sec
A (b)	1	255K	28.2	.1958	3.50×10^{-3}	.46	7.05×10^{-4}	.183	S
A (c)	2	240K	25.1	.2545	4.917×10^{-3}	.78	9.88×10^{-4}	.232	S
	3	225K	21.4	.3105	6.722×10^{-3}	1.16	1.35×10^{-3}	.284	S
	4	200K	14.4	.356	1.078×10^{-2}	1.53	2.17×10^{-3}	.326	S
	5	175K	11.6	.468	1.707×10^{-2}	2.64	3.45×10^{-3}	.429	S
	6	150K	7.14	.463	2.757×10^{-2}	2.58	5.56×10^{-3}	.424	S
	7	120K	3.89	.464	5.331×10^{-2}	2.59	1.09×10^{-2}	.433	S
	8	100K	3.18	.2305	.168	4.12	Non-Oscillatory		S
	9	85K	2.58	.461	.082	6.02	4.72×10^{-2}	.625	S
	10	70K	2.00	1.943	.120	8.56	1.75×10^{-2}	.771	S
	11	50K	1.12	1.572	.355	10.85	3.9×10^{-2}	.777	S
	12	35K	.747	.665	.449	8.70	4.32×10^{-2}	.209	S
	13	26K	.608	.659	520	8.45	5.54×10^{-2}	.131	S
B (b)	14	2K	.362	.69	.695	7.46	7.71×10^{-2}	.187	S
	15	1K	.329	.61	.706	6.36	8.53×10^{-2}	.105	S
	16	1K	.272	.534	.721	4.33	9.76×10^{-2}	.028	S

*1 See Ref 7, Subsection 8.3.3.5 for definition
*2 Damping requirement for level 2, $\zeta \geq .25$
*3 S = Stable

TABLE 8.3.3-4 LATERAL DIRECTIONAL STATIC TRIM

FLIGHT CONDITION	α_{TRIM}, deg	$\delta_{e_{TRIM}}$, deg	$\delta_{a_{TRIM}}$, deg	$\delta_{r_{TRIM}}$, deg	ϕ, deg	β, deg
30 Kt Crosswind T.O. h=0 V=170 Kt	13.4	-4.9	-15.0	6.8	16.7	10.0
30 Kt Crosswind Landing h=0 V=160 Kt	10.7	-4.3	-12.6	6.5	17.2	9.5
30 Kt Crosswind Landing h=2000 Ft V=240 Kt	6.4	-4.1	-7.3	4.9	22.9	7.1
$\beta=10^{o}$ V=V_{TD} h = 0 V=180 Kt	10.7	-4.3	-13.2	6.85	18.2	10.0
1 Eng. Out on T.O. h=0 V=170 Kt	13.4	-4.9	-4.3	-.1	5	2.1
$\beta=15^{o}$ in Operational Service V=180 Kt $\delta a < .75\,\delta a_{MAX}$	10.7	-4.3	-19.8	10.3	27.9	15.0
2 Eng. Out Go Around h=0 V=180 Kt	10.7	-4.3	-3.8	-1.5	5	1.2

Maximum Control Deflections:

$\delta e = -40^{o}, \pm 10^{o}$

$\delta a = \pm 20^{o}$ $(M \geq 4.)$

$= \pm 50^{o}$ $(M < 4.)$

$\delta R = \pm 35^{o}$

Table 8.3.3-5 is a tabulation of the other characteristic roots of the lateral directional mode, also included is the ϕ/β ratio of the dutch roll mode. This value indicates the basic vehicle tends to be sensitive to a lateral gust. The high level of ϕ/β tends to overwhelm the significance of the roll time constant's conventional implications. This term is tabulated, however, and compared with maximum values from Reference 7, Section 8.3.3.5. The requirement is met below Mach 2.0.

The spiral mode is stable and thus satisfies the requirement of Reference 7, Subsection 8.3.3.5. Hypersonically, there exist flight conditions where the spiral and roll modes tend to combine into a second oscillatory mode called the lateral directional phugoid. The period of this mode is extremely long and therefore should not present a problem.

TABLE 8.3.3-5 H-33 ORBITER LATERAL DIRECTIONAL DYNAMIC STABILITY CHARACTERISTICS

Flight Condition	Altitude, ft	Mach	τ_i + ~sec	τ_s ~sec	ϕ/β	$\omega\phi/\omega_{nd}$	$\zeta\phi/\zeta_d$	$\omega_{L/D_{ph}}$, rps	$\zeta_{L/D}$	$T_{L/D}$ sec
1	255,000	28.2	260.	2,410.	3.94	*	*	-	-	-
2	240,000	25.0	331.	882.	3.94	*	*	-	-	-
3	225,000	21.4	-	-	3.94	*	*	.00253	.787	4016.
4	200,000	14.4	-	-	3.94	*	*	.00406	.582	1904.
5	175,000	11.6	-	-	3.94	*	*	.00641	.201	1001.
6	150,000	7.1	-	-	3.94	*	*	.0103	.214	622.
7	120,000	3.9	-	-	3.94	*	*	.0198	.209	324.
8	100,000	3.2	-	-	6.54	*	*	.0319	.679	269.
9	85,000	2.6	12.9	38.4	4.93	.842	.911	-	-	-
10	70,000	2.0	5.15	43.0	5.31	.833	.676	-	-	-
11	50,000	1.1	1.99	18.8	10.0	.900	.755	-	-	-
12	35,000	.75	1.64	42.6	5.32	.923	.950	-	-	-
13	26,000	.61	1.36	37.5	5.12	.910	.985	-	-	-
14	2,000	.36	.945	21.9	4.84	.910	1.13	-	-	-
15	1,000	.33	1.01	24.4	4.49	.850	1.22	-	-	-
16	1,000	.27	1.26	22.0	3.84	.740	1.65	-	-	-

*All Real Roots

+ τ_r requirement from Ref 7, Subsection 8.3.3.5, Level 1 $\tau_r < 1.4$

Level 2 $\tau_r < 3.0$

The levels of $\omega\phi/\omega_{n_d}$ as well as $\zeta\phi/\zeta_d$ in the conventional flight regime give an indication of the relative location of the zeros to the poles in the roll rate to aileron transfer function. The relative location indicates the pilot induced oscillation is unlikely. Further indications of the roll rate response dynamics of the basic vehicle is shown in the time response to a step aileron input in Fig. 8.3.3-51 at the approach flight conditions (240 kt and 2000 ft), which points out the ample lateral control power, low roll time constant and low time to bank to 30 deg.

8.3.3.4.6 Basic Vehicle Controllability in Presence of Atmospheric Disturbance

In a preliminary effort to access the adequacy of the aerodynamic control power during entry through atmospheric wind shears, the basic vehicle response to a ramp gust was determined. The vehicle response to a wind shear of 7.85 ft/sec per 1000 ft altitude, at a 50,000 ft altitude are presented in Fig. 8.3.3-52 and 8.3.3-53 for both the longitudinal and lateral directional mode respectively. This flight condition corresponds to the lowest forward vehicle velocity in the high-wind shear region on the trajectory. The wind shear can be related to the ramp gust disturbance in both α and β via the vehicle's rate of descent and forward velocity. This ramp is only $.23^{o}$/sec, which is a very gradual increase in either α gust or β gust. As a result, no difficulty was expected which was borne out in the figures. The α and β traces shown correspond to the incremental angular change from the initial zero gust flight path direction. The acceleration time histories vividly reflect the vehicle's ability to align itself with the wind. From the magnitude of the maximum acceleration levels, no acute dynamic situation that the aerodynamic control cannot handle in flight through this regime is expected. A more detailed 6 DOF simulation will be made to confirm this preliminary finding.

8.3.3.4.7 Additional Hypersonic Flying Qualities Considerations

Further insight to the basic vehicle flying qualities can be obtained by evaluating the vehicle response to a miscoordinated roll input; (i.e., the roll input acceleration vector is misaligned with respect to the velocity vector by an angle α_ϵ). This appears to be the most likely cause of error disturbance since gust disturbances in the high altitude/ hypersonic flight are expected to be minimal. Fig. 8.3.3-54 compares the H-33 Orbiter

lateral directional characteristics during entry with various limits. For example, the boundary at which an incipient roll reversal may occur during a 5 deg miscoordinated roll input and the boundary where the maximum sideslip angle in the response will be 5 deg (assumed thermal constraint) are noted. Also noted on the figure is the bound where the dutch roll frequency is equal to .5 rad/sec. This figure shows at which point in the entry trajectory the vehicle will possess the characteristics noted by these boundaries if a 5 deg miscoordinated roll input is made. Subsequent attitude error studies discussed in Section 8.3.4 indicate expected errors to be less than 5 deg during entry.

8.3.3.4.8 Six-Degree of Freedom Flying Qualities Analysis

Due to the high angle-of-attack during the hypersonic flight regime, coupling of both the longitudinal and the lateral directional modes exist. A joint Grumman-Dornier study effort to evaluate the flying qualities of the basic vehicle with various proposed control systems has been completed; the results are described in detail in Reference 8, Subsection 8.3.3.5. Some of these results are presented in Fig. 8.3.3-55 through 8.3.3-62.

The data used in this analysis is for an earlier configuration with and without ventral fin. The results are representative of the H-33 Orbiter. Fig. 8.3.3-55 shows the 6 DOF response of the bare airframe to a finite pulse input from the lateral stick with and without an aileron to rudder interconnect (ARI). The finite pulses were opposite in sign for the two cases, but of equal magnitude, sufficient to give an approximate 5 deg/sec roll rate ($\dot{\Phi}_V$ = 5 deg/sec) about the velocity vector. This figure points out that without an aileron to rudder interconnect, the ventral-on configuration would result in an undamped oscillation, at an essentially constant angle of attack. The effect of the ARI is to give a better roll rate response as seen in the $\dot{\Phi}_V$ trace, but the inertia coupling is stronger resulting in an angle of attack oscillation.

The angle of attack oscillation is an important consideration since the present guidance scheme assumes constant angle of attack. This angle of attack variation can couple with the guidance logic causing excessive bank reversal to maintain trajectory control.

The effect of a stability augmentation system (SAS), described in Subsection 8.3.4.2.10 which utilizes aerodynamic controls about all axes (assuming a movable ventral), is shown in Fig. 8.3.3-56. The response is to a $\dot{\Phi}_V$ command of 6.3 deg/sec. The lateral response is good, but there is still a deviation in pitch from trim due to the inertia coupling. The longitudinal dynamics is well damped due to the pitch rate damper.

The Z-dap response to a bank angle and a velocity roll rate command are shown in Fig. 8.3.3-57 and 8.3.3-58 respectively. ACPS controls were assumed in this study for yaw, roll, pitch, but the reaction engines used do not reflect the current baseline. Thus the fuel consumption shown can only be interpreted on a relative basis. Fig. 8.3.3-57 and 8.3.3-58 point out that the angle of attack oscillation is well damped, but has a limit cycle with an amplitude of .5 deg, and that the ventral-on configuration shows a significant improvement in fuel consumption over the ventral-off configuration. It is noted that a constant roll rate command is somewhat incompatible with the Z-dap phase plane logic and resulted in extraneous low amplitude oscillations. This can be remedied by redefinition of the rate input to the phase plane logic.

Fig. 8.3.3-59 and 8.3.3-60 points out the advantage of an X-dap system for the ventral-on configuration which has positive body axis static directional stability. It is interesting to note the fuel consumption is reduced by 50% from the Z-dap levels. The lateral directional response appears better and longitudinal about the same as the Z-dap.

Fig. 8.3.3-61 and 8.3.3-62 presents the Z-dap control logic with aerodynamic controls in pitch and roll and ACPS in yaw. A longitudinal SAS is included and a ventrals-off configuration is assumed. The response is excellent in both the longitudinal and the lateral directional modes for both a constant bank angle and constant roll rate command. Angle of attack returns to trim quickly and lateral directional response is good save the 3 deg maximum sideslip during the transient. Fuel consumption is reduced by 50% over the Z-dap with ACPS about all axis.

Refer to Table 8.3.3-6 for a summary of aerodynamic trade studies.

1. USAF Stability and Control DATCOM; Hoak, D. E., dated Oct. 1960, revised June 1969

2. Subsonic Aerodynamic Characteristics of the GAC Orbiter; SADSAC Data Report DMS-DR-1081; Jung, W., Francinella, M., Quan, M.; dated April 1971

3. SADSAC Data Report on the 1/75th Scale GAC Orbiter at the NASA Ames Research Center 6 ft Wind Tunnel; SADSAC Data Report DMS-DR-1112; Quan, M.; in publication

4. SADSAC Data Report on the 1/200th Scale GAC Orbiter at the GAC 26 in. Transonic Wind Tunnel; Johannesen, B.; in publication

5. SADSAC Data Report on the 1/200th Scale GAC Orbiter at the GAC 15 in. Supersonic Wind Tunnel; Johannesen, B.; in publication

6. Moore, K; GSA High-Cross-Range Shuttle Vehicle - Trade Off of ACPS and Aerodynamic Control for Entry Roll Command Guidance Maneuver: GAC Memo 552-170 MO-1 April 16, 1971

7. Staff of NASA Flight Research Center: Preliminary Flying Qualities Specification for the Space Shuttle Vehicles, January 28, 1970

8. Matecki, R.; Wuennenberg, H., Jenkins, F.: Hypersonic 6 Degrees of Freedom Flying Qualities of the Basic Orbiter with Different Stability and Control Systems. Results of the Joint GAC-Dornier Study Effort. (Space Shuttle Task Number 4). GAC Memo B 35 100 RP-106, May 28, 1971

9. SADSAC Data Report DMS-DR-1030; dated November 1970

TABLE 8.3.3-6

SUMMARY OF AERODYNAMIC TRADE STUDIES (Sheet 1 of 2)

Study	Trade Options	Results	Reference
Launch Configuration	Belly-to-Back vs. Belly-to-Belly	Belly-to-Belly offers advantages during ascent.	NA
Hypersonic Directional stability	Fuselage Forebody Design Tip Fins Ventral Fin(s)	Ventral is best Aerodynamic means for improving static directional stability	B35-170MO-76, Sect 8.3.3.2
Wing Planform Optimization	Wing Loading, Aspect Ratio, Taper Ratio, Leading Edge Sweep, Variations in center of gravity position, Subsonic Static Margin & Hypersonic Trim Margin.	Output from program results in optimum wing planform for a given set of physical and aerodynamic constraints	Grumman Computer Program
Entry Control	Aero vs ACPS	Aerodynamic controls are as effective as ACPS down to dynamic pressures of 20 lb/ft^2	552-170MO-1
Effect of Hypersonic Lateral Directional Stability Levels	Ventral vs no-Ventral	Ventrals or improved C_{n_β} increases tolerance of roll miscoordination	B35-170MO-84
Control System Effect on Vehicle Flying Qualities	Aero SAS vs Z-Dap vs. X-Dap	Preliminary results show aero control in roll & pitch & ACPS in yaw with Z-DAP looks good	B35-100 RP-106

TABLE 8.3.3-6

SUMMARY OF AERODYNAMIC TRADE STUDIES (Sheet 2 of 2)

Study	Trade Options	Results	Reference
Evaluate various Air Breathing Propulsion Systems	Four & five engine air breathing propulsion systems were traded-off with several available off-the-shelf engines.	Recommended the JTF 22-A-4 engine with four engines for orbital mission & five engines for ferry missions	NA
Parametric Study of Landing Performance	Evaluate various deceleration devices (e.g. drag chutes, speed brakes, nose wheel brakes) to determine optimum landing system	Selected (2) 30 ft dia drag chutes, split tail speed brakes, & main wheel brakes only (permits stopping on 10,000 ft FAA factored field even with one chute failed)	NA

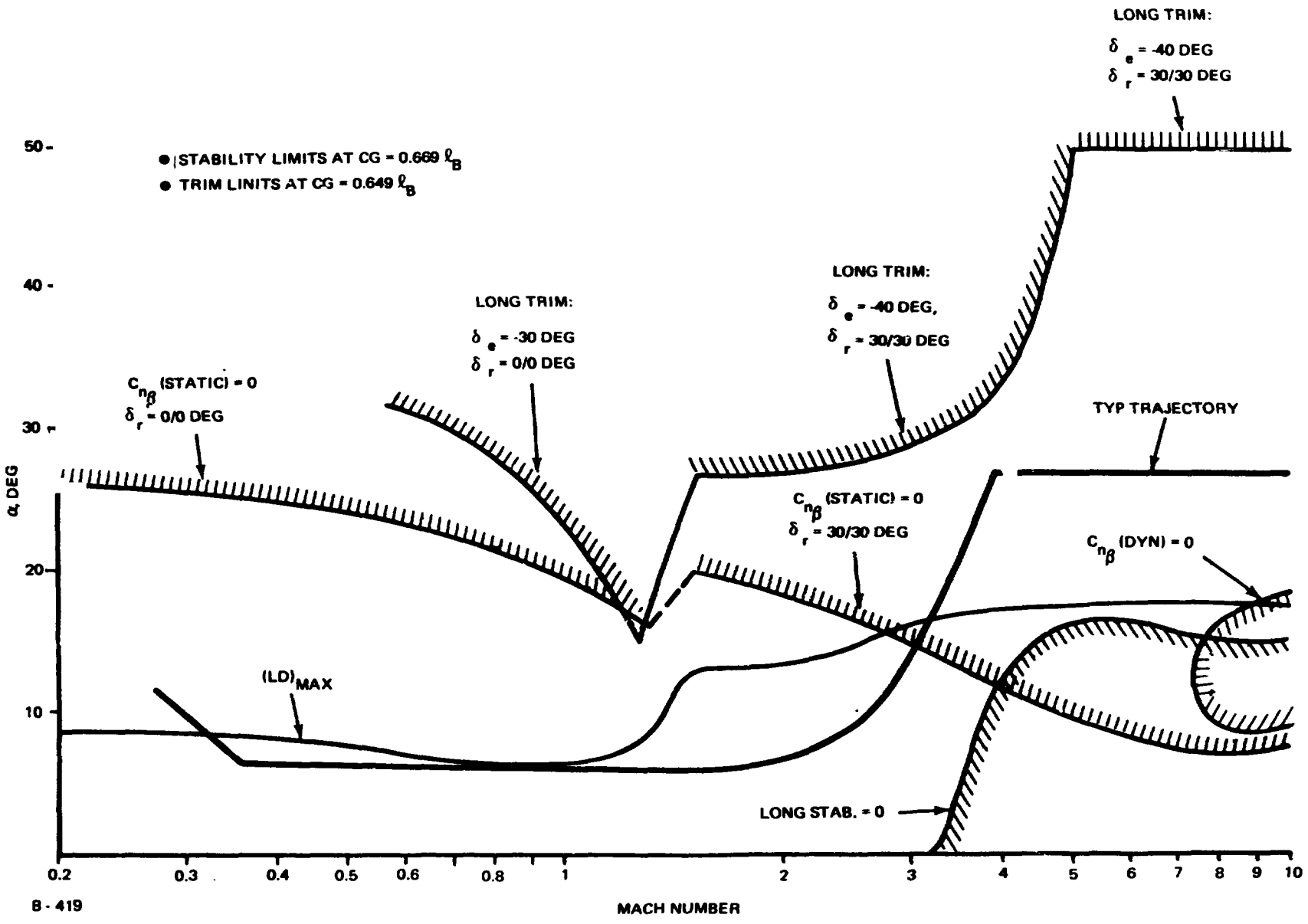

Fig. 8.3.3-1 H-33 Mach ~α Envelope

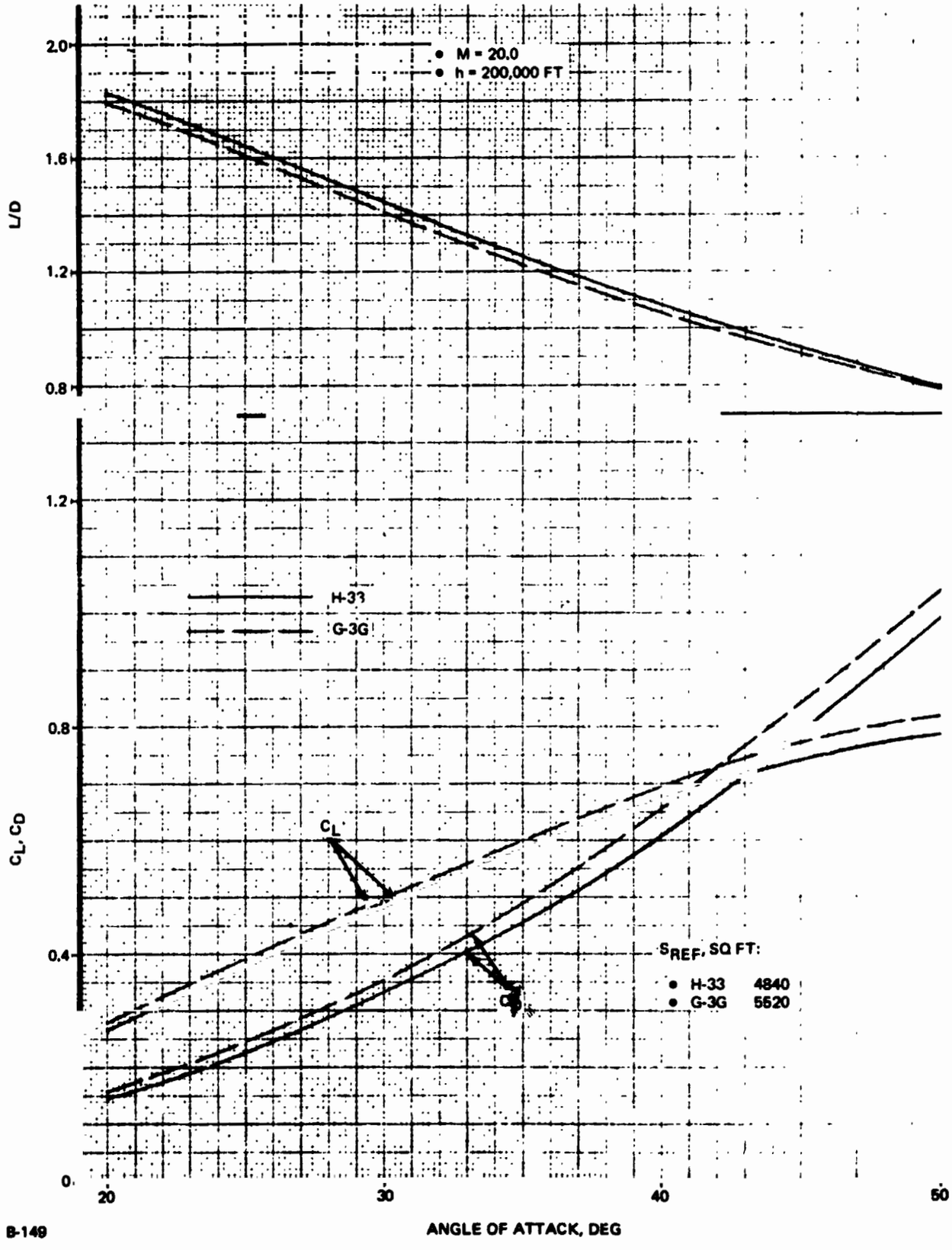

Fig. 8.3.3-2 Hypersonic Longitudinal Performance Characteristics, Trimmed

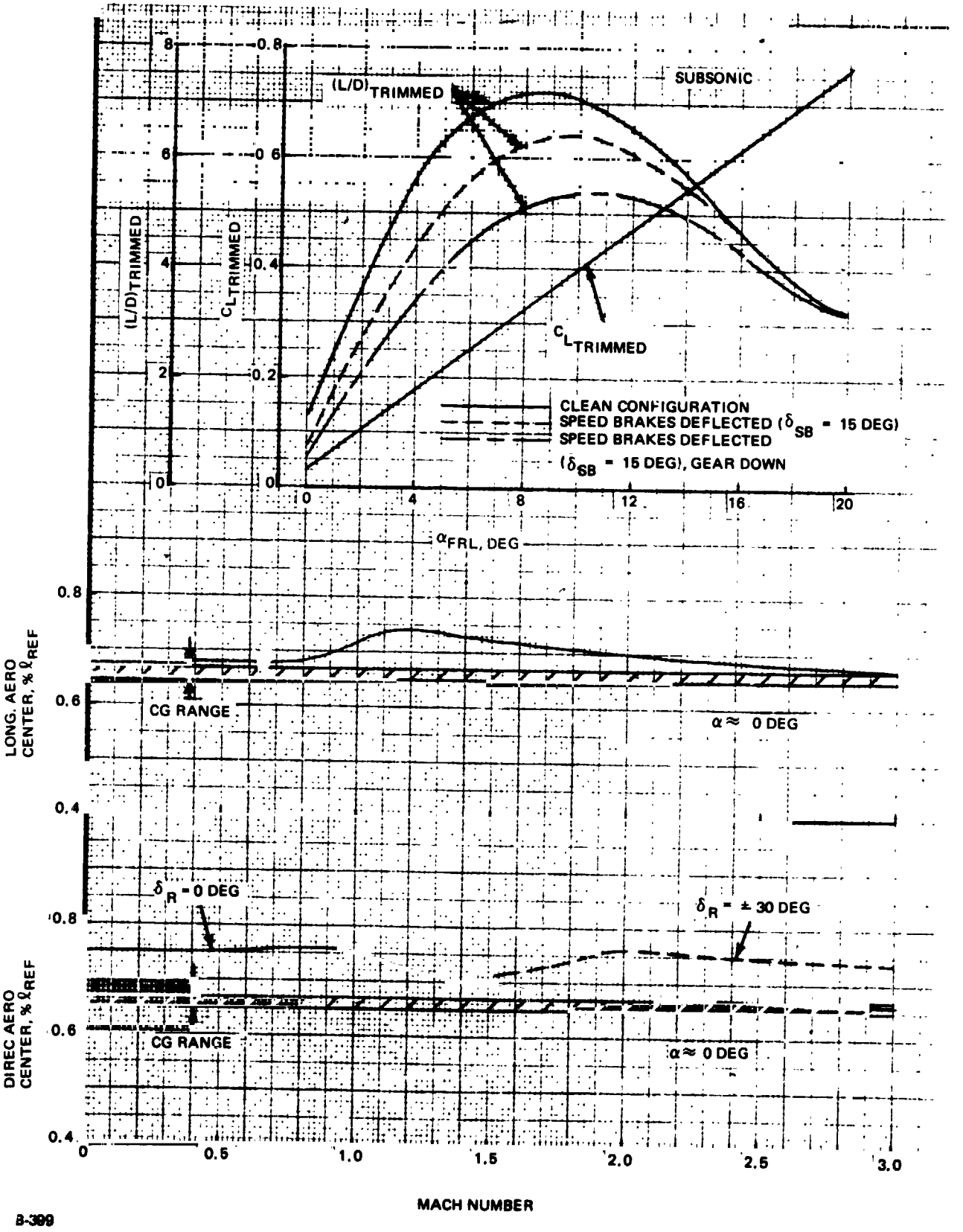

Fig. 8.3.3-3 H-33 Orbiter Post Entry Aerodynamic Characteristics Summary

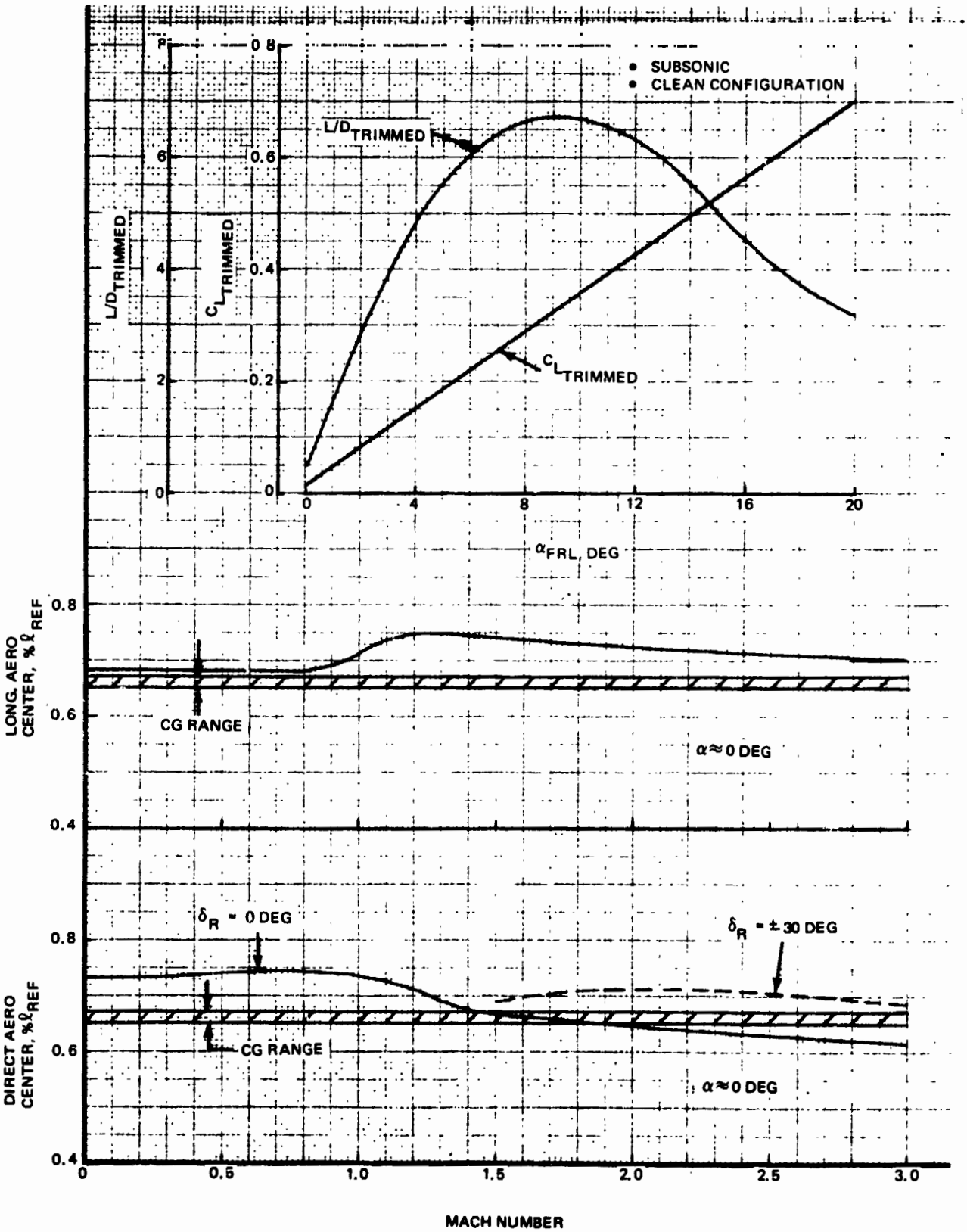

B-398

Fig. 8.3.3-4 G-3G Orbiter Post Entry Aerodynamic Characteristics Summary

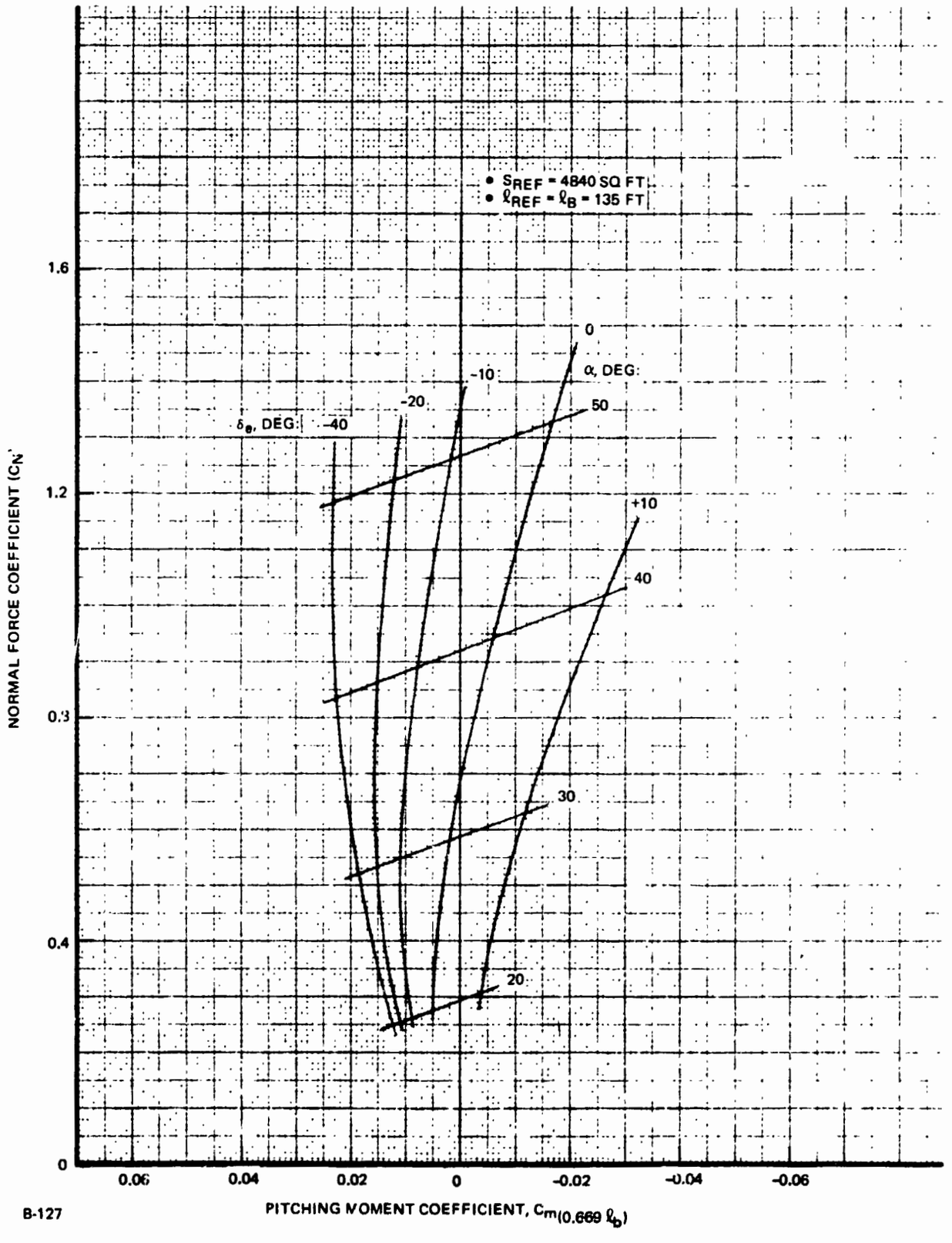

Fig. 8.3.3-5 H-33 Hypersonic Longitudinal Stability and Control

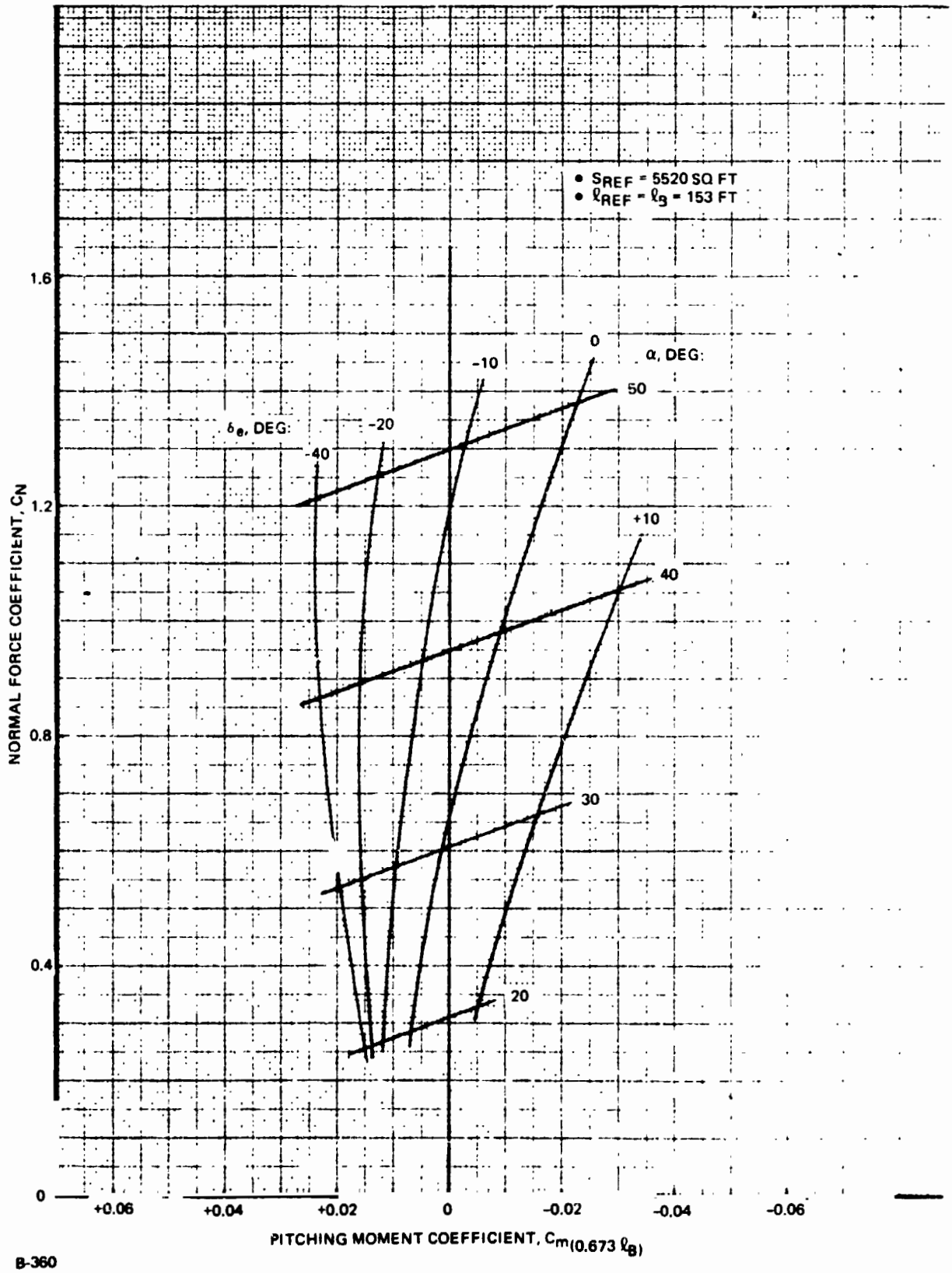

Fig. 8.3.3-6 G-3G Hypersonic Longitudinal Stability and Control

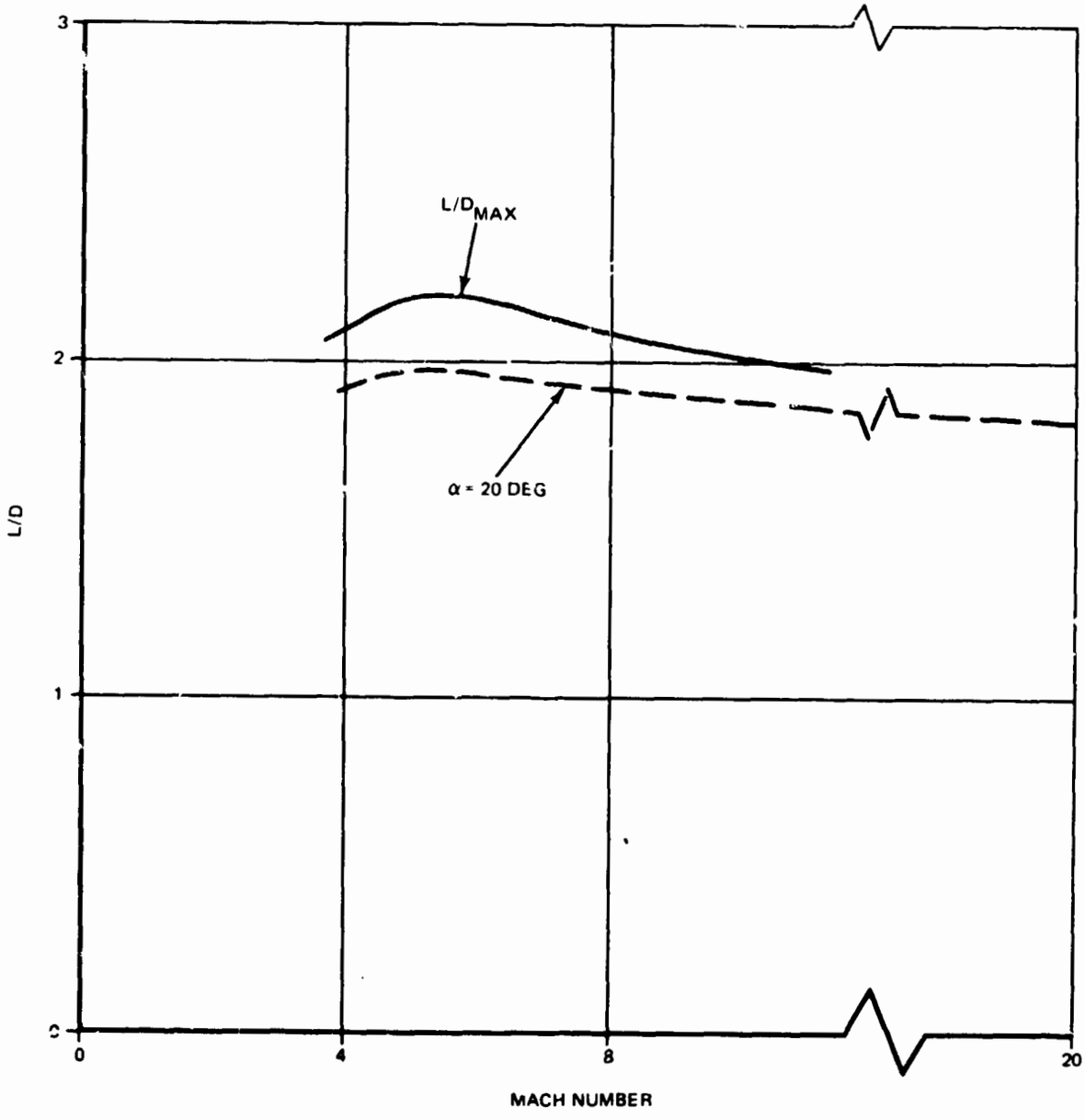

Fig. 8.3.3-7 Variation of H-33 Lift-Drag Ratio With Mach No.

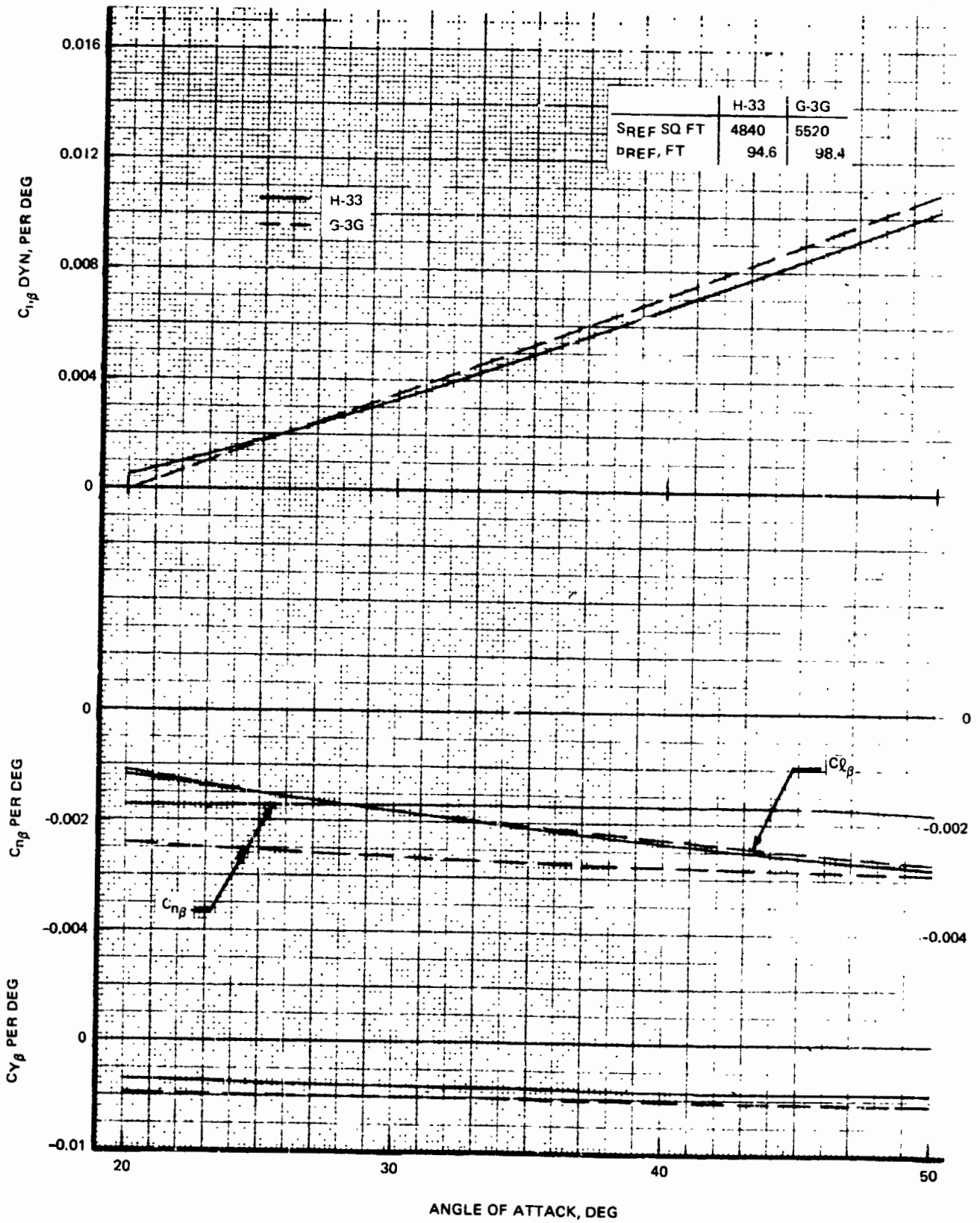

Fig. 8.3.3-8 Hypersonic Lateral-Directional Stability, Body Axis

B-112

B

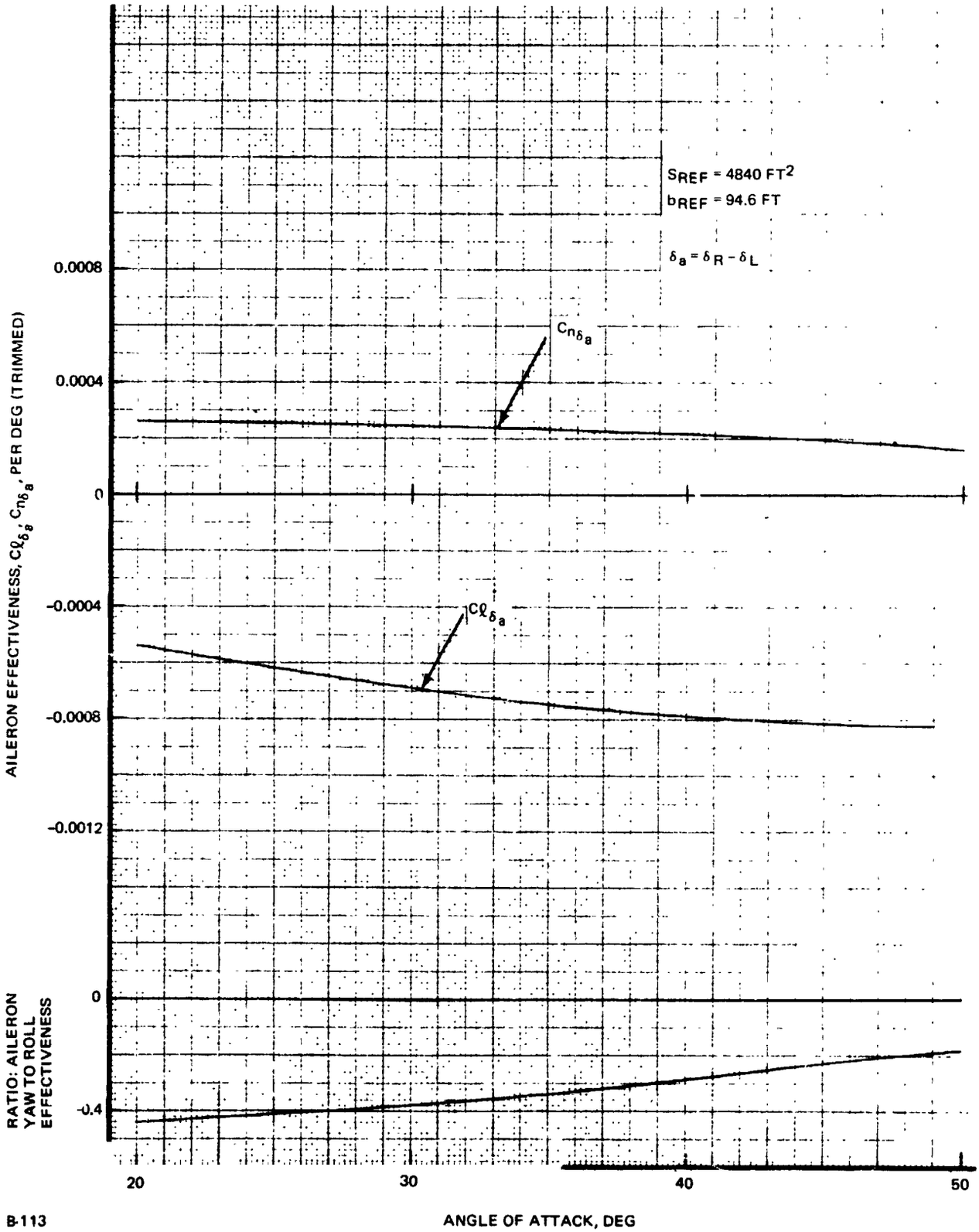

Fig. 8.3.3-9 H-33 Hypersonic Aileron Effectiveness, Body Axis

GRUMMAN
BOEING

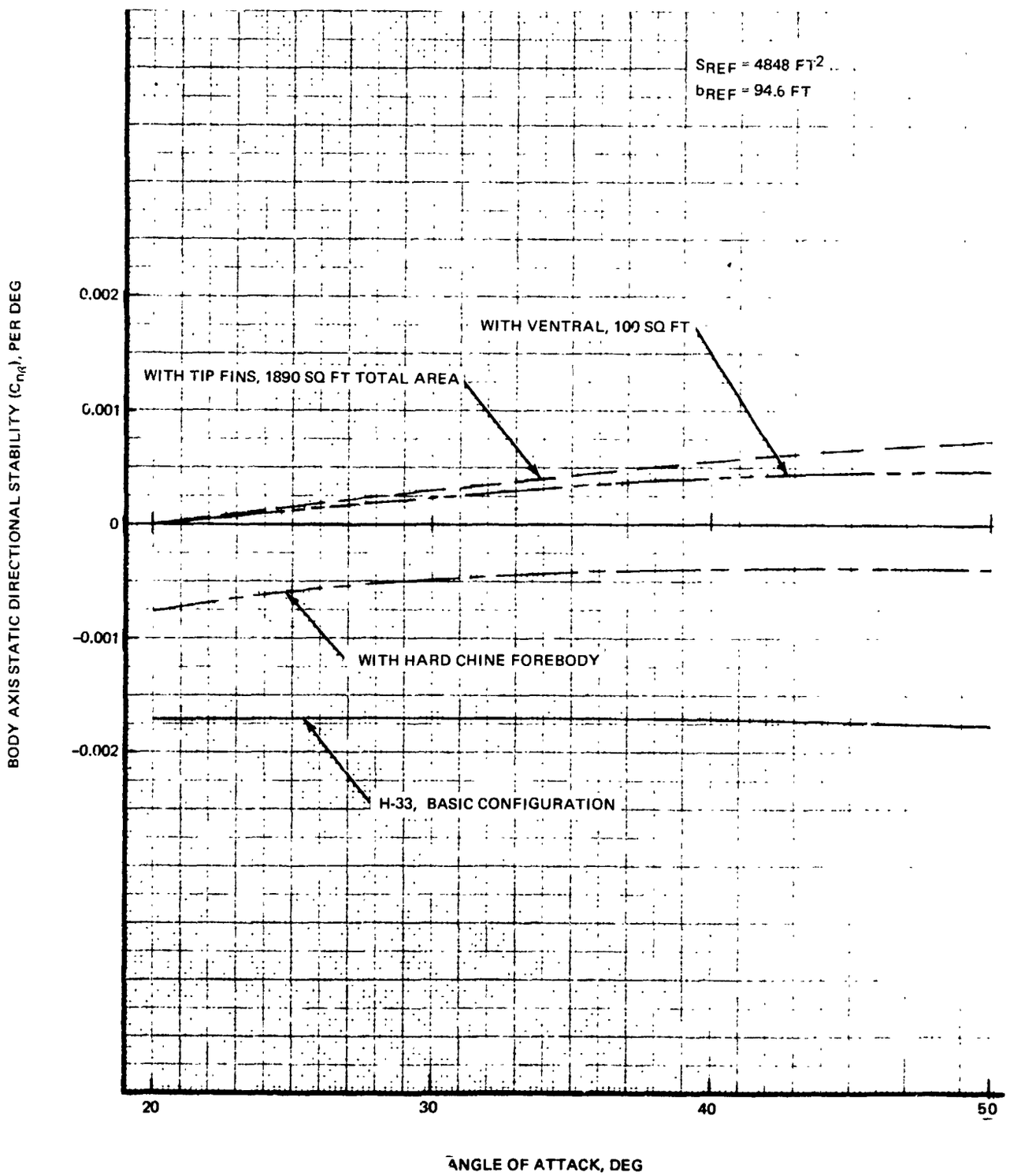

B-111

Fig. 8.3.3-10 Aerodynamic Trade-Offs, Hypersonic Directional Stability

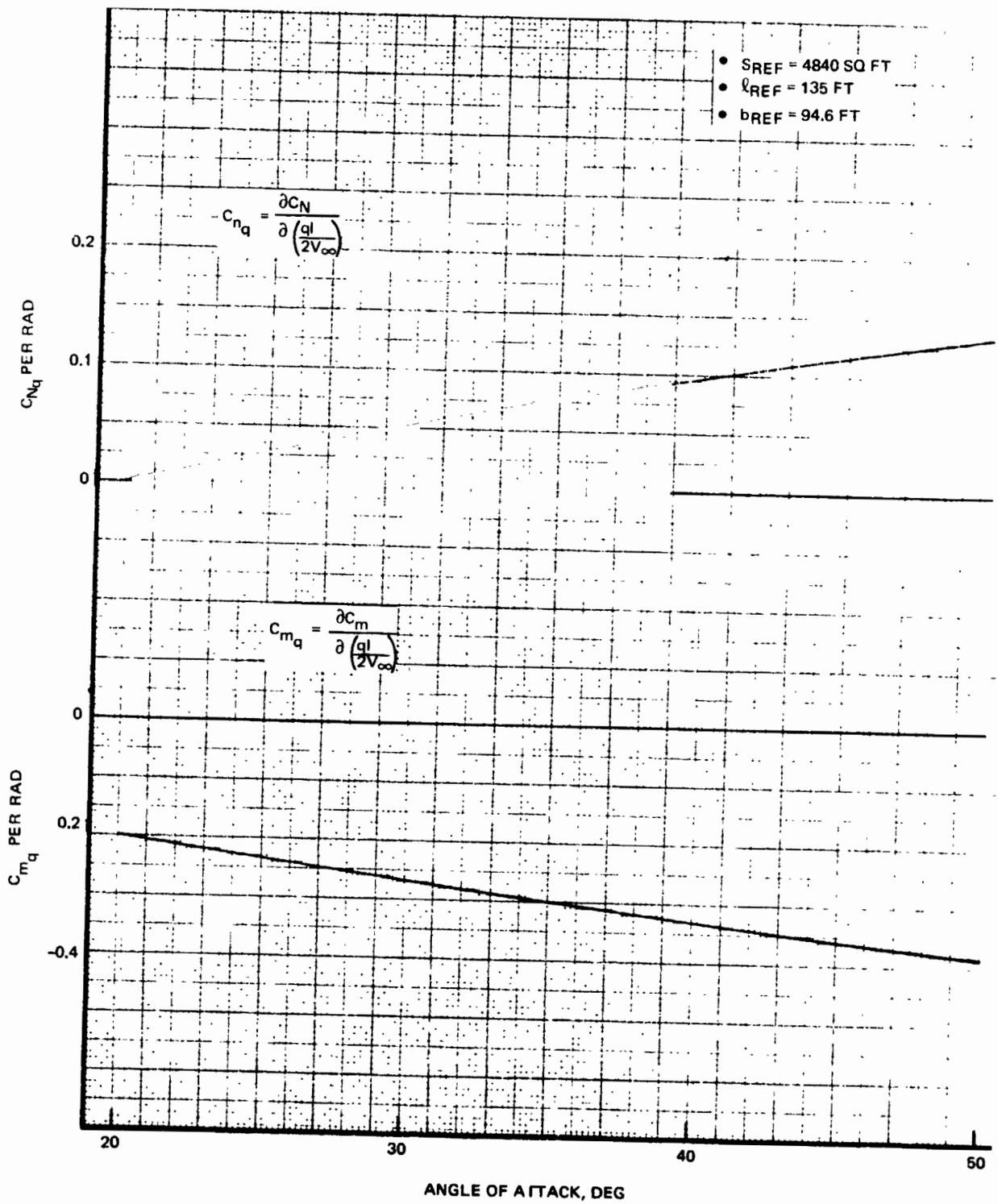

B-147

Fig. 8.3.3-11 H-33 Hypersonic Longitudinal Dynamic Derivatives

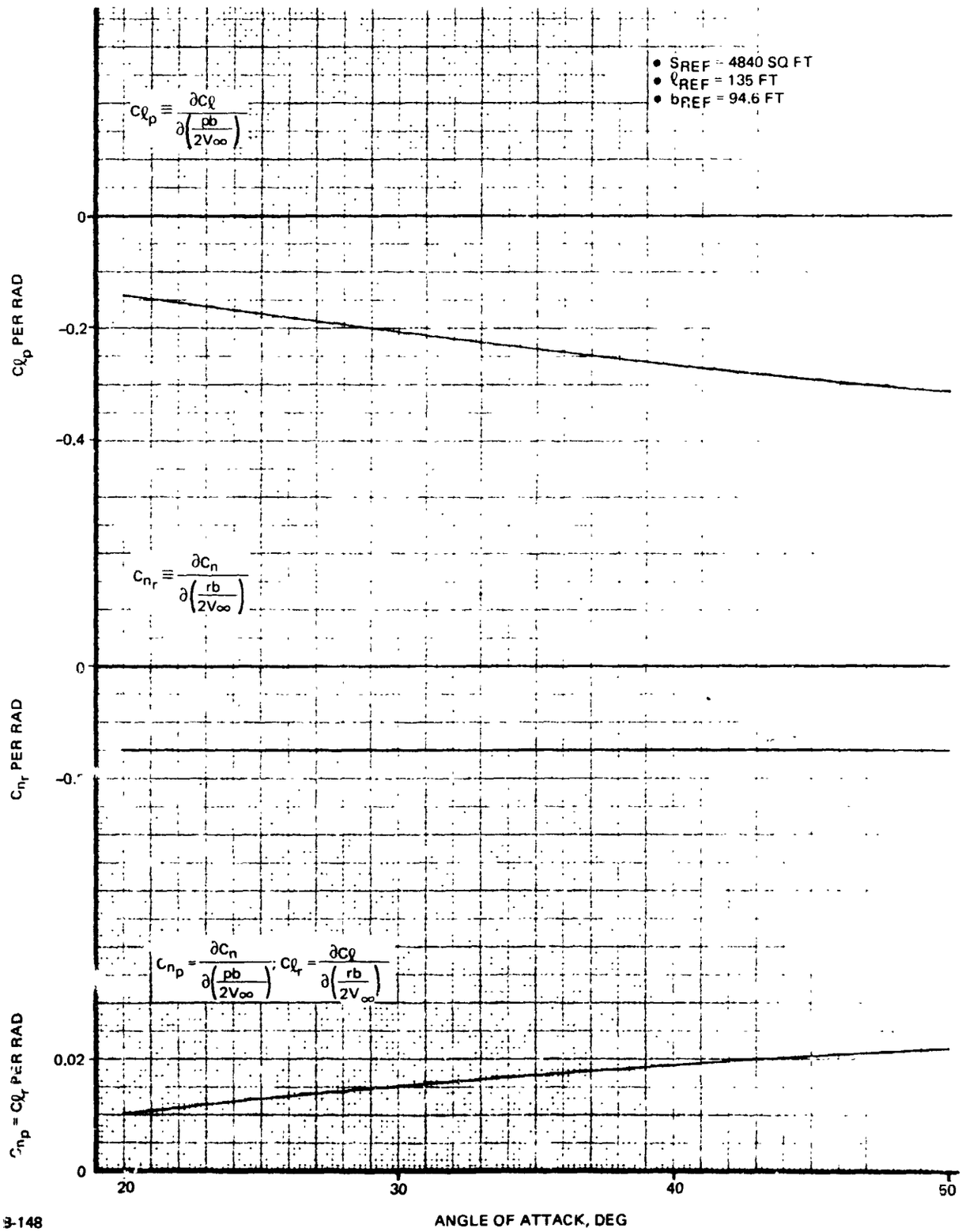

Fig. 8.3.3-12 H-33 Hypersonic Lateral-Directional Dynamic Derivatives

FOLDOUT FRAME 1

B/8.3

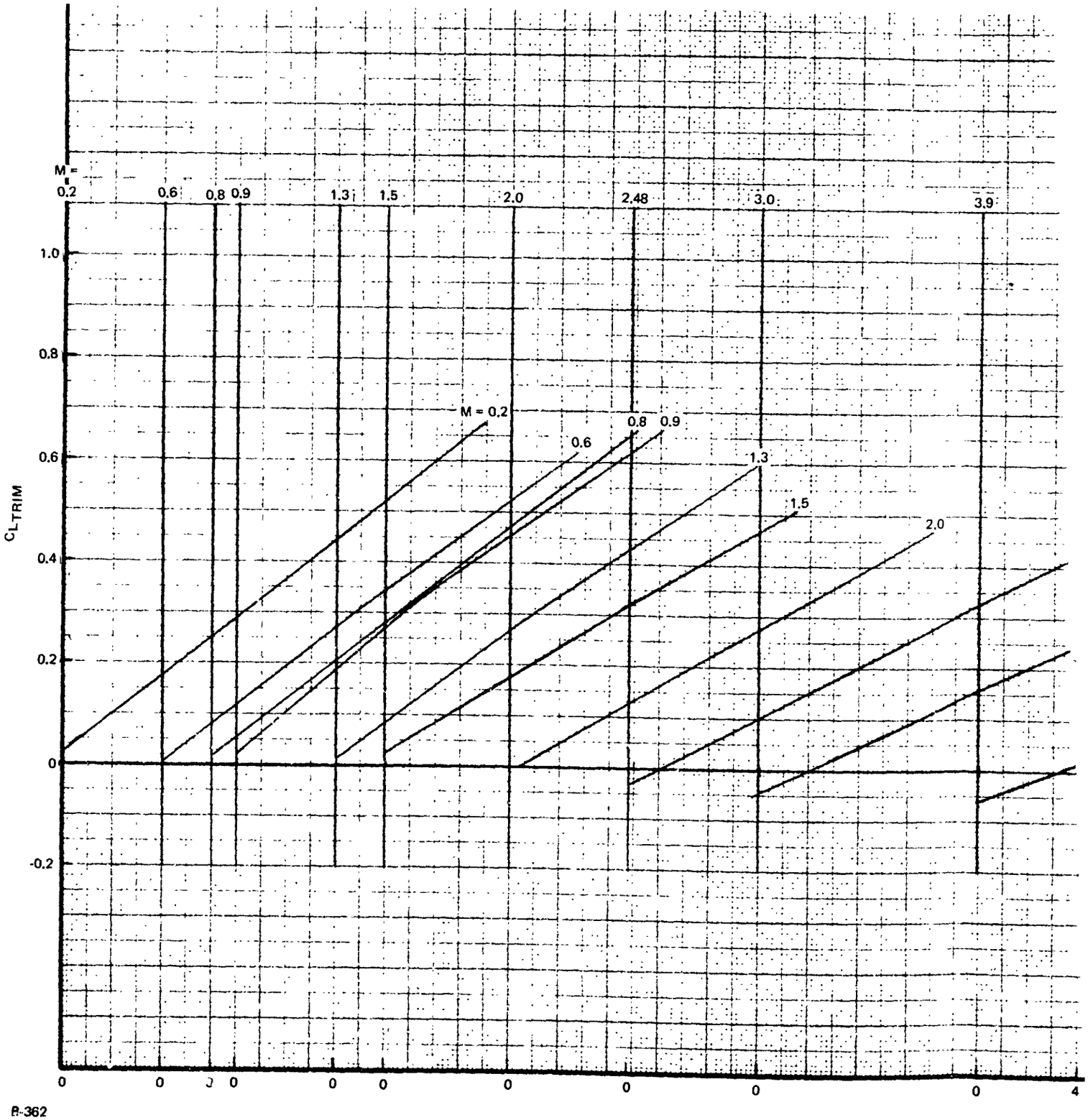

B-362

FOLDOUT FRAME 2

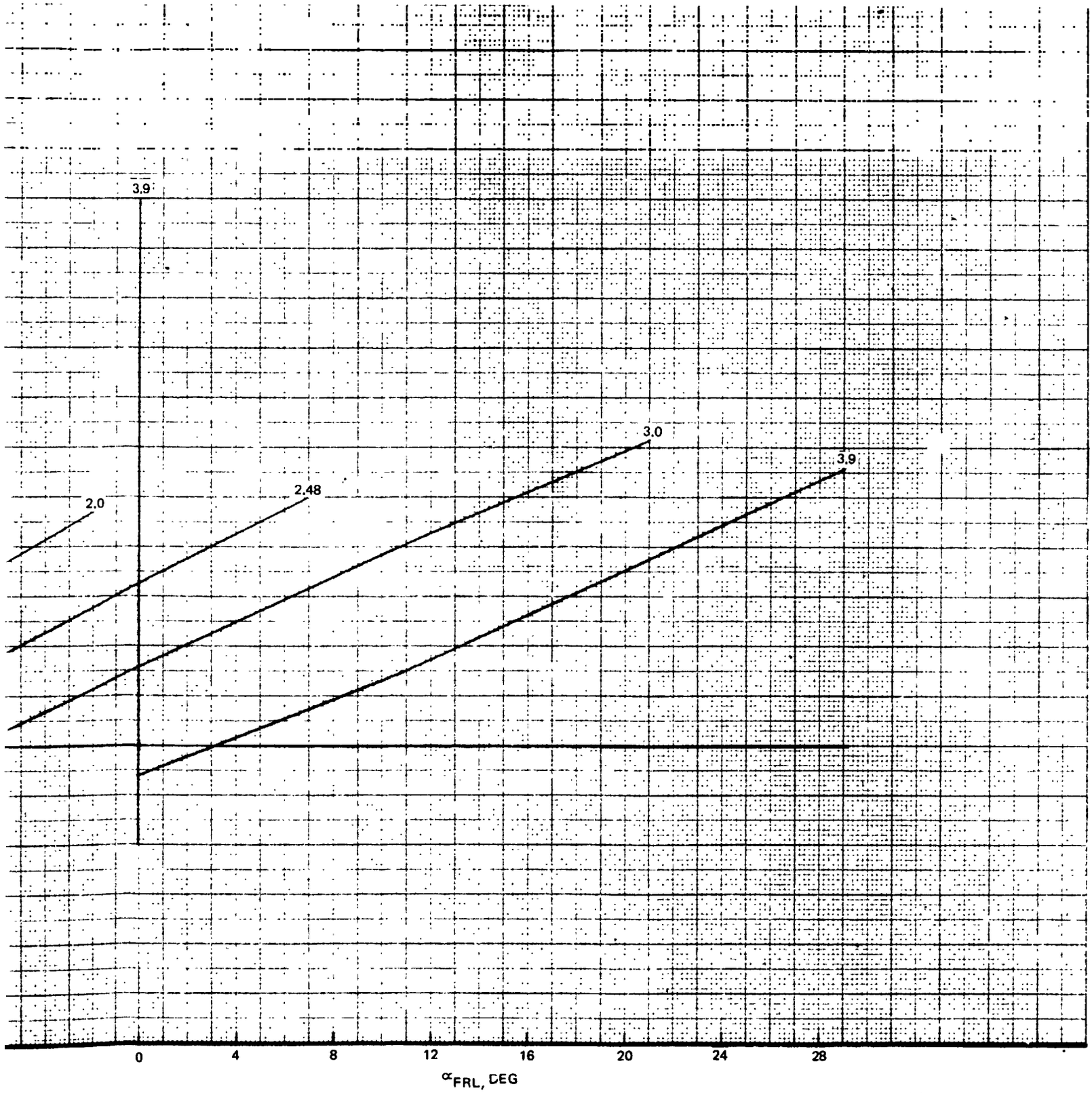

Fig. 8.3.3-13 H-33 Orbiter Trimmed Lift Characteristics

GRUMMAN BOEING

FOLDOUT FRAME |

B/8.3

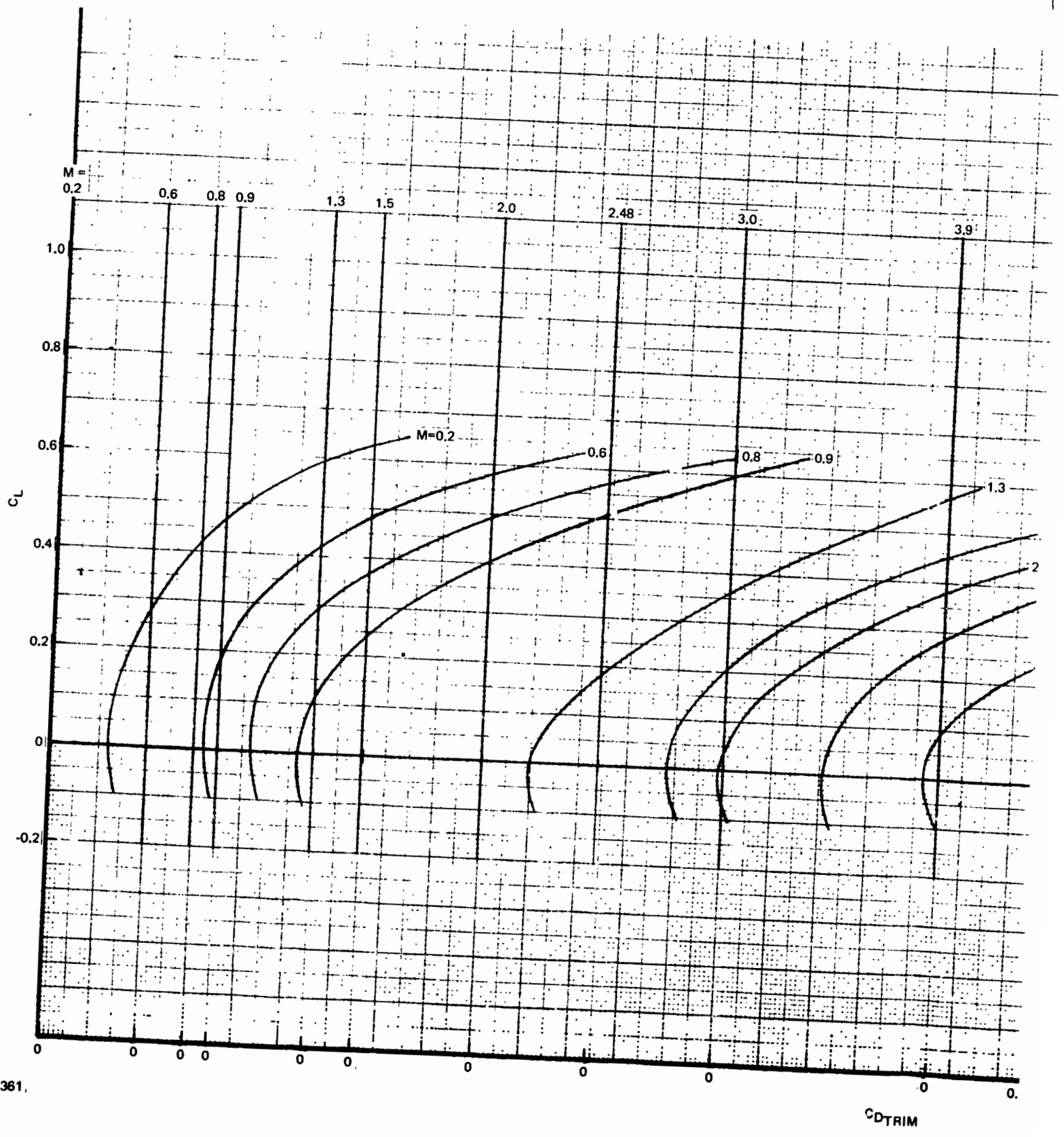

B-361,

FOLDOUT FRAME 2

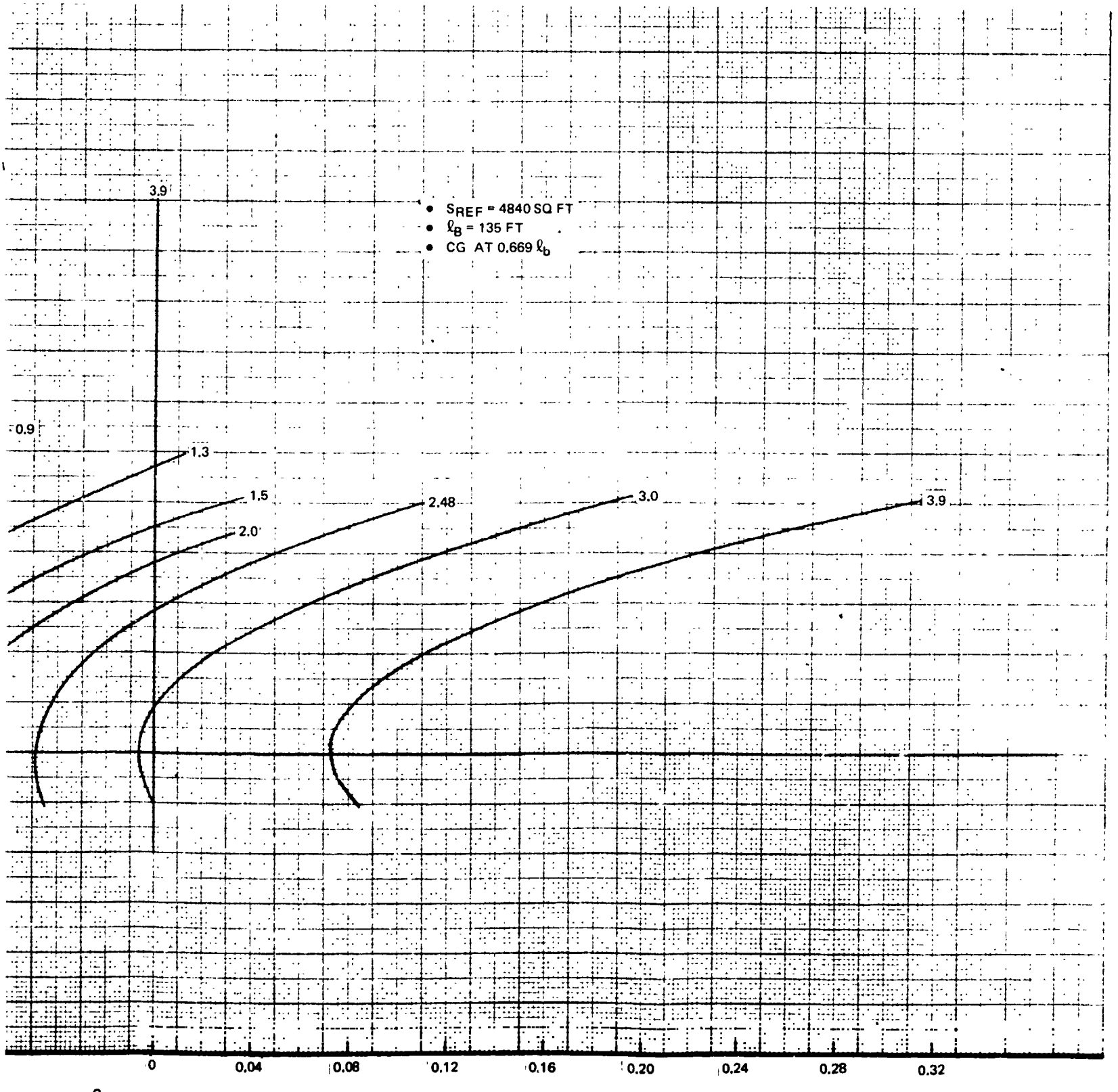

Fig. 8.3.3-14 H-33 Orbiter Trimmed Drag Polars

GRUMMAN
BOEING

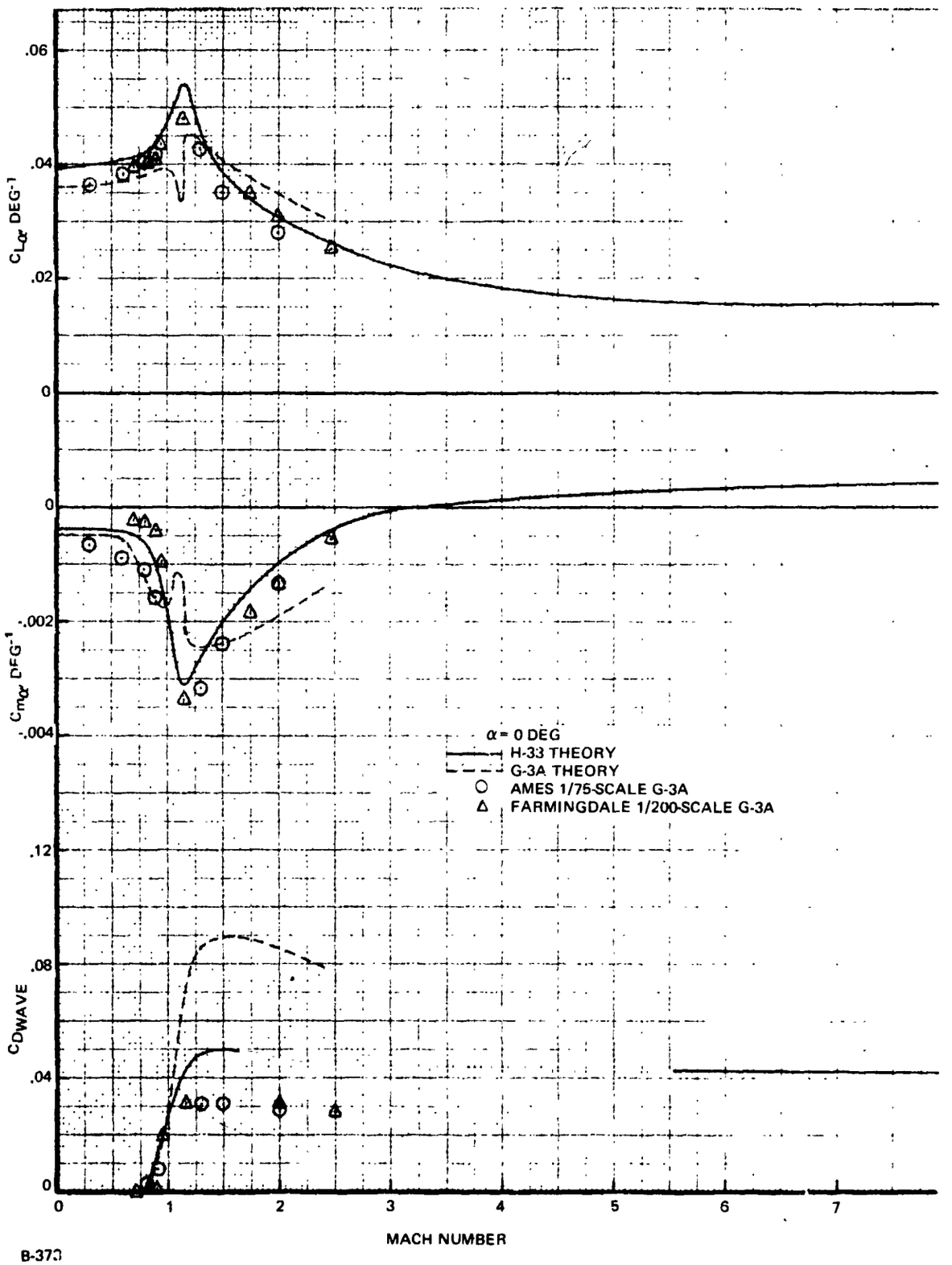

Fig. 8.3.3-15 H-33 Orbiter Longitudinal Characteristics

FOLDOUT FRAME 1

B/8.3

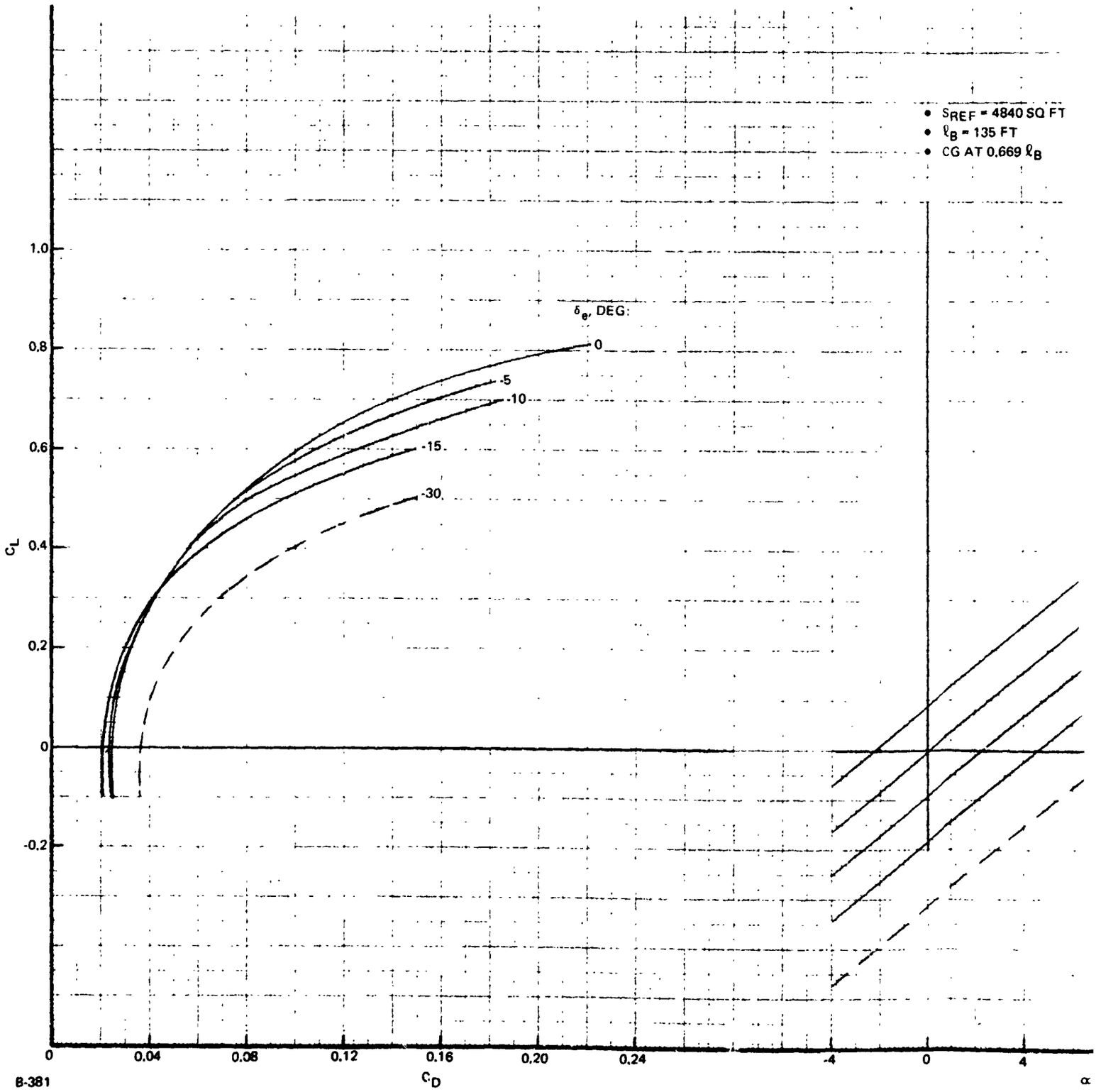

B-381

FOLDOUT FRAME 2

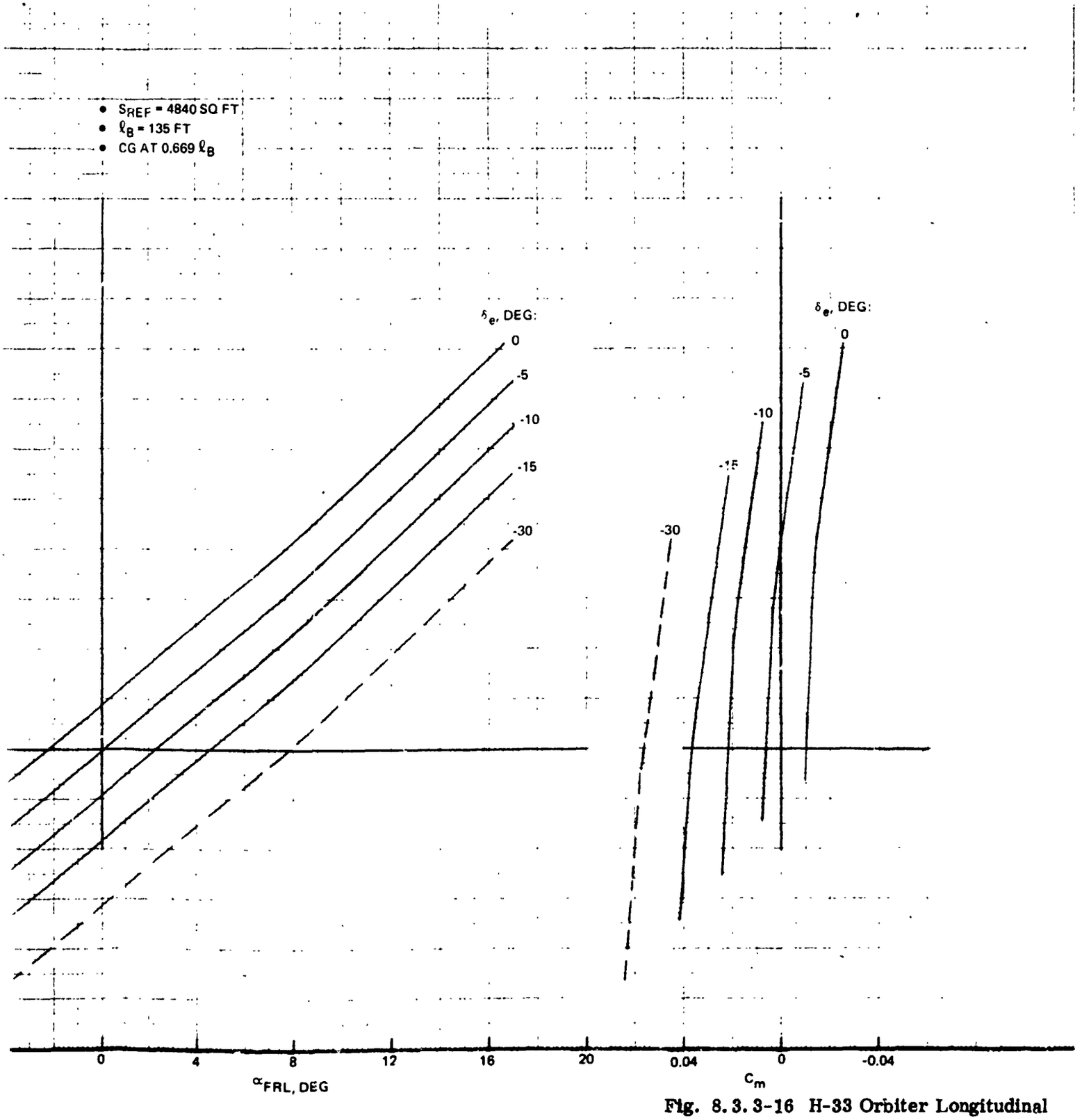

Fig. 8.3.3-16 H-33 Orbiter Longitudinal Aerodynamic Characteristics, Mach=0.2

GRUMMAN BOEING

FOLDOUT FRAME |

B/8.3

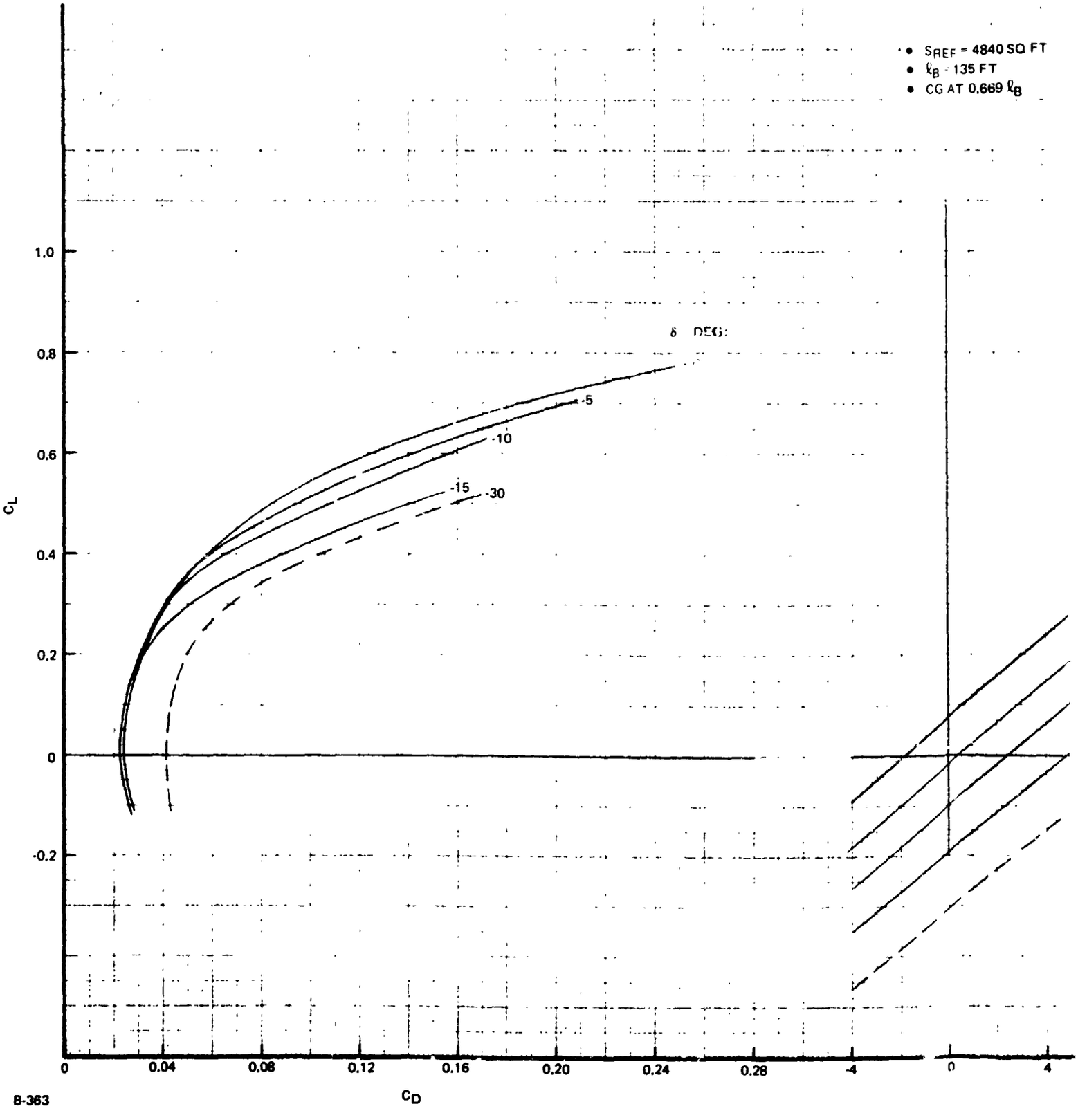

B-363

FOLDOUT FRAME 2

- S_{REF} = 4840 SQ FT
- ℓ_B = 135 FT
- CG AT 0.669 ℓ_B

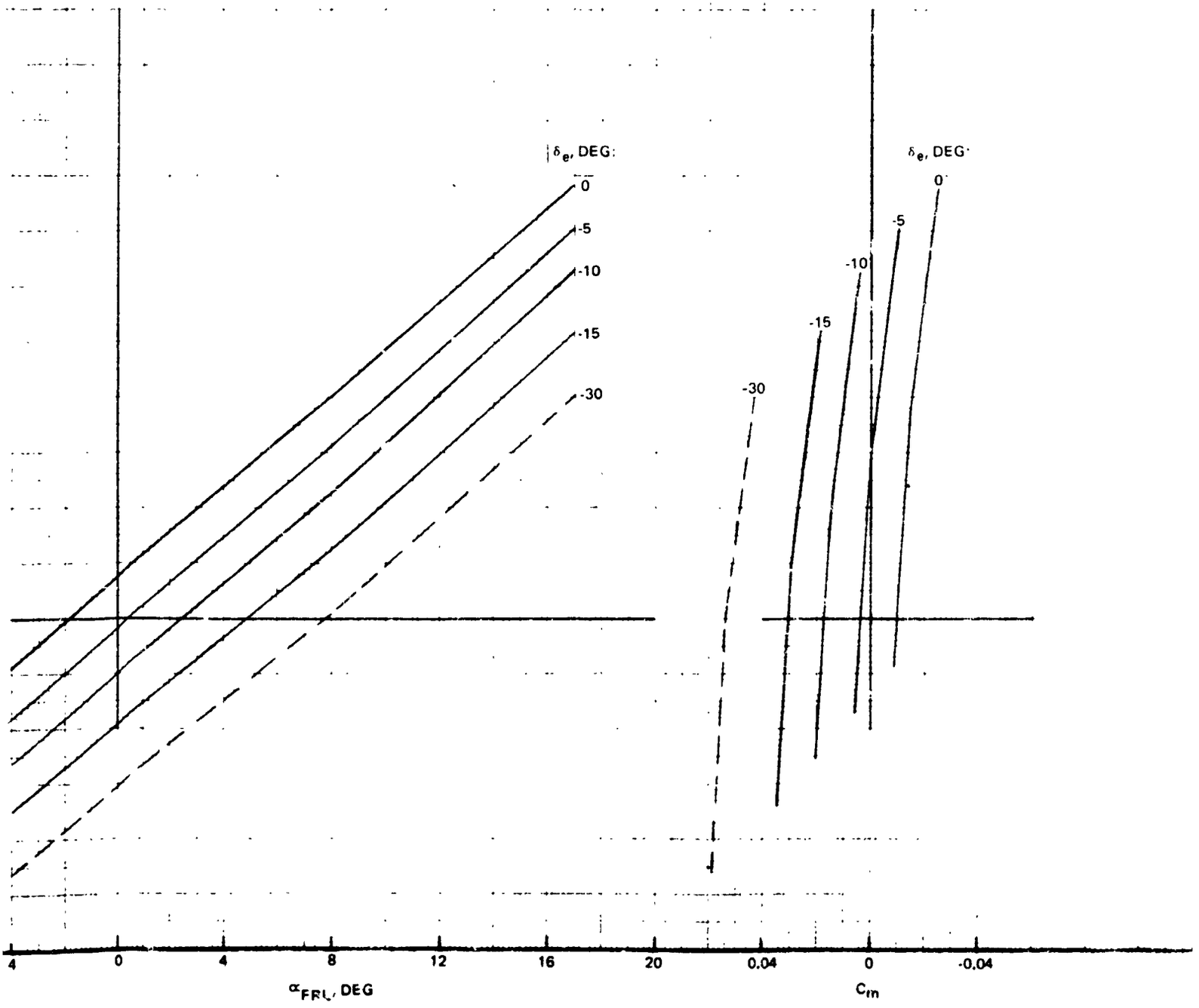

Fig. 8.3.3-17 H-33 Orbiter Longitudinal Aerodynamic Characteristics, Mach = 0.6

FOLDOUT FRAME

B/8.3

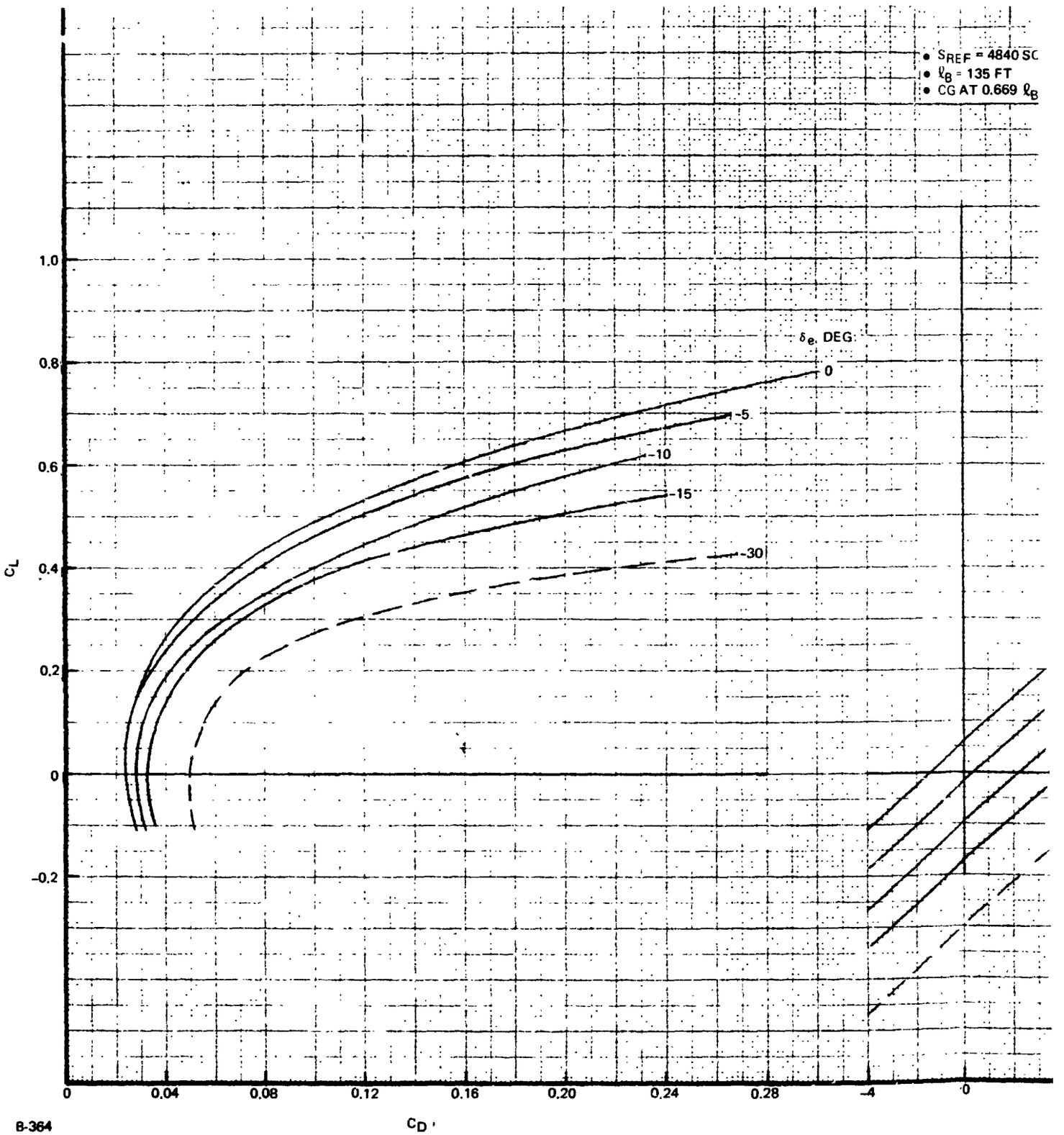

FOLDOUT FRAME 2

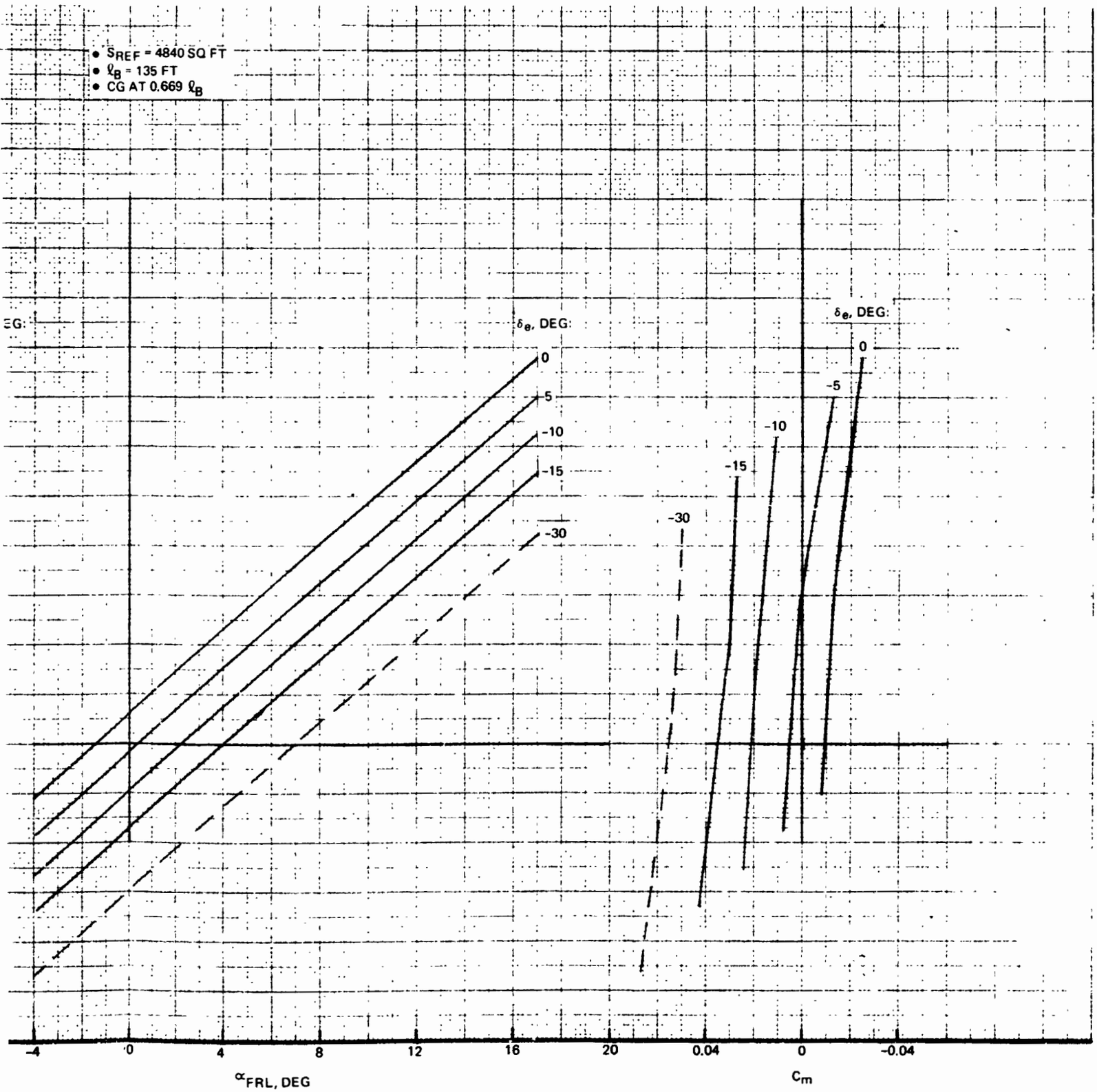

Fig. 8.3.3-18 H-33 Orbiter Longitudinal Aerodynamic Characteristics, Mach = 0.8

GRUMMAN
BOEING

FOLDOUT FRAME

B/8.3

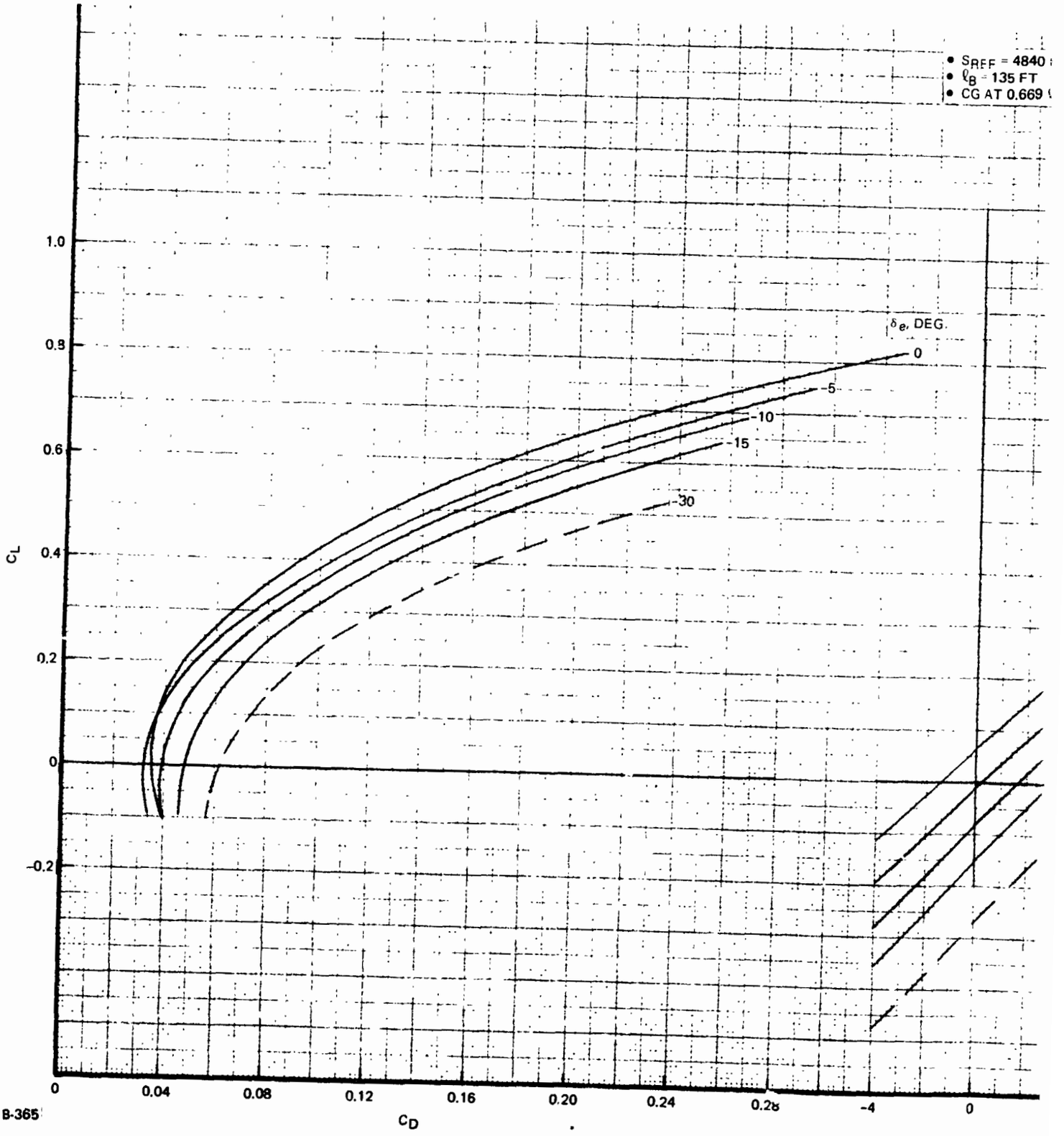

FOLDOUT FRAME 2

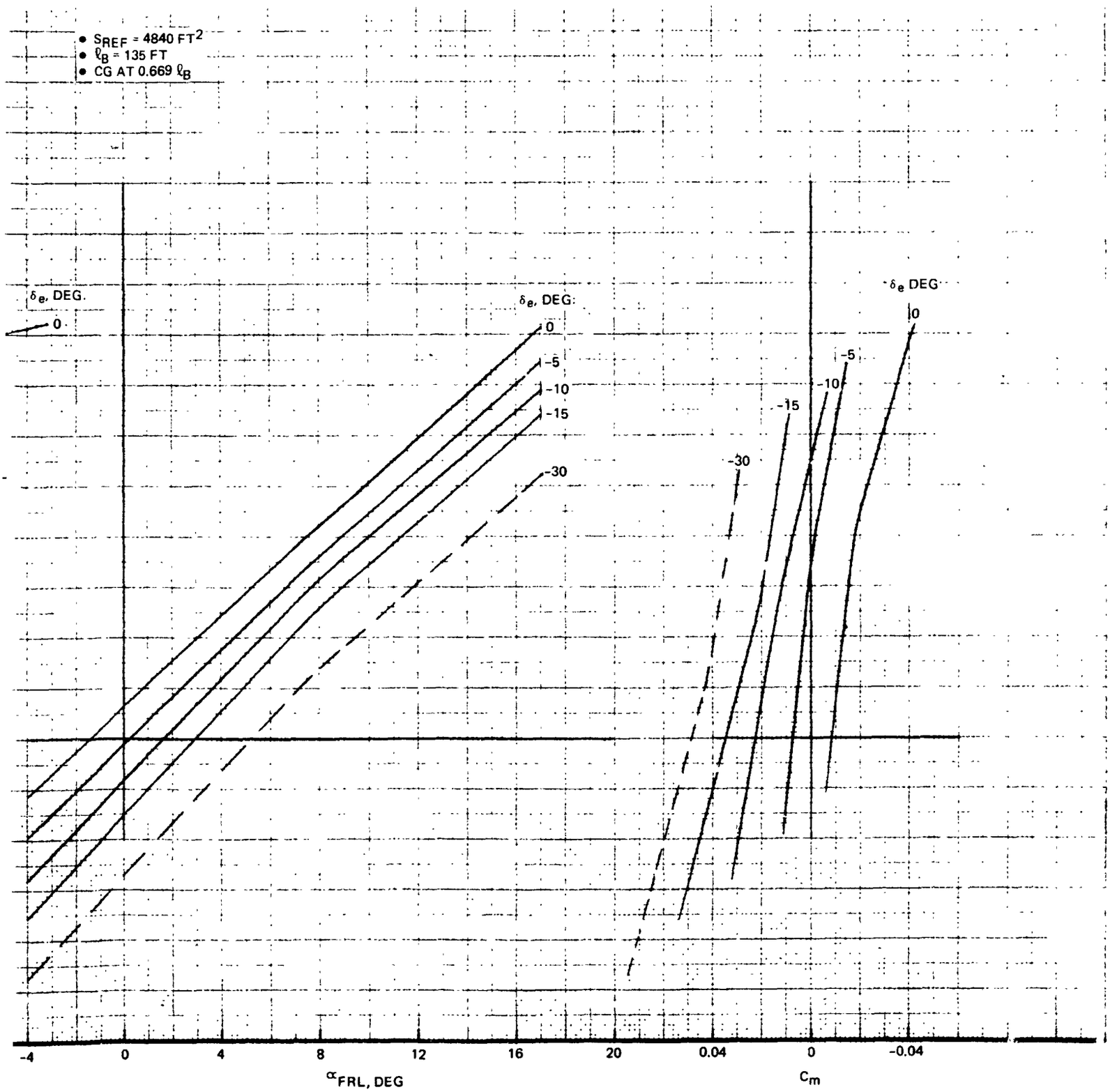

Fig. 8.3.3-19 H-33 Orbiter Longitudinal Aerodynamic Characteristics, Mach = 0.9

GRUMMAN
BOEING

FOLDOUT FRAME

R/8.3

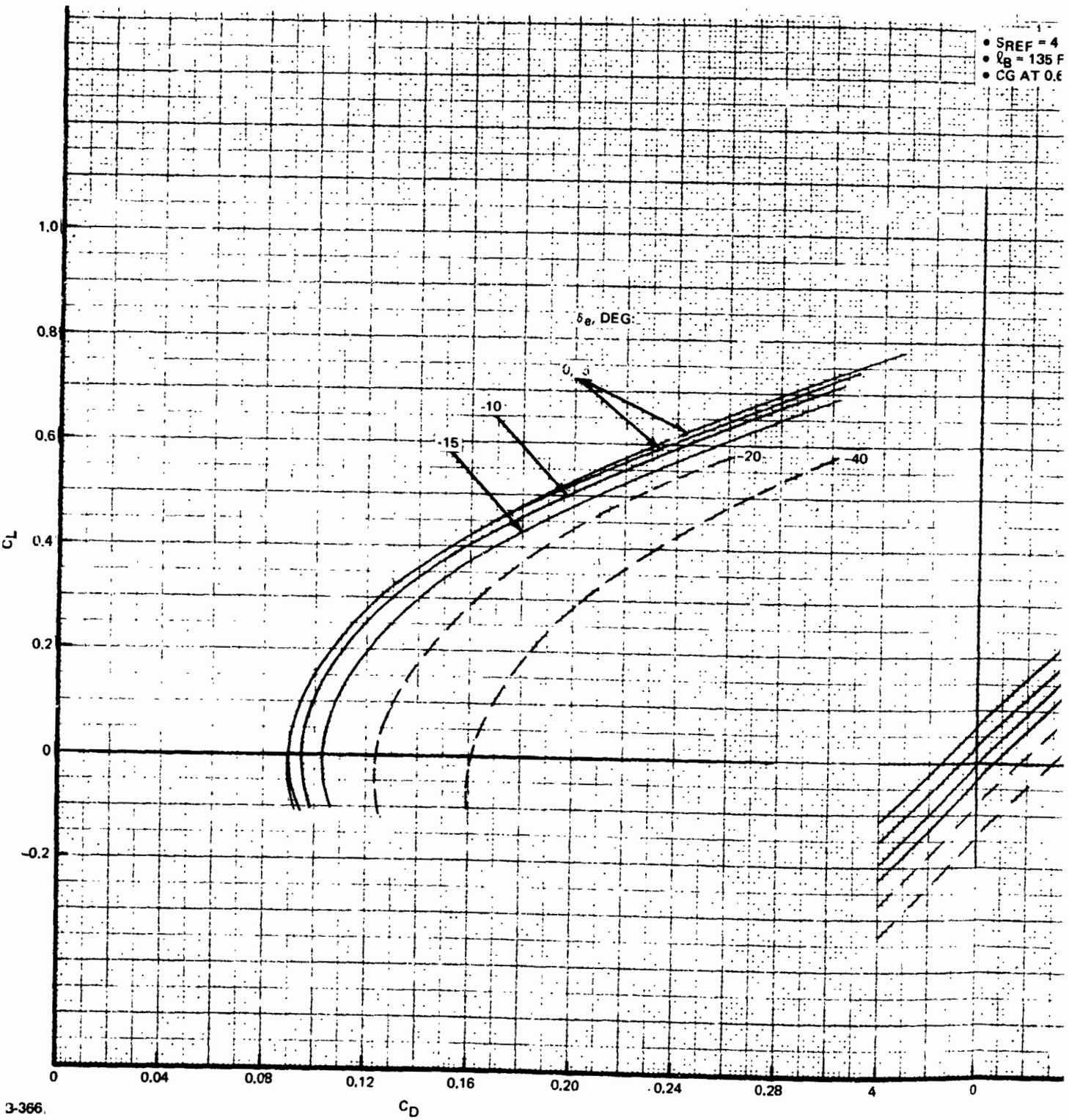

3-366

FOLDOUT FRAME 2.

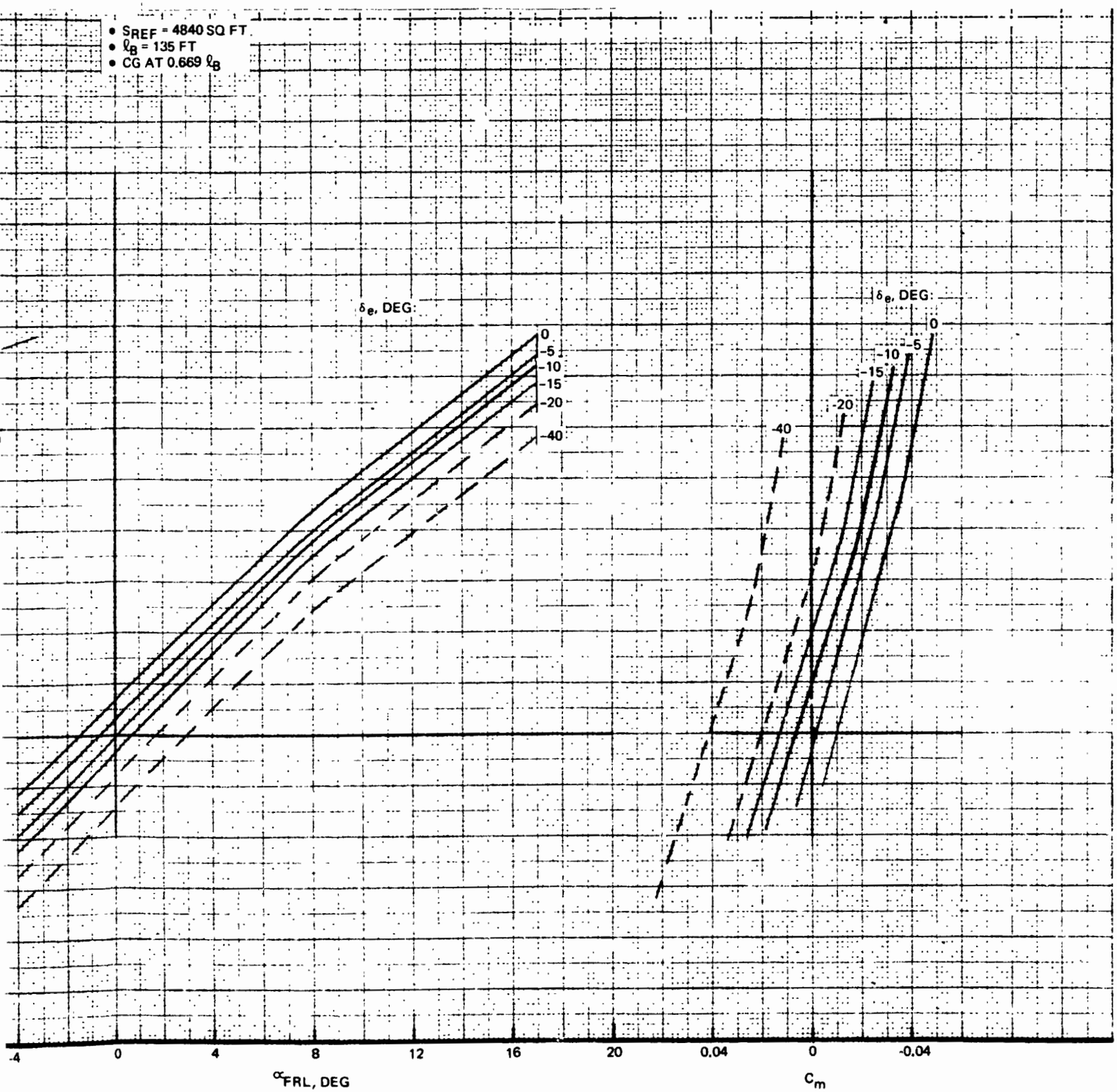

Fig. 8.3.3-20 H-33 Orbiter Longitudinal Aerodynamic Characteristics, Mach = 1.3

GRUMMAN
BOEING

FOLDOUT FRAME

B/8.3

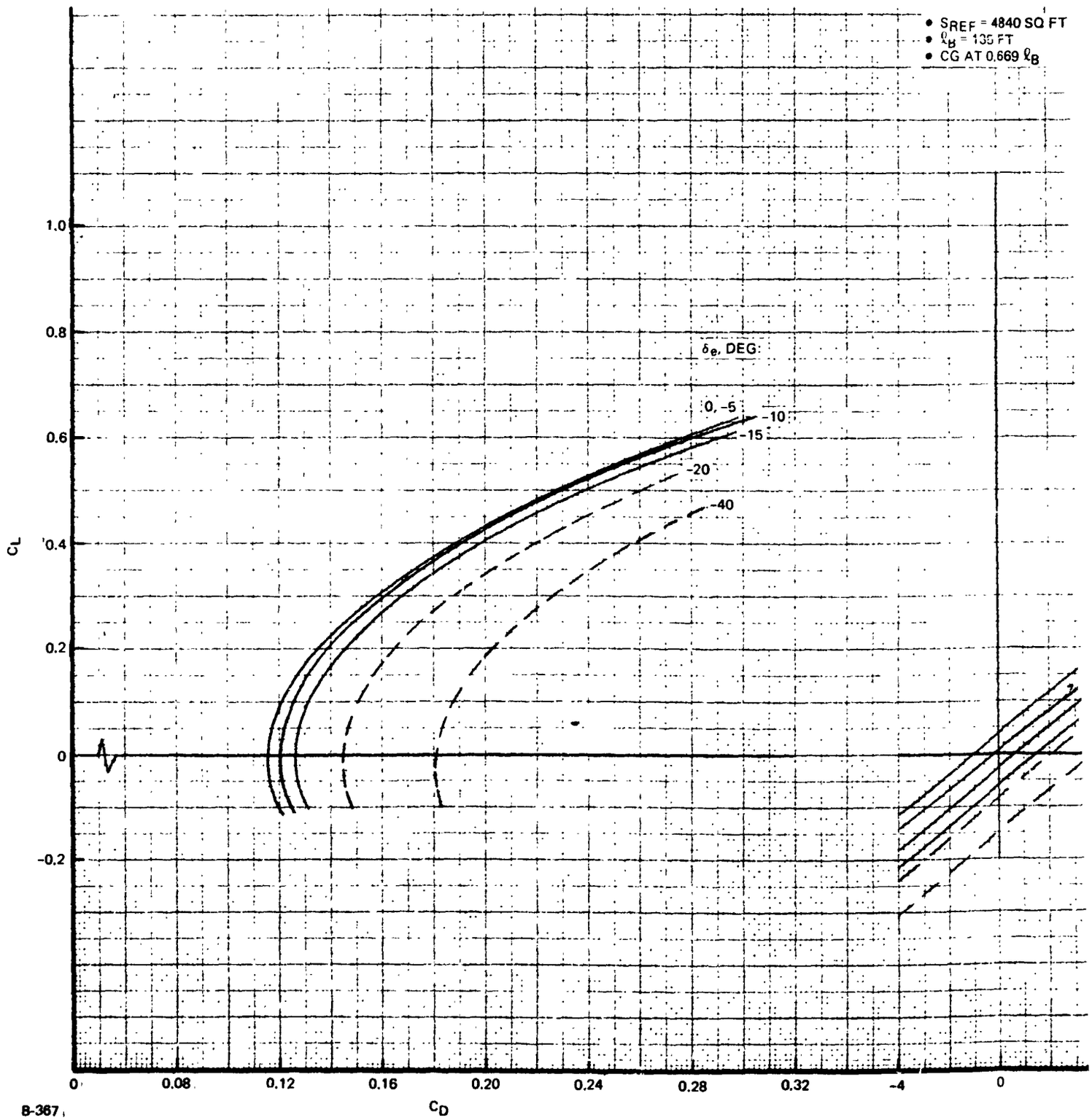

B-367

FOLDOUT FRAME 2

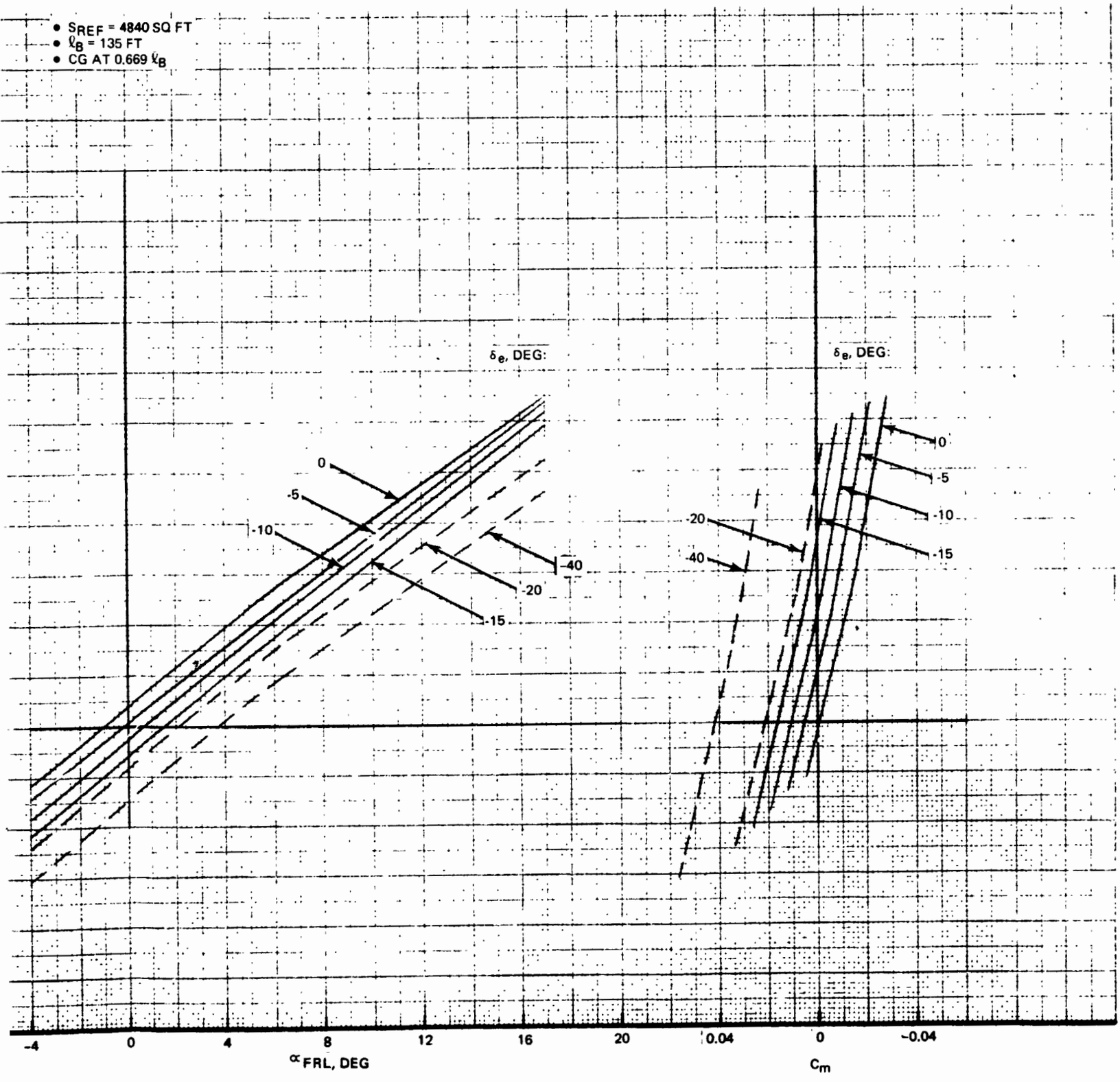

Fig. 8.3.3-21 H-33 Orbiter Longitudinal Aerodynamic Characteristics, Mach = 1.5

GRUMMAN
BOEING

FOLDOUT FRAME 1

B/8.3

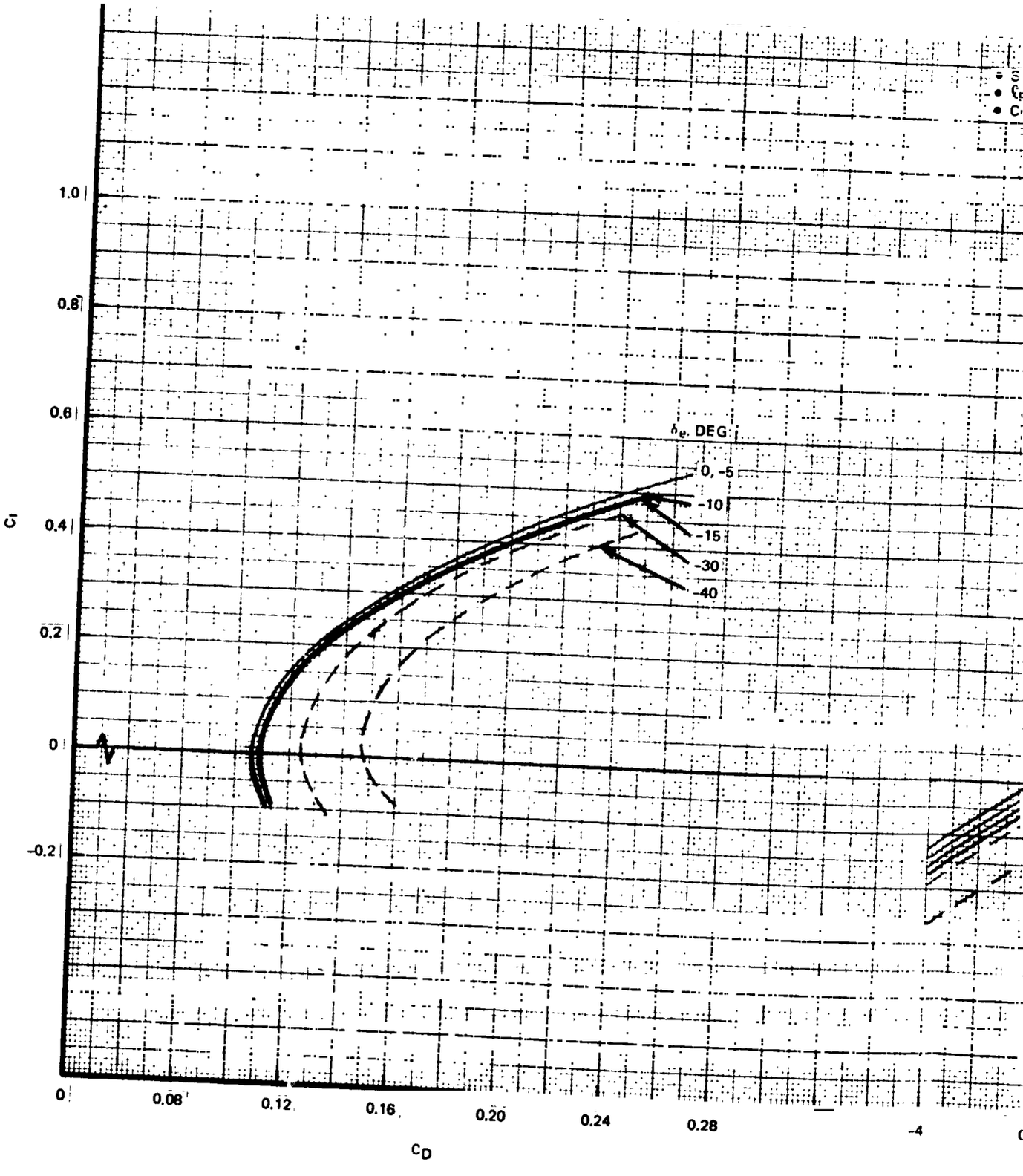

B-368

FOLDOUT FRAME 2

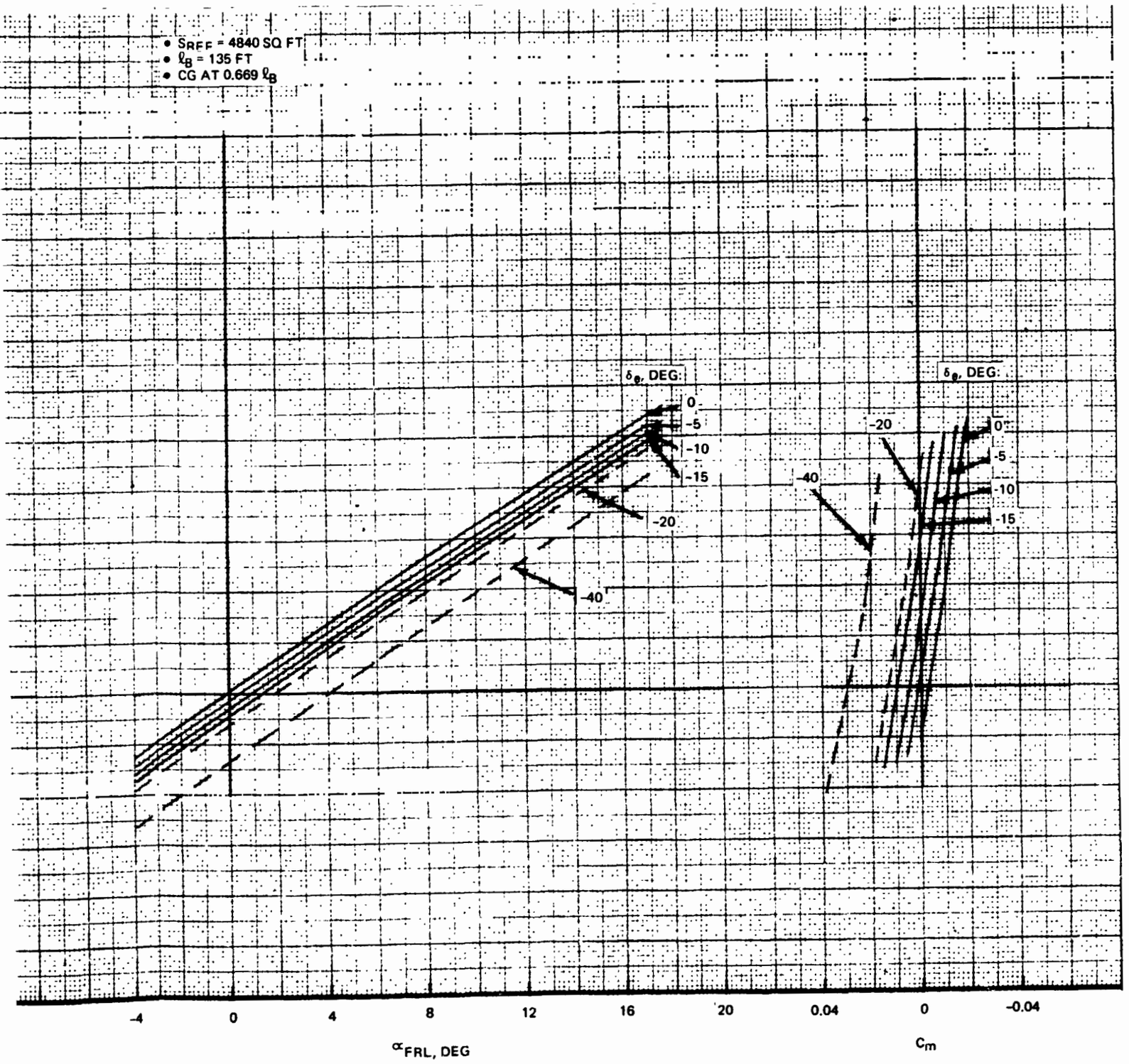

Fig. 8.3.3-22 H-33 Orbiter Longitudinal Aerodynamic Characteristics, Mach = 2.0

FOLDOUT FRAME 1

FOL

B/8.3

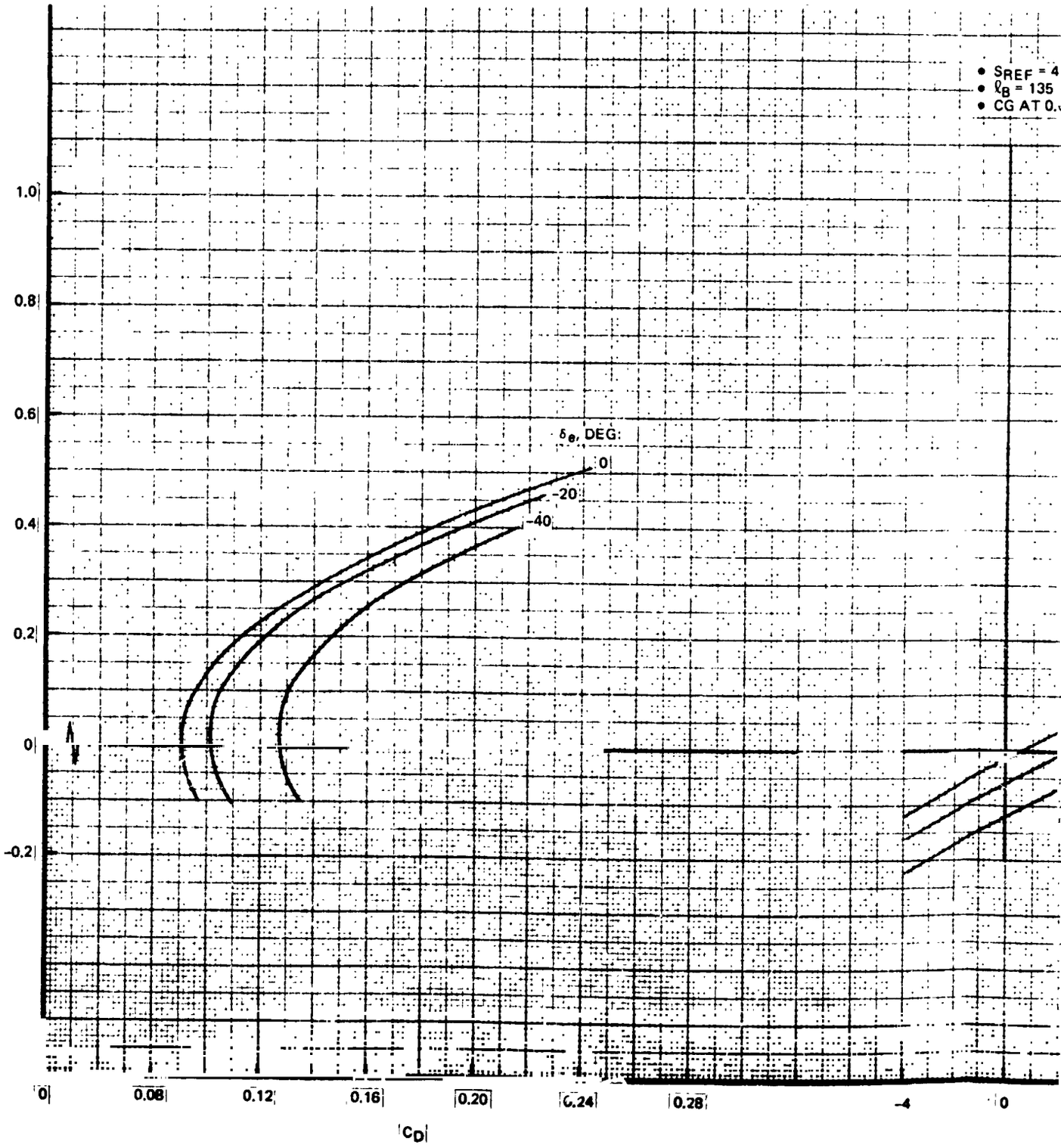

B-369

FOLDOUT FRAME 2

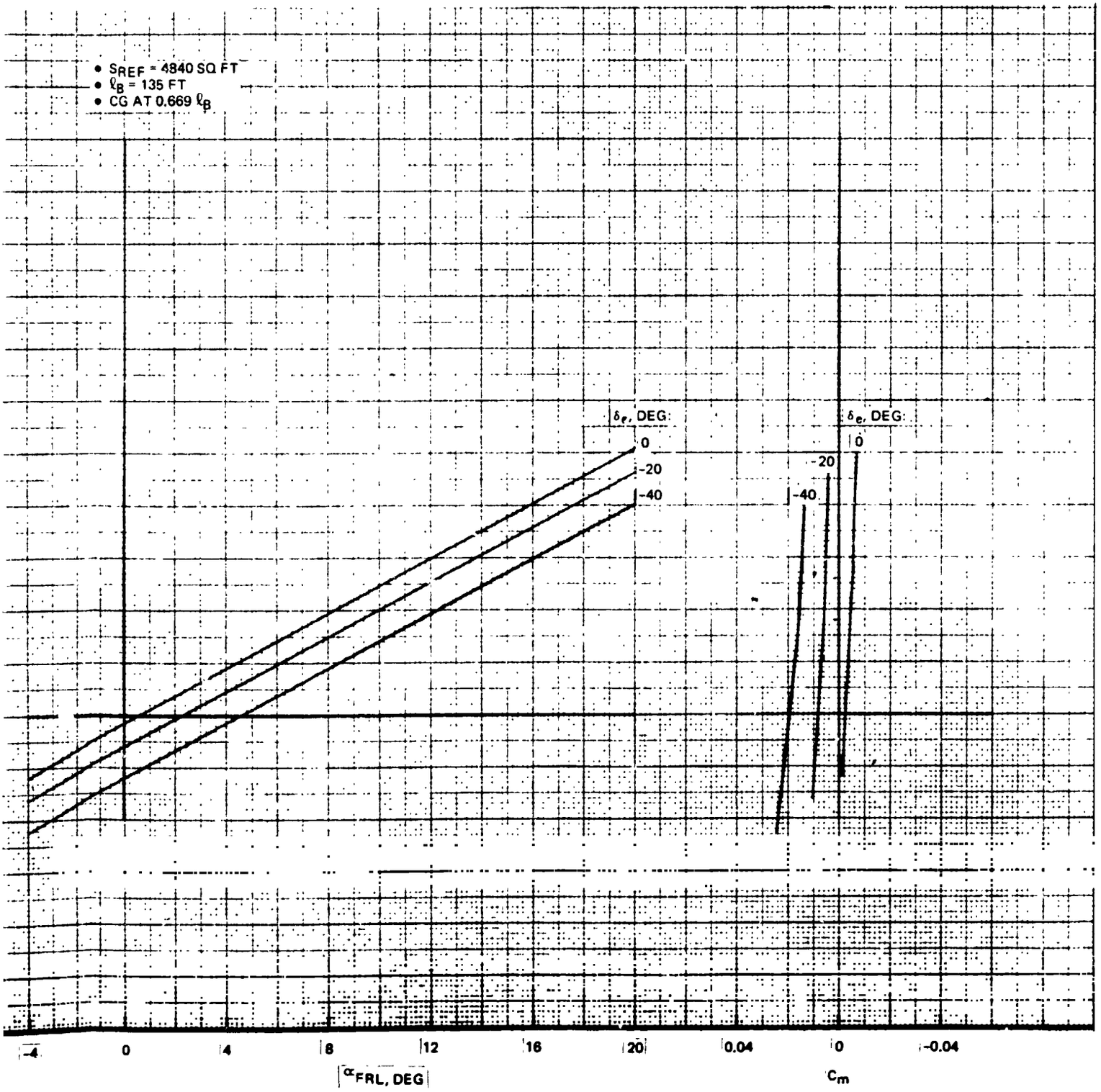

Fig. 8.3.3-23 H-33 Orbiter Longitudinal Aerodynamic Characteristics. Mach = 2.48

FOLDOUT FRAME

B/8.3

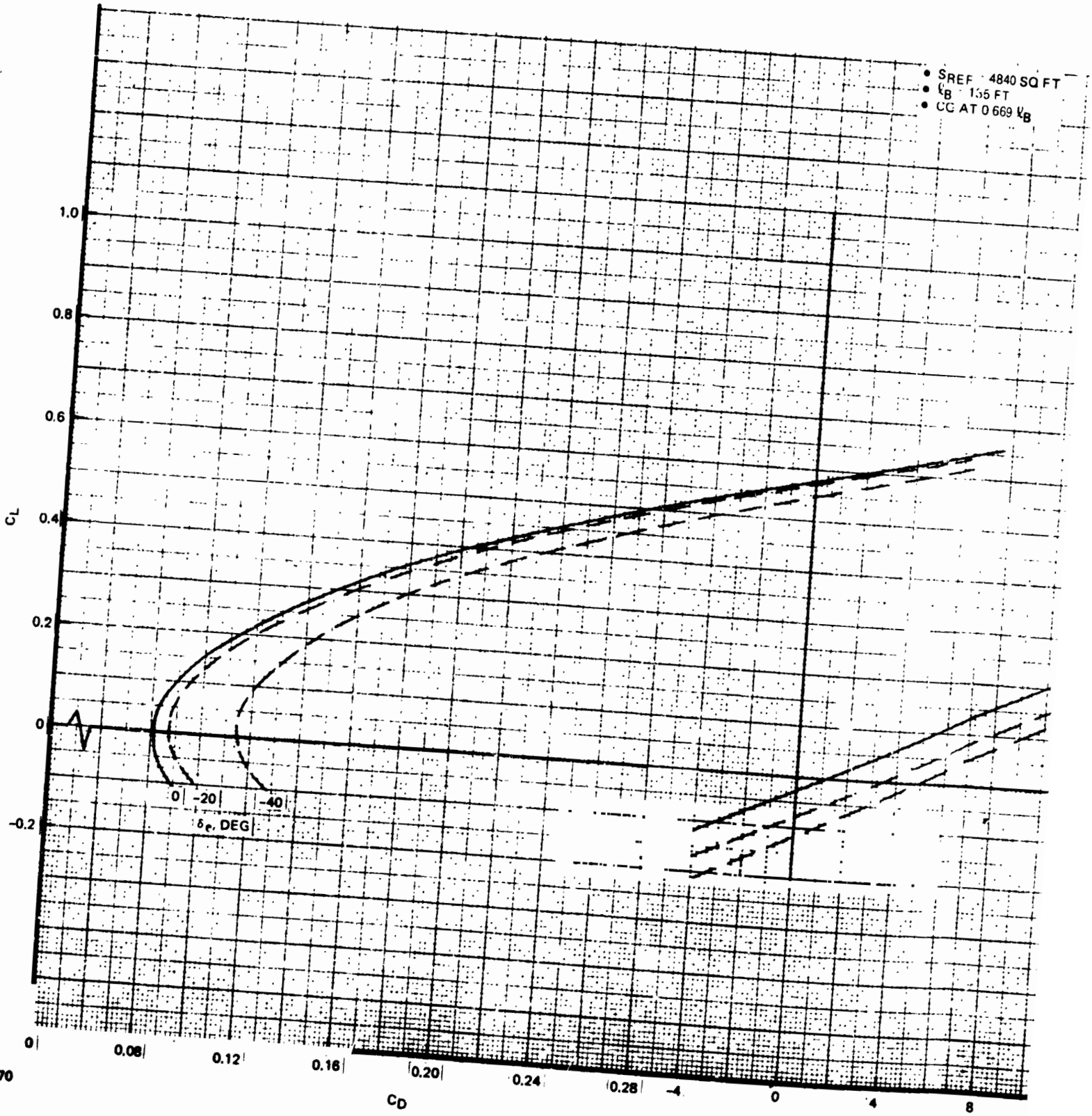

FOLDOUT FRAME 2

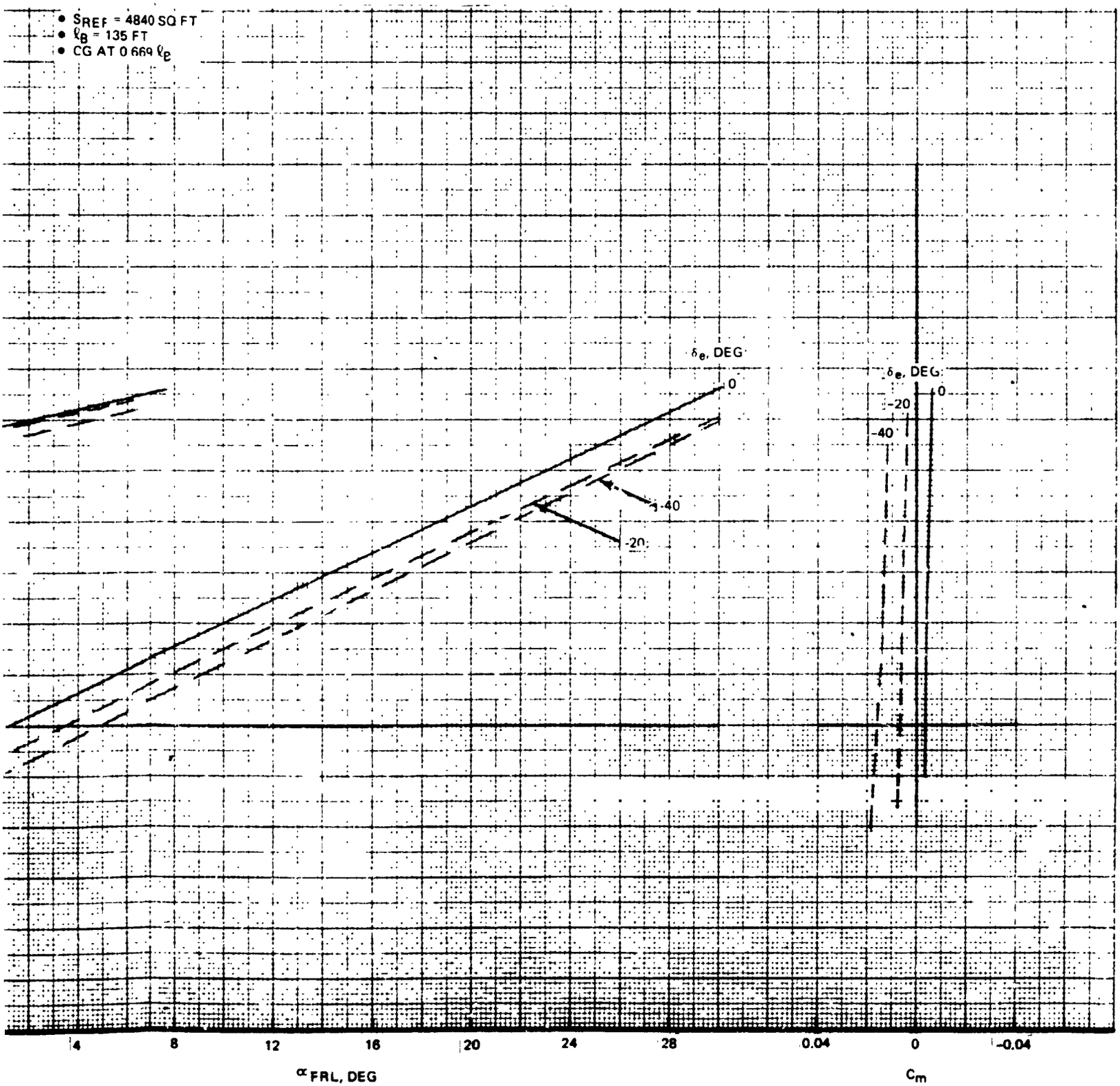

Fig. 8.3.3-24 H-33 Orbiter Longitudinal Aerodynamic Characteristics, Mach = 3.0

FOLDOUT FRAME

B/8.3

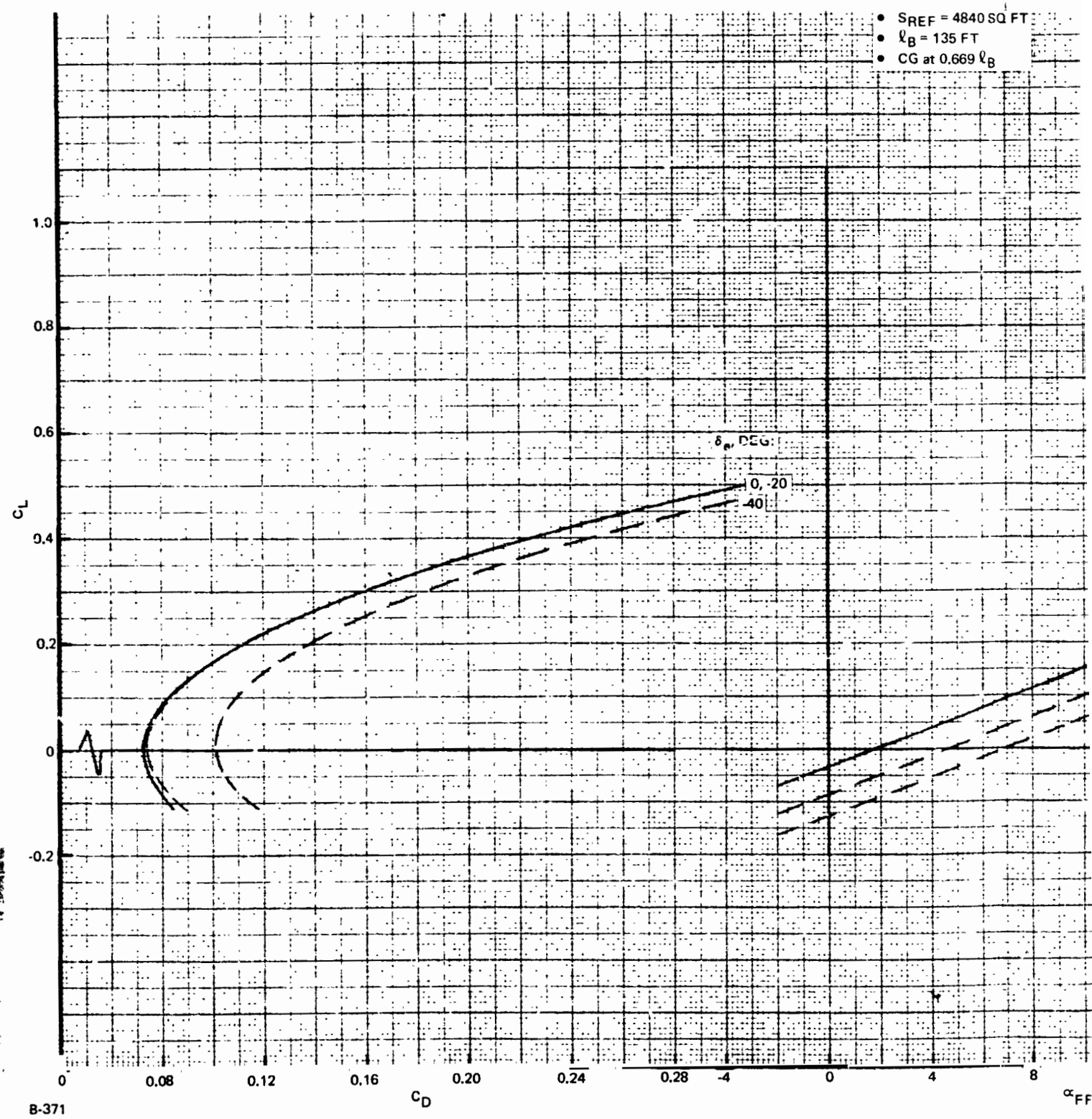

FOLDOUT FRAME 2

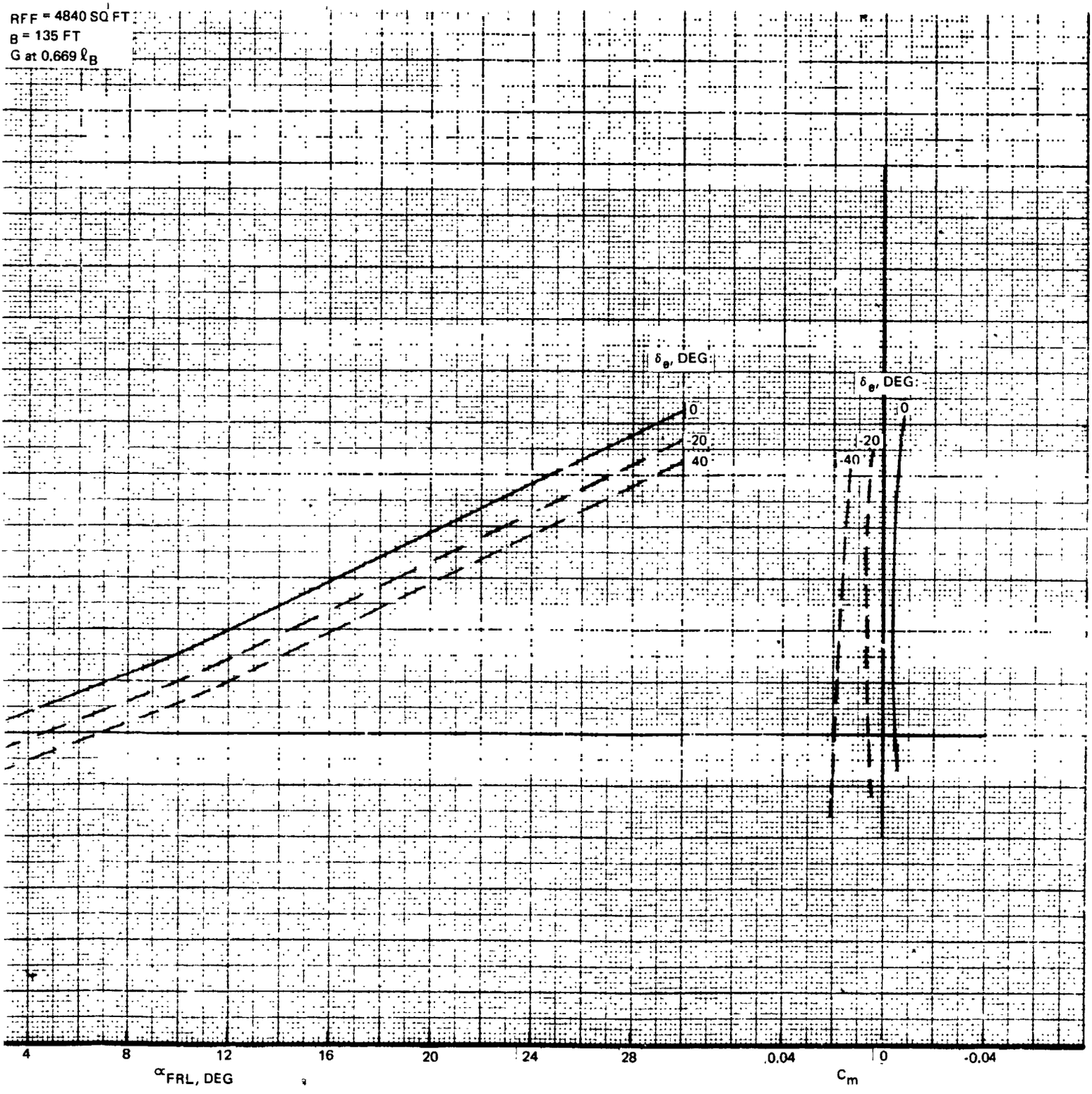

Fig. 8.3.3-25 H-33 Orbiter Longitudinal Aerodynamic Characteristics, Mach = 3.9

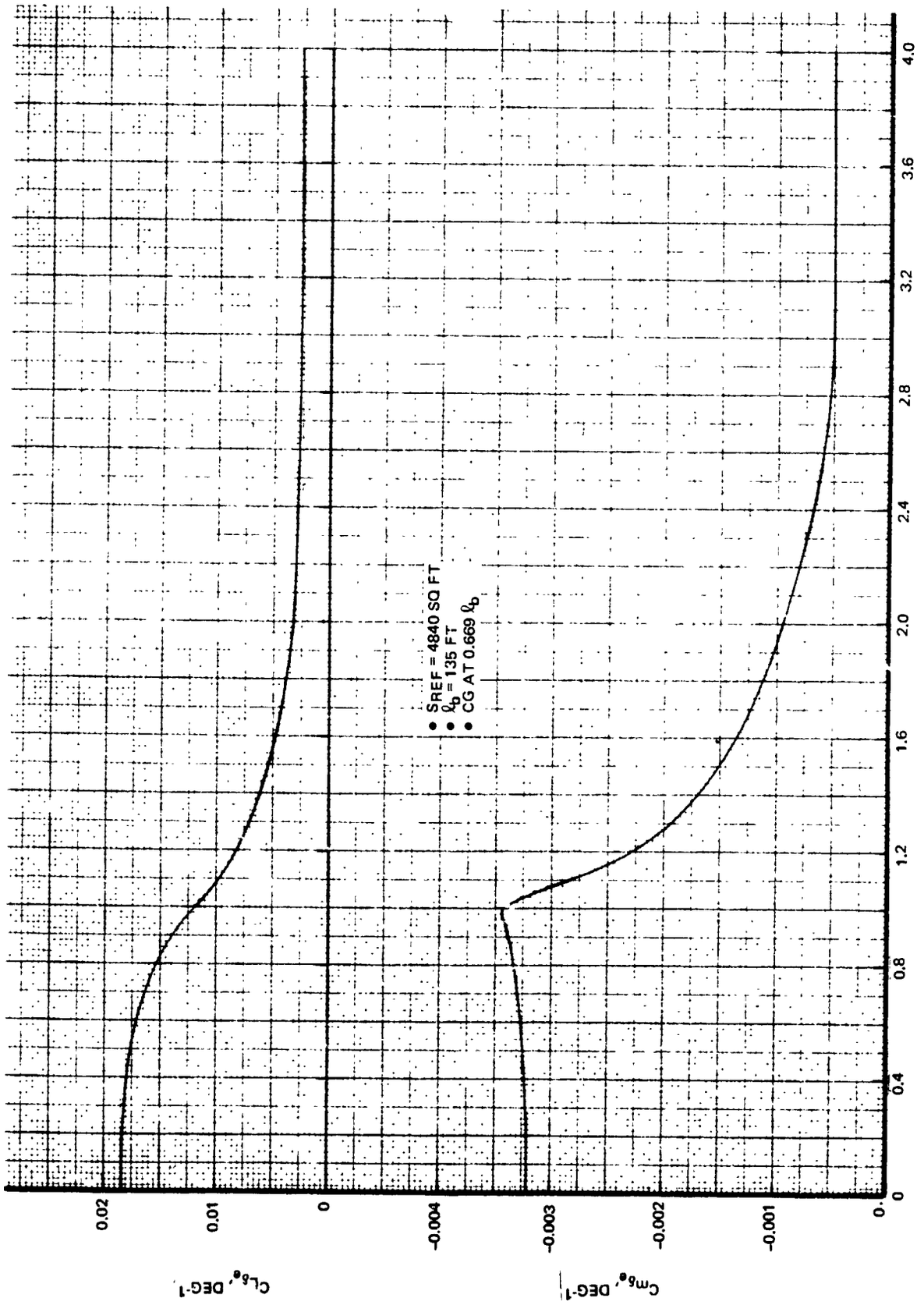

Fig. 8.3.3-26 H-33 Elevator Effectiveness

GRUMMAN
BOEING

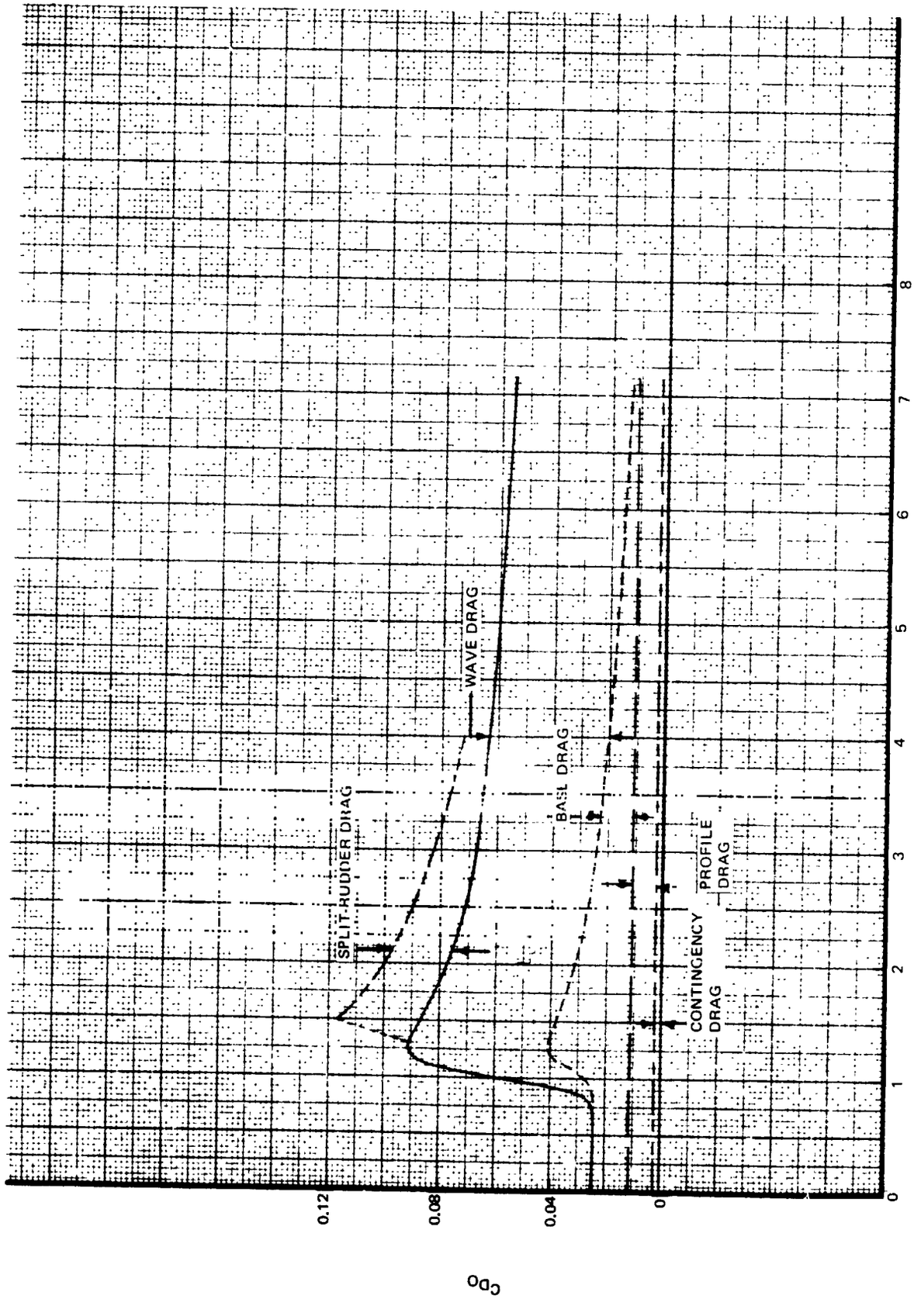

Fig. 8.3.3-27 H-33 Orbiter Zero-Lift Drag Versus Mach Number

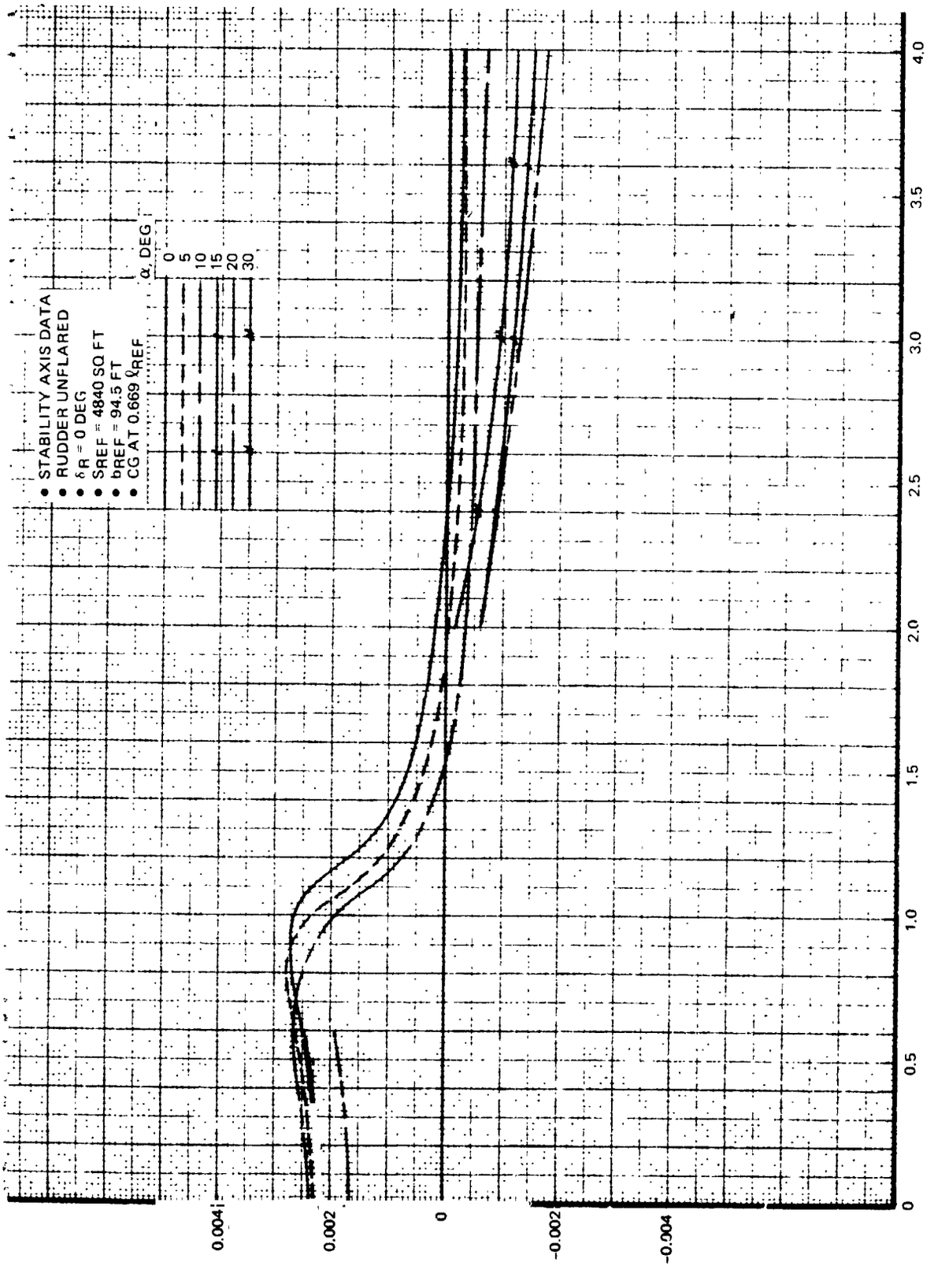

Fig. 8.3.3-28 H-33 Orbiter Estimated Static Directional Stability vs. Mach Number

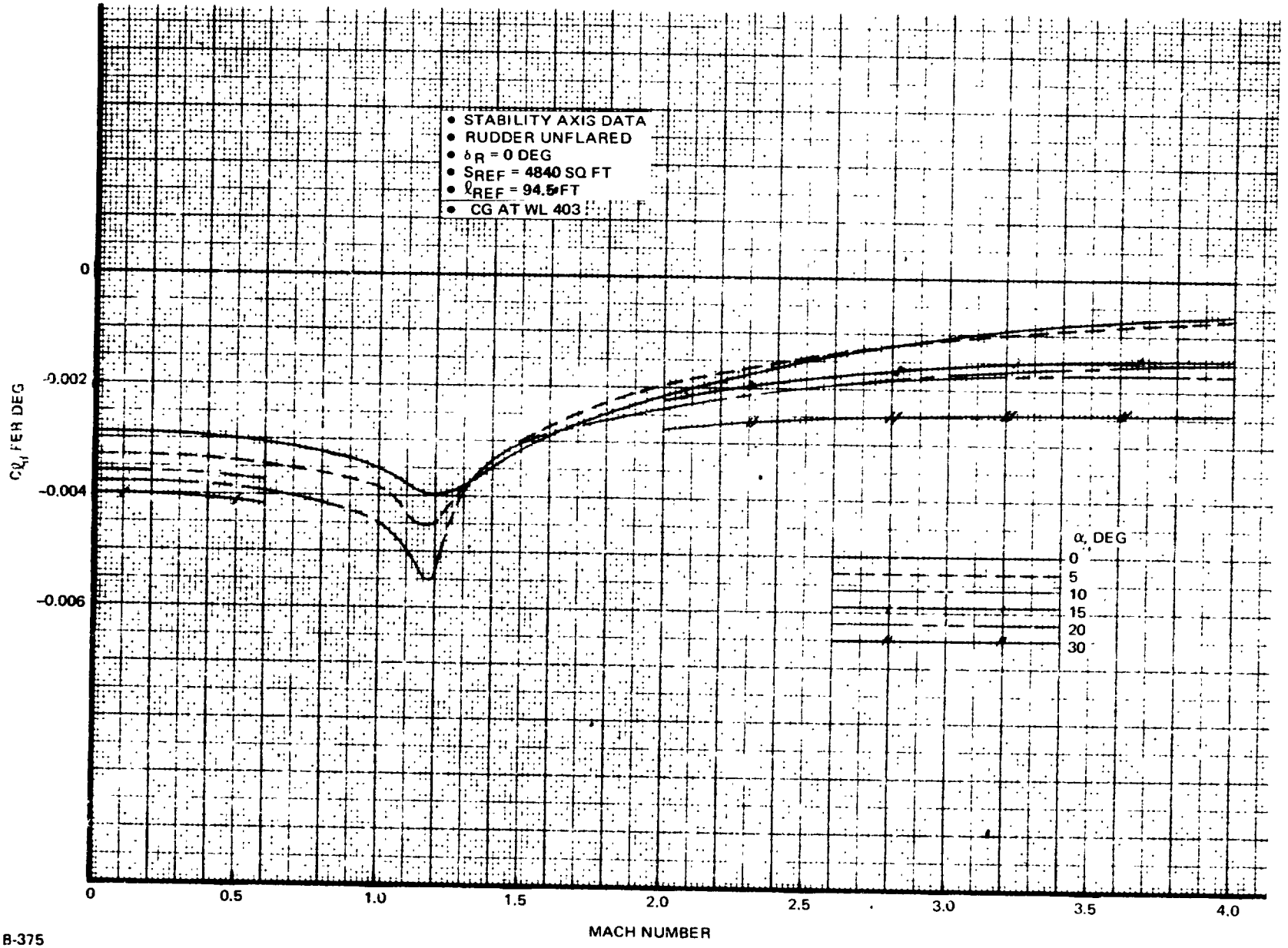

Fig. 8.3.3-29 H-33 Orbiter Estimated Lateral Stability Variation with Mach Number

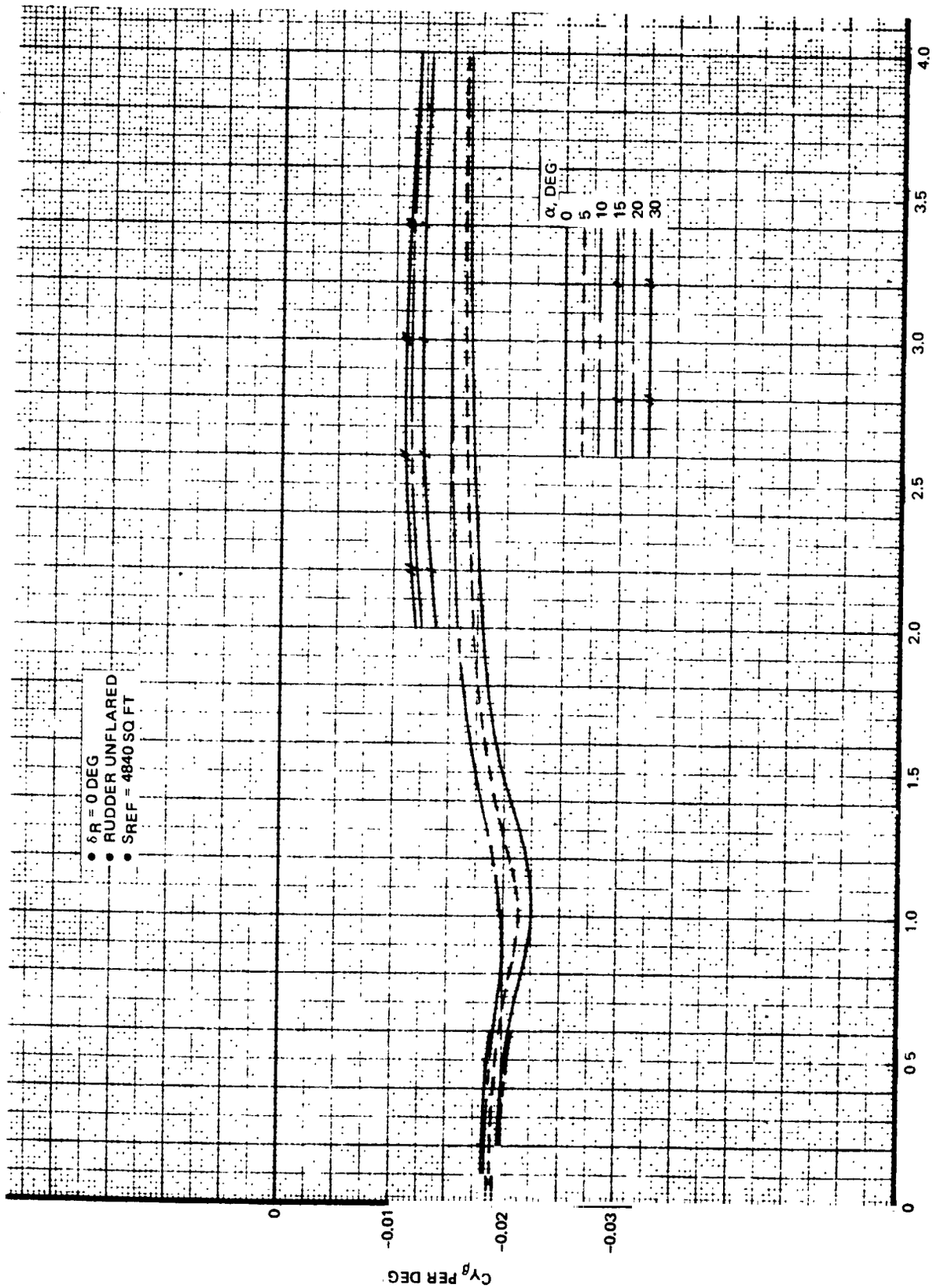

Fig. 8.3.3-30 H-33 Orbiter Estimated Side Force Variation with Mach Number

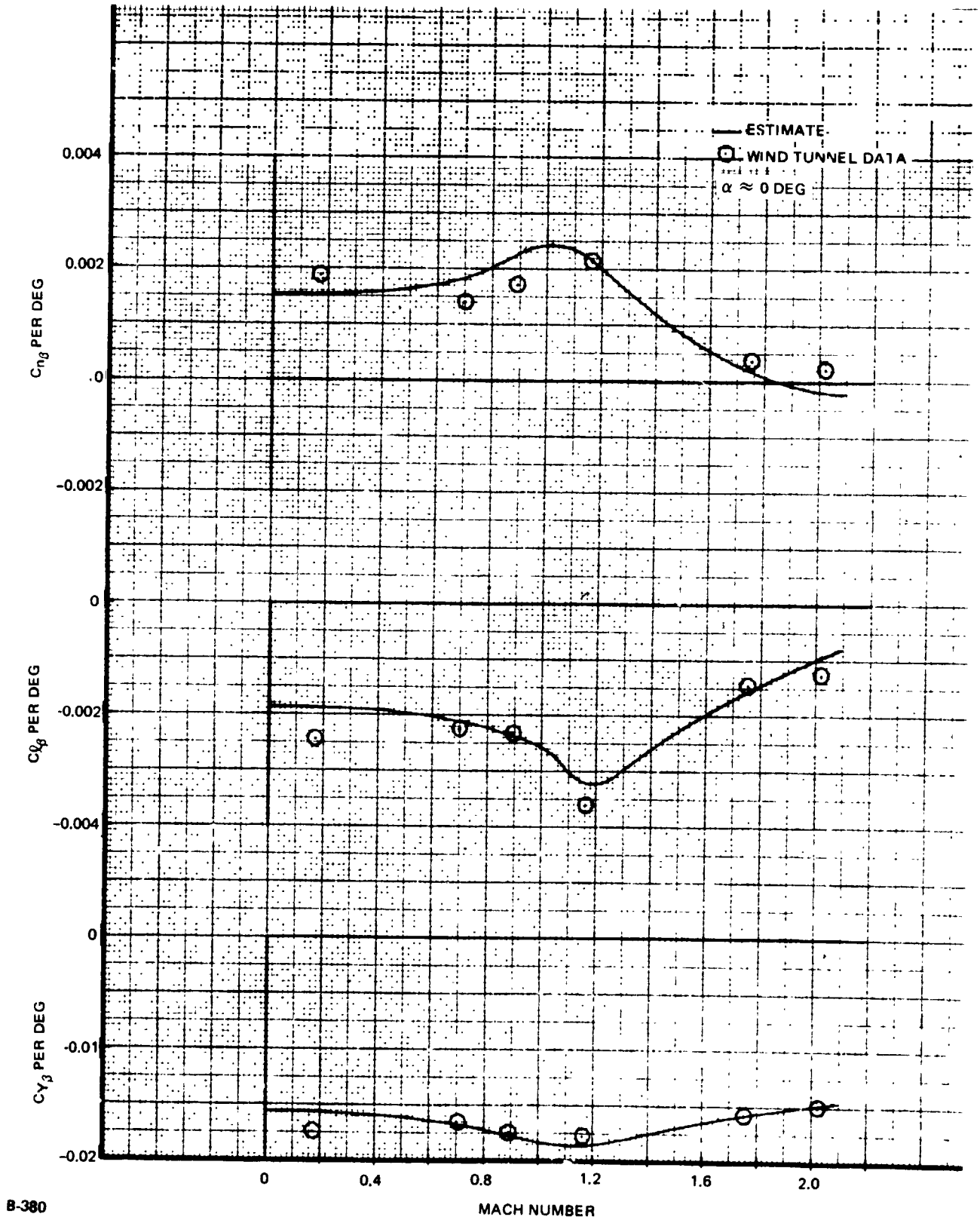

Fig. 8.3.3-31 Correlation of Test Data with Estimation Techniques, G-3A Orbiter

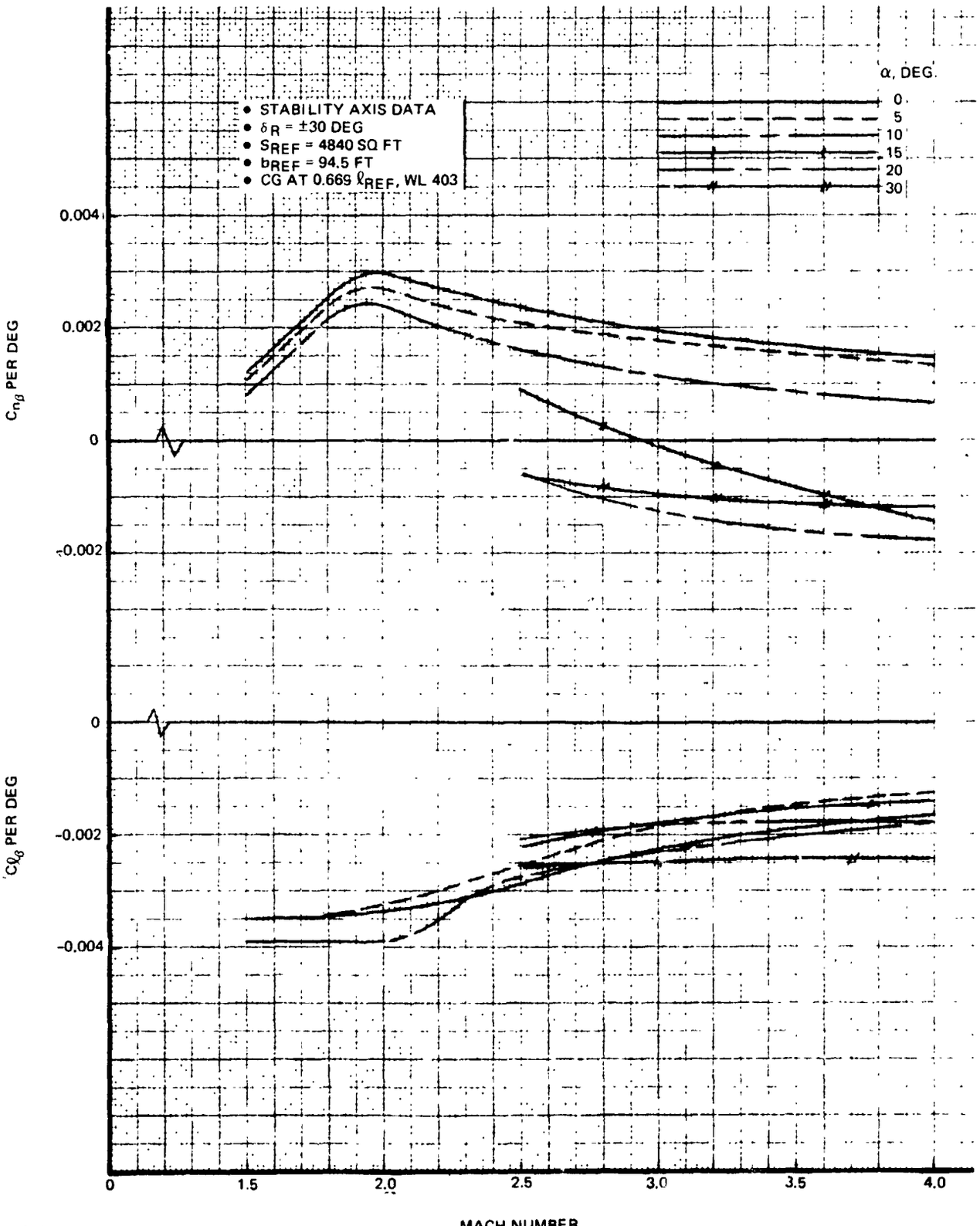

Fig. 8.3.3-32a H-33 Orbiter Estimated Lateral-Directional Characteristics with Flared Rudder Deployed

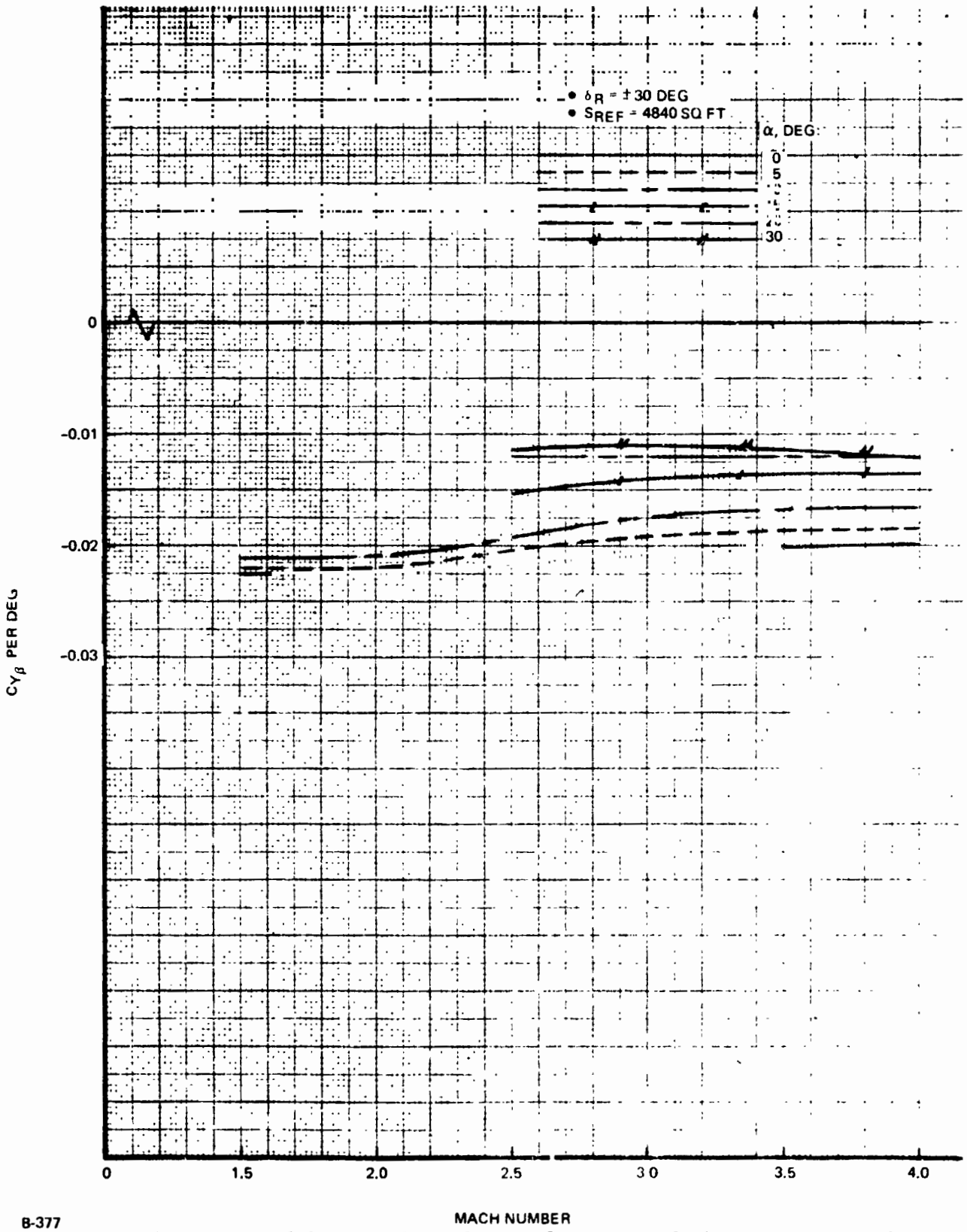

8-377

Fig. 8.3.3-32b H-33 Orbiter Estimated Lateral-Directional Characteristics with Flared Rudder Deployed

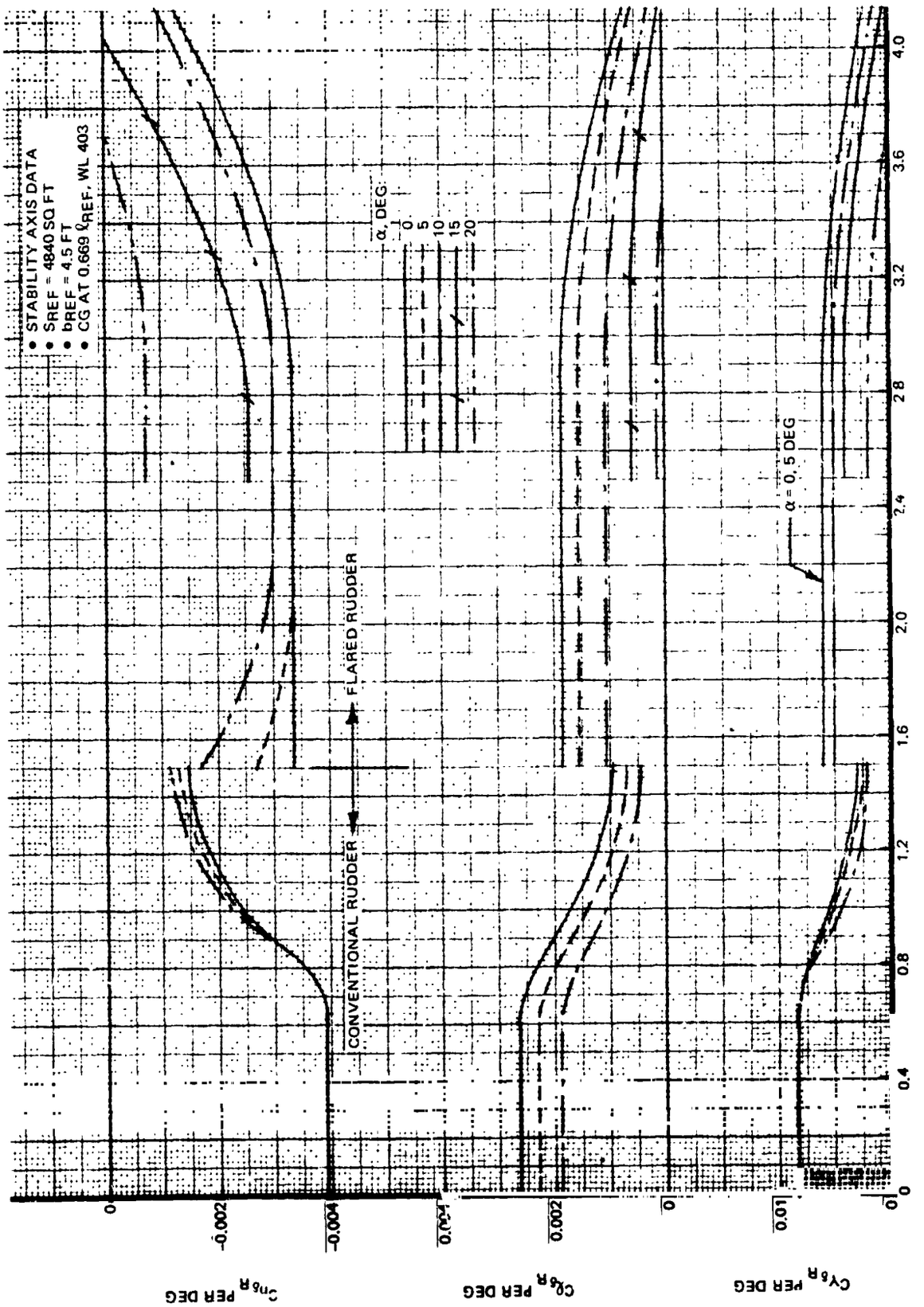

Fig. 8.3.3-33 H-33 Orbiter Estimated Rudder Effectiveness

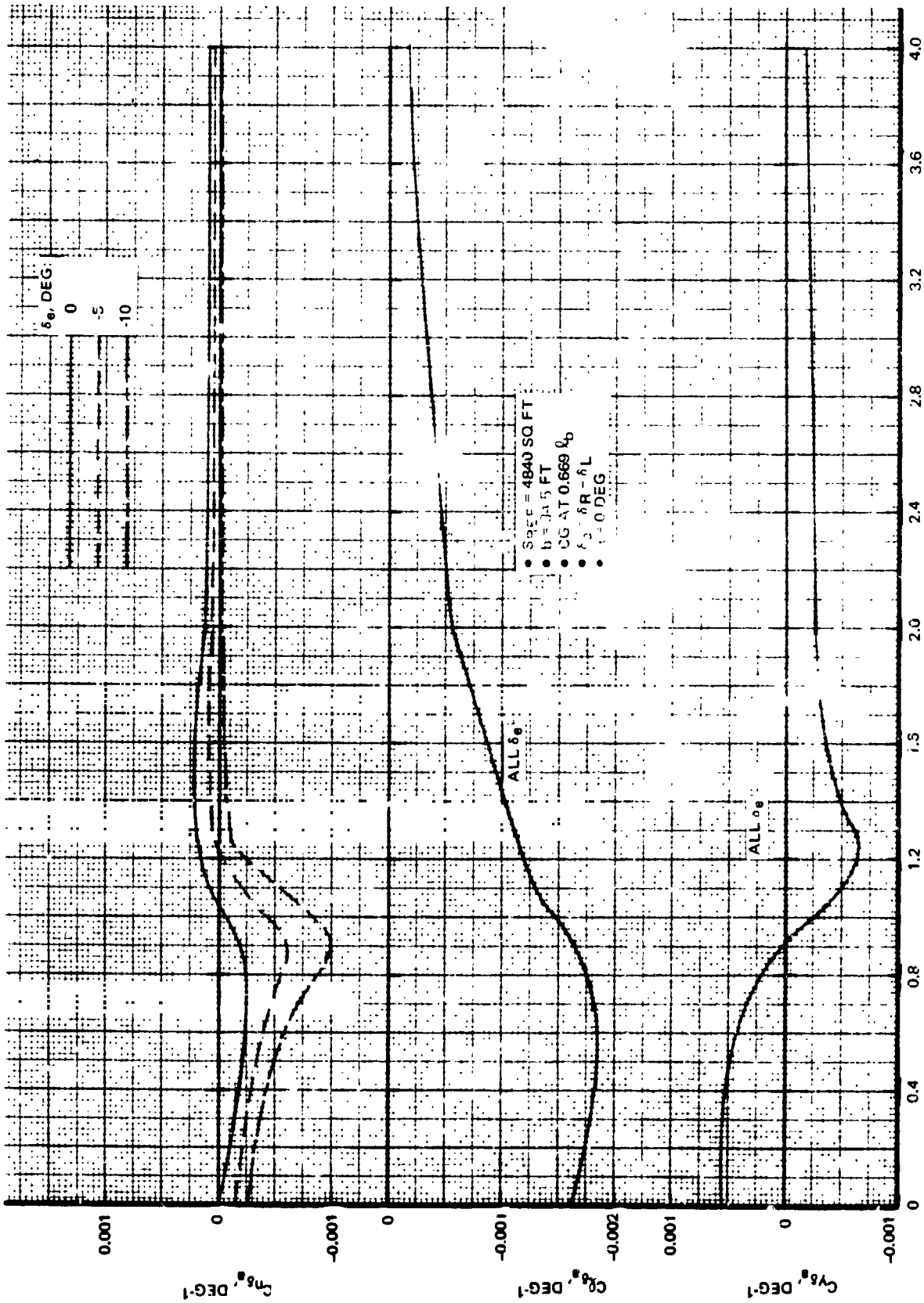

Fig. 8.3.3-34 H-33 Aileron Effectiveness

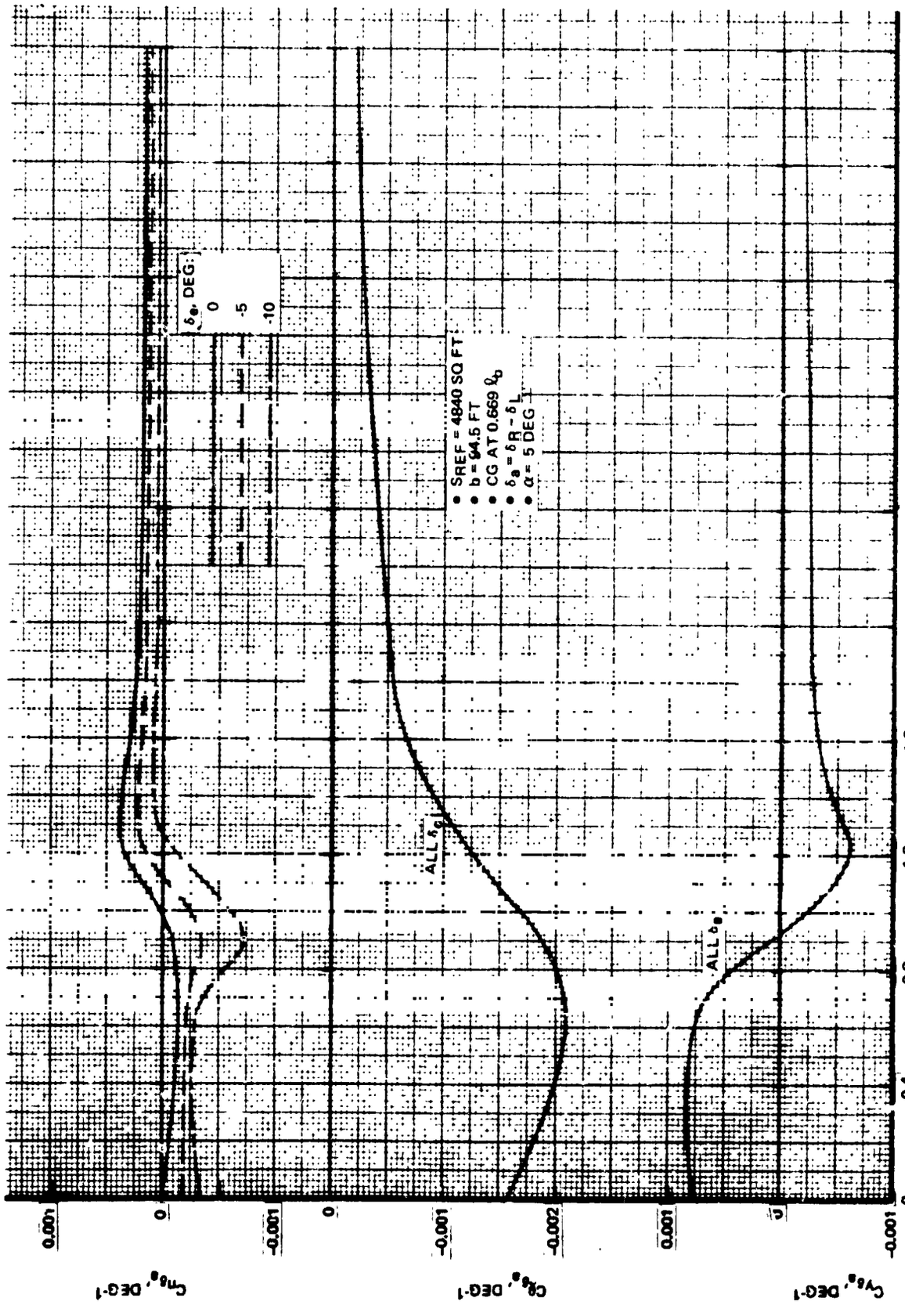

Fig. 8.3.3-35 H-33 Aileron Effectiveness

B-125

GRUMMAN
BOEING

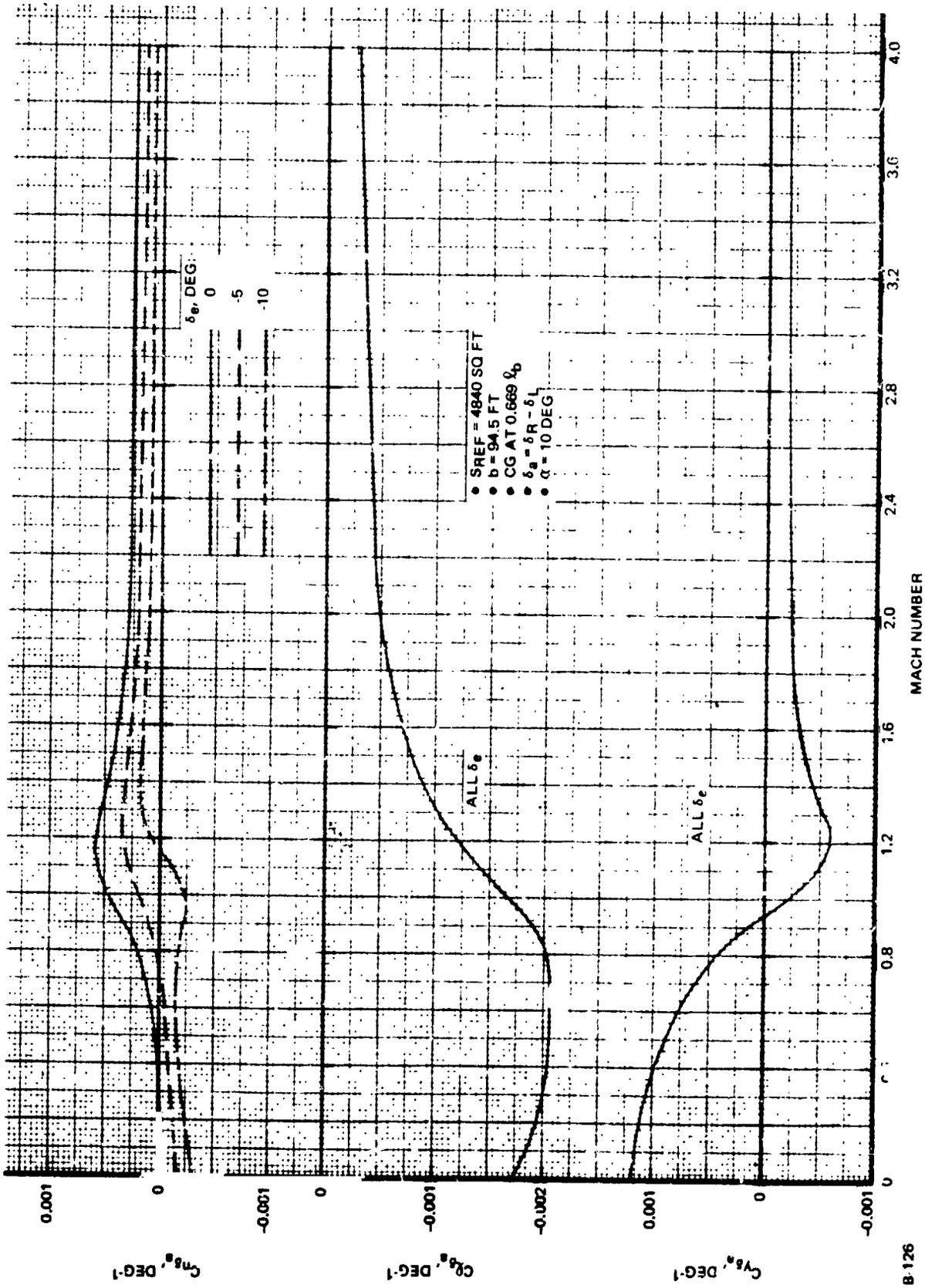

Fig. 8.3.3-36 H-33 Aileron Effectiveness

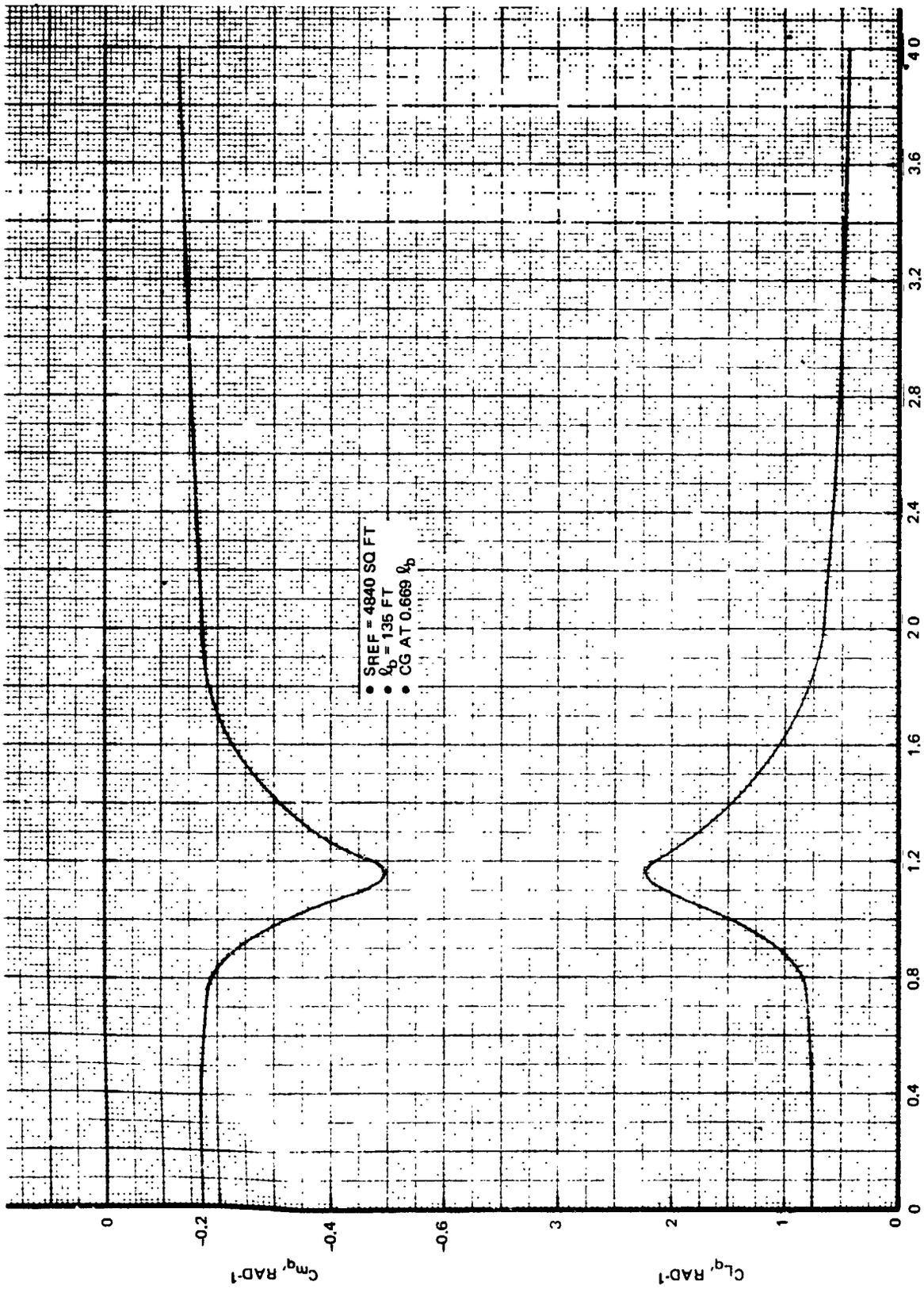

Fig. 8.3.3-37 H-33 Pitching Derivatives

GRUMMAN
BOEING

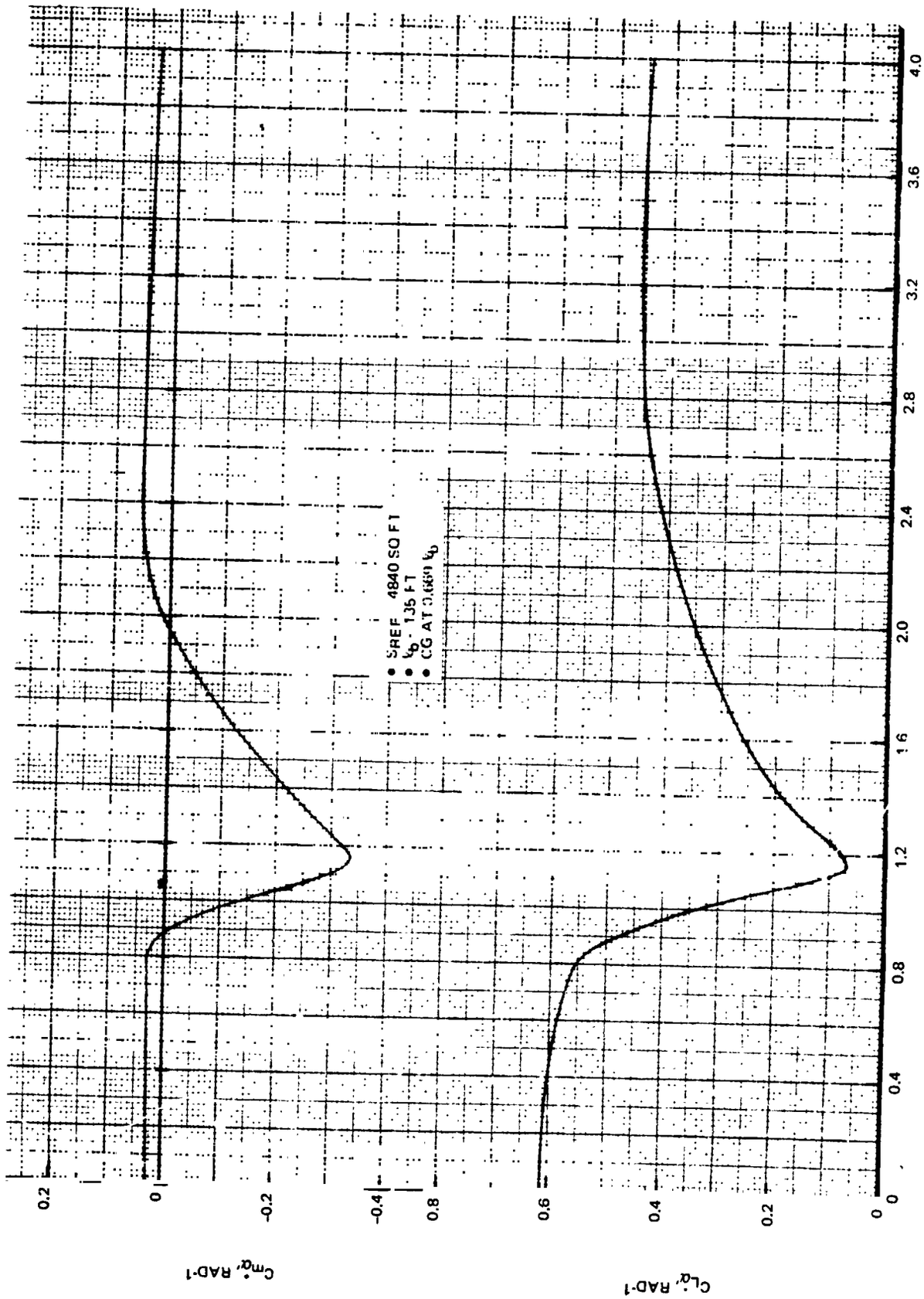

Fig. 8.3.3-38 H-33 Acceleration Derivatives

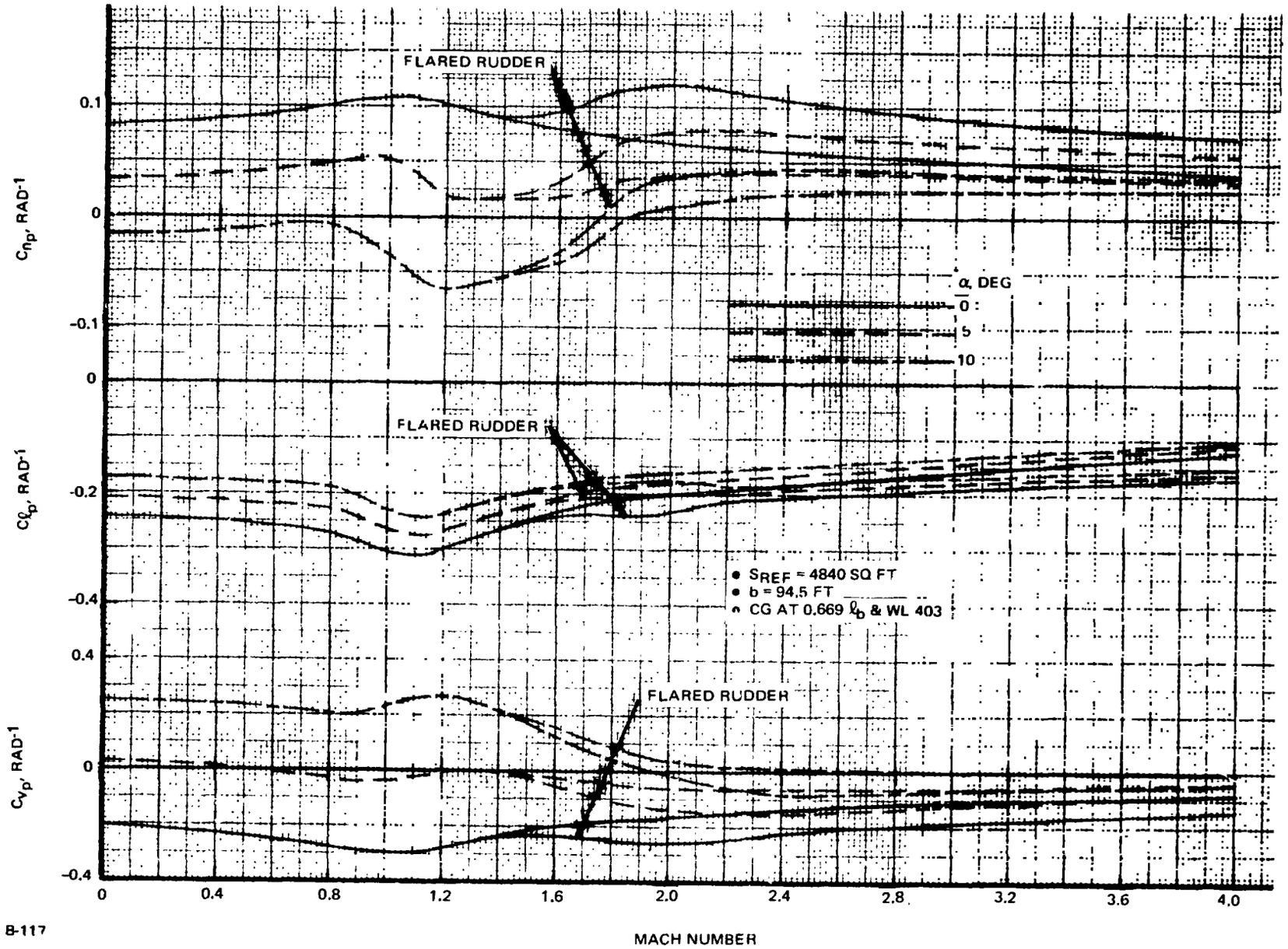

B-117

Fig. 8.3.3-39 H-33 Roll Dynamic Derivatives

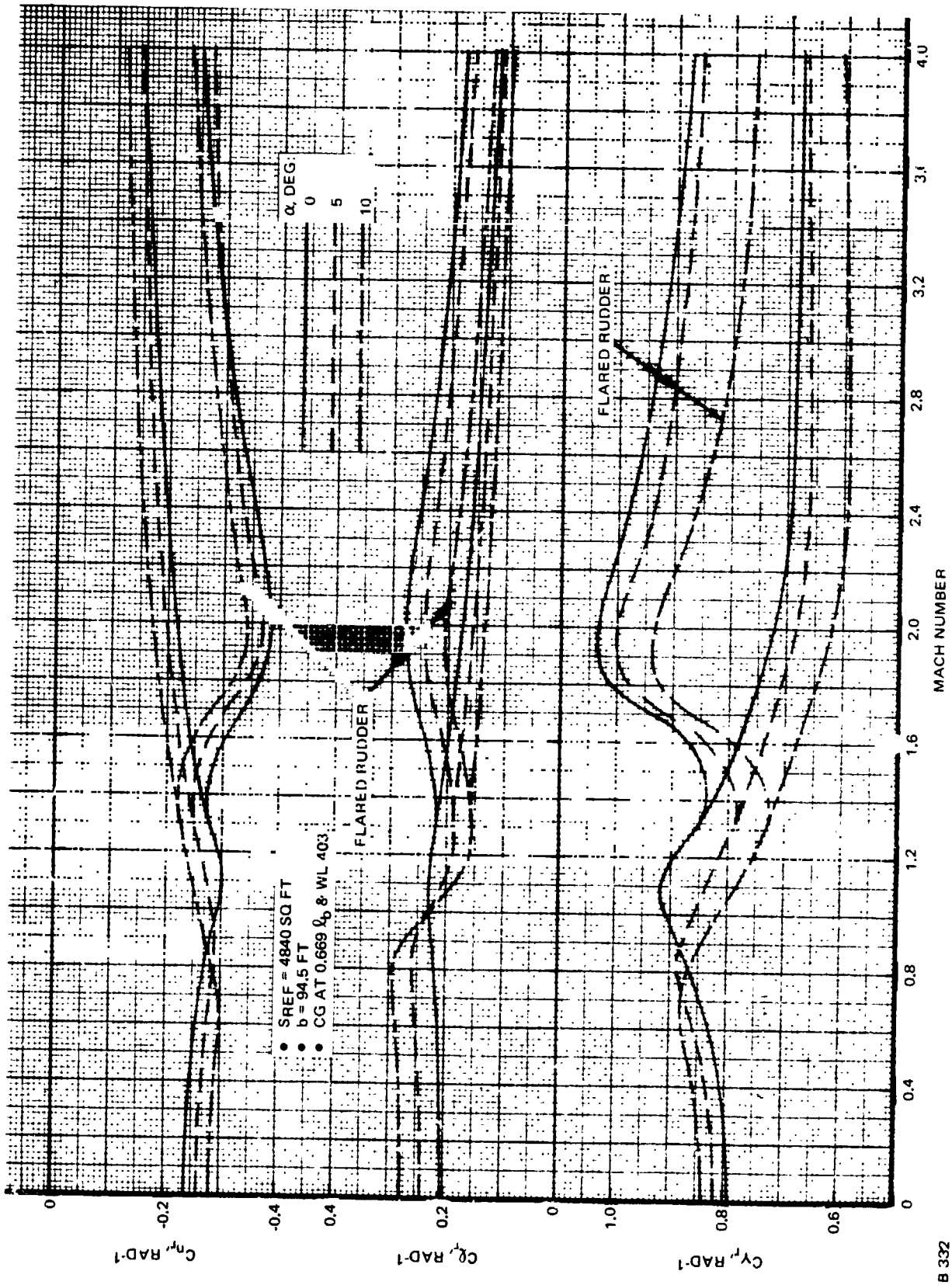

Fig. 8.3.3-40 H-33 Yaw Dynamic Derivatives

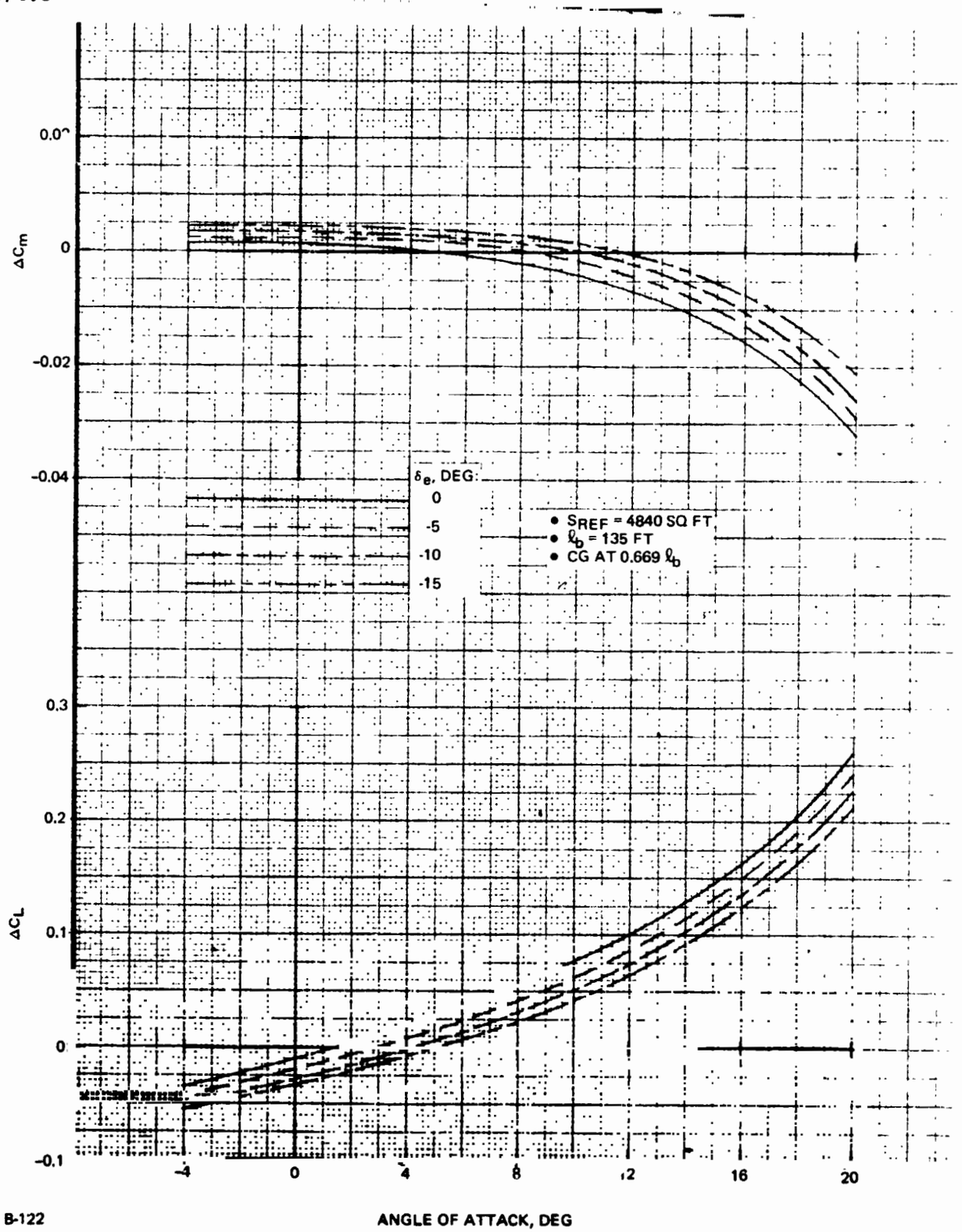

Fig. 8.3.3-41 H-33 Incremental Subsonic Longitudinal Characteristics Due to Ground Proximity

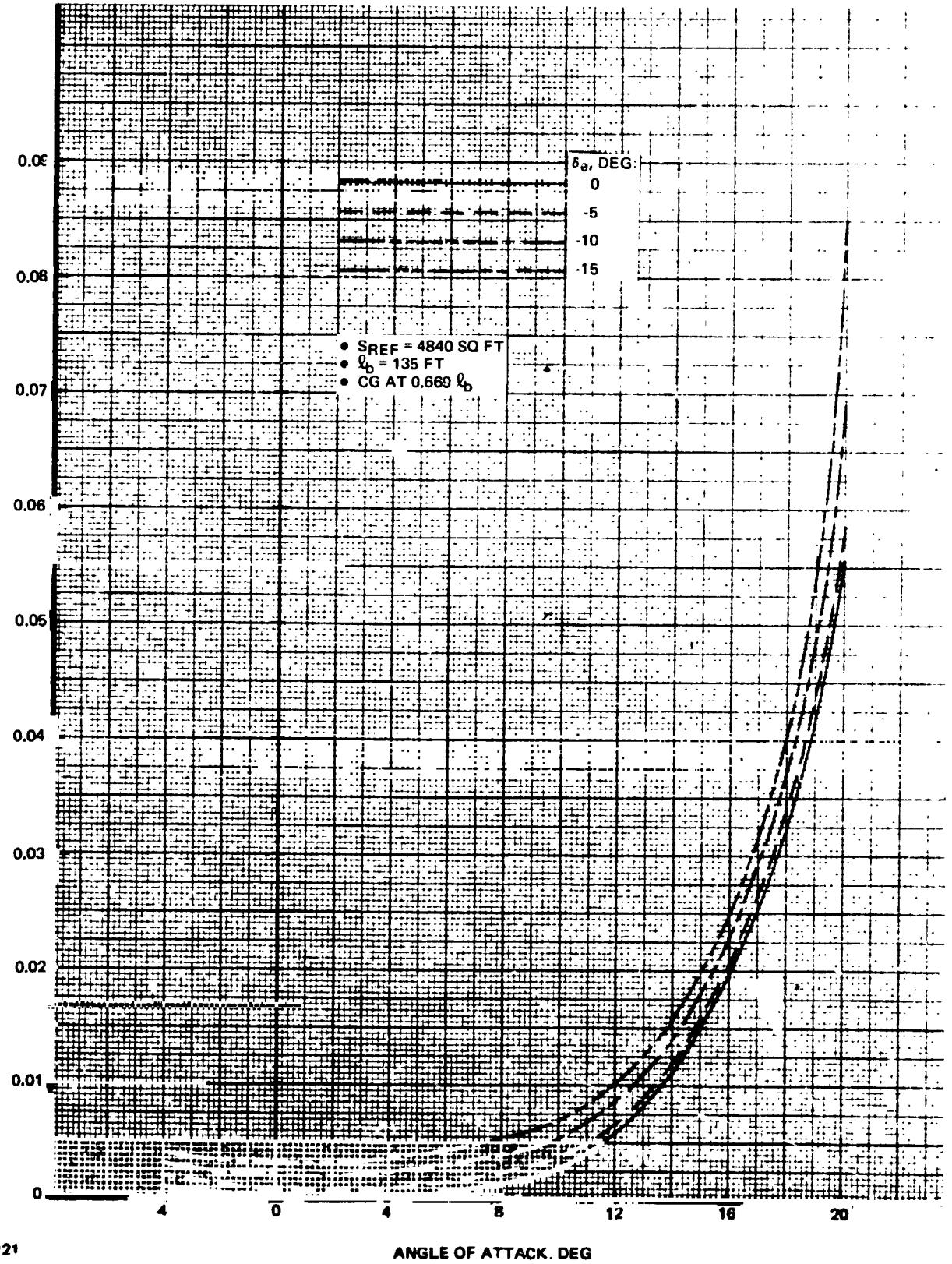

Fig. 8.3.3-42 H-33 Incremental Subsonic Drag Coefficient Due to Ground Proximity

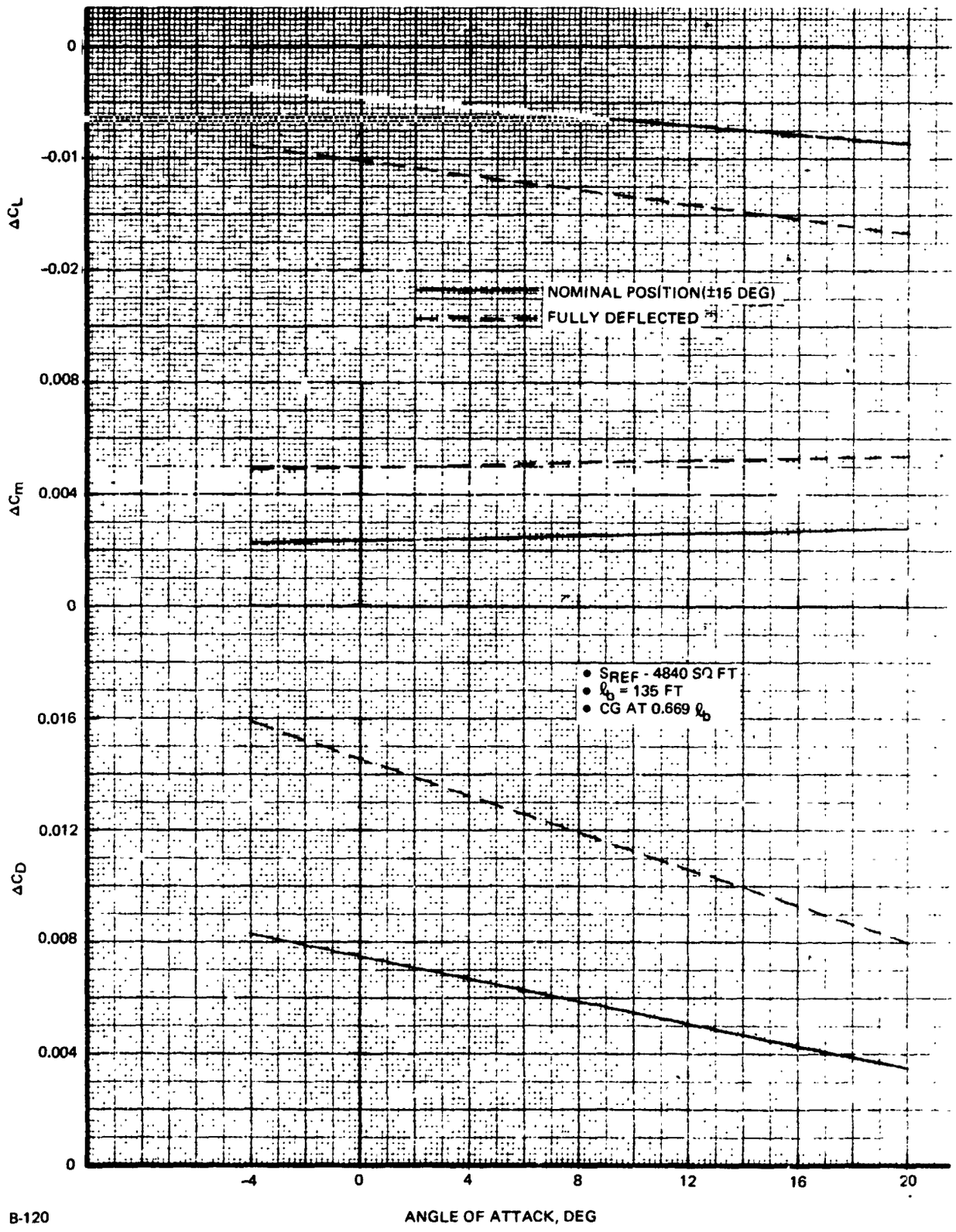

Fig. 8.3.3-43 H-33 Subsonic Longitudinal Speedbrake Increments

GRUMMAN
BOEING

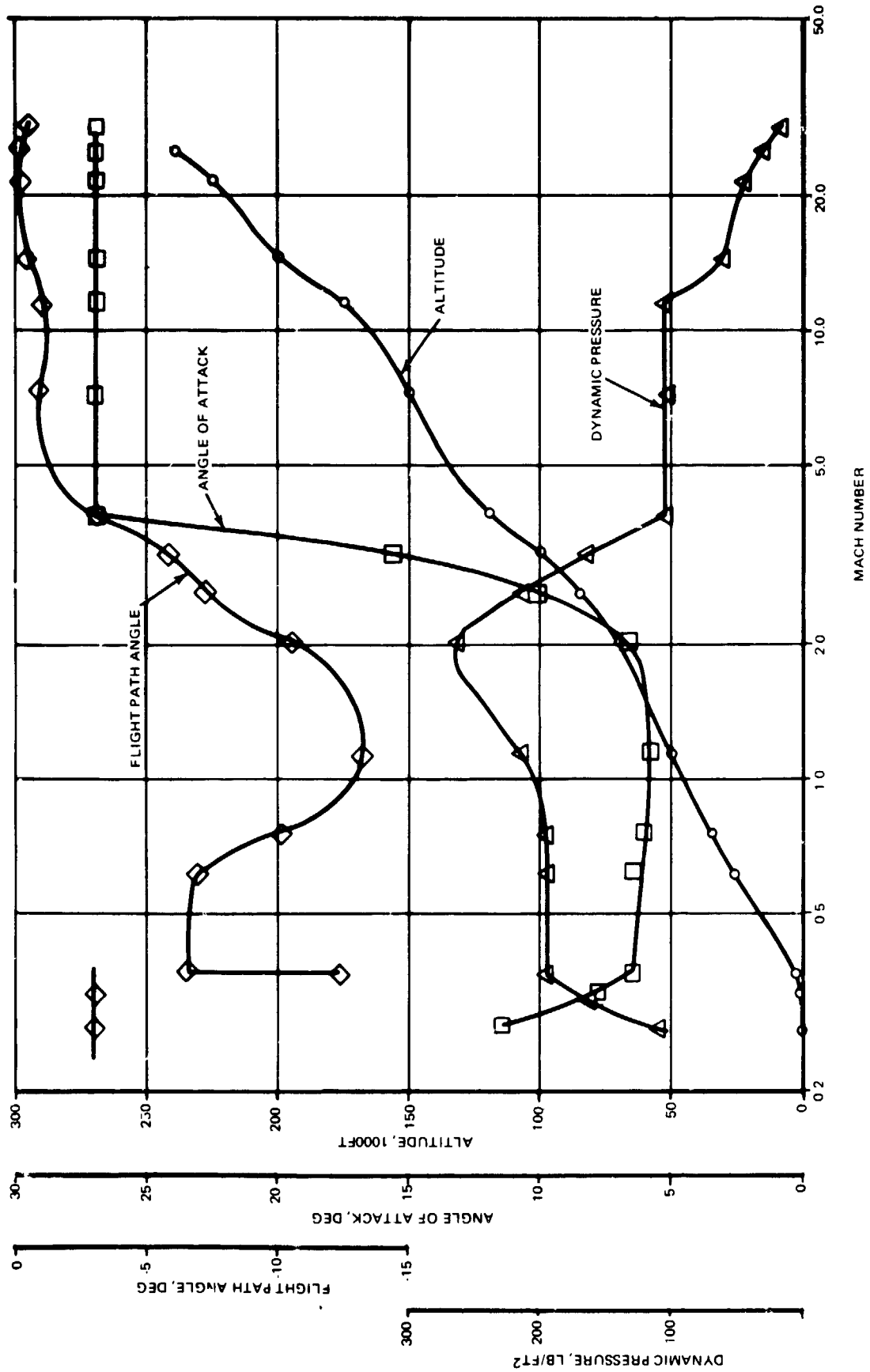

Fig. 8.3.3-44 H-33 Orbiter Design Trajectory

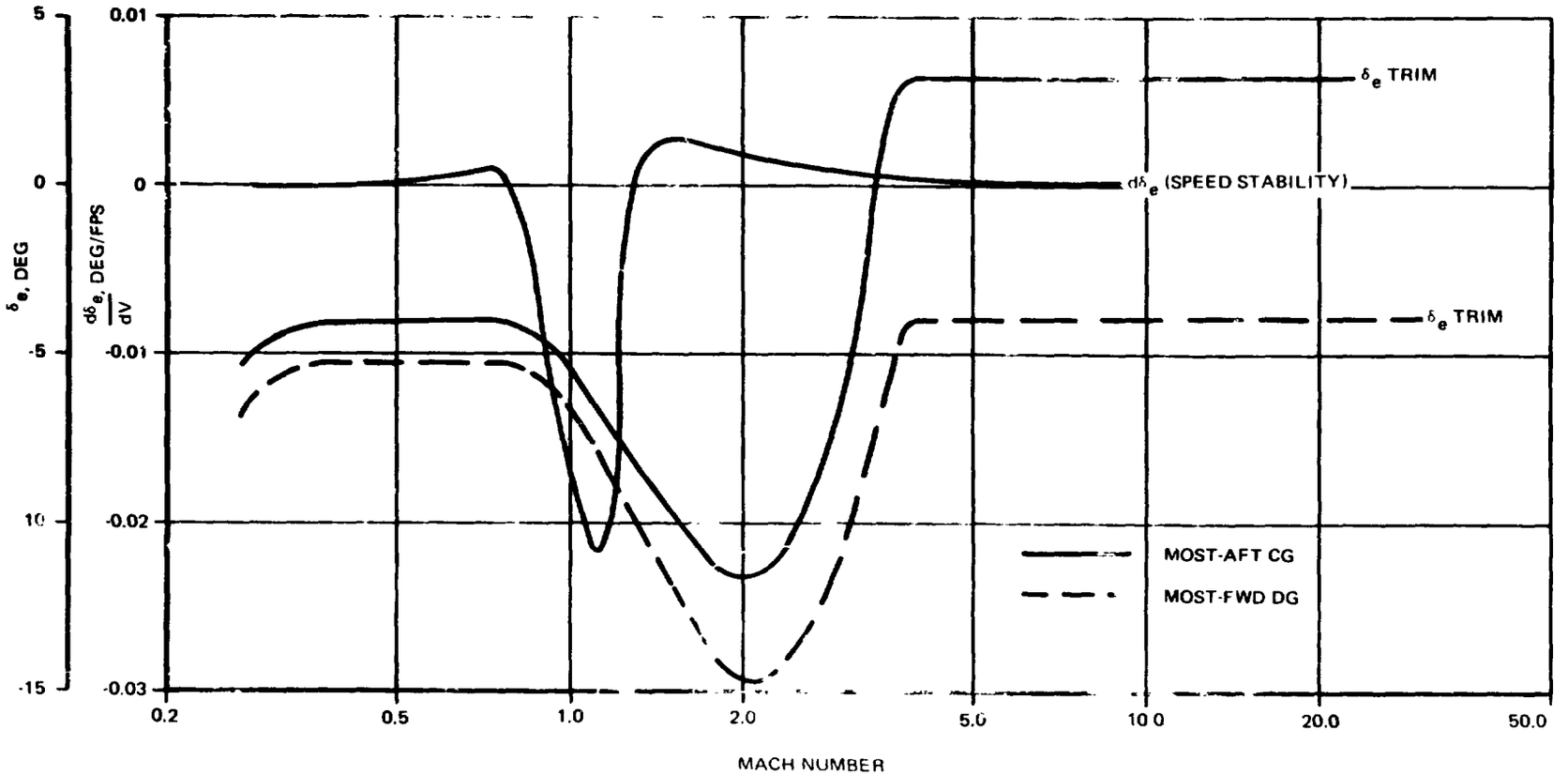

Fig. 8.3.3-45 H-33 Orbiter Longitudinal Speed Stability and Trim Requirement

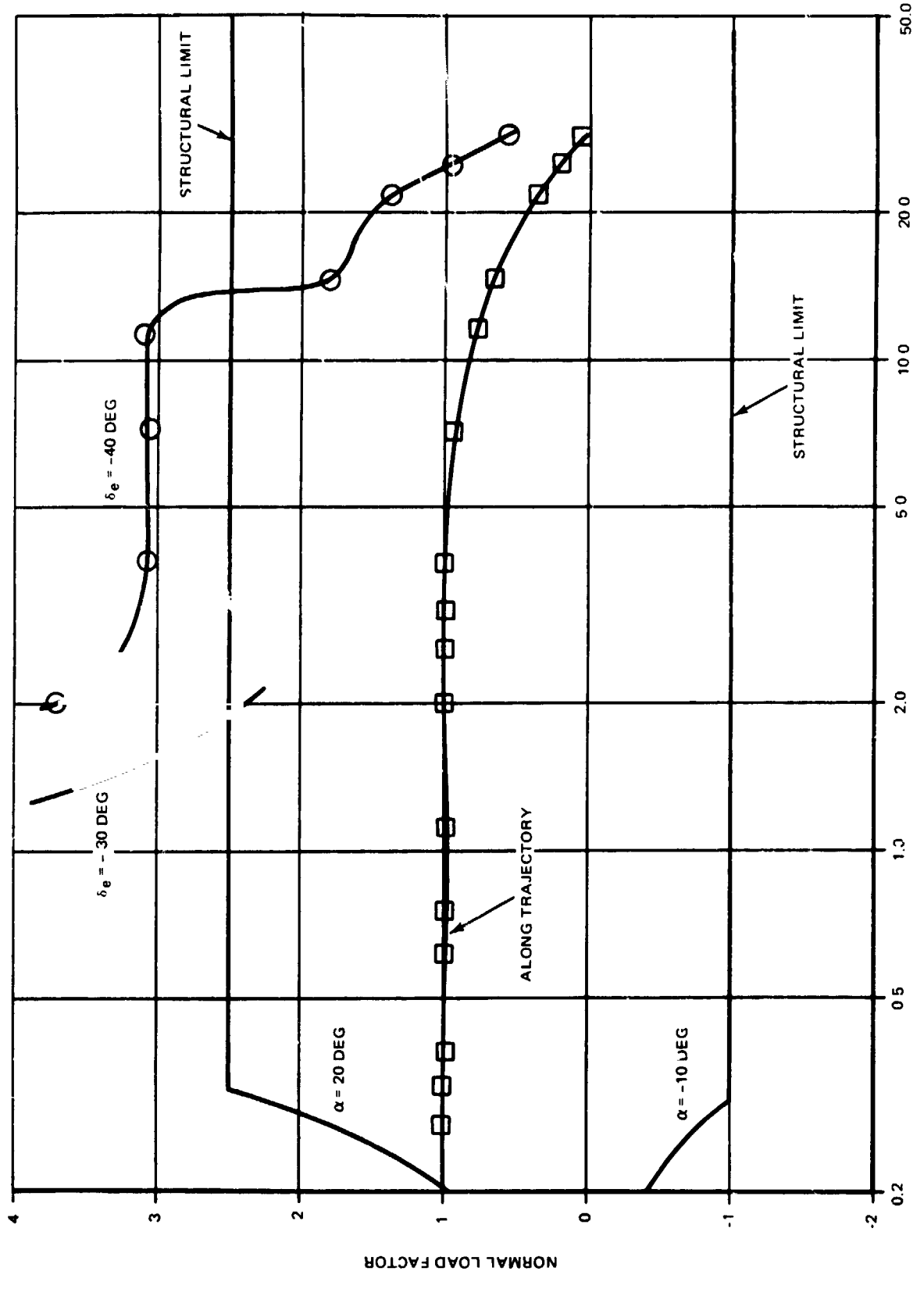

Fig. 8.3.3-46 H-33 Orbiter Longitudinal Control Power

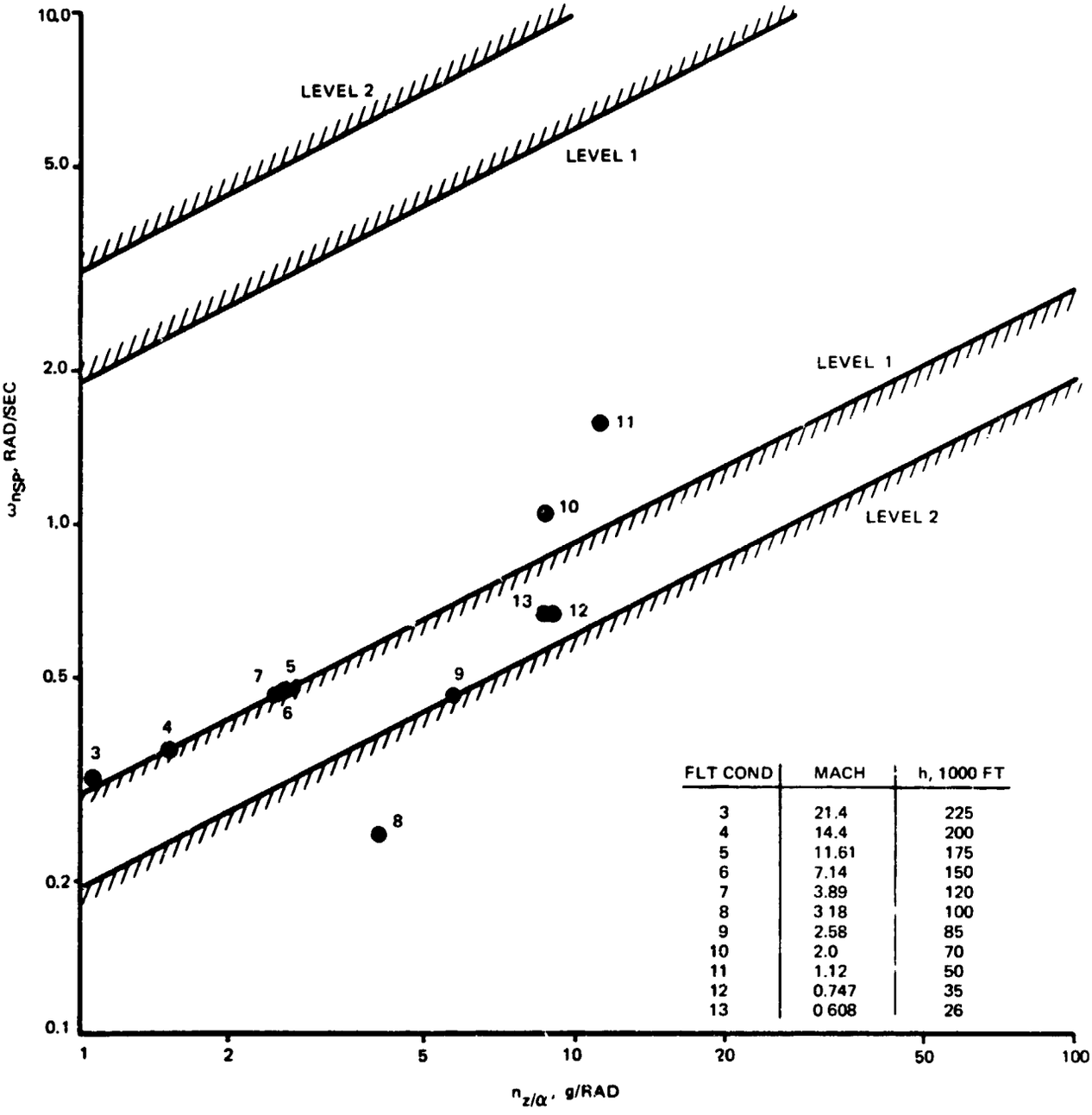

FLT COND	MACH	h, 1000 FT
3	21.4	225
4	14.4	200
5	11.61	175
6	7.14	150
7	3.89	120
8	3 18	100
9	2.58	85
10	2.0	70
11	1.12	50
12	0.747	35
13	0 608	26

Fig. 8.3.3-47 H-33 Orbiter Longitudinal Short Priced Dynamic Characteristics During Entry and Cruise

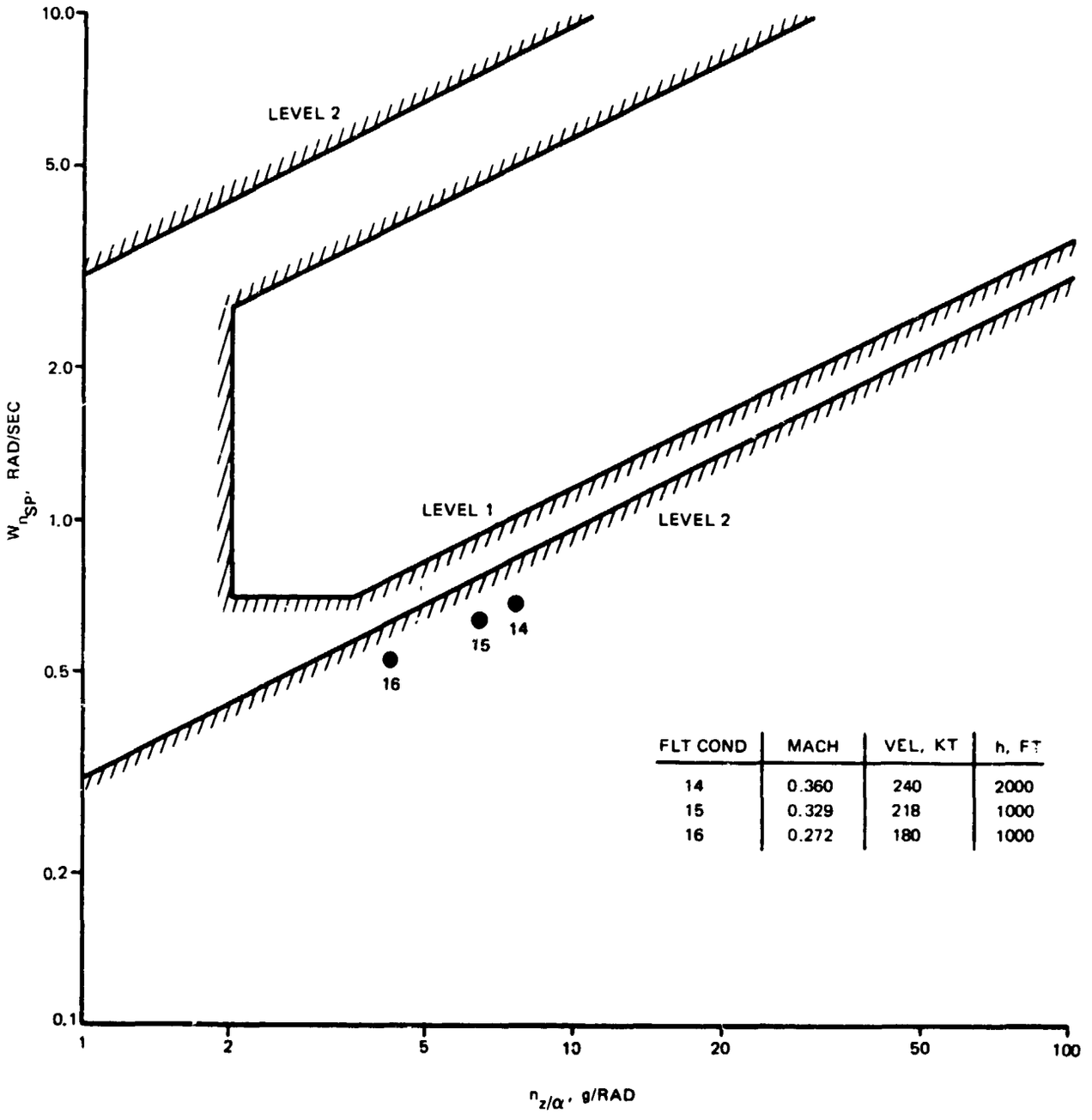

FLT COND	MACH	VEL, KT	h, FT
14	0.360	240	2000
15	0.329	218	1000
16	0.272	180	1000

B 404

Fig. 8.3.3-48 H-33 Orbiter Longitudinal Short Period Dynamic Characteristics During Approach and Landing

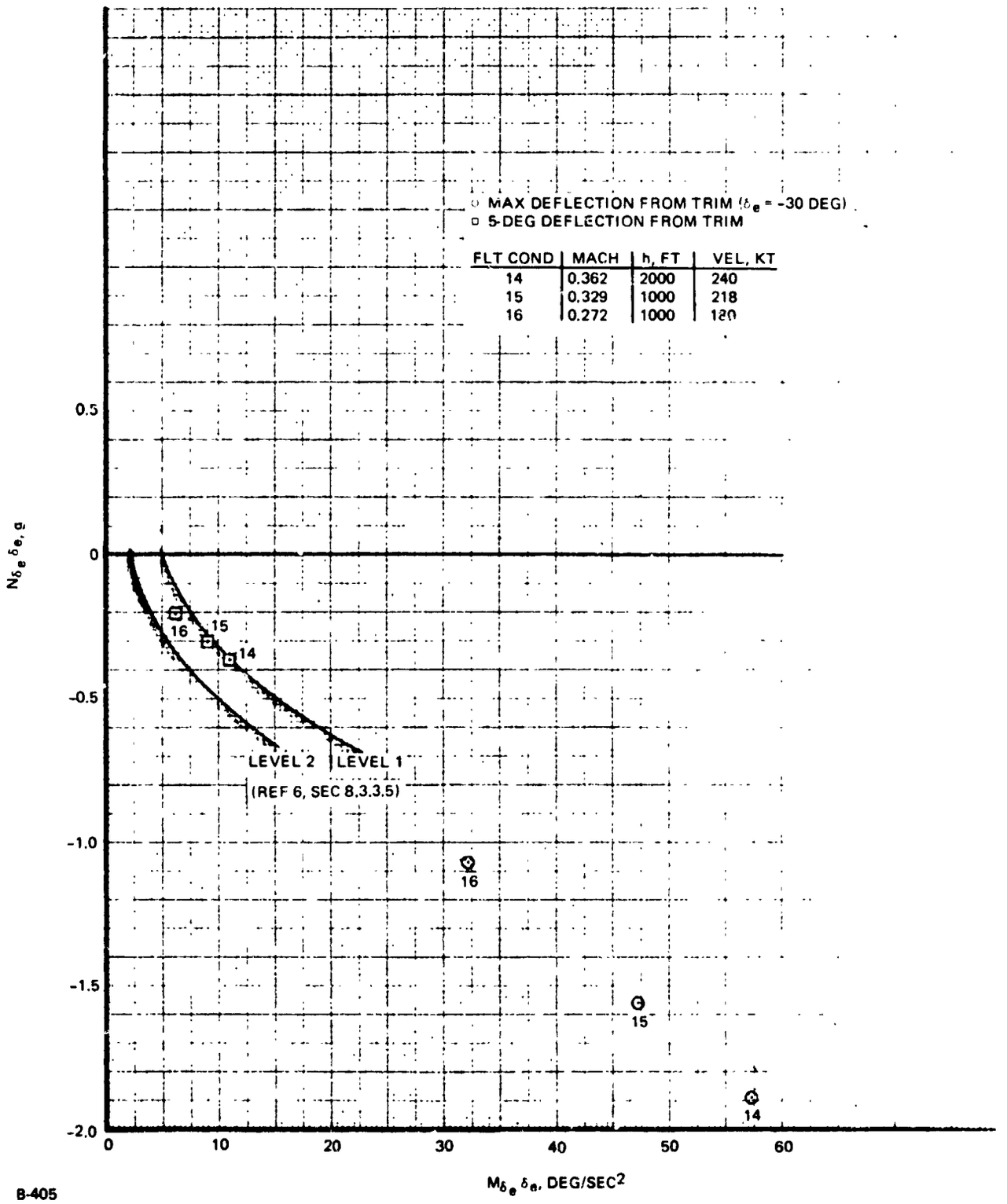

Fig. 8.3.3-49 H-33 Orbiter Longitudinal Control Lift Loss Requirement in Approach

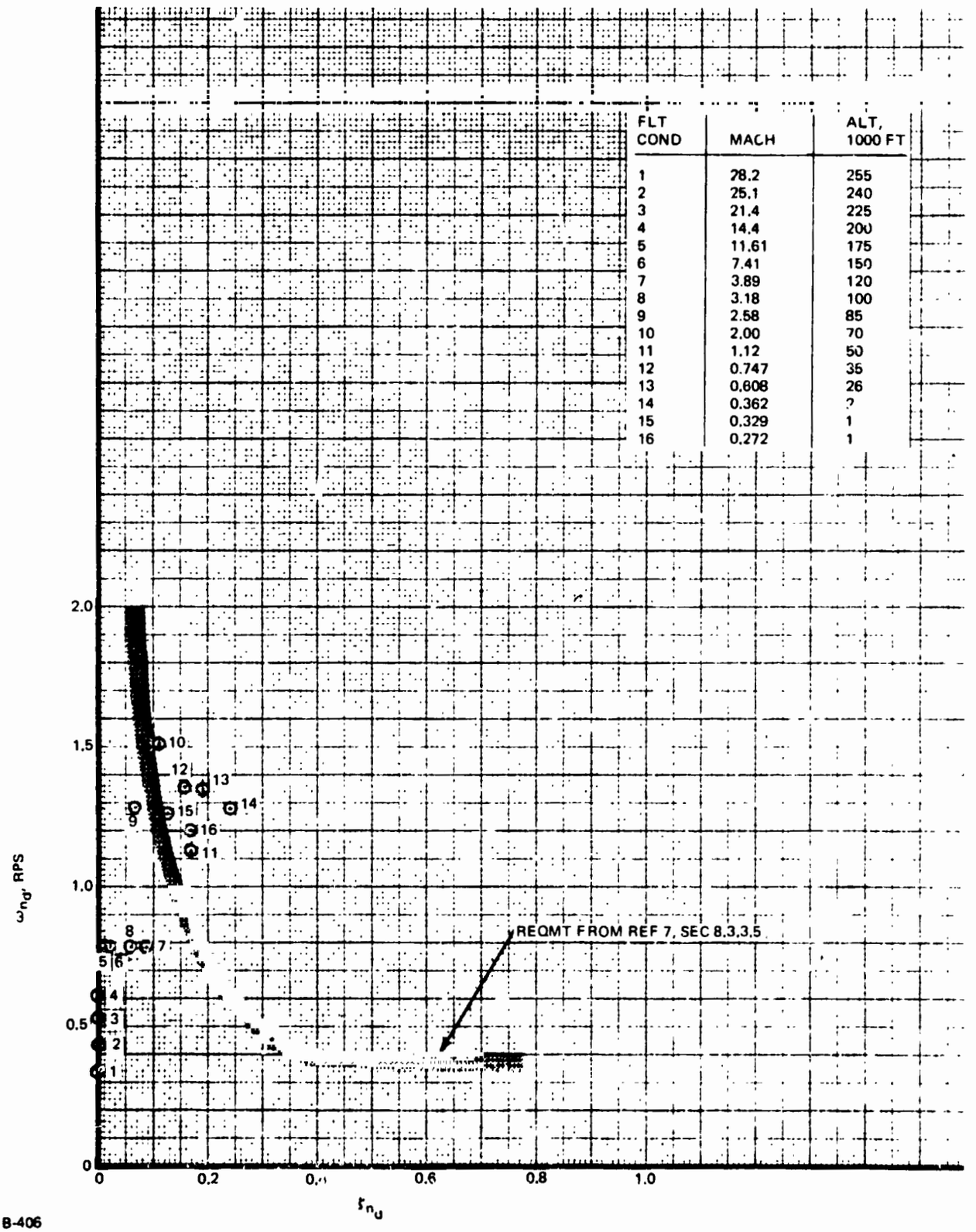

Fig. 8.3.3-50 H-33 Orbiter-Dutch Roll Mode Characteristics

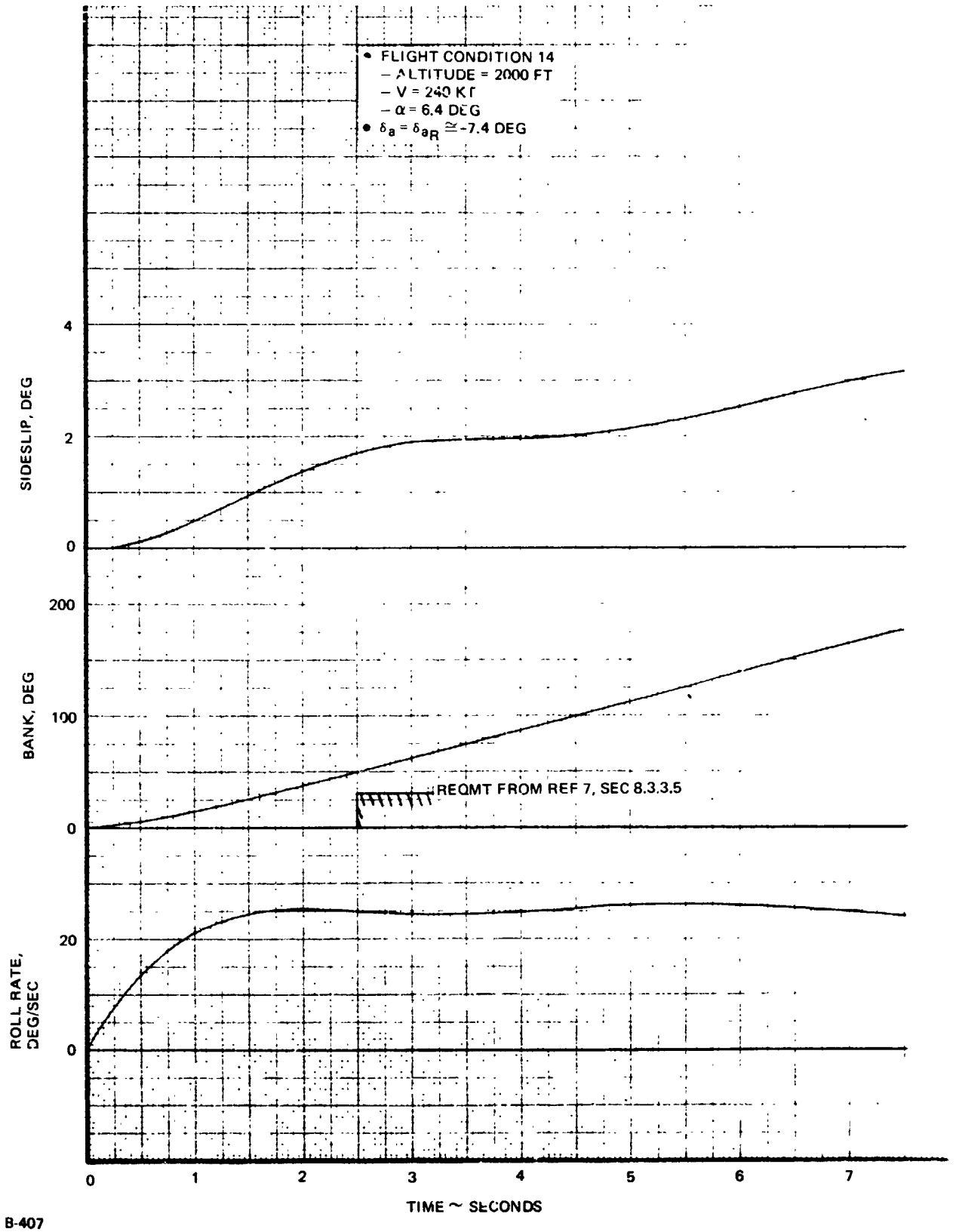

Fig. 8.3.3-51 H-33 Orbiter Roll Rate Response to Step Aileron Input

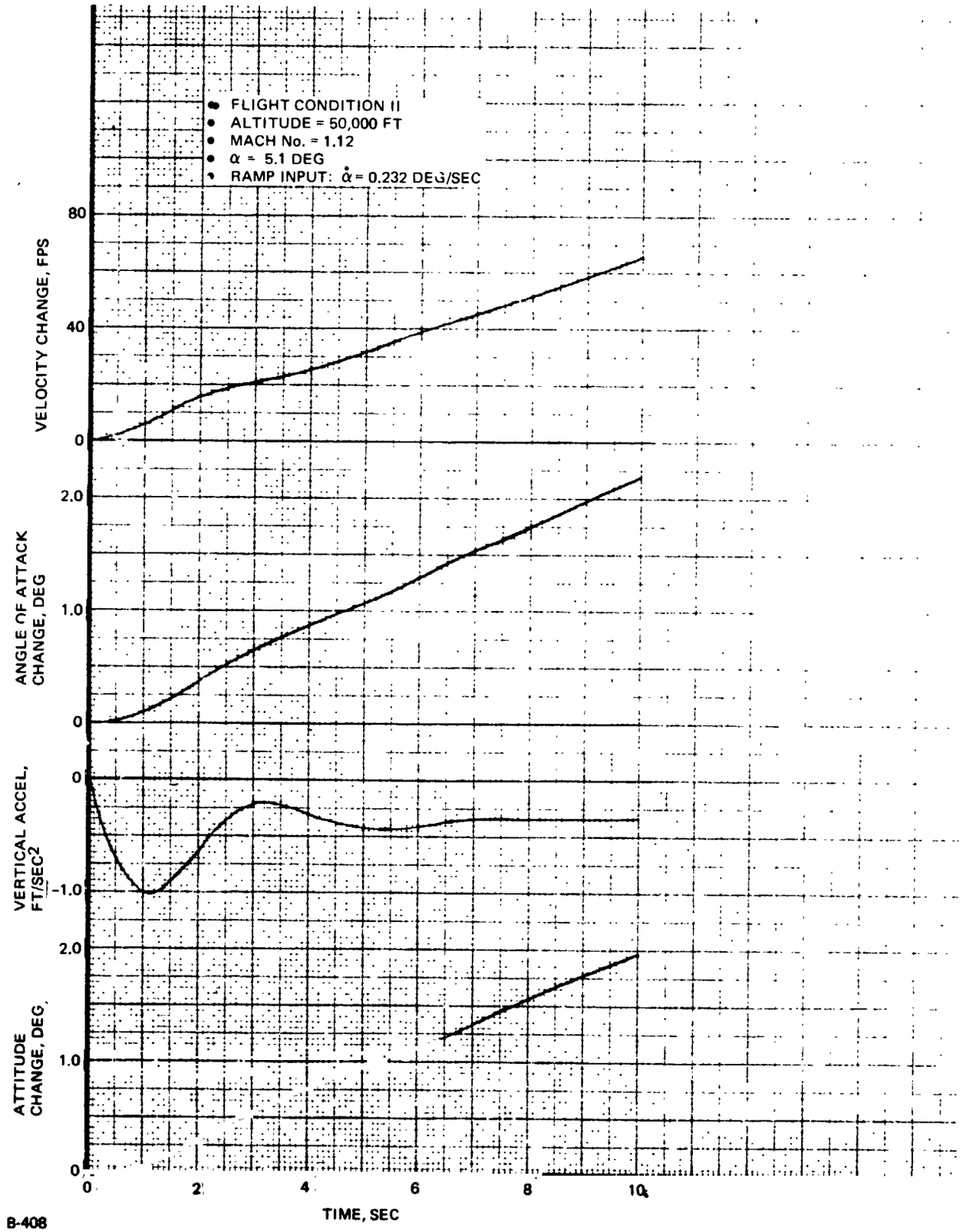

Fig. 8.3.3-52 H-33 Orbiter Basic Vehicle Response to Ramp Vertical Gust

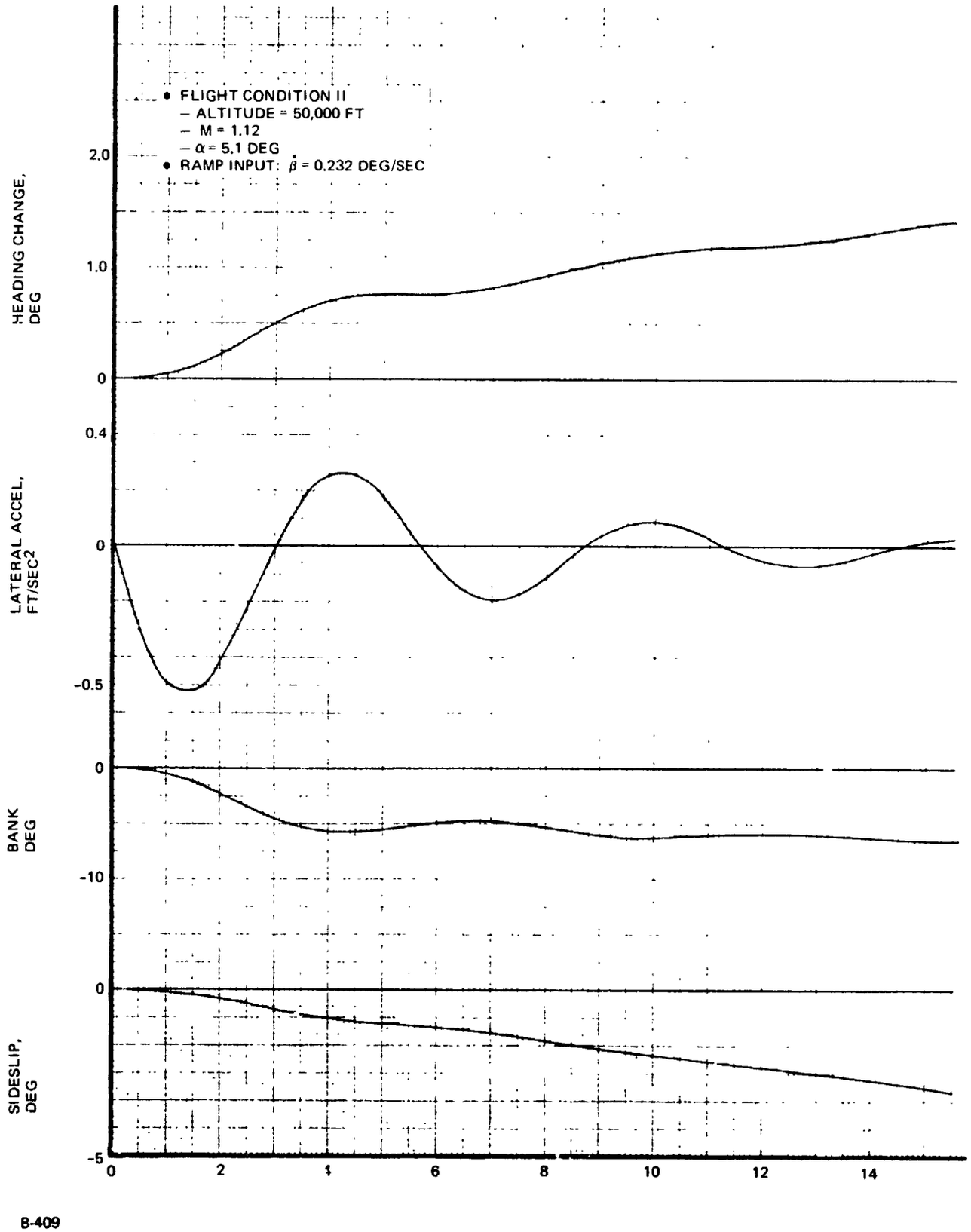

Fig. 8.3.3-53 H-33 Orbiter Basic Vehicle Response to Ramp Side Gust

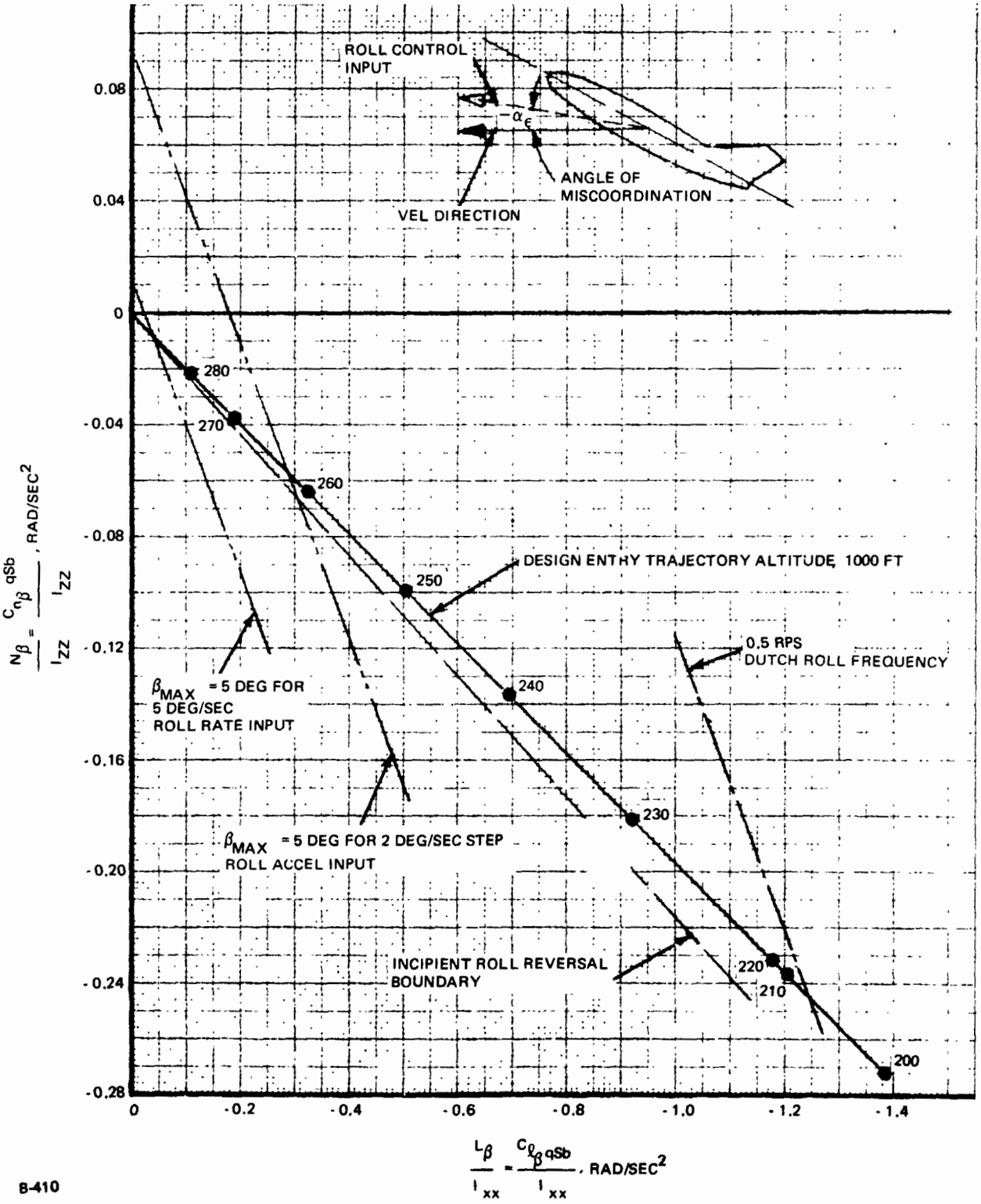

Fig. 8.3.3-54 Basic Vehicle Response to Miscoordinated Roll Control Input at Hypersonic Entry Flight ($\alpha = -5^0$)

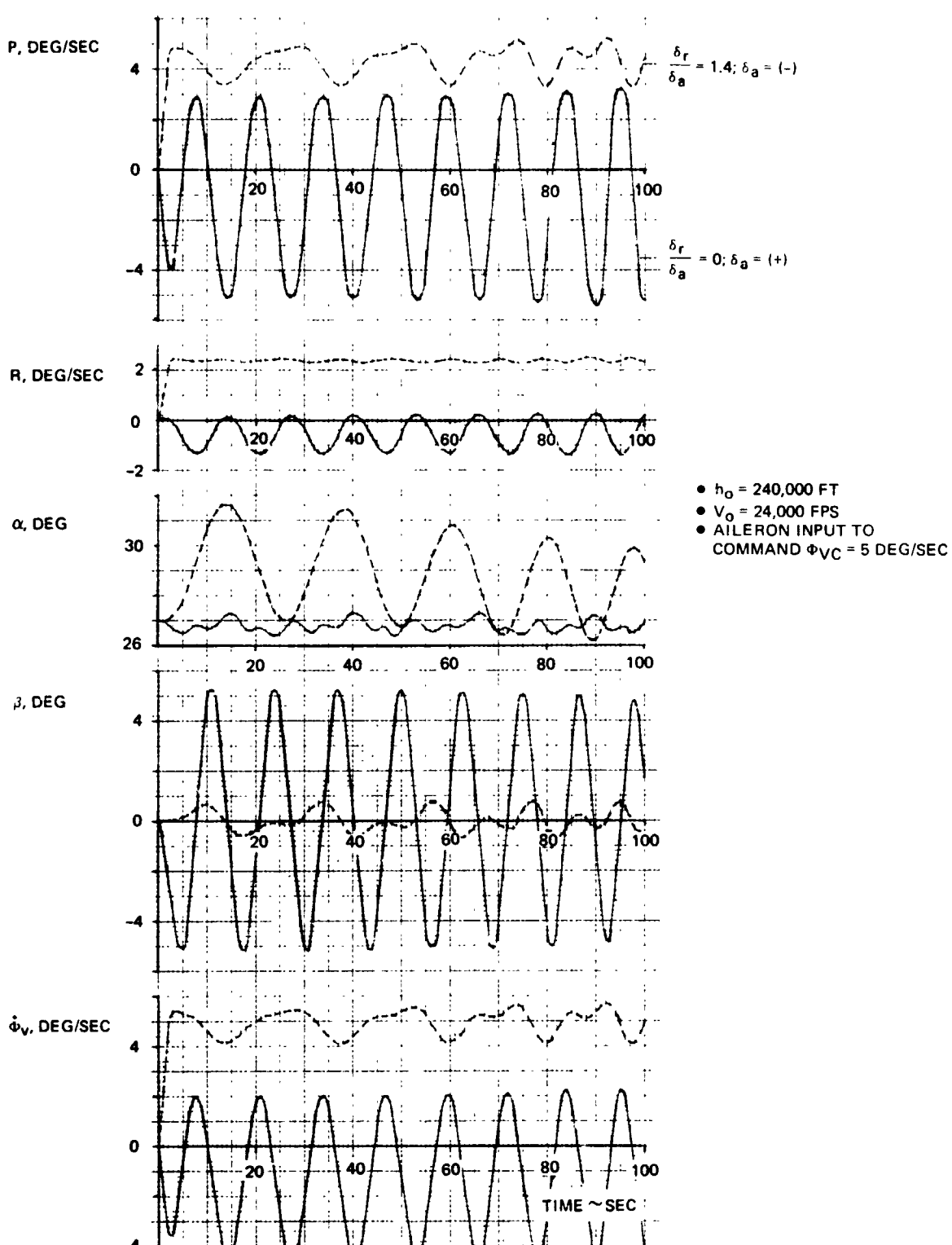

Fig. 8.3.3-55 Effect of ARI on Bare Airframe Dynamics

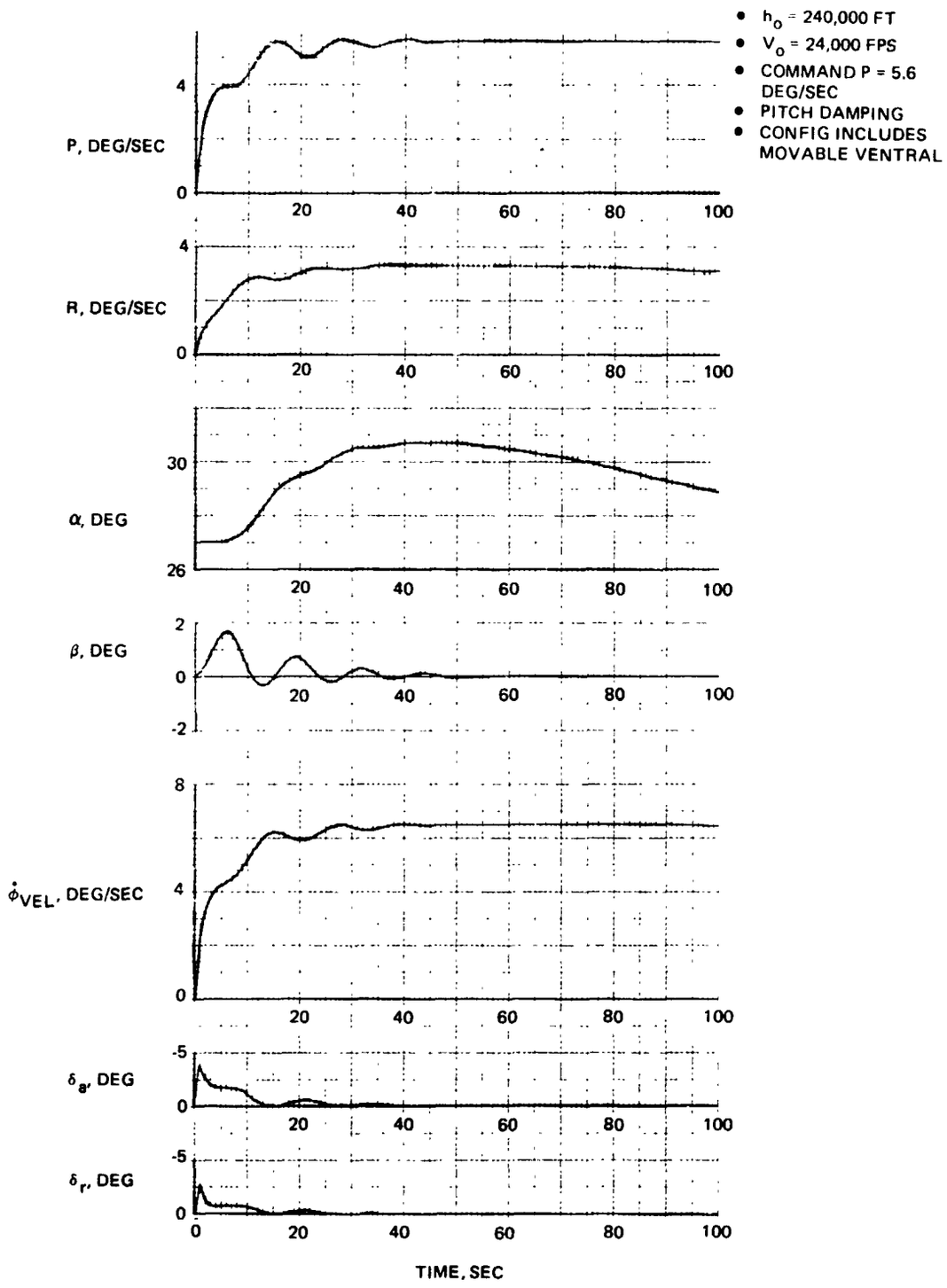

Fig. 8.3.3-56 Dynamic Response of Orbiter with SAS to Roll Rate Command (Φ_V = 6.3°/sec)

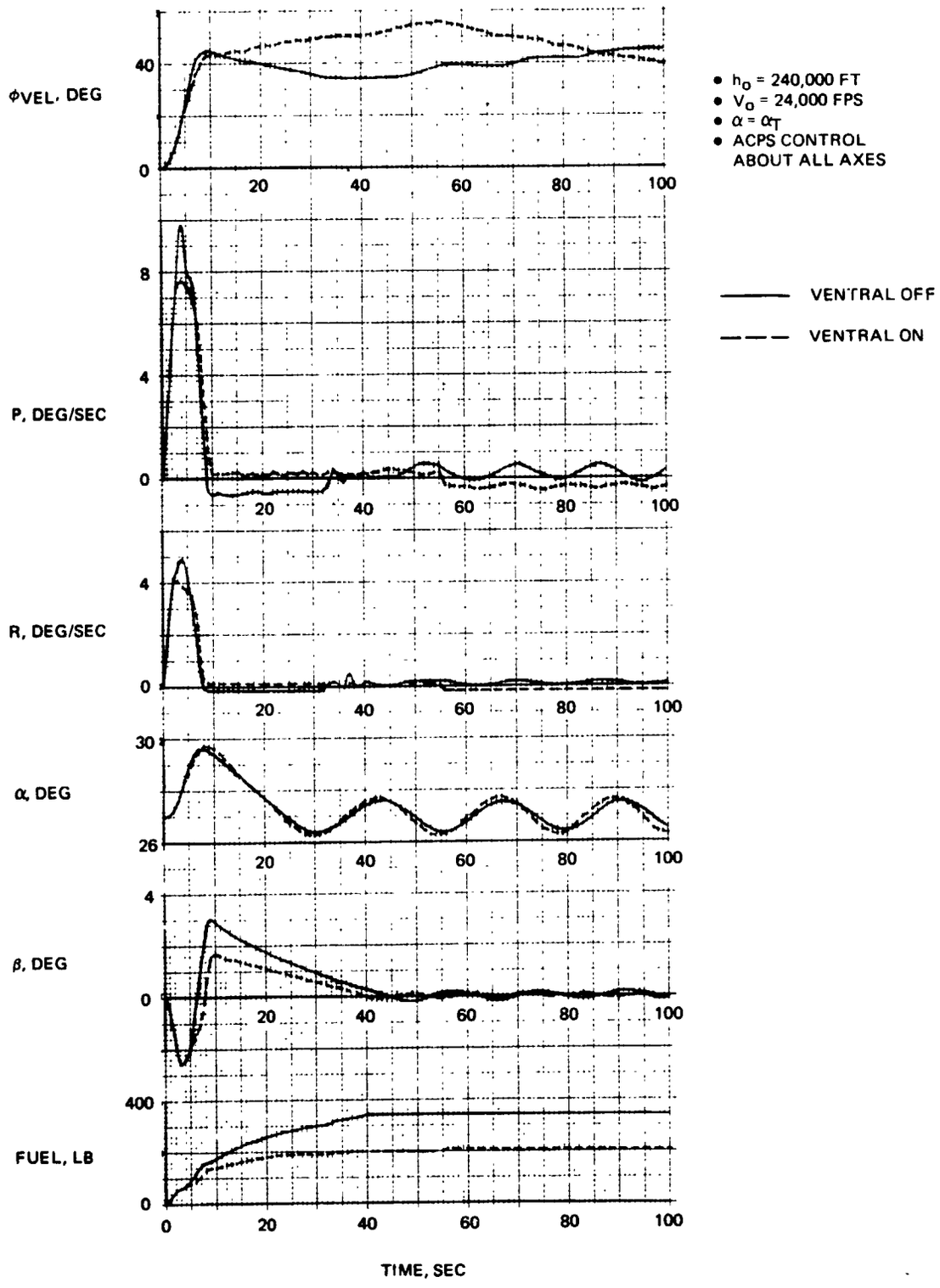

Fig. 8.3.3-57 Dynamic Response of Orbiter with Z-Dap to Bank Angle Command ($\Phi_V = 45^O$)

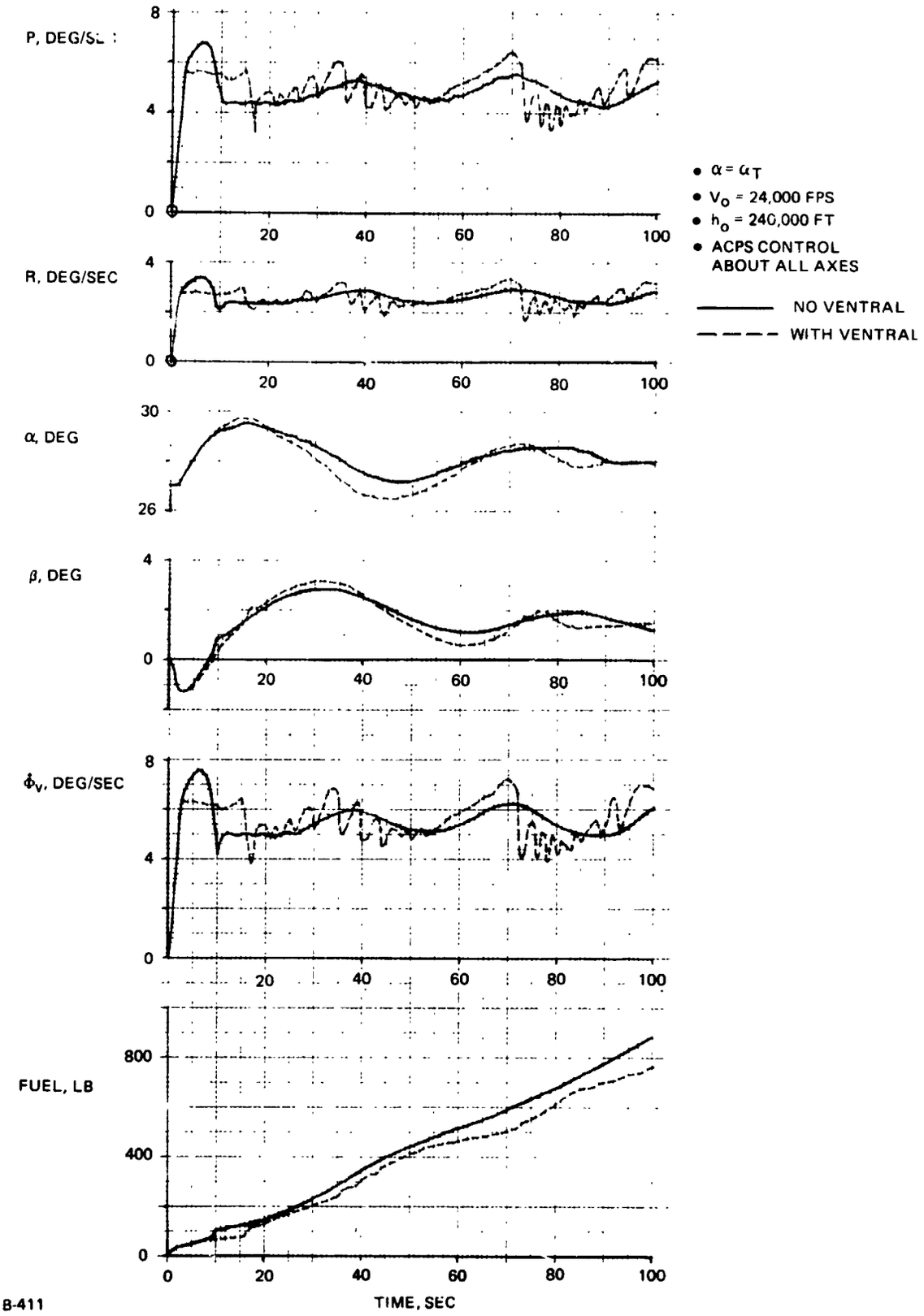

Fig. 8.3.3-58 Dynamic Response of Orbiter with Z-Dap to Roll Command ($\Phi_V = 5^o$/sec)

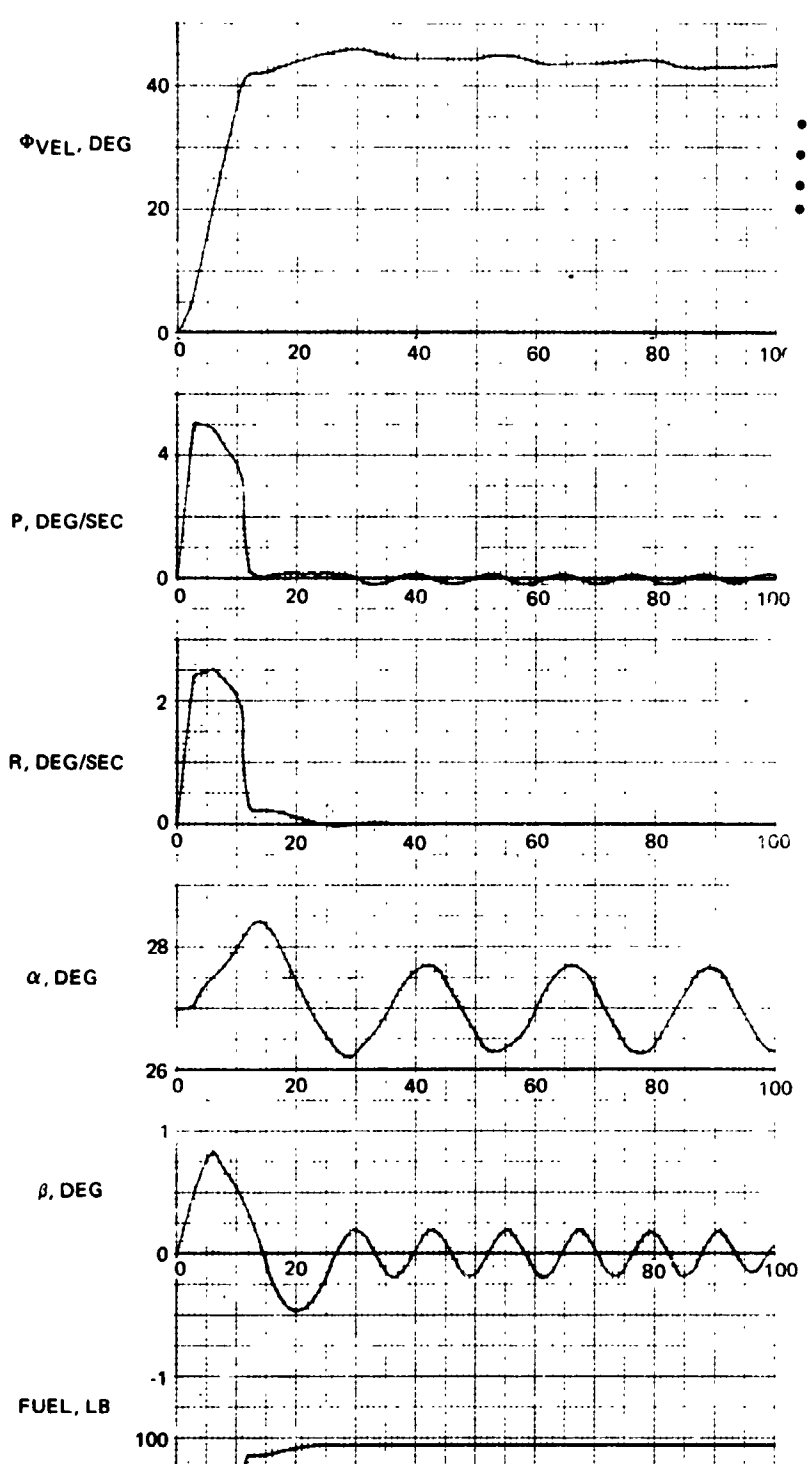

B-417

Fig. 8.3.3-59 Dynamic Response of Orbiter with X-Dap to Bank Angle Command ($\Phi_V = 45^o$)

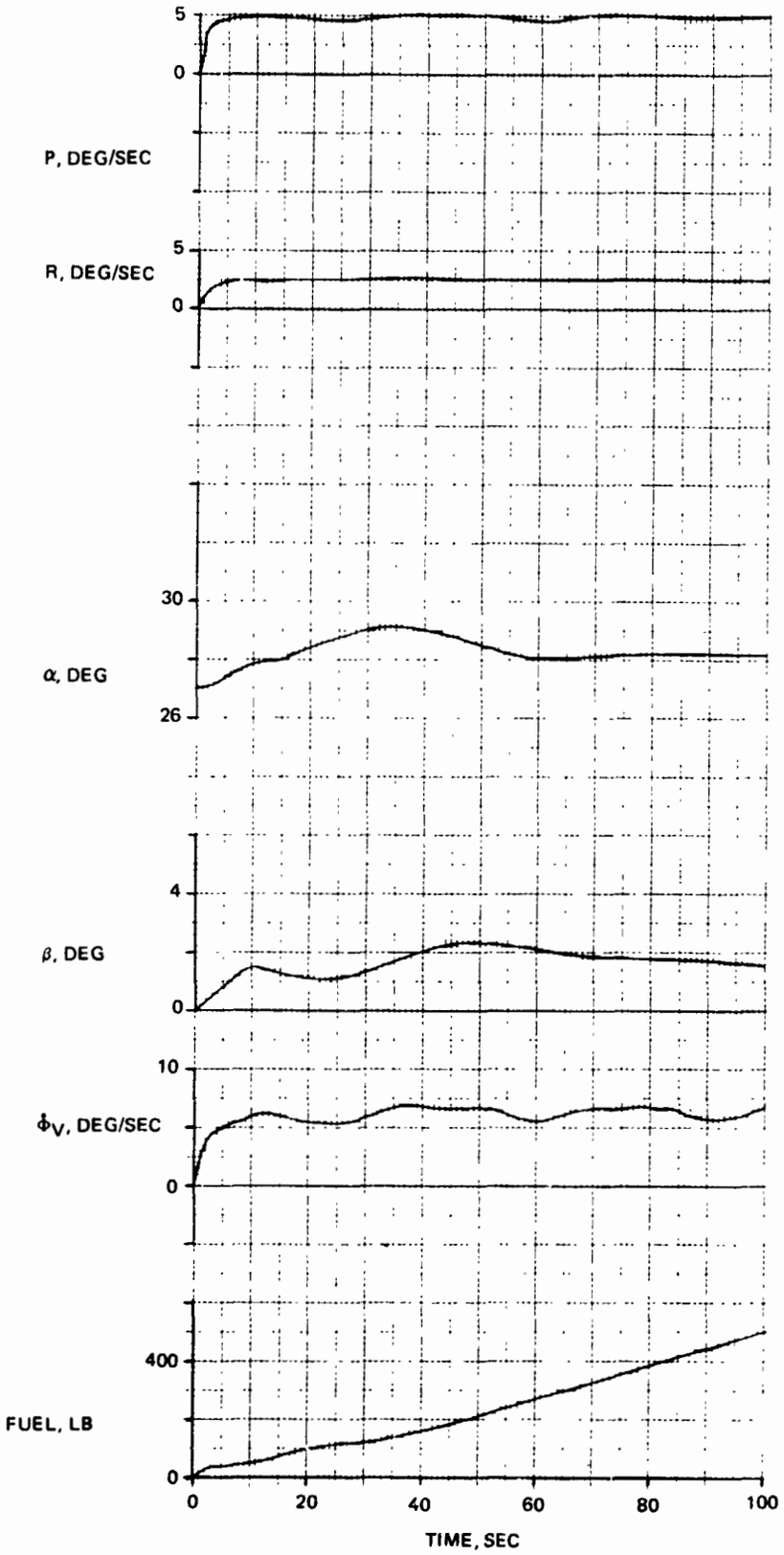

Fig. 8.3.3-60 Dynamic Response of Orbiter with X-Dap to Roll Rate Command ($\Phi_V = 5^o$/sec)

FOLDOUT FRAME 1

B/8.3

- FLIGHT CONDITIONS
  - V = 24,000 FPS
  - h = 240,000 FT
- AERODYNAMIC CONTROL IN PITCH & ROLL, ACPS CONTROL IN YAW (0.0336 RAD/SEC^2)

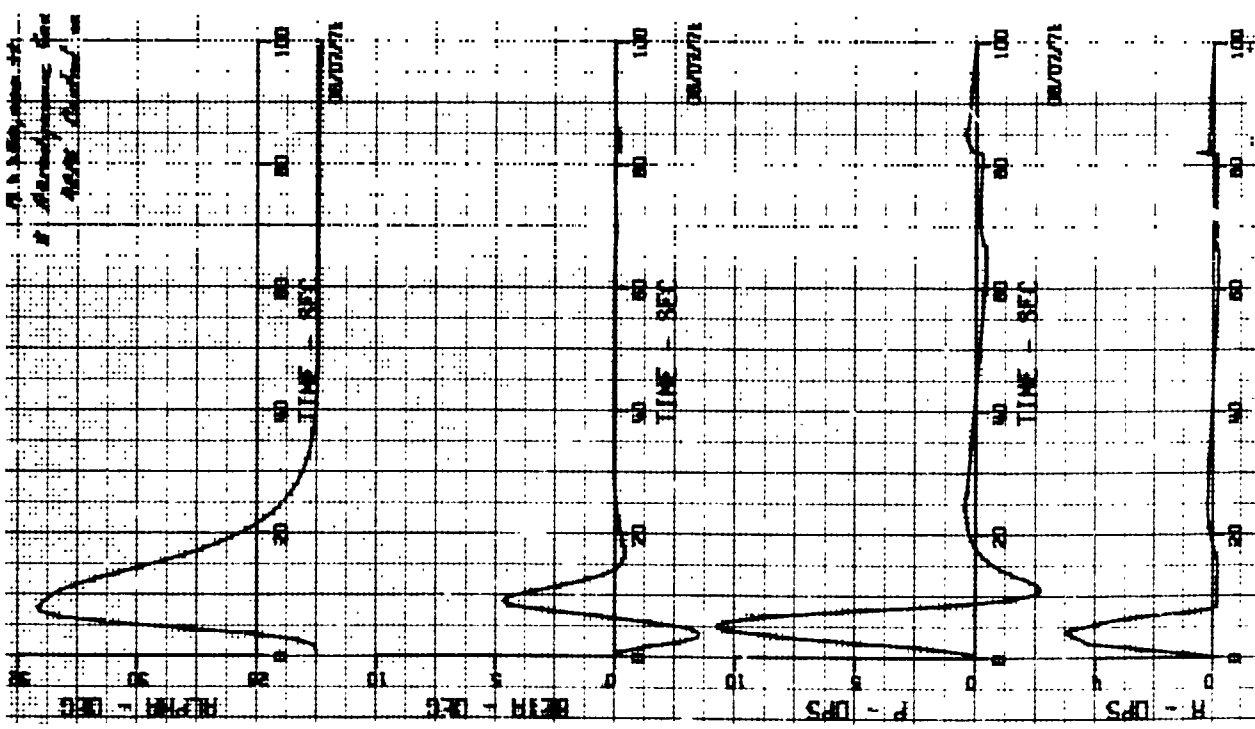

FOLDOUT FRAME 2

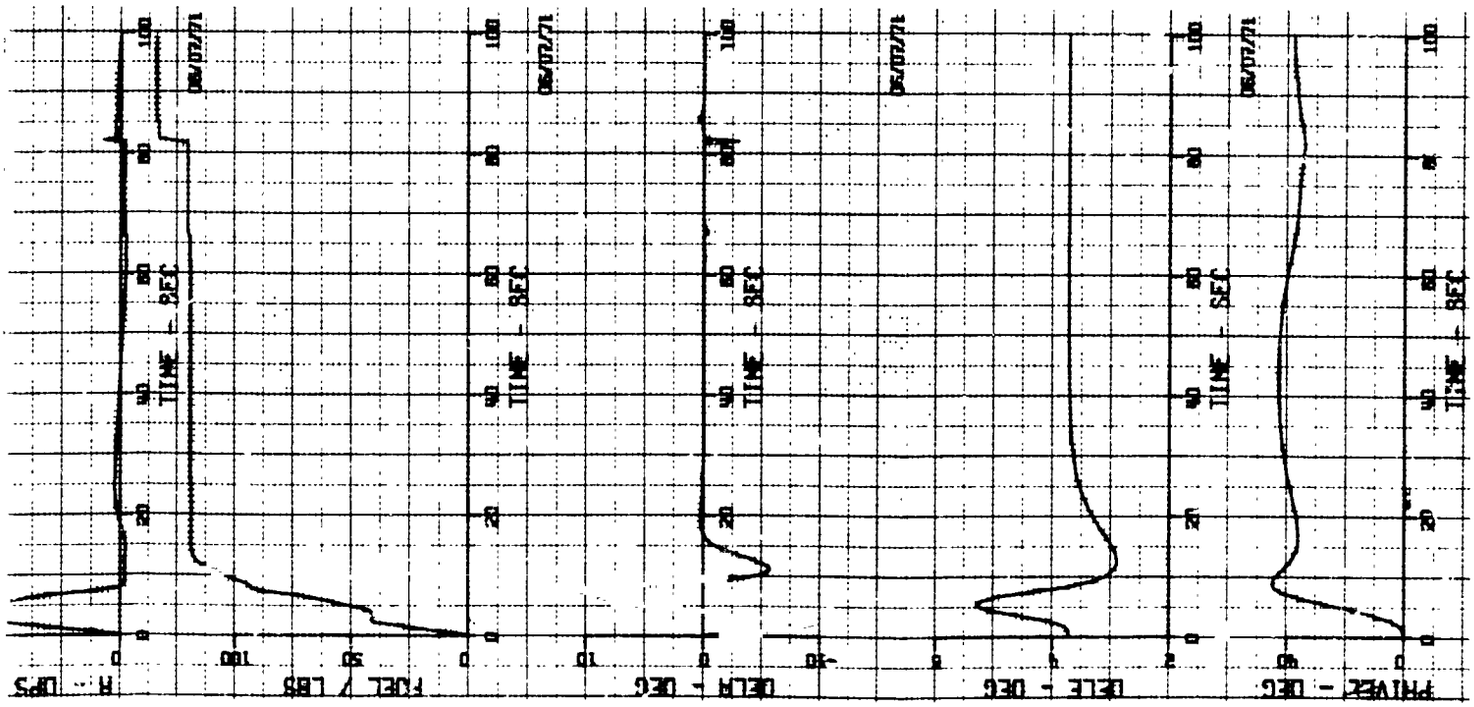

Fig. 8.3.3-61 Dynamic Response of Orbiter With Aero/ACPS Control System To Bank Angle Command ($\Phi_V = 45^o$)

GRUMMAN
BOEING

- FLIGHT CONDITIONS
  - V 24,000 FPS
  - h 240,000 FT
- AERODYNAMIC CONTROL IN PITCH & ROLL, ACPS CONTROL IN YAW (0.0336 RAD/SEC^2)

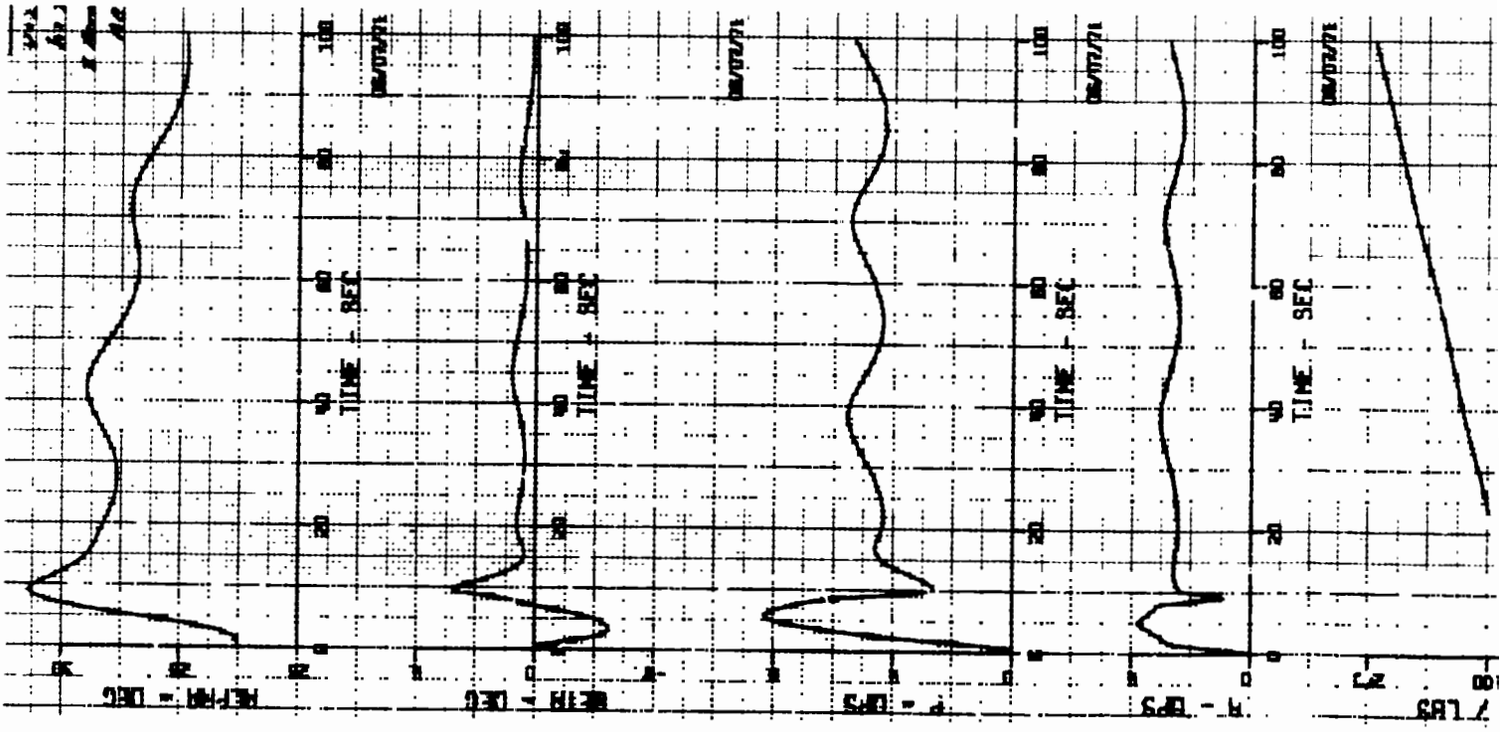

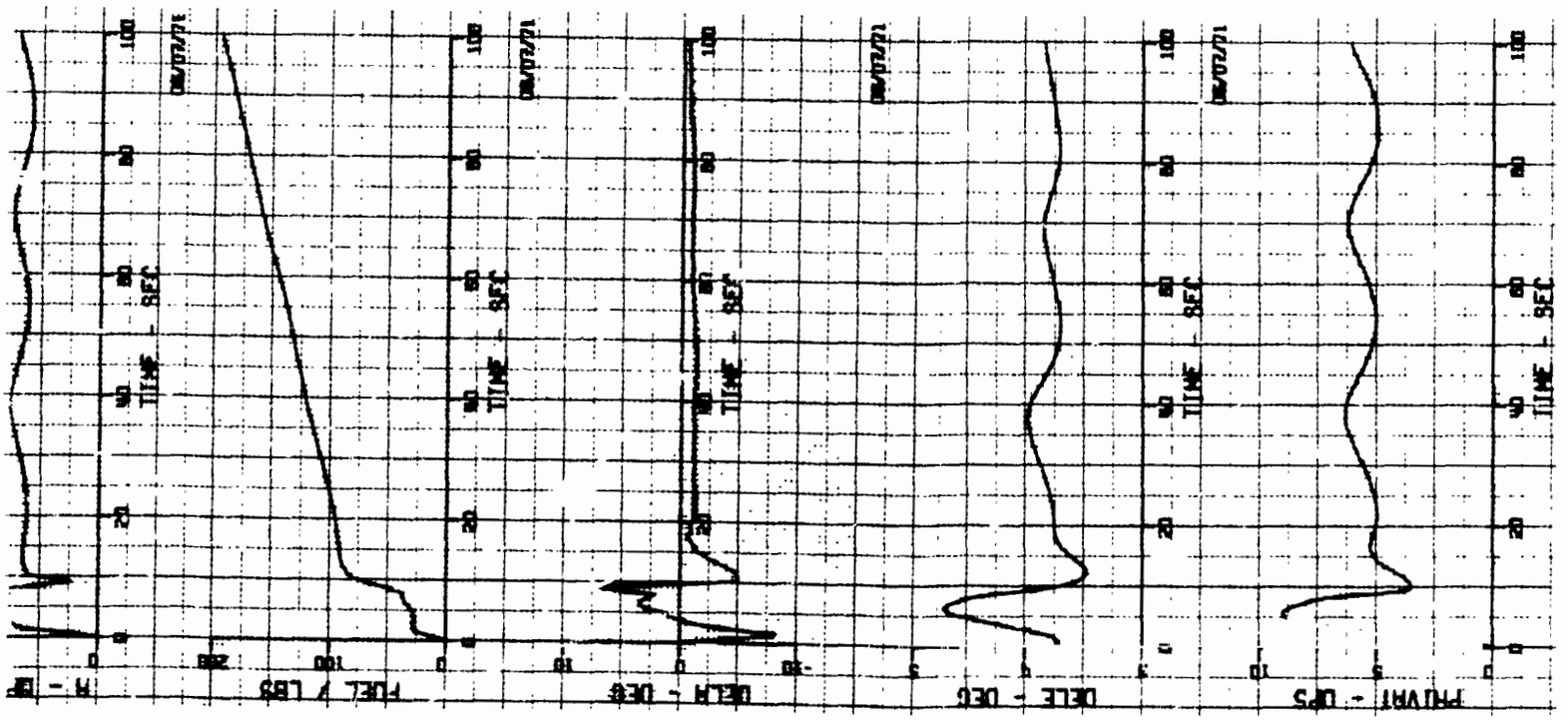

Fig. 8.3.3-62 Dynamic Response of Orbiter With Aero/ACPS Control System to Roll Rate Command ($\Phi V = 5^{0}$/Sec)

GRUMMAN
BOEING

8.3.4 PERFORMANCE

This subsection contains a general performance summary for the H-33 External Tank Orbiter design mission profiles. Where appropriate, discussion of the G-3 internal hydrogen tank orbiter has been included for comparison purposes.

Orbital operations are described for the space station resupply mission. Delta-V budgets have been determined and various system tradeoffs are presented. Of significance, it was found that it is feasible to de-orbit using the ACPS as a back-up to the RL-10 with a small 40 fps penalty. In addition, the use of ACPS in the igniter-only mode was found to reduce attitude control propellant requirements by 250 lb during the rendezvous as well as providing a potential fine control mode for missions requiring high pointing accuracies. Minimum impulse body rates of 0.0010 deg/sec are achievable.

Our entry studies have investigated entry guidance techniques, crossrange performance capability as well as control requirements. Aeroheating and load restrictions have been included to determine the overall effects on TPS design and ACPS propellant requirements. The results of these studies indicate that a high crossrange polar entry from a 0 n mi circular orbit would generate the critical design heating environment. For our baseline entry design mission an 1100 n mi cross range relative to an earth fixed great circle was selected. The aeroheating environment contained in Subsection 8.3.5 and TPS designs described in Subsection 8.4.6 have been based on this critical design mission. Our studies are continuing, to determine the impact, if any, of the abort to onceround requirement on TPS design.

Our studies indicate a large footprint is available for operational flexibility within the underbody temperature limitation of 1610° F (representative of large percentage of vehicle underbody). Downrange capability from heel to toe averages 4000 + n mi, crossrange up to 165 + n mi. This performance was obtained using entry guidance control policies for underbody thermal and target control, with a realistic ACPS/aero-trim entry autopilot as described in Subsection 8.3.4.2.

Entry autopilot studies have included studies of ACPS thruster sizing, trajectory control, aero surface trim systems for cg offsets and uncertainties, and use of aero flight control during entry. Significant results indicate ACPS thruster size can be reduced on the orbiter to 1000 lb with substantial savings in ACPS propellant at slight expense to terminal miss distances. The energy management capability of the orbiter is sufficient to tolerate this increase. An aero surface trim system has been formulated using moment unbalance compensation techniques developed in the Apollo program; results indicate that with assumed lateral cg offsets of 2 in. aero trim is achieved within 20 sec with minimum ACPS propellant consumption.

After the transistion maneuver, which is characterized as a slow nose down pitch maneuver starting at M = 4 and 120,000 ft and terminating at M = 2 at 70,000 ft, a spiral glide is initiated from high key. Energy management techniques results in a terminal footprint capability of from 30 to 80 n mi from 35,000 ft depending on heading change required to landing site. This glide range capability is adequate for all entry and conditions anticipated at this time. At low key, the vehicle is aligned with the runway; approach glide path is adjusted by use of the speed brake at apprach speeds on the "front" side of the drag curve, with a final flare and touchdown at approximately 180 kt. Detailed approach and landing performance data are presented in paragraph 8.3.4.3.

For the ferry mission an additional airbreathing engine is required to meet the one-engine-out 10,000 ft ceiling requirements. A discussion of the installation provisions is contained in Subsection 8.5. The ferry package is sufficient to provide 300 n mi range with reserves for a 20 min hold, missed approach and a go-around. It should be noted that the basic orbiter propulsion system (four engines) marginally satisfied the ferry requirements as stated by the NASA (ceiling of approximately 9200 ft). The addition of the fifth engine for ferry purposes does provide a significant improvement in tropic day performance which appears reasonable for expected summer ferry conditions encountered in CONUS.

8.3.4.1 Orbit Operations

Performance studies have been made to support the OMS and ACPS on-orbit consumables analyses presented in Section 4. Table 8.3.4-1 summarizes the data used in Section 4 for the 270 n mi, 55 deg inclination resupply mission with the external tank orbiter. The total on-orbit OMS propellant loading is 28,605 lb and 1698 lb for translational and

rotational requirements, respectively. Included in the propellant allocation is a 280 fps delta-V margin in translation to account for dispersions prior to the terminal rendezvous phase (160 fps), during terminal rendezvous (50 fps) and deorbit reserves (70 fps). A 5% margin is included for attitude maneuver propellant margins. Similar consumables profiles were prepared for the South Polar and Due East missions and are summarized in Section 4.

The remainder of this section is used to discuss the results of orbit performance analyses which will be the basis for more detailed consumables analyses in the future. The results of these studies can be summarized as follows:

- The 210 fps delta-V allocation for rendezvous dispersion is conservative for a mission in which the height adjustment maneuver is performed one-half orbit after the phasing maneuver. The results of a Monte Carlo Analysis indicates that 26 fps for dispersion would be sufficient for the nominal rendezvous
- A 70 fps delta-V de-orbit reserve is sufficient to provide an ACPS de-orbit back-up capability
- A propellant savings of 250 lb is achieved during the rendezvous mission by using the 50 lb ignitor engines during attitude hold functions
- A propellant savings of 230 lb could be achieved in the space station resupply mission if the OMS engines were gimballed. This savings is based on an assumption that the OMS thrust vector misalignment would be no greater than 3 deg. Further, in-depth study is required to determine the desirability of not gimballing the OMS engines

8.3.4.1.1 Translational Performance

a. Rendezvous

An evaluation of the shuttle rendezvous was performed to support mission planning for the Space Station resupply mission and to define requirements for the synthesis and design of the navigation and on-orbit propulsion system. The following summarizes the assumptions made in these evaluations:

- The shuttle navigation system is calibrated, aligned and initialized prior to liftoff
- Inertial sensors are employed during the launch/boost-to-orbit insertion phase

TABLE 8.3.4-1 OMS TANK LOADING REQUIREMENT, SPACE STATION RESUPPLY MISSION (Sheet 1 of 2)

Event	OMS ΔV, (fps)	OMS Propellant, (lb)	ACPS Translation, (lb)	ACPS Rotation Propellant (lb)
1) Attitude Maneuver Following Insertion, Ullage, Tank Jettison, and Maneuver Prior to Phasing			234	300
2) Phasing Maneuver and Attitude Control	120	2330		40
3) Attitude Maneuver After Phasing, Attitude Hold During Coast and Maneuver Prior to Height Adjustment Burn				104
4) Height Adjustment and Attitude Control	280	5460		104
5) Attitude Maneuver After Height Adjustment to Tracking Attitude, Coast and Maneuver Prior to Coelliptic Burn				104
6) Coelliptic Maneuver and Attitude Control	240	4760		92
7) Maneuver to Tracking Attitude, Coast and Maneuver Prior to TPI				106
8) TPI Maneuver and Attitude Control	21	390		8
9) Maneuver to Tracking Attitude After After TPI, Coast and Maneuver Prior to Braking Sequence				105
10) Braking Maneuvers and Attitude Control	25		540	155
11) Station-keeping	3		64	90
12) Docking	25		400	140
13) Undocking, Coast and Maneuver to De-Orbit Attitude	1		20	110
14) De-Orbit Burn and Attitude Control	486	9200		95
15) Maneuver to Reentry Attitude				60
Subtotal	1211	22140	125[a]	1613

TABLE 8.3.4-1 OMS TANK LOADING REQUIREMENT
SPACE STATION RESUPPLY MISSION (Sheet 2 of 2)

Event	OMS V, fps	OMS Propellant, lb	ACPS Translation, lb	ACPS Rotation Propellant, lb
Reserves and Margin	280	5207		85
Total	1490	28,605		1698

- The state vectors are extrapolated by coasting flight integration between orbit insertion and rendezvous sensor acquisition
- Navigation is similar to Apollo rendezvous techniques
- All maneuvers are performed under control of the onboard computer

b. Coelliptic Sequence

The logic associated with the initial targeting of the rendezvous is presented in Fig. 8.3.4-1.

The first three orbital burns occur at apogee of the appropriate orbits. The phasing maneuver is performed to achieve the proper in-plane central angle between the shuttle and the target for initiation of the terminal rendezvous under the desired lighting conditions. This phase adjustment can be performed in one or several orbits to privide a substantial launch window. Under the most severe out-of-phase condition, as much as 24 hr may be required for this leg of the rendezvous. The height adjustment is targeted to 10 n mi below the passive vehicle for the subsequent catchup mode prior to Terminal Phase Initiation (TPI). Variations in this maneuver can be made (i.e., target 10 n mi above the passive vehicle for a subsequent slow down maneuver) as a means of decreasing the rendezvous flight time. The TPI maneuver is executed when the line of sight between the target and the shuttle local horizontal is 28 deg. The Braking Sequence consists of a series (nominally three) of ACPS maneuvers to reduce velocity, of and continuous line-of-sight rate adjustments.

The nominal elapsed time, traversed central angle, required delta-V, maneuver duration and range to the target for the various burns of rendezvous is given in Table 8.3.4-2.

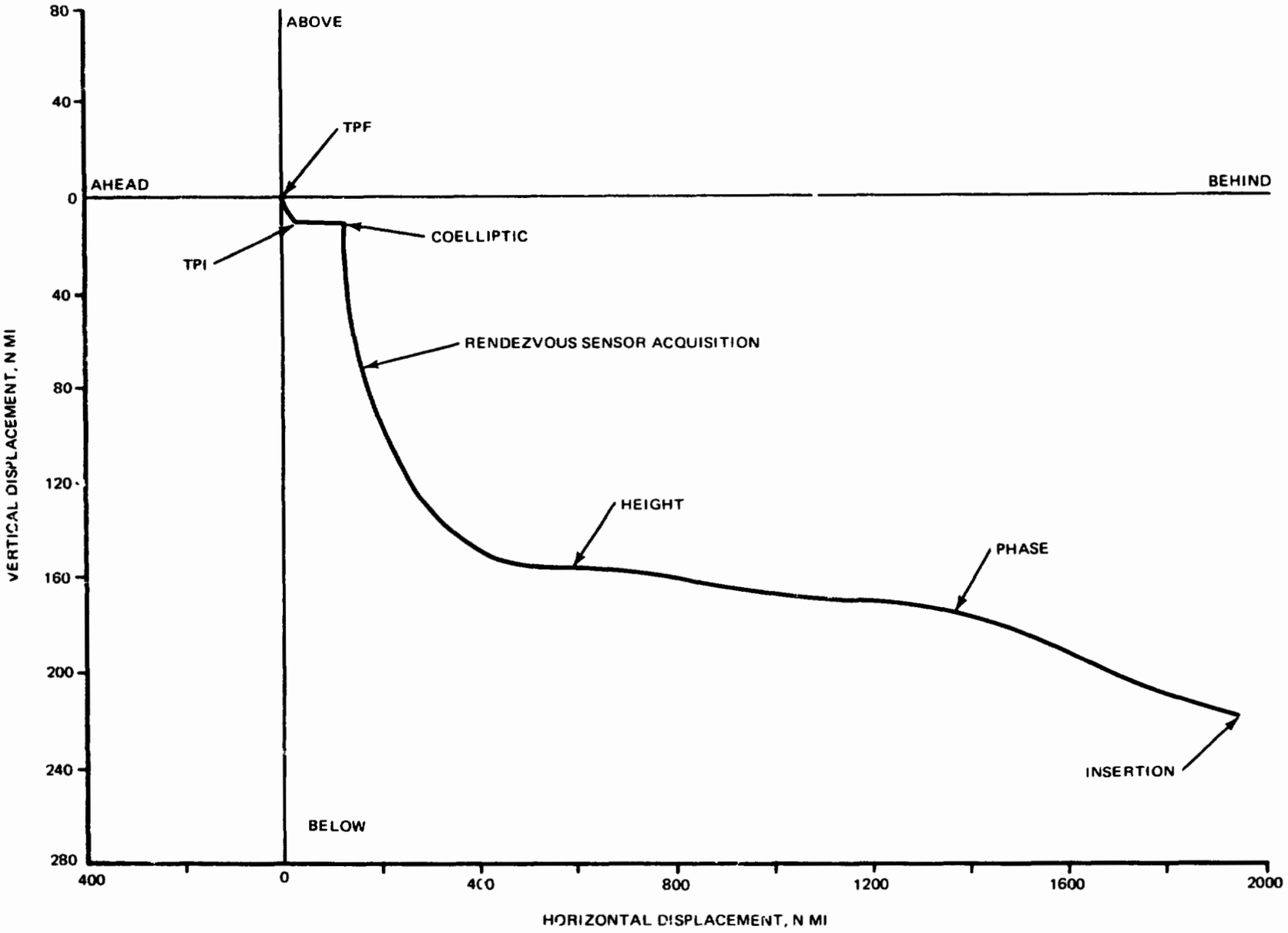

Fig. 8.3.4-1 Shuttle Position Relative to Target Coelliptic Rendezvous Curvilinear Coordinates

TABLE 8.3.4-2 INITIAL PHASE OF RENDEZVOUS - TRAJECTORY PARAMETERS

Maneuver	Inertial Central Angle From Insertion, Deg	Time From Insertion Hr, Min	Inertial Central Angle From Last Burn, Deg	Required Delta-V, fps	Duration of Maneuver, sec	Range to Target, n mi	Resultant Pergee/ Apogee, n mi	Time From Last Maneuver Hr, Min
Insertion	0	0	0	0	-	2092	50/100	0
Phase	180	43 m	180	120	62	1246	100/116	43 m
Height	360	1h, 27 m	180	280	145	527	116/260	44 m
Coelliptic	540	2h, 13 m	180	249	128	131	260/260	46 m
TPI	969	4h, 5 m	429	21	12	21	130° transfer	1h, 52 m
MCC	1000	4h, 15 m	39	0	0	11	130° transfer	10 m
Braking				25				
			Total	695				

The nominal braking schedule for terminal rendezvous is:

Range	Desired Range Rate	Delta V
2 n mi	- 25 fps	2.1
5000 ft	- 10 fps	12.9
1000 ft	- 2 fps	7.8
200 ft	0 fps	2.2

The results of a Monte Carlo analysis of the rendezvous sequence was performed assuming that rendezvous sensor angle information and ranging information are available at a range of 300 n mi. Apollo CSM SXT/VHF sensor characteristics, and IMU performance was assumed. Table 8.3.4-3 summarizes the performance characteristics of this mission. The total delta V for the automatic rendezvous is 721 fps or 26 fps greater than the ideal. The rms variation in initiation of TPI is 9.1 min with a maximum mistiming of 15.5 min. If ranging information was made available at 800 n mi (angle information at 300 n mi), the variation in TPI time can be reduced to an rms of 3.1 min with a maximum mistiming of 4.4 min. In addition, the total delta-V requirement is reduced to 712 fps for an OMS propellant savings of 180 lb.

a. Modified Coelliptic Sequence

Figure 8.3.4-2 presents a modified coelliptic rendezvous in which a second phasing maneuver and a plane change are incorporated into the sequence for added flexibility. The addition of the second phasing maneuver would permit use of a 300 n mi ranging system by providing the time for a correction maneuver after tracking data is made available and prior to the coelliptic maneuver. This approach is being used in the Skylab mission.

b. Other Rendezvous Requirements

Requirements for a rendezvous and a de-orbit in less than one orbit will necessitate direct insertion at launch into an intercept trajectory or a direct powered ascent utilizing the throttling capability of ascent engines. Rendezvous with passive targets (no-ranging transponders) will necessitate adjustments to the rendezvous sequence to allow tracking of the target over an orbit pass at relatively small ranges prior to initiation of the terminal rendezvous.

TABLE 8.3.4-3 RENDEZVOUS PERFORMANCE CSM SXT AND VHF WITH 300 N MI ACQUISITION RANGE

1. Delta-V Expended

Maneuver	Expended Delta-V	
	Mean, fps	Standard Deviation, fps
Phase	119	0.7
Height	281	2.1
Coelliptic	265	9.3
TPI	19.5	10.8
MCC	0.4	1.4
TPF_1	2.0	1.6
TPF_2	11.3	6.8
TPF_3	6.4	4.1
Stop	2.0	1.2
Total	706.6	4.8

2. Relative State Vector Subsequent to Stop Burn

		Range	Altitude	Track
Relative Position, ft	Mean	80	-191	-11
	Standard Deviation	51	60	34
Relative Velocity, fps	Mean	-1.9	0.3	0.1
	Standard Deviation	0.2	0.5	0.5

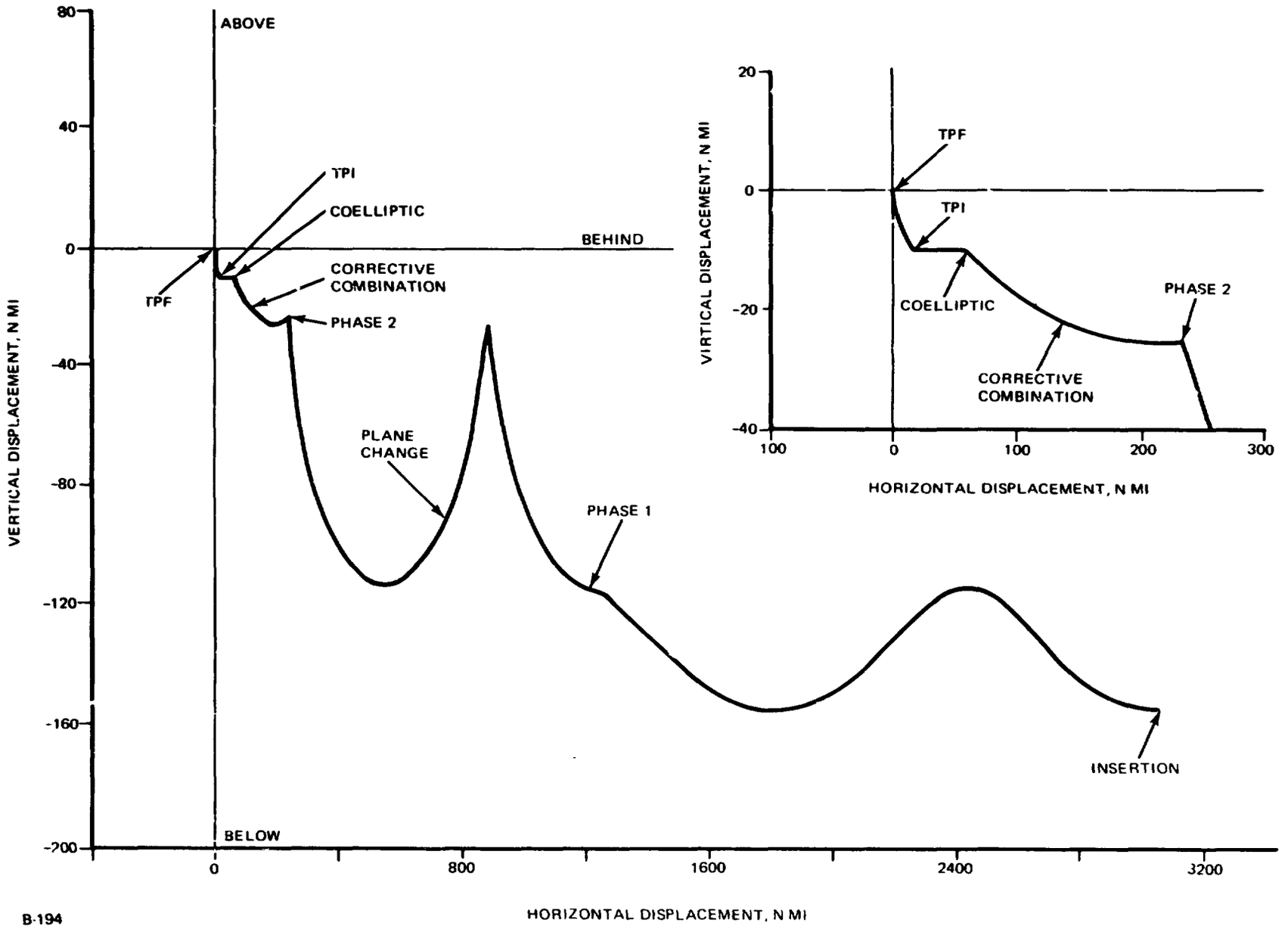

B-194

Fig. 8.3.4-2 Shuttle Position Relative to Target, Modified Coelliptic Rendezvous Curvilinear Coordinates

The stable orbit rendezvous approach lends itself to this function. Fig 8.3.4-3 is a relative motion plot of this rendezvous sequence and Table 8.3.4-4 summarizes the results of an error analysis which indicates a requirement for range measurements within 10 n mi and angle measurements within 75 n mi of the passive target.

c. OMS Maneuvers

Fig 8.3.4-4 presents the delta-V penalty as a function of thrust-to-weight ratio (T/W) of the OMS for the rendezvous and de-orbit phases of the Space Station resupply mission. For T/W ratios greater than 0.015, the delta-V required is relatively constant. The delta-V penalty for systems having a T/W equal to 0.015 is 49 fps, which is 3.3% of the total ideal delta-V required for the mission. The listing below summarizes the expected delta-V penalty for the H-33 and G-3 vehicles for the resupply mission.

	2 RL 10's		1 RL 10		4 ACPS Engines	
	T/W	Delta-V Penalty, fps	T/W	Delta-V Penalty, fps	T/W	Delta-V* Penalty, fps
H-33	0.108	0	0.054	2.5	0.014	40
G-3	0.094	0	0.047	3.7	0.012	55
* de-Orbit Only						

Both configurations have sufficient thrust from the 15,000 lb thrust RL 10's to minimize losses during orbital operations. The penalty of performing de-orbit with the ACPS jets is on the order of 40 to 60 fps. From a performance standpoint it is feasible to de-orbit with the ACPS as a backup to the RL 10's. However, the burn arc associated with these maneuvers will be of such a long duration that the coast period between the end of the maneuver and entry interface may not be of sufficient length for crew preparation for reentry.

d. Stationkeeping

Preliminary evaluation of the orbiter station-keeping requirements have considered stationkeeping above and in front of the target vehicle. The study considered the effect of velocity uncertainties due to navigation and delta-V application error. It is assumed the stationkeeping boundary consists of a 20 degree half angle cone and that all velocity

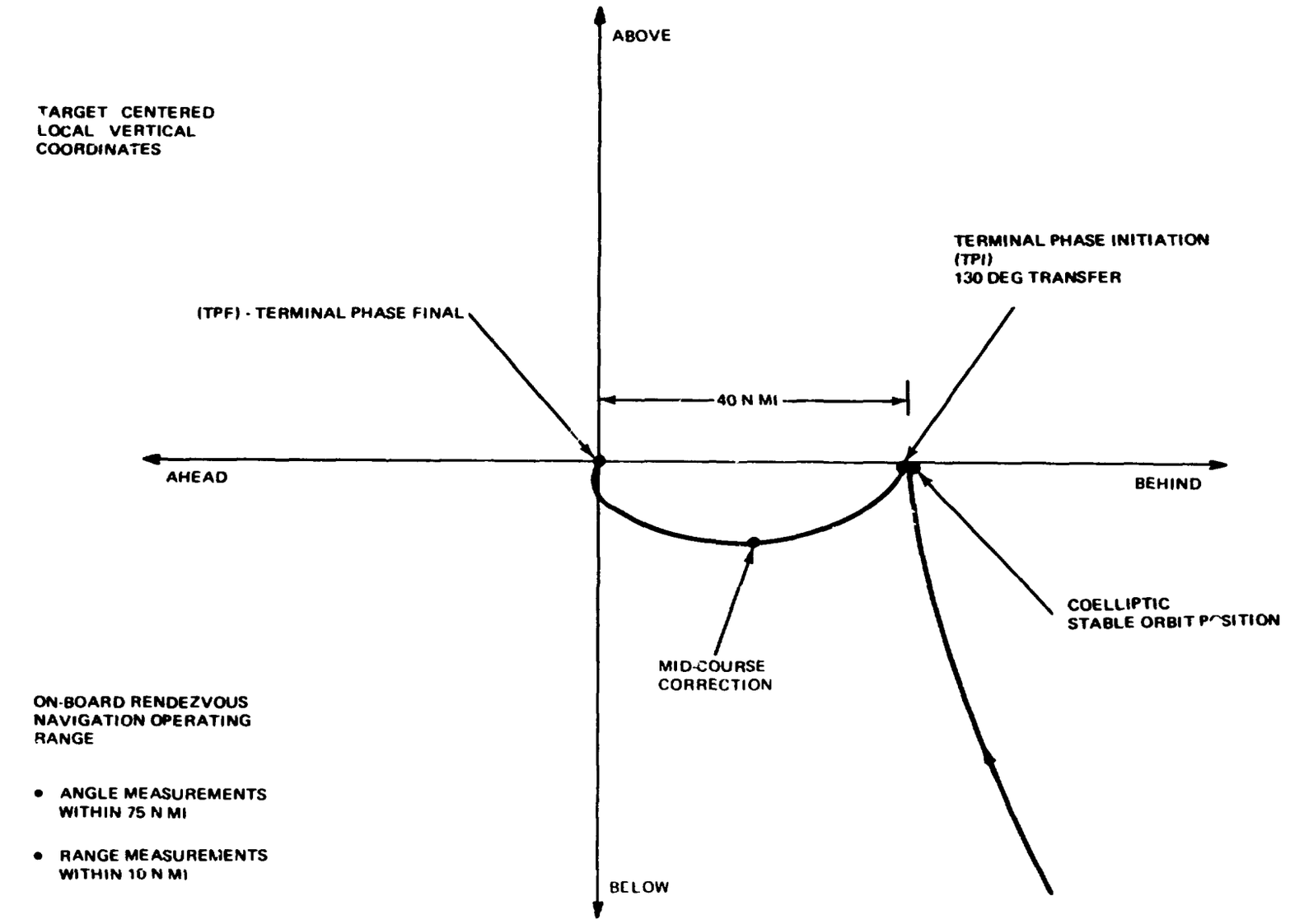

Fig. 8.3.4-3 Shuttle Position Relative to Target, Stable Orbit Rendezvous, Non-Cooperative Target

TABLE 8.3.4-4 NAVIGATION PERFORMANCE - UNCOOPERATIVE TARGET

	1 δ Position Error - ft			1 δ Velocity Error - fps		
	Range	Altitude	Track	Range	Altitude	Track
Insertion	1,100	1,200	1,000	3.0	4.0	4.0
Phase	12,193	7,523	2,753	2.2	11.6	1.5
Height	14,500	2,558	2,025	5.1	16.0	2.1
Coelliptic	19,141	3,198	2,169	3.9	23.0	1.2
(a)						
TPI	21,683	2,392	357	2.2	23.6	0.8
Mid-Course	20,575	5,535	383	7.4	15.6	0.8
(b)						
TPF_1	150	1,250	101	3.8	7.9	0.1
TPF_2	80	71	22	0.2	0.3	0.1
TPF_3	15	29	5	0.1	0.1	0.1
Stop	10	20	5	0.1	0.1	0.1

(a) Begin Angle Tracking
(b) Begin Ranging

Shuttle Orbit Navigation (1 δ) 2000 ft, 2 fps Each Axis

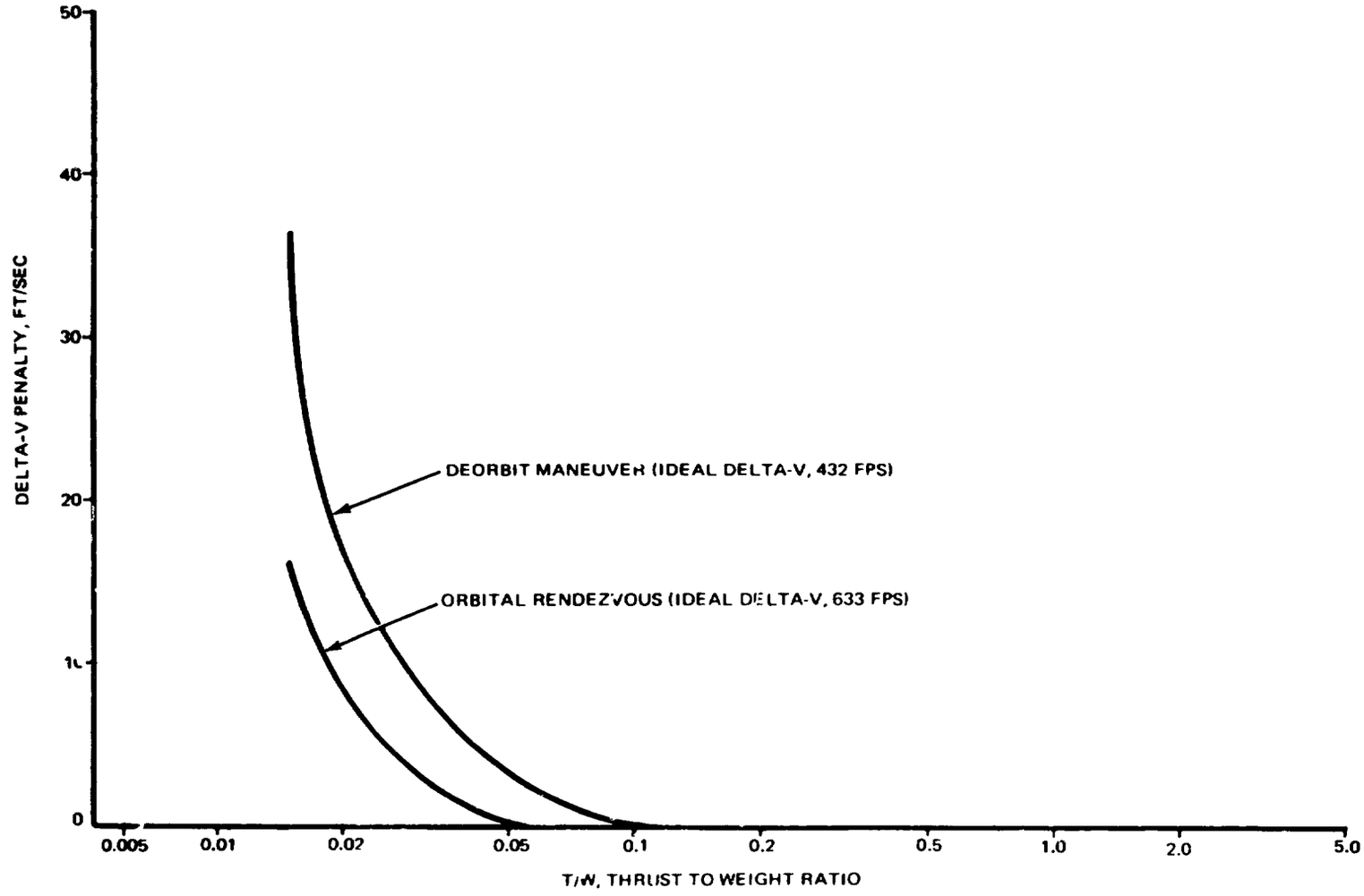

Fig. 8.3.4-4 Delta-V Penalties for De-Orbit and Orbital Rendezvous Maneuvers

corrections are impulsively applied at the boundary. Fig. 8.3.4-5 presents the boundaries for stationkeeping both above and ahead of the target vehicle. For stationkeeping at an altitude of 270 n mi, Table 8.3.4-5 presents the delta V requirements per orbit as a function of velocity uncertainties for station-keeping distances ranging from 100 to 600 ft. As can be seen from the table, station-keeping requirements are more severe when the orbiter station keeps above rather than in front of the target for ranges above 400 ft. For ranges below 400 ft there is no appreciable difference between delta-V requirements.

8.3.4.1.2 Rotational Performance

a. OMS Engine Gimballing

The Orbit Manuevering System (OMS) engines are not gimballed in the baseline vehicle design. This saves checkout, production and maintenance costs that would otherwise be required for the OMS gimbal subsystem and its interface equipment. This advantage is offset by additional OMS/ACPS propellant requirements. It is estimated that the ACPS propellant penalty (for the H-33 Orbiter on the 270 n mi, 55 deg inclination rendezvous mission) amounts to 140 lb/deg of misalignment of the OMS thrust vector with respect to the vehicle mass centroid. A 3 deg tolerance has been assumed, based on LM experience, and used in the calculation of on-orbit propellant requirements.

b. ACPS Igniter - Only Capability Option

The ACPS engines are designed with small (50 lb) igniter engines. These smaller thrusters could be used to provide a two-thrust level system that would have several performance advantages during on-orbit operations. The igniter engines, if used for all-attitude hold functions during the coasting phases of the rendezvous in the space station mission, could provide a 250 lb ACPS propellant savings. Such a system would enable the orbiter attitude control system to provide pointing accuracies as tight as 10^{-4} deg. Thus, the orbiter could provide the stable platform for a variety of short duration, precision pointing experiments.

During on-orbit coasting flight a rate of usage of ACPS propellant will occur for the purpose of holding the orbiter attitude within some attitude deadband. This ideal limit cycle propellant usage rate is directly proportional to the square of the product of engine thrust and the minimum impulse firing period.

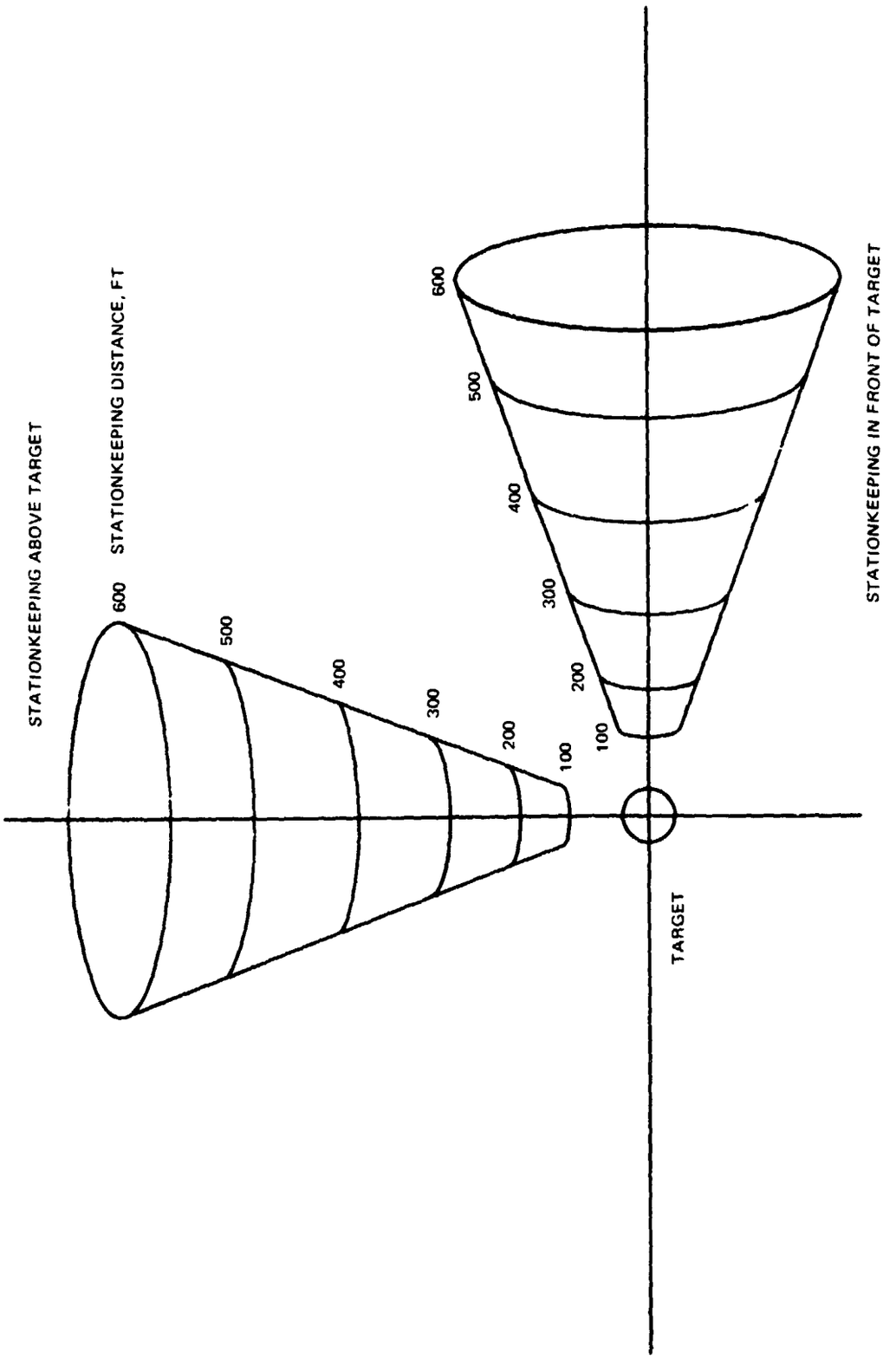

Fig. 8.3.4-5 Stationkeeping Boundaries

A-18

TABLE 8.3.4-5 STATIONKEEPING DELTA-V REQUIREMENTS PER ORBIT

		Delta-V Requirements Per Orbit, fps				
		Velocity Uncertainty, fps				
	Stationkeeping Distance, ft	1.0	0.5	0.3	0.1	0
Stationkeeping Above Target	600	19.0	14.1	13.1	12.6	12.5
	400	18.1	10.9	9.2	8.4	8.3
	200	23.7	9.1	5.9	4.4	4.2
	100	41.1	11.8	5.6	2.9	2.1
Stationkeeping In Front of Target	600	9.6	4.8	3.7	3.2	3.1
	400	11.8	4.5	3.0	2.2	2.1
	200	20.5	5.9	2.8	1.2	1.0
	100	39.5	10 3	4.0	0.9	0.5

The ACPS thruster igniters have about 1/20 the thrust and about 1/5 the minimum impulse firing period of the full thruster capability. Thus, there is ideally, a propellant usage rate reduction of about 10,000 to 1 in going from thruster control to igniter control.

Table 8.3.4-6 presents the itemized limit cycle propellant rate in pounds per hour (as a function of attitude deadband) for two-jet thruster attitude control versus two-jet igniter attitude control for the H-33 Orbiter. This is based upon ACPS thruster characteristics of 1000 lb thrust, 50 millisec minimum impulse firing period, and a minimum specific impulse of 300 sec.

TABLE 8.3.4-6 H-33 ORBITER IDEALIZED TWO-JET COAST PHASE LIMIT CYCLE PROPELLANT RATE

Attitude Deadband, deg	10	1.0	0.1
Thruster Control, lb/hr	5.0	50.	500.
Igniter Control, lb/hr	0.0005	0.005	0.05

Another advantage of the igniter method for attitude hold is that it enables a 100 to 1 reduction in limit cycle rates. This enables high pointing accuracies with a relatively stationary vehicle. This will make possible many space experiments that could not be performed with the much higher vehicle rates of rotation resulting from full thruster control.

Table 8.3.4-7 presents the two-jet minimum impulse attitude rate change in degrees per second about each axis for the H-33 Orbiter, for thruster and for igniter control.

TABLE 8.3.4-7 H-33 ORBITER TWO-JET MINIMUM IMPULSE BODY AXES RATE CHANGE INCREMENT

	X-AXIS	Y-AXIS	Z-AXIS
Thruster Control, deg/sec	.100	.0344	.0312
Igniter Control, deg/sec	.0010	.000344	.000312

For technical clarity, it must be emphasized that the propellant usage rates presented in Table 3.3.4-6 are for idealized limit cycle characteristics. Some of these

idealizations neglect all orbiter disturbance torques (due to gravity gradients, electromagnetic field interaction, etc.) and cross-axes coupling effects (due to the inertia tensor, thruster alignment tolerances, mass centroid locations, etc.). For example, it has been estimated that the maximum gravity gradient torque on the H-33 Orbiter could be about 15 ft-lb, which could cause an additional propellant usage rate of about 2.4 lb per hour.

8.3.4.1.3 On Orbit ACPS Control Acceleration Requirements

The following table summarizes the on-orbit translational and rotational ACPS acceleration requirements.

		Requirement	Min Fail Operational Orbiter External H_2 Tank Capability
Translation, ft/sec^2	X	+ 0.1, - 0.2	+ 0.13, - 0.27
	Y	0.2	0.4
	Z	0.2	0.4
Rotation, deg/sec^2	X	.4	1.4
	Y	.4	0.44
	Z	.4	0.5

The translational requirements are based on the CSM acceleration levels (two-jet x-axis translation) while in lunar orbit. The CSM is required, and is capable of, rendezvous with LM in the event of a LM failure which precludes rendezvous by that vehicle. The rotational requirements are based on manned simulation studies of docking performed during the LM-A Apollo Applications Program. (Reference: ARP 250-007, "Apollo Applications Program LM-A/ATM Docking Feasibility Study Summary Report," J. Boudreau, 20 Dec 1967).

8.3.4.2 Entry

This subsection summarizes the entry guidance and control performance characteristics, and the interrelationship of the mission requirements, aerodynamic performance, and thermal and structural design environment. The following briefly describes the baseline entry guidance and control system and associated procedures:

- After the deorbit maneuver, the vehicle is oriented to the nominal angle-of-attack (27deg) and bank angle (60deg) required for the initial phase of entry using ACPS control. The orbiter elevons are prepositioned to provide longitudinal trim at this angle-of-attack
- At a sensed accelerometer measurement of 0.1g, the yaw control autopilot and the guidance thermal control mode is activated. The pitch axis ACPS control system remains in an attitude hold mode using inertial system angle-of-attack and attitude rate information. Both the longitudinal and lateral-directional integral trim systems are activated to reposition the elevons to account for center-of-mass uncertainties. When elevon trim command error signals fall below threshold limits, the control surfaces are frozen in position to avoid surface motions during peak heating periods. The pitch axis ACPS is then placed in a rate-hold mode
- At trajectory pull-out (as the relative flight path angle approaches zero), guidance begins to issue bank angle commands to control the vehicle drag levels as sensed by the inertial system accelerometers. Drag commands are generated to provide the desired underbody thermal environment. Drag is related to underbody temperatures in the software through the density and relative velocity terms common to the definition of both parameters, i.e.,

$$\text{Drag} = 1/2\rho\, V^2 C_D S \qquad\qquad \text{Temp} = f\ (\rho^N,\ V^M)$$

Hence, the bank angle rotations effectively control altitude by modulating the in-plane (vertical) component of lift

- Lateral targeting is controlled by continuously computing the cross range capability of the vehicle. When the actual cross range to the target exceeds three-fourths of the predicted vehicle performance, a bank angle reversal is initiated with the ACPS to place the out-of-plane component of L/D toward the target

- In-plane targeting is achieved by computing the range-to-go between the vehicle and the landing-site assuming a constant drag terminal phase. When the actual drag reaches the level required to achieve the range to the target, the thermal control mode is discontinued and target control is activated. During target control, drag commands are continuously computed and drag levels adjusted for accurate acquisition of the landing site. Lateral control during terminal guidance is performed in the same manner as described above

- At Mach 4, the aerodynamic control surfaces are activated and the split rudder is deployed. A gradual pitch down maneuver is performed and at an angle-of-attack of 15 deg, Mach 3, the vehicle is placed under complete aerodynamic surface control

Trade studies have indicated that the required thermal and structural load environment can be achieved with constant angle-of-attack flight between entry interface and Mach 4. Footprint flexibility is achieved by selecting the angle of attack to be flown prior to entry interface. Fig. 8.3.4-6 is the performance footprint in which the vehicle temperature at the 100 ft underbody centerline point is less than 1610°F (representative of 80% of the underbody) and the vehicle maximum load is less than 1.15g. Once an angle of attack is selected, footprint flexibility can be achieved by varying the peak temperatures and load levels. (See Fig. 8.3.3-14)

Reentry control is performed with the ACPS with the elevon providing both longitudinal- and lateral-directional trim. Studies that indicate that the minimum acceptable ACPS jet size for entry is 1000 lb have been performed. The ACPS propellant consumption during entry is 2500 lb. Simulations are currently being performed to determine the acceptability of this jet size for manually controlled entries. The results of an alternate aerodynamic control system study, which evaluated the use of an active ventral for complete aerodynamic control during reentry, are discussed in subsection 8.3.4.2.10.

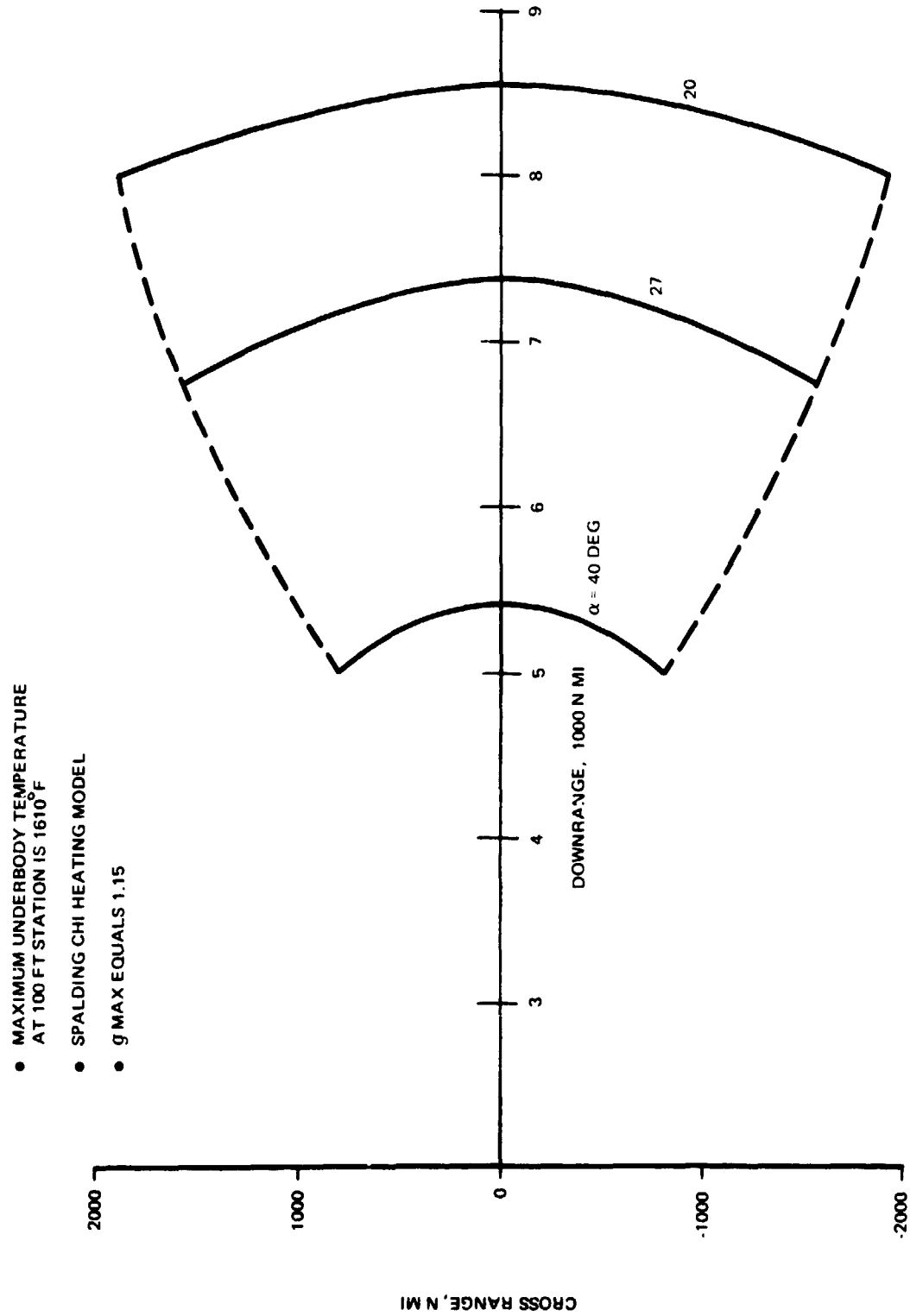

Fig. 8.3.4-6 Downrange and Cross Range Capability For Different Angles-of-Attack

8.3.4.2.1 Mission Requirements

The orbiter cross-range requirement is derived from the one-orbit 100 n mi polar-orbit mission, launched from, and returned to, ETR. A total requirement of 1244 n mi is obtained by summing the cross range between two successive groundtracks, a correction to account for the shaping of the ascent trajectory, a correction to compensate for the difference between satellite time and entry flight time required to traverse the entry range angle, and a correction to allow for atmospheric aerodynamic, and navigation uncertainities experienced during entry. A similar computation indicates that the total requirement for launch from Vandenberg AFB and return is 1170 n mi (Fig. 8.3.4-7). A launch from Vandenberg and a return to Edwards requires 1254 n mi.

The high cross-range design heating environment is more severe for a polar entry than for an inclined eastward entry. This result can be explained by noting that for a given relative velocity, the inertial speed and centrifugal lift decreases as the orbit inclination increases. To maintain aerodynamic equilibrium at the lower value of centrifugal lift, the aerodynamic lift must be increased, thereby, requiring flight at a lower altitude and increased atmospheric density and heating rates. Design reference trajectories used for TPS design and weight estimates (subsection 8.4.6) are generated for the polar entry case.

8.3.4.2.2 De-Orbit and Entry Flight Path Angle

The impulsive delta-v required for de-orbit from a 100 n mi circular orbit is shown in Fig. 8.3.4-8 as a function of entry flight path angle. The reference heating rate, altitude and down-range distance traveled to pullout are presented as a function of path angle with the baseline angle selected to provide the desired heating rate at pullout and to insure flight at 1000 ft altitude above the thermal boundary (1610°F laminar heating at the 20 ft underbody centerline point).

8.3.4.2.3 Aero-Thermodynamic Performance

The relationship between underbody temperature and maximum achievable cross range is shown as a function of target down range (measured from entry interface) in Fig. 8.3.4-9 for flight at 20, 27 and 40 deg angles of attack. Each of the trajectories computed consists of a phase with constant underbody temperature at the 100 ft centerline station (T_{UB}), a transition phase to a constant terminal applied aerodynamic acceleration (G_A) phase.

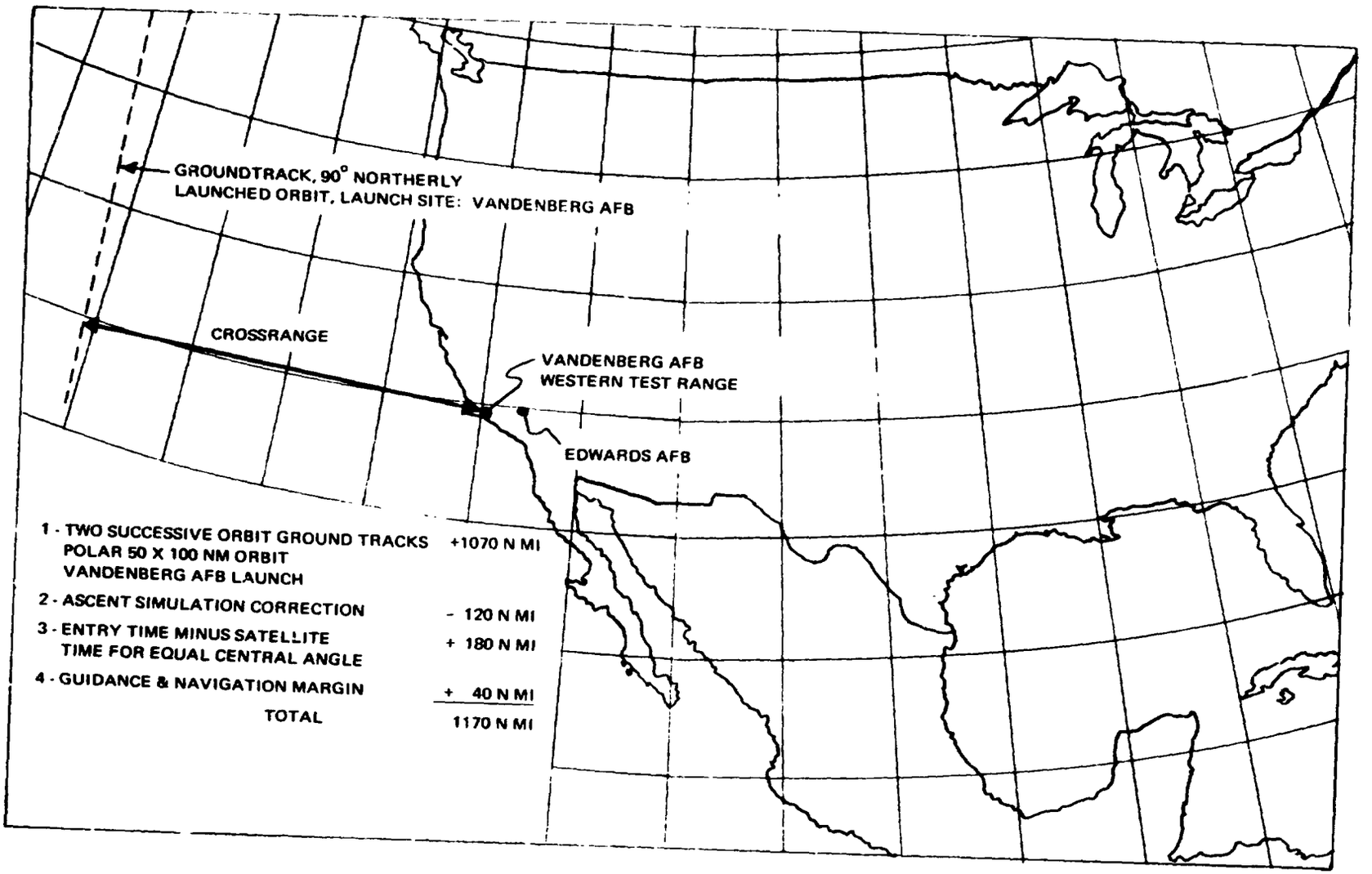

Fig. 8.3.4-7 Crossrange Required

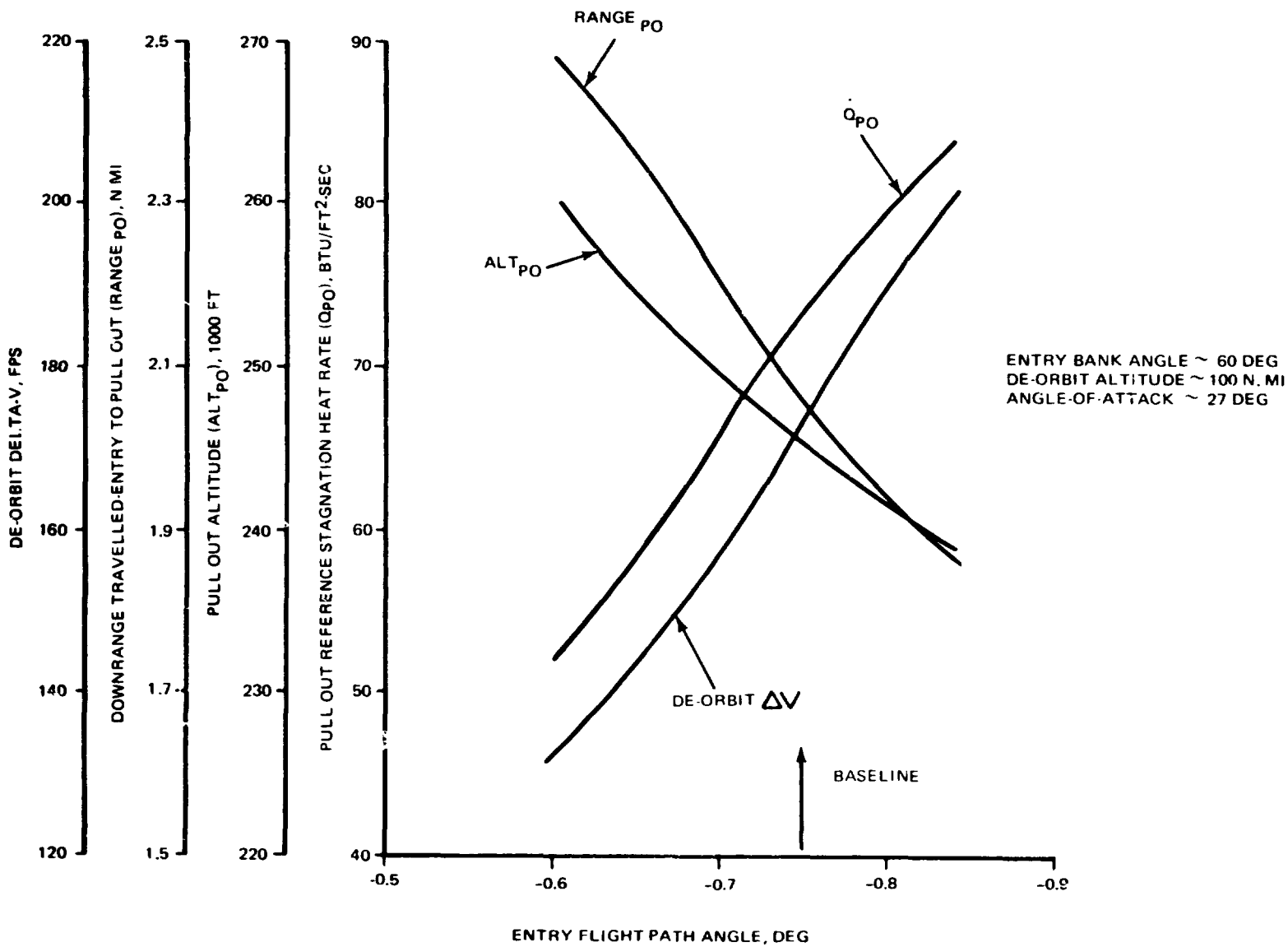

Fig. 8.3.4-8 Entry Flight Path Angle Tradeoff

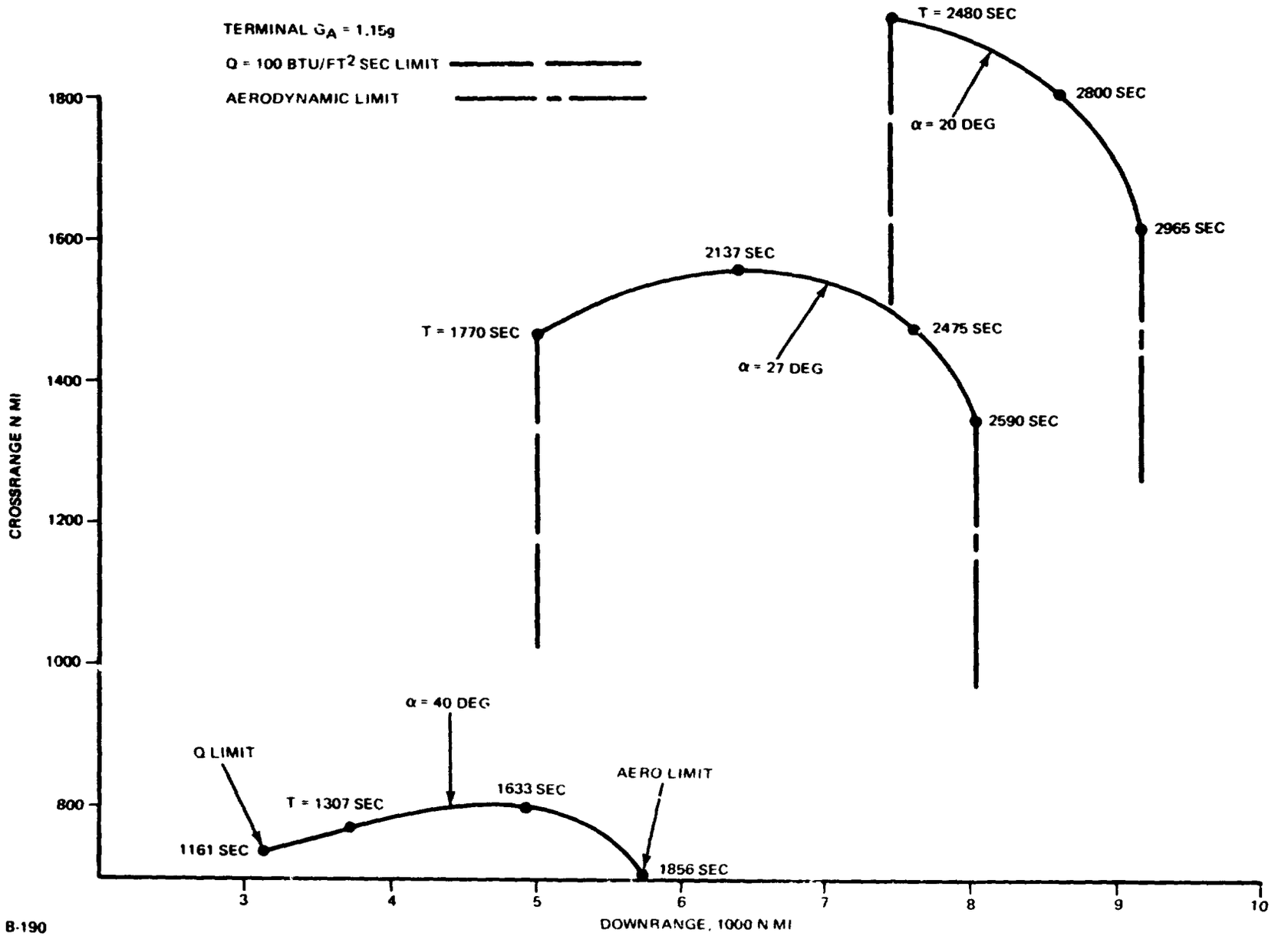

Fig. 8.3.4-9 Maximum Cross[illegible]nd Time of Flight vs Downrange and Angle-of-Attack

The minimum achievable down range boundary for a given angle-of-attack entry is determined by a reference stagnation heating rate of 100 BTU/ft^2/sec, which represents the limit conditions for carbon/carbon used in the nose region. The maximum boundary is defined by the aerodynamic lift capability of the vehicle during the constant temperature phase. Flight to targets further than this limit will result in trajectories that lose equilibrium. Times of flight from entry interface to a speed of 2000 fps are indicated in the figure.

The maximum temperature and total heat load (Q_{UB}) at the 100 ft station for the different down range locations are shown in Fig. 8.3.4-10. The results demonstrate that the excess cross-range capability available at low α can be converted to a lower temperature, a lower reference stagnation heating rate, and a shorter flight time by flying at a higher angle of attack. Most missions will not require the maximum capability of the vehicle, and could be flown at the higher angle of attacks to increase TPS operational life.

The underbody heat load remains approximately constant with increasing downrange distance travelled at a 40 deg angle of attack. In the cases of 27 and 20 deg, the heat load decreases with increasing downrange. Flight at α = 27 deg to targets located 7000 n mi down range, provides flight operation at the minimum end of the temperature and heat load curves, achieves the required cross range, and retains additional thermal maneuvering capability.

8.3.4.2.4 Entry Trajectory Control

The entry guidance policy controls the vehicle's thermal environment for velocities greater than half circular. For lower velocities, a desired aerodynamic acceleration level is maintained while the vehicle is steered to a specified latitude and longitude at the given terminal speed. The lower limit of the thermal environment is ultimately defined by the orbiter aerodynamic performance.

a. Thermal Control

The thermal boundaries that maintain the underbody centerline below 1800°F, aft of the 20 ft station are shown in Fig. 8.3.4-11 and discussed in subsection 8.3.5. These boundaries have been defined by the conservative reference enthalpy method for computing thermal transition. The trajectory program employs these boundaries iteratively, to determine the

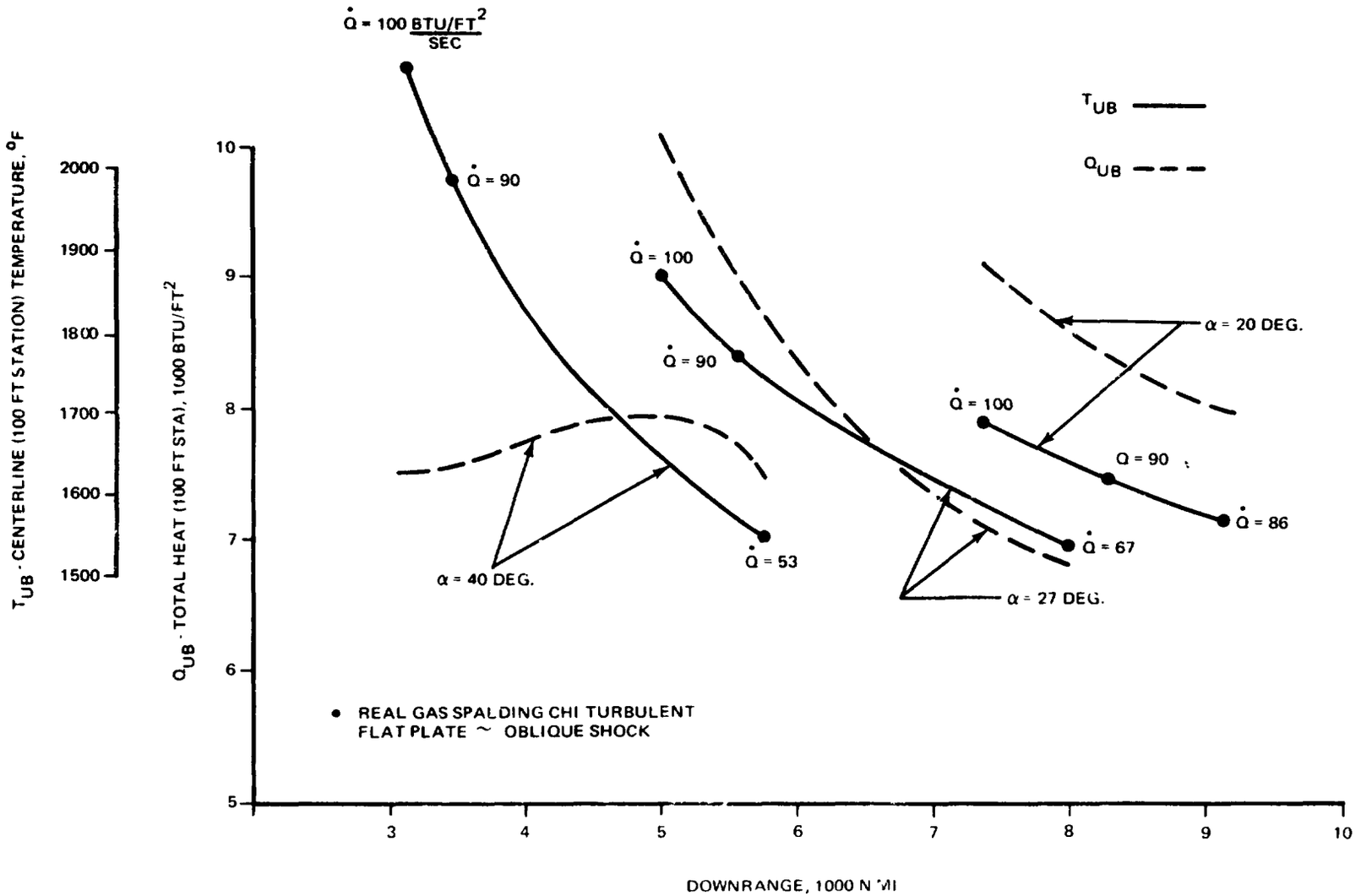

B-189

Fig. 8.3.4-10 Maximum Centerline Temperature and Total Heat vs Angle-of-Attack

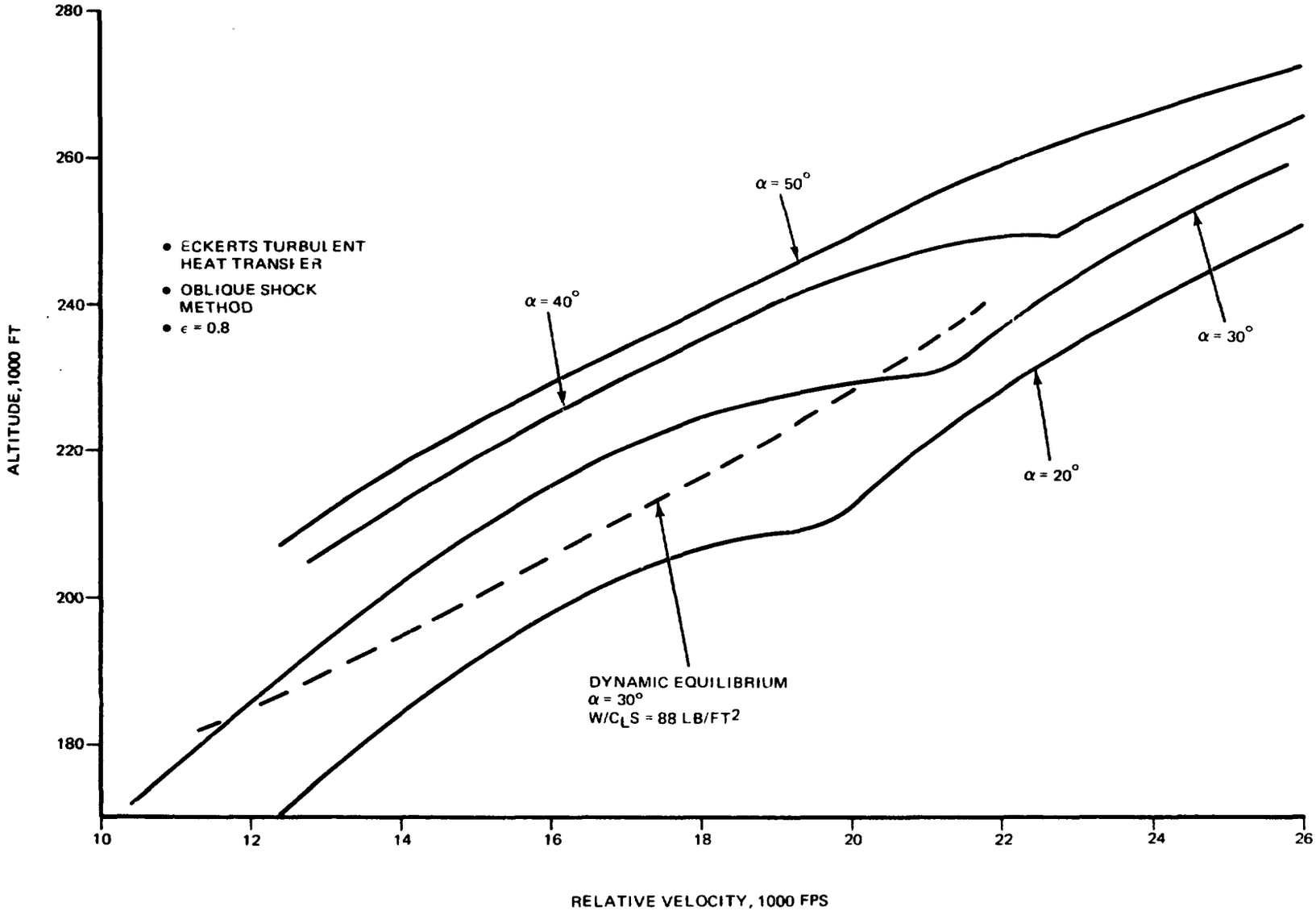

Fig. 8.3.4-11 Thermal Boundaries to Maintain Centerline Aft of 20 Ft Station Below 1800°F

control law that minimizes the centerline temperature profile and satisfies the cross-range requirement. The boundaries are defined by laminar heating at the forward stations during the initial portion of entry. The break in the initial slope of the boundary is due to the onset and realization of turbulent heating at the aft stations. This critical heating region requires the constant angle-of-attack orbiter to maintain altitude, as the velocity decreases, by rotating the lift vector toward the vertical plane. The minimum temperature thermal boundary capable of being flown by the orbiter is determined by the maximum lift available during the critical heating period.

b. Target Control

The desired terminal latitude and longitude are achieved at the specified final speed by computing the point of departure from the thermal boundary as a function of the range to the target. The terminal phase of flight simultaneously reduces the speed to the desired final value and drives the remaining down-range and cross-range distances to the target to zero.

8.3.4.2.5 Baseline Entry Trajectory

The fixed angle-of-attack baseline entry (Fig. 8.3.4-12) controls the centerline temperature for speeds greater than half-circular and achieves an 1100 n mi cross-range distance relative to an earth-fixed great circle. The -0.75 deg entry flight path angle provides a 1000 ft altitude margin with respect to the thermal boundary at pullout for a polar mission. A transition from thermal to target control is initiated at a speed of 12,300 fps with the subsequent terminal phase flown at an applied acceleration of 1.2g (Fig. 8.3.4-13). A time history of the underbody centerline station temperatures computed from the real gas Spalding Chi turbulent flat plate method is presented in Fig. 8.3.5-20. The maximum value at the 100 ft station is 1610°F, which occurs at a speed of 15,958 fps. This trajectory has been used as the basis for the isotherms presented in subsection 8.3.5 and for design of the TPS discussed in subsection 8.4.6.

a. Target Control Capability

The entry footprint for an angle of attack of 27 deg is shown in Fig. 8.3.4-14, as a function of terminal acceleration (G_A) and variations in underbody temperature (ΔT_{UB}).

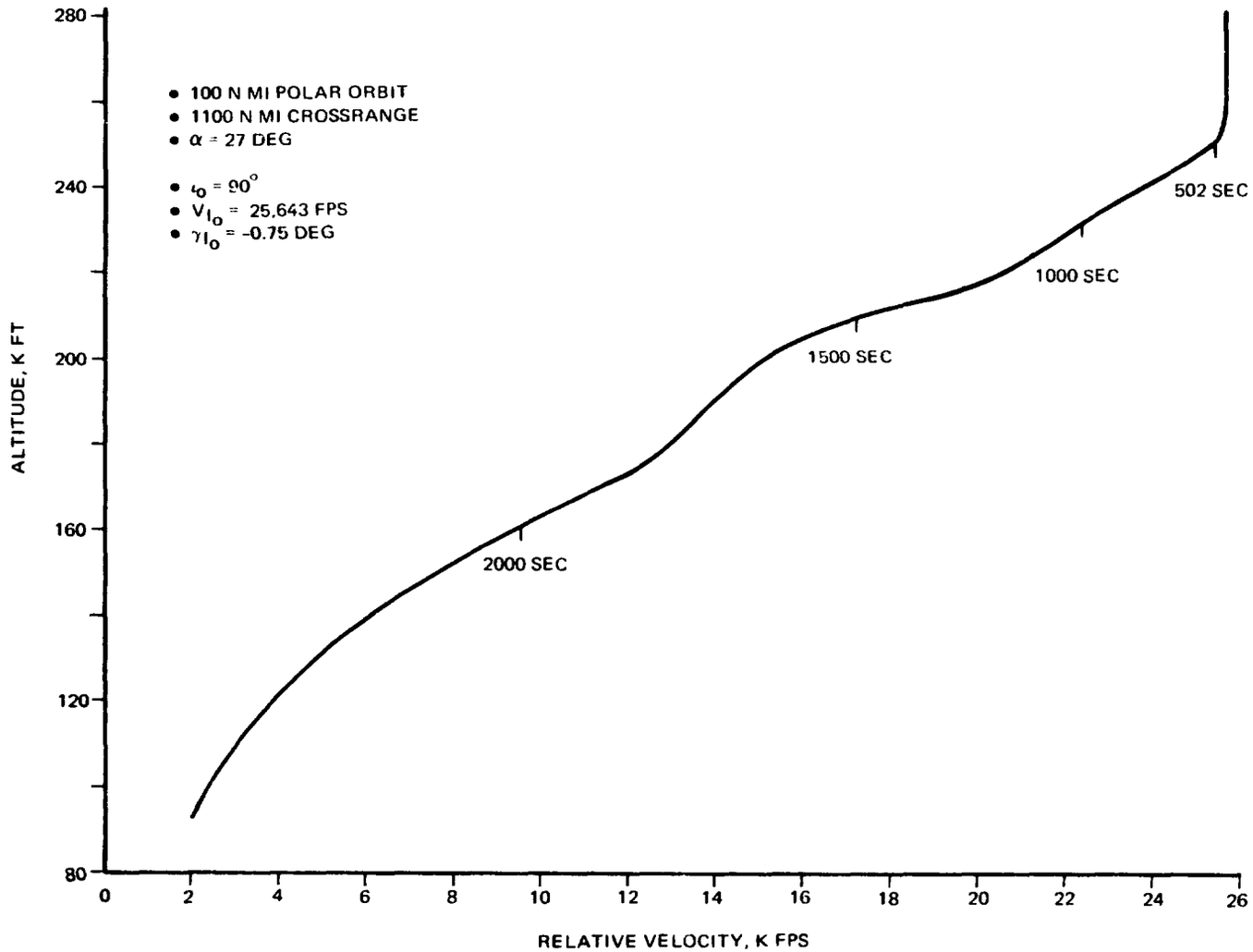

Fig. 8.3.4-12 Baseline Entry

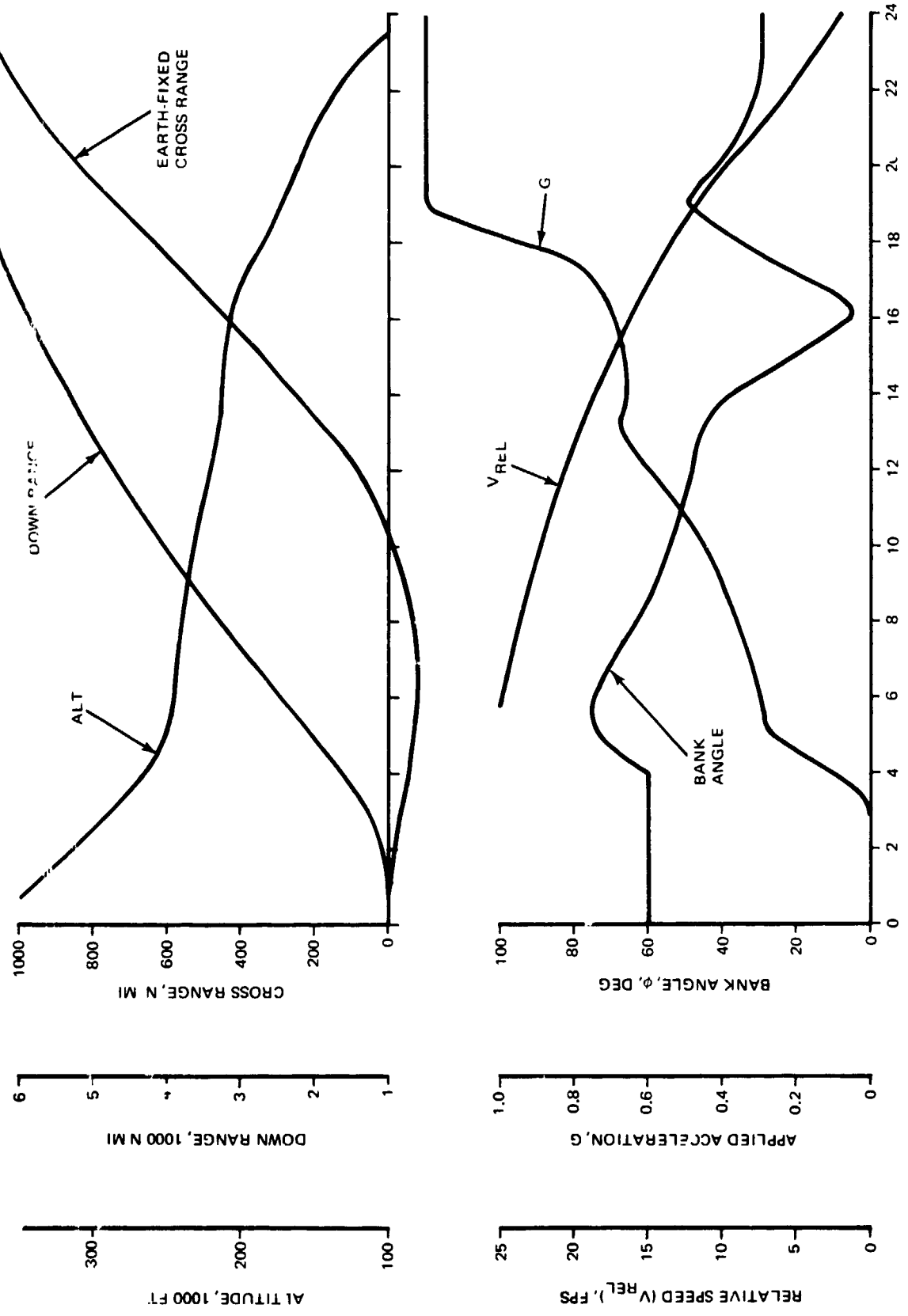

Fig. 8.3.4-13 Entry Trajectory Time History

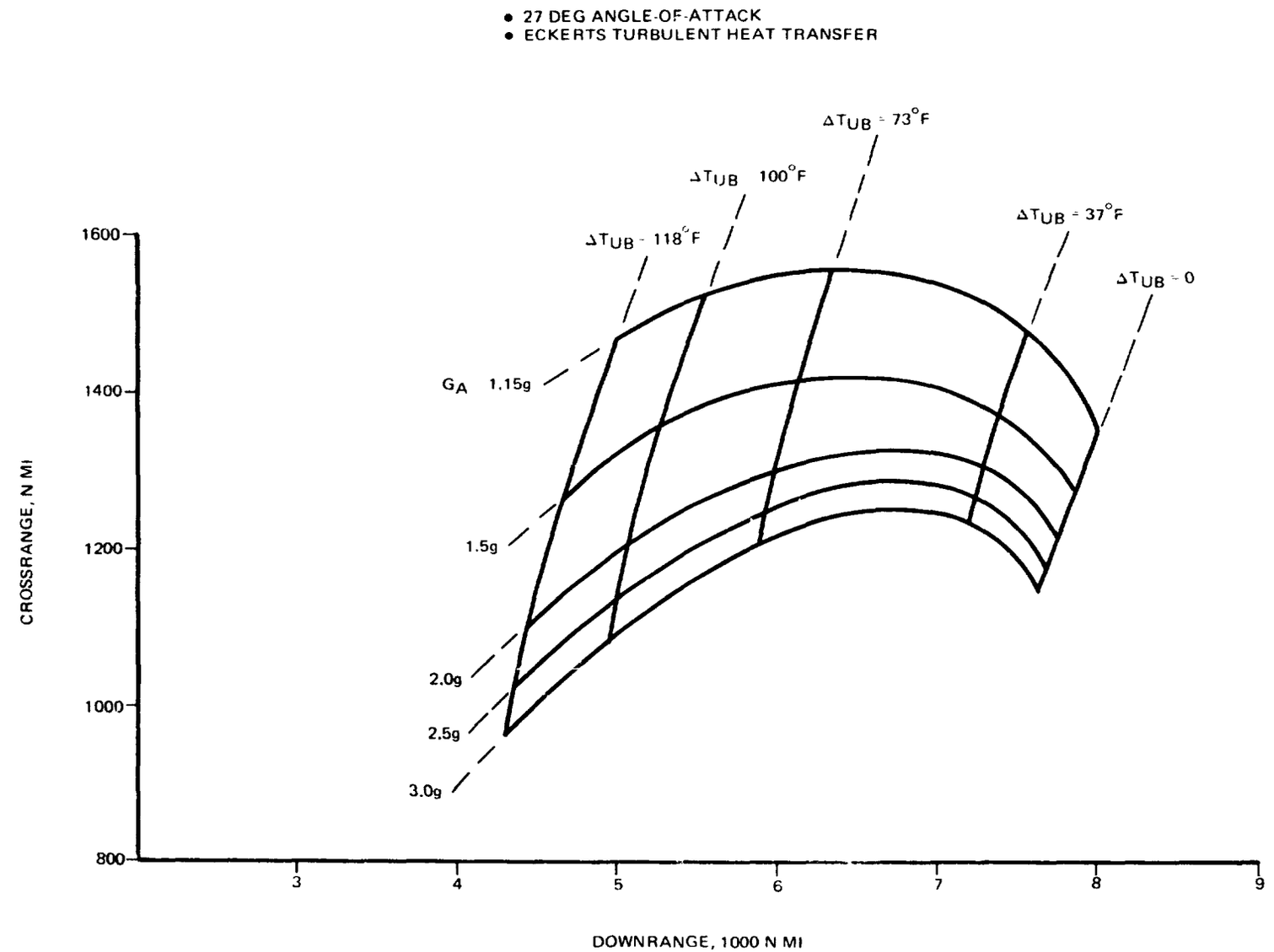

Fig. 8.3.4-14 Maximum Crossrange and Downrange vs 100-Ft Station Temperature (T_{UB}) and Applied Acceleration (G_A)

Varying the applied acceleration (G_A) along the minimum temperature boundary ($\Delta T_{UB} = 0$) enables the down range distance to be changed by 350 n mi. Increasing the centerline temperature by 37°F enlarges the footprint to 800 n mi in the down range direction.

b. Angle-of-Attack Modulation

The thermal boundary, computed from the conservative Eckert's turbulent heat transfer method, is compared to an aerodynamic equilibrium trajectory for a 30 deg angle of attack in Fig. 8.3.4-11. For the 20,000 to 12,000 fps velocity interval, the equilibrium trajectory lies below the 1800°F boundary and results in higher centerline temperatures. An entry employing angle-of-attack modulation (Fig. 8.3.4-15) is considered in order to take advantage of the smaller increases in the thermal boundary altitude as α is increased to 50 deg.

The maximum temperature at the 100 ft station for this entry, based upon the Eckert thermal model, is 100°F lower than that for the fixed angle-of-attack entry. The cross range achieved, to a speed of 2,000 fps, is 1225 n mi relative to the inertial plane at entry interface.

8.3.4.2.6 Entry Control System Description

Fig. 8.3.4-16 presents a schematic of the ACPS/aero-trim entry attitude control logic. The schematic illustrates the automatic guidance command input data to the control logic. The output of the control logic consists of jet thruster firing commands and elevon trim angle commands.

A breakdown of the control logic can be made in terms of the functional response to the guidance bank angle command and the guidance angle-of-attack command. The bank angle control logic is based upon the Z-DAP logic. Thus, the bank angle error is converted to an equivalent yaw body axis attitude error which, with the yaw rate, is used in the phase plane logic to command a yaw body axis torque (i.e., a yaw jet firing command). The yaw rate is converted to a roll rate command and the roll error is used to command a roll angular acceleration.

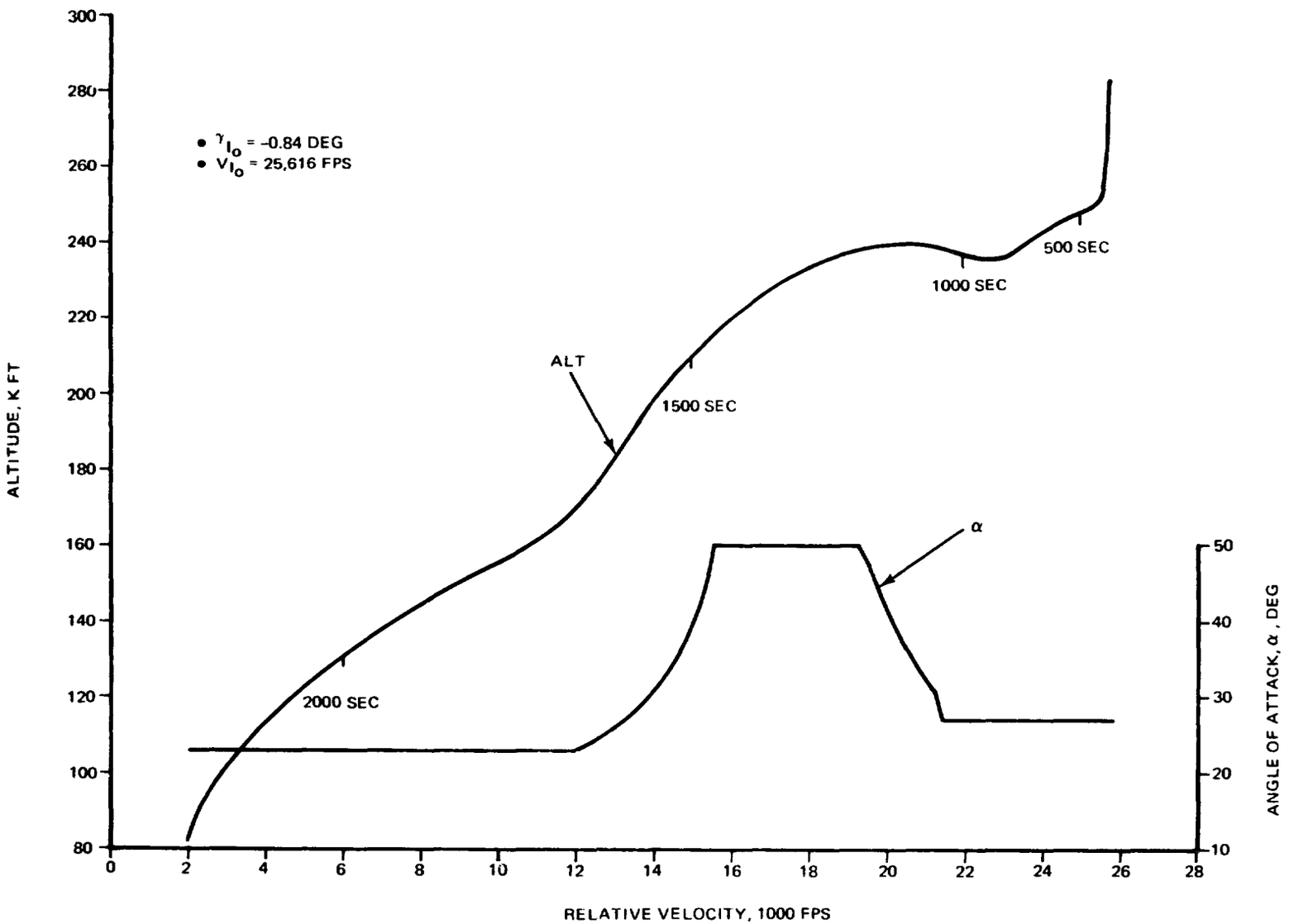

GRUMMAN
BOEING

B-231

Fig. 8.3.4-15 Entry With Angle-of-Attack Modulation, 100 n mi Polar Orbit

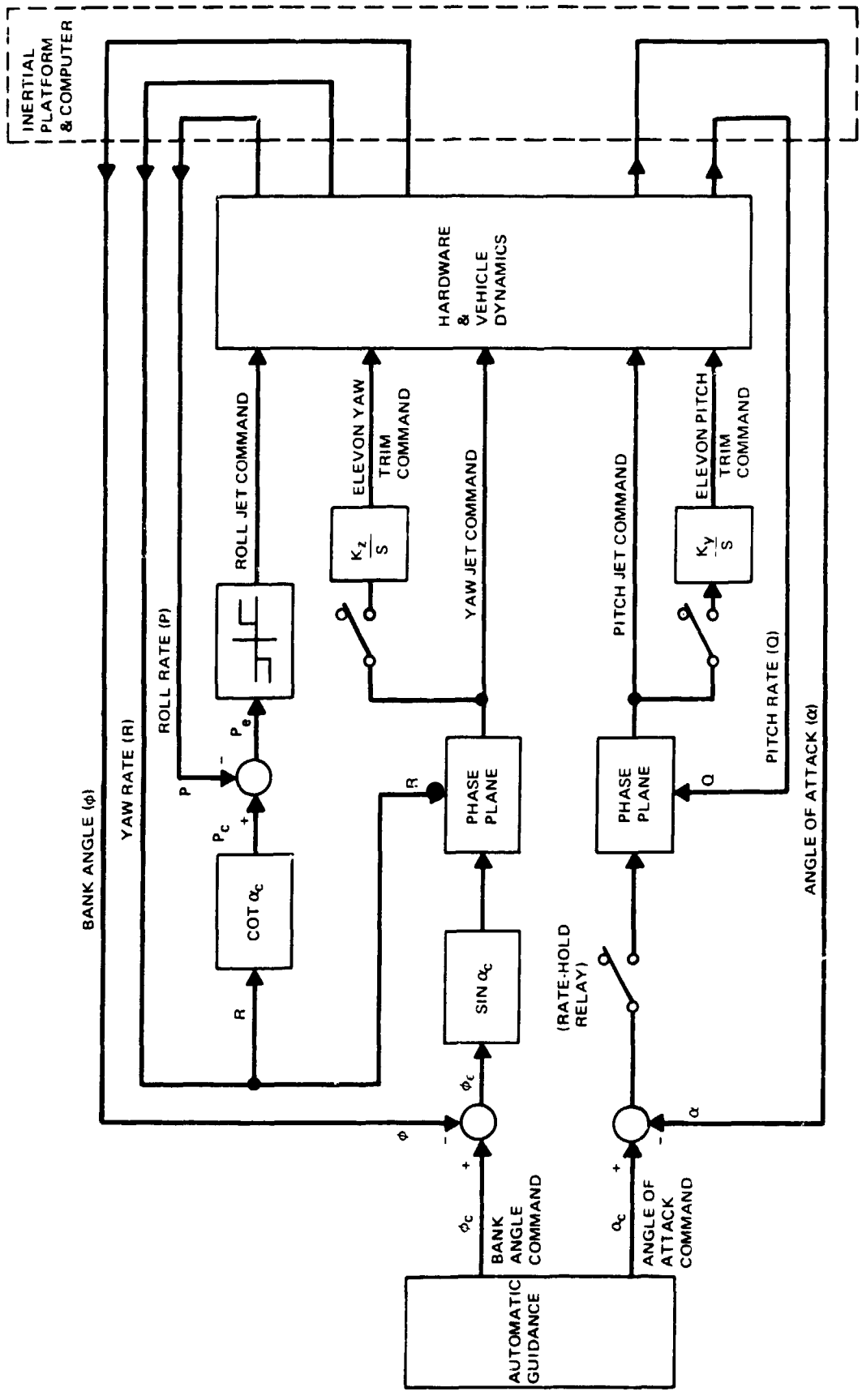

Fig. 8.3.4-16 ACPS/Aero-Trim Attitude Control Logic

The angle-of-attack control logic is based upon angle-of-attack feedback (early in the entry phase) and pitch rate inputs to the phase plane, which provide pitch jet firing commands to hold the commanded angle of attack.

Since a small lateral offset between the mass centroid and the aerodynamic pressure centroid can cause a large ACPS propellant usage during entry, the elevons are differentially trimmed during entry to account for the lateral offset uncertainties. The integral trim compensation for differential elevon control of lateral offset-induced disturbance torques is illustrated in Fig. 8.3.4-16. The elevons are positioned during entry to account for the longitudinal offset uncertainties. The integral trim compensation for elevon control of a longitudinal offset is illustrated in Fig. 8.3.4-16.

The characteristics of the nonlinear phase plane logic are significant parameters in the evaluation of ACPS entry control performance. The particular phase plane logic used is illustrated in Fig. 8.3.4-17. It consists of six zones which are functionally defined in the figure.

The parameters used to control the parabolic switch lines are of particular significance and are illustrated in Fig. 8.3.4-18. The steepest (right-most) parabolic line represents the estimated nominal jet thruster acceleration capability. With the parameter FSHRT ("Fire-Short") set to zero, the high parabola would fall exactly on that line. However, it is not desirable to have the high parabola fall right on the estimated jet capability line because the nominal uncertainties (in cross-axis coupling effects, aerodynamic interactions, jet thruster performance tolerance or undetected failures) could cause propellant-wasting vehicle attitude overshoots during attitude maneuvers. With a FSHRT of 1 the (derivative of) slope of the high parabola is reduced and corresponds to a control acceleration that is one half of the estimated jet thruster capability. The equation that expresses the fraction of corresponding high parabola acceleration to estimated capability is $\frac{1}{1 + \text{FSHRT}}$.

Because the FSHRT variable reduces the slope of the high parabola below that of the jet capability, the vehicle state might go from Zone III to Zone IV (Fig. 8.3.4-17). This would cause the thrusters to stop firing momentarily until the vehicle coasts to Zone III or Zone II. This tvpe of Fire-Short response is less undesirable than an overshoot of the deadband region. A nominal FSHRT value of 1 is used in the baseline autopilot.

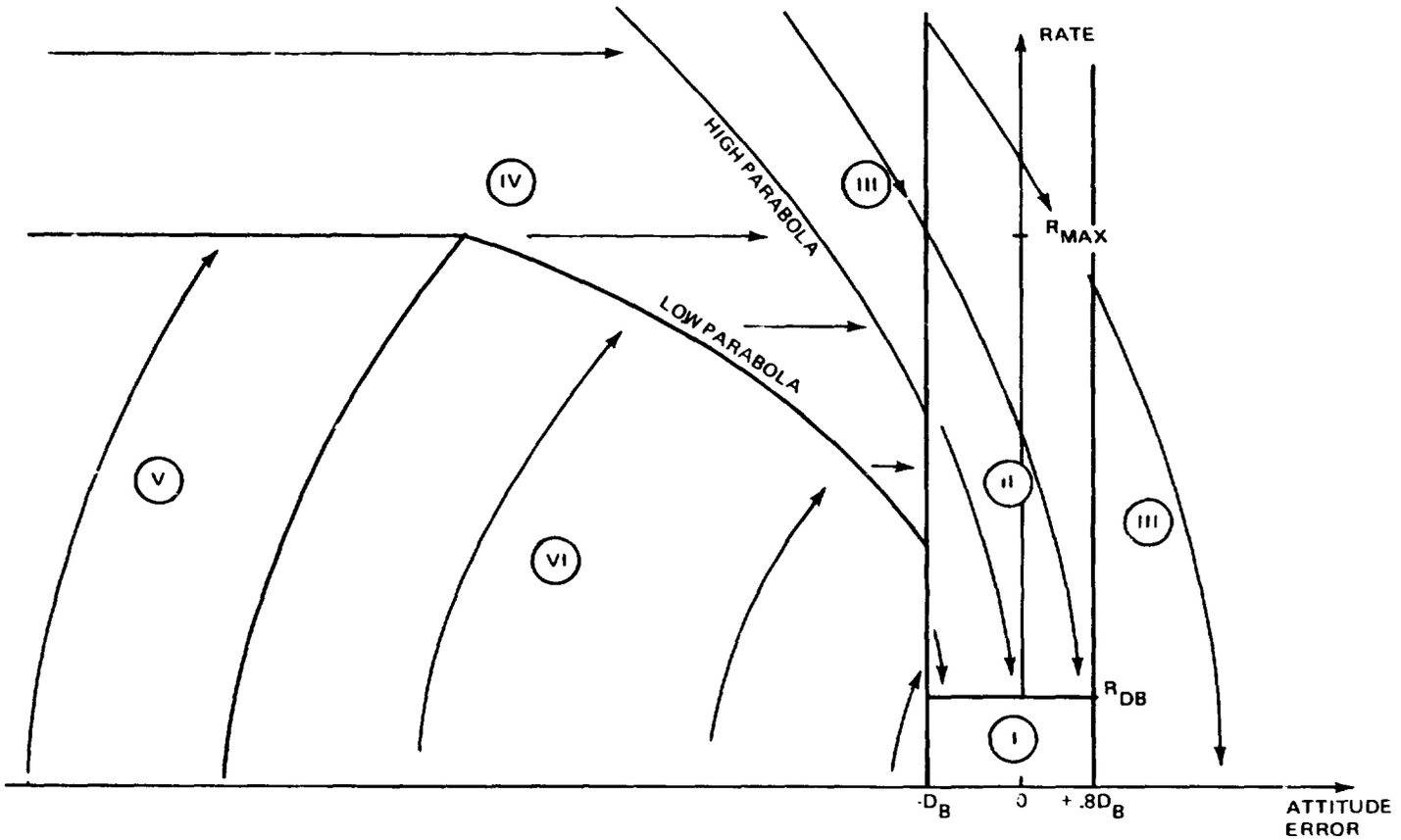

ZONE DEFINITIONS

I. NO-FIRE LIMIT CYCLE
II. FIRE TO REDUCE RATE (UNTIL R_{DB})
III. FIRE TO ZERO RATE
IV. HOLD COASTING RATE UNTIL HIGH PARABOLA
V. FIRE TO INCREASE RATE TO R_{MAX}
VI. FIRE TO INCREASE RATE TO LOW PARABOLA

B-169

Fig. 8.3.4-17 ACPS Jet Thruster Firing Command Schematic for the Upper-Half Phase Plane

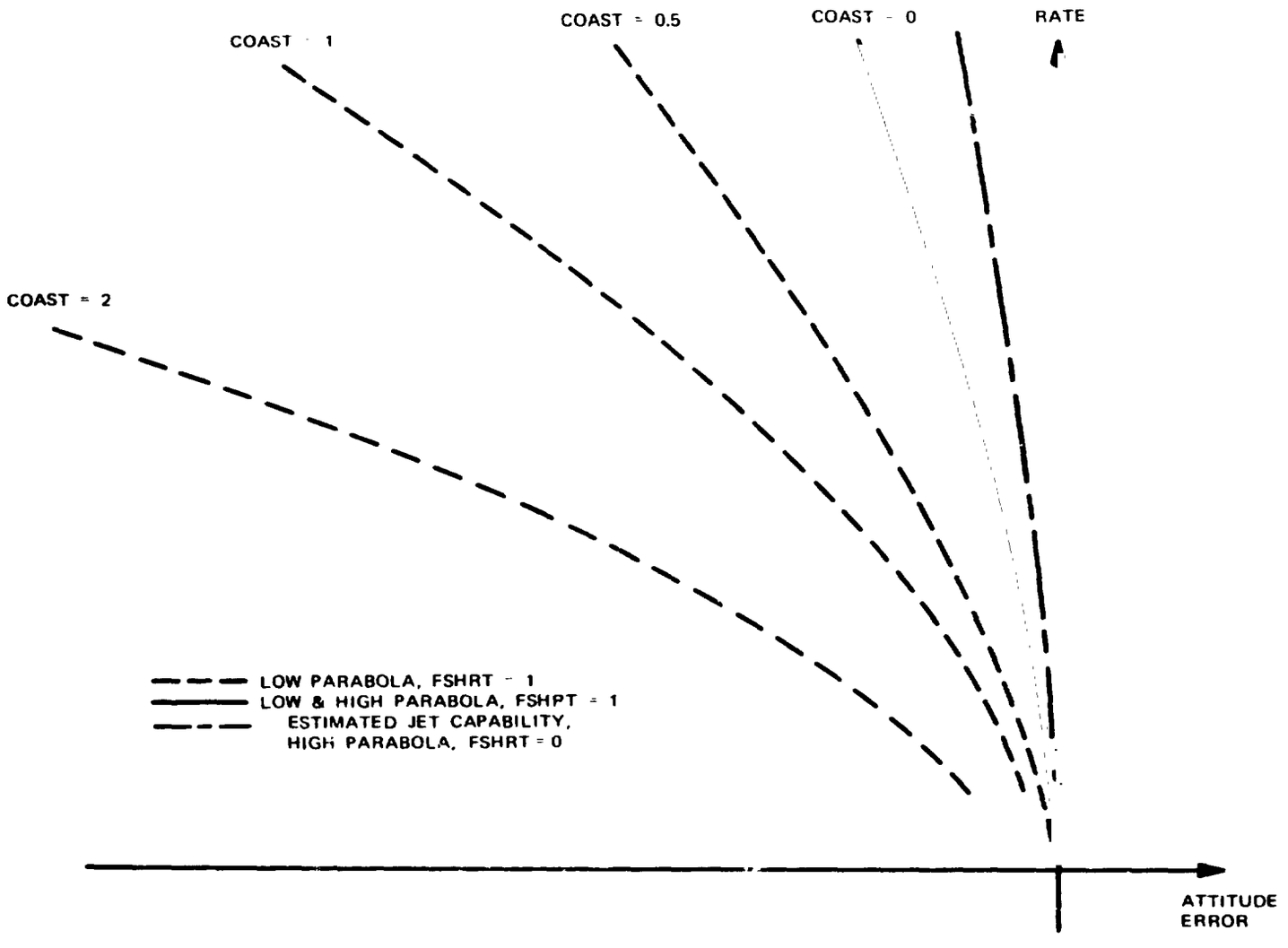

Fig. 8.3.4-18 Parabolic Switch Line Adjustment Variables ("Coast", "FSHRT") Effectiveness

With a COAST parameter of zero the low parabola and the high parabola become identical as is illustrated in Fig. 8.3.4-18. As COAST takes on larger values, the low parabola is shifted leftward of the high parabola. For a given value of rate, a point on the low parabola is shifted to the left by the multiplier function $(1 + COAST)^2$ on the given high parabola point.

As can be seen in Fig. 8.3.4-17, the more leftward the shift of the low parabola (for a given attitude error in Zone VI), the lower the coasting rate in Zone IV that the jets will be required to produce. Thus, the total rate change for any given attitude maneuver will be less, and the ACPS propellant usage will be less. The low parabola performs the function of a rate limit that is proportional to the square root of attitude error.

The parameter COAST would never be set to zero because, if the vehicle were moved from Zone III back into the high parabola (i.e., to "fire short"), it is more desirable for it to move into the Zone IV coast region rather than the opposite-firing Zone VI region.

8.3.4.2.7 Entry ACPS Thruster Size Selection And Propellant Requirements

Evaluation of the reentry attitude control system was performed using a 6-degree-of-freedom simulation, which includes the effects of guidance/control interactions resulting from attitude corrections during the thermal control and target control phases of the trajectory. Total ACPS entry propellant usage as affected by jet size and number used is shown in Fig. 8.3.4-19 for a typical 1100 n mi cross-range maneuver. The yaw control system (Z-DAP, refer to subsection 8.3.4.2.6) was used. Fig. 8.3.4-20 presents the corresponding body-axis control accelerations for these thruster sizes on the external tank configuration assuming the same thruster location. Trajectory control as measured by the effectiveness of the control system to maintain nominal peak accelerations and heating rates are shown in Table 8.3.4-8 along with the resulting terminal target accuracies as a function of the thruster jet size. Better trajectory control and terminal targeting can be achieved with the larger control accelerations associated with the 3500 lb thrusters, but uses ACPS propellants in excess of 6000 lb. Use of the 1000 lb thruster results in propellant usage below 2500 lb. However, good trajectory control and terminal targeting capability is compromised with these lower thruster sizes. The trajectory and target parameters for an entry simulation using instantaneous control response is also indicated in Table 8.3.4-8 for comparative purposes.

- Z-DAP CONTROL LAWS (COAST 2)
- DEADBAND 5° YAW ATTITUDE
  .1°/SEC PITCH RATE
  .3°/SEC ROLL/YAW RATE
- ENTRY TRIM α = 27°
- TERMINAL G LIMIT = 1.5
- ISP = 375 SEC

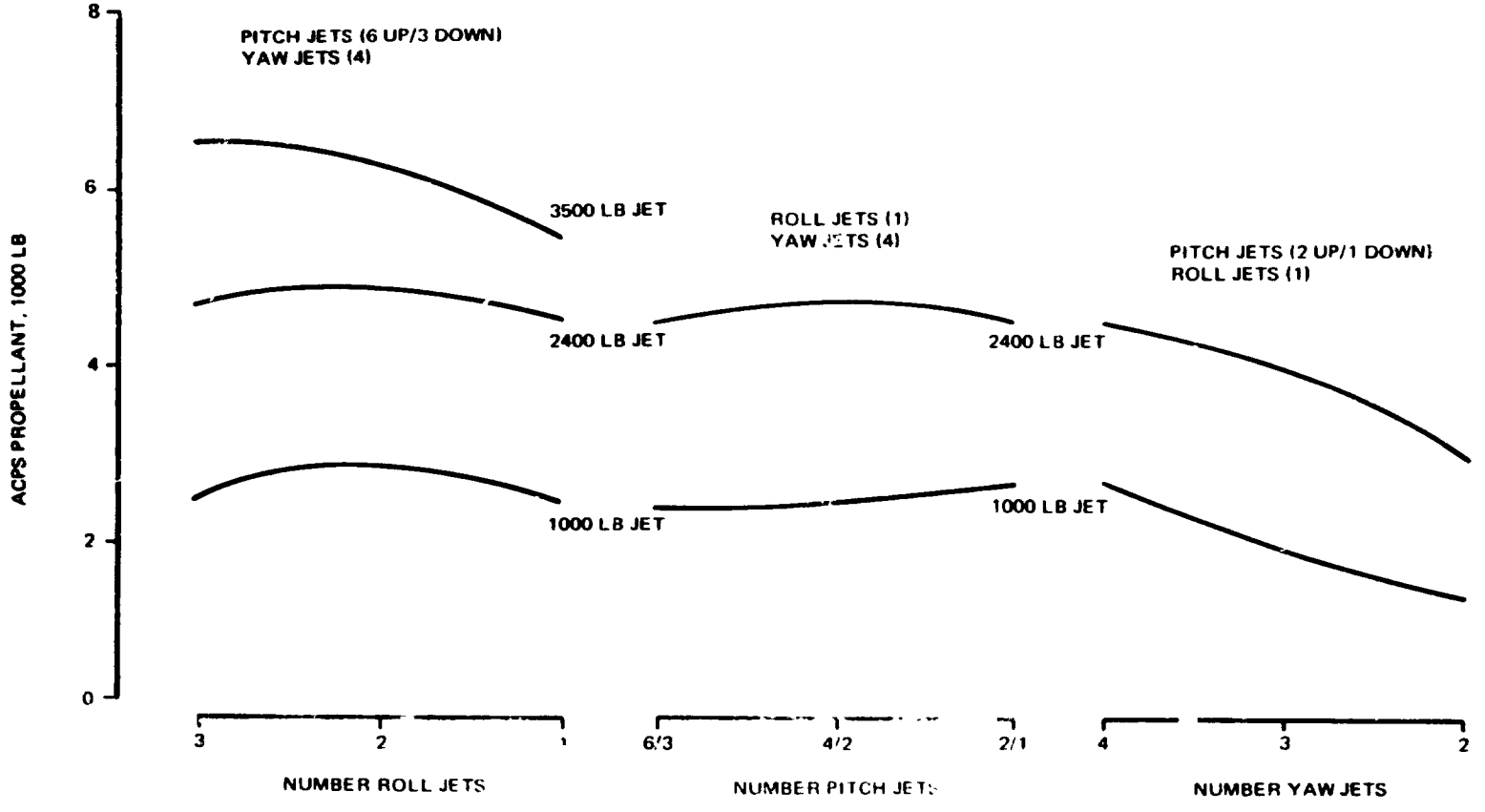

B-175

Fig. 8.3.4-19 Total ACPS Propellant - High Cross Range Entry Effect of Jet Thruster Size and Number

ROTATIONAL INERTIAS
- I_{XX} = 1.72 X 10^6 SLUG-FT^2
- I_{YY} = 16.4 X 10^6 SLUG FT^2
- I_{ZZ} = 14.3 X 10^6 SLUG FT^2

CONTROL MOMENT ARMS

ROLL	41.67 FT
PITCH }	79.17 FT FWD
YAW }	45.83 FT AFT

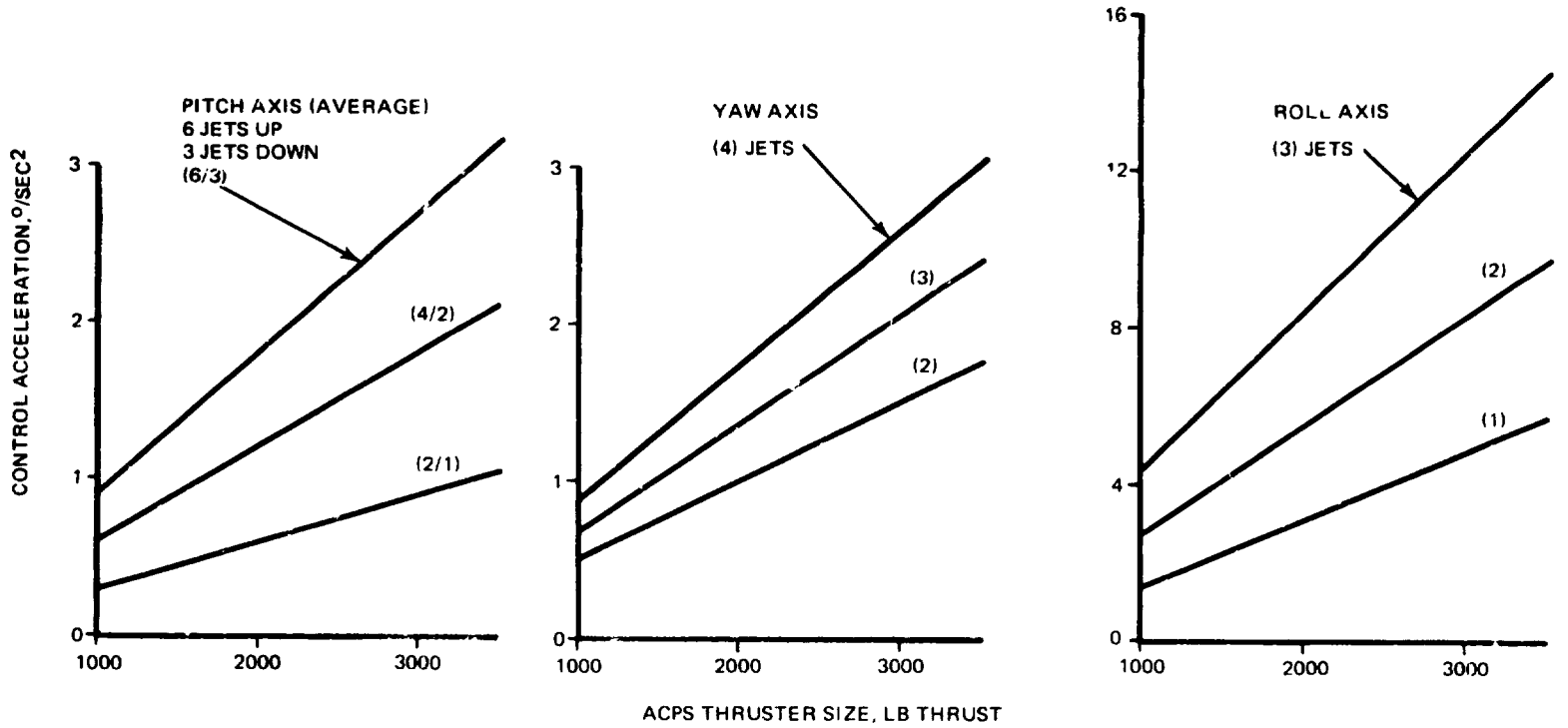

B-212

Fig. 8.3.4-20 ACPS Control Accelerations per Axis for Selected Jet Thruster Size and Number

TABLE 8.3.4-8 - ACPS JET THRUSTER SIZING ENTRY
TRAJECTORY CONTROL WITH GUIDANCE/
CONTROL INTERACTION, HIGH
CROSS-RANGE ORBITER

Z - DAP Control Laws
Coast = 2.
Deadband Yaw Attitude - 5.0°
Pitch Rate - 0.1°/sec
Roll/Yaw Rate - 0.3°/sec

Entry α time = 27°
Terminals G-Limit = 1.5

Jet Thrusters				G_{MAX}	$\dot{Q}_{MAX}$	Cross Range
Size lb	Number Roll	Pitch	Yaw	g's	BTU/ft²/sec	Target Dispersion, - n mi
3500	3	6/3	4	3.25	56.5	2.8
↓	2	↓	↓	2.20	↓	0.9
↓	1	↓	↓	2.16	↓	-2.5
2400	3	↓	↓	3.12	56.8	-4.6
↓	2	↓	↓	4.14	↓	-4.4
↓	1	↓	↓	5.32	↓	-10.0
↓	↓	4/2	↓	3.07	↓	-3.9
↓	↓	2/1	↓	4.45	↓	-7.0
↓	↓	↓	3	6.19	56.5	-16.6
↓	↓	↓	2	5.60	57.2	-10.6
1000	3	6/3	4	6.45	60.4	8.1
↓	2	↓	↓	4.98	59.6	15.7
↓	1	↓	↓	3.43	58.3	3.7
↓	↓	4/2	↓	5.06	59.3	15.4
↓	↓	2/1	↓	6.31	60.9	15.9
↓	↓	↓	3	2.19	67.5	40.1
↓	↓	↓	2	4.09	71.2	22.3
Inst Control Response				1.99	56.3	-2.9

In an attempt to achieve the propellant benefits associated with the 1000 lb. thruster and to define minimum torque requirements, further optimization of the guidance/control system was performed. Table 8.3.4-9 presents the effects of the following parameters on a 1000 lb system:

- Variation in pitch and roll/yaw rate deadbands
- Variation in the level of the terminal g-profile (G_{HIGH})
- Variation in the phase-plane parameter "COAST" (Subsection 8.3.4.2.6)

Tightening the parameter "COAST" from 3 to 1 improves the system performance to acceptable levels during the thermal control phase, but at the expense of a 1000 lb increase in propellant consumption. The g-rise experienced during the termainl targeting phase was still found to be unacceptable due to the loss in drag control during a bank reversal. Once drag control is lost (during the bank reversal) guidance commands higher g-levels to prevent overshoot of the target. The effects of this guidance/control interaction can be minimized using several approaches:

- Minimize the number of bank reversals
- Provide guidance targeting software which takes into account the reduction in drag during the bank reversal
- Significantly increase the control torque to reduce the time for a bank reversal or increase the rate at which the reversal is performed
- Perform the terminal guidance phase at lower g-levels to provide more margin for a guidance g-rise

The latter two approaches were investigated using the 1000 lb thruster. The nominal terminal g-level was reduced to 1.2g from 1.5g, and the parameter "COAST" was decreased to 1 when the roll error signal exceeded a specified high level (i.e. 30 degrees). The tightening in the phase plane switch logic causes the vehicle to accelerate to higher rotational rates. The combination of these approaches resulted in acceptable trajectory and target control using the 1000 lb thruster with 2500 lb of ACPS propellant consumption.

TABLE 8.3.4-9 ENTRY TRAJECTORY CONTROL, TARGETING AND ACPS PROPELLANTS WITH 1000 LB ACPS THRUSTERS GUIDANCE/CONTROL INTERACTION HIGH CROSS-RANGE ORBITER (Sheet 1 of 2)

Z-DAP Control Laws
Yaw Attitude Deadband = 5.0°

Entry α Trim = 27°
ISP = 375 sec

Jet Thrusters				Rate Deadband		Coast Parameter	G_{High} g's	G_{Max} g's	$\dot{Q}_{Max}$ BTU/ft^2/sec	Cross Range Target Dispersion, n mi	ACPS Propellant, lb
Size, lb	Number Roll	Pitch	Yaw	Pitch deg/sec	Roll/Yaw deg/sec						
1000	1	2/1	4	0.10	0.30	2	1.5	6.31	60.9	15.9	2640
			3			2		2.19	67.5	40.8	1970
			2			2		4.09	71.2	22.2	1380
			4			1		5.30	56.9	-11.4	3740
			3			1		5.26	57.3	-12.1	3200
			2			1		5.03	59.6	14.7	2150
			4			2	1.2	1.70	66.5	-11.1	2490
			4			1		1.92	58.5	8.5	3410
			4		0.50	2		1.65	67.6	- .4	2430
			4			1		4.4	59.5	-10.3	4191
			4			$3/1\phi_\epsilon \geq 40^\circ$		3.19	59.2	14.9	2560
			4			$3/1\phi_\epsilon \geq 30^\circ$		1.87	59.1	8.5	2440
			4	0.05		$2/1\phi_\epsilon \geq 40^\circ$		1.50	59.1	3.0	2580
			3	0.10		$3/1\phi_\epsilon \geq 30^\circ$		2.40	65.2	-15.5	2220
			3	0.10		$3/.5\phi_\epsilon \geq 20^\circ$		2.35	58.5	-10.0	2420

TABLE 8.3.4-9 ENTRY TRAJECTORY CONTROL, TARGETING AND ACPS PROPELLANTS WITH 1000 LB ACPS THRUSTERS GUIDANCE/CONTROL INTERACTION HIGH CROSS-RANGE ORBITER (Sheet 2 of 2)

Z-DAP Control Laws
Yaw Attitude Deadband = 5.0°

Entry α Trim = 27°
ISP = 375 sec

Jet Thrusters				Rate Deadband		Coast Parameter	G_{High} g's	G_{Max} g's	$\dot{Q}_{MAX}$ BTU/ft^2/sec	Cross Range Target Dispersion, n mi	ACPS Propellant, lb
Size, lb	Number Roll	Pitch	Yaw	Pitch deg/sec	Roll/Yaw deg/sec						
1000	1	2/1	3	0.05	0.50	$2/.5\phi_\epsilon \geq 40^\circ$	1.2	1.73	58.9	6.9	2300
Inst Control Response							1.5	1.99	56.3	-2.9	-
Inst Control Response							1.2	1.85	57.5	1.8	-

Deadband selections of 5.0 deg yaw attitude, 0.1 deg/sec pitch rate, and 0.50/sec roll/yaw rate, provide minimum propellant usage with the 1000 lb thruster. The minimum acceptable control torques for reentry are:

Roll:	1.4 deg/sec^2
Yaw:	0.65 deg/sec^2
Pitch:	0.3 deg/sec^2

The level of roll torque indicated above can be reduced further without adverse effect. These torque levels represent the minimum acceptable levels for safe entry using automatic guidance between entry interface and Mach 4. Further study is being performed using a manned simulation to determine man-in-the-loop requirements, the impact on jet sizing required during the transition to low α , and the impact of winds on jet size selection.

The presence of a lateral cg offset from the lift center of pressure will impose a steady state roll torque disturbance during entry. If left untrimmed, this offset will result in an excessive ACPS propellant usage and prevent good attitude control, (Fig. 8.3.4-21 and Table 8.3.4-10. For a vehicle with unstable static directional stability (Negative C_{n_β}) and a 2 in. cg offset, the ACPS propellant will increase as much as 5000 lb for the configurations being studied. Fig. 8.3.4-21 indicates that an increase in C_{n_β} to a neutral stability level will minimize the impact of this lateral cg offset. Addition of approximately 140 sq ft of fixed ventral fin (weight $\approx$ 3000 lb) offers a means of providing these favorable stability levels. Since further evaluation of the ventral in terms of thermal integrity are required, the base line configuration does not include this empennage. Differential actuation of the orbiter elevons, using its adverse yaw characteristics, is being employed as an aerodynamic means to trim out the lateral cg torque distrubance without increase in ACPS propellant usage.

8.3.4.2.8 Entry Control Trim System: Longitudinal

During the initial phase of entry, the vehicle attitude will be oriented to a nominal angle-of-attack (27 deg) utilizing inertial system state vector information. The ACPS will provide attitude stability about this orientation to within a $\pm 1^o$ attitude deadband. The elevons will be prepositioned to provide the longitudinal trim at an angle of attack of 27 deg. At a sensed g = 0.1, the yaw control autopilot (Z-DAP) will be activated. At this

- Z-DAP CONTROL LAWS (5° YAW ATT DEADBAND)
- ENTRY TRIM α = 27°
- TERMINAL G LIMIT = 1.2
- ISP = 375 SEC

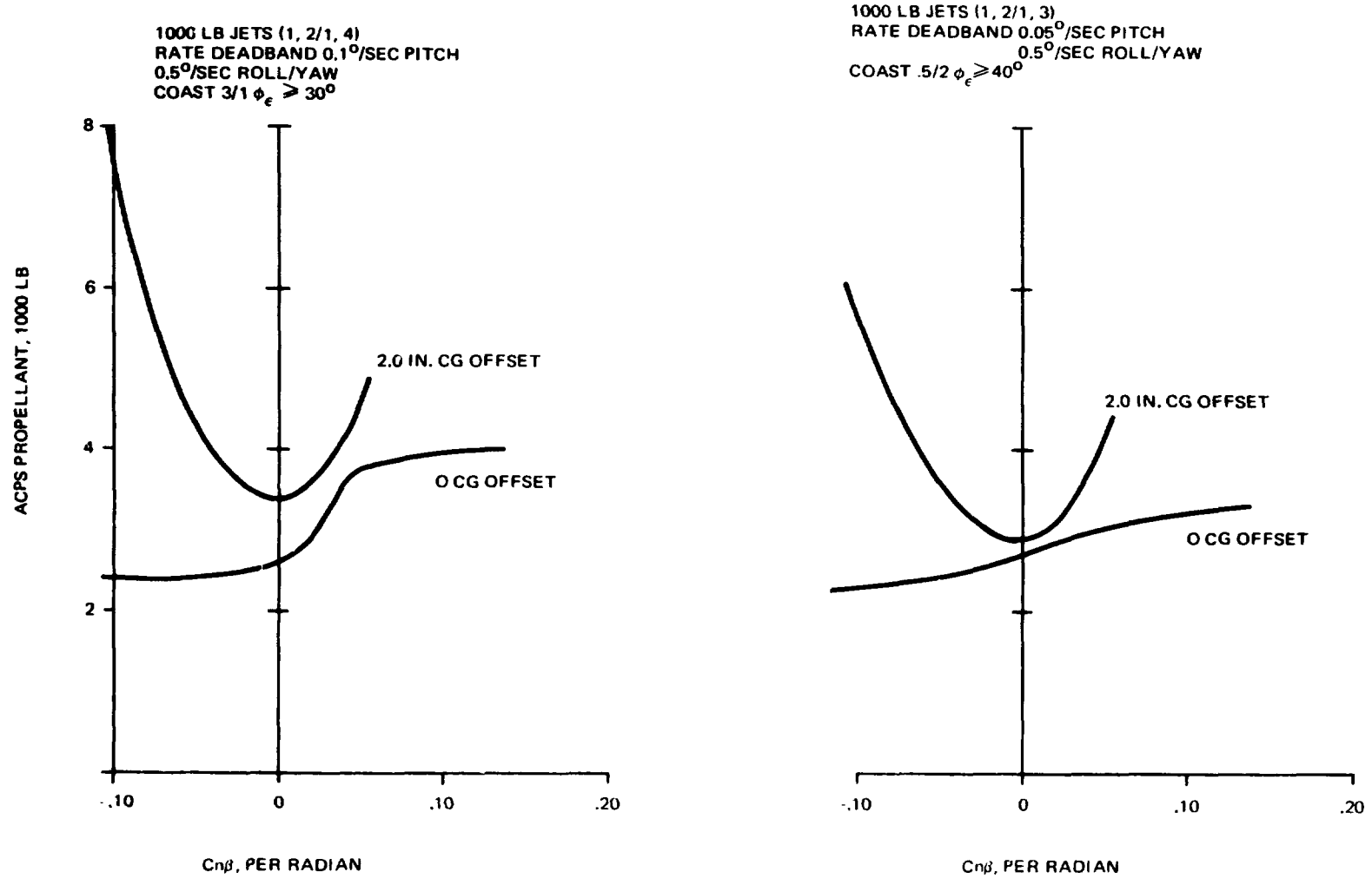

B-174

Fig. 8.3.4-21 Total ACPS Propellant - High Crossrange Orbiter Effect of Lateral CG Offset and Directional Aerodynamic Stability

TABLE 8.3.4-10 ENTRY TRAJECTORY CONTROL, TA
THRUSTERS; EFFECT OF LATERAL CG OFFSET
GUIDANCE/CONTROL INTERACTION

Z-DAP Control Laws
Yaw Attitude Deadband = 5°

Jet Thrusters				Rate	Deadband	Coast	C_{n_β}	Late
Size, lb	Number			Pitch, deg/sec	Roll/Yaw deg/sec	Parameter	per rad	CG C in
	Roll	Pitch	Yaw					
1000	1	2/1	4	0.10	0.3	2	-0.10	0.
							0	
							0.05	
							0.12	
					0.5		-0.10	
							0	
							0.05	
							0.12	
						$3/1\phi_E \geq 30°$	-0.10	
							0	
							0.05	
							0.12	
							-0.10	2.
							0	
							0.05	
							0.12	
	1	2/1	3	0.05		$2/.5\phi_E \geq 40°$	-0.10	0.
							0	
							0.05	
							0.12	
							-0.10	2.
							0	
							0.05	
							0.12	

FOLDOUT FRAME 2

;Y CONTROL, TARGETING AND ACPS PROPELLANTS WITH 1000 LB ;RAL CG OFFSET AND LATERAL AERODYNAMIC STABILITY; ;OL INTERACTION HIGH CROSS-RANGE ORBITER

Entry $\alpha_{Trim} = 27^{o}$
Isp = 375 sec

C_{n_β} per rad	Lateral CG Offset, in.	G_{HIGH}, g's	G_{MAX}, g's	$\dot{Q}_{MAX}$ BTU/ft^2/sec	Cross Range Target Dispersions n mi	ACPS Propellant, lb
-0.10	0.0	1.2	1.7	66.5	-11.1	2490
0			1.89	65.5	4.1	2430
0.05			1.64	63.9	2.2	2750
0.12			1.96	64.1	4.3	3160
-0.10			1.65	67.6	- .4	2430
0			2.75	66.9	6.2	2800
0.05			2.43	66.2	2.1	2970
0.12			4.14	61.5	- 7.6	4010
-0.10			1.87	59.1	8.5	2440
0			1.58	58.8	.8	2570
0.05			3.60	58.9	8.6	2770
0.12			3.72	58.7	- 5.8	3970
-0.10	2.0		1.74	59.5	- .3	7480
0			3.24	59.3	4.6	3380
0.05			2.54	59.2	15.8	4540
0.12			UNCONTROLLABLE			-
-0.10	0.0		1.73	58.9	6.9	2300
0			2.85	59.4	- .1	2700
0.05			1.66	59.6	1.2	3040
0.12			1.60	59.1	3.9	3290
-0.10	2.0		1.81	59.1	4.0	5770
0			2.19	57.7	- 2.5	2840
0.05			3.07	57.4	18.7	4140
0.12			UNCONTROLLABLE			-

GRUMMAN BOEING

time the pitch channel will remain in an attitude hold mode using inertial system angle-of-attack and rate information. The elevons will be repositioned to achieve trim at the command angle of attack with an integral compensation network. Fig. 8.3.4-22 illustrates this integral compensation logic, which utilizes the pitch jet-on-time command.

This trim system can remain active for the remainder of the entry or, once a steady-state elevon command is achieved, the elevon can be fixed while switching the ACPS into a rate hold mode. This mode of control will be used to Mach 4 where preparation for the transition to lower angle-of-attack is made and full aero surface control is activated.

The issue of inertial system accuracy has been evaluated in terms of angle-of-attack estimation for use in the trim system early in the entry trajectory. Navigation performance was determined by propagating the true and estimated state vector through the once-around abort mission. It was assumed that no external information was used to update the state vector. Fig. 8.3.4-23 shows a time history of the 3σ α and β errors during entry using the Carousel IV inertial platform. The figure indicates that α and β can be estimated to within 1 degree for most of the entry maneuver. At about 2000 seconds into entry, the increasing vertical velocity error combined with the decreasing horizontal velocity cause a significant increase in α error, indicating the requirement for barometric measurement updates.

8.3.4.2.9 Entry Control Trim System: Lateral-Directional

Studies have shown that a relatively small lateral (Y-axis) offset between the vehicle center of mass and its aerodynamic center of pressure will cause relatively high ACPS propellant requirements during entry. This characteristic is undesirable because the additional ACPS propellant weight has a severe impact upon the shuttle liftoff weight. Moreover, the high sensitivity of propellant usage to lateral offset tolerance imply potentially high operational costs to continuously ensure an acceptable vehicle configuration.

The initial effect of a 2 in offset step input is to provide a roll torque distrubance about the roll (X) axis. However, as the simulation results of Fig. 8.3.4-24 indicate, this roll torque interacts with the Z-DAP autopilot to cause the vehicle to build up to a steady-state side-slip (β) angle and a steady-state bank angle error (ϕ). The final result consists of a side-slip angle (β), which balances out the roll (X-axis) torque

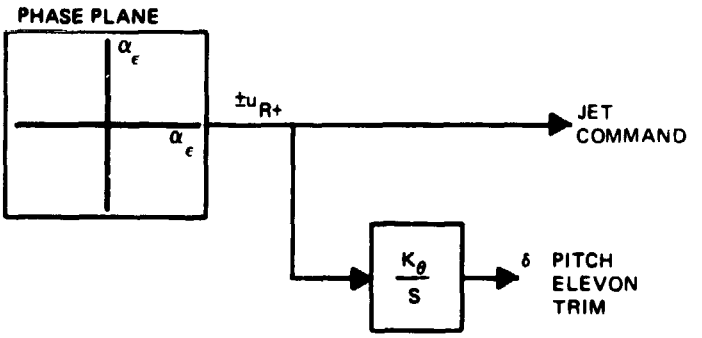

Fig. 8.3.4-22 Pitch Trim System Jet On-Time Integral Compensation

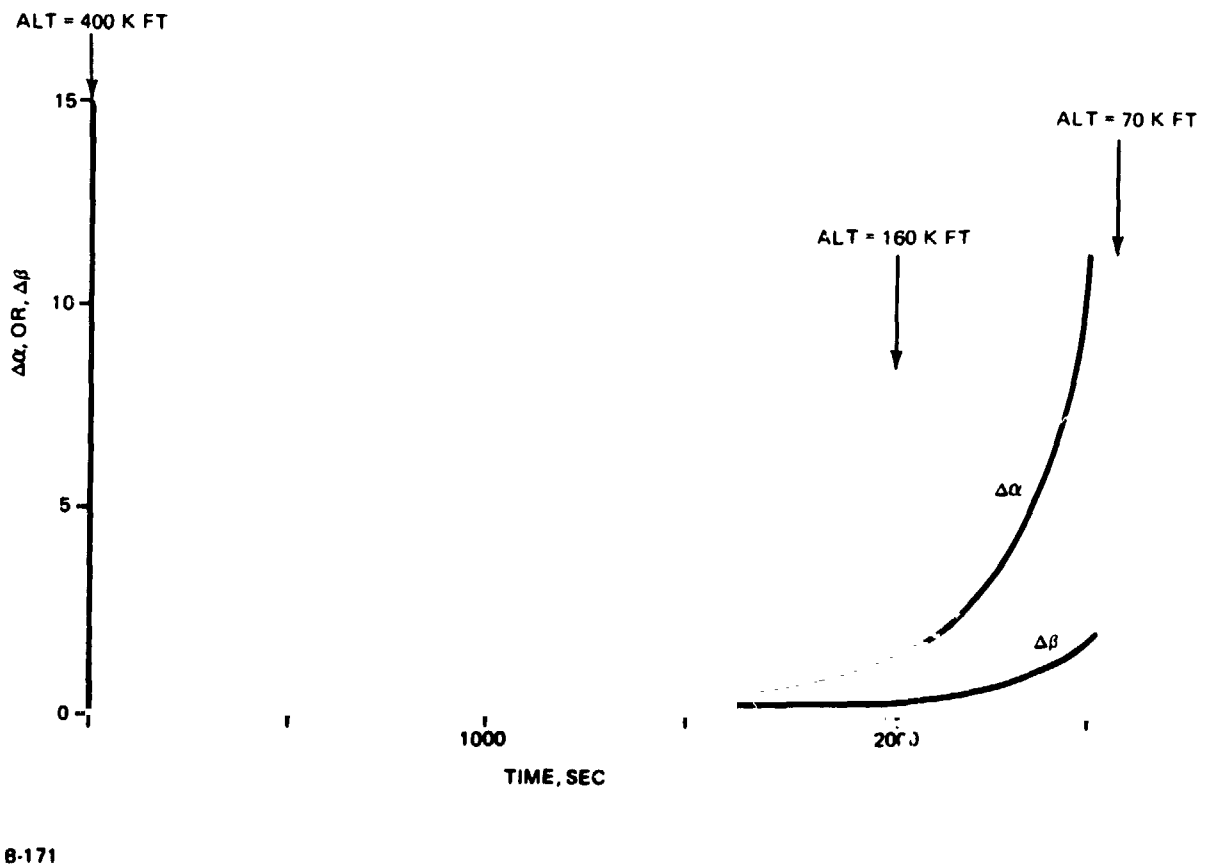

Fig. 8.3.4-23 3σ $\Delta\alpha$ And $\Delta\beta$ Errors During Entry Using Carousel IV Platform

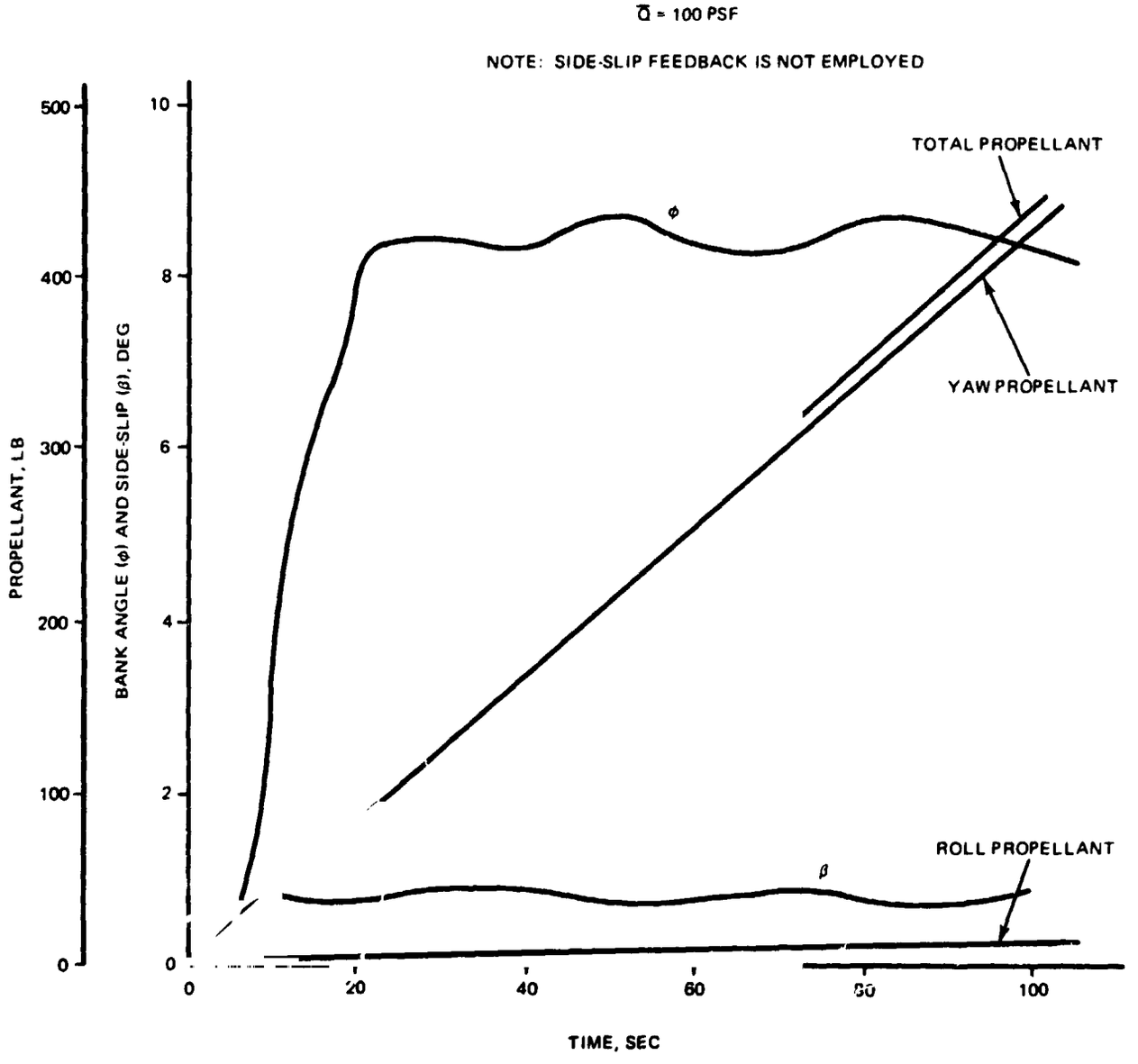

B-172

Fig. 8.3.4-24 Response to 2 In. Lateral CG Offset, No Aero Trim

caused by the offset, and a bank angle error which is sufficient to activate the ACPS autopilot to counteract the yaw (Z-axis) torque that results from the side-slip angle.

Note, that if the static directional stability (C_{n_β}) is zero, then the yaw torque resulting from the side-slip angle will be zero. This, then, is the mechanism which explains the results of previous studies where it was shown that a zero value of C_{n_β} will minimize the entry propellant penalty induced by a lateral offset (Refer to Subsection 8.3.4.2.7).

The shuttle elevons provide both roll (X-axis) and yaw (Z-axis) torques when differentially deflected. Thus, it becomes apparent that the elevons could be deflected to trim out the induced steady state yaw moment. Rapid trim motions of the elevons are to be avoided for vehicle dynamic considerations. Thus, a relatively simple and slow integral compensation trim command algorithm is an advantage. It is desirable for the variable that is selected for integration (to provide the elevon trim command) to be effective, efficient, and readily available. One variable that meets all of these qualifications is the autopilot-computed yaw axis thruster firing command.

With the ACPS yaw thruster integrated firing command being used to provide an elevon trim angle command, the simulation results are as shown in Fig. 8.3.4-25. It can be seen that, after a 20-sec transient response, the effective reduction in yaw axis ACPS propellant rate amounts to at least two orders of magnitude with respect to Fig. 8.3.4-24. Moreover, a total steady-state elevon angle of about 1.5 deg is sufficient to counteract the effects of a 2 in. offset, and the resulting side-slip angle has been reduced.

8.3.4.2.10 Aerodynamic Entry Autopilot

An alternate aerodynamic autopilot is under study to supplement the ACPS entry autopilot described in Subsection 8.3.4.6. Although the study is not complete at this time, this approach could potentially reduce overall ACPS propellant consumption and improve handling qualities.

Partial aerodynamic vehicle control is possible beginning with a dynamic pressure of approximately 4 psf, and complete control is obtained at 20 psf. Reaction control to aerodynamic control transitions are being performed in a 6-degree-of-freedom digital computer program supplemented by a 6-degree-of-freedom analog computer study for the autopilot

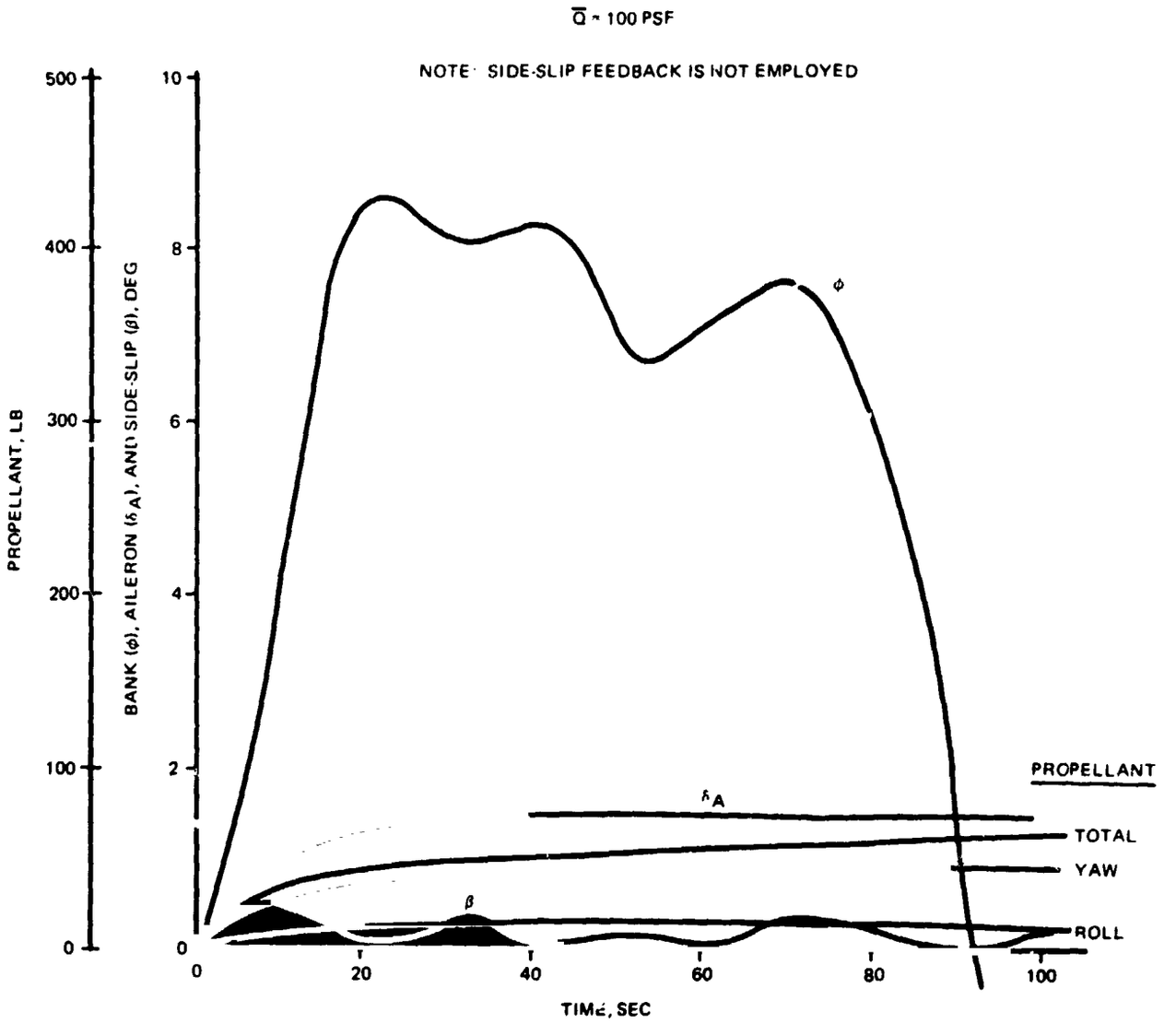

B-173

Fig. 8.3.4-25 Response to 2 In. Lateral CG Offset, Aero Trim Active

investigations. It should be noted that hypersonic control capability is required during entry; for the configuration studied, a moveable ventral was assumed for full aerodynamic control.

a. Autopilot Configuration

Block diagrams of the aerodynamic control system are illustrated in Fig. 8.3.4-26.

The longitudinal axis system uses body pitch rate and Euler pitch angle feedback. Both of these quantities are directly measureable on the vehicle, thus eliminating the computation of transformations in the control loop. The lateral-directional system also uses body rate and Euler angle measurements as shown. This total configuration is also advantageous in that it lends itself to direct adaptation to conventional autopilot and automatic landing systems.

The overall characteristics shown here are in general agreement with conventional airplane autopilot design practices. Minor modifications to general designs are the inclusion of an integral path in the longitudinal axis and heading angle feedback and commands. The integral path in the longitudinal axis is required to compensate for vehicle trim changes necessary when an angle of attack change is made on the vehicle. Without this compensation serious positional errors would occur due to the low forward gain of the vehicle and phugoid cancellation during the entry phase. Positive direction control is necessary to control the vehicle bank angle about the velocity vector at large angles-of-attack.

The results presented here are preliminary and demonstrate the feasibility of aerodynamic attitude control during the entry phase. It is emphasized that the control system presented here uses fixed gains and configuration. There are no gain changes nor are there any system or program changes during entry. Thus, this represents the simplest control system which can be mechanized. More sophisticated compensation using filters, programmed and parameter controlled gains and more extensive feedbacks can be incorporated into the control system to improve performance. However, the cost of this performance is the resultant complexity of the control system.

b. Linear Analysis

Results of a linear analysis of the stability augmentation system (SAS) and autopilot are shown in Fig. 8.3.4-27. The path of the lateral-directional SAS dominant root for a

D

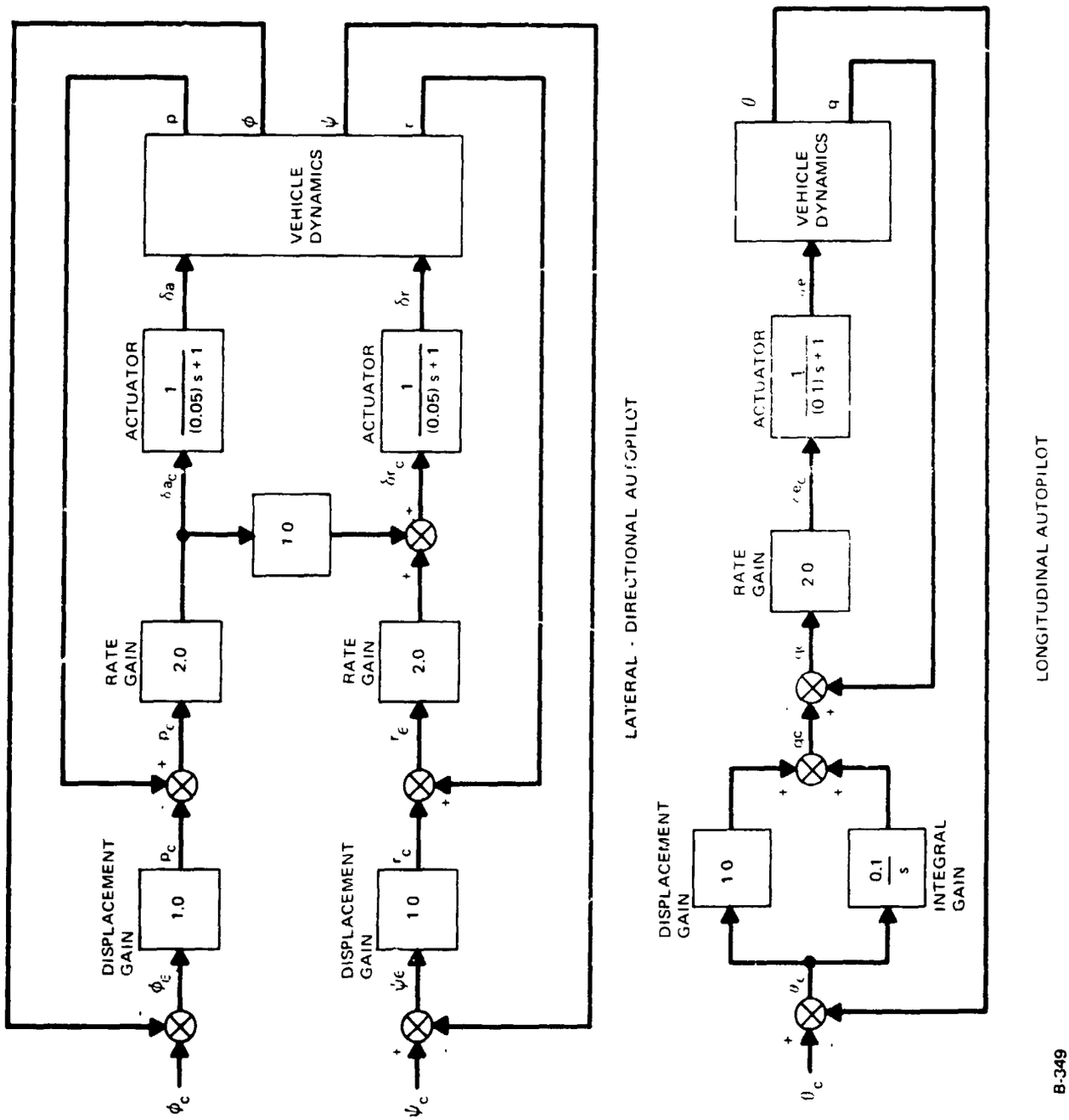

Fig. 8.3.4-26 G-3 30°α Aerodynamic Entry Autopilot Block Diagram

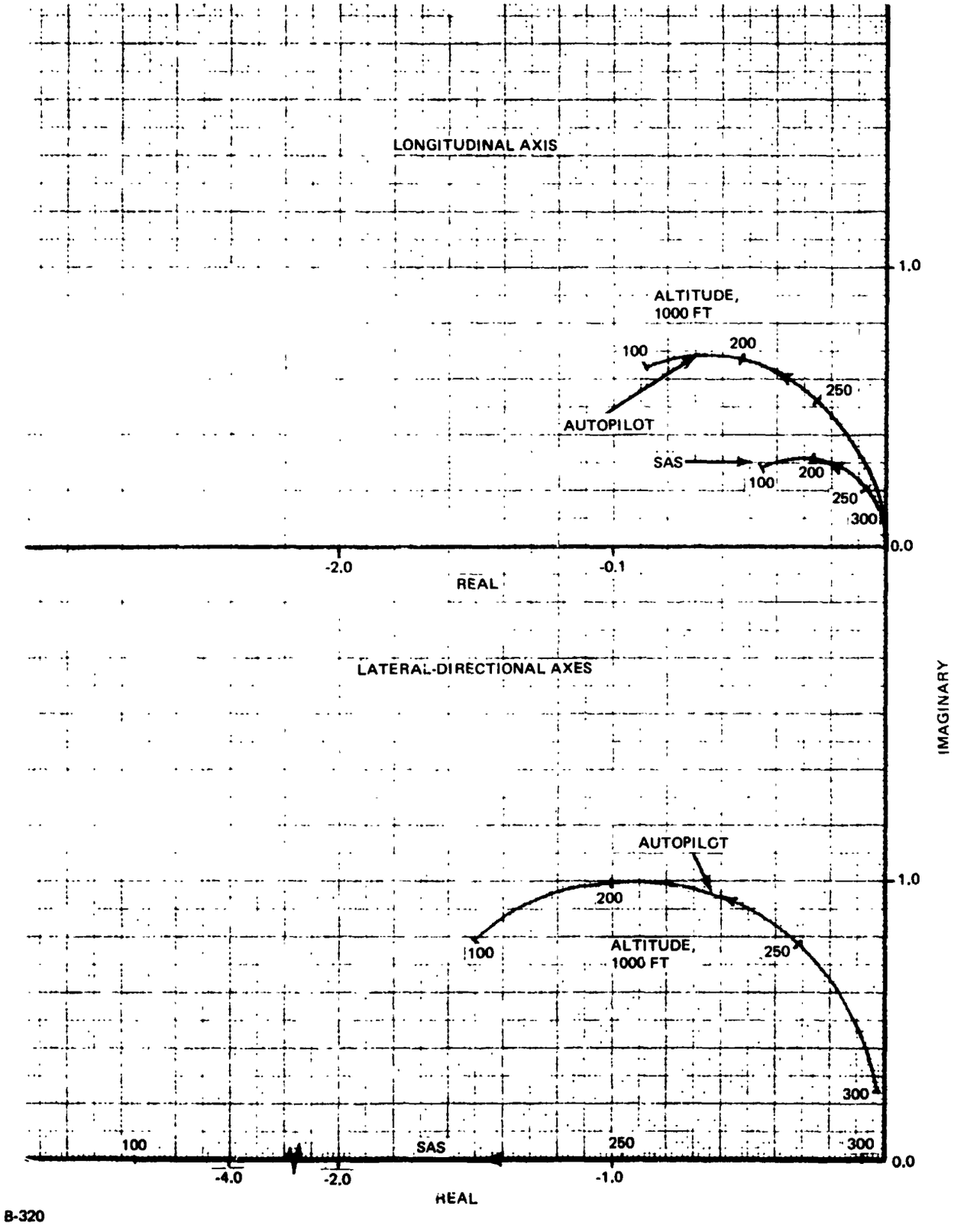

Fig. 8.3.4-27 Paths of Dominant Roots for 30^{o} α Equilibrium Entry

30 deg angle of attack equilibrium entry trajectory is shown in the figure. This root path is on the negative real axis and indicates that the system has increasing bandpass as the vehicle enters the atmosphere. This effect results from the increase in dynamic pressure along the trajectory. The dutch roll mode is not shown in this figure because it contributes very little to the output response. This is due to the energy cancelling effect of the numerator zero (ω_β) throughout the trajectory. Thus the roll rate SAS is governed by a first-order lag response.

The autopilot root path shows the characteristics for a body roll-angle command autopilot. The dominant behavior is that of a second-order system comprising what originally were the roll subsidence and spiral modes. The dutch roll mode is also cancelled in the roll response by the numerator zeros.

The path of the short-period roots for the longitudinal SAS describes the dominant longitudinal axis behavior since the phugoid is cancelled by the numerator zeros (Reference 1 and 2 of Subsection 8.3.4.5). The damping ratio of this response is greater than 0.5 for altitudes less than 230,000 ft. While this damping is generally acceptable in the preliminary handling quality specifications, the undamped natural frequency, about 0.3 to 0.4 radian per sec, is low. Preliminary investigations have shown that notch filter compensation can increase the undamped natural frequency somewhat. However, if large values (greater than 1.0 rps) are required during entry a high-gain system will probably be necessary.

The path of the roots for a body pitch command autopilot are also shown in this figure. Here the bandpass is much improved over the SAS because of the addition of a displacement gain. This system generally satisfies the preliminary control system response requirements.

c. Time History Responses

The vehicle response in the lateral-directional axis are demonstrated by the analog computer traces in Fig. 8.3.4-28. The first response is for a 5 deg per second body roll rate command at an altitude of 200,000 ft and a velocity of 15,000 ft/sec. The input command was shaped to prevent system saturation and coordination was provided by having heading rate commanded as a function of angle of attack. Capture of the commanded rate is

accomplished smoothly and with moderate control activity. Direct coordination commands provide an excellent transient with minimum side-slip excursion as shown.

The second transient response in Fig. 8.3.4-28 is for a 20 deg bank command about the velocity vector. To perform this maneuver, and to maintain vehicle body axis control, the command was transformed into roll and heading (Euler) body axis angle commands. These commands were then executed as shown again giving smooth and positive body axis control.

The pitch autopilot is demonstrated in Fig. 8.3.4-29 for a 5 deg pitch command at 230,000 ft and a velocity of 20,400 ft/sec. The response is smooth and well controlled and demonstrates the moderate effect of pitch attitude on the flight path angle.

8.3.4.3 Cruise and Landing

8.3.4.3.1 Terminal Phase Entry

After transition to conventional aerodynamic flight, (M = 2.0, 70,000 ft) a spiral glide is flown to target the vehicle into the final approach path. Use of energy management techniques permits considerable latitude in guiding the vehicle to a target point with a specified heading angle.

Previous studies indicate that it is desirable to define two points of reference as milestones on the glide path: the high key and the low key. The low key is established a priori as the target point for the descent glide.

The high key on the glide path is a cardioid-shaped area, or a "window," in the x-y plane, which defines the ranging capabilities of the orbiter for all heading angles, the limitation being the maximum lift-to-drag ratio of the vehicle. This energy management window expands with altitude, as the potential energy of the gliding vehicle increases. The window in Fig. 8.3.4-30 for example was calculated for an altitude of 35,000 ft for convenience, since below that altitude the vehicle aerodynamic characteristics remain invariant with Mach number. In an actual mission operations manual, the high key would be

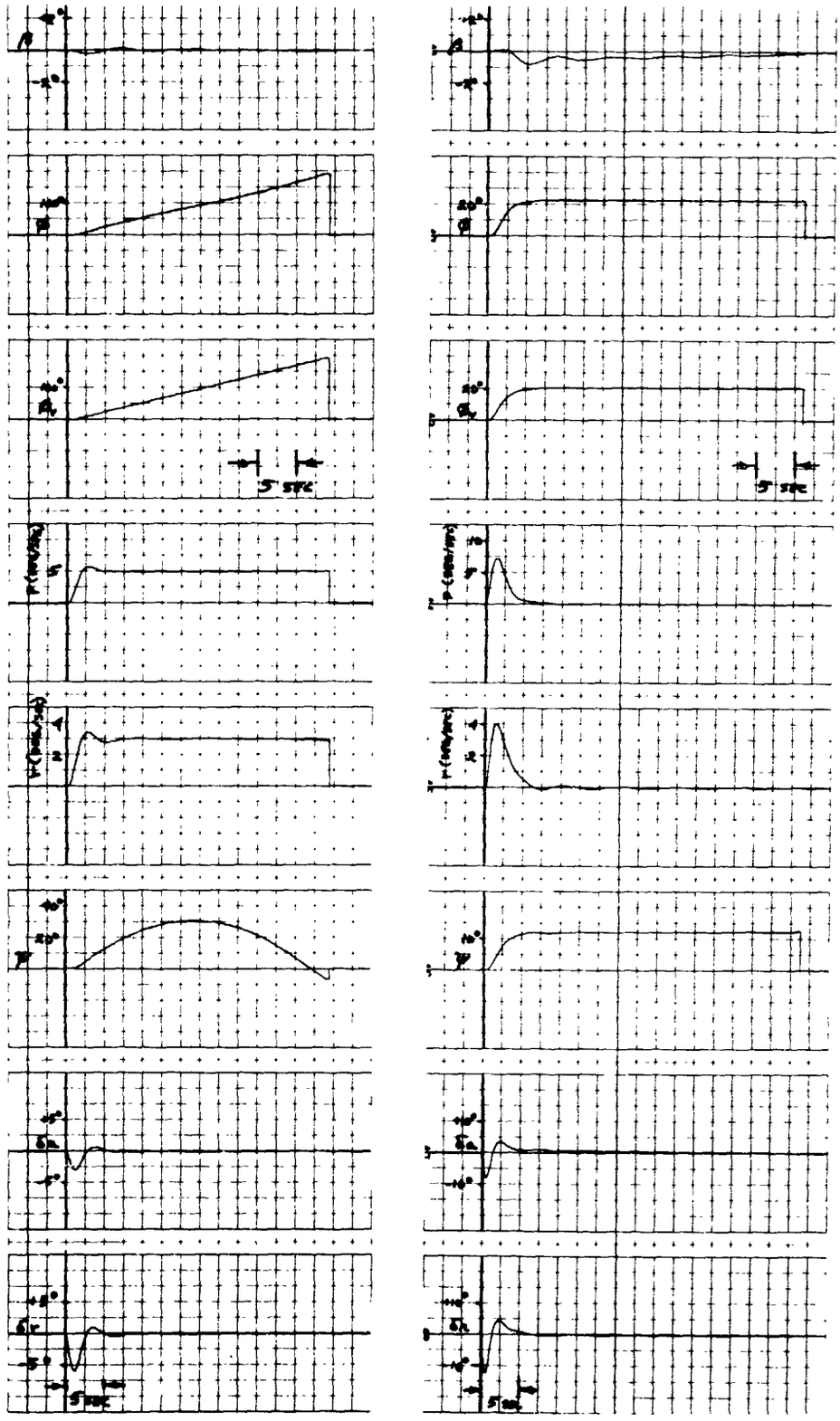

TRIM CONDITIONS
- h = 200,000 FT
- V = 15,000 FPS
- α_T = 30 DEG
- $\bar{q}$ = 59.0 PSF

B-321

5-DEG/SEC ROLL RATE COMMAND

20-DEG ROLL ABOUT VELOCITY VECTOR COMMAND

Fig. 8.3.4-28 G-3A Aerodynamic Entry Autopilot

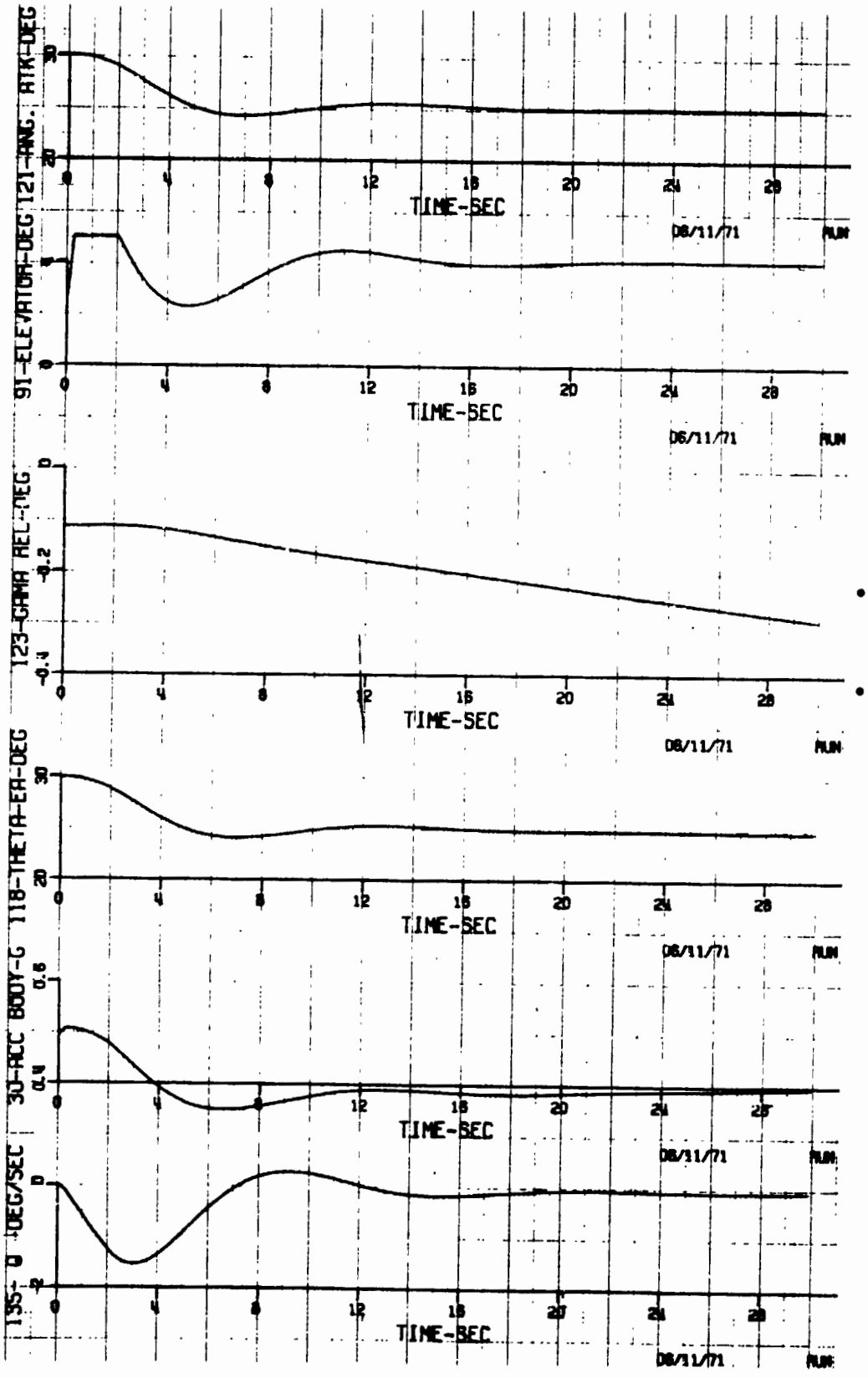

B-322

Fig. 8.3.4-29 G-3A Aerodynamic Entry Autopilot

defined for every altitude, presenting a three-dimensional inverted pyramid of expanding cardioids. The low key must be within the ranging capabilities of the orbiter at all times during the descent, ideally in the center of the cardioid.

Upon acquisition of a "funnel" that rises above the low key, a spiral glide is initiated. The altitude for acquisition of the funnel of course depends on the errors accumulated during the initial entry.

The spiral glides described by the orbiter are conducted at constant equivalent airspeed, bank angle, and load factor; i.e., the craft is very nearly in a state of steady maneuvering flight. The only departure from such steady flight is a very gradual decay in velocity accompanying descent into the denser lower atmosphere. It is this increase in atmospheric density that causes a decrease in the vehicle's turning radius, which results in a descending, inward-spiraling, funnel shaped trajectory. The variation of atmospheric density with altitude is accounted for in this analysis and the two typical descent spirals shown in Fig. 8.3.4-31 and 8.3.4-32 are judged to be a reasonable representation of pilot landing pattern execution.

The bank angle selected determines the final heading and altitude at the beginning of the final approach. The maximum bank angle (and the narrowest funnel) is that angle which will permit equilibrium turning flight at the maximum lift-to-drag ratio. For the H-33 vehicle, at entry weight, and nominal speed brakes, the $(L/D)_{max}$ - bank angle combination for the tightest spiral is 6.4 and 55 deg. The corresponding trajectory is shown in this figure as the inner spiral.

The wider spiral trajectory shown was constructed for a descent at a constant load factor 1.1g. Both trajectories were constructed to end at the same nominal low key, and illustrate how variation in initial conditions could be accommodated in setting up the final approach.

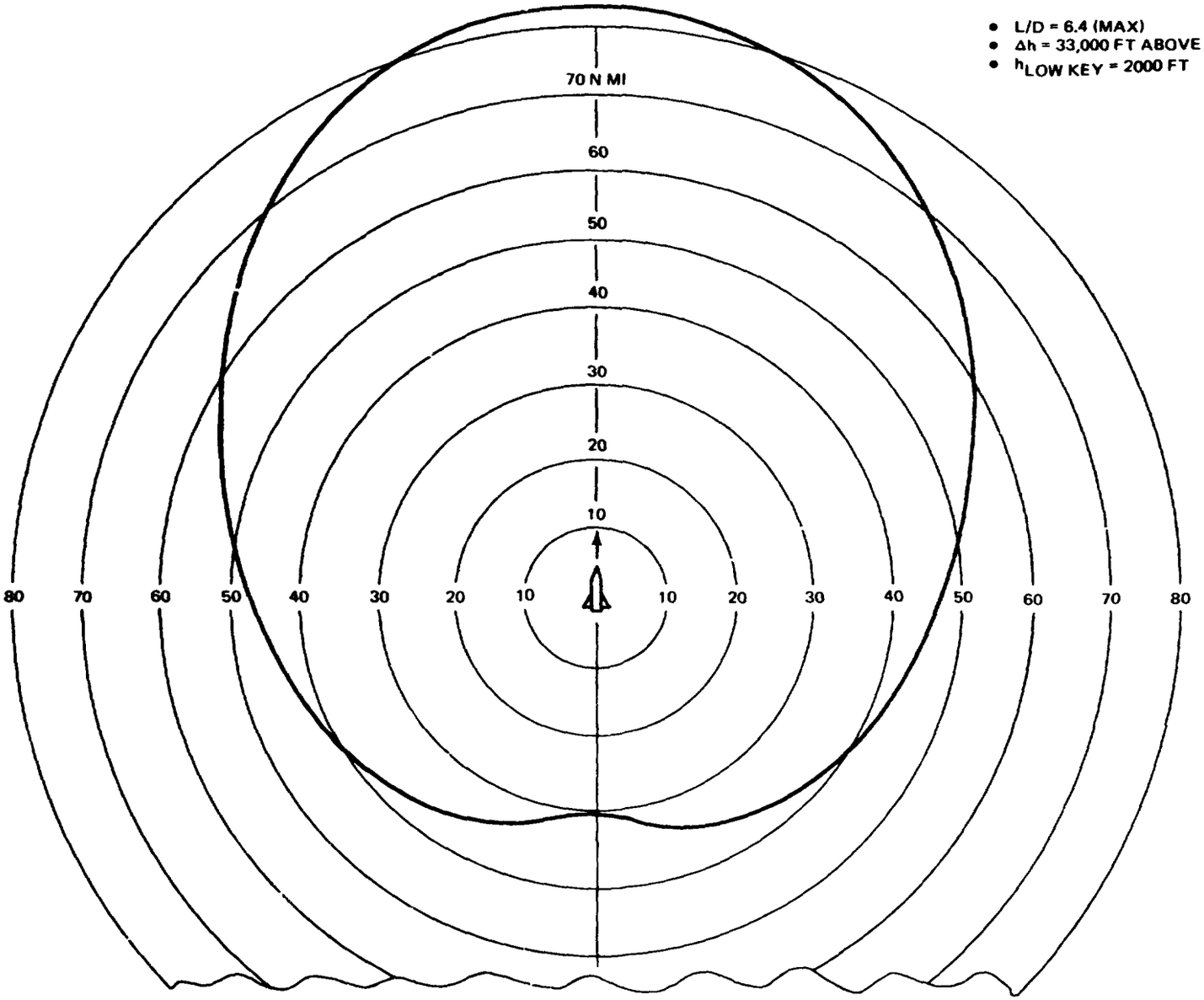

Fig. 8.3.4-30 H-33 Orbiter Terminal Footprint

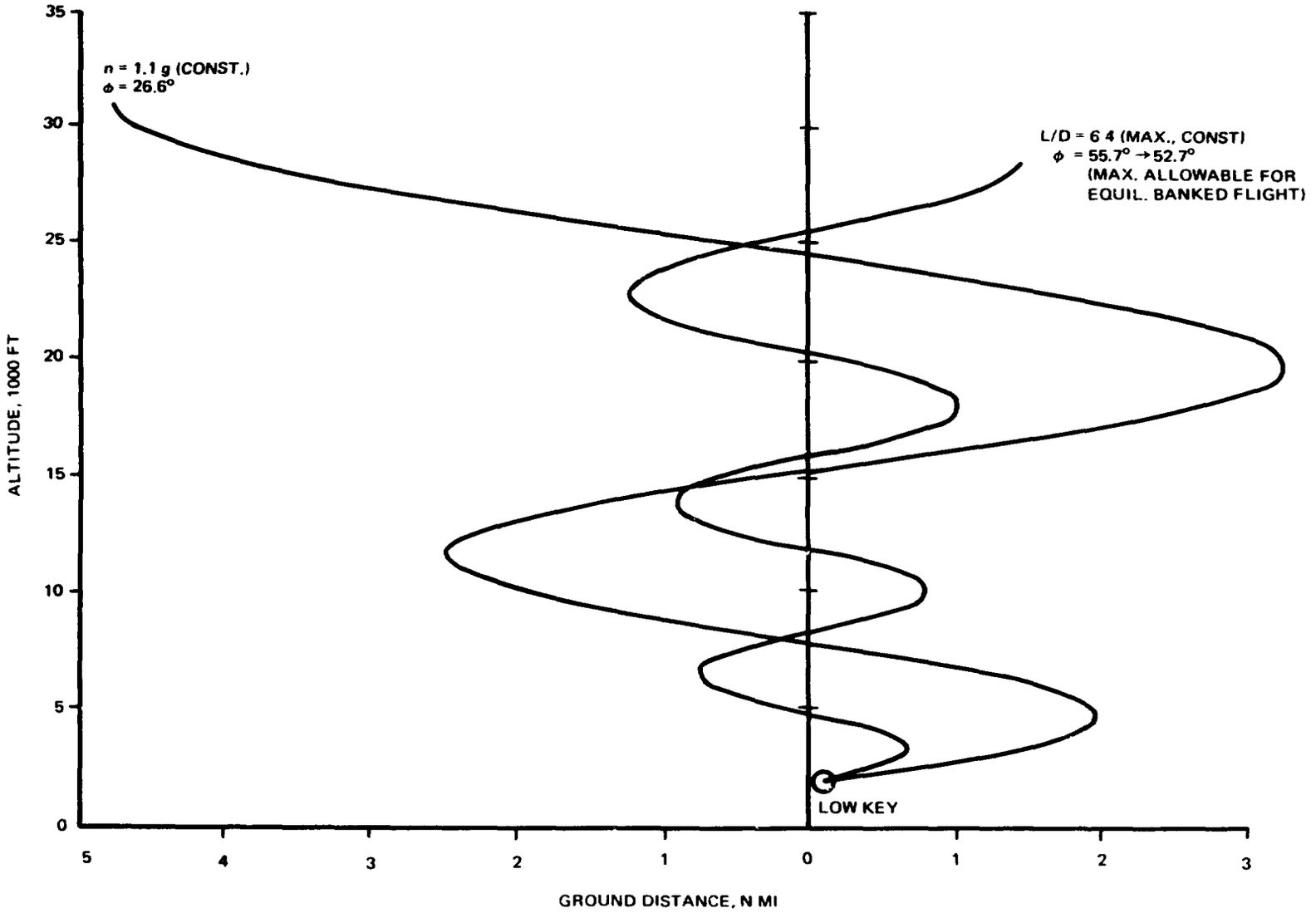

Fig. 8.3.4-31 Spiral Glide Descent Trajectories to Initiation of Final Approach (Side View)

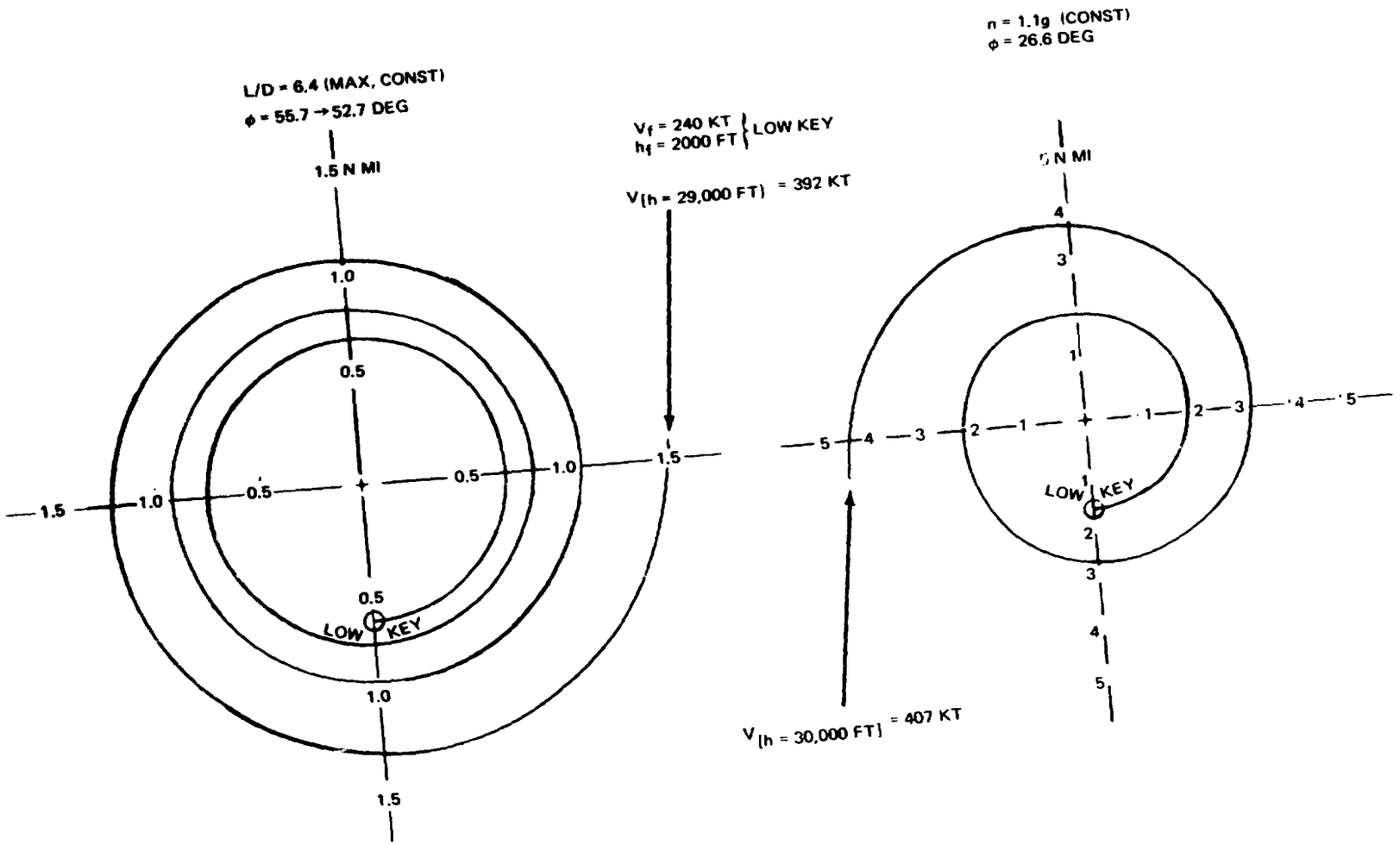

8.3.4-67

B-383

Fig. 8.3.4-32 Orbiter Ground Track in Spiral Glide Descent Polar View

8.3.4.3.2 Landing Procedures

The low key is the threshold of the final approach and landing path. At this point the vehicle must be correctly aligned with the runway at the correct speed and attitude for good landing performance. The final approach and landing path consists of three adjacent flight segments: an equilibrium glide, a flare at constant normal load factor, and a deceleration to touchdown on a 3 deg glide slope.

An important criterion for acceptable dead-stick landing characteristics is the "float time," or available deceleration time. A certain minimum float time is required for the pilot to complete any configuration changes and correct any last-minute deviations. In addition, the flare must be flown "hot" to provide stall margin for possible near-end-flare maneuvering.

Since the speed at touchdown is desired to be 180 kt based on the speed stability criteria of MILF8785B (Fig. 8.3.4-34), it is convenient to construct the maneuver backwards. The H-33 vehicle, whose landing is shown in Fig. 8.3.4-33 has a maximum lift-to-drag ratio of 4.6 with gear down. Given the vehicle characteristics and touchdown speed, an end-flare velocity is determined by selecting an appropriate deceleration time. Based on pilot experience in glide landings of the X-15, HL-10, and X-24 vehicles, a float time of about 12.5 sec is adequate yet not prohibitive in distance required before touchdown.

Continuing backwards from the end-flare velocity just determined, a suitable flare initiation altitude-flare load factor combination must be selected to provide roundout on the 3 deg glide slope. In this choice, a compromise is made between the extremes of early high-altitude flare initiation, with diminished accuracy, and late commencement requiring high load factors. A typical tradeoff of flare initiation altitude for normal load factor appears in the boxed sketch on Fig. 8.3.4-33. Piloting considerations suggest use of an altitude-load factor combination near the knee of the curve. The 1.4g load factor selected for the H-33 Orbiter reflects these considerations. For this analysis, the landing gear is assumed to be deployed prior to flare, but this configuration change may occur at any point in the flight sequence, depending on energy requirements.

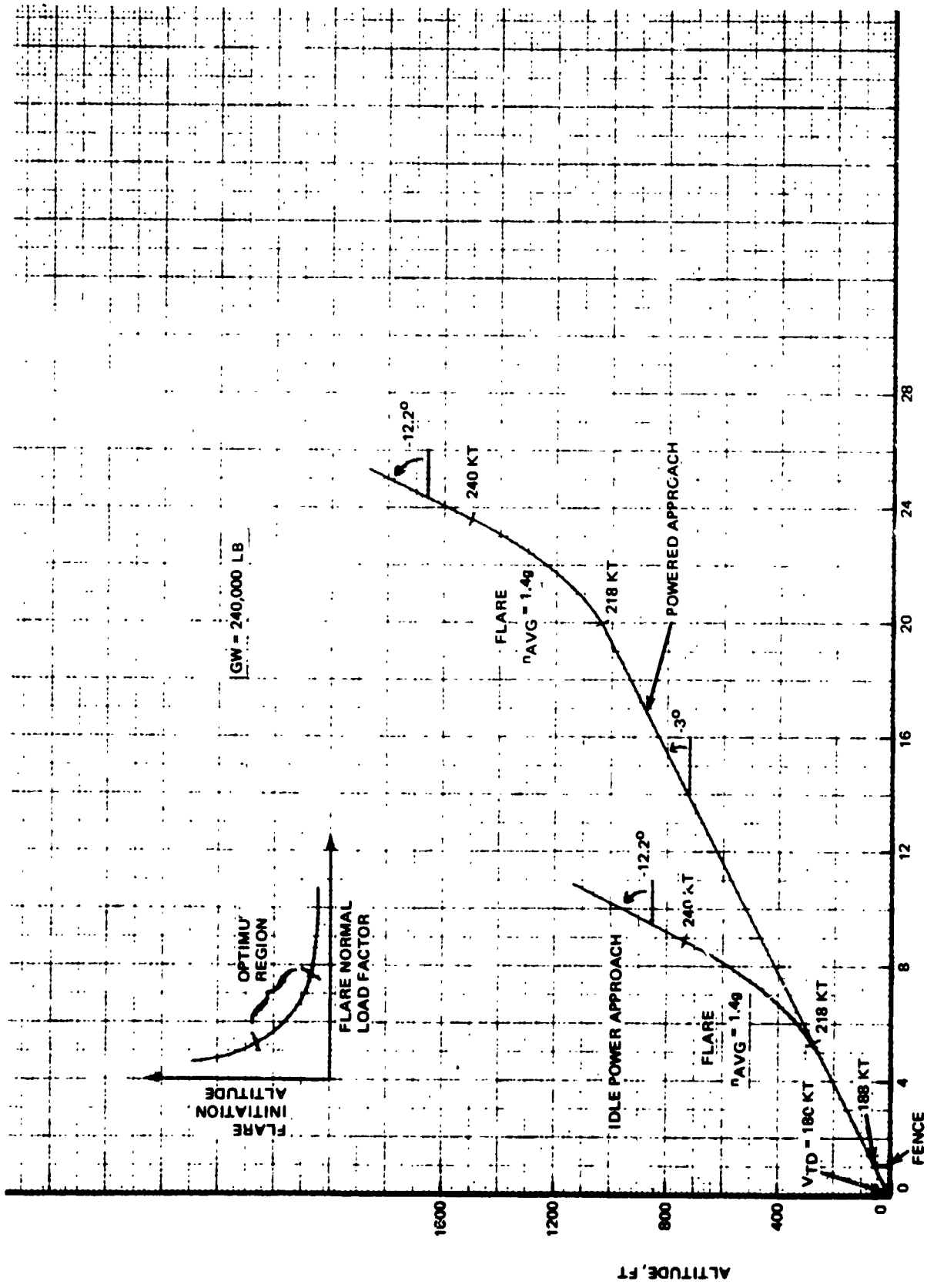

Fig. 8.3.4-33 H-33 Final Approach Profile

B-296

For the case where air-breathing engines are on board the approach is flown in exactly the same manner except that the flare is initiated at a higher altitude, permitting more time on the 3 deg glide slope, under powered conditions.

As mentioned above the touchdown speed selection was based on the speed stability criteria of MIL-F-8785B. The approach speed selection is also based on providing sufficient speed stability. In the approach configuration (gear up, speed brakes in mid-position) it is desired to fly well on the "front side" of the drag curve. The selection of 240 kt provides a 40 kt margin before any "back side" operation is expected (see Fig. 8.3.4-34). Speed brake capability has also been provided so that a constant glide path angle can be maintained over a ± 40 kt speed variation from the nominal 240 kt approach speed.

Fig. 8.3.4-35 presents the variation of approach and landing climb gradients as a function of weight, altitude and temperature for the re-entry configuration (four air-breathing engines). As can be seen the orbiter satisfies the FAA requirements spotted on the figure for reference.

Landing distance over a 50 ft obstacle is presented in Fig. 8.3.4-36. The actual stopping distance at a nominal landing wt of 240,000 lbs is 4850 feet. This distance when multiplied by 1.15/.6 to account for all weather operation equals 9300 ft, which satisfies the 10,000 FAA field length criteria. The mission landing go-around profile is presented in Fig. 8.3.4-37. The landing go-around fuel allowance is based on this profile and the fuel used in each phase is noted. A 10% reserve is also included. A summary of the approach and landing procedure is present in Table 8.3.4-11.

8.3.4.4 Ferry

For the ferry mission, the air-breathing engine system must provide for takeoff with a fuel load sufficient to provide the desired ferry range. In addition, there must be sufficient thrust to maintain 10,000 ft with one engine out. (Critical engine sizing condition.) As a consequence of these requirements, an additional engine was added to the baseline mission configuration. Because the air-breathing engine system is sized by the 10,000 ft ceiling condition the take-off, cruise, and go-around requirements are satisfied.

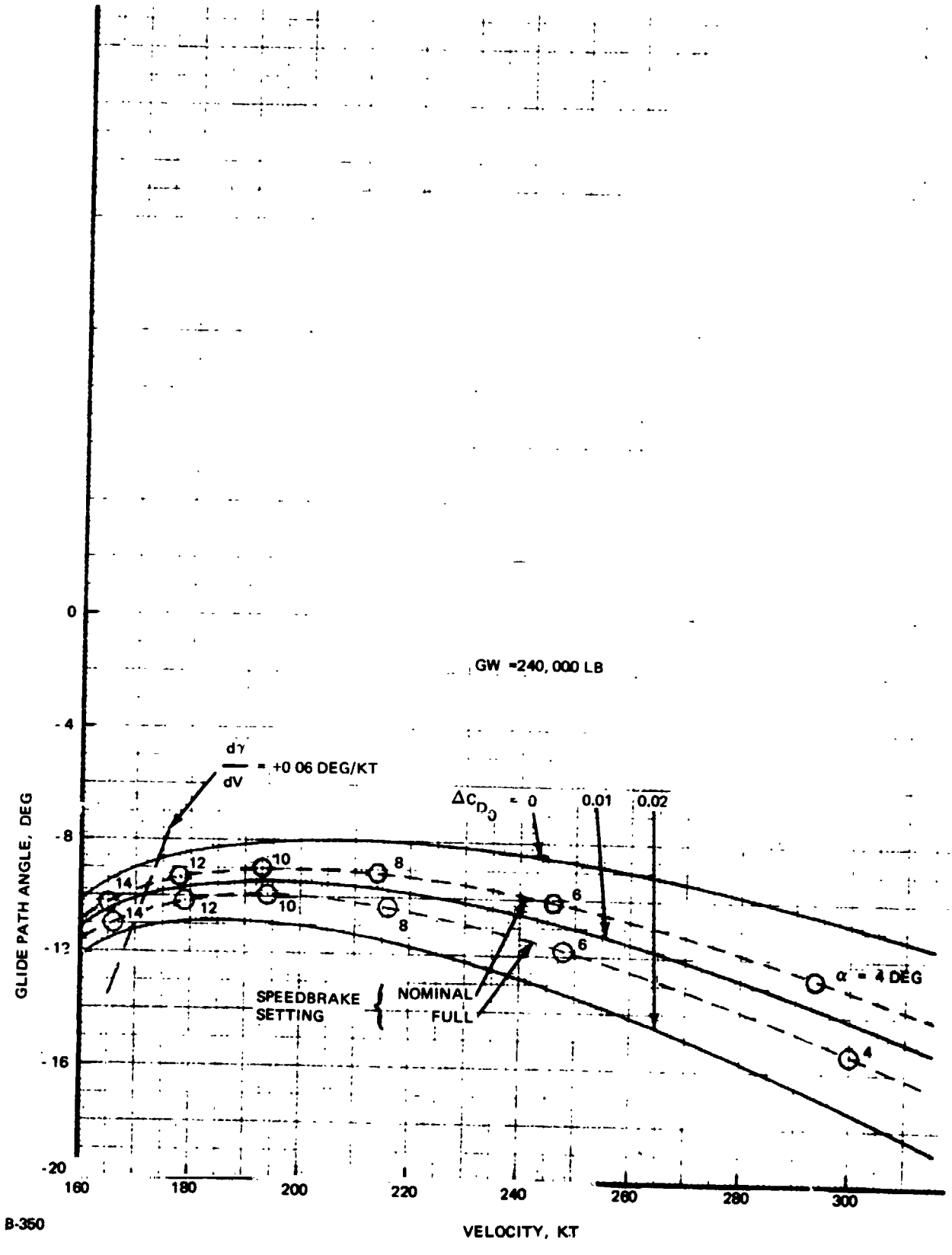

Fig. 8.3.4-34 Glide Path Control

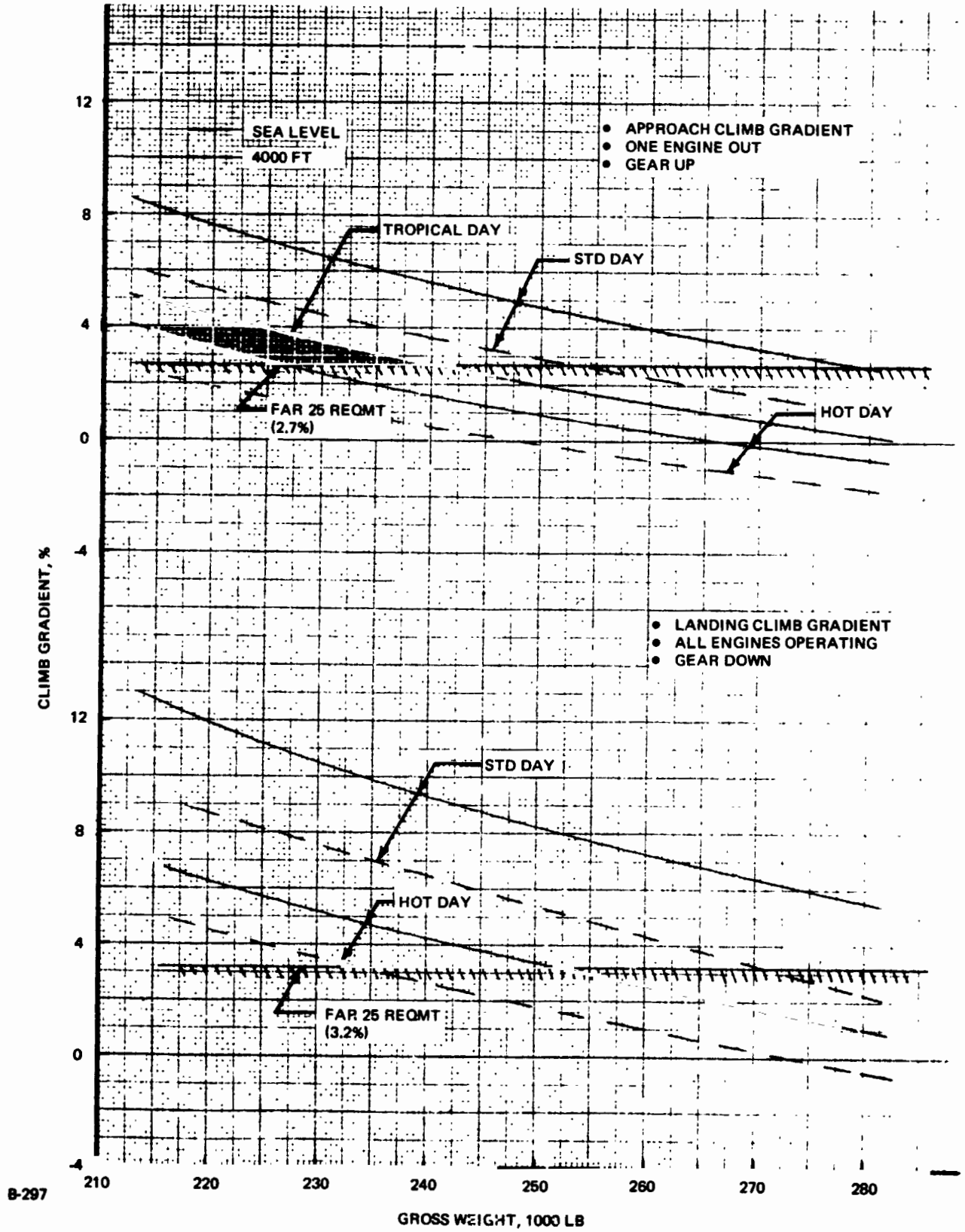

Fig. 8.3.4-35 H-33 Orbiter Operational Climb Performance

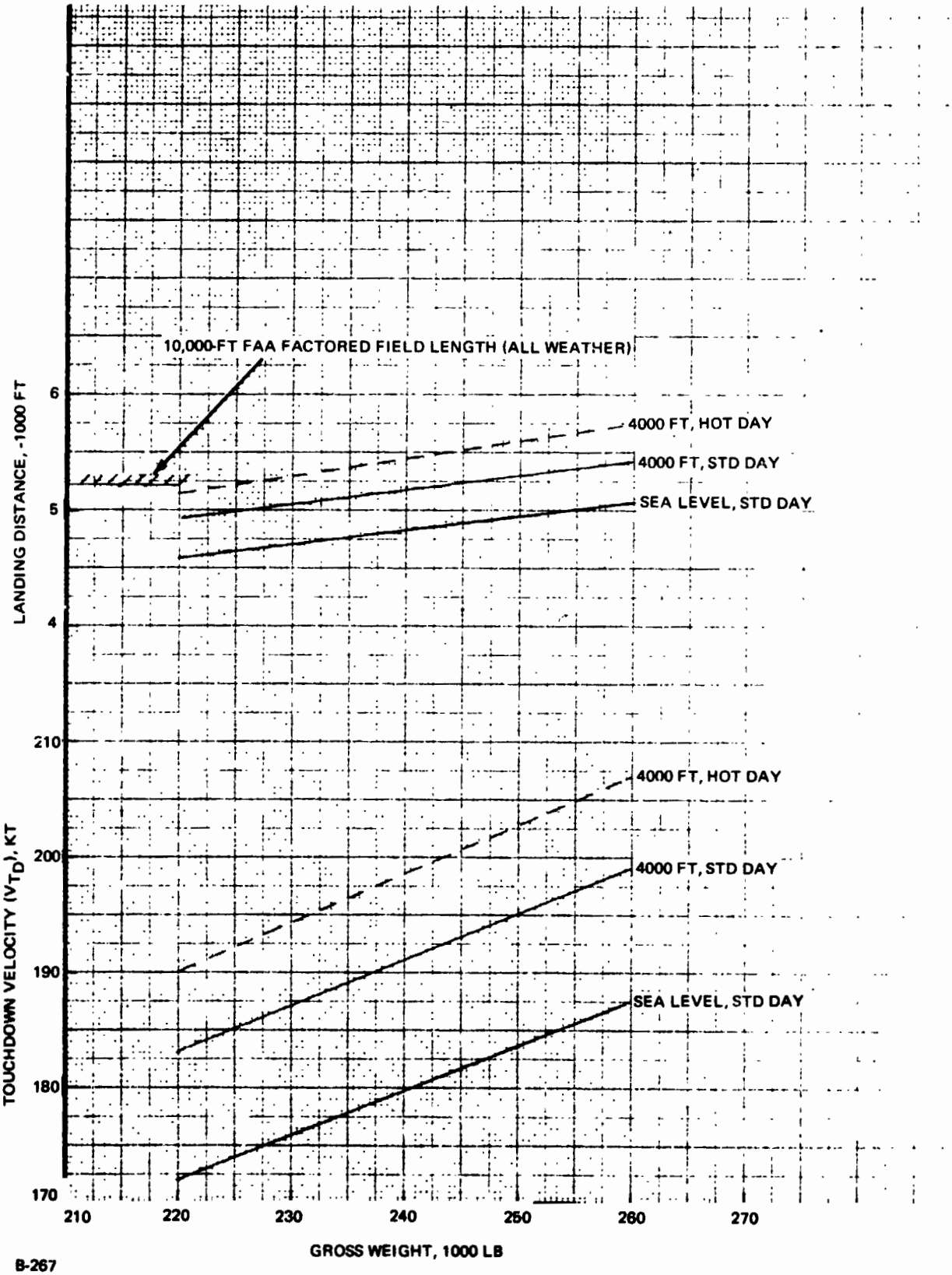

Fig. 8.3.4-36 H-33 Touchdown Velocity and Landing Distance Over 50 Ft Obstacle

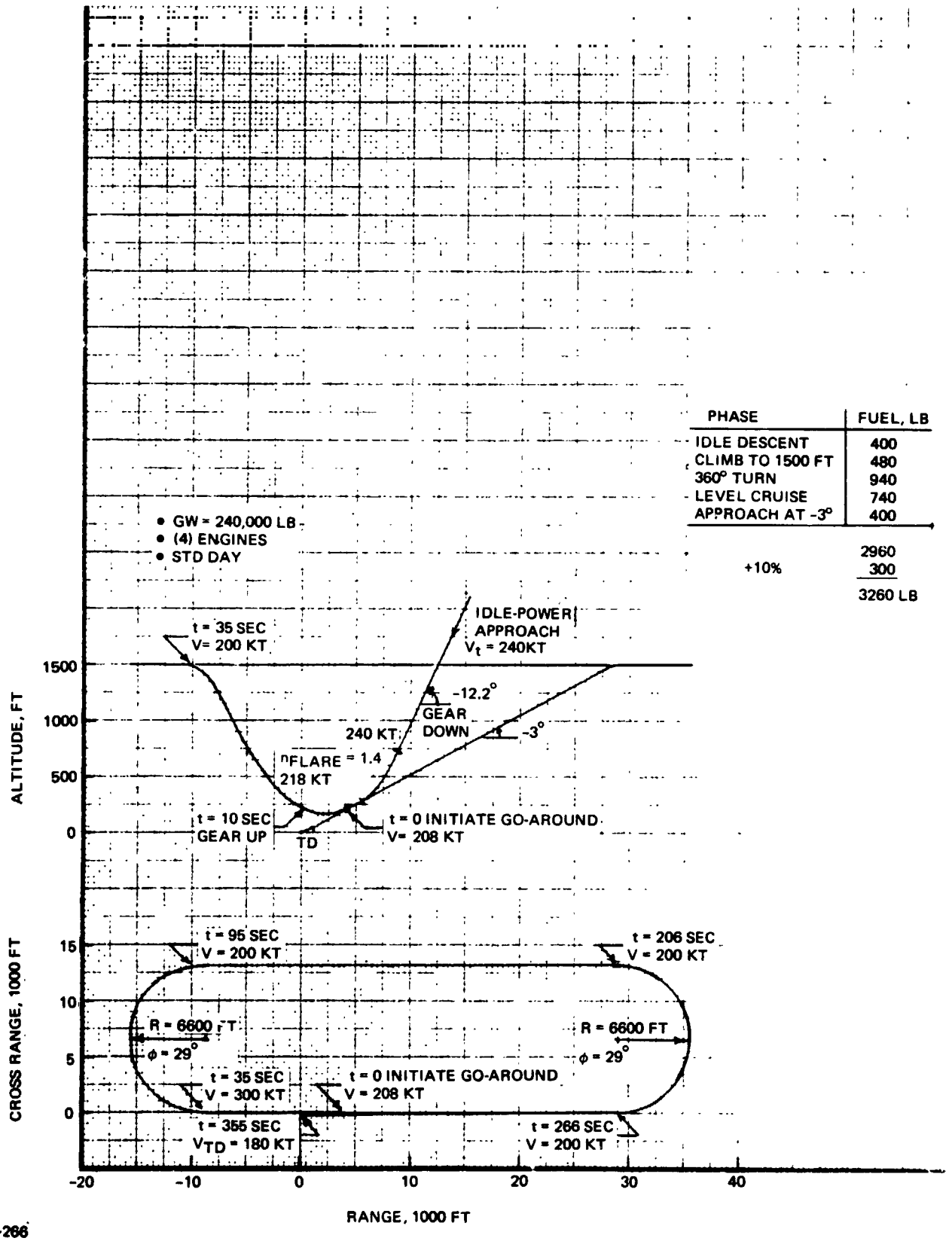

Fig. 8.3.4-37 H-33 Approach and Go-Around Profile

TABLE 8.3.4-11 H-33 ORBITER APPROACH AND LANDING PROFILE (Sheet 1 of 2)

Procedure	Configuration
• Descend at optimum speed for flight path stability (V = 240t, γ = -10.5° to 2000 ft	Idle power, gear up, partial speed brakes
• Deploy gear at 2000 ft altitude, continue descent (V = 240kt, γ = -12.2° L/D = 4.6)	Idle power, gear down, partial speed brakes
• Initiate flare at 715 ft altitude to change flight path angle to constant -3° ($H_{END\ FLARE}$ = 275 ft. $V_{END\ FLARE}$ = 218kt)	Idle power, gear down, partial speed brakes
• Pick up ILS beam at 275 ft alt 4280 ft from runway threshold; decelerate along constant -3° flight path	Idle power, gear down, partial speed brakes
• Decision altitude at 200 ft altitude (IFR ceiling): if runway positioning is correct, proceed to next step; if not, initiate go-around maneuver.	Idle power, gear down, partial speed brakes
• At 50 ft above runway threshold (V = 188 kt) reduce sink rate to acceptable gear loads (< 10 fps)	Idle power, gear down, partial speed brakes
• Touchdown at 180 kt, allow 3 sec free roll, deploy (2) 30 ft dia. drag chutes ($\Delta C_{D\pi}$ = .55 Δt_{DEPLOY} = 2 sec), extend speed brakes fully, apply main wheel brakes (μ = .38)	Power off, gear down, full speed brakes, chutes out
• Decelerate, release chutes at 40 kt. stop in 4850 ft (= 9300 $\frac{(.6)}{(1.15)}$)	Power off, gear down, full speed brakes
Go-Around Maneuver	
• Rotate to optimum lift coefficient ($C_{L_{PULLOUT}}$ = .35) maintain FAR approach go-around climb gradient of 2.7 %	Intermediate power, gear up, speed brakes retracted

TABLE 8.3.4-11 H-33 ORBITER APPROACH AND LANDING PROFILE (Sheet 2 of 2)

Procedure	Configuration
Go-Around Maneuver (Continued) • Climb to 1500 ft. above runway, execute race track pattern to intercept nominal approach path (Fig. 8.3.4-37)	Power required for level flight, gear up, speed brakes retracted

8.3.4.4.1 Takeoff Performance

Takeoff distance is determined by the higher of the critical field length (balanced field length) or 115% of the calculated all engines takeoff distance. Takeoff distance as a function of gross weight for several altitude and temperature combinations is presented in Fig. 8.3.4-38. The corresponding second segment climb gradients calculated at the lift-off speed are presented in Fig. 8.3.4-39. It is noted that on a hot day at 4000 ft and weights about 246,000 lb that the climb gradient remains constant. This results from the fact that the lift-off speed is increased until the required climb gradient is achieved. For all other conditions, lift-off occurs at approximately five knots above the minimum nose wheel unstick speeds presented in Fig. 8.3.4-40. The ground rules assumed in calculating the takeoff distance are presented in Table 8.3.4-12.

8.3.4.4.2 Cruise and Climb Performance

All engines and one engine out specific range versus gross weight is presented in Fig. 8.3.4-41. As can be seen, the degradation in cruise performance due to an engine loss is less than 10%. In addition to the specific range, the velocity for maximum range, the corresponding best cruise altitudes, and the engine-out service ceiling are shown. The 10,000 ft ceiling requirement can be met at weights up to 280,000 lb. Fig. 8.3.4-42 and 8.3.4-43 present time, fuel and distance to climb from S.L to cruise altitude and the corresponding climb speeds. Fig. 8.3.4-44 presents the level flight operational envelope for both the four and five engine configuration. Loiter fuel flows used to calculate mission reserves are presented in Fig. 8.3.4-45.

TABLE 8.3.4-12 H-33 ORBITER TAKEOFF PROCEDURES

One Engine Out Takeoff

- Vehicle accelerates with all engines operating to the critical engine failure speed
- An engine failure is experienced and the vehicle continues to accelerate with one engine out to the minimum nose wheel unstick speed
- Rotation is initiated either at the minimum nose wheel unstick speeds for the lighter weights or at the speed necessary to meet the required climb gradient for the heavier weights. Lift-off is accomplished approximately 5 kt later
- A constant speed equal to the lift-off speed is maintained up to the 35 ft obstacle height.

Accelerate - Stop

- Vehicle accelerates with all engines operating to the critical engine failure speed
- An engine failure is experienced at which time the throttles are chopped to idle and the vehicle free rolls for 3 sec
- At the end of the free roll, two 30 ft diameter drag chutes are deployed within 2 sec providing an incremental drag coefficient equal to 0.55 based on chute frontal area
- After chute deployment (after a total of 5 sec) the wheel brakes are applied and the speed brakes activated until the vehicle comes to a stop. This segment assumes a dry runway (μ = .38) and the speed brakes provide an additional incremental drag coefficient of 0.0150 based on the 4840 sq ft reference area. Drag chutes are released at 40 kt
- The all engines takeoff distance is calculated in a manner similar to the one engine out takeoff distance. Rotation is accomplished at the minimum nose wheel unstick speeds and yield more than adequate climb gradients.

8.3.4.4.3 Ferry Range

Fig. 8.3.4-46 presents ferry range as a function of gross weight. At a takeoff weight of 264,820 lb the range is 300 n mi in still air. Should a 50 kt headwind be encountered the 20 min fuel reserve is sufficient to offset this contingency. Fig. 8.3.4-47 presents a breakdown of the mission phases and fuel, time, and distance consumed during each phase.

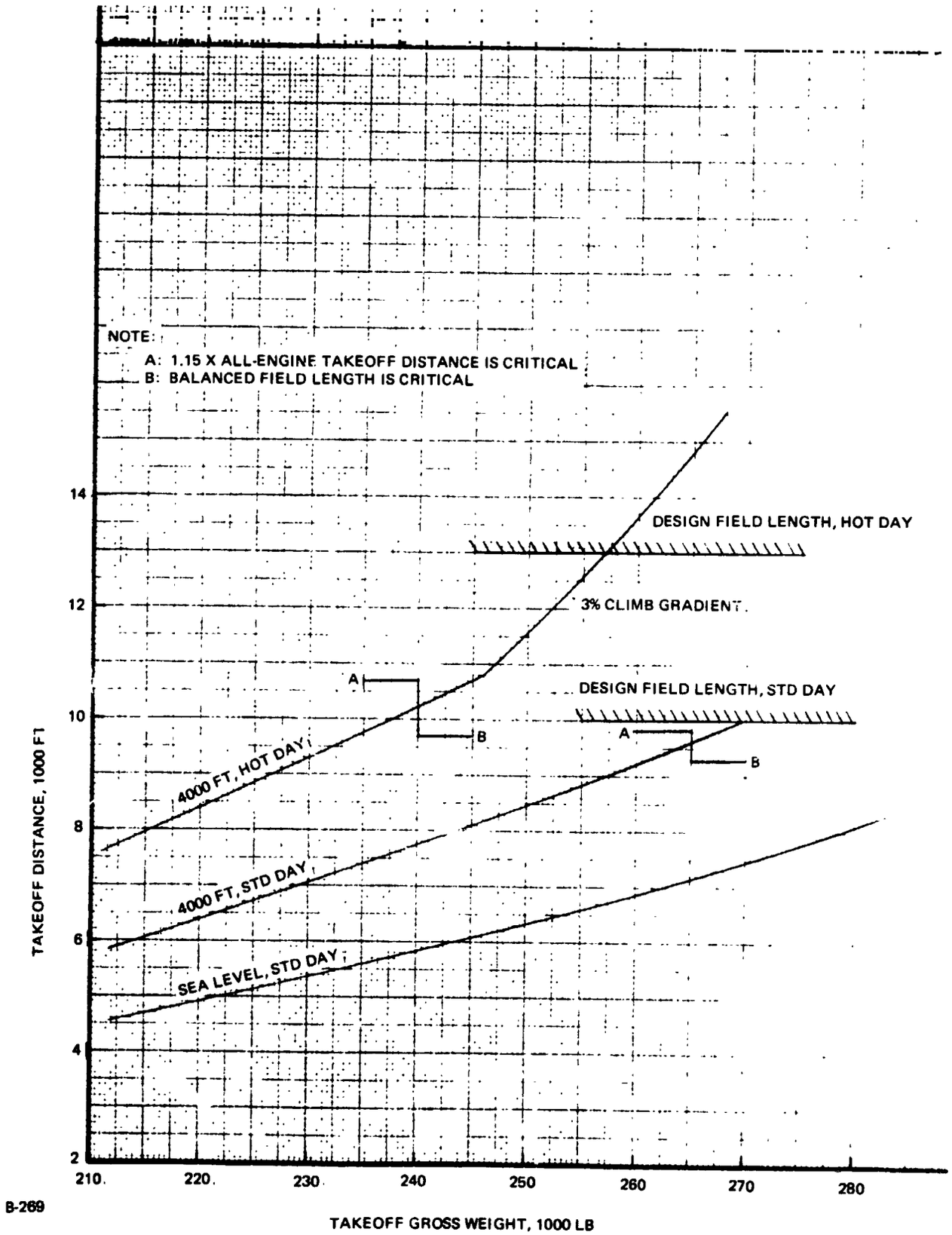

Fig. 8.3.4-38 H-33 Orbiter Ferry Package Takeoff Distances

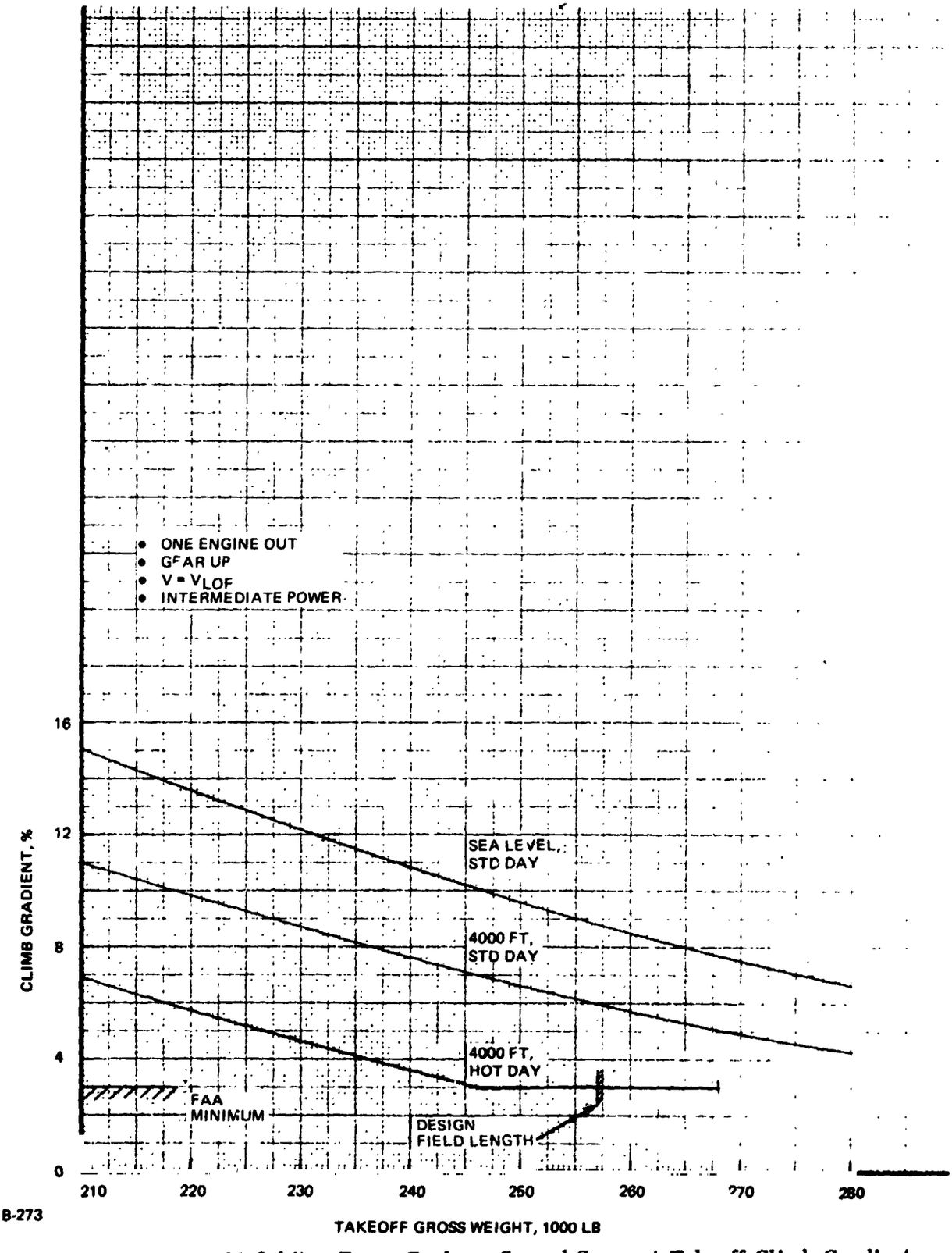

Fig. 8.3.4-39 H-33 Orbiter Ferry Package Second Segment Takeoff Climb Gradients

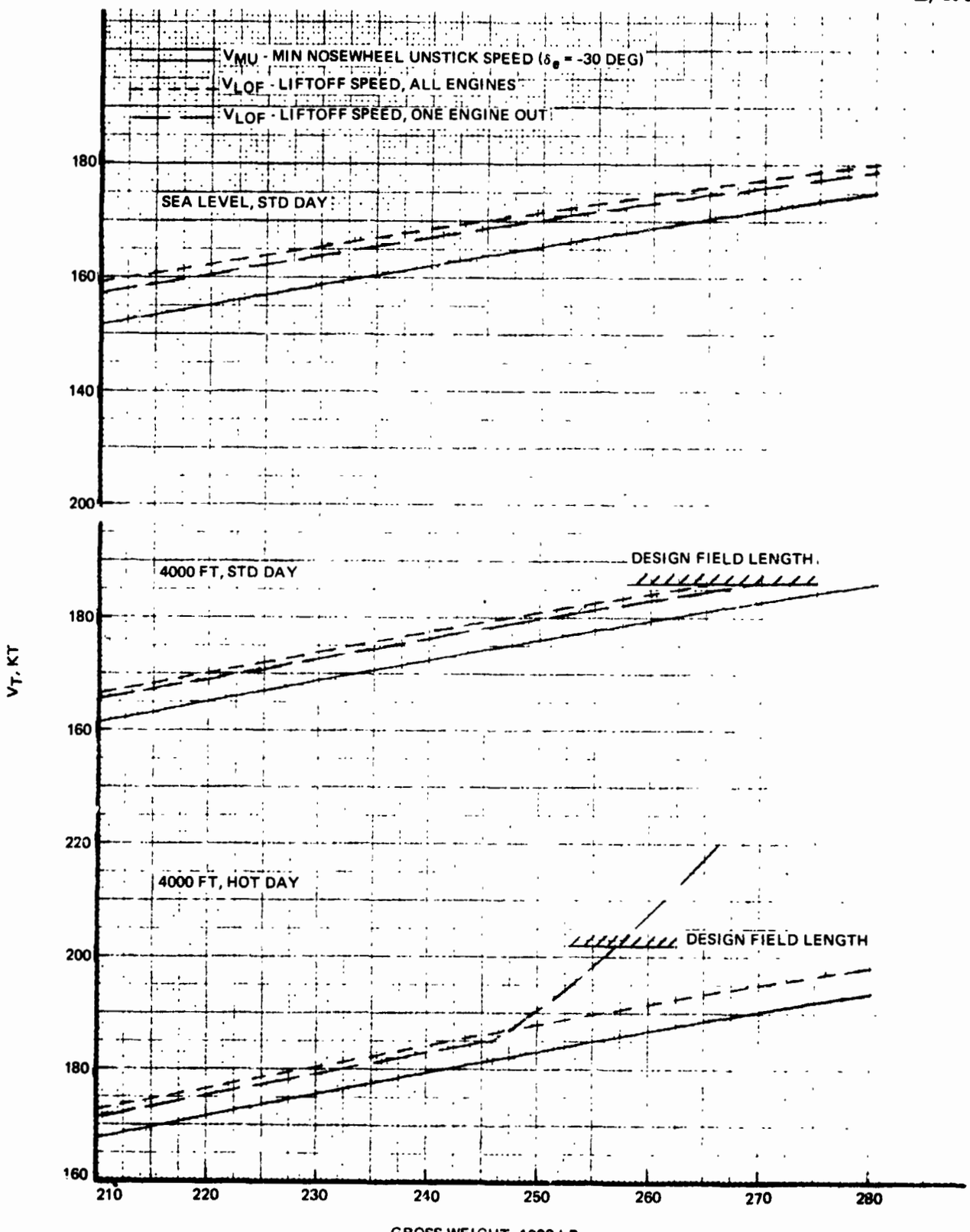

B-268

Fig. 8.3.4-40 H-33 Orbiter Ferry Package, V_{MU} - Minimum Nosewheel Unstick Speed, V_{LOF} - Liftoff Speed

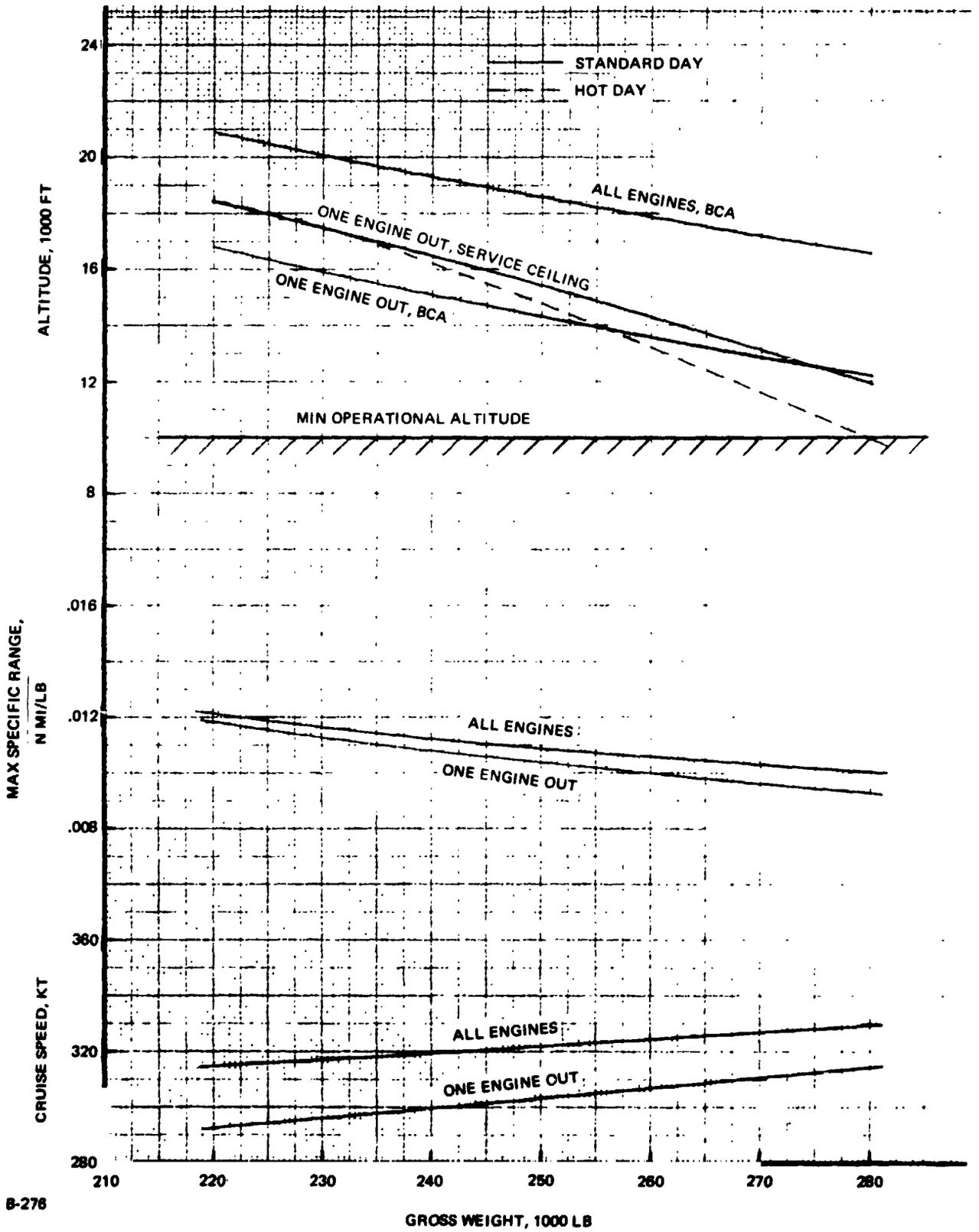

Fig. 8.3.4-41 H-33 Cruise Performance

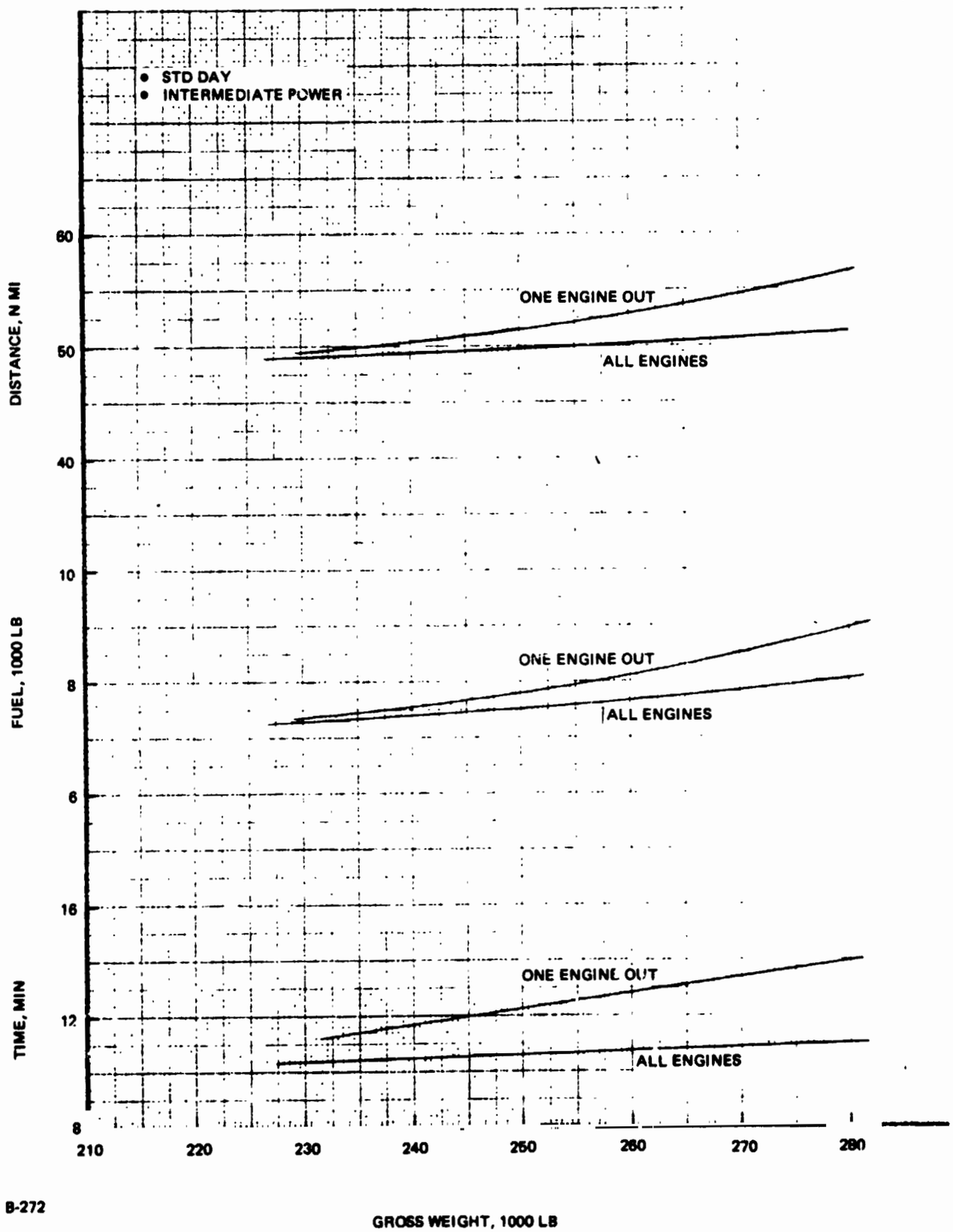

Fig. 8.3.4-42 H-33 Orbiter Ferry Package Time, Fuel, and Distance in Climb From Sea-Level to Best Cruise Altitude

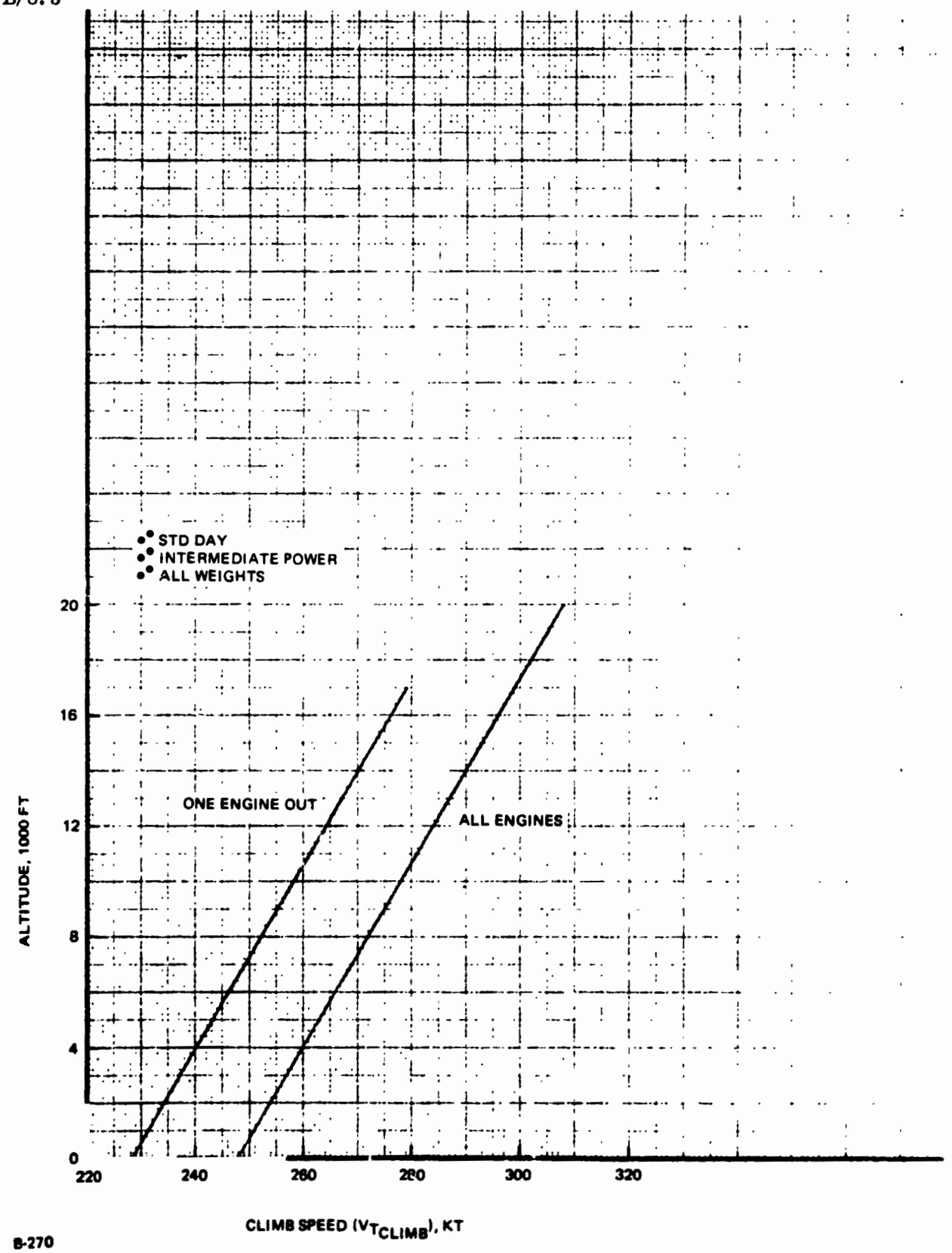

Fig. 8.3.4-43 H-33 Orbiter Ferry Package Best Climb Speeds

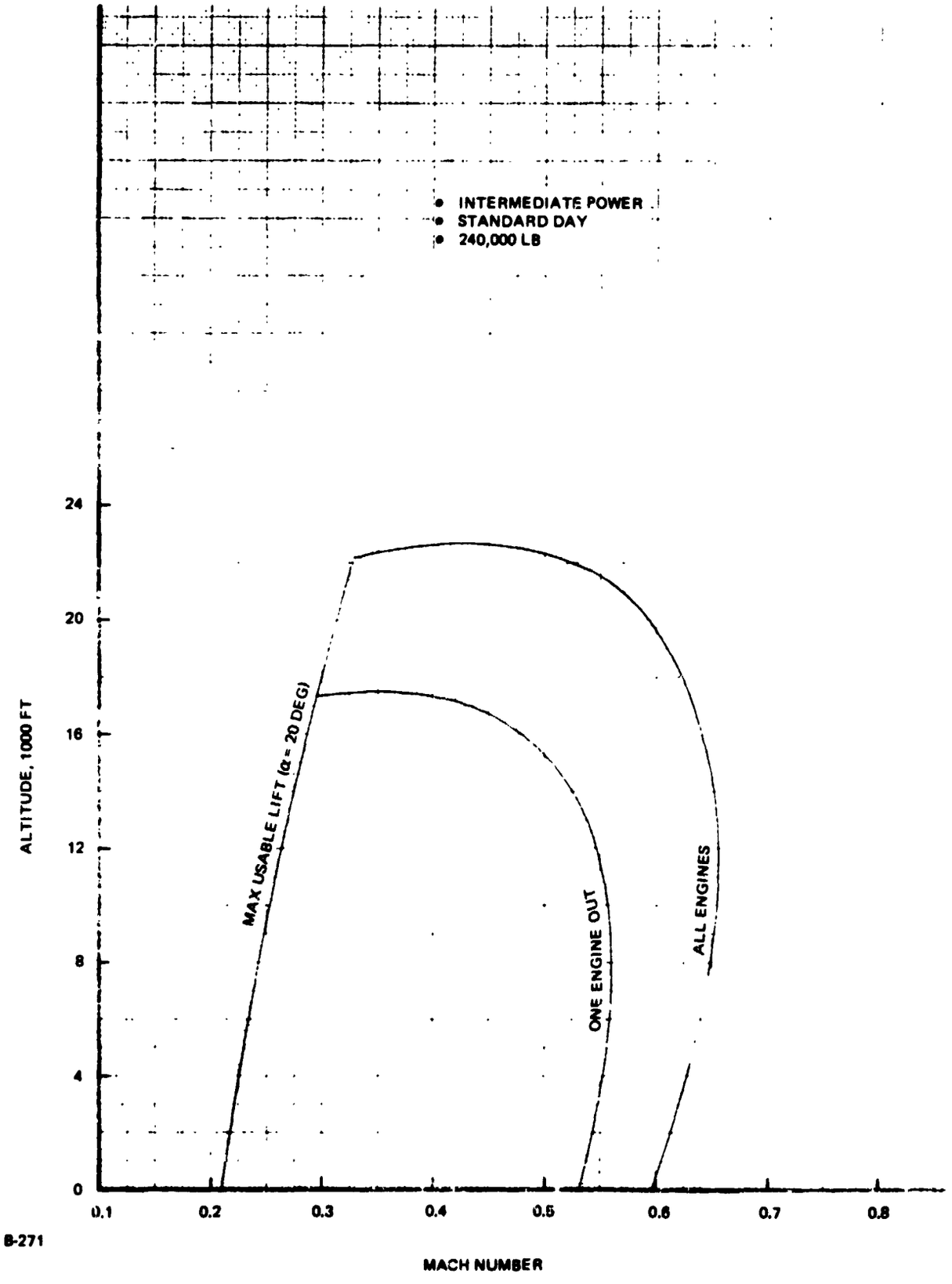

Fig. 8.3.4-44 H-33 Flight Envelope, Intermediate Power

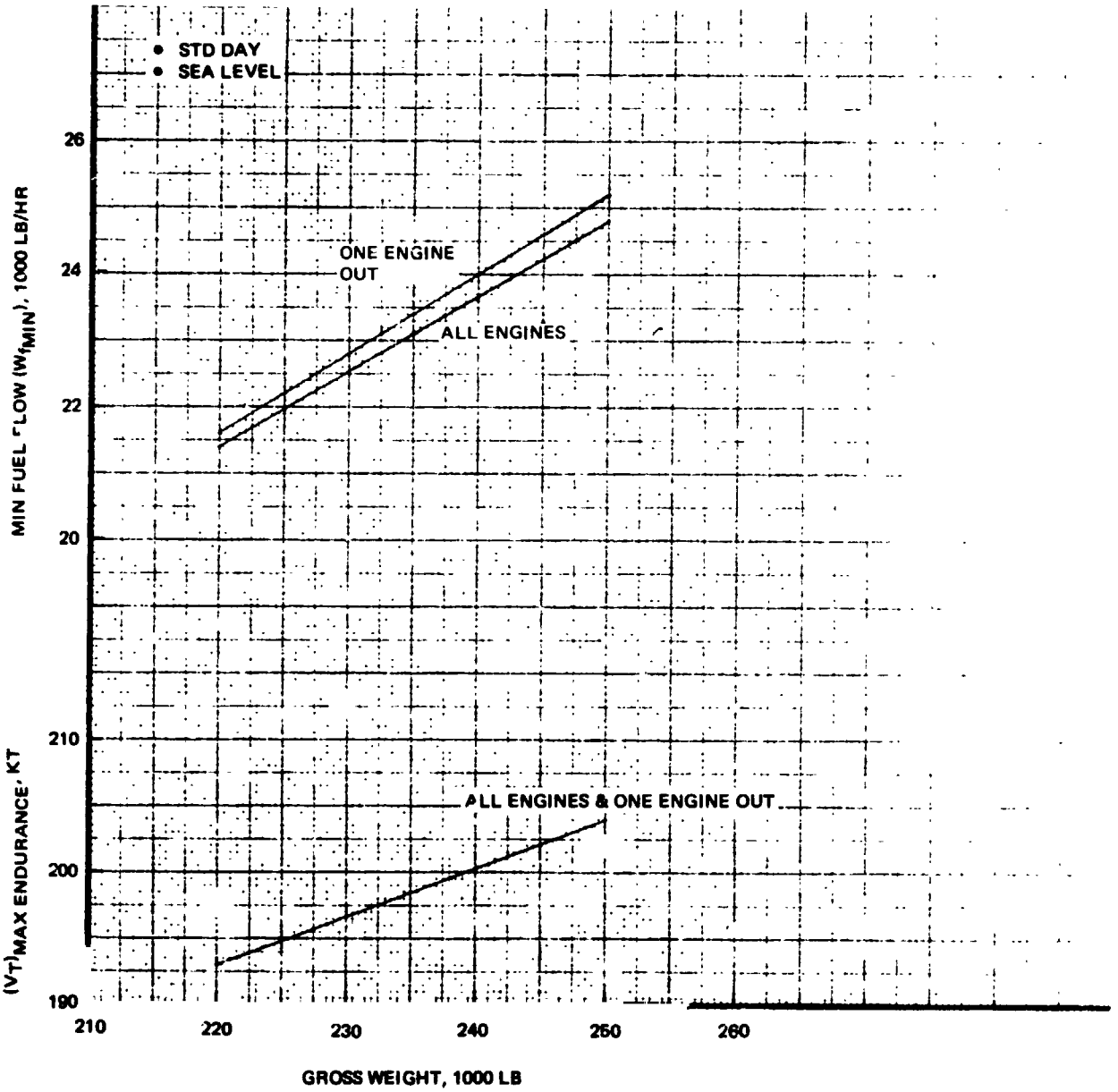

B-274

Fig. 8.3.4-45 H-33 Orbiter Ferry Package Minimum Loiter Fuel Flows and Corresponding Velocities

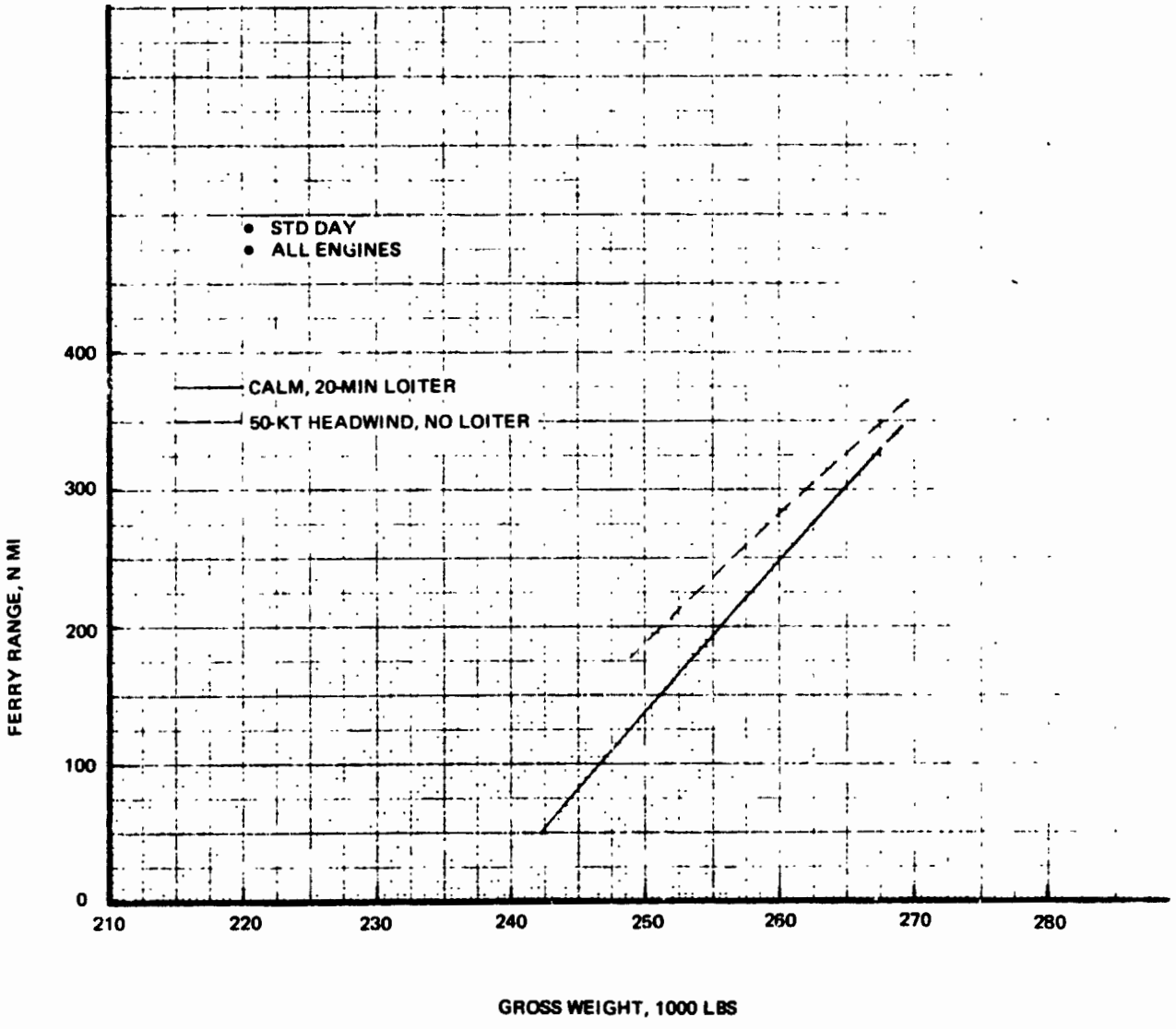

B-277

Fig. 8.3.4-46 H-33 Orbiter Ferry Package Ferry Range

- NO WIND
- 20-MIN HOLD AT SEA LEVEL
- ALL ENGINES OPERATING

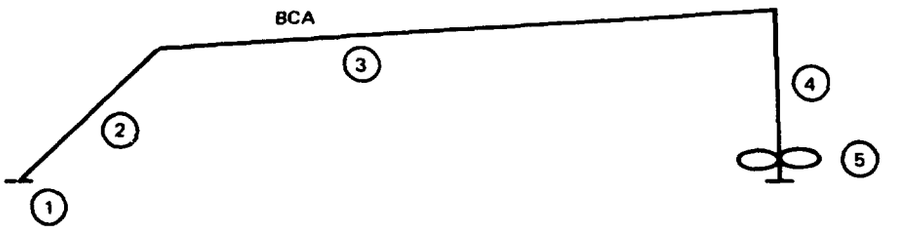

	MISSION PHASE	POWER SETTING	ALTITUDE, FT	SPEED, KT	INITIAL WT, LB	TIME, MIN	FUEL LB	DIST, N MI
1	WARMUP, TAXI, TAKEOFF	INT	0	0	264,820	5 0	5340	–
2	ENROUTE CLIMB TO BCA	INT	17,900	275	259,480	10.6	7610	51
3	CRUISE AT BCA	PART		320	251,870	46.7	22230	249
4	DESCEND TO SEA LEVEL	PART	0	250	229,640	0 0 (1)	0	–
5	RESERVE							
	• HOLD AT SL, MAX ENDURANCE	PART	0	195	229,640	20.0 (2)	7335	–
	• MISSED APPROACH ALLOWANCE	INT	0	–	222,305	–	2450	–
	ZERO-FUEL GROSS WEIGHT				219,855			
	TOTAL MISSION TIME					1.04		
	TOTAL MISSION FUEL						44,965	
	TOTAL MISSION DISTANCE							300

(1) NO TIME, FUEL OR DISTANCE ACCREDITED
(2) NOT INCLUDED IN TOTAL MISSION TIME

Fig. 8.3.4-47 H-33 Ferry Mission Summary

8.3.4.5 References

1. Klafin, J.F., Barnhart, B.P., Aerodynamic Entry Autopilots, Presented at Meeting 27 of SAE Aerospace Vehicle Flight Control Systems Committee, 17-19 March 1971, Grand Junction, Colorado

2. Etkin, B., "Longitudinal Dynamics of a Lifting Vehicle in Orbital Flight", J. Aero/Space Sciences, October 1961

8.3.5 THERMODYNAMICS

The thermodynamic environment is discussed for each major mission phase, in sequence, starting with prelaunch and proceeding through ascent, on-orbit and reentry. Each of these phases exerts a critical design condition on one or more of the systems or subsystems affected by the transfer of heat. Examples of this are as follows:

- Prevention of ice/frost formation during ground hold sizes the external LH_2 tank insulation and LOX tank purge requirements (8.3.5.1).
- Ascent provides the design environment for the external LH_2 tank fairing, the spray-on ablative coating over a portion of the external LH_2 tank foam insulation and a relatively small section of the leeside TPS (8.3.5.2).
- Stage separation, with the main orbiter engines firing in close proximity to the booster, impacts the design of the booster's vertical tail and some of its leeside heat sink material (8.3.5.3).
- The weight of the TPS insulation is strongly dependent on the temperature of the internal structure prior to entry; a temperature governed by the orbital environment (8.3.5.4).
- The majority of the TPS, including the base heat shield, is designed by reentry considerations (8.3.5.5).

The OMS tankage is discussed as a separate entity since its design is dependent on the entire spectrum of environments (8.3.5.6).

8.3.5.1 Pre launch

8.3.5.1.1 External LH_2 Tank Insulation

Thermal protection is required for the external LH_2 tanks to limit boil-off (and stratification) and the freezing of condensables during ground hold. External spray foam (Saturn II) insulation was selected for this purpose because of its low thermal conductivity

and density and its successful use in the Saturn program in a similar application. Since the tanks are expendable, the requirement for the development of a reusable cryogenic insulation is eliminated. In regions of relatively high aerodynamic heat loads, the foam will be protected by a spray-on ablator to prevent high heat loads to the propellant and excessive tank wall temperatures.

The required thickness of the foam is determined by considering the effects of insulation thickness on propellant stratification and the probability of ice/frost conditions during ground hold. The present baseline, based on these considerations, is 3/4 in. of foam.

A tradeoff of insulation thickness (weight) against propellant residual (due to stratification) indicates that 1/2 in. of foam insulation is the optimum thickness (3/4 in. of foam represents approximately a 95 lb penalty). However, a study of ground hold conditions, discussed in detail in Subsection 8.14.9, indicates that severe ice/frost conditions will result from the use of 1/2 in. of insulation.

The first step in the ground hold study was to determine whether the conditions are such that ice/frost will form on the outer tank surface. The approach used is to solve for the surface temperature as a function of ambient temperature and insulation thickness. Having determined the combinations of insulation thickness and ambient temperature which result in surface temperatures equal to or less than 32°F, the temperature occurrence probability for the Cape Kennedy area was investigated. Using this temperature probability data and the surface temperature analysis, the probability of an ice/frost condition existing was determined as a function of insulation thickness. The results are shown in Fig. 8.3.5-1.

The curve shows that: for 1/2 in. of insulation there is a 90% chance of the surface temperature going below 32°F (ice/frost condition), for 3/4 in. there is a 25% chance, for 1 in. there is a 6% chance, and for 1 1/4 in. there is a 2% chance. This shows that the probability of the existence of an ice/frost condition decreases rapidly with increasing insulation thickness up to approximately one inch of insulation.

The second part of this study was to determine the probability of the extent of the accumulation. This was done by estimating the accumulation rates for the various

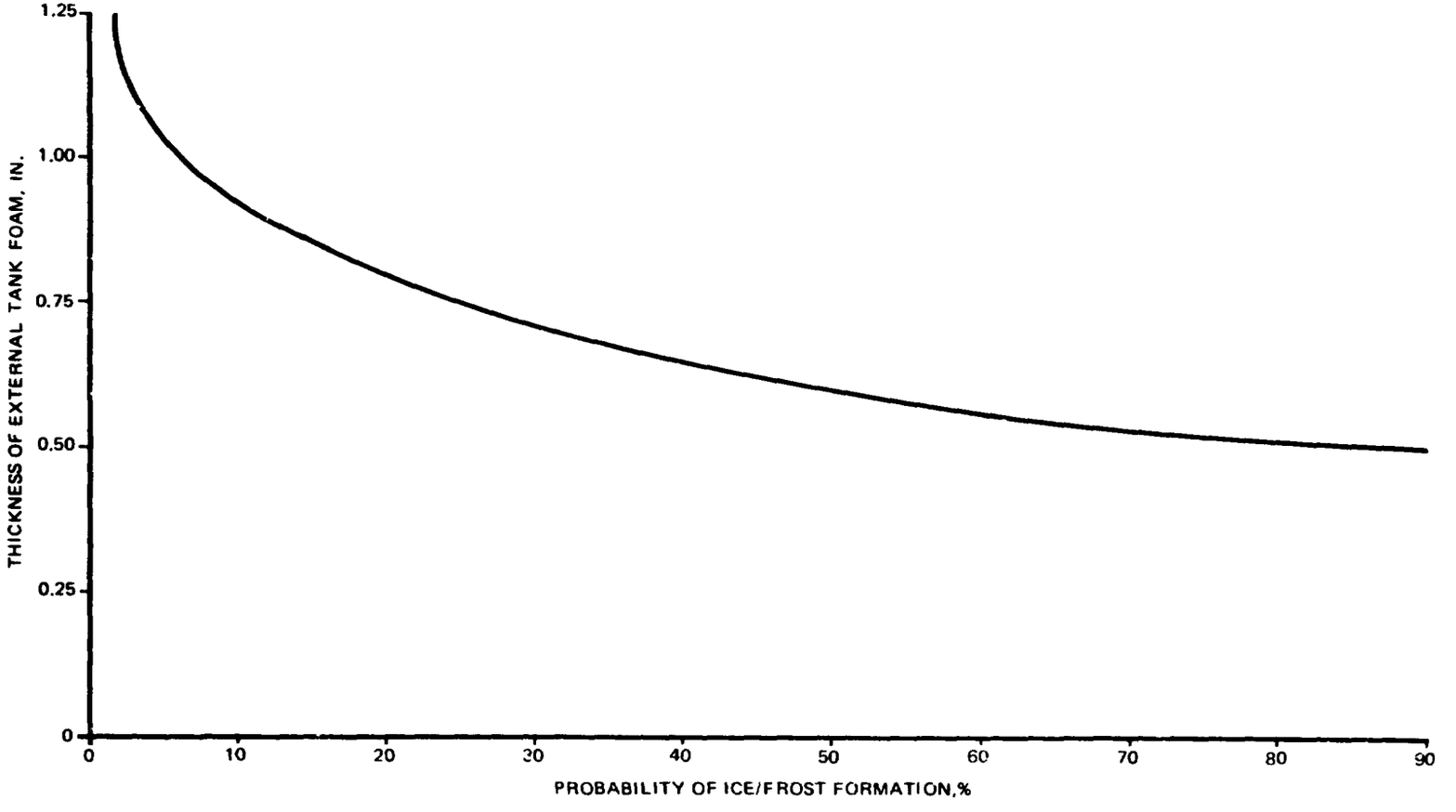

Fig. 8.3.5-1 Ice/Frost Formation Probability

ice/frost conditions and correlating the results with the temperature and rain probabilities for the Cape Kennedy area. The results of this analysis are shown in Fig. 8.3.5-2. The accumulations under rain conditions are much higher than those under humid conditions, but the probabilities of occurrence are reduced, since there is less chance of the simultaneous occurrence of rain and cold ambient conditions.

From Fig. 8.3.5-1 and 8.3.5-2, it can be seen that the use of 1/2 in. insulation represents a severe ice/frost problem. Accordingly, 3/4 in. insulation, which improves the condition considerably, was selected as the baseline.

8.3.5.1.2 LOX Tank Purge

The LOX tanks are uninsulated and will require purging during ground hold. Purging is required to inert the tankage area, minimize condensation of water on vehicle surfaces, and to provide an acceptable thermal environment for equipment located in the tankage area. The baseline system to accomplish this is to purge the tankage area with dry nitrogen gas (-63.5°F dew point). The flow is introduced forward of the LOX tank by a distribution manifold and exits at the aft portion of the vehicle. Unheated purge gas at a flow rate of approximately 30,000 lb/hr is required. This system requires no thermal conditioning of the gas and the flow rate is well within present Cape Kennedy capabilities.

The performance of this system under 95 percentile maximum and minimum temperatures for the Cape Kennedy area is shown in Fig. 8.3.5.3. The external vehicle surface temperature is above 32°F under all conditions investigated and no problem of ice formation on the exterior surface is anticipated. A flow rate of approximately 30,000 lb/hr is required to prevent moisture condensation on the inner skin (-63.5°F) and to ensure an exit gas temperature greater than -50°F. An exit gas temperature greater than -50°F is desirable to maintain a suitable thermal environment for any mil spec equipment or hydraulic lines located in the tankage area.

Some condensation of moisture on the LOX tank cannot be avoided due to the low temperature of the surface ($T_s \simeq -297°F$). However, the moisture content of the gas is so low that for a purge flow rate of 30,000 lb/hr the water vapor introduced is less than

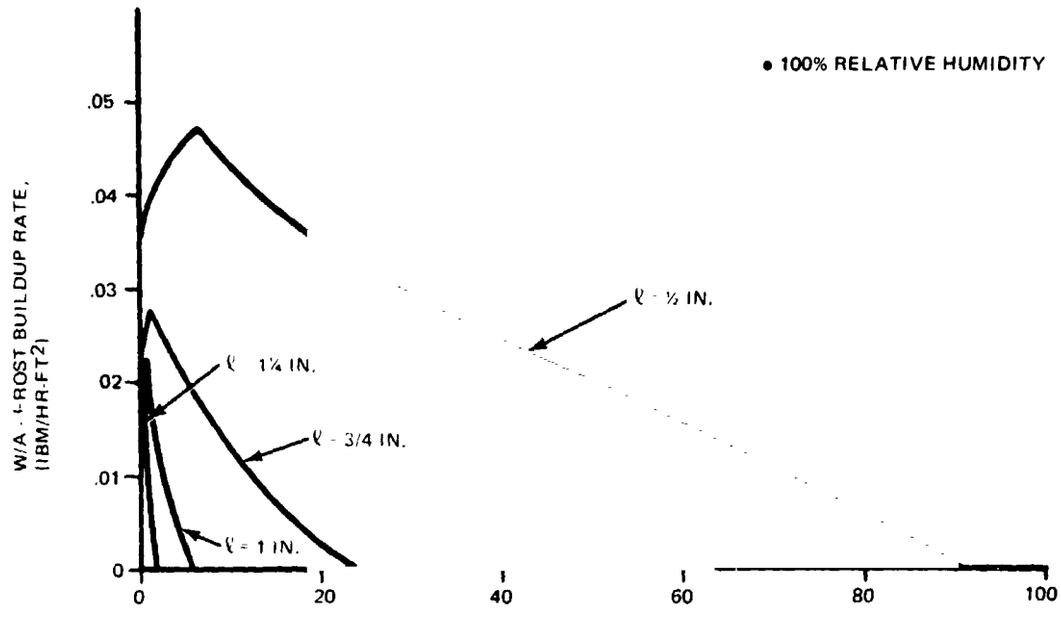

(a) FROST BUILDUP (NO RAIN CASE)

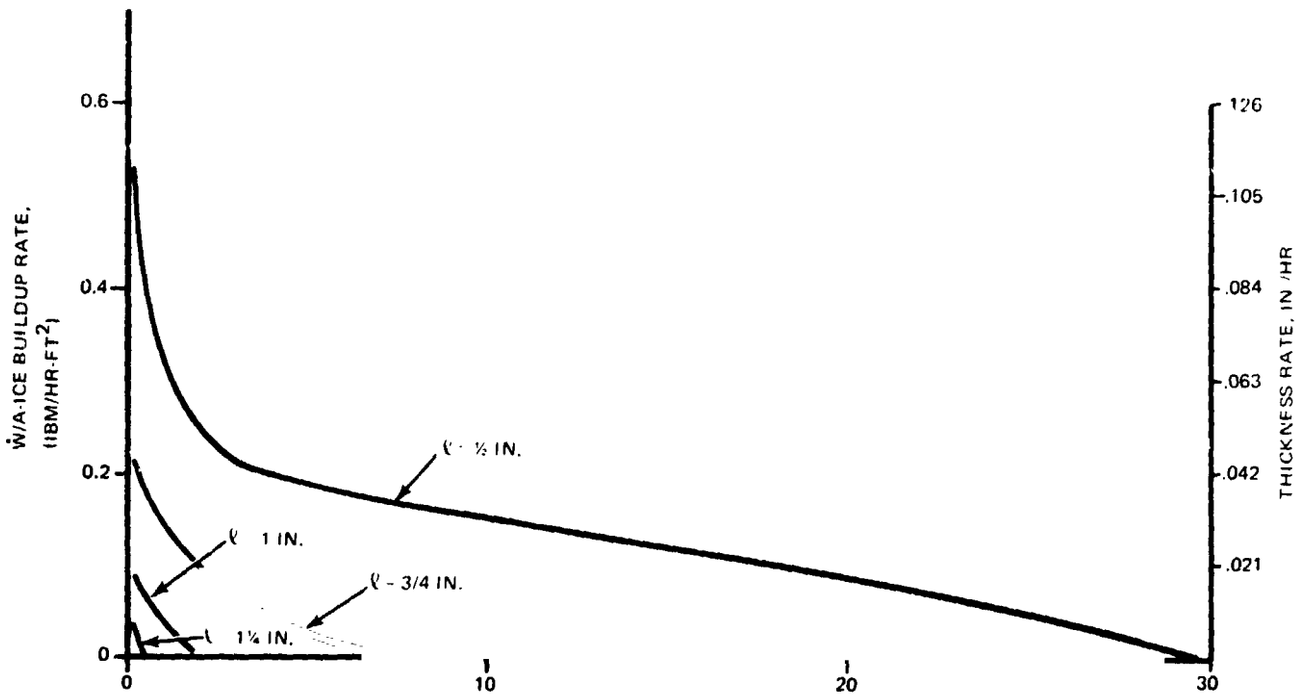

(b) ICE BUILDUP (RAIN CASE)

B-70

Fig. 8.3.5-2 Probable Ice/Frost Buildup

GRUMMAN BOEING

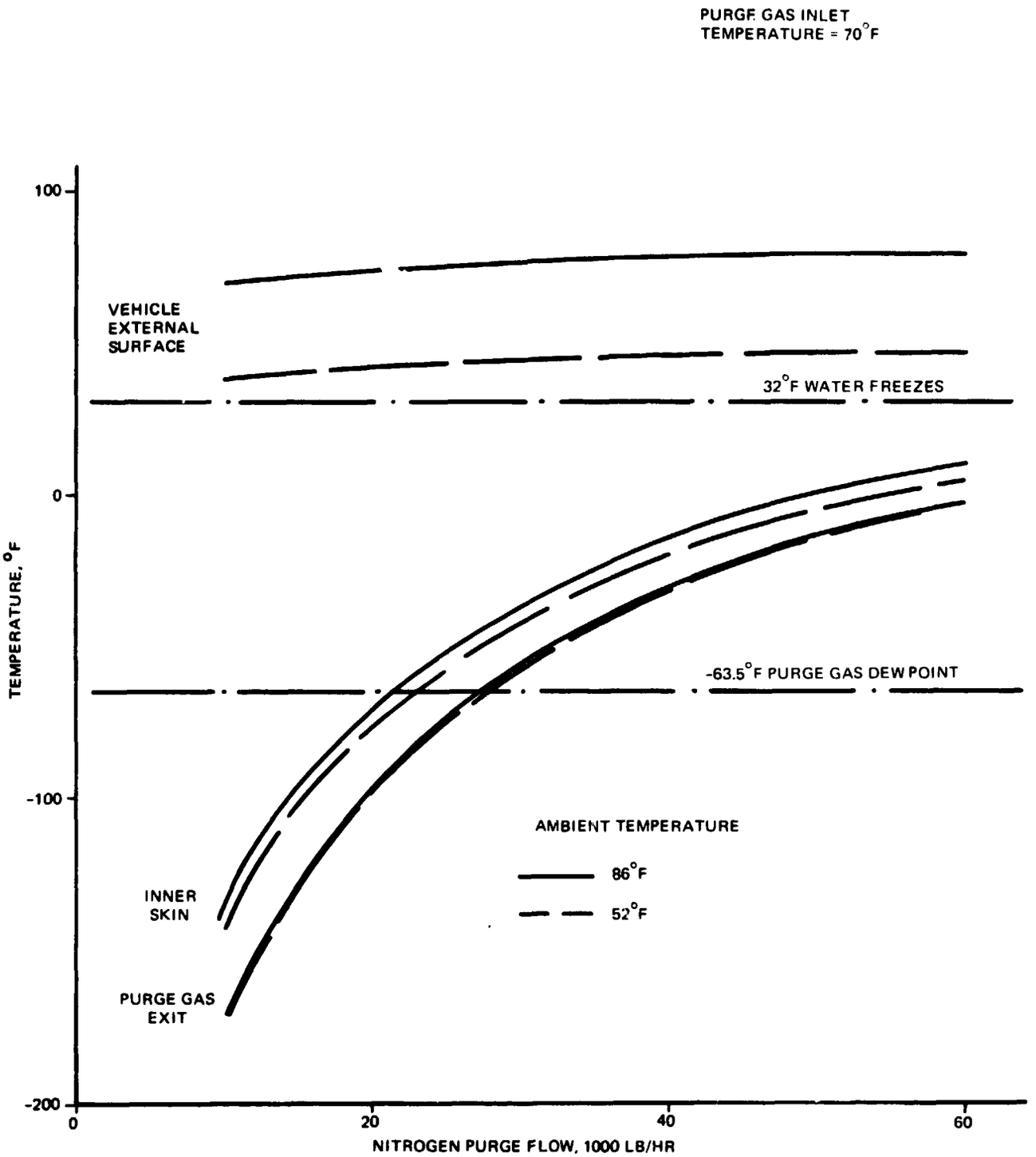

Fig. 8.3.5-3 Liquid Oxygen Tank Purge

0.5 lb/hr. Since the frost formation rate will be even less than this, no problem is anticipated.

A potential problem with this system is the possible formation of frost on the interior surfaces of the microquartz insulation due to diffusion of water vapor from the environment to this area (the inner surfaces of the microquartz will be close to the temperature of the inner skin). This condition is presently being evaluated; however, it is anticipated that leakage of the dry nitrogen purge gas will preclude frost formation. In order to prevent this condition by raising the temperature of these surfaces, the purge flow rate would have to be increased to over 100,000 lb/hr (exceeding the present Cape Kennedy capability) or the purge gas would have to be heated. An analysis of a heated purge gas system is shown in Fig. 8.3.5-4. The purge gas inlet temperature was assumed to be 200^{o}F for this system. A flow rate of approximately 40,000 lb/hr would be required with this system to prevent any moisture condensation on the interior portions of the microquartz. This system, however, will result in high GSE penalties due to increased LOX boil-off rate and the thermal conditioning requirements of the purge gas. The increase in boil-off rate of LOX during groundhold for this system is on the order of 4,000 lb/hr while purge gas thermal conditioning will require approximately 1.2×10^{6} BTU/hr. Because of these penalties and until it is determined whether a problem actually does exist, the baseline system employing unheated purge gas will be used.

8.3.5.2 Ascent

8.3.5.2.1 Ascent Environment and External Temperatures

Only a small portion of the fully reusable orbiter is thermally designed by the ascent environment. For the external tank orbiter, this mission phase takes on greater significance since it provides the critical design environment for the external tanks and sizes portions of the orbiter TPS in leeward regions on the fuselage and wing and the side of the vertical tail. The low staging velocity associated with the H-33 concept does, however, have the salutary effect of minimizing mated booster/orbiter interference heating levels (Fig. 9.3.4-7).

Reference heating for the H-33 ascent trajectory, Fig. 8.3.5-5, indicates that the portion of the trajectory after staging is more severe in terms of heating level and

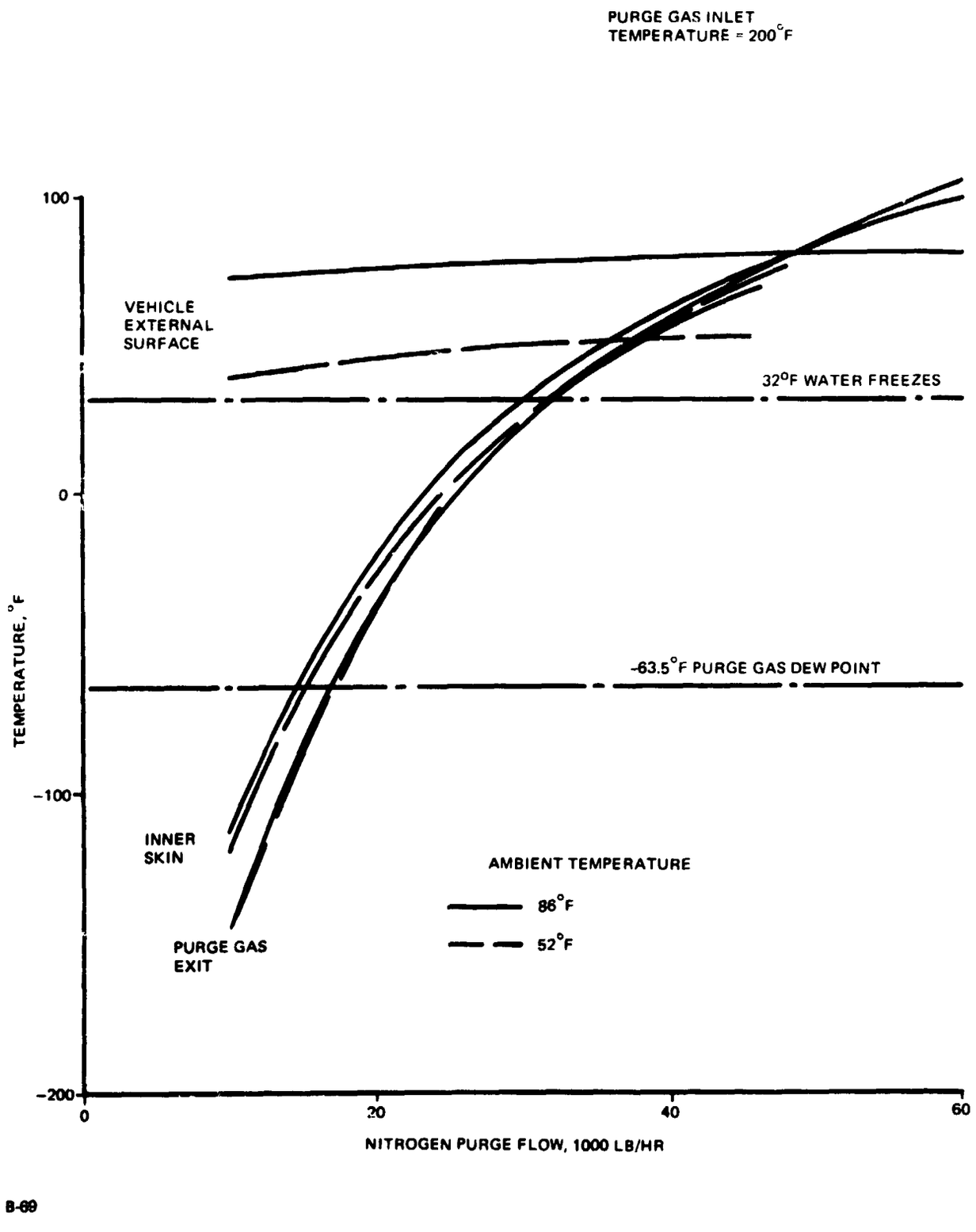

Fig. 8.3.5-4 Liquid Oxygen Tank Heated Purge

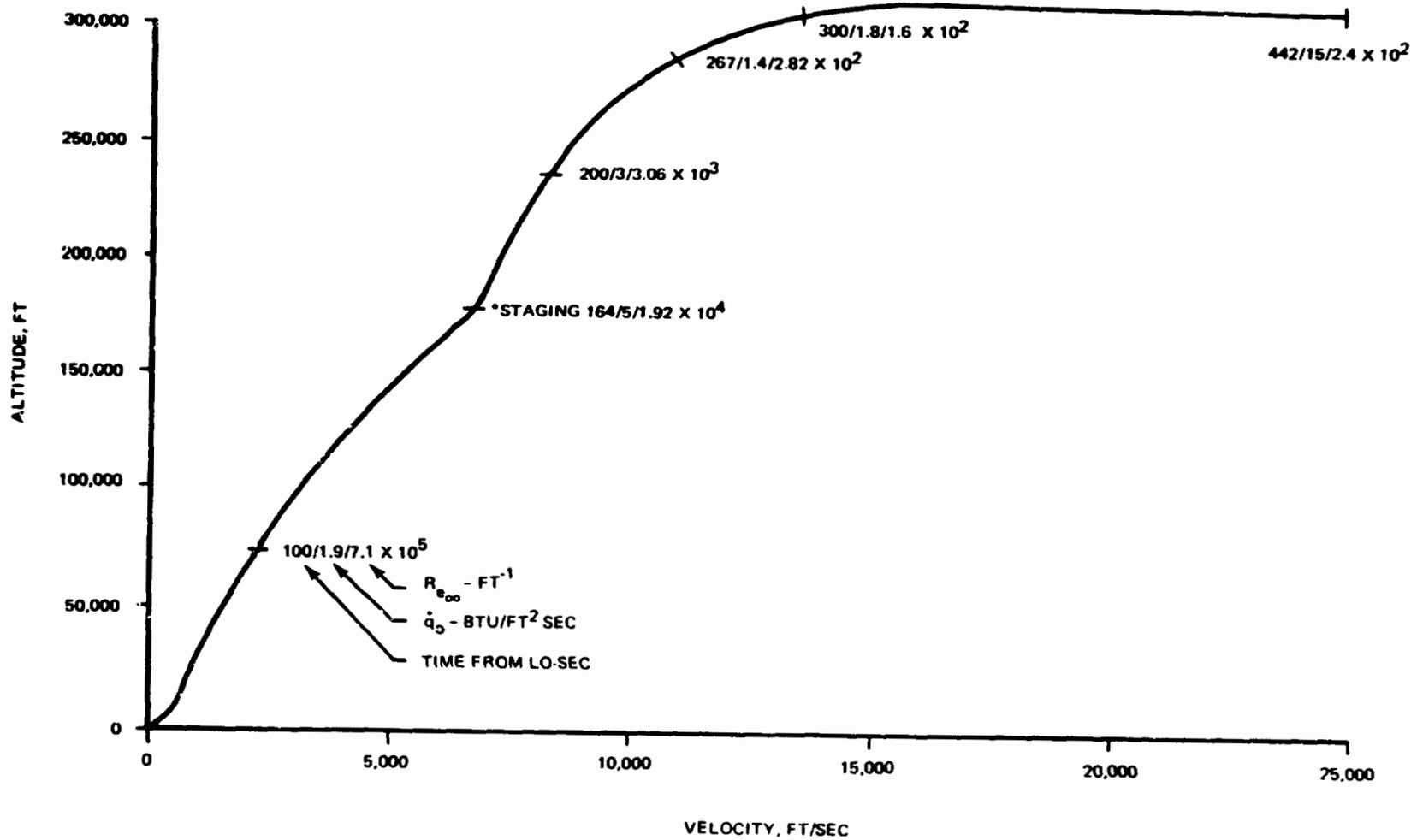

Fig. 8.3.5-5 H-33 Ascent Trajectory

duration than that prior to staging. The levels of Reynolds number after staging are sufficiently low, however, that laminar flow conditions prevail over the orbiter.

Interference heating has a major influence on the cost and weight of the tanks and orbiter for the H-33 concept. Inability to analyze the complex flow field in the vicinity of the tanks makes theoretical analysis of shock interference heating questionable. Reliance has, therefore, been placed on experimental data.

Three heat transfer tests have been conducted to date which have explored the effects of tank geometry and positioning on the resulting heat transfer. The first of these tests was run at the Grumman HWT ($M_\infty = 8$, Re_∞ /ft = $0.5 \times 10^6 - 2.0 \times 10^6$); the second and third at the NASA Langley 31 in. CFHT ($M_\infty = 10.3$, Re_∞ /ft = 10^6). Tank geometries considered include a spherically blunt cylinder, a conically tipped cylinder and a cylinder with a front end contoured fairing. Fig. 8.3.5-6 shows phase change paint models of the three configurations after being subjected to identical environments. The high heating regions are those which are black. This figure and Fig. 8.3.5-7, which shows the distribution of amplified heating rates on the orbiter, graphically illustrate the relative advantages of the contoured tank configuration. A full discussion of these tests is contained in References 8.3.5-1, -2 and -3.

The measured heating rates to the tanks and the vehicle are given in Fig. 8.3.5-8 and -9. Since the tests and the critical flight conditions are for the laminar boundary layer, scaling test results to flight conditions is somewhat simplified. In regions of shock amplified heating, scaling was accomplished using laminar pressure interaction theory, in other regions the heating rates were scaled with stagnation point heating. The maximum temperatures the orbiter experiences during ascent are contained in Fig. 8.3.5-10.

In the region of the contoured fairing, the vehicle is completely shielded. Extending the fairing to protect the cylindrical portion of the tank is prohibitively heavy. Fortunately, heating rates between the tank and fuselage, and tank and wing are low. While the poor radiation view factors to space in these regions might cause concern, the TPS skin heat capacity and radiation heat sink provided by a low temperature ablator (250°F) on the cylindrical tank wall combine to limit temperatures to those shown.

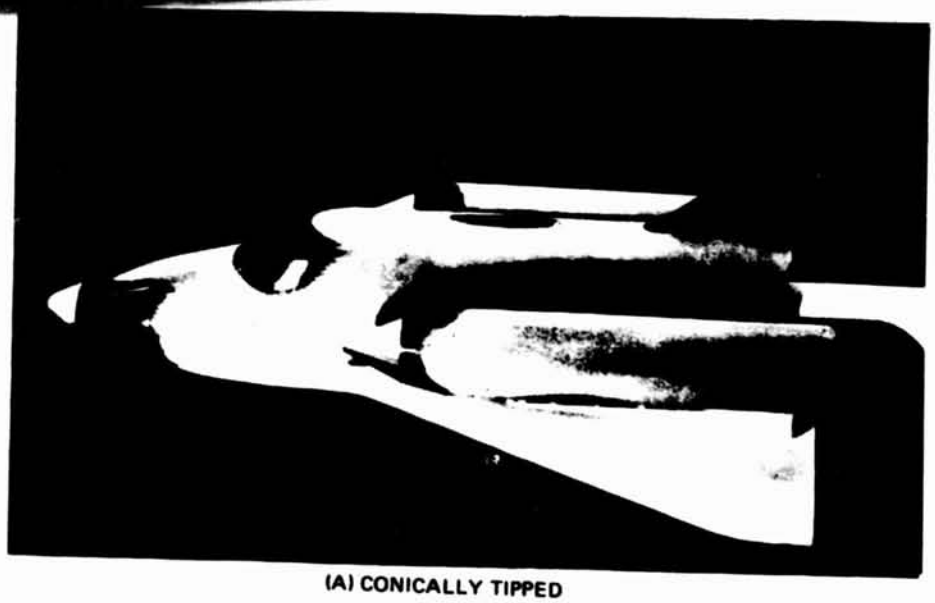

(A) CONICALLY TIPPED

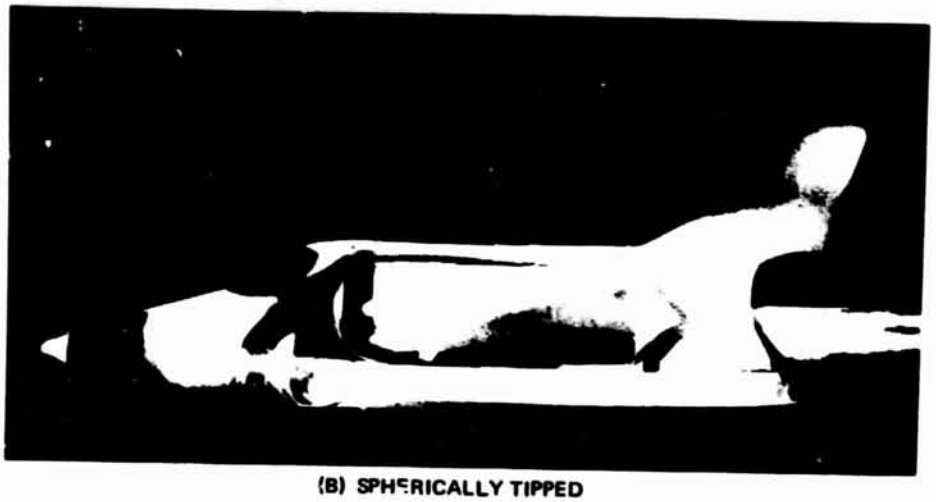

(B) SPHERICALLY TIPPED

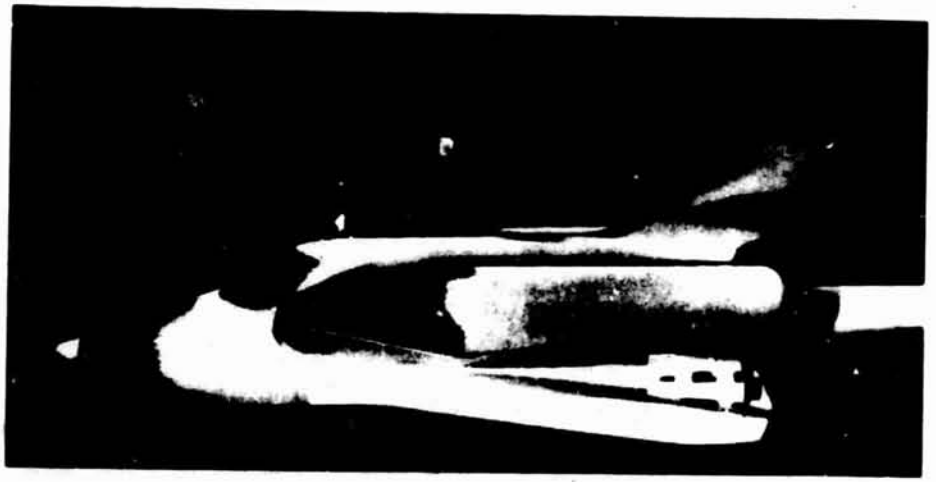

(C) CONTOURED TANK

B-90

Fig. 8.3.5-6 Tank Configurations After Phase Change Paint Test in LRC Hypersonic Wind Tunnel

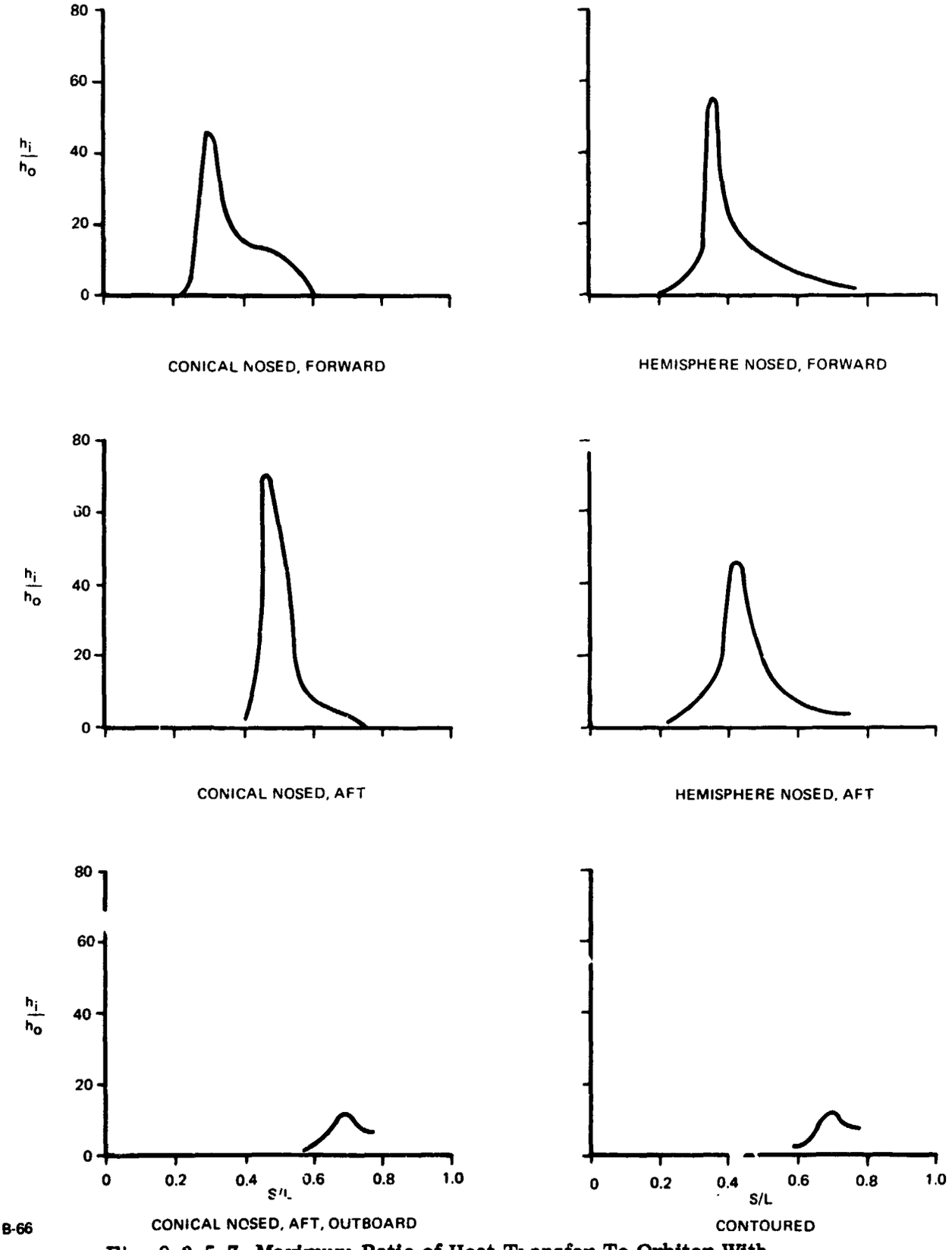

B-66

Fig. 8.3.5-7 Maximum Ratio of Heat Transfer To Orbiter With Flow Disturbed & Undisturbed by Tanks

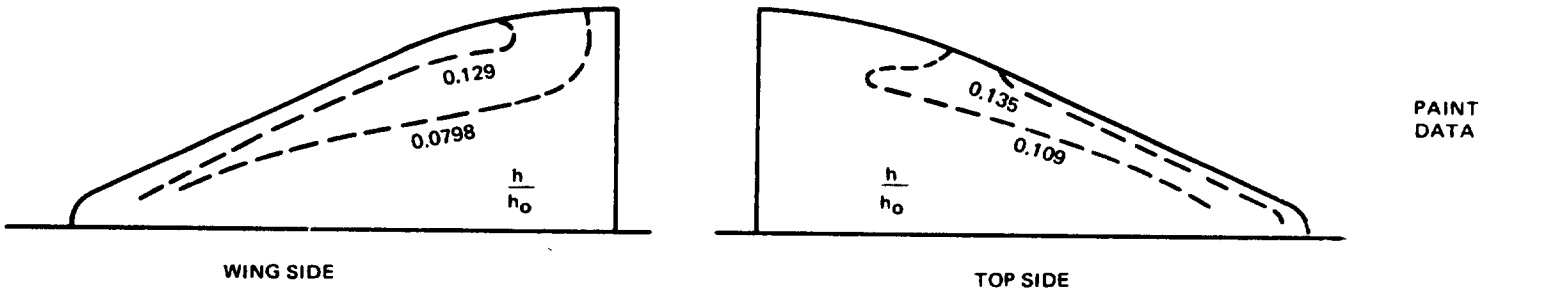

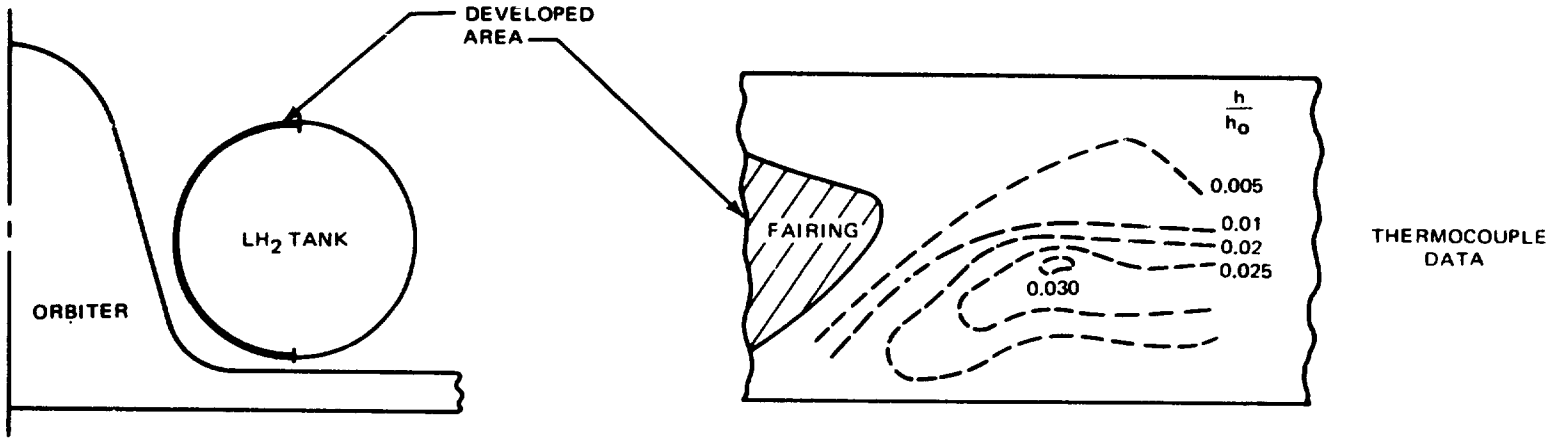

Fig. 8.3.5-8 Measured Heating Rates To H-33 Contoured External LH_2 Tanks

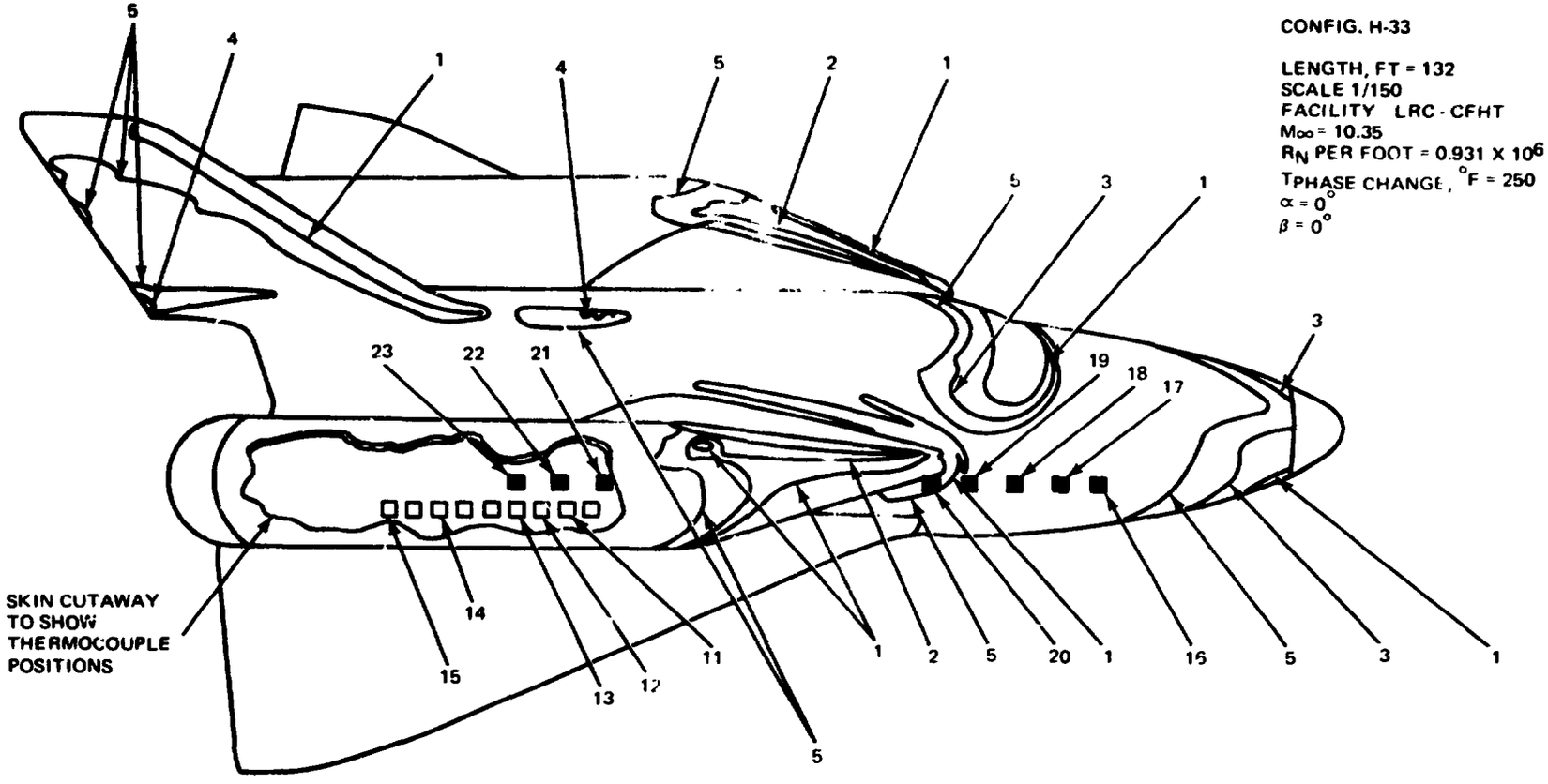

PAINT DATA

ISOTHERM	$\frac{h}{h_{r=1'}}$
1	.1554
2	.1090
3	.0908
4	.0821
5	.0662
6	
7	
8	
9	
10	

B-77

THERMOCOUPLE DATA

THERMOCOUPLE	$h/h_{r=1'}$
11	0.0048
12	0.0170
13	0.0250
14	0.0250
15	0.0260
16	0.0200
17	0.0140
18	0.0076
19	0.0185
20	0.0580
21	0.0053
22	0.0330
23	0.0420

■ FUSELAGE MOUNTED THERMOCOUPLE

□ TANK MOUNTED THERMOCOUPLE

NOTE
THERMOCOUPLES ARE MOUNTED ON THE INBOARD SURFACE OF THE TANK

Fig. 8.3.5-9 Measured Ascent Heating

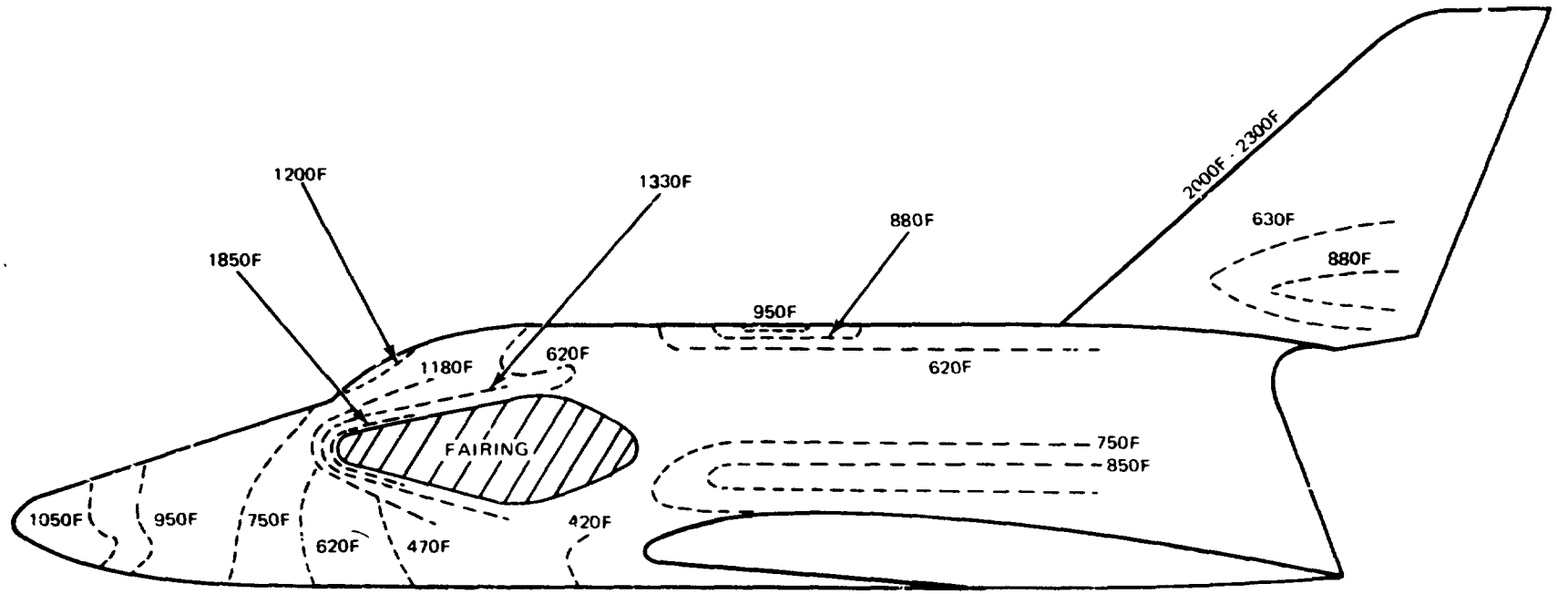

Fig. 8.3.5-10 Maximum Vehicle Temperatures During Ascent

8.3.5.2.2 External LH_2 Tank TPS

The ablative coating used on the cylindrical section of the LH_2 tank must limit the foam-ablator interface temperature to approximately 200°F, thereby maintaining the integrity of the foam, which in turn limits ascent LH_2 boil-off. The baseline material for this application is a low temperature spray-on ablator which cures at room temperature. This is desirable for low cost and ease of application. From a thermal viewpoint, the low temperature of the ablator minimizes the insulation thickness required of the ablator and acts as a heat sink for those portions of the vehicle TPS in close proximity to the tank.

Firex 250 (Pfizer) has been selected, at this time, as representative of this type of material for purposes of cost and weight estimating. Tests were run in the Aerotherm Corporation arc tunnel on aluminum-foam-Firex 250 samples. Foam samples (3 x 3 x 3/4 in.) were spray-coated with .050 in. of Firex 250 and tested under conditions simulating the expected average and peak heating rates (at the center of the sample). Fig. 8.3.5-11 shows an unheated specimen, a specimen subjected to the average ascent heating rate, one subjected to the peak ascent heating rate and an uncoated heated specimen. The specimen heated to the average level performed well. When heated to the maximum level, the uncoated sample was eroded to the aluminum substrate and the coated sample, while showing deep erosion, fared somewhat better. In all cases, the aluminum substrate showed no temperature rise. Subsequent analysis showed that the heat loads at the leading edge of the model were approximately twice the design value indicating that the present baseline thickness of the ablator, 0.1 in., may be somewhat conservative.

The tank fairing does not contain LH_2. Therefore, the TPS for the nose fairing need only provide for the structural integrity of its aluminum frame. This is best accomplished with an ablator in the 30 lb/cu ft class, placed on the frame in thicknesses up to 0.8 in. AVCOAT 5026-39 has been selected at this time as representative for purposes of cost and weight estimating.

8.3.5.3 Stage Separation/Plume Effects

The orbiter main propulsion engines are fired in close proximity to the booster during stage separation. The separation sequence analyzed consists of two engines firing until the thrust-to-weight ratio is equal to 0.5. Although the separation sequence heating duration is short, the magnitude of heating from the orbiter engines is

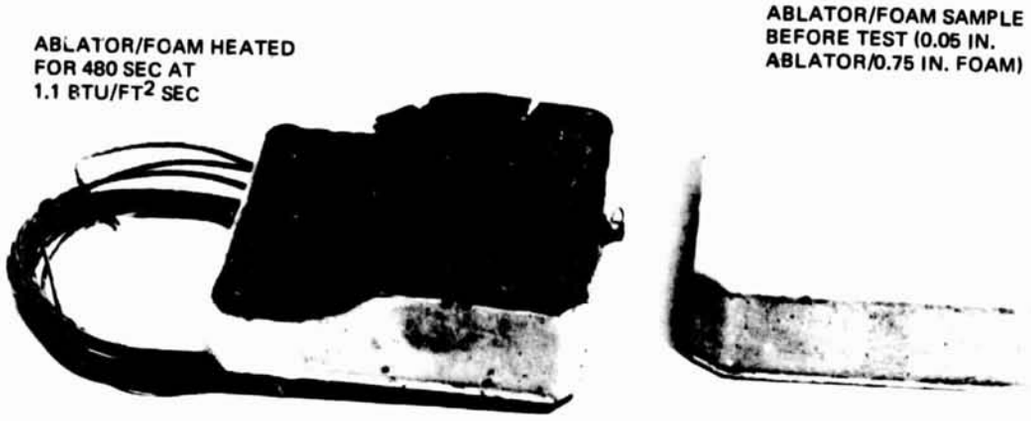

A BEFORE ARC JET TEST

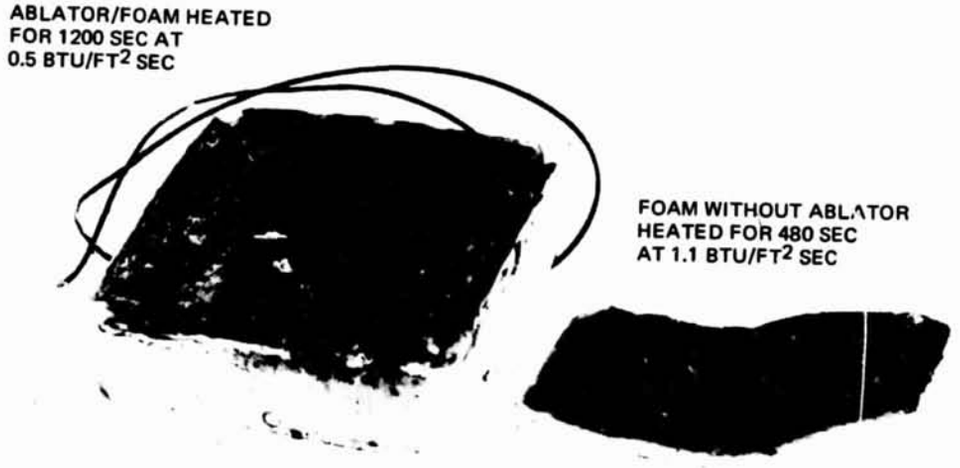

B AFTER ARC JET TEST

B-83

Fig. 8.3.5-11 External LH_2 Tank Ablator Foam Samples

sufficient to design the booster's vertical tail leading edge and some of the fuselage leeside as discussed in Subsection 9.3.4.2.2. Because of the impact of plume heating on booster design, other separation sequences are being investigated. These include: three engines firing (higher heating rates, but shorter duration) and two engines firing while gimballed outboard at the maximum nominal angle (lower heating rates, but longer duration). Prediction of multiple engine, hydrogen/oxygen plume effects is, therefore, of more than academic interest for the heat sink booster configuration.

Available analytical methods for predicting rocket plume impingement heating are generally not applicable for the complex orbiter/booster stage separation problem as shown diagramatically in Fig. 8.3.5-12. The complexities include multiple intersecting plumes from two- and three-engine configurations, nozzle generated internal shocks, three-dimensional impingement surfaces with streamwise corner flows, non-uniform oncoming streams, separated and reattachment regions, etc. Consequently, prediction of plume impingement heating must rely heavily on experimental data.

An experimental program was conducted in the Grumman detonation tube shock tunnel plume facility to examine the effects of dual hydrogen/oxygen plumes on the booster afterbody. The tests consisted of 1/100 scale, one and two engine firings on a flat plate, a flat plate with a swept vertical fin (shown in Fig. 8.3.5-13) and a cylinder model. The models were all instrumented with standard shock tunnel thin film heat transfer gages. Tests were conducted under full scale enthalpy conditions but, because of facility safety and size limitations, the Reynolds numbers were 1/300th of the full scale values. This precluded studying transition and turbulent phenomena. However, based on LM experience, the large favorable pressure gradients characteristic of plume flows should act to maintain the laminar boundary layer except, perhaps, in regions of strong shock-boundary layer interactions.

The more pertinent results from the test, reported in detail in Reference 8.3.5-4, are summarized in Fig. 8.3.5-14 through 8.3.5-16. Fig. 8.3.5-14 shows the flat plate heating distribution on the nozzle centerline plane. The important effects to be noted from the figures include: 1) two-engine firing increases peak heating, moves the location of peak heating further aft, and decreases the heating rate in the near field;

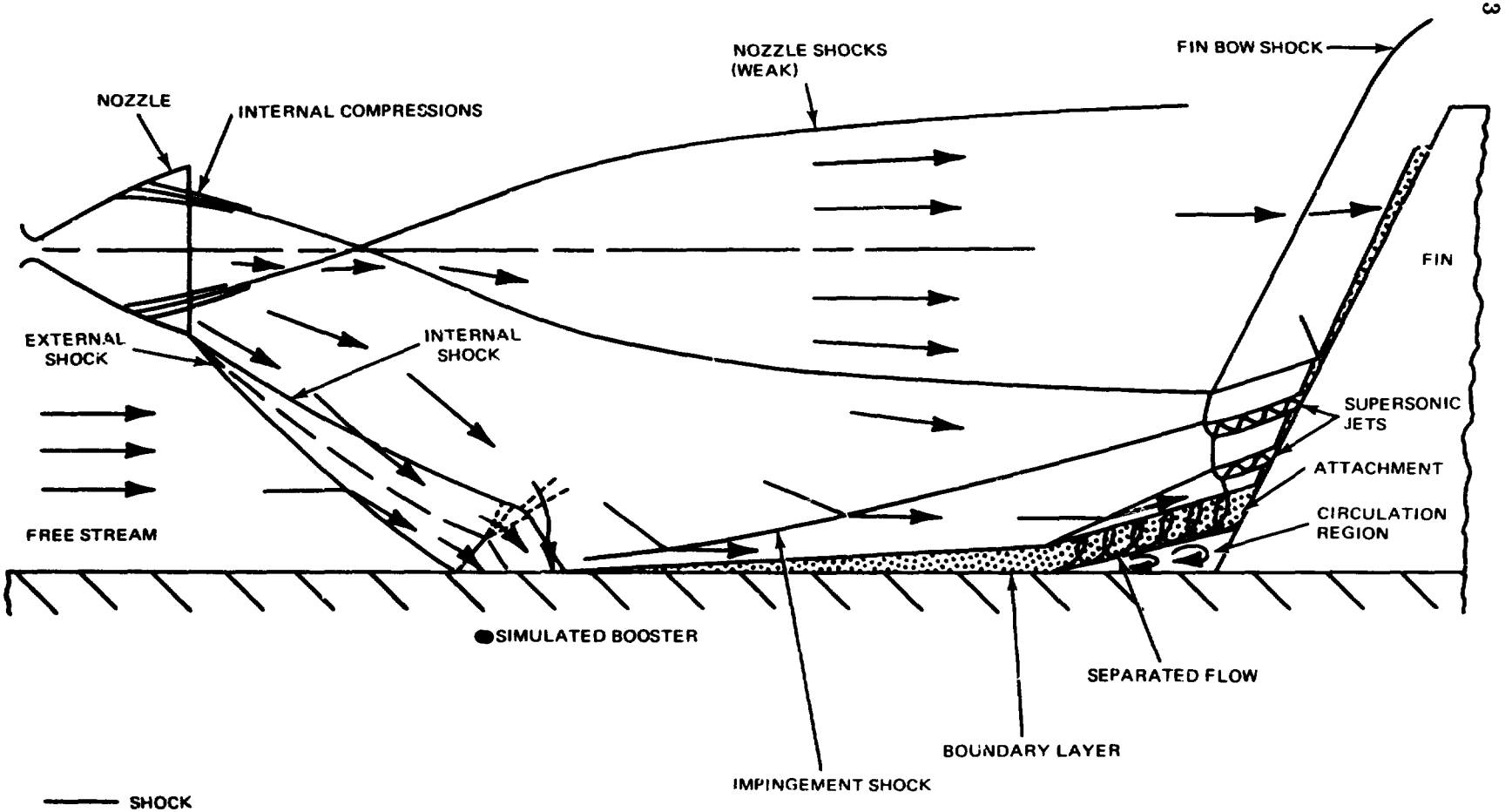

SHOCK
EXPANSION
CONTACT SURFACE
STREAMLINE
BOUNDARY LAYER

Fig. 8.3.5-12 Complex Rocket Exhaust; Booster Flow Field

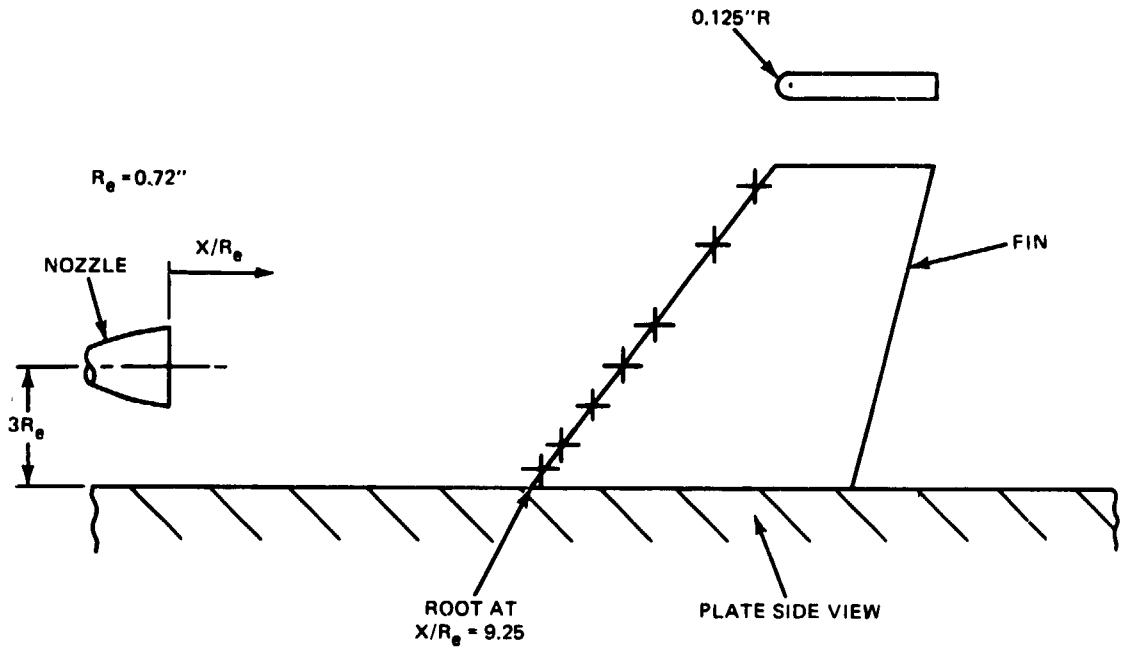

+ THERMOCOUPLE LOCATIONS

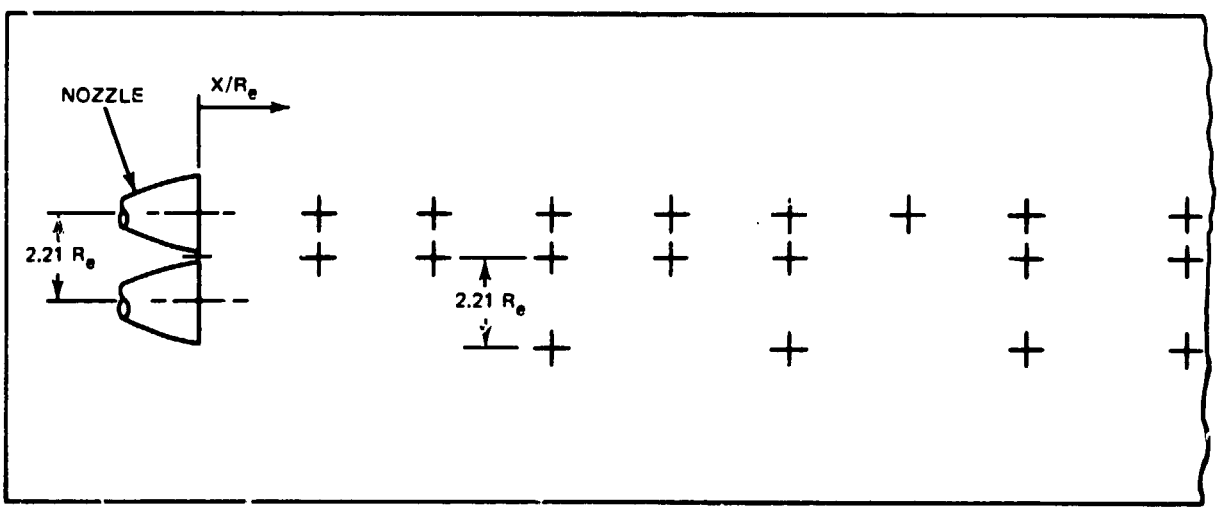

TOP VIEW

B-85

Fig. 8.3.5-13 Plume Impingement Test Model

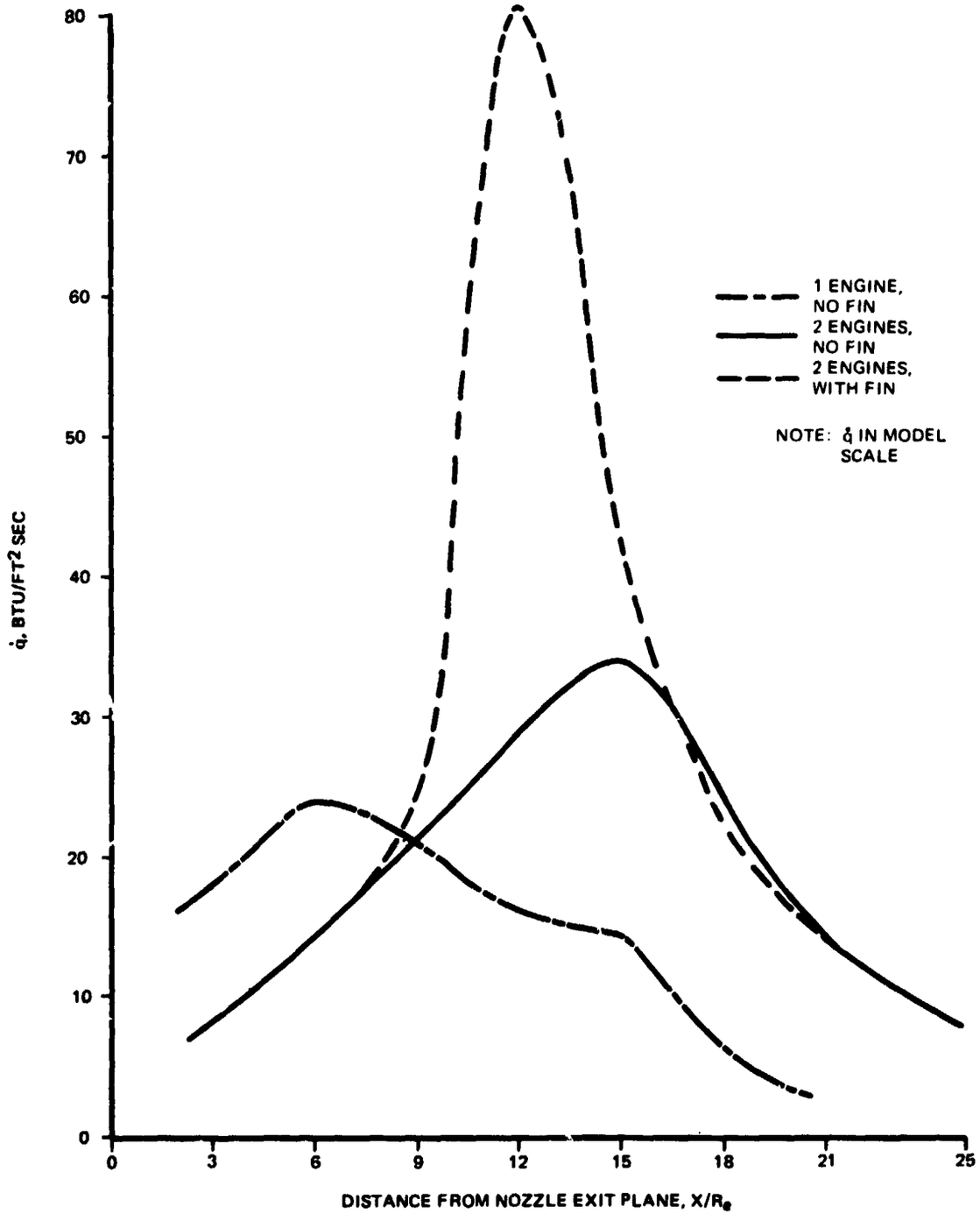

B-75

Fig. 8.3.5-14 Flat Plate Heat Transfer Rate Distribution On Nozzle Centerline Plane

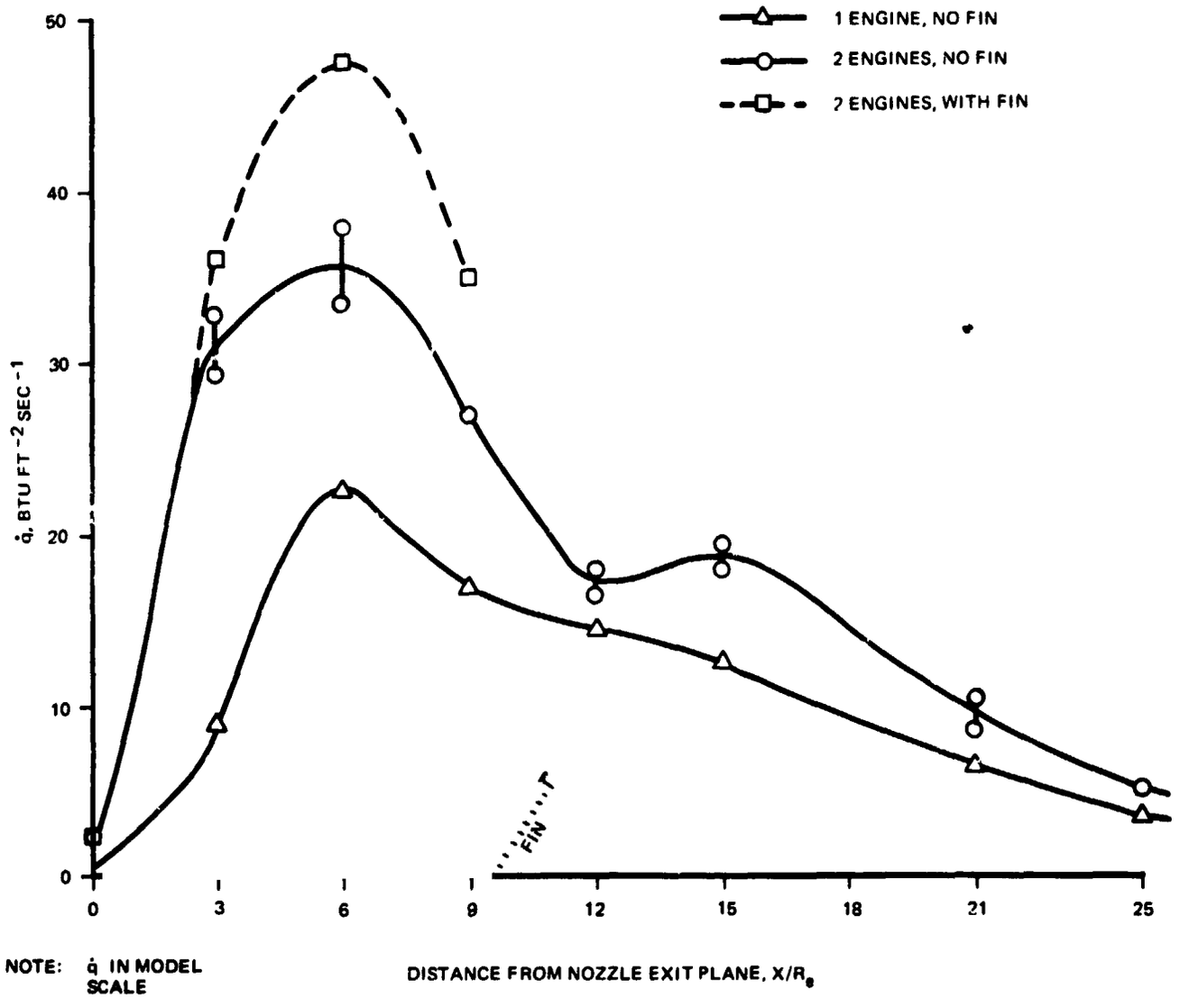

B-76

Fig. 8.3.5-15 Flat Plate Heat Transfer Distribution On Body Centerline Plane

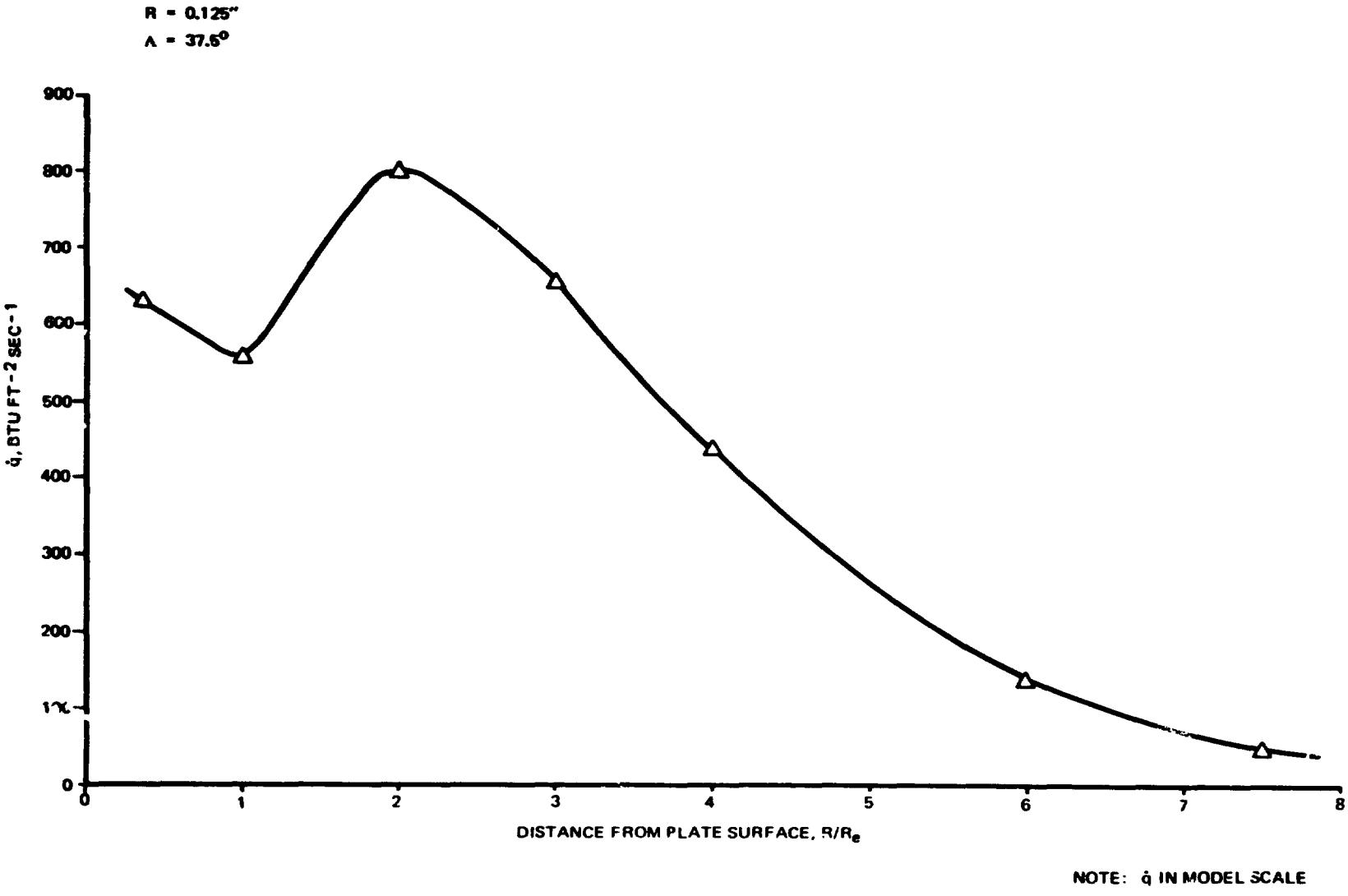

Fig. 8.3.5-16 Fin Heat Transfer Rate Distribution on Leading Edge and Side (Two Engines Firing)

and 2) a fin on the body centerline plane between the two engines causes a dramatic increase in heating on the plate surface outboard and aft of the fin leading edge, due to the fin bow shock.

Fig. 8.3.5-15 shows the flat plate heating on the body centerline plane between the two nozzles. Two-engine firing increases substantially the heating rates due to the increased mass flow but leaves the peak point location unchanged. The addition of the fin further increases the heating, though not to the degree shown on the nozzle centerline plane. Similar trends are found for the cylinder and, as expected, heating rates are higher than those on the plate along the centerline plane by approximately thirty percent.

Heating along the fin leading edge, Fig. 8.3.5-16, with two-engine firing, is an order of magnitude greater than those on the flat plate surface. The upswing in heating rate near the fin root is due to the plate-surface shock wave which in GLOW photographs could be seen to impinge near the lowest fin leading edge gage.

The model heating rates were scaled to flight heating rates assuming that laminar conditions prevail. With 1/3 full scale pressure and 1/100 full scale lengths, $\dot{q}$ flight/$\dot{q}$ model = 0.17. If the flow were fully turbulent, this ratio would be 0.95. As model scale or pressure is increased, the uncertainty will be reduced.

8.3.5.4 On-Orbit Thermodynamics

On orbit environments have a significant influence on the sizing of TPS insulation thickness for reentry (lower initial temperatures result in lesser weights) and on the sizing of ECS hardware for orbital flight. To gain an appreciation for structural temperatures at reentry initiation and the environmental effects on the ECS system, three typical orbital attitudes were analyzed. Two of these correspond to "delivery/retrieval" missions and the third to an experimental mission.

8.3.5.4.1 On-Orbit Natural Environments

For both "delivery/retrieval" missions, the vehicle was oriented with its centerline parallel to the velocity vector, wings normal to the orbital plane and the cargo bay looking to space (earth-oriented mode). In one case, the orbital plane was taken parallel to the ecliptic plane and in the other a polar orbit was assumed. For the polar case, the maximum possible angle between the solar vector and orbital plane was used in

determining the natural environment. For the experimental mission, the vehicle centerline was maintained in the orbital plane with its vertical axis parallel to the solar vector and the lee side insolated (solar inertial mode). The experimental mission was flown with the solar vector normal to the orbital plane.

In either mode of orbital operation (earth-oriented or solar inertial), the orbital average environment can be characterized by the angle of incidence of the solar vector on the orbital plane. These environments are shown in Fig. 8.3.5-17 and 8.3.5-18 for the range of possible solar angles and shuttle surface orientations.

8.3.5.4.2 On-Orbit Vehicle Temperatures and Heat Loads

In analyzing the "delivery/retrieval" missions, the cargo bay was assumed empty with the bay doors open. For the experimental mission, the instrumentation package was considered to fill the cargo bay and provide its own environmental conditioning so that the interface between the package and vehicle structure was considered adiabatic. Here, also, the bay doors were open. Steady-state temperatures were calculated using a thermal nodal network together with the orbital natural environment. External surfaces were assumed to have an absorptivity to emissivity ratio of 1.0.

The results of the analysis for a typical fuselage station (station 900) are shown in Fig. 8.3.5-19. For the "delivery/retrieval" mission with the orbit parallel to the ecliptic plane, LOX tank temperatures range from 20°F to 45°F with the remaining internal structure between 35°F and 70°F. The temperature distribution is symmetric about the vehicle centerline. The polar "delivery/retrieval" mission shows a much wider range of tank temperatures; -100°F to 90°F. There is also a significant temperature gradient across the vehicle. The experimental mission is by far the coldest overall and has tank temperatures as low as -100°F. However, there is not a significant temperature gradient within the vehicle in this case.

"Worst case" situations can be generated which give temperatures far in excess of those resulting from realistic missions and orientations. For example, if one assumes that the payload bay is open and empty when the vehicle is in the previously described experimental orientation, internal temperatures can range upward toward 200°F. Low α/ϵ coatings on internal surfaces could be used to alleviate this situation, but, when

FOLDOUT FRAME
B/8.3

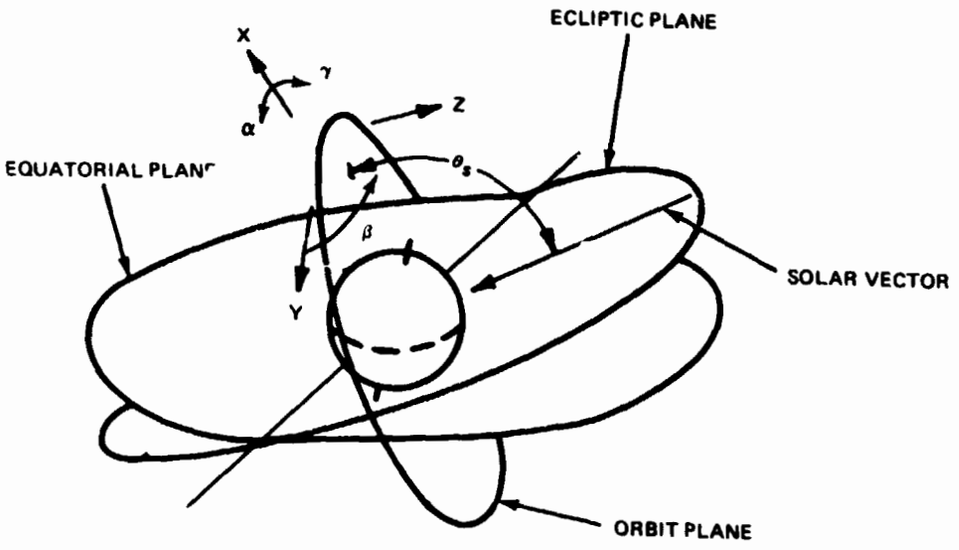

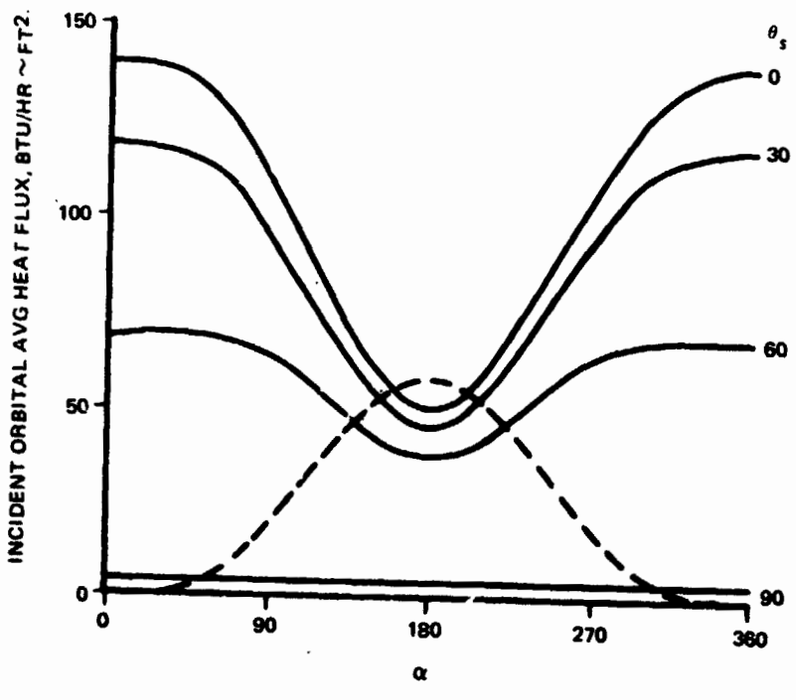

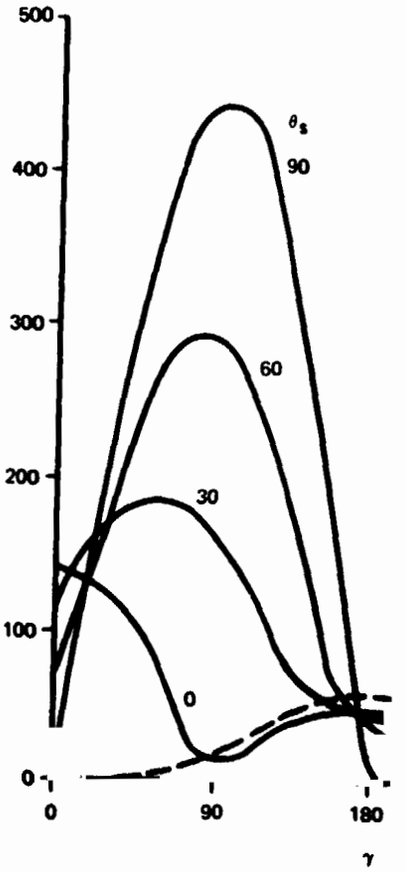

B-330

FOLDOUT FRAME 2

SOLAR AND EARTH ALBEDO
EARTH IR
α = SURFACE NORMAL IN X-Y PLANE
β = SURFACE NORMAL IN Y-Z PLANE
γ = SURFACE NORMAL IN X-Z PLANE

TOR

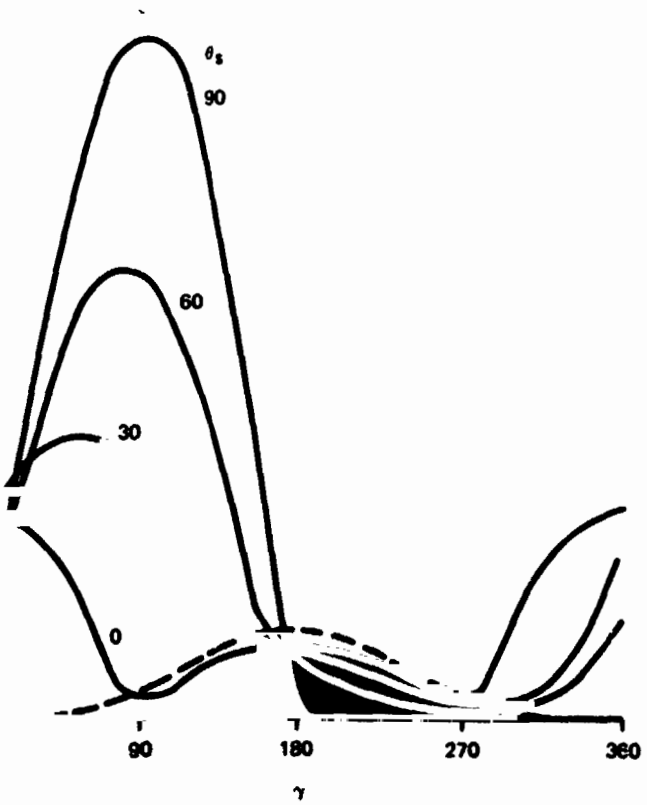

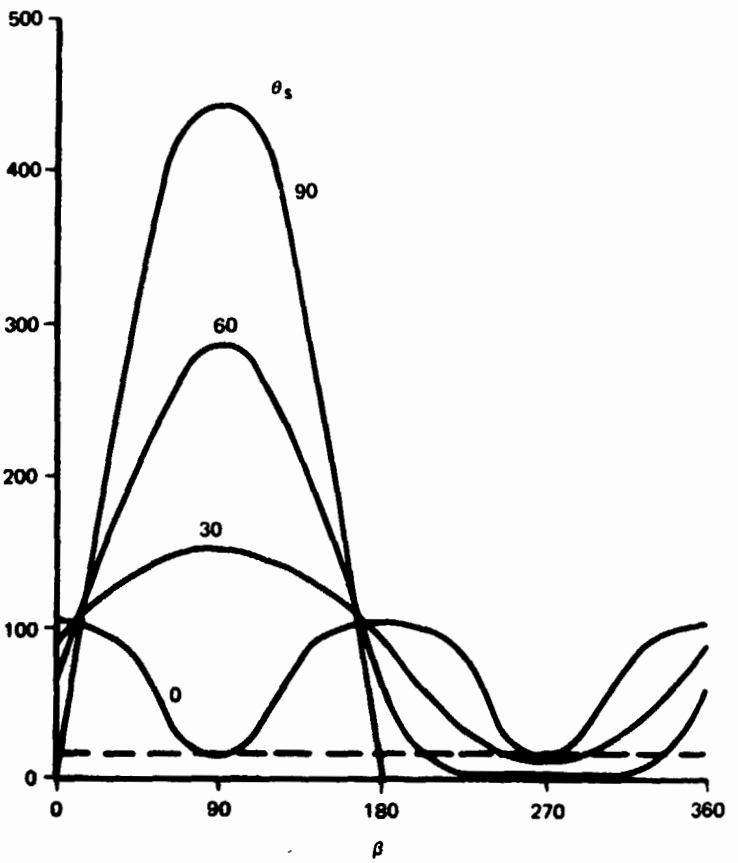

Fig. 8.3.5-17 Orbital Average Heat Flux, Earth Oriented

GRUMMAN
BOEING

FOLDOUT FRAME

B/8.3

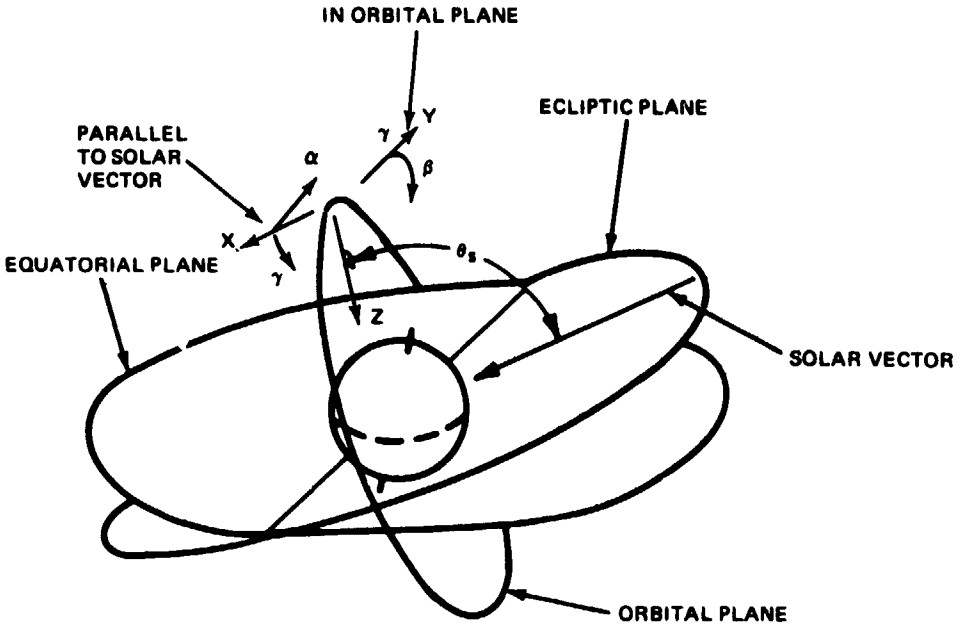

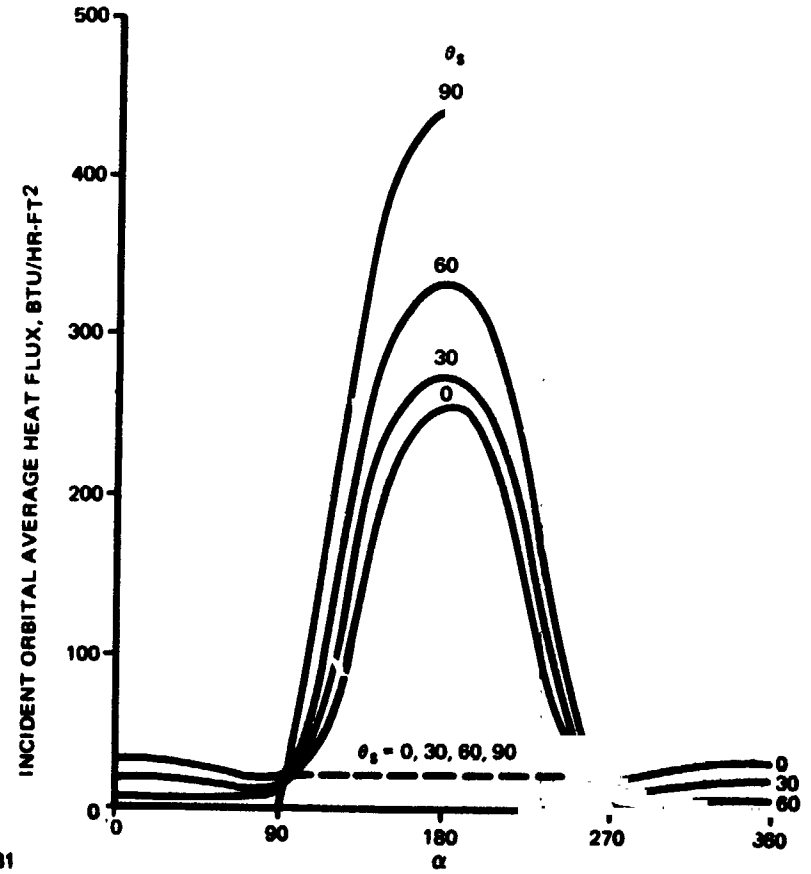

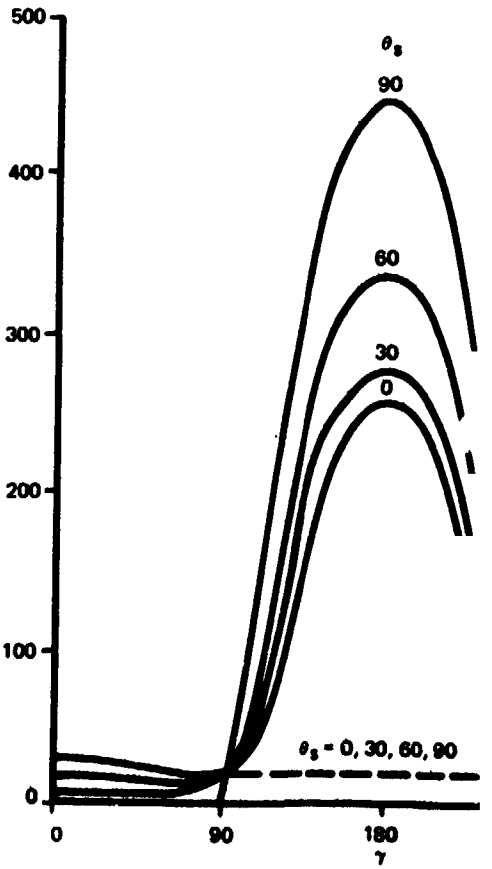

B-331

FOLDOUT FRAME 2

SOLAR AND EARTH ALBEDO
EARTH IR
α = SURFACE NORMAL IN X-Y PLANE
β = SURFACE NORMAL IN Y-Z PLANE
γ = SURFACE NORMAL IN X-Z PLANE

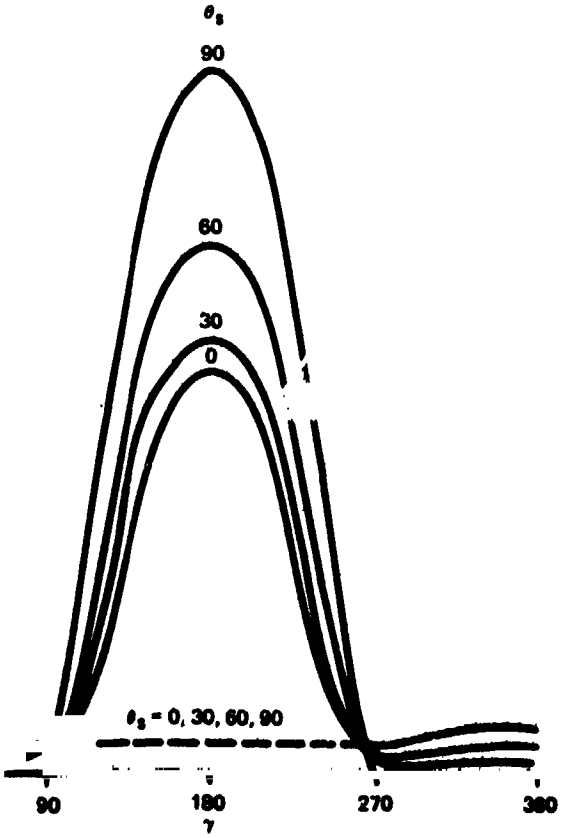

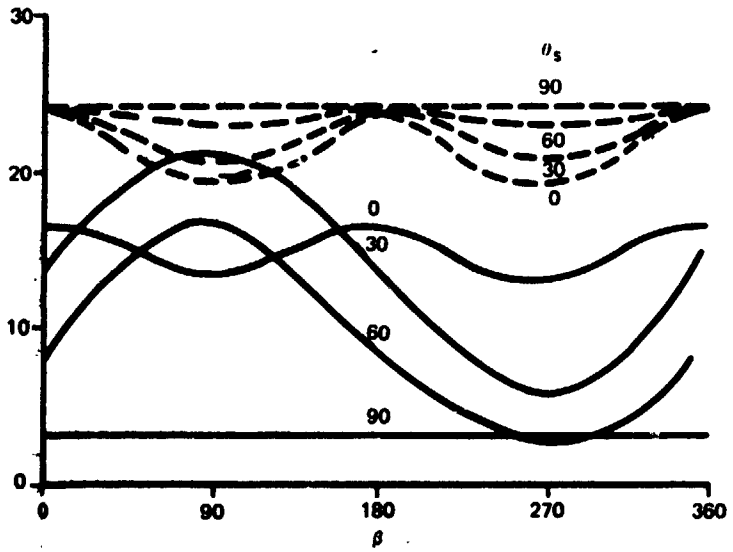

Fig. 8.3.5-18 Orbital Average Heat Flux, Solar Inertial

GRUMMAN
BOEING

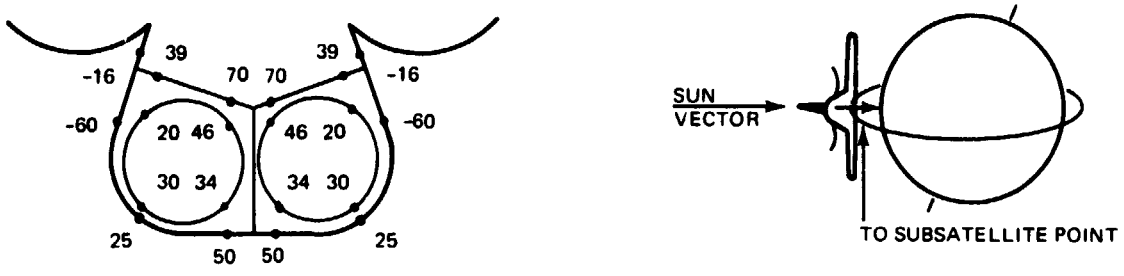

DELIVERY/RETRIEVAL MISSION, ORBITAL PLANE
PARALLEL TO ECLIPTIC PLANE

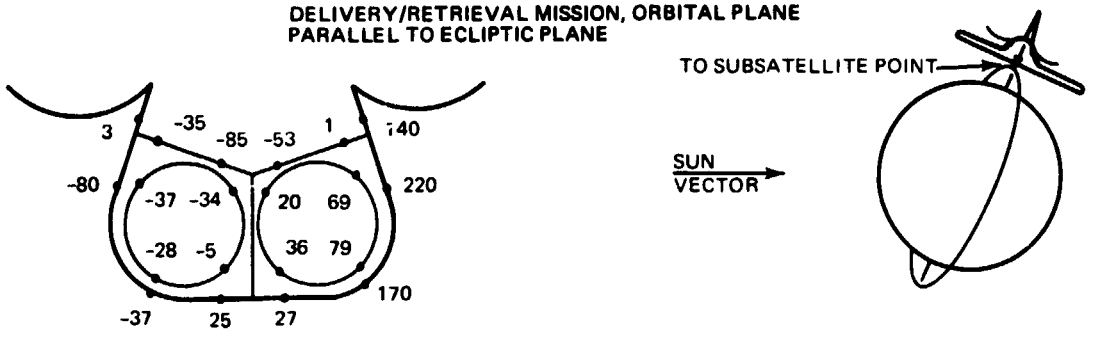

DELIVERY/RETRIEVAL MISSION, POLAR ORBIT

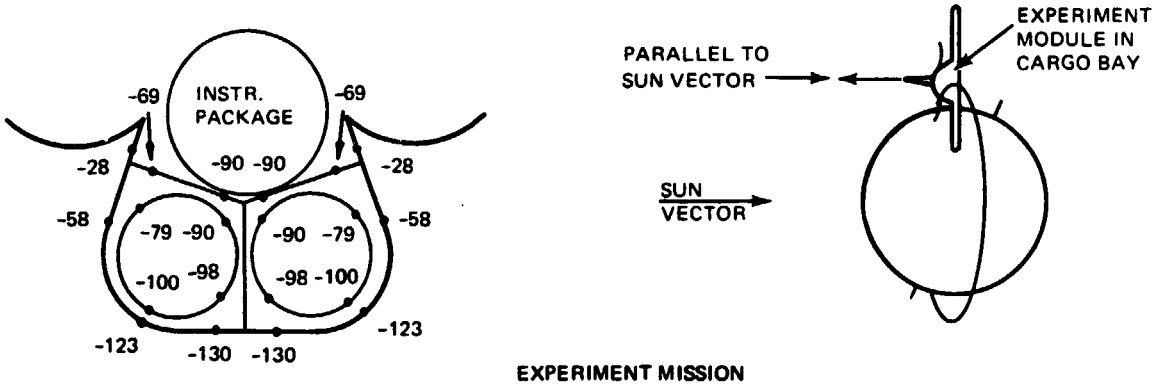

EXPERIMENT MISSION

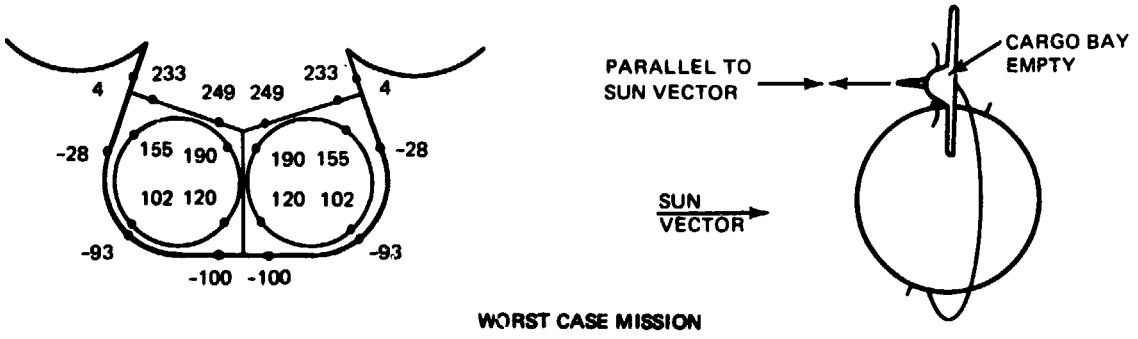

WORST CASE MISSION

B-88

Fig. 8.3.5-19 On-Orbit Temperatures, ^{o}F, Fuselage Station 900

reusable coatings must be applied to external surfaces to prevent high temperatures, the state-of-the-art is severely challenged.

While it is poor design practice to constrain vehicle orientations for thermal reasons, it is equally poor to design with the conservatism necessary to accommodate unrealistic worst case situations. Further work is required to define the full spectrum of orientations. However, based on the cases considered, the initial structure temperature of 100°F used in sizing TPS insulation appears realistic.

Two prime considerations in sizing the ECS on-orbit hardware are structural heat loads to the cabin and radiant energy incident on the space radiators. Structural heat loads were determined for the two "delivery/retrieval" missions previously described. A thermal model was employed which included the effects of the natural environment, window heat loads and that portion of the cabin electrical loads which are not actively cooled. The structural heat loads to the cabin air for polar orbit and ecliptic orbit are 600 BTU/hr and 1500 BTU/hr, respectively. The effect of the incident energy on the space radiators is minimized by the use of a low α/ϵ coating; silver teflon with $\alpha/\epsilon = 0.125$. In the presently proposed system, the radiators can experience full solar irradiation with a small effect on cabin comfort.

8.3.5.5 Reentry

Orbiter reentry temperature-time histories and maximum vehicle isotherms are shown in Fig. 8.3.5-20, -21 and -22. The underbody is dominated by turbulent heat transfer with the exception of the forward 30 ft, the chines and wing leading edge. Chine temperatures are low because of the large chine radius (80 in.) afforded by the moderate L/D configuration. The wing leading edge, optimized for subsonic aerodynamic performance, experiences temperatures in the 3000°F range. The high lee side temperatures reflect our concern for this most difficult problem and is based on both shuttle model data (NAR, LaRC) and our in-house studies on simple shapes, Reference 8.3.5-5.

External hydrogen tank reentry heat transfer is discussed in detail in Subsection 8.9.5. Basically, the tanks are allowed to break up and subsequently burn up in the atmosphere during reentry. To ensure intact reentry, approximately 3000 lb of

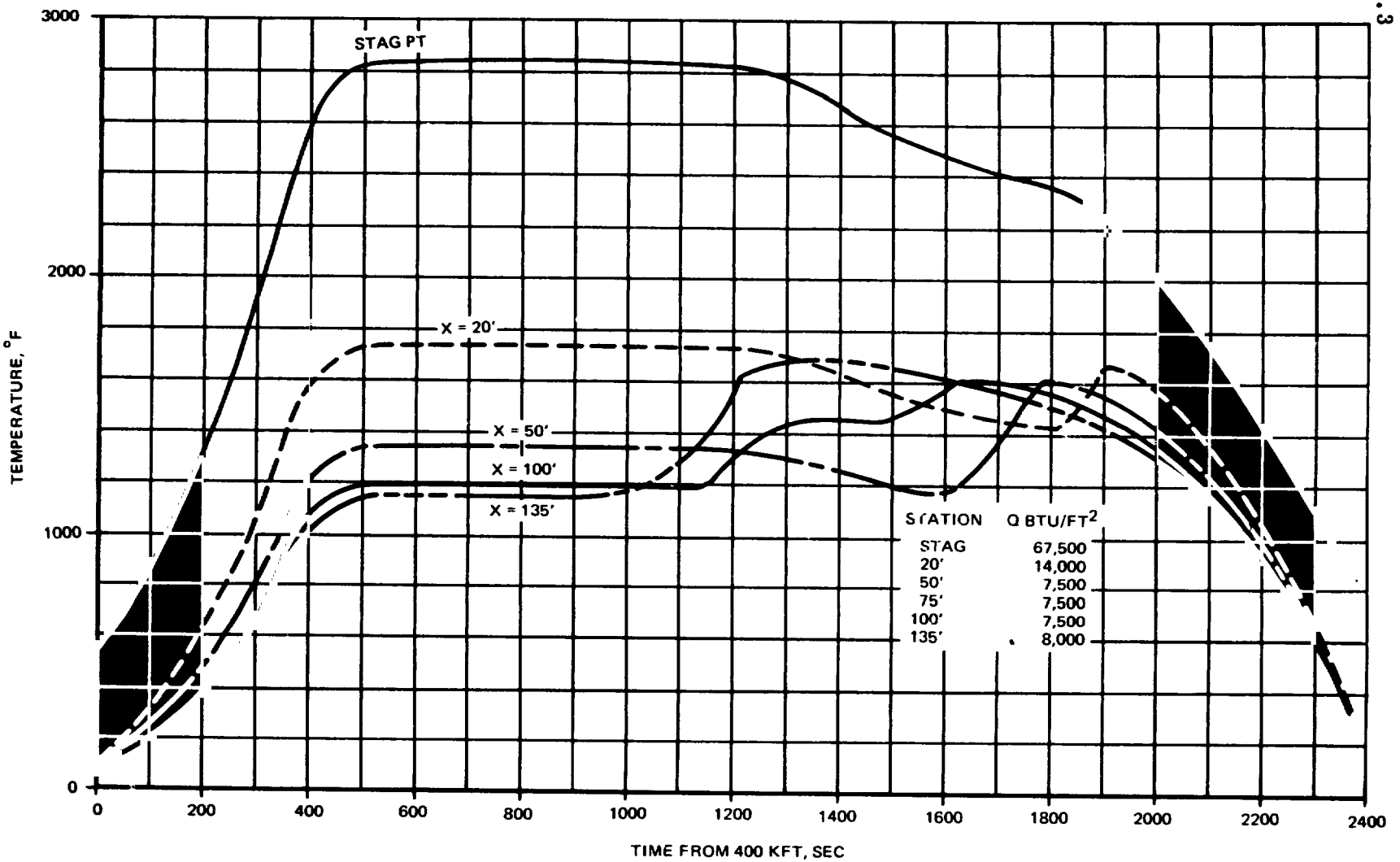

Fig. 8.3.5-20 H-33 Temperature Time History on Windward Centerline

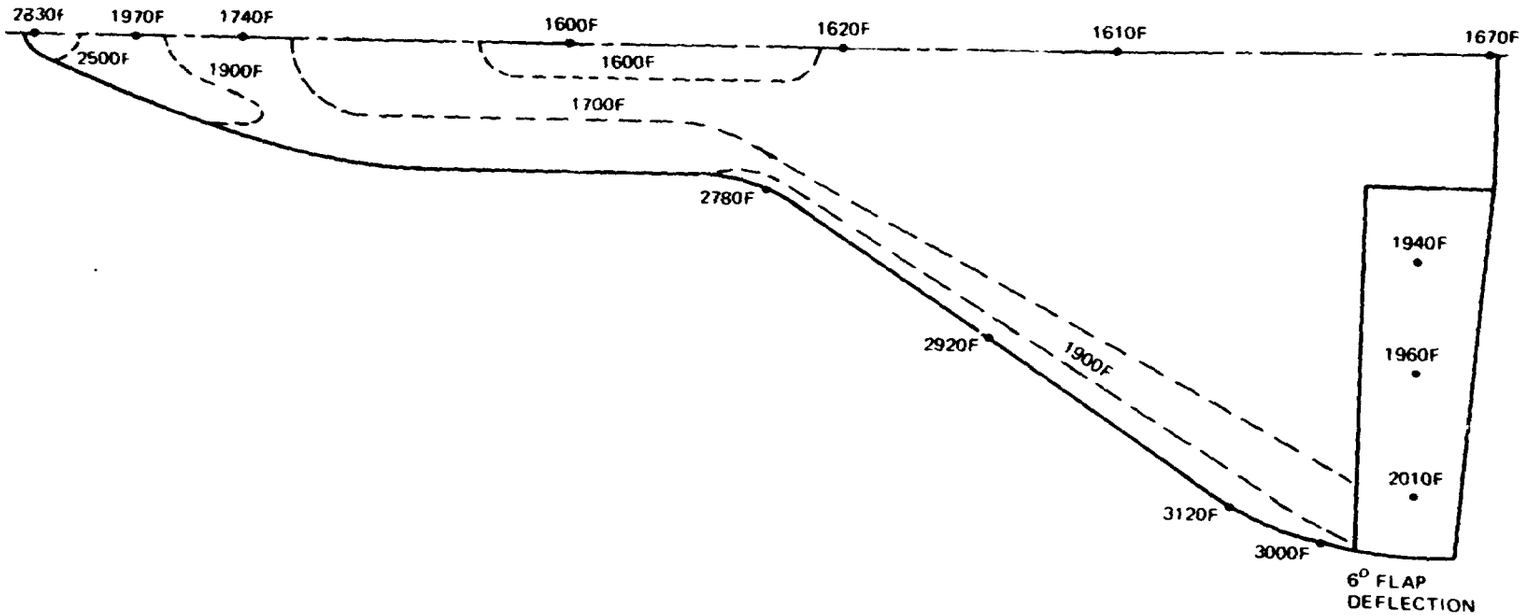

B-62

Fig. 8.3.5-21 Maximum Vehicle Temperatures During Reentry - Windward, = 0.8

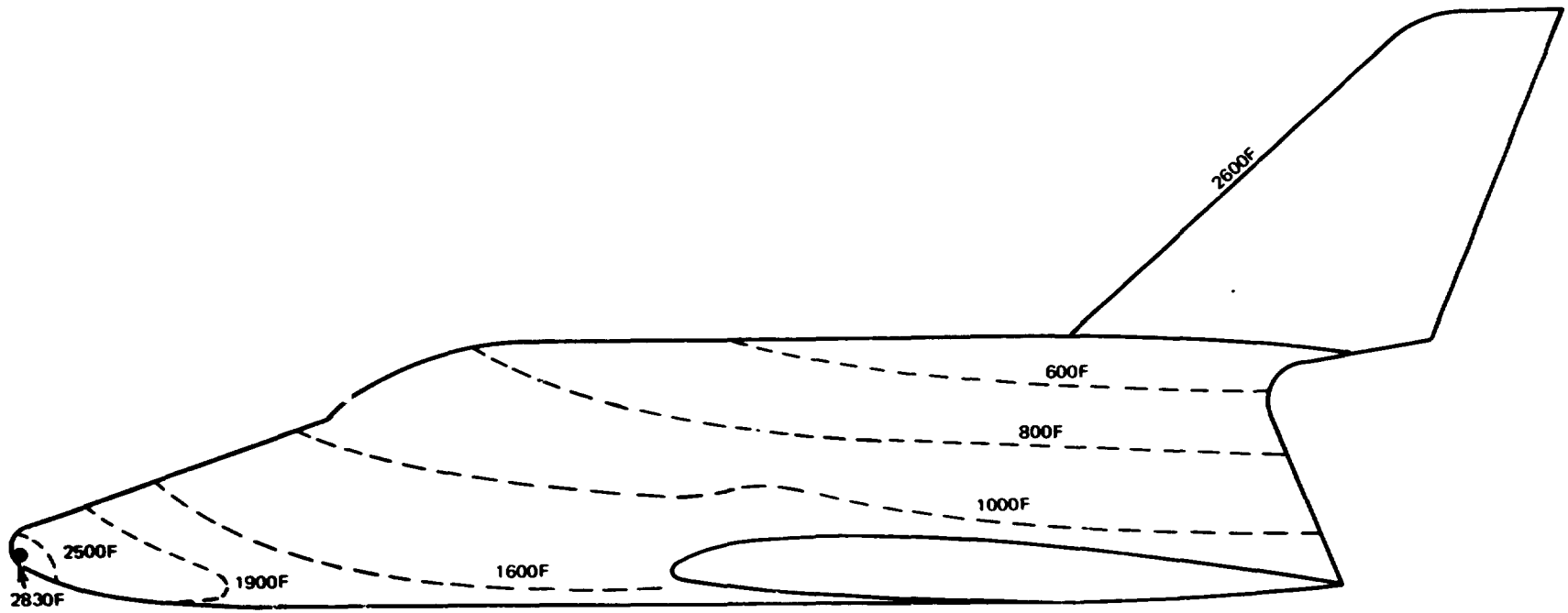

Fig. 8.3.5-22 Maximum Vehicle Temperatures During Reentry - Lee Surfaces, a = 27°, e = 0.8

additional ablator would be required per tank; an excessive weight penalty which would only serve to further constrict a quite tolerable impact dispersion zone. Since the tanks are designed only to survive ascent, and since the total integrated heating during reentry is some five times greater than ascent, the probability of all major pieces burning up is great.

8.3.5.5.1 Trajectory

The H-33 reentry trajectory is shaped to limit maximum underbody temperatures to values below 1800°F. This is done by first prescribing boundaries in altitude-velocity space such as those shown in Fig. 8.3.5-23. These boundaries are the locus of the highest windward centerline radiation equilibrium temperatures aft of the 20-ft station. Trajectories are then flown which, through either bank modulation or a combination of bank and angle of attack modulation, attempt to meet both the temperature constraint and achieve the design crossrange.

Vehicle reentry temperatures are based on a constant angle of attack trajectory ($\alpha = 27^{\circ}$) which meets the above stated objectives and at the same time yields reasonable values of total integrated heating. Examination of α modulated trajectories indicate that small perturbations in α are of no value since benefits derived from increased C_L are offset by increases in heat transfer. For α modulation to be effective, the perturbations must be on the order of 25° to 30°. Even then, the value of α modulation appears marginal from a thermal standpoint. By flying at constant α, simplifications can be effected in aerodynamics and guidance/control. The design trajectory is shown in Fig. 8.3.5-24.

8.3.5.5.2 Analytical Methods and Sensitivity

Prediction of the reentry environment on the orbiter is sufficiently complex to warrant strong reliance on experimental results, with judicious use of analytical methods, to extrapolate to flight conditions or supply information not yet obtained in test. The analytical methods employed are based on correlations obtained from and substantiated for basic shapes. A summary of these techniques, including the estimation procedures for determining the boundary layer state, is given in Table 8.3.5-1. Special effects, such as the effects of yaw, heating to deflected control surfaces, and the effects of surface roughness have been studied and are reported in References 8.3.5-6, -7, -8. For all

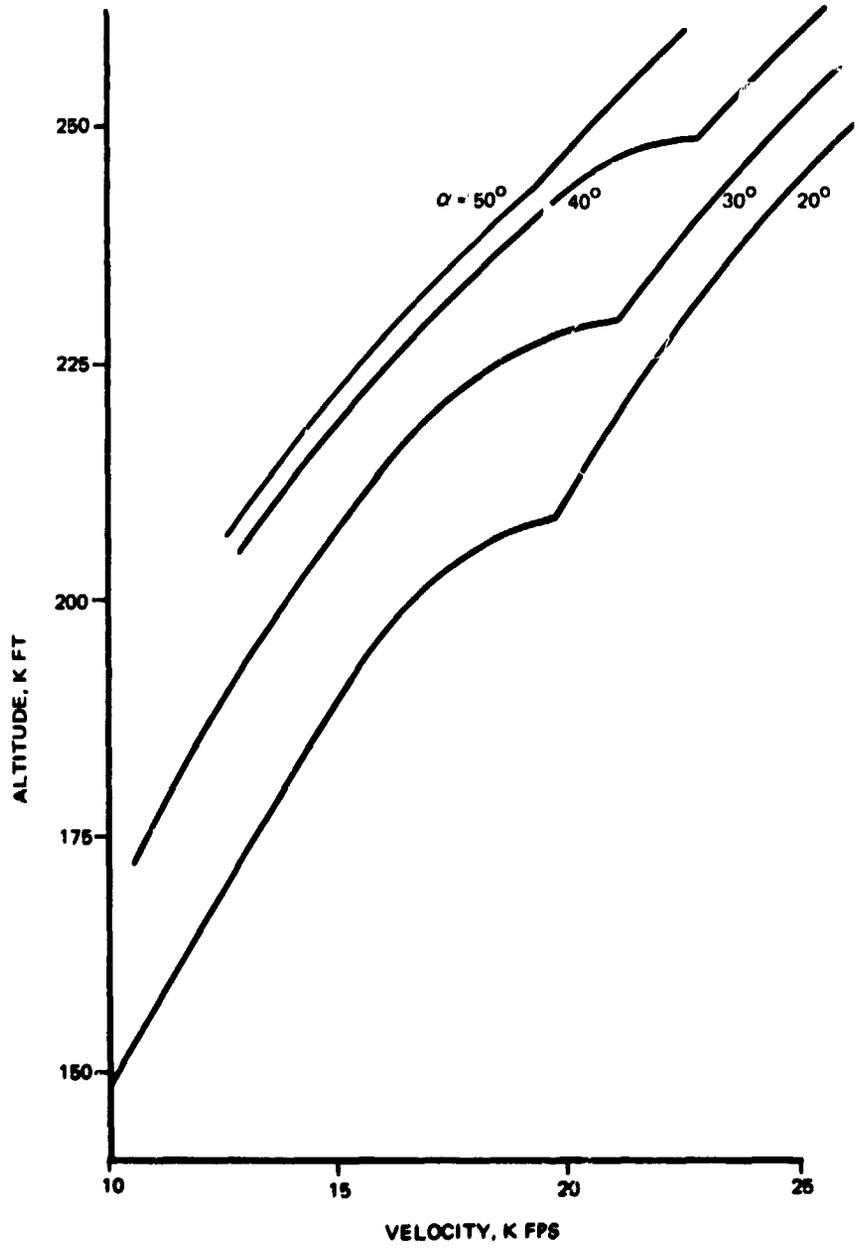

B-98

Fig. 8.3.5-23 1800°F Windward Surface Temperature Boundaries

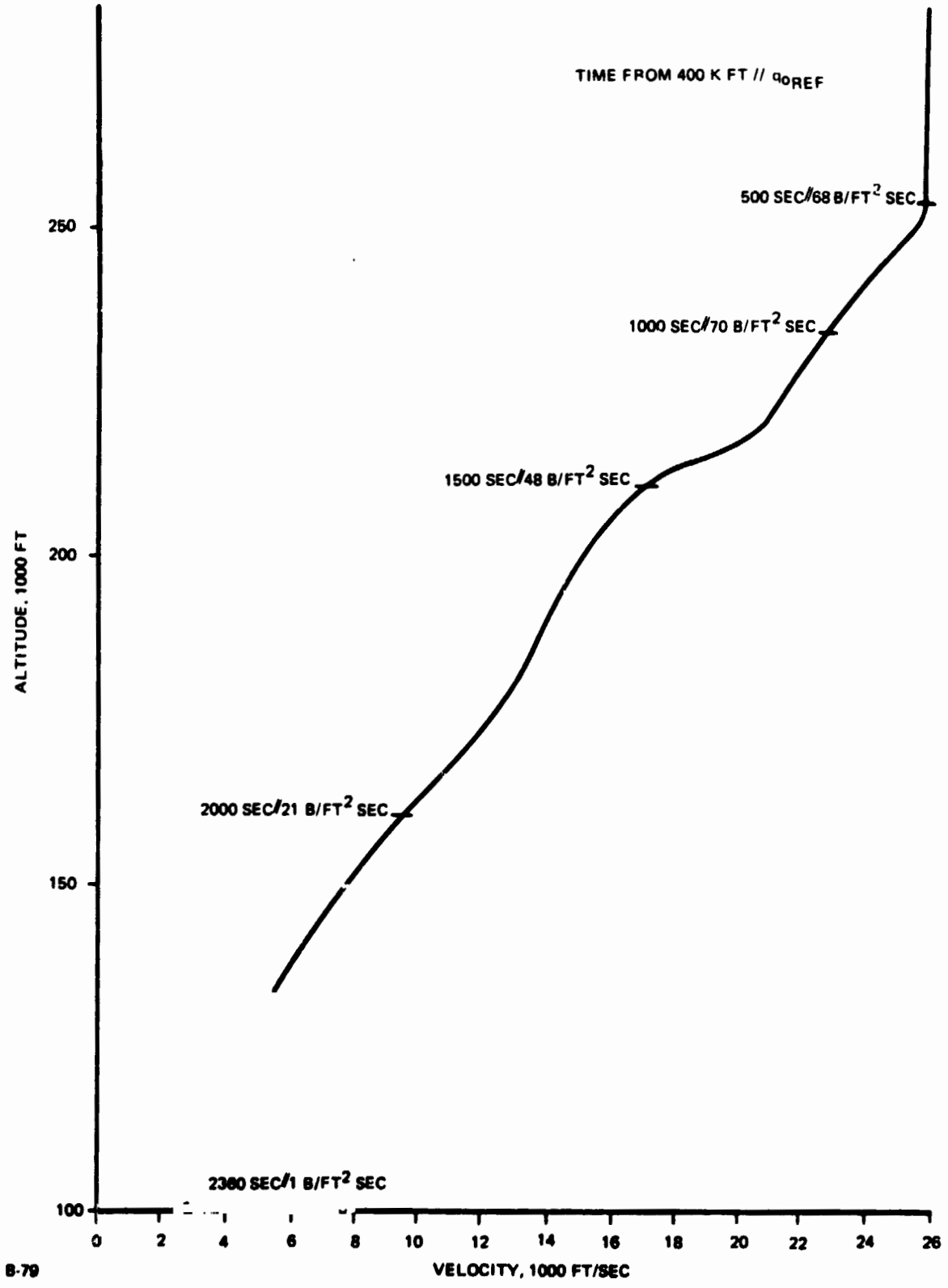

Fig. 8.3.5-24 H-33 Design Reentry Trajectory, a = 27°

TABLE 8.3.5-1 SUMMARY OF ANALYTICAL AERODYNAMIC HEATING METHODS

Region	Method of Analysis		Transition Criteria
	Correlative Method	Edge Property Assumption	
I. Orbiter Nose (Launch & Reentry)	Fay & Riddell Stagnation Point Theory	Normal shock	All Laminar
II. Fuselage			
a) Launch	Eckert's Reference Enthalpy Method for laminar flow, Real Gas Spaiding-Chi for turbulent flow	Normal shock entropy with tangent-cone pressures	$(Re_x)t = f(M_e, H_w/H_R)$ $(Re_x)T(Re_x)t = 2$ (Fig. 8.3.5 - 25
b) Reentry	Same as for launch	Plane oblique shock	$(Re_x)t = f(M_e)$ $(Re_x)T/Re_x)t = 2$ (Fig. 8.3.5 - 26
III. Wings & Tail			
a) Launch	Swept Cylinder for Leading edges	Parallel shock	$(Re_\infty)dt = 2 \times 10^5$ $(Re_\infty)dT/Re_\infty)n$
	Method for planform areas same as for fuselage (launch)	Normal shock entropy with tangent-wedge pressures	Same as for fuselage (launch)
b) Reentry	Leading edges same as for launch	Parallel shock	Same as launch
	Planform areas same as launch	Plane oblique shock	Same as for fuselage (Reentry)
IV. Chines (Launch & Reentry)	Swept Cylinder Theory	Parallel shock	Same as for wing & tail leading edges

methods of analysis, the assumption is made that the gas within the boundary layer is in thermal and chemical equilibrium. Ambient atmospheric conditions are based upon the 1962 U. S. Standard Atmosphere.

Even after deciding upon an analytical correlation based on agreement with test, care must be exercised in applying that method to flight conditions. For example, the Spalding-Chi method has as its base the empirical correlation of flat plate ideal gas skin friction data. One could apply this method directly to the flight situation, use an expedient pseudo real gas correction, or evaluate the factors F_c and $F_{R\delta}$ using real gas properties within the boundary layer. The differences as shown for a representative flight condition in Table 8. 3. 5-2 are not trivial. We have adopted the correction using real gas properties in evaluating the factors F_c and $F_{R\delta}$ as defined in the original paper by Spalding and Chi.

The Grumman transition criteria are shown in Fig. 8. 3. 5-25 and -26 and discussed in Reference 8. 3. 5-9. The criteria is based on an extensive body of sphere-cone flight and ground test data. Other criteria have been proposed based on combinations of momentum thickness Reynolds number, unit Reynolds number and edge Mach number. We have found these criteria lacking since they fail to correlate the most accurate flight transition data obtained to date.

The effect on the maximum windward surface centerline temperatures of using 1) the various postulated transition criteria, 2) Eckert's Reference Enthalpy turbulent heat transfer correlation rather than Spalding-Chi, and 3) a commonly used trajectory dispersion factor of lowering altitude by 2500 ft is shown in Fig. 8. 3. 5-27. In all cases the analytical model was supplemented by experimental data, with regard to the streamline divergence. The effect of using the Re_θ/M_e and $Re_\theta/M_e\,(Re_\theta/L).^2$ correlations decrease and increase temperatures by 200°F, respectively. Similarly, Eckert's method, when contrasted directly with Spalding-Chi, raise temperatures by 200°F. It is only the trajectory dispersion factor which has little influence on temperature, indicating that this simple design expedient is a poor substitute for a realistic assessment of trajectory dispersions. This limited sensitivity study points up the fact that work still remains to be done in the areas of methods, criteria and mission definition.

TABLE 8.3.5-2 COMPARISON OF RESULTS
FOR SPALDING - CHI METHOD
(Using Various Corrections)

EXAMPLE 1

Flight Condition:

Z = 200,000 Feet

∞ = 15,199 Fps

$\alpha = 27^{O}$

	Ideal Gas	Local γ	Effective M_e	Real Gas*	Eckert Method
$\dot{q}$ (BTU/ft^2 sec)	5.26	6.70	7.62	6.40	9.20
T (^{O}F) $\epsilon = 0.8$	1468	1590	1656	1560	1760

EXAMPLE 2

Flight Condition:

Z = 210,000

∞ = 18,294

$\alpha = 27^{O}$

	Ideal Gas	Local γ	Effective M_e	Real Gas*	Eckert Method
$\dot{q}$ (BTU/ft^2 sec)	6.78	10.80	11.66	9.50	13.53
T (^{O}F) $\epsilon = 0.8$	1595	1850	1890	1780	1978

* Grumman adopted method

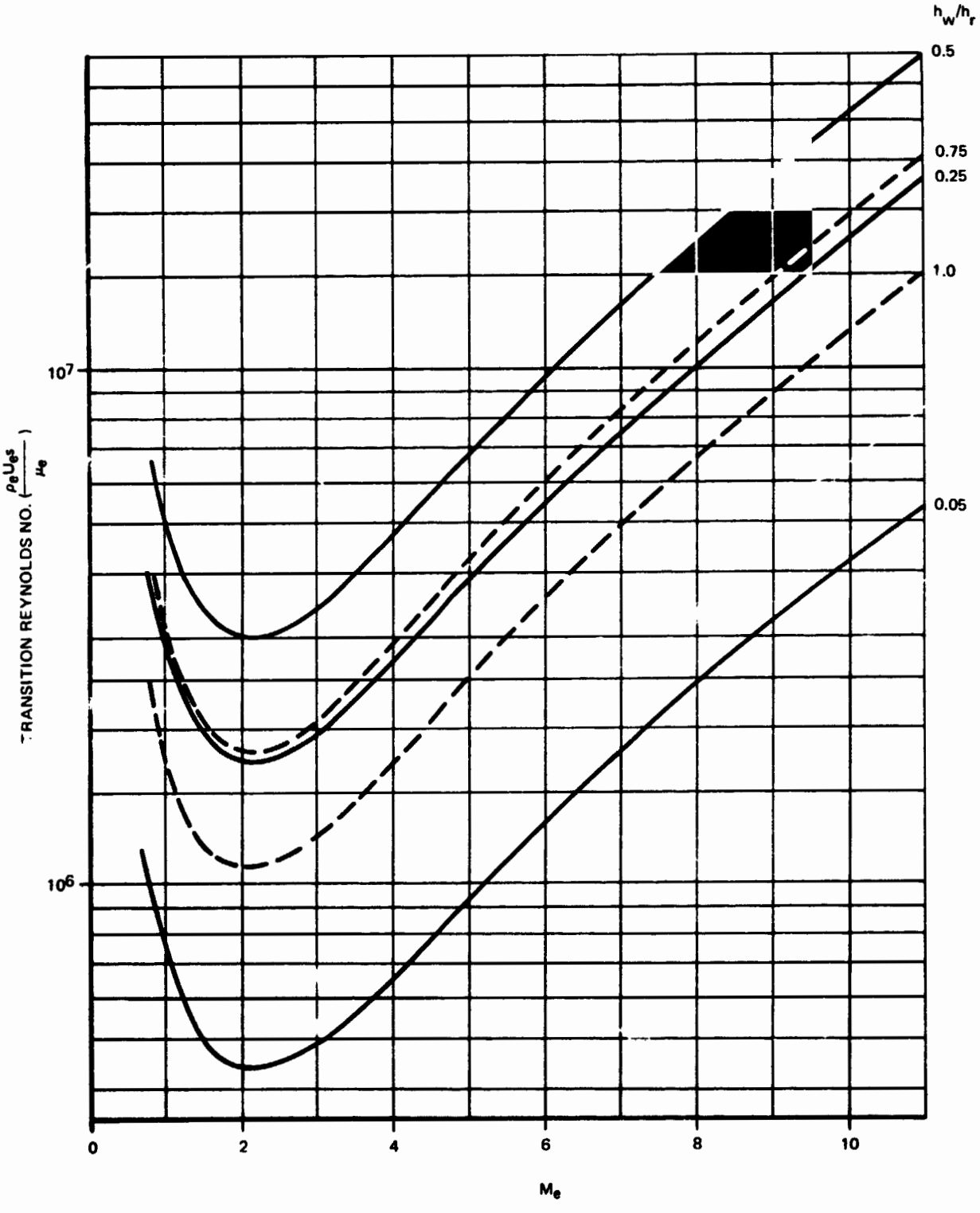

Fig. 8.3.5-25 Ascent Transition Criteria

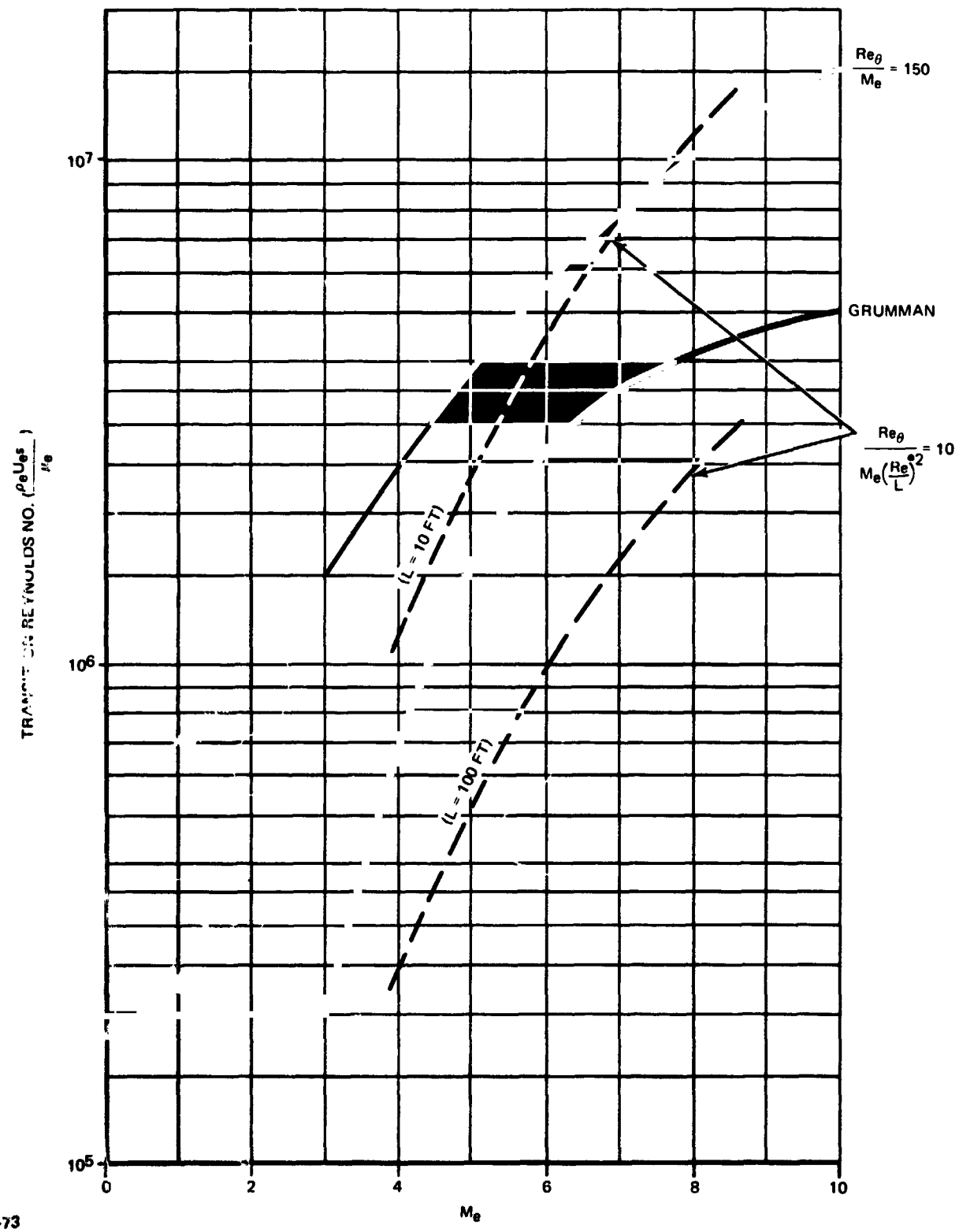

Fig. 8.3.5-26 Reentry Transition Criteria

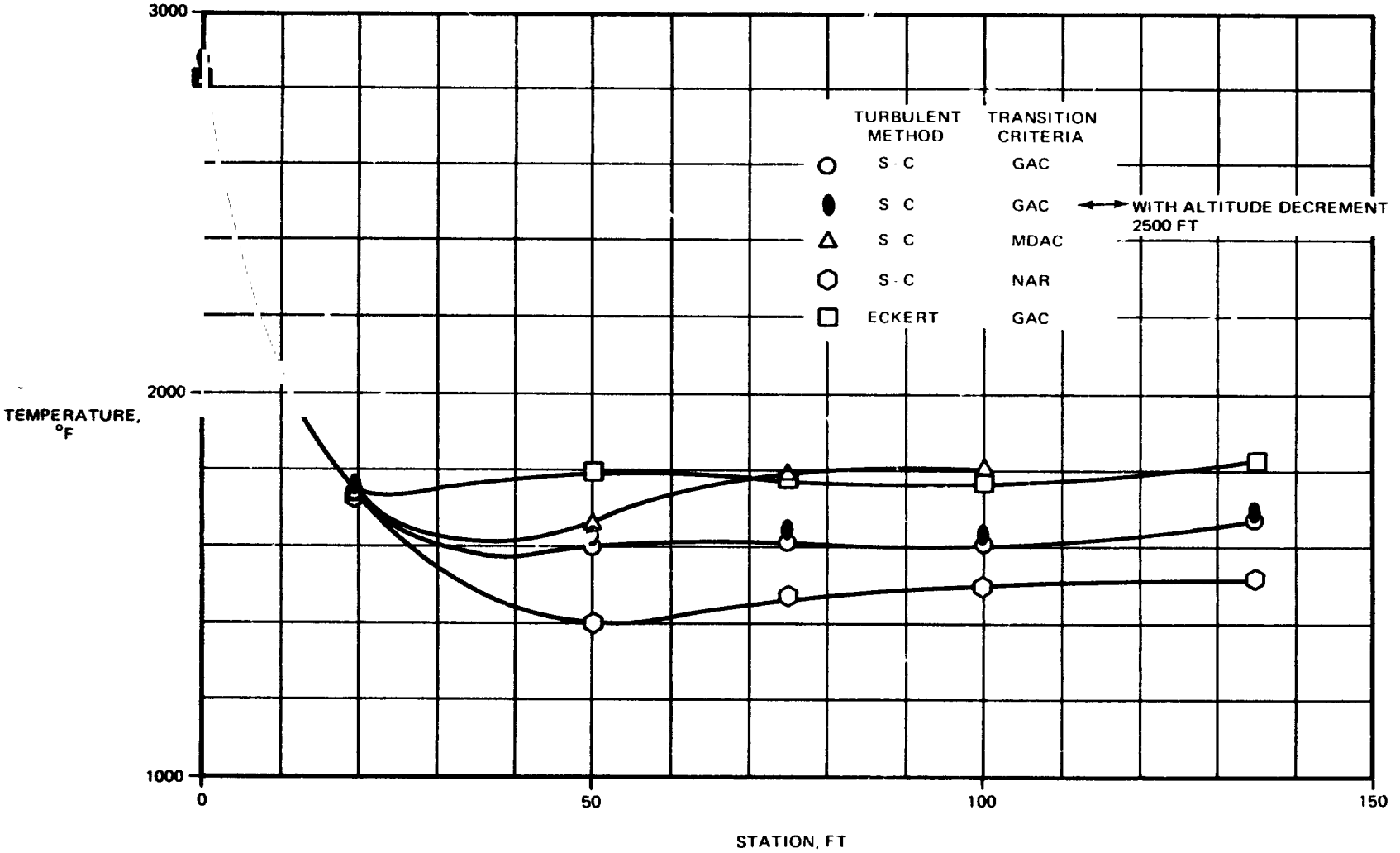

Fig. 8.3.5-27 Sensitivity of Reentry Maximum Temperature On The Windward Centerline To Methods & Criteria, a = 27°

8.3.5.5.3 Leeside Heating

Analytical definition of the heating environment on lee surfaces is complicated by vortical fluid motions involving complex viscous inviscid interactions. A complete description of this fluid behavior is not currently in hand so that one must rely upon experimental heat transfer results, with the full realization that such information is not without limitations. It must be appreciated that the particular test facility employed will not duplicate all relevant fluid dynamic and thermodynamic parameters such as the freestream Mach number, Reynolds number, and enthalpy levels. However, in the absence of closer simulation or more reliable scaling laws, the weight of experimental results as evidenced on both simple shapes and shuttle configurations cannot be dismissed.

Examination of experimental heat transfer results obtained on the lee surfaces of basic configurations (cones, half-cones, delta bodies) at angle of attack indicates that the leeward meridian, when shadowed (i.e., in the separated flow region) can experience heating values appreciably higher than when the meridian is not shadowed. These results are shown in Fig. 8.3.5-28 and the attendant higher heat transfer is postulated to be the result of vortical reattachment. Similar results were obtained from a series of tests performed at Grumman on two models, one cylindrical in running length and the other pyramidal in running length, both with triangular cross-sections. These results are shown in Fig. 8.3.5-29.

Although the results of the leeside heating to the basic configurations previously described are not directly applicable to the shuttle configuration, they do provide an insight into the problems that can exist. Experimental data obtained on two different delta wing orbiters (Fig. 8.3.5-30) shows that the leeward meridian, fuselage sides, and wing upper surfaces can experience heating which results in temperatures in excess of 800°F. These results tend to substantiate the trends found on the simple shapes.

The H-33 orbiter leeside temperatures are based upon the experimental results suitably extrapolated to flight conditions. This approach results in a TPS weight penalty on the order of several thousand pounds; a conservatism which is warranted at this point in time, considering the level of the state-of-the-art.

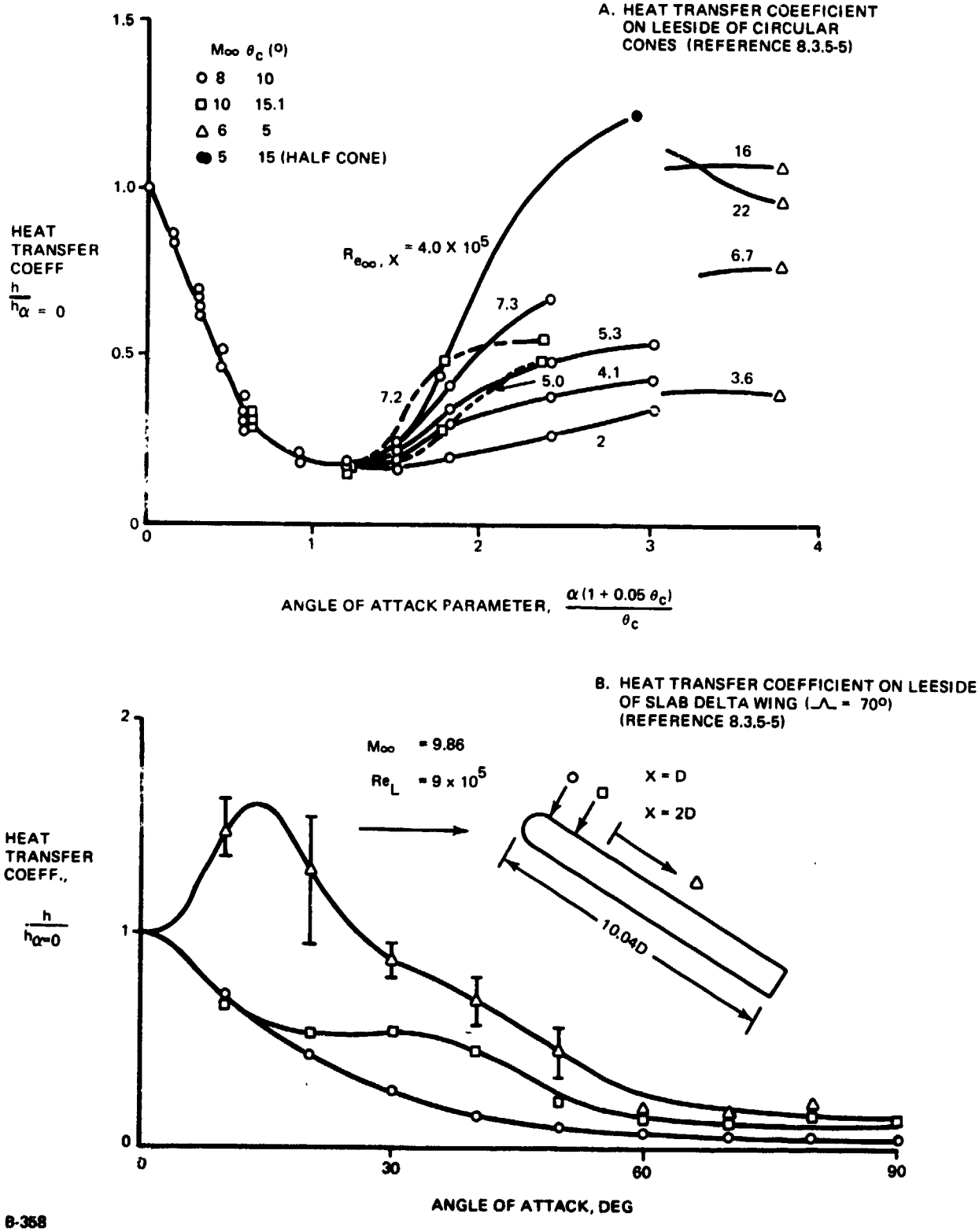

Fig. 8.3.5-28 Leeside Heating on Simple Shape

B/8.3

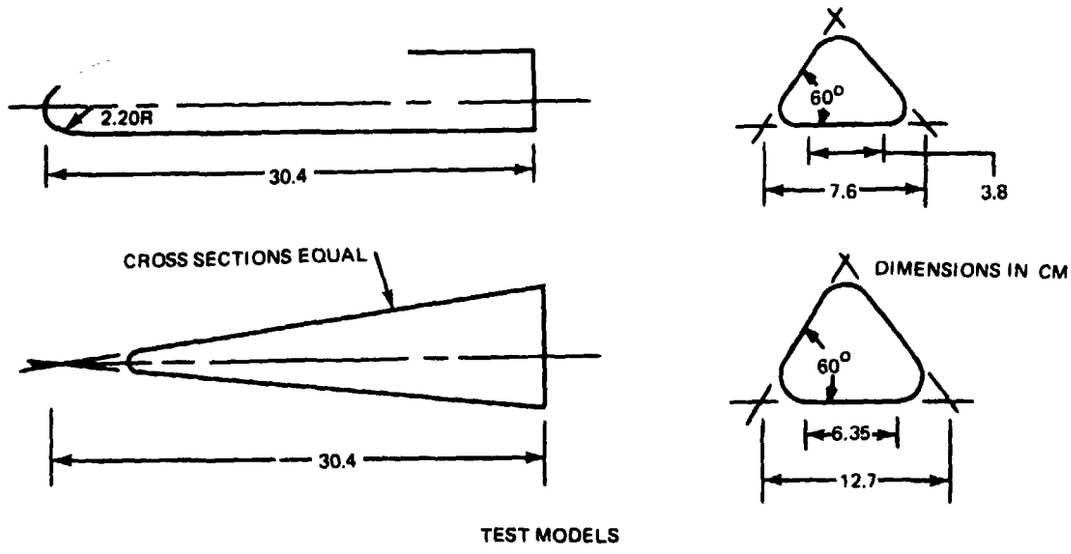

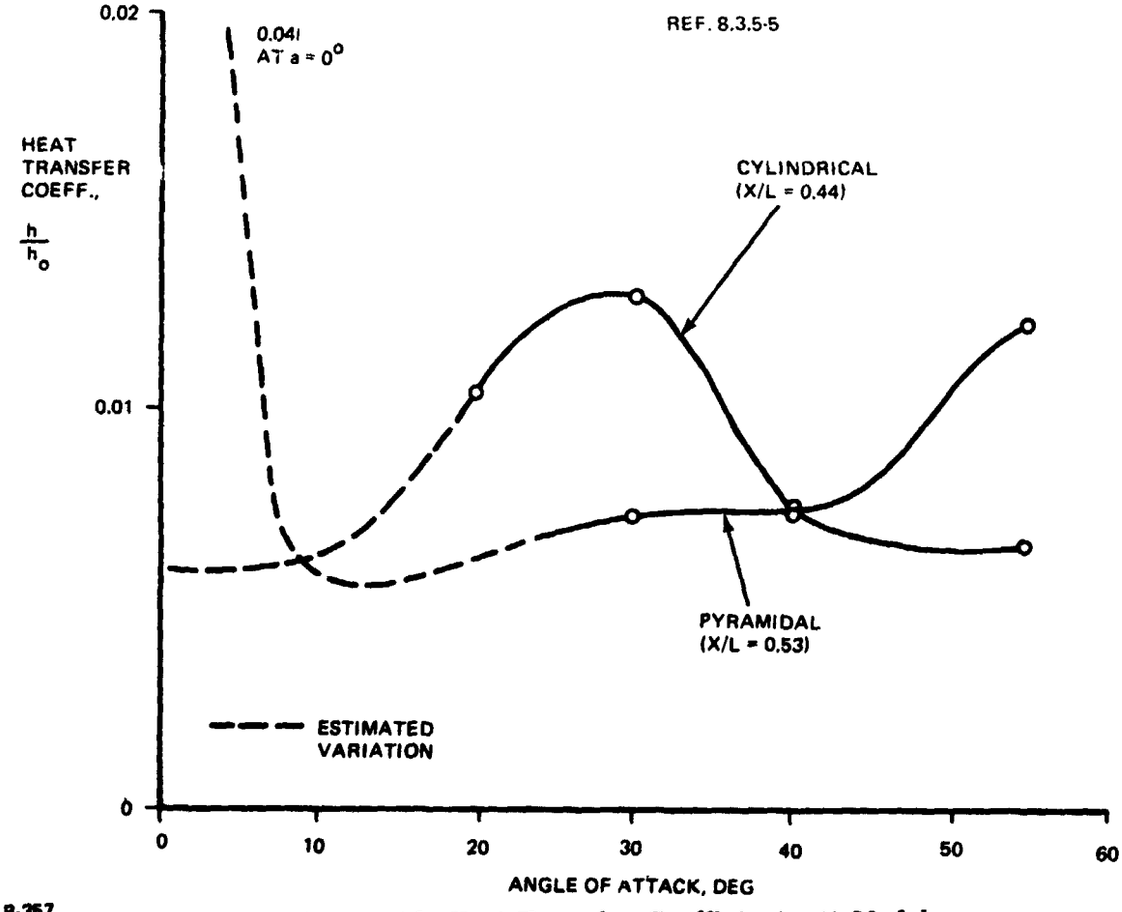

B-357

Fig. 8.3.5-29 Leeside Heat Transfer Coefficients At Model Stations With Equal Cross-Sectional Areas and Running Length Reynolds Numbers

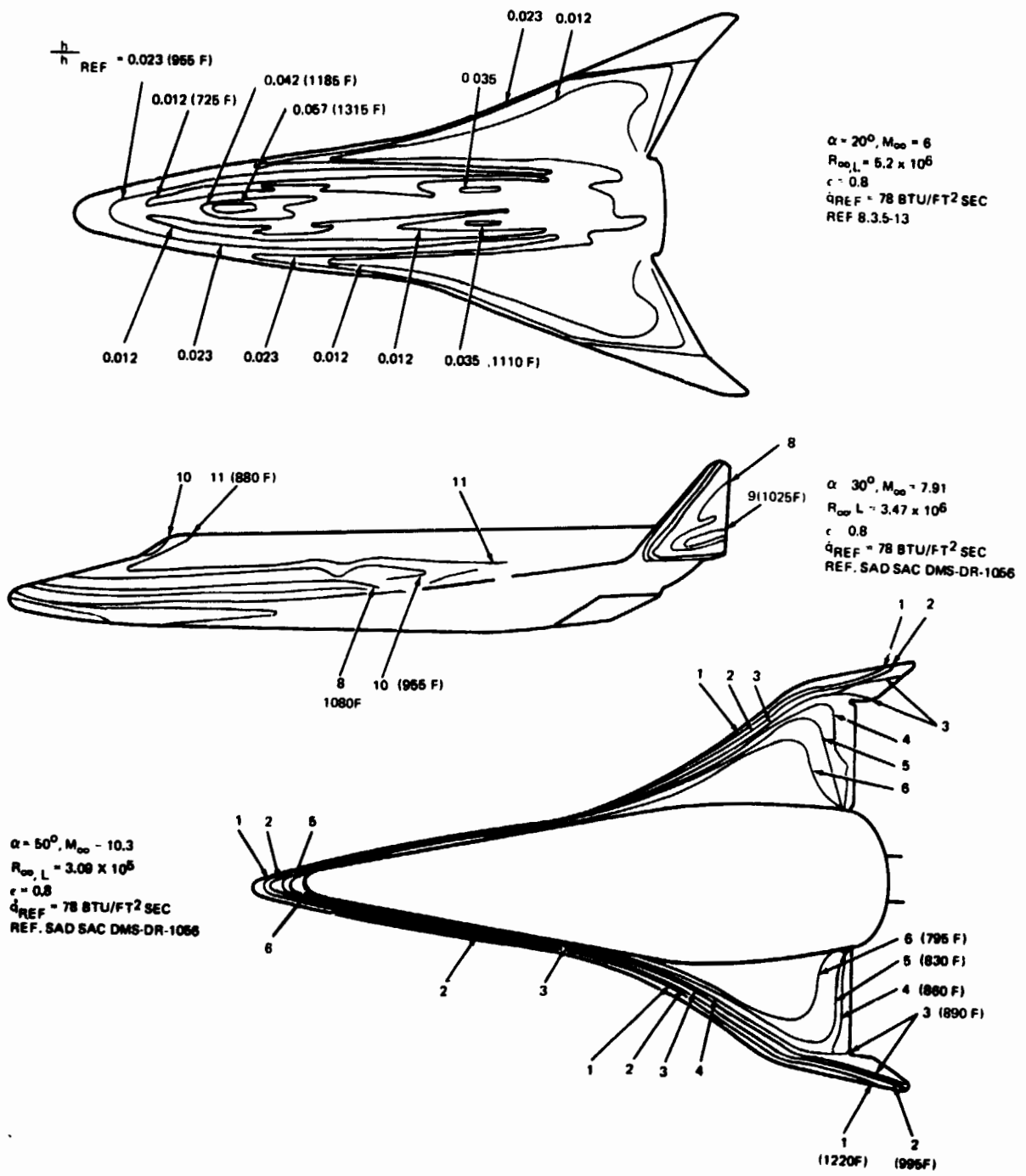

Fig. 8.3.5-30 Heating on Leeside of Delta Wing Orbiters

8.3.5.5.4 Base Heating

The orbiter reentry base heating was determined by the criteria established by MSC in the engine ICD. This method defines the laminar base heating as 0.3% of the stagnation point heating to a one-ft reference sphere. A review of free-flight lifting reentry body base heating data indicated that an accepted correlation procedure is to relate the laminar base heating rate to a percentage of the stagnation point heating rate based on a one-ft reference sphere. However, there exists a rather large disparity of percentages to use for orbiter application: 0.3% (MSC), 2% (MSFC), and 1% maximum (ASSET). A comparison with Korst-Page theory, a standard for theoretical base flow calculations, indicated a percentage slightly less than 0.3%. The 0.3% value is, therefore, a reasonable design value.

Transition to turbulent base heating and the completion of transition were prescribed to coincide with the same occurrence at the aft-most windward centerline position. The completion of transition occurred when the instantaneous local Reynolds number was twice the local transition Reynolds number. The amplification factor relating laminar to turbulent base heating at the completion of transition was defined to be 2.5. To account for the Reynolds number effect in the amplification factor for the remainder of the trajectory, a correction based on the ratio of the stagnation point Reynolds number to its value at the completion of transition was used.

The engine-on ascent base heating values are also based on engine ICD values. These values indicate that the critical design case is the reentry situation. Dornier has completed a study of the engine-on base environment which shows values even lower than those contained in the ICD, further supporting the latter statement. This study is described in Trade Study B35-100RP-104.

8.3.5.6 On-Orbit Tankage Insulation

8.3.5.6.1 Purged HPI System

The baseline insulation for the on-orbit tanks is a purged HPI system. The insulation system consists of a combination of high performance multi-layer insulation (MLI) and external foam insulation. The foam is sprayed on the outer surface of the tank. The MLI blankets are mounted over the foam. It was found that some foam was desirable

for this design to prevent the freezing of condensables and to reduce the cryogen boil-off during ground hold and reentry. The MLI design incorporates reflective shields of double goldized 0.15 mil mylar with 2 layers of thin silk net spacer material interspersed between shields. The outboard portion of the blanket is a buffer of goldized kapton with spacers of Nomex or betaglass netting to withstand the elevated temperatures sustained during the reentry-soakback condition. The shields are perforated (0.5%) to allow for rapid venting of the blankets during ascent.

The insulation scheme is shown in Fig. 8.3.5-31. The insulation layers are held together and laterally supported by injection molded reinforced plastic grommets which are inserted into the blanket after lay-up. The fabricated insulation blanket assembly is attached to the tank by securing the grommets to injection molded reinforced plastic standoffs which are bonded to the foam surface at approximately 4-ft intervals. The long struts on the stand-offs are used to minimize the heat leak. Radiation shield continuity is maintained with layer-to-layer taped over-lap joints. Minimum degradation of the MLI at support and plumbing penetrations is assured by matching the blanket and penetration temperature gradients in order to approximate adiabatic termination.

The purge bag is a clam shell design (Fig. 8.3.5-32). The bag is closed during purging conditions in order to minimize purge gas requirements and can be opened to expose nearly half of the blanket surface area to provide rapid acquisition of interstitial pressure, inside the blanket layers, of 10^{-5} torr during ascent. The insulation is purged during ground hold with GN_2 (GSE) and during reentry with GHe (on board supply).

The installed blanket thermal performance projected for the MLI composite is presented in Fig. 8.3.5-33 and 8.3.5-34, for cryogen temperatures of $40^{\circ}R$ and $170^{\circ}R$ respectively. The performance shown is predicated on Grumman insulation tests conducted with small scale 16 in. dia tanks. The tests were performed with a .25 mil aluminized mylar/nylon netting composite. The spacer material was 5.5 mil unstarched nylon netting of 15 denier. Six fiberglass support struts, plus fill and vent lines penetrating the insulation blanket were integrally wrapped with MLI at a controlled density. This scheme yielded a gross thermal performance of 0.20 BTU/hr-sq ft for a 50 layer blanket based on a tank surface area of 5.58 sq ft and boundary temperatures of $140^{\circ}R$ and $540^{\circ}R$. Confidence in this figure as a realistic and realizable performance

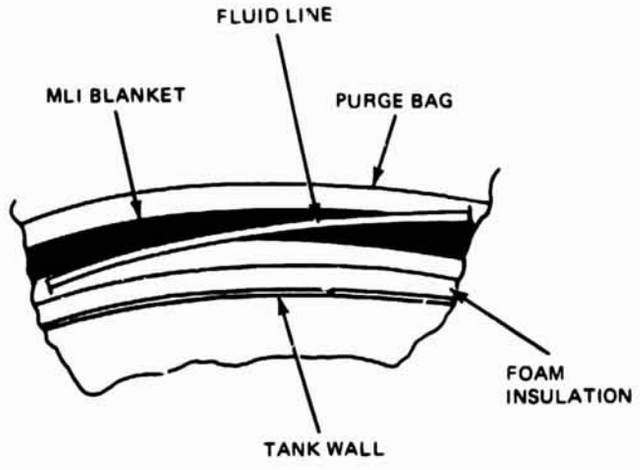

TYPICAL BLANKET WRAP FOR PLUMBING LINE PENETRATION

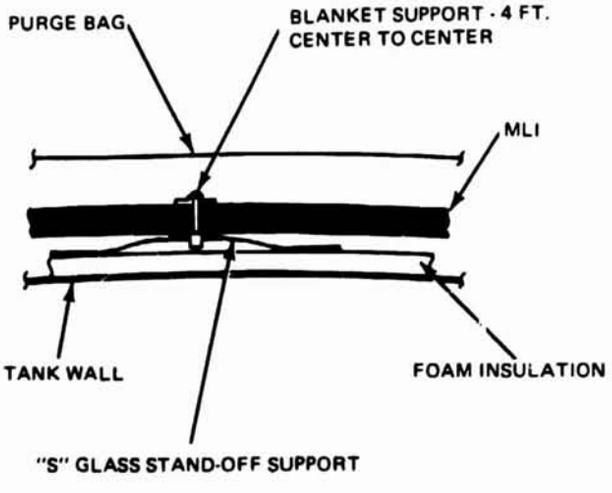

STAND-OFF

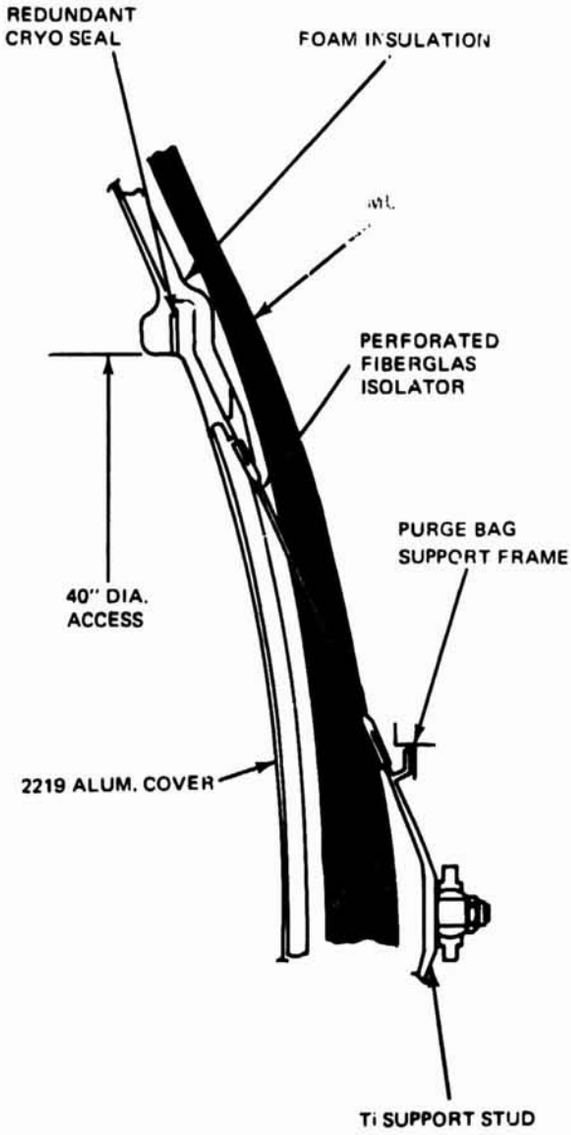

TANK SUPPORT

B-89

Fig. 8.3.5-31 Purged HPT Insulation Scheme

GRUMMAN BOEING

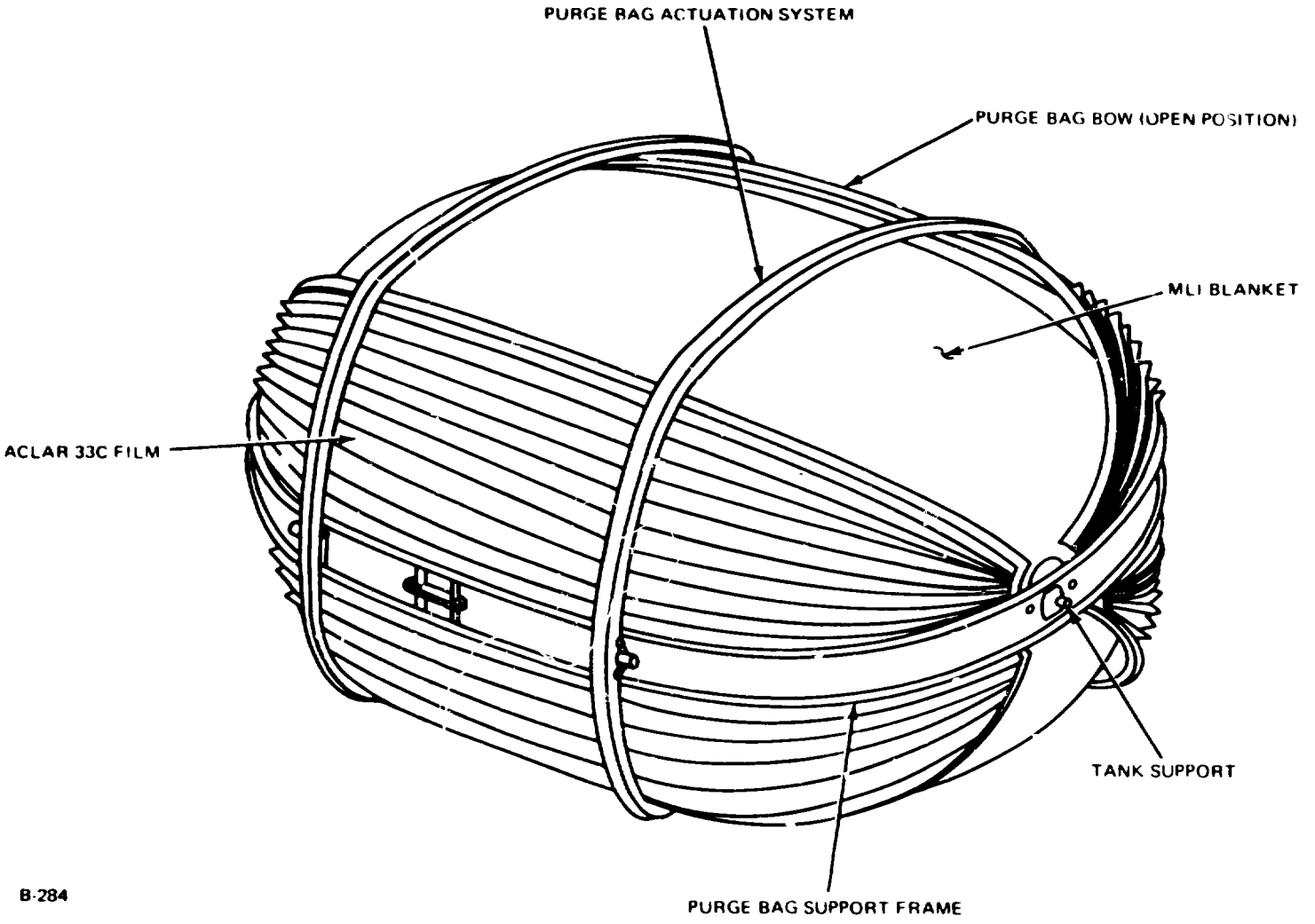

Fig. 8.3.5-32 OMS Purge Bag

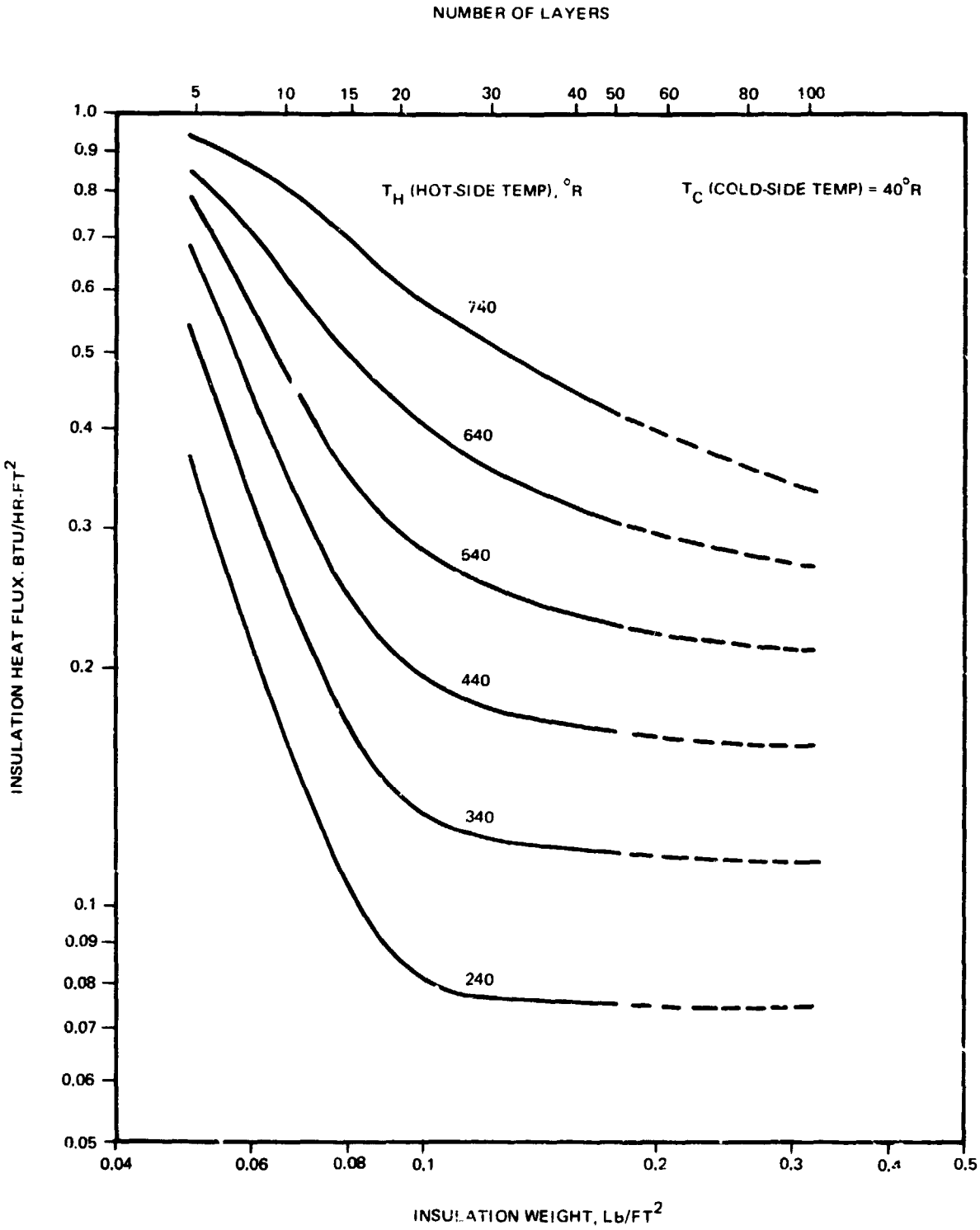

B-286

Fig. 8.3.5-33 MLT Thermal Performance, $T_C = 40^oR$

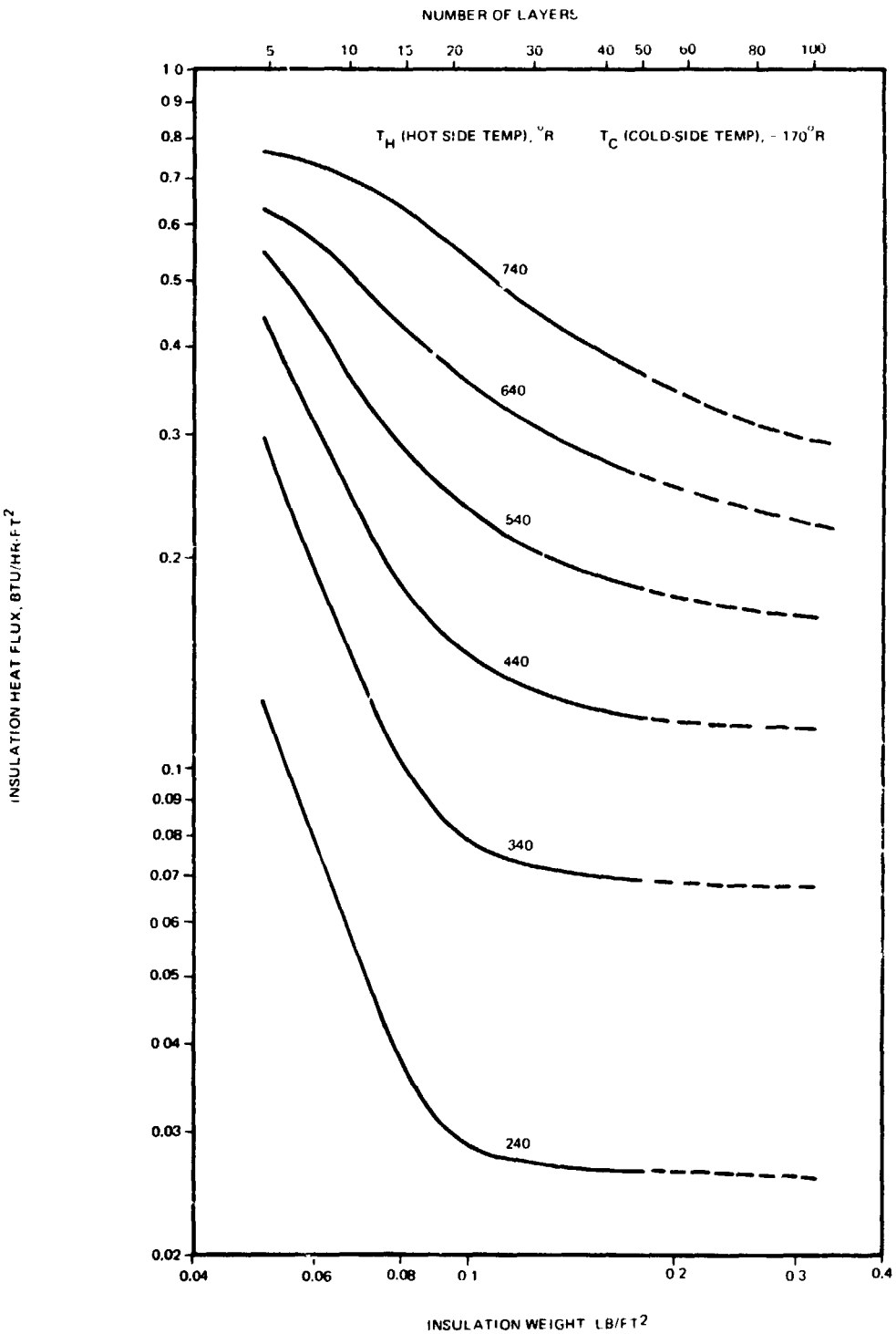

B-267

Fig. 8.3.5-34 MLT - Thermal Performance, $T_C = 170^oR$

in a tank of larger scale is based on the correlation of experimental data with analytical studies and theoretical modeling. The results of this work were presented at the AIAA 5th Thermophysics Conference, June 1970 (Reference 8. 3. 5-10). While the materials tested were not the same as the candidate insulation composite design, they provided the best available data for design purposes, based on the following considerations:

1. The radiation shield used for test was double aluminized mylar which, except for a slightly higher emittance, is similar to the double goldized mylar candidate selected for the design. Since the radiation contribution to the total heat leak can be calculated for the test data, predicted performance can be adjusted for the difference in emissivities of gold and aluminum.

2. The spacer material in the Grumman tests was a double layer of 15 denier nylon net. This material closely approximates the weight and thickness of the candidate silk net cited in Ref. 8. 3. 5-11 and it is expected that it will have similar heat transfer characteristics.

3. The higher temperature Nomex and β- glass netting spacers, selected for the outer layers of the composite, are heavier, stiffer, and denser than the double layer nylon netting spacer, but they have approximately the same thickness. The error involved in assuming identical performance will have relatively little effect on the overall blanket value, since the high temperature composite is a relatively small portion of the overall blanket.

A thermodynamic vent system is used in conjunction with the MLI to maintain subcooled propellants. A number of heat exchange approaches are being considered, with preliminary selection of tank cooling shrouds as the baseline (Subsection 8. 5. 3. 2. 4). Further study of this and alternative approaches, discussed in Subsection 8. 5. 3. 3. 5, is in progress. The insulation designs for the OMS tanks were optimized for the 7 day mission and are presented in Table 8. 3. 5-3.

TABLE 8.3.5-3 PURGED HPI
INSULATION SYSTEM

Cryogen	LH_2	LOX
Tank size	13.5 ft dia x 18.4 ft long	(2) 8 ft dia spheres
Cryogen weight	8150 lb	38,400 lb
Insulation		
No. layers	40	50
Thickness	.8 in.	1 in.
Foam thickness	1 in.	1/2 in.
He purge gas	185 lb	104 lb
Cryogen weight loss	322 lb	278 lb

8.3.5.6.2 Dewar System

The Dewar system offers several advantages over the purged system. These advantages include: lower operational costs and complexity, protection of the MLI from the environment, substantially better thermal performance during ground hold and reentry (and ferry flight) and simplification of ground test requirements. In addition, the Dewar system does not require the development of a reusable ground hold insulation. Based on these considerations, a Dewar system for the OMS tanks is presently being investigated. The configurations being evaluated include: self-supporting vacuum jackets of both sandwich and stiffened skin construction, and a tension membrane vacuum jacket supported longitudinally on the internal pressure vessel.

Sandwich and ring-stringer designs resist external pressure by means of their compressive capability and are designed to resist buckling. Due to the magnitude of the load and the size of the structure, the materials involved work at low or moderate stress levels. In an attempt to use material at a higher stress level, the tension membrane design resists pressure over large areas by using the material in tension with intermediate compression rings carrying the transverse component of the membrane load. End dome loads and the longitudinal membrane load component are transferred to the

inner vessel. For the diameters and volumes being considered, this loading has little effect on the design of the pressurized inner vessel. Assuming that the hoop load in the membrane is zero, a shape was determined to carry the pressure load in the desired fashion. A schematic of the tension membrane design is shown in Fig. 8.3.5-35. A more detailed description of these designs is contained in Reference 8.3.5-12.

The primary insulation system for OMS Dewar tanks is a high performance, lightweight multilayer insulation (MLI) which provides essentially identical thermal performance for ground hold and on-orbit periods. The blanket composite and support system are similar to that described for the purged system. The Dewar design will employ gold coatings on the MLI, as in the purged scheme, in order to mitigate the consequences of accidental exposure of the MLI to moisture during the operational life of the tank. The buffer region required to withstand the elevated temperatures during reentry will be smaller for the Dewar tank, due to the heat sink capability of the outer shell.

A summary of the insulation designs and performance are shown in Table 8.3.5-4.

TABLE 8.3.5-4 DEWAR INSULATION PARAMETERS & PERFORMANCE

Cryogen	LH_2	LO_2
Tank size	13.5 ft dia x 18.4 ft long	(2) 8 ft dia
Cryogen weight	8150 lb	38,400 lb
Insulation		
No. layers	40	50
Thickness	.8 in.	1 in.
Cryogen weight Loss	175 lb	168 lb

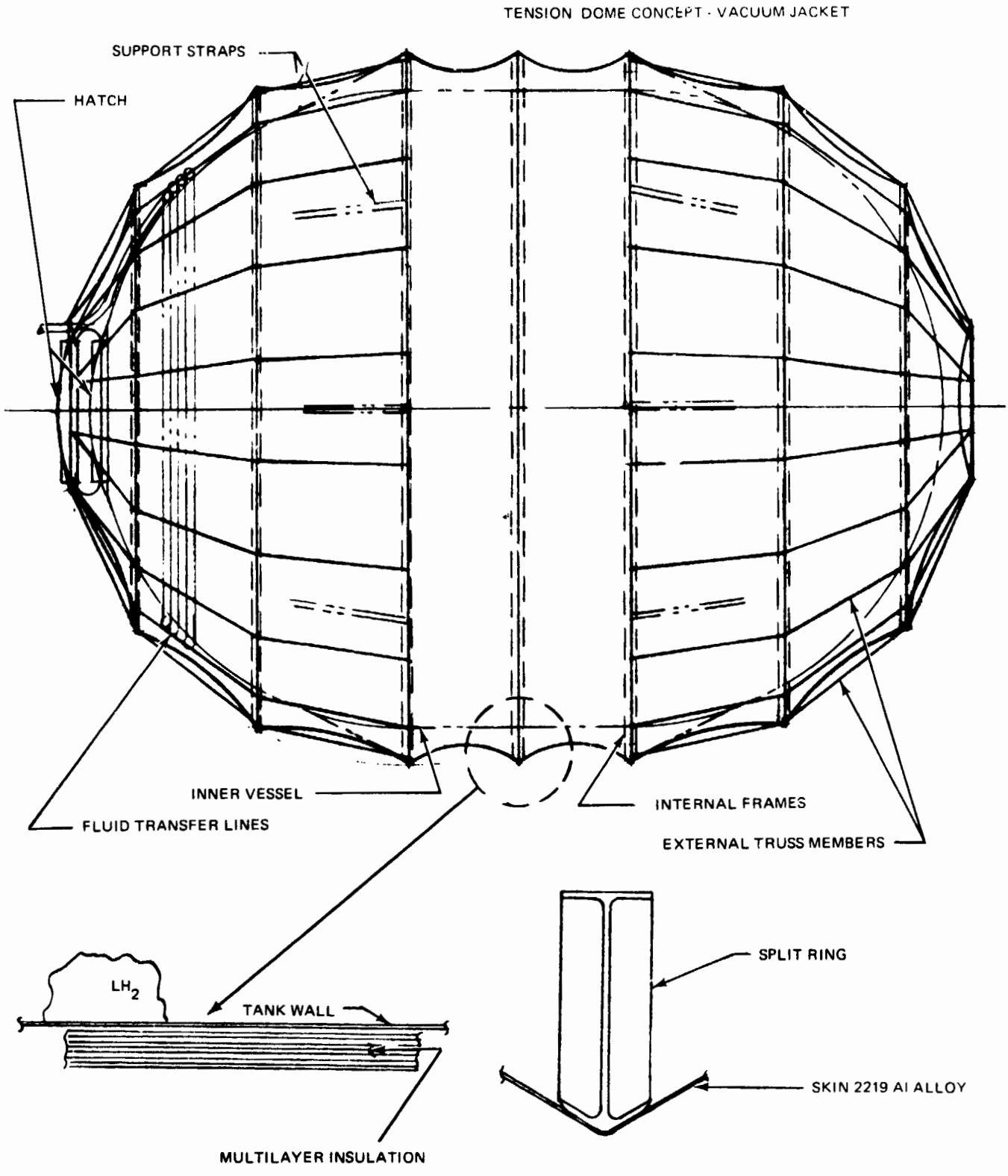

Fig. 8.3.5-35 Schematic of Dewar Tension Membrane

B/8.3

Studies of the Dewar system indicate that the tension membrane represents the lightest weight approach. An aluminum sandwich construction is the next lightest while the ring-stringer design is the heaviest. A comparison of these designs with the purged HPI system is presently being pursued. Indications are that the lightest weight Dewar designs are competitive with the purged system. If this is substantiated, the baseline for the OMS tanks will be revised to a Dewar system based on the advantages noted previously.

8.3.5.7 References

1. "Results of Phase - Change Paint Investigations of Windward, Profile and Leeside Aerodynamic Heating to 1/150 Scale ROS - NB1 and ROS-WB1 Configurations at Mach 8," GAC RPT GFHT -017, April 1971.

2. "Grumman Delta Wing Orbiter ROS-NB2 With External Tanks Tested in the 31" LRC - Continuous Flow Hypersonic Tunnel," AER/T - LRC -1, June 1971.

3. Bourbin, M. "Review of Tank Interference Heating Data from Test H-0602," to be Published.

4. Leng, J., Osonitsch, C., Konopka, W., "Experimental Study of Plume Impingement Heating from Orbiter Main Engines," GAC RPT. 552-1200RD-31, May 1971.

5. Maise, G., "Leeside Heating Investigations," NASA Space Shuttle Technology Conference, Vol. I - Aerothermodynamics, Configurations, and Flight Mechanics, NASA TM X -2272, March 1971.

6. Jew, M., "Perturbations in Aerodynamic Heating Due to Orbiter Sideslip," GAC Memo B35-170M0-42, January 1971.

7. Bourbin, M., "Estimation Procedure for Turbulent Reattachment Heating in Hypersonic Flow," GAC Memo B35-170MO-47, February 1971.

8. Lake, W., "Variations in the Heat Transfer Coefficient for Hypersonic Flow over a Sinusoidal Wall," GAC Memo B31-173MO-23, July 1970.

9. Jew, M., "Boundary Layer Transition Criteria," GAC Memo B35-170M0-75, March 1971.

10. Chau, H. and Moy, H., "Thermal Characteristics of Multilayer Insulation," AIAA Progress in Astronautics and Aeronautics, 24, 1970.

11. "High Performance Thermal Protection Systems," LMSC RPT. A964947, December 1969.

12. "Lightweight Dewar Cryogen Storage System for the Space Shuttle," GAC Report ADR-04-02-71.02.

13. Hefner, J. N., & Whitehead, A. H. Jr., "Leeside Heating Investigations," NASA Space Shuttle Technology Conference, Vol. 1 - Aerothermodynamics, Configurations, and Flight Mechanics, NASA TM -X 2272, March 1971.

SUMMARY OF THERMODYNAMICS TRADE STUDIES

Study	Trade Options	Results	Response
Plume Heating	Single vs. double plume on cylindrical vs. flat booster	Flat Booster - Double Plume is most severe, & test data is a necessity	552-1200RD-31
External Tank Interference Heating	Hemisphere vs. conical vs. contoured tanks	Contour tanks are by far the best from a thermodynamic point of view	AER/T-LRC/CFNT-1
Ice/Frost	Ice/frost formation & propellant residual vs. insulation thickness	Baseline insulation thickness was selected	See Section 8.14.9
Effects of length to dia eter ratio (L/d) on the OMS LH_2 tank	L/d of LH_2 OMS tank vs. tank and insulation weight & propellant boil-off	Low L/d configuration for LH_2 OMS tank is used to optimize vehicle configuration	B35-170 MO-27
Main LOX Tank Purge Requirements	Vehicle temperatures vs. flow rate & inlet temperature	Baseline purge system selected	Memo to be published-results discussed in Section 8.3.5.1
Configuration of OMS Tanks	Dewar design vs. purge bag design	Study in progress.	See discussion in Section 8.3.5.6
OMS Tank Dewar Designs	Sandwich design vs. ring-stringer design vs. tension membrane design	The tension membrane design is the lightest weight approach & has lower fabrication costs than the sandwich construction	GAC Report ADR-04-02-71.02

SUMMARY OF THERMODYNAMICS TRADE STUDIES

Study	Trade Options	Results	Response
Influence of Hypersonic L/D on Vehicle Weights & Temperatures	L/D vs. vehicle weight & temperature for 1500 n. mi. crossrange	Optimum L/D is ~ 15% greater than minimum required to reach given crossrange	GAC Rpt . 552-170RP-1

8.3.6 LOADS AND DYNAMICS

The analyses reported in this section are performed on an early version of the two-engine orbiter designated as the H-3T. A comparison of some significant parameters of the H-3T and H-33 is shown in Table 8.3.6-1.

TABLE 8.3.6-1. COMPARISON OF H-3T AND H-33 PHYSICAL CHARACTERISTICS

Parameter	H-3T	H-33
Gross Lift-Off Weight - lb	4.362M	3.925M
Booster Lift-Off Weight - lb	3.400M	2.824M
Orbiter Lift-Off Weight - lb	962,013	1101,260
Orbiter Landed Weight - lb	237,851	241,172
Design Staging Velocity - fps	8500	7000
Booster Overall Length - ft	261	239
Orbiter Overall Length - ft	156.67	155.2
No. of Booster Injection Engines	10	12
No. of Orbiter Injection Engines	2	3
Sea Level Engine Thrust (each) - lb	550K	415K
Orbiter Exposed Wing Area - sq ft	3100	2900
Orbiter Exposed Fin Area - sq ft	675	855
Forward Interstage - Orbiter Sta	548	412
Aft Interstage - Orbiter Sta	1400	1572

The primary differences result from the use of three smaller engines on the H-33 instead of the original two, and the reduction in booster staging velocity from 8500 to 7000 fps.

The decision to change from a two-engine to a three-engine orbiter was a recent development. As a result, the time remaining until the end of the contract was too short to permit inclusion of the loads and dynamics analysis of the H-33 in this final report.

However, the two configurations have fundamental similarities. The key differences are: The H-3T 2-engine orbiter fuselage has been extended locally to provide room for the feed line to the third engine on the H-33. The oxygen tank has been enlarged by making better use of existing fuselage space and the external hydrogen tanks extend further aft over the wing. The wing planform has been modified slightly to provide a properly balanced vehicle. The method of interstage connection has been modified on the baseline H-33 arrangement to include a single point drag connection and a longer distance between the fore and aft connections so as to span the booster hydrogen tank and to allow booster interstage structure to be external to the tankage.

The baseline H-33 support arrangement is shown in Fig. 8.3.6-1. An alternate arrangement similar to the H-3T is also shown. The alternate demonstrates the ease with which the baseline H-33 can be modified to be more nearly identical to the H-3T.

An appraisal of the three configurations thus indicates that there are no significant unique problems in the loads and dynamics area on the alternate H-33. Therefore the proper solution of the H-3T design problems can be used directly in the H-33 alternate design. On this basis, the analysis of the H-3T was continued and the results of that work are reported herein.

The baseline H-33 configuration with its significantly different load paths, interstage arrangement and expected change in dynamic response can be only partially evaluated with the present H-3T analyses. It will be necessary to perform additional load and dynamic response calculations to substantiate the extent to which the conclusions formed in regard to the H-3T are applicable to the baseline H-33. However, our experience with the analyses reported herein leads us to believe the H-33 will be satisfactory and will have no significiant new design problems. The final decision as to which H-33 arrangement is best will await the outcome of further studies to determine weight and cost of alternate arrangements.

8 3.6.1 Vehicle Description - H-3T

The loads and dynamic analyses were performed on the H-3T configuration. The applicability of the H-3T analysis to the H-33 is discussed in subsection 8.3.6. The mated H-3T configuration is shown in Fig. 8.3.6-2.

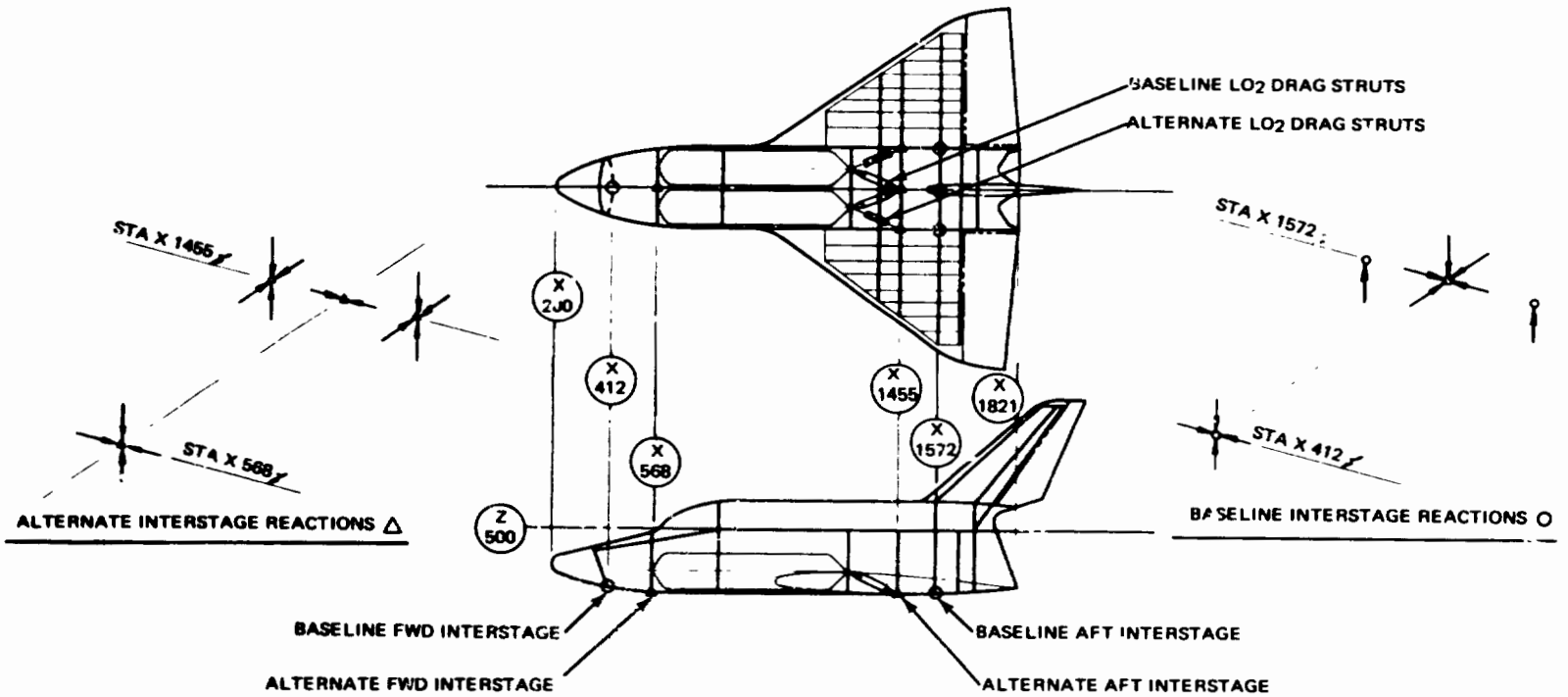

NOTE: FOR CLARITY HYDROGEN TANKS NOT SHOWN

Fig. 8.3.6-1 H-33 Baseline and Alternate Interstage Arrangement

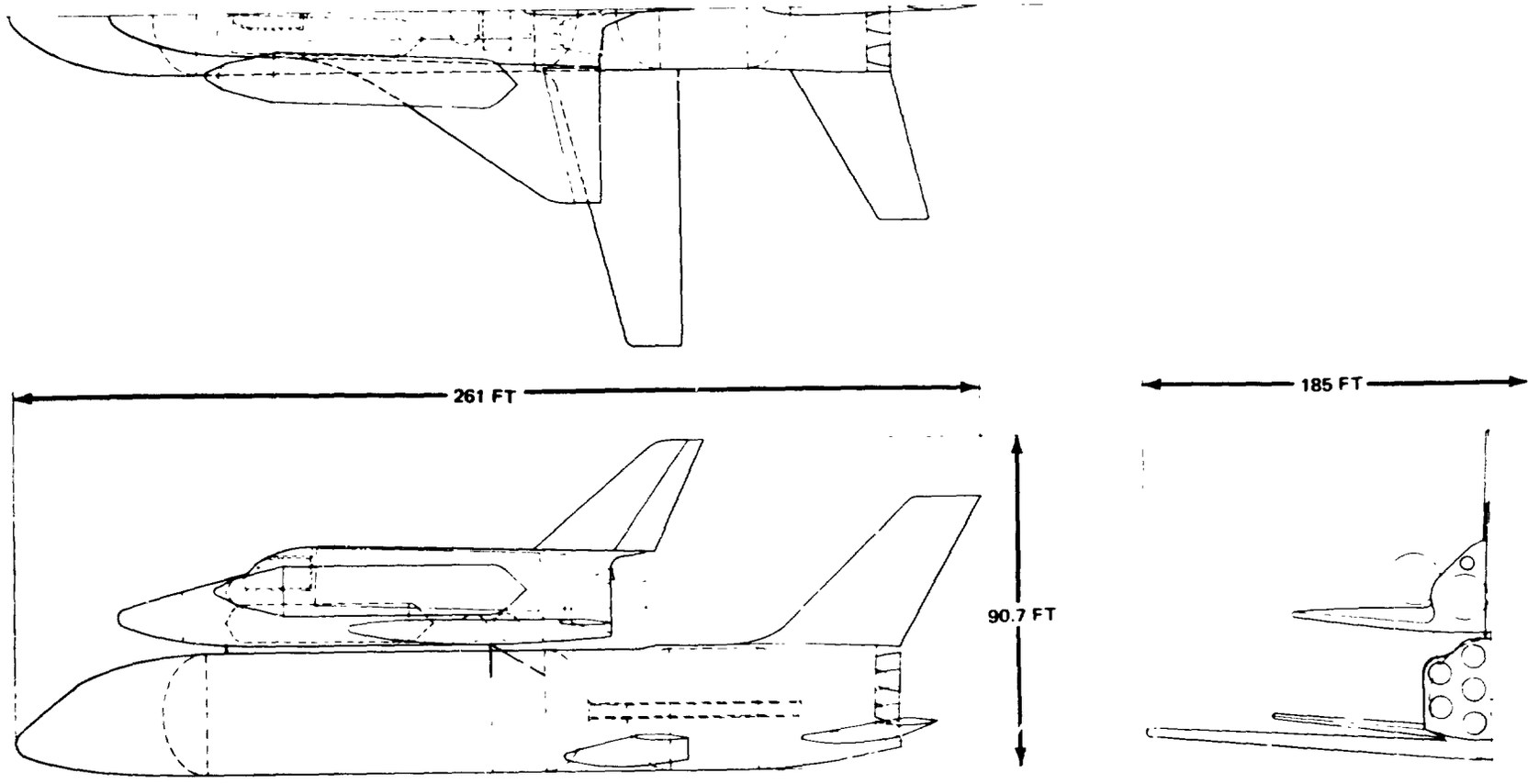

B-115

Fig. 8.3.6-2 Mated H-3T External Hydrogen Tank Orbiter/Heat Sink Booster

The H-3T heat sink booster has a straight wing, ten rocket engines, and nine air breathing engines. It has a lift-off weight of 3,400,000 lb, an injection weight of 726,000 lb, and a landed weight of 637,800 lb.

The H-3T orbiter shown in Fig. 8.3.6-3 has a delta wing, a single vertical tail, and two injection engines. It has a 65,000 lb payload capability for the due east mission. The H-3T orbiter has a lift-off weight of 962,013 lb and a landed weight of 237,851 lb. The H-3T orbiter weight summary is shown in Table 8.3.6-2.

The injection propellant is carried by two internal non-integral, removable LO_2 tanks at 286,796 lb each and two externally mounted LH_2 tanks at 55,080 lb each. The LO_2 tanks are mounted as directly as possible to the interstage supports to minimize the length of load paths and associated flexibilities. The forward LO_2 tank support is attached directly to the interstage bulkhead at orbiter station 548. The aft support is at station 1213 and is 187 inches forward of the aft interstage to accommodate the structure which transfers the drag load from the tank center line to the interstage support. The external hydrogen tank forward supports also attach to the forward interstage bulkhead. The aft supports attach to the aft end of the orbiter fuselage.

8.3.6.2 Net Rigid Body Loads

8.3.6.2.1 Design Conditions

The H-3T orbiter rigid body loads are based on the design conditions summarized in Table 8.3.6-3. Orbiter fuselage axial loads, shears, bending monents, etc. were calculated for each of the design conditions. In addition, orbiter wing loadings for the max $q\alpha$ and 2.5 g pullout conditions and orbiter fin loadings for the max $q\beta$ condition were obtained. Results of each of the design conditions are discussed in subsection 8.3.6.2.3.

8.3.6.2.2 Basic Loads Data Information

The orbiter rigid body loads were calculated using H-3T weight and rigid body aerodynamic data, together with the results of a six-degree-of-freedom trajectory simulation. The trajectory simulation was performed using synthetic wind profiles and a load alleviation control system which is discussed in more detail in subsection 6.3.1.4. Two orbiter weight configurations were used, namely a liftoff weight of 962,013 lb and a landed

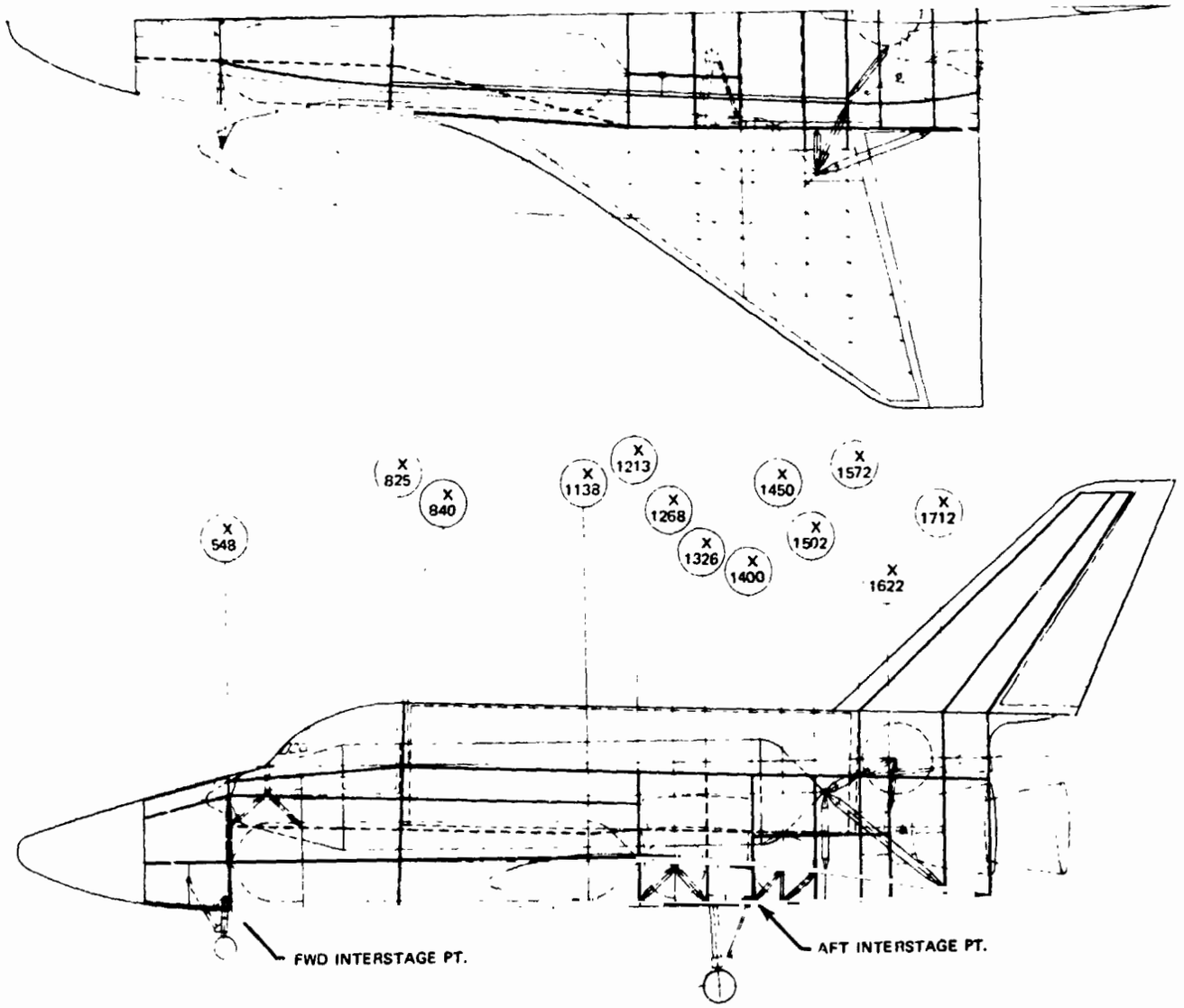

B-132

Fig. 8.3.6-3 H-3T Orbiter Configuration

TABLE 8.3.6-2. H-3T ORBITER WEIGHT SUMMARY

Condition	Lift-off			Landed		
	Weight (lb)	$\bar{X}$	$\bar{Z}$	Weight (lb)	$\bar{X}$	$\bar{Z}$
Body + Contents	217,056	1237.64	433.11	168,520	1193.16	418.613
Wing + Contents (LH)	26,730	1452	322	26,730	1456	314
Wing + Contents (RH)	26,730	1452	322	26,730	1456	314
Tail + Contents	7745	1840	728	7745	1840	728
External H_2 Tank (LH)	55,080	1044	452	-	-	-
External H_2 Tank (RH)	55,080	1044	452	-	-	-
Internal LO_2 Tank (LH)	286,796	875	348	4063	875	347
Internal LO_2 Tank (RH)	286,796	875	348	4063	875	347
Total:	Gear Up			Gear Down		
Weight (lb)	962,013			237,851		
$\bar{X}$ (in.)	1016			1262		
$\bar{Y}$ (in.)	0			0		
$\bar{Z}$ (in.)	380			402		
I_{xx} (slug-ft^2)	4,824,852			2,091,774		
I_{yy} (slug-ft^2)	21,852,500			8,266,965		
I_{zz} (slug-ft^2)	24,486,600			9,275,204		
I_{xz} (slug-ft^2)	1,457,069			122,613		

TABLE 8.3.6-3. H-3T ORBITER DESIGN CONDITIONS

Launch Loads with Ground Winds

Max q α (head and tail winds)

Max q β

Initial 3 g

End Boost

Orbiter Ignition

Orbiter 2.5 g Fullout

Orbiter Landing (five critical conditions)

weight of 237,851 lb. Table 8.3.6-2 presents the orbiter weight summary. The orbiter fuselage weight distribution, without main propellant tanks is given separately in Table 8.3.6-4.

An overlay of three design ground wind profiles is shown in Fig. 8.3.6-4 for the mated H-3T configuration. Ground wind loads were investigated for three directions: (+) wind, (-) wind and side wind. The wind profiles are 10-min mean steady state winds from NASA TMX - 53872 representing the following conditions:

- Two-week standby exposure, 1% risk of exceedance, full tanks, pressurized
- One-day hold exposure, 1% risk of exceedance, full tanks, pressurized
- One-hour exposure, 5% risk of exceedance, full tanks, pressurized

The maximum aerodynamically induced structural loading conditions, max $q\alpha$ and max $q\beta$, occur 63 sec after launch and at an altitude of 28,000 ft. Flight winds and gusts of 95% design wind speed modified to include 99% wind shear and gusts from NASA TMX - 53872 were used. The synthetic wind profile used to calculate the max $q\alpha$ and $q\beta$ loads at 28,000 ft is shown in Fig. 8.3.6-5.

8.3.6.2.3 Discussion of Loads for Each Design Condition

The load conditions and summary of loads are shown in Table 8.3.6-3 and Table 8.3.6-5 respectively. The corresponding orbiter distributed fuselage loads are shown in Fig. 8.3.6-8 through 8.3.6-18. Conditions which have airload distributions as well as inertia distributions include launch, $\pm$ max $q\alpha$, max $q\beta$ and 2.5 g pullout. Landing conditions include air loads with the center of pressure at the vehicle cg. The end boost orbiter ignition conditions include inertia distributions only since the dynamic pressures at these altitudes are negligible. Fig. 8.3.6-6 shows orbiter geometry and sign convention.

Components of the orbiter such as internal LO_2 tanks and external hydrogen tanks have front and rear attachment points. The net loads for each of the tanks are transmitted into the fuselage at these attachment points. Wing net loads given in Table 8.3.6-6, shown acting on the fuselage at one fuselage station, are distributed during structural analysis over redundant wing-fuselage mating structure.

TABLE 8.3.6-4. H-3T ORBITER FUSELAGE WEIGHT DISTRIBUTION (Sheet 1 OF 2)

Condition		Liftoff				Landed			
Panel	Fuse Sta.	Weight	$\bar{X}$	$\bar{Z}$	I_{yy} - slug-ft^2	Weight	$\bar{X}$	$\bar{Z}$	I_{yy} - slug-ft^2
1	200 - 300	1372	260	370	303.8	1372	260	370	403.8
2	300 - 400	1865	353	370	744.7	1865	353	370	744.7
3	400 - 500	4748	450.3	360	2897.2	3742	444	373	2018.3
4	500 - 600	8505	544.3	362.3	1687.5	9511	547.2	346.2	10,127.1
5	600 - 700	9532	642.4	438.1	11,051.6	9532	642.4	438.1	11,051.6
6	700 - 800	8763	751	441	11,565.3	8763	751	441	11,565.3
7	800 - 900	12,517	856.4	456	19,006.2	10,433	853.7	447.7	16,785.2
8	900 - 1000	13,927	950	464.7	21,188.5	10,455	950	454.7	17,925.8
9	1000 - 1100	13,868	1050	463	20,636.2	10,396	1050	453.4	17,446.3
10	1100 - 1200	13,839	1150	460.8	20,067.7	10,367	1150	451.4	16,923.7
11	1200 - 1300	16,955	1245	439.7	27,494.4	13,483	1243.9	427.8	23,101.9
12	1300 - 1400	19,088	1353.9	423.5	34,083.4	13,976	1355.3	419.7	25,544.1
13	1400 - 1500	20,267	1447.8	415.5	35,041.9	14,377	1446.9	414.3	25,186.4
14	1500 - 1600	16,132	1544.6	426.5	20,718.6	14,048	1546.8	419	18,114.9
15	1600 - 1700	50,412	1652.7	435.6	61,203.9	30,934	1660.7	391.9	20,095.4
16	1700 - 1784	5266	1746	418	7014.4	5266	1746	418	7014.4

TABLE 8.3.6-4. H-3T ORBITER FUSELAGE WEIGHT DISTRIBUTION (Cont'd) (Sheet 2 OF 2)

Total		
Wt (lb)	217,056.	168,520
$\bar{X}$ (in.)	1237.64	1193.16
$\bar{Z}$ (in.)	433.11	418.613
I_{xx} (slug-ft^2)	485,284.	400,058
I_{yy} (slug-ft^2)	7136,938.	6,015,946
I_{zz} (slug-ft^2)	7038,266.	5,961,498
I_{xz} (slug-ft^2)	69,977.6	- 28,327

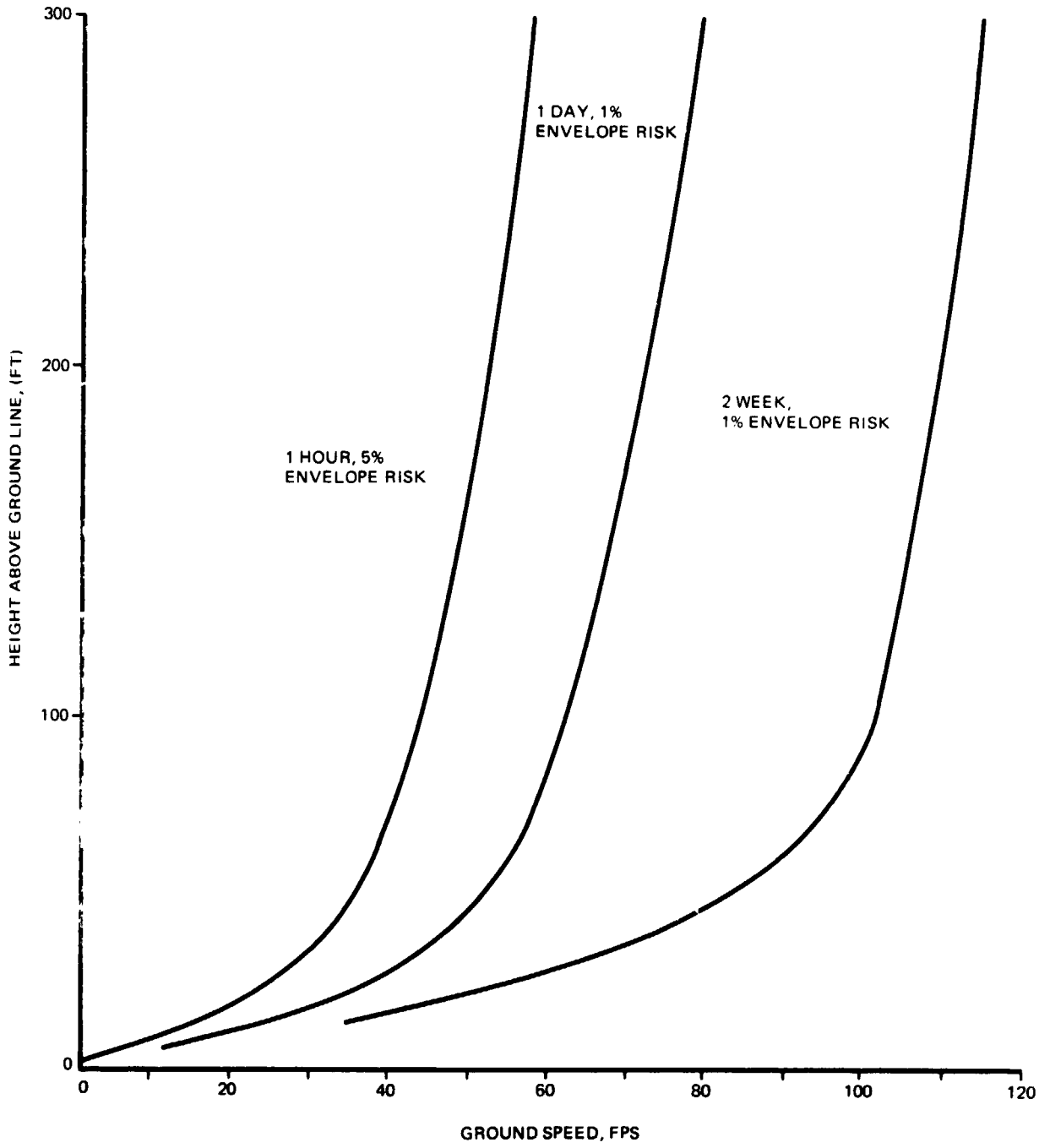

Fig. 8.3.6-4 Ground Wind Profiles

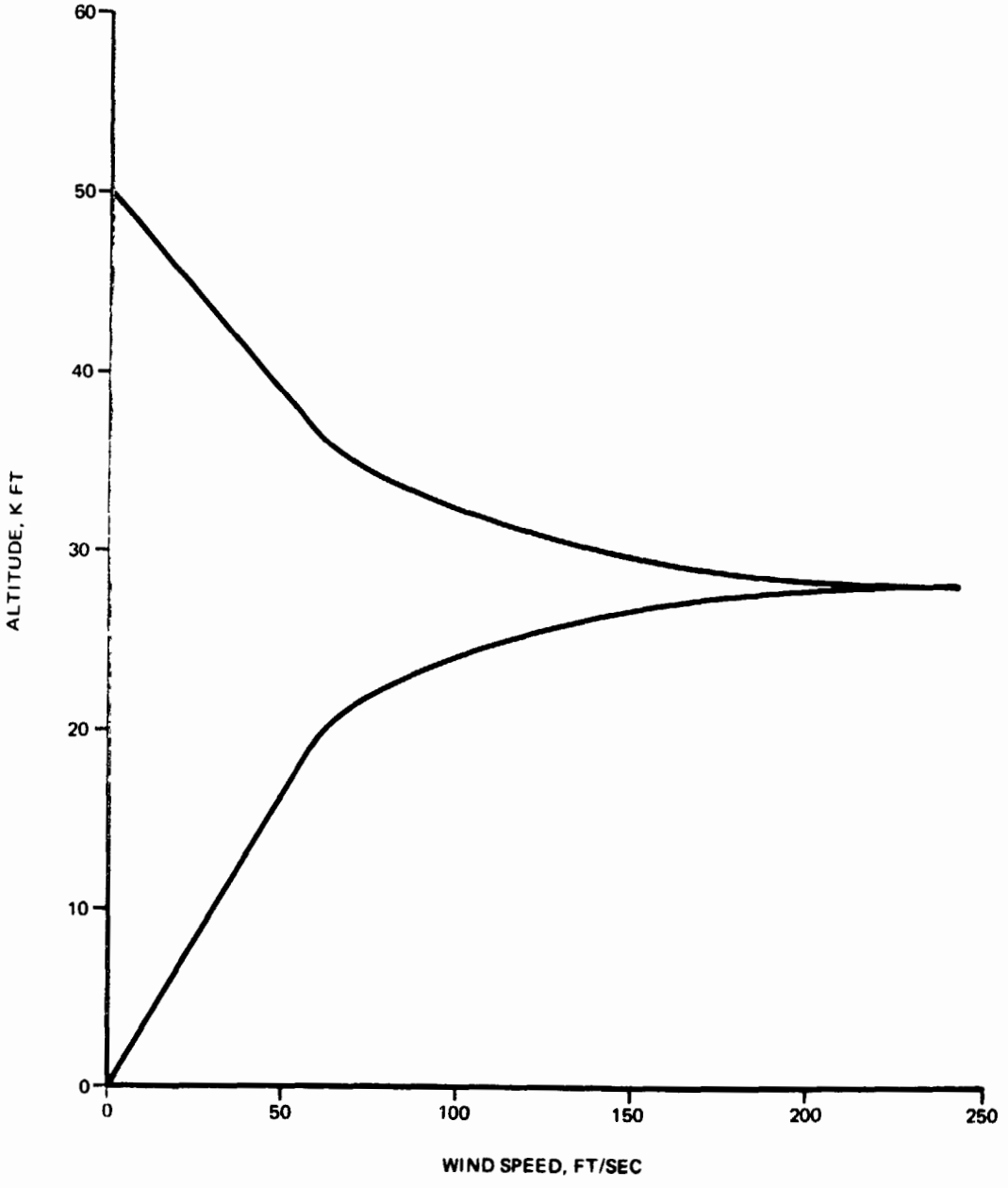

B-130

Fig. 8.3.6-5 Synthetic Wind Profile Corresponding to Maximum Aerodynamic Loading at 28,000 Foot Altitude

TABLE 8.3.6-5. SUMMARY OF APPLIED LIMIT LOADS & LOAD FACTORS OF THE H-3T ORBITER (Sheet 1 of 3)

		Launch Loads with Ground Wind	Max Q α Headwind	Max Q α Tail Wind	Max Q β $+\beta$	Initial 3.0 g	End Boost	Orbiter Ignition	2.5 g Pull-Out	Landing-2 Pt. Tail Down Spin Up	Landing-2Pt Tail Down Spring Back	Landing-2Pt Level Spin Up	Landing Nose Gear Impact-Spin Up	Landing-Nose Gear Impact Spring Back
Flight Parameters														
M		-	1.10	0.952	1.04	5.5	8.4	8.4	0.5	-	-	-	-	-
q	lb/sq ft	3	585.9	435	523.3	0	0	0	300	-	-	-	-	-
α	deg	-	2.22	-7.82	-1.711	-	-	-	-	-	-	-	-	-
β	deg	-	0	0	5.722	-	-	-	0	-	-	-	-	-
Mated vehicles														
n_x		-1.7445	-1.33034	-1.40016	-1.42963	-2.97765	-2.97417	-	-	-	-	-	-	-
n_y		-	-	-	0.20527	0	0	-	-	-	-	-	-	-
n_z		0.13866	0.625536	-0.49496	0.09179	0.36561	0.39294	-	-	-	-	-	-	-
Orbiter														
n_x		-1.7445	-1.32722	-1.39393	-1.42822	-2.97765	-2.97417	-1.45320	0.032785	0.552447	-1.299133	1.000026	0.214420	-.039941
n_y		0	0	0	0.342780	0	0	0	0	0	0	0	0	0
n_z		0.13866	0.635483	-0.47501	0.096311	0.36561	0.39294	-0.018812	2.50	3.093327	2.92533	2.957780	1.904974	2.058011
$\ddot{\theta}_x$	rad/sec^2	0	0	0	-0.08369	0	0	0	0	0	0	0	0	0
$\ddot{\theta}_y$	rad/sec^2	0	0.00526	0.01055	0.00239	0	0	0	0	-0.736629	0.418713	-0.982493	-0.010147	0.38722
$\ddot{\theta}_z$	rad/sec^2	0	0	0	0.01335	0	0	0	0	0	0	0	0	0
Wing Net Loads														
Left Panel	F_z	-15920	178976	-186568	25709	-9773	-10503	503	151819	-92577	-72574	-92256	-50928	-49806
@ WL 310	F_x	46631	141166	188208	71204	79593	79500	38841	-2588	-19254	37275	-32731	-5793	3427
	F_y	0	0	0	-9214	0	0	0	0	0	0	0	0	0
@ sta 1400	M_y	1985800	-2629300	3733914	-32620	1463293	1500156	439942	7188600	7071979	3096523	7655935	2855905	1769568
Right Panel,	F_z	-15920	178976	-186568	8641	-9773	-10503	503	151819	-92577	-72574	-92256	-50928	-49806
@ WL 310	F_x	46631	141166	188208	70610	79593	79500	38841	-2588	-19254	37275	-32731	-5793	3427
	F_y	0	0	0	-9214	0	0	0	0	0	0	0	0	0
@ sta 1400	M_y	1985800	-2629300	3733914	421940	1463293	1500156	439942	7188600	7071979	3096523	7655935	2855905	1769568
Vertical Tail Net Loads														
@ WL 753.66	F_y	0	0	0	136111	0	0	0	0	0	0	0	0	0
	F_x	0	24975	19736	24617	23062	23035	0	1896	540	7323	-1323	-1594	-2224
@ WL 343.5	M_x	0	0	0	-53377290	0	0	0	0	0	0	0	0	0

TABLE 8.3.6-5. SUMMARY OF APPLIED LIMIT LOADS & LOAD FACTORS OF THE H-3T ORBITER (Sheet 2 of 3)

		Launch Loads with Ground Wind	Max Q α Headwind	Max Q α Tail Wind	Max Q β + β	Initial 3.0 g	End Boost	Orbiter Ignition	2.5 g Pull-Out	Landing-2 Pt. Tail Down Spin Up	Landing-2Pt Tail Down Spring Back	Landing-2Pt Level Spin Up	Landing Nose Gear Impact-Spin Up	Landing-Nose Gear Impact Spring Back
Internal LO_2 Tanks														
Left Tank	$F_{y\ front}$	0	0	0	-47647	0	0	0	0	0	0	0	0	0
	$F_{z\ front}$	-20183	-92954	68230	-11732	-53217	-57195	2739	-5155	-4498	-7102	-3592	-3902	-5232
	$F_{y\ aft}$	0	0	0	-47108	0	0	0	0	0	0	0	0	0
	$F_{z\ aft}$	-19584	-89852	66896	-11228	-51638	-55498	2657	-5002	-5070	-6489	-4425	-3796	-4707
	$F_{x\ aft}$	500316	380767	400023	410449	853978	852980	416738	-133	-2671	5520	-4634	-877	387
Right Tank	$F_{y\ front}$	0	0	0	-47647	0	0	0	0	0	0	0	0	0
	$F_{z\ front}$	-20183	-92954	68230	-16717	-53217	-57195	2739	-5155	-4498	-7102	-3592	-3902	-5232
	$F_{y\ aft}$	0	0	0	-47108	0	0	0	0	0	0	0	0	0
	$F_{z\ aft}$	-19584	-89852	66896	-16066	-51638	-55498	2657	-5002	-5070	-6489	-4425	-3796	-4707
	$F_{x\ aft}$	500316	380767	400023	408881	853978	852980	416738	-133	-2671	5520	-4634	-877	387
Net Loads LH_2 Tanks														
Left Tank	$F_{y\ front}$	0	0	0	8660	0	0	0	-	-	-	-	-	-
	$F_{z\ front}$	-5935	-10504	-4492	-5779	-9820	-10554	507	-	-	-	-	-	-
	$F_{y\ aft}$	0	0	0	-14755	0	0	0	-	-	-	-	-	-
	$F_{z\ aft}$	-4946	-17368	12247	-1580	-10318	-11089	530	-	-	-	-	-	-
	$F_{x\ aft}$	96087	112132	103608	114089	164009	163817	80036	-	-	-	-	-	-
Right Tank	$F_{y\ front}$	0	0	0	8660	0	0	0	-	-	-	-	-	-
	$F_{z\ front}$	-5935	-10504	-4492	-8539	-9820	-10554	507	-	-	-	-	-	-
	$F_{y\ aft}$	0	0	0	-14755	0	0	0	-	-	-	-	-	-
	$F_{z\ aft}$	-4946	-17368	12247	-4480	-10318	-11089	530	-	-	-	-	-	-
	$F_{x\ aft}$	96087	112132	103608	113186	164009	163817	80036	-	-	-	-	-	-

TABLE 8.3.6-5. SUMMARY OF APPLIED LIMIT LOADS & LOAD FACTORS OF THE H-3T ORBITER (Sheet 3 of 3)

		Launch Loads with Ground Wind	Max Q α Headwind	Max Q α Tail Wind	Max Q β + β	Initial 3.0 g	End Boost	Orbiter Ignition	2.5 g Pull-Out	Landing-2 Pt. Tail Down Spin Up	Landing-2Pt Tail Down Spring Back	Landing-2Pt Level Spin Up	Landing Nose Gear Impact-Spin Up	Landing-Nose Gear Impact Spring Back
Interstage Loads														
	$F_{y\ front}$	0	0	0	111115	0	0	-	-	-	-	-	-	-
	$F_{z\ front}$	-140613	4521	-347168	-168,115	-194502	-182239	-	-	-	-	-	-	-
Left Aft	F_z	164550	22025	267763	236190	273112	280126	-	-	-	-	-	-	-
	F_x	-839116	-871420	-902343	-836015	-1432269	-1430595	-	-	-	-	-	-	-
Right Aft	F_z	164550	22025	267763	9080	273112	280126	-	-	-	-	-	-	-
	F_x	-839116	-871420	-902343	-836015	-1432269	-1430595	-	-	-	-	-	-	-
Total $F_{y\ aft}$		0	0	0	-63301	0	0	-	-	-	-	-	-	-
Landing Gear Loads														
Nose Gear	F_z	-	-	-	-	-	-	-	-	0	0	0	54600	91000
	F_x	-	-	-	-	-	-	-	-	0	0	0	32000	-28500
Main Gear	F_z	-	-	-	-	-	-	-	-	497900	457990	465660	351000	351000
(Total)	F_x	-	-	-	-	-	-	-	-	131400	-309000	238000	19000	19000

Notes:
1. Orbiter geometry & sign convention shown in Fig. 8.3.6-6.
2. Nose & main gear F_z loads include 1.3 magnification factor.

TABLE 8.3.6-6. SUMMARY OF APPLIED LIMIT LOADS FOR EXPOSED WIND AND VERTICAL TAIL

A) Exposed Wing Panel (per side)

- Moments about fus sta 1400; BL ± 180; WL 310.
- Exposed wing area 1550 sq ft per side.

Condition		F_z, lb	M_y, in-lb	M_x, in-lb (left panel shown)
Maximum	Airload	195,804	-3,916,070	32,895,072
+ $q\alpha$	Inertia	-16,828	1,286,752	-2,372,748
	Net	178,976	-2,629,318	30,522,324
Maximum	Airload	-199,584	3,991,670	-33,530,112
- $q\alpha$	Inertia	13,016	-257,756	1,835,256
	Net	-186,568	3,733,914	-31,694,856
Pullout	Airload	218,644	3,724,251	36,732,192
2.5 g	Inertia	-66,825	3,464,350	9,422,325
	Net	151,819	7,188,601	27,309,867

B) Vertical Tail

- Moments about fus sta 1784; BL 0; WL 577.
- Vertical tail exposed area 675 sq ft.

Condition		F_y, lb	M_z, in-lb	M_x, in-lb
Maximum	Airload	±139,088	±3,428,519	∓22,045,448
± $q\beta$	Inertia	∓2977	∓166,712	±449,527
	Net	±136,111	±3,261,807	∓21,595,921

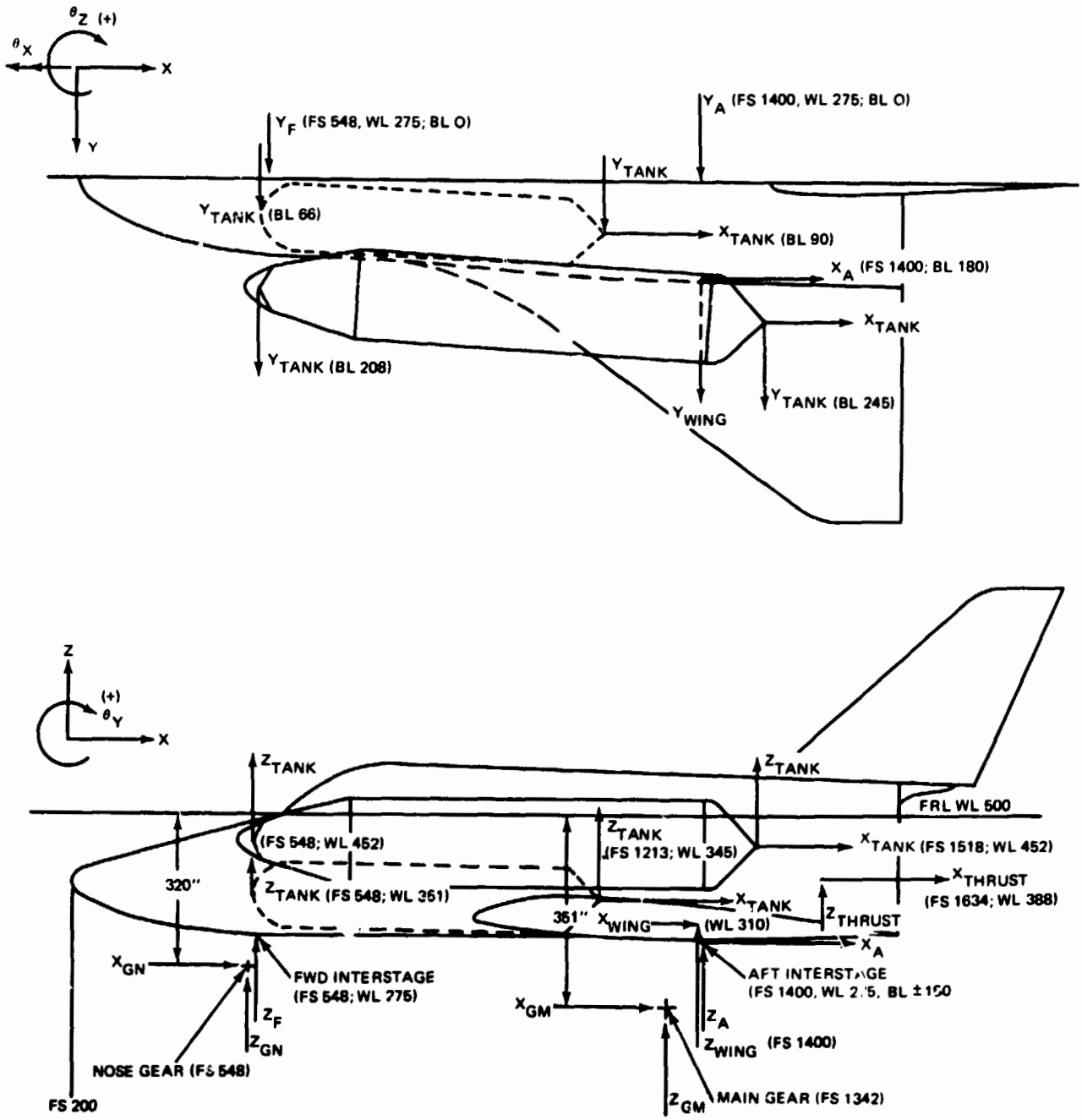

B-131

Fig. 8.3.6-6 H-3T Orbiter Geometry and Sign Convention

The air load distributions over the orbiter are obtained by conventional aerodynamic methods with modification over the orbiter fuselage to account for orbiter-booster aerodynamic interference.

A brief description of each condition follows:

a. Launch Loads with Ground Winds

Ground winds provide critical loads for much of the booster structure. This is discussed elsewhere under booster loads in the present report. For the orbiter, ground winds are not critical and become significant only during launch at lift-off. Rebound (emergency engine shutdown on the pad) is considered less severe for the orbiter than nominal launch, based upon previous dynamic response studies of similarly mated configurations and is not considered here as a critical orbiter design condition.

Wind loads have been calculated using a drag coefficient of $C_D = 1.0$ for exposed wing and fin surfaces and projected areas of the fuselage; and for the external tanks exposed beyond the wing planform $C_D = 0.58$. Also differences in drag of portions of the orbiter fuselage when in the leeside, as opposed to the windward side of the booster, have been taken into account. Steady state horizontal wind loads are multiplied by a factor of 3.0 to account for gusts, dynamic structural response and vortex shedding.

For launch in one-hr winds, a dynamic magnification factor is applied to the interstage thrust fitting to account for release transients. The factor is derived from the assumption that the line of thrust acts through the combined vehicle center of gravity at lift-off. Further, the magnification of net axial load is assumed to vary linearly from 1.25 at the booster gimbal to 3.0 at the booster nose. The resulting longitudinal load factor is 1.75 at the thrust interstage fitting.

A summary of interstage loads for all ground winds is shown in Fig. 8.3.6-7. The most severe ground wind condition for the orbiter occurs at lift-off in a (-) wind. Here, one-hr ground wind loads have been superimposed on no-wind launch loads. Distributed axial loads, shears, and bending moments are shown in Fig. 8.3.6-8.

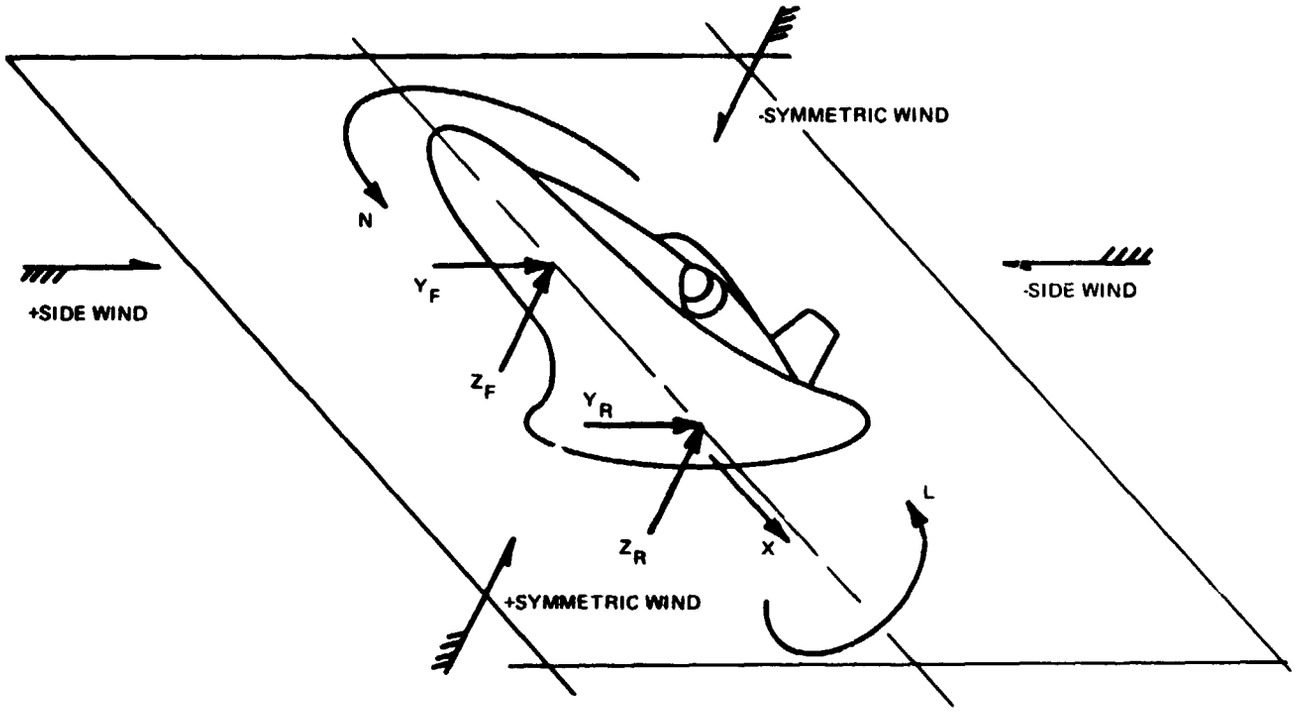

CONDITION	Z_F	Z_R	X	$(Y_F + Y_R)$	L	N
2-WEEK WIND						
+SYM. WIND	-53,557	-171,569	-237,851	—	—	—
-SYM. WIND	+6,744	+244,824	-237,851	—	—	—
±SIDE WIND			-237,851	∓93,816	∓1,872,640	±1,275,790
NO WIND	-36,850	+36,850	-237,851	—	—	—
ONE-DAY WIND						
+SYM. WIND	-131,929	+41,749	-962,013	—	—	—
-SYM. WIND	-104,833	+206,455	-962,013	—	—	—
±SIDE WIND			-962,013	∓37,671	∓731,058	±588,357
NO WIND	-124,208	+124,208	-962,013	—	—	—
ONE-HOUR WIND						
+SYM. WIND	-128,684	+80,900	-962,013	—	—	—
-SYM. WIND	-113,305	+167,393	-962,013	—	—	—
±SIDE WIND			-962,013	∓19,791	∓390,540	±337,000
NO WIND	-124,208	+124,208	-962,013	—	—	—
LAUNCH/REBOUND						
+SYM. WIND	-144,167	+231,140	-1,678,230	—	—	—
-SYM. WIND	-140,613	+329,101	-1,678,230	—	—	—
±SIDE WIND	-146,703	+280,096	-1,678,230	∓19,791	∓390,540	±337,000
NO WIND	-146,703	+280,096	-1,678,230	—	—	—

B-129

Fig. 8.3.6-7 H-3T Interstage Reactions for Design Ground Winds

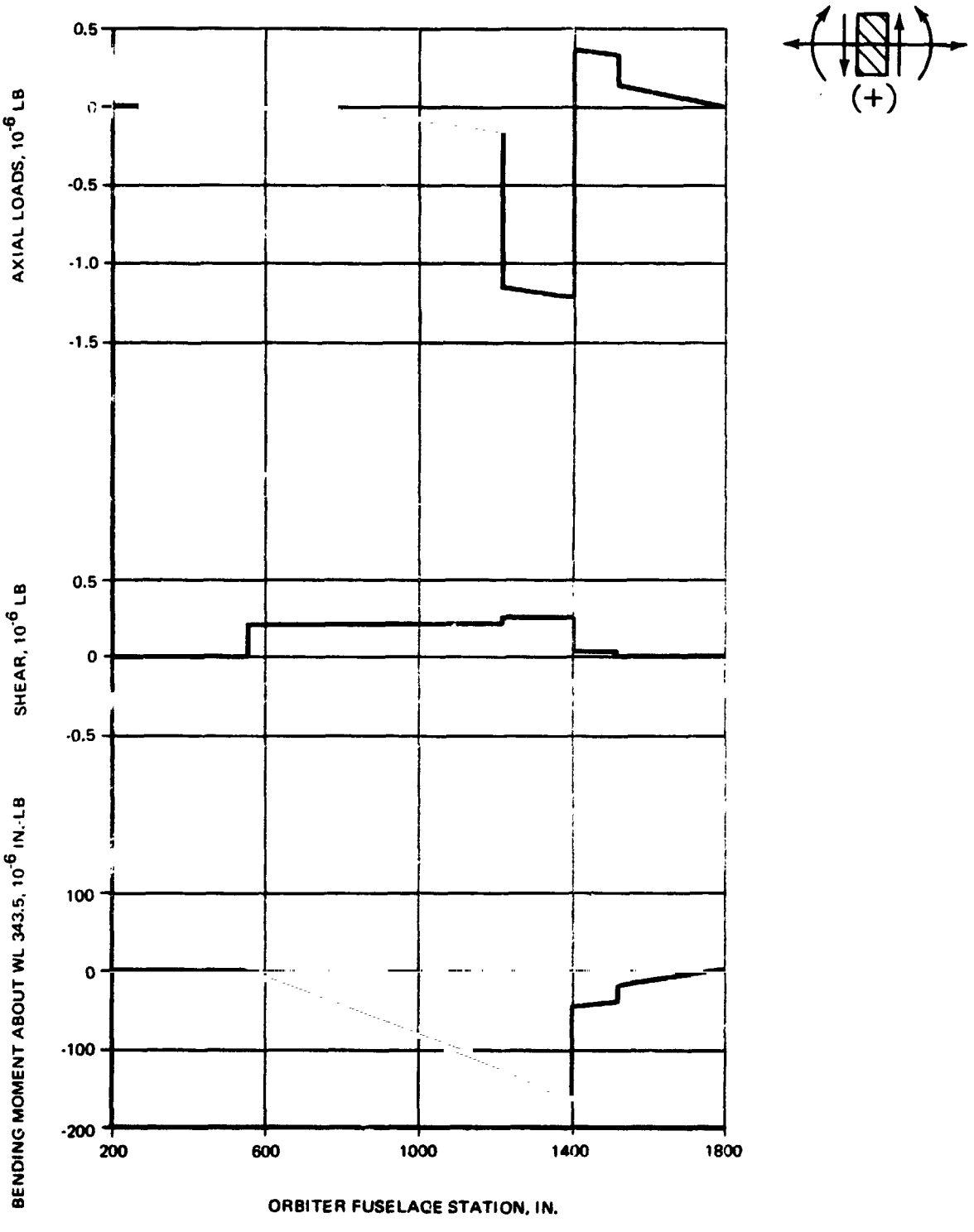

B-136

Fig. 8.3.6-8 H-3T Orbiter Fuselage Distributed Limit Loads, Launch Loads With Ground Winds

b. Max qα

The max qα condition was chosen at a point during the ascent trajectory where the effect of wind speed, vehicle relative velocity, dynamic pressure, and vehicle lift curve slope resulted in a maximum aerodynamic loading. The maximum aerodynamic loading for the H-3T occurs at 63 sec into the flight and at an altitude of 28,000 ft. The max qα as well as the max qβ loads were obtained at this point.

Max qα values of 1300 deg-psf for head winds and -3400 deg-psf for the tail winds were obtained from the trajectory simulation (subsection 6.3.1.4). The value of alpha is referenced to the FRL. These q α's together with the orbiter responses were used to obtain the distributed fuselage loads shown in Fig. 8.3.6-9 and the concentrated loads and load factors shown in Table 8.3.6-5. The wing loadings are shown in Table 8.3.6-6.

The aerodynamic stability of the mated configuration is essentially neutral or slightly unstable in the transonic range where maximum wing loads are encountered. This allows minimum drift guidance to be achieved simultaneously with substantial load relief for the wings. No aerodynamic control such as the use of elevons is required for load relief in the control scheme discussed in subsection 6.3.1.4. Moverever, the line of thrust and wing incidence of the orbiter and booster have been adjusted to provide wing root bending moments which are nearly equal in absolute magnitude regardless of wind direction, as shown in Table 8.3.6-6. Wing root incidence is 2 1/4 deg for the orbiter and 2.0 deg for the booster. Final adjustment of wing root incidence, twist and angular displacement of vehicle centerlines for optimum performance and load relief will depend upon wind tunnel test results.

c. Max qβ

The max qβ condition was attained at the same point of the ascent trajectory as the max qα condition. A qβ of ± 3000 deg-psf combined with a qα of -896 deg-psf results from the side synthetic wind profile shown in Fig. 8.3.6-5.

Max qβ of ± 3000 deg-psf is achieved without the use of aerodynamic control surfaces. Without load relief, the max qβ can be 60% higher and the available 10° of gimbal authority is inadequate to provide roll control. Control mechanization for reducing max qβ is discussed in subsection 6.3.1.4.

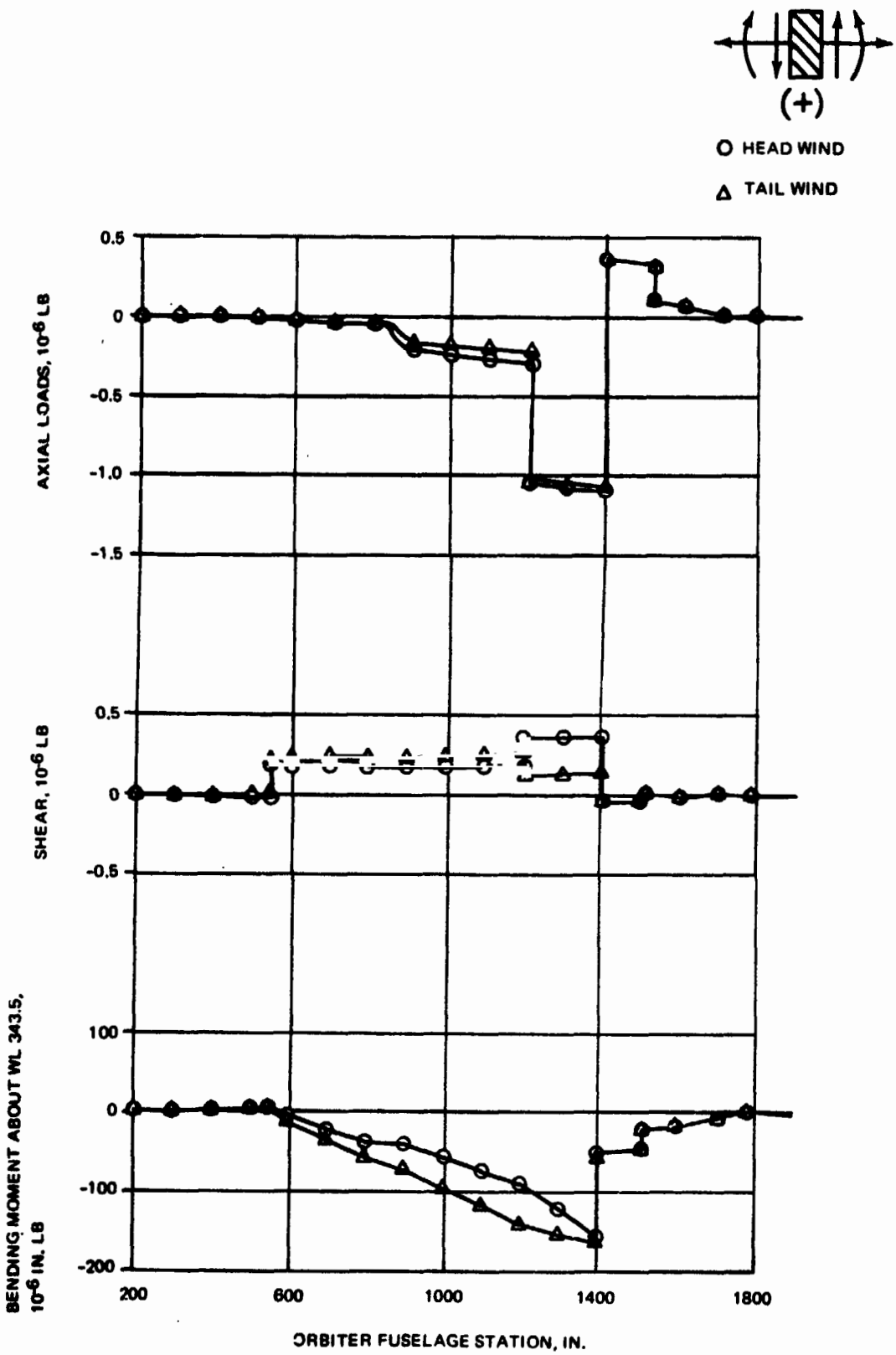

B-137

Fig. 8.3.6-9 H-3T Orbiter Fuselage Distributed Limit Loads, Max Qα Condition

Max q β orbiter fuselage distributed longitudinal loads are shown in Fig. 8.3.6-10 and distributed lateral loads are shown in Fig. 8.3.6-11. The lateral fuselage distributed loads of Fig. 8.3.6-11 and Table 8.3.6-5 are for a $\beta = 5.7$ deg. For a wind from the opp site direction, or $\beta = -5.7$ deg, the distributed lateral loads and concentrated lateral load and lateral load factors will be of opposite direction.

d. Initial 3.0 g and End Boost

The maximum allowable resultant acceleration during ascent is 3.0 g. Initially the 3 g acceleration is reached at 157 sec and at an alittude of 161,500 ft. The final mated 3.0 g acceleration occurs at end boost or 185 seconds and at an altitude of 207,000 ft. Both of these conditions were investigated since they have different vehicle weights and centers of gravity and therefore different axial and normal components of the resultant acceleration. The initial 3.0 g condition imposes higher axial acceleration and the end boost condition ha. higher normal acceleration. The aero forces were neglected during these conditions since they are expected to be very small due to both low dynamic pressure and low lift and drag coefficients at the high Mach numbers. The distributed fuselage loads for the initial 3.0 g and end boost conditions are shown in Fig. 8.3.6-12 and 8.3.6-13 respectively.

e. Orbiter Ignition

Orbiter ignition occurs at 185 sec and at an altitude of 207,000 ft. This condition was chosen because of its compressive loads at the fuselage section between the drag interstage fitting and the thrust structure. The aero forces during the orbiter ignition were neglected for the same reasons that they were neglected during initial 3.0 g and end boost. The orbiter thrust level used for this condition is 699,000 lb per engine which corresponds to the emergency power level which is 7.7% above nominal. Distributed fuselage loads for the oribiter ignition condition are shown in Fig. 8.3.6-14.

f. Orbiter 2.5 g Pullout

Reentry transition to conventional aircraft flight and normal aircraft maneuver has been limited to 2.5 g at q = 300 pst maximum. At q = 300 psf with an arbitrary M = 0.50, the corresponding altitude is 5000 ft. The air load distribution along the orbiter fuselage approximates the inertia distribution, see Fig. 8.3.6-15, indicating a non-critical fuselage shear and bending moment condition. Net wing loads listed in Table 8.3.6-6 are somewhat

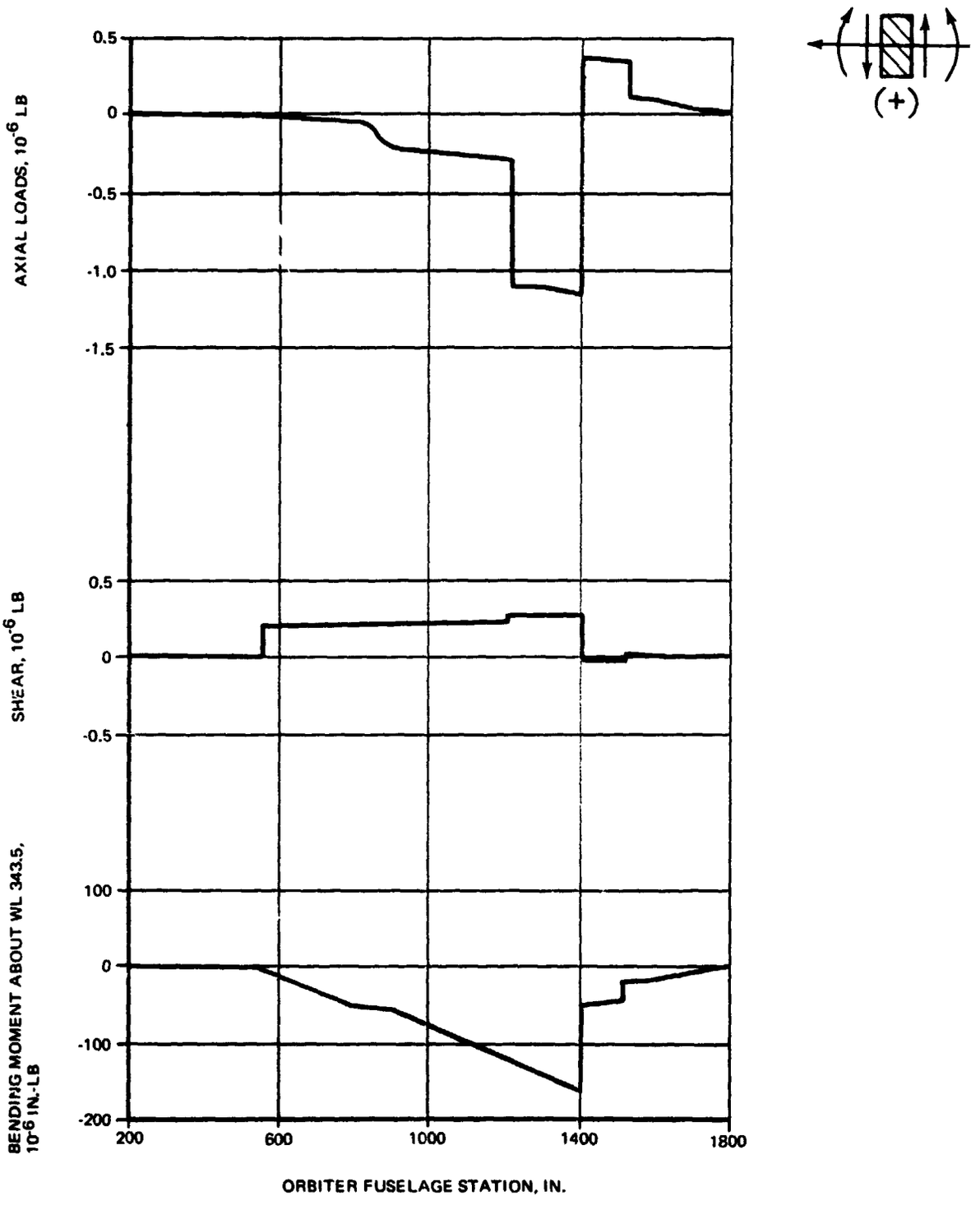

B-136

Fig. 8.3.6-10 H-3T Orbiter Fuselage Distributed Limit Loads, Max QB - Longitudinal Loads

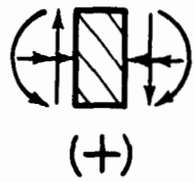

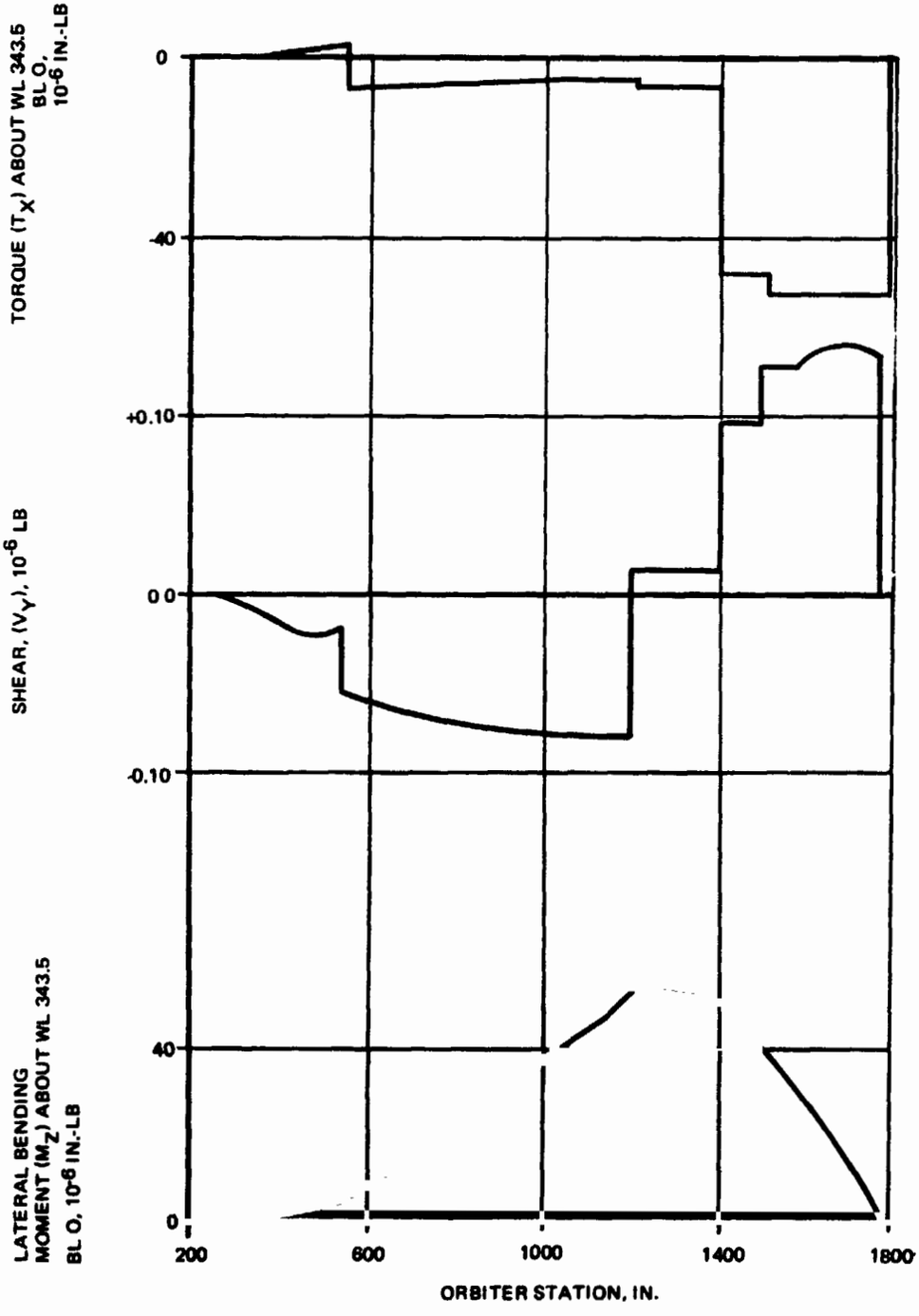

B-139

Fig. 8.3.6-11 H-3T Orbiter Fuselage Distributed Limit Loads, Max Qβ, Yaw Plane Loads

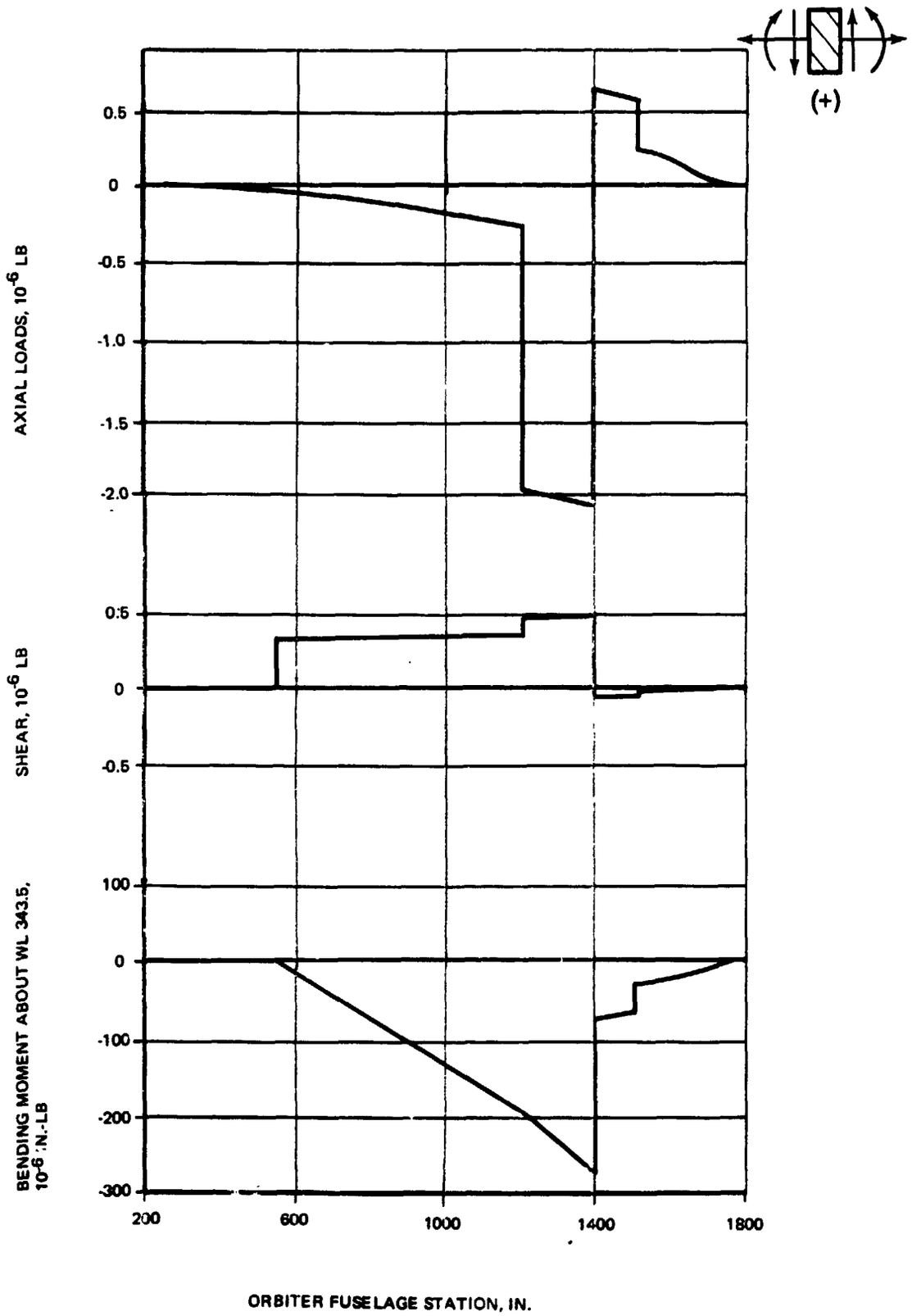

Fig. 8.3.6-12 H-3T Orbiter Fuselage Distributed Limit Loads, Initial 3.0G Conition

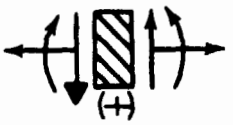

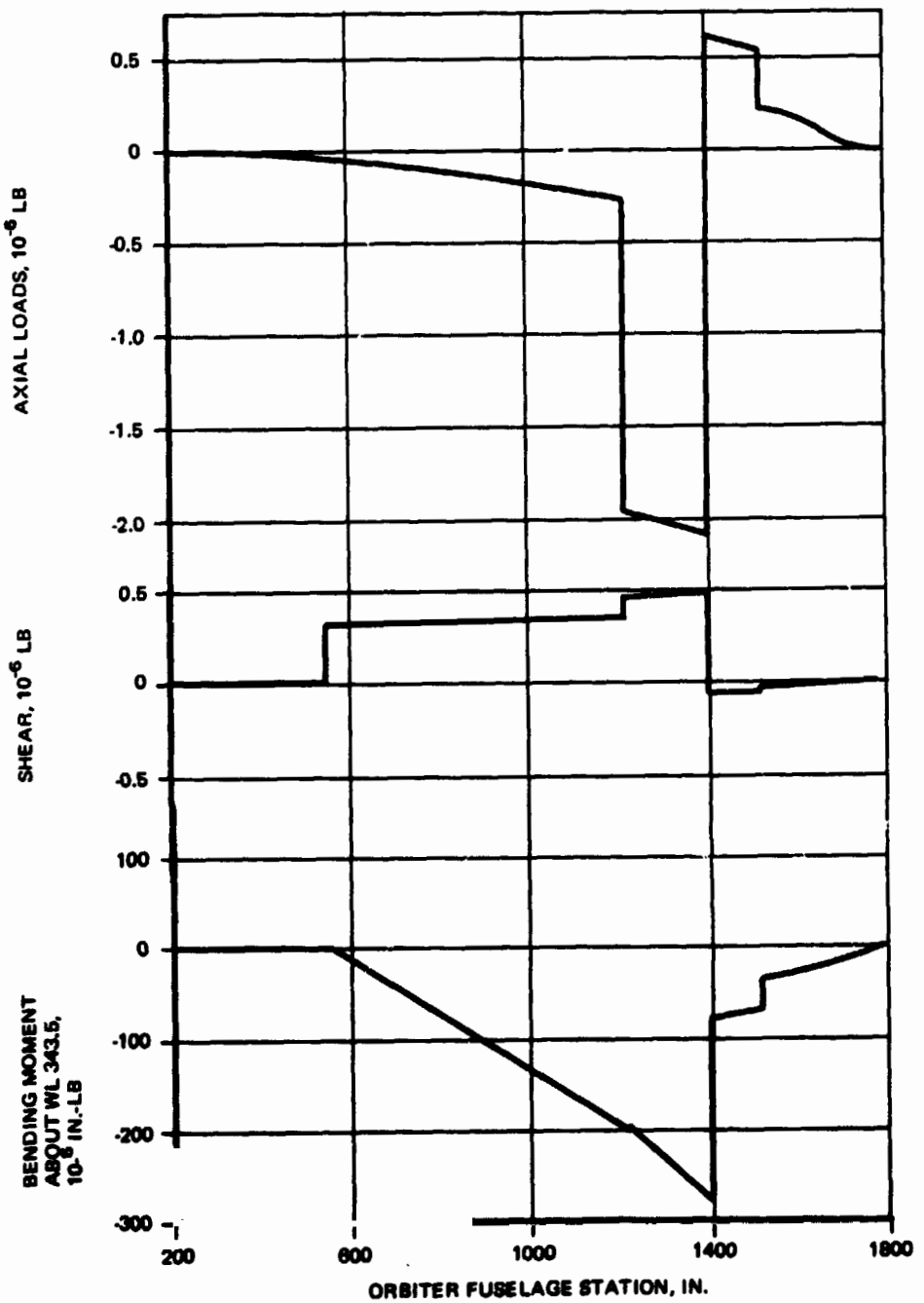

B-141

Fig. 8.3.6-13 H-3T Orbiter Fuselage Distributed Limit Loads, End Boost Condition

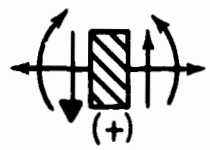

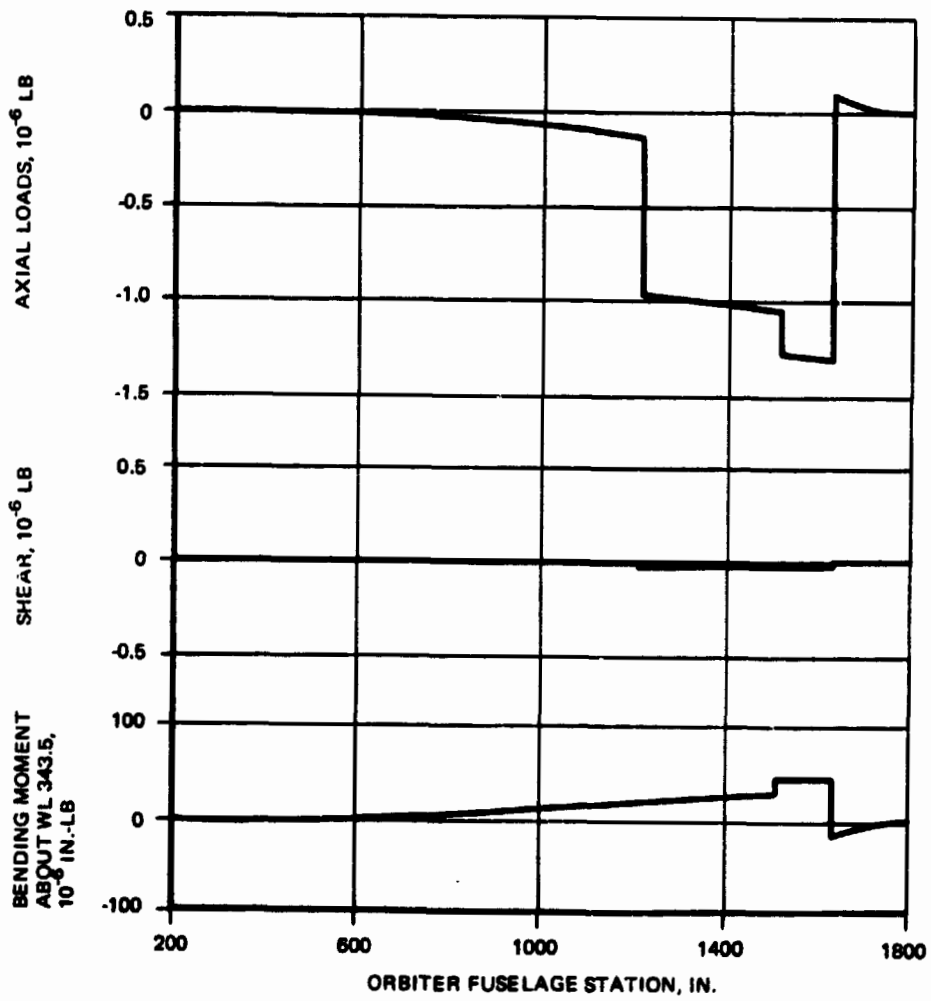

B-142

Fig. 8.3.6-14 H-3T Orbiter Fuselage Distributed Limit Loads, Orbiter Ignition-Emergency Power

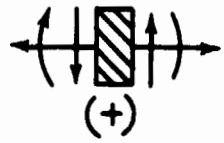

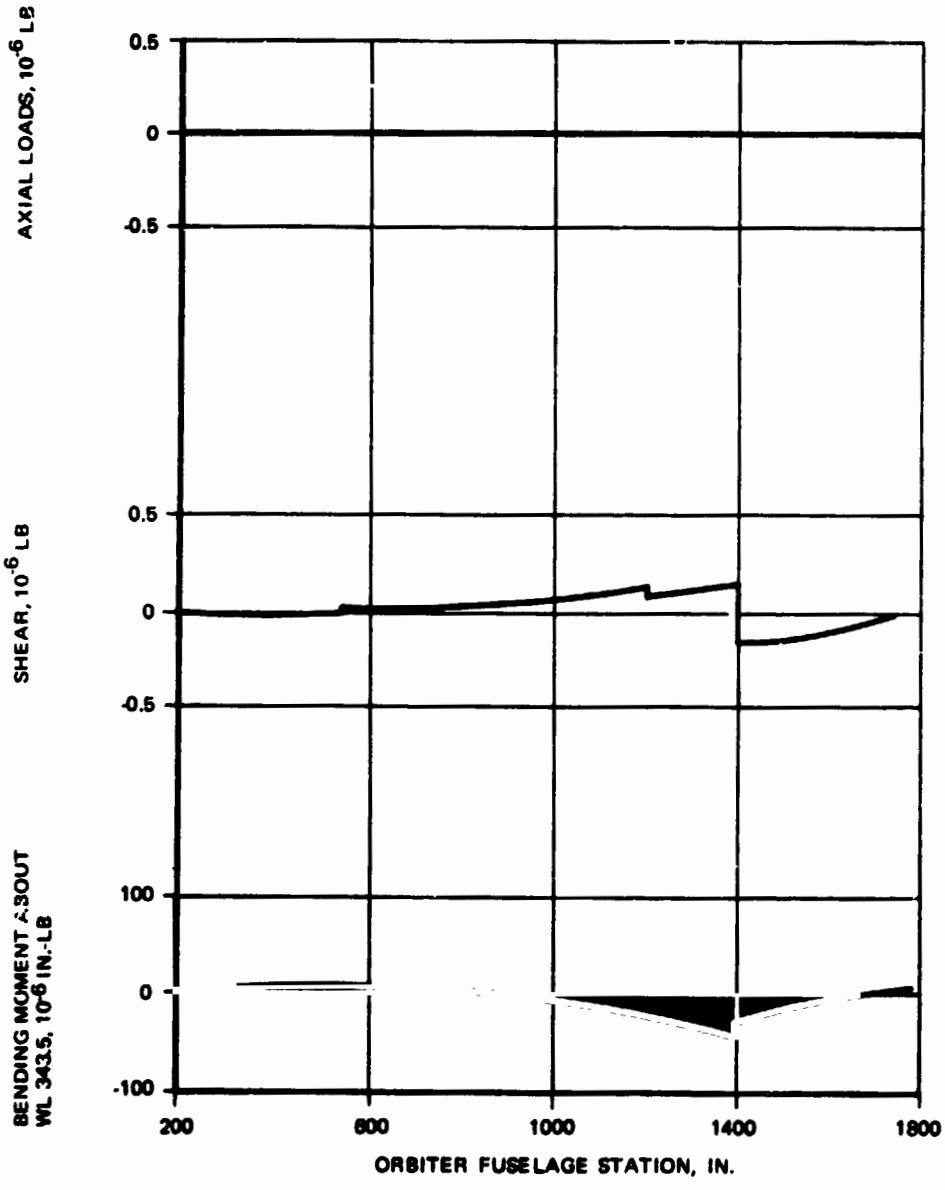

8-143

Fig. 8.3.6-15 H-3T Orbiter Fuselage Distributed Limit Loads, Orbiter 2.5G Pullout

lower than the max q α conditions. However, for the 2.5 g pullout, heated structure reduces the available strength.

g. Orbiter Landings

Five critical symmetric landing conditions were considered:

- Two point-tail down, spin-up
- Two point-tail down, spring back
- Two point-level, spin-up
- Nose gear impact, spin-up
- Nose gear impact spring-back

The two point landing loads were obtained using a vertical gear load factor of 1.6 and an aerodynamic lift equal to the vehicle weight with the center of pressure assumed at the cg. The nose gear impact loads depend on vehicle motion subsequent to the main gear touchdown and are based on an assumed vehicle rotational velocity at the instant of nose wheel impact of 7 deg/sec. The corresponding aerodynamic lift is assumed to be 0.2 g and the main gear load equal to 1.15 g. For all conditions a dynamic magnification factor of 1.3 was applied to all vertical loads to account for fuselage response.

Orbiter fuselage distributed loads for the two point tail down, spin-up, and spring-back conditions are shown in Fig. 8.3.6-16; the two point-level, spin up are shown in Fig. 8.3.6-17; and the nose gear impact spin-up and spring-back conditions are shown in Fig. 8.3.6-18. Load factors and concentrated loads for the landing conditions are shown in Table 8.3.6-5.

8.3.6.2.4 External Tank Design Loads

a. Preliminary Design Loads - H-3T Tanks

Preliminary design loads were calculated for the axisymmetric H-3T tanks using a adaptation of NASA/NACA experimental data. The calculation of aerodynamic loads began with an estimated surface pressure distribution. This was integrated to get normal loads, shears, etc. Inertial loads were included when there was a component of acceleration in the direction of the loads being calculated.

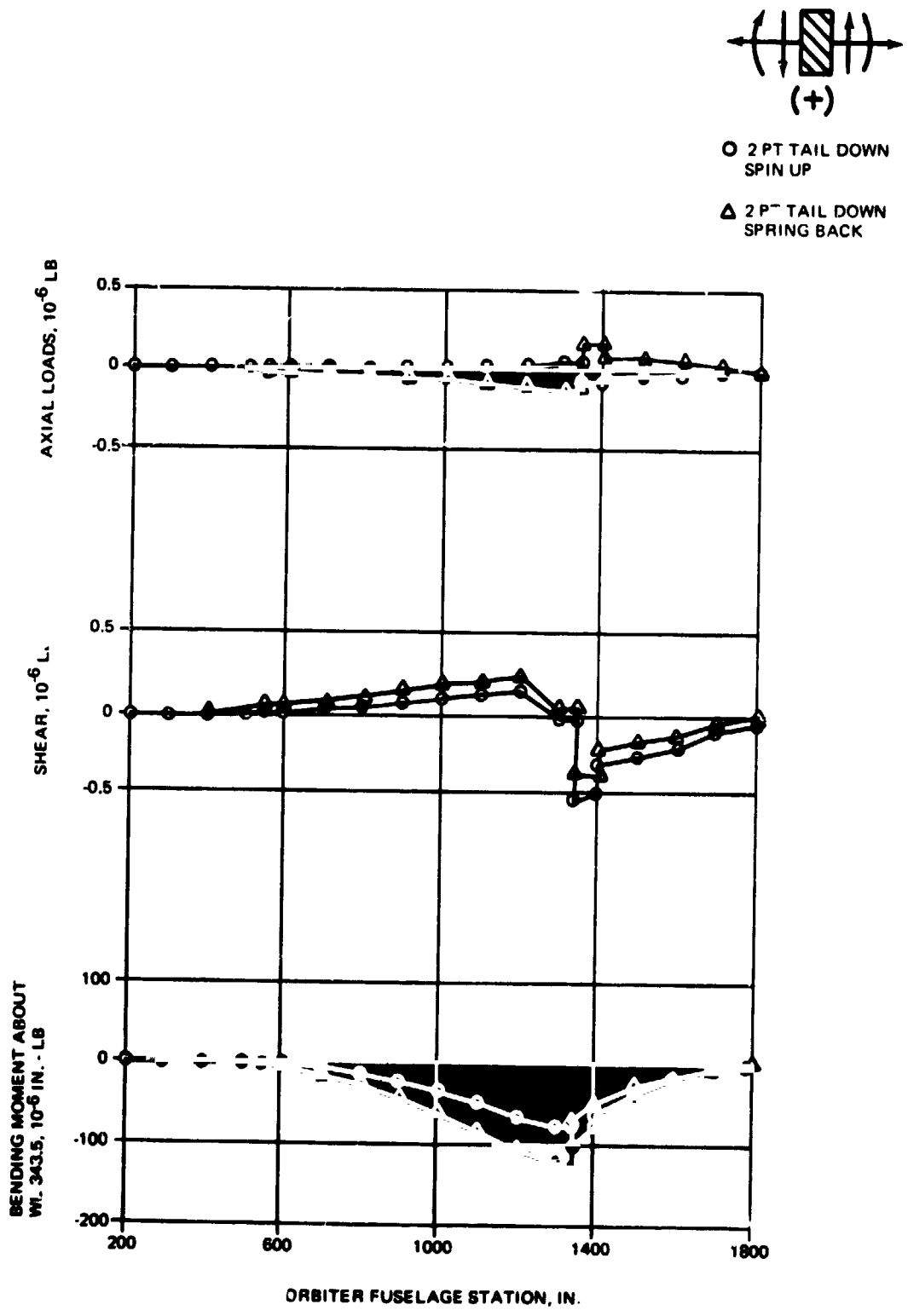

Fig. 8.3.6-16 H-3T Orbiter Fuselage Distributed Limit Loads, Landing Loads

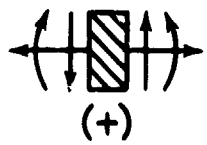

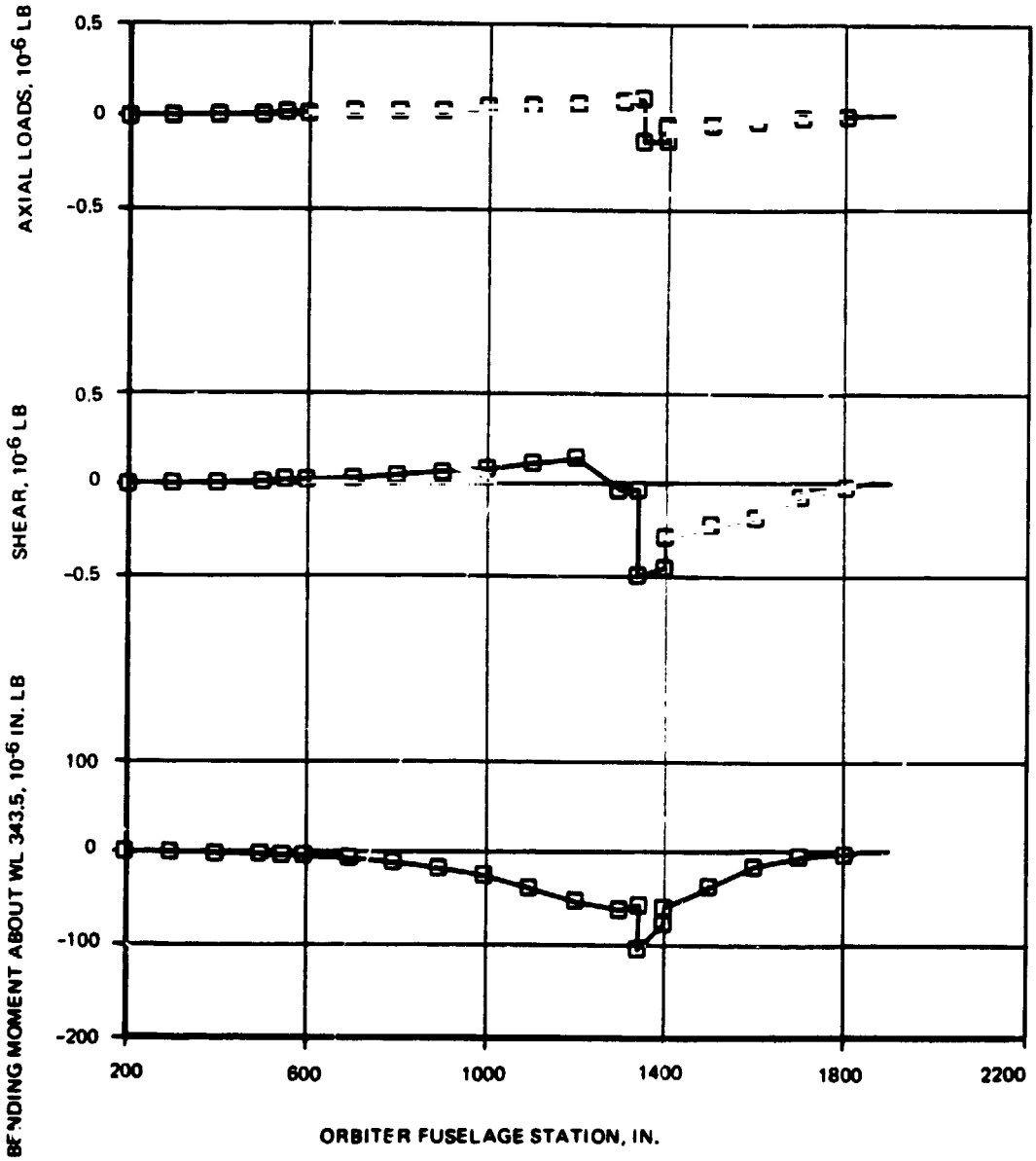

B-145

Fig. 8.3.6-17 Orbiter Fuselage Distributed Limit Loads, Landing Loads (2 Point Level, Spin Up)

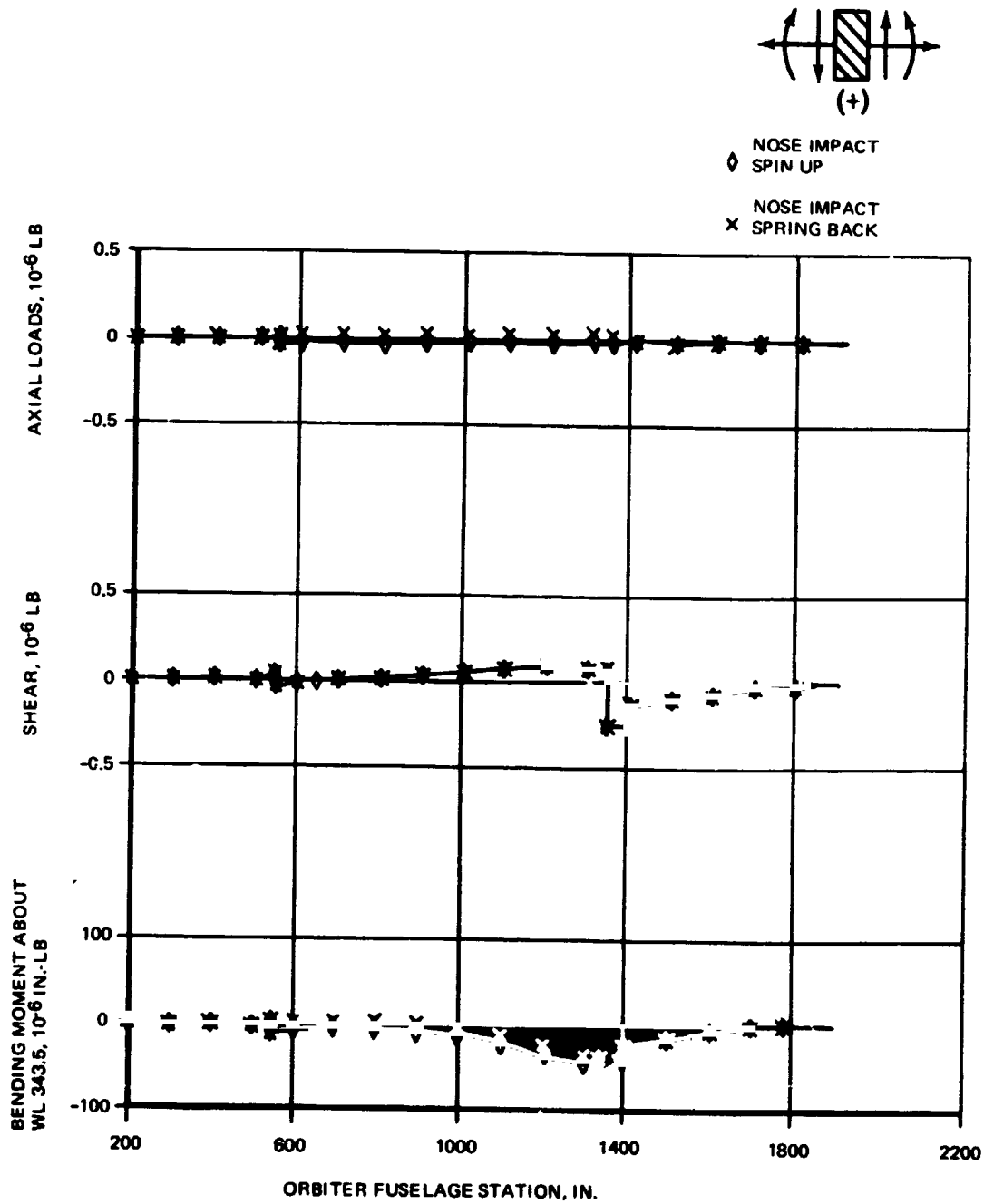

Fig. 8.3.6-18 H-3T Orbiter Fuselage Distributed Limit Loads Landing Loads

(1) Maximum Normal Loads, Shears, and Bending Moments

Vertical and lateral loads were calculated for the maximum q α condition. A pressure distribution over the tank alone and free from interference was estimated using NASA Scout data from TN D-945 as a guide. This distribution was then corrected to account for the proximity of the orbiter fuselage and wing and is shown in Fig. 8.3.6-19.

Vertical and lateral components of the cross sectional pressures were combined with inertia forces to give the net normal load distributions shown in Fig. 8.3.6-19. The net normal load distributions were successively integrated to give shear and bending moment distributions, also shown in Fig. 8.3.6-19.

The total axial air plus inertia load accompanying the above net normal loads is 130,502 lb.

(2) Maximum Axial Load

The maximum tank axial load occurs at the End Boost condition. Since aerodynamic drag at this condition is negligible, the net load was calculated as a pure inertia load and was 170,439 lb.

b. Design Loads - H-3T Tanks

Subsequent to the completion of the preliminary design loads of item (a) above, Ames wind tunnel test program No. 66-551 for measuring axisymmetric tank surface pressures in the Boost Configuration was completed. A comparison of estimated vs. wind tunnel measured pressures indicated that the preliminary design loads were of the proper order of magnitude, yet conservative. The preliminary loads indicated a maximum bending moment in the lateral direction. The wind tunnel results indicated a maximum bending moment in the vertical direction and having a somewhat smaller magnitude. Since each external tank is structurally symmetrical, the distributed tank loads can be safely carried and only minor changes in the tank attachments need be considered.

Since the baseline external tank configuration was changed from the H-3T axisymmetric to the H-33 contoured tanks, detailed axisymmetric tank loads based on wind tunnel measurements were not calculated.

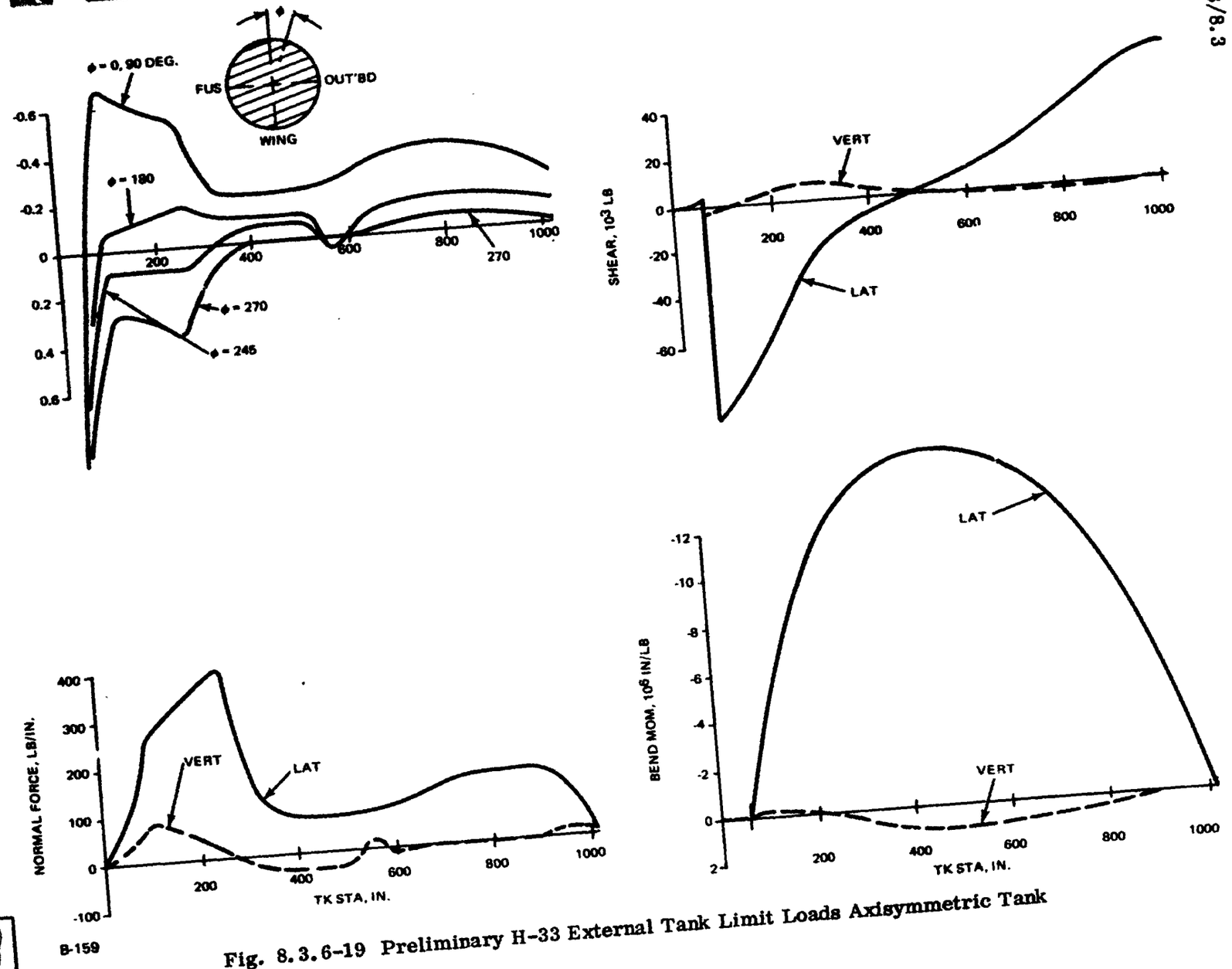

B-159

Fig. 8.3.6-19 Preliminary H-33 External Tank Limit Loads Axisymmetric Tank

c. Design Loads - H-33 Contoured Tanks

Tank normal loads were recalculated to take into account the configuration change associated with the contoured tanks. This time the maximum negative $\bar{q}\alpha$ condition was selected as critical. Following the procedure outlines in paragraph (a) above, surface pressures, normal loads, shears, and bending moments were calculated and are presented in Fig. 8.3.6-20.

After the design loads were estimated, Ames wind tunnel test program No. 66-551 measuring tank aerodynamic loads was completed. One tank was strain-gaged for force-moment tests.

A comparison of estimated and measured loads indicated results similar to that of paragraph (b) above. Again the lateral load was lower and the vertical load was almost exactly equal to the maximum estimated lateral load. Although the longitudinal distribution of the wind tunnel load was not known with certainty, the centerof pressure appeared reasonable.

Since the wetted volume of each tank is structurally symmetrical, the tank can safely carry the wind tunnel measured vertical load and only minor changes in the tank attachments need be considered.

8.3.6.3 Structural Math Model

Structural math models of the H3T Orbiter and Booster have been established to determine stiffness characteristics for dynamic analyses of the orbiter and booster, and to enable calculation of internal load and deflection distributions for the orbiter.

The primary intent has been to arrive at a structural idealization of minimum complexity which can still provide adequate confidence regarding the accuracy of calculated mode shapes, frequencies, and inertia loads associated with transient or oscillatory loading conditions. Accordingly, the structure has been idealized to represent all primary structure by using discrete finite elements and by using stiffness matrices calculated for specific primary structural components. (Less complex "beam" or "stick" models were used for initial mode shape and frequency checks.)

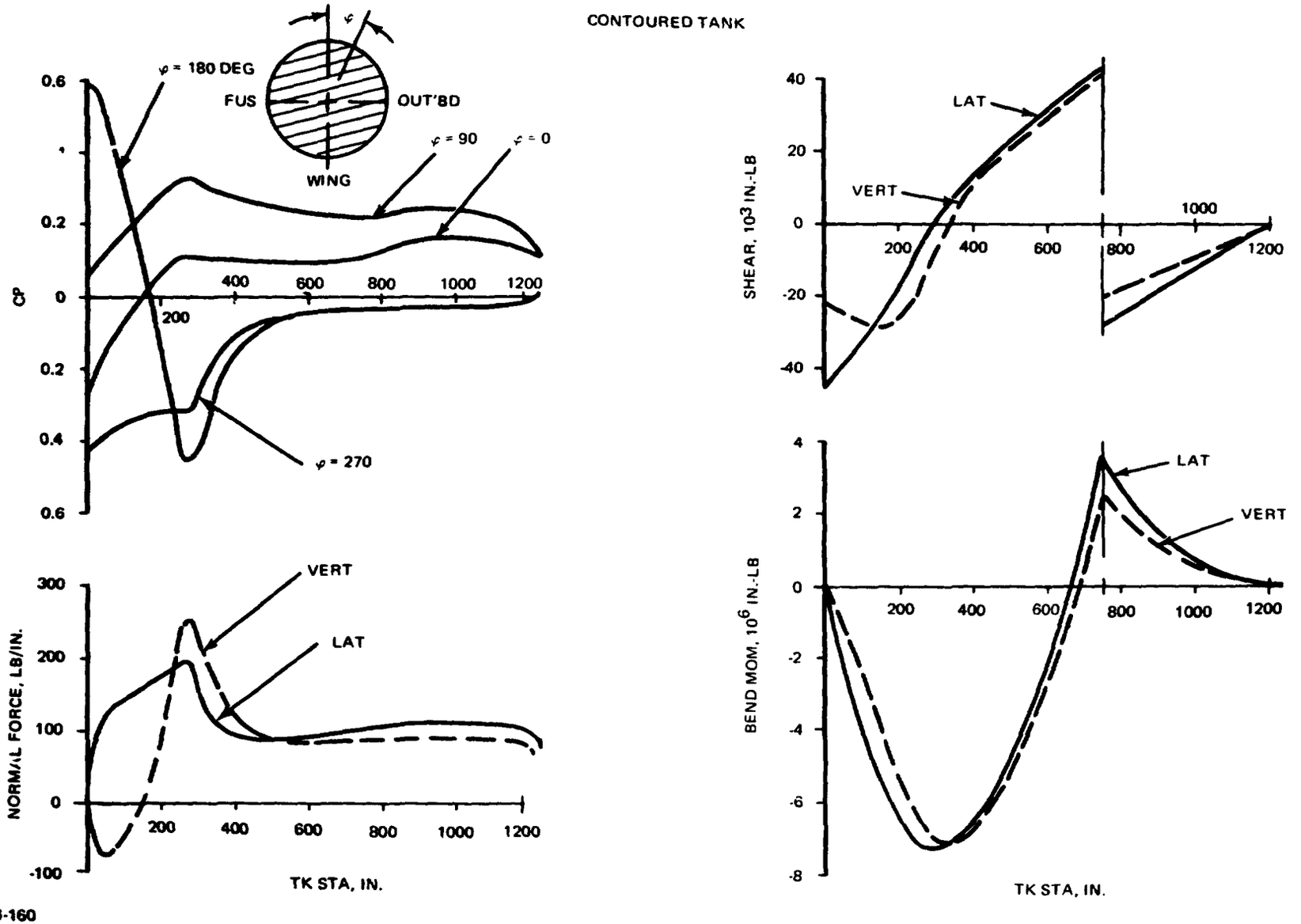

8.3.6-37

B-160

Fig. 8.3.6-20 Preliminary H-3T External Tank Limit Loads

The Orbiter has been modeled in sufficient detail to provide accurate stiffness data for dynamic analyses, and to also allow complete internal load and deflection distribution calculations. By using the same structural model for both stiffness and internal load calculations, complete consistency can be obtained in regard to the sizing of primary structure to simultaneously satisfy the various requirements of dynamic response, strength, and aeroelastic or other deflection constraints.

The detail associated with booster modeling has been chosen to satisfy all requirements of dynamic analyses, but is not intended to provide redundant structure internal load and deflection analysis capability.

8.3.6.3.1 Orbiter Structural Math Model

a. Idealization of Structure

The H-3T Orbiter (see Fig. 8.3.6-3) primary structure has been idealized by considering five major components as separately discussed below.

Primary structure and associated preliminary critical design conditions are as follows:*

- Fuselage:

  Longerons and shear webs forward of station 1400:
  Critical for End Boost

  Longerons and shear webs aft of station 1400:
  Critical for Max. $q\beta$ and Orbiter Engine Thrust (EPL)

- Bulkheads:

  Stations 548 and 1218: Critical for End Boost and Max $q\alpha$
  Station 1400: Critical for End Boost, Max $q\alpha$ and Max $q\beta$
  Station 1572: Critical for Max $q\alpha$ and Max $q\beta$
  Station 1622: Critical for Max $q\beta$ and Orbiter Engine Thrust (EPL)
  Station 1712 and 1748: Critical for Max $q\beta$

*Updated internal loads for the design conditions given in paragraph 8.3.6.2 will be presented in Grumman Report B36-100RP-105. Note that landing is critical only in local areas at or near gear attachment points.

- Tank Supports: Critical for End Boost and Max qα (decks, longerons, struts)
- Engine Support Box Beam: Critical for Orbiter Engine Thrust (EPL)
- Main Propulsion LH_2 Tankage: Critical for pressure combined with Max qα Max qβ or End Boost
- Main Propulsion LO_2 Tankage: Critical for pressure combined with Max qα or End Boost
- Wing and Wing Carry-Thru: Critical for Max qα
- Fin: Critical for Max qβ

1. Basic Fuselage Structure

The basic fuselage shell of H3T Orbiter is a conventional semi-monocoque design. Tankage is non-integral. Longerons are represented as bars; shear webs are represented as quadrilateral panels, some of which are warped; bulkheads are comprised of beams, bars and quadrilateral panels. Fuselage shell material is titanium 6A1-6V-2Sn (Ti 6-6-2). Material selection is discussed in paragraph 8.4.1.2.

2. Engine Thrust Structure

The two main rocket engines used in the H-3T Orbiter are supported by a continuous box beam with its longitudinal axis in the Y direction. The box beam is located between bulkheads at stations 1572 and 1622. The beam spans from +Y to -Y extremes of the fuselage contour and is supported at +Y, centerline and -Y butt lines for X components of thrust. Y and Z components of engine thrust are reacted by the bulkheads mentioned above. The box beam, as idealized, consists of bars and quadrilateral shear webs of Ti 6-6-2.

The theoretical points of application of engine thrust (gimbal points) are X = +1634, Y = +79, Z = +388 for the left engine, and X = +1634, Y = -79, Z = +388 for the right engine.

3. Primary Tankage

Primary tankage is non-integral and consists of:

- Two main propulsion internally mounted cylindrical LO_2 tanks
- Two main propulsion externally mounted cylindrical LH_2 tanks

- Two on-orbit propulsion internally mounted cylindrical LH_2 tanks
- One on-orbit propulsion internally mounted spherical LO_2 tank

The on-orbit tanks are not structurally idealized in the model. Their mass properties and local supporting structure are included.

Each of the four main propulsion tanks is idealized as several monocoque cylindrical sections with appropriate end-domes. Aluminum alloy 2219-T87 material is used throughout and is discussed in paragraph 8.4.1.2. Each tank is supported in a statically determinate manner. Drag loads are reacted at the aft end of each tank. All local supporting structure is Ti 6-6-2.

4. Wing Structure

The H-3T Orbiter wing structure is an all titanium (Ti 6-6-2) structure built-up of corrugated cover panels on a gridwork of spars and ribs. Five primary wing spars are built into the fuselage bulkheads of Fuselage Stations 1213, 1326, 1400, 1502, and 1572 to provide continuity of wing through the fuselage. Cover panels are corrugated and are idealized as warped quadrilateral or triangular panels both of which are capable of carrying direct stress. The spar and rib caps are included with the cover panels except for portions of the fuselage carrythrough structure where the spar caps are idealized as bar elements. The spar and rib webs are idealized as shear panels. Posts are required at the intersections of spars and ribs to stabilize nodes in the direction normal to the wing. These posts are idealized as bar elements.

5. Fin Structure

The fin model is based on a hot structure which is an alternate to the baseline fine which has a TPS protected titanium structure.

The fin structure material is composed of Rene 41 and Inconel 718. Construction consists of corrugation stiffened sheet covers supported by three spars and truss type ribs which are spaced at thirty inches. Spars are idealized as bars and shear webs.

The fin box beam structure was idealized in a manner which compares closely with the actual structure. Covers are treated as direct stress carrying orthotropic panels with the stiff axis in the spanwise direction. All remaining structure is idealized as bars and shear panels.

b. Sizing of Structural Elements

Subsequent to establishing the geometry and identity of all structural members, the process of computing the member sizes was initiated. Sizing of the five major constituents of structure was accomplished in accordance with the criteria of paragraph 8.4.1.1, the tankage design data of Table 8.3.6-7 and the procedures described below:

1. Sizing of Basic Fuselage Shell

The fuselage shell is sized through an iteration procedure using four basic design conditions. The conditions are:

- End of Booster Boost
- Maximum $q\alpha$ (+) Wind
- Symmetrical Orbiter Engine Thrust (Emergency Power Level)
- Maximum $q\beta$

Fig. 8.3.6-21,-22,-23, and-24 document the applied loads for these conditions. Nodal geometry is covered in paragraph 8.3.6.3.3. Wing and fin root load distributions shown in these figures were estimated. Landing was found to be critical only in local structure.

Thermal loads and deformations were not included in the analysis but will be accounted for in the next iteration of conditions as described in the Engineering Development Plan, Section 2.9.1 and paragraph 8.3.6.6 of this report.

The iteration procedure noted in the first sentence under this subparagraph was carried out, as described below, with the objective of converging on the final definition of structural member sizes for the fuselage shell.

Step I: Compute internal loads by slide-rule methods using assumptions to establish redundant load distributions and longeron member sizes.

Step II: Using the loads of Step I, determine all remaining structural member sizes. (Minimum structural sizes assumed are: longeron area = .40 sq in., bulkhead cap area = .25 sq in., shear web thickness = .016 in.).

Step III: Using the preliminary sizes of Step II and the four loading conditions, determine, by computer, the internal member loads. This is a COMAP ASTRAL solution.*

Step IV: Using the loads of Step III, re-size all structural members.

Step V: Using the revised member sizes of Step IV, re-run the computer solution mentioned in Step III to get member loads.

Step VI: Compare the member loads of steps III and VI.

The above procedure was carried to completion and it was judged that the member sizes as determined in Step IV adequately defined the fuselage Structural Model.

2. Sizing of Engine Thrust Structure

The engine thrust structure was sized using an assumed transmissibility factor of 1.0. Emergency power level (EPL) thrust quoted in Engine ICD 13M15000B, change 1, dated March 12, 1971 was used for design. A subsequent transient response analysis of the thrust structure was performed and has validated this assumption. The analysis included mass and thrust data quoted in the aforementioned Engine ICD in establishing the 1.0 transmissibility factor.

3. Sizing of Primary Tankage

As previously mentioned, the tankage structure included in the Structural Model is that of the main propulsion LO_2 and LH_2 tanks. The design and environmental criteria used in sizing these tanks appear in Table 8.3.6-7 and paragraph 8.4.1.1.

4. Sizing of Wing structure

A finite element fully stressed design analysis** is used to size the H-3T wing structure. Instability data is used to obtain sizes for cover panels and spar caps critical in compression. These data are inputs to the computer analysis.

*Grumman Ideas Program S-3, IDEAS Vol IIA

**An Automated Procedure for the Optimization of Practical Aerospace Structures, Grumman, Report No. ADR 02-01-71.1, March 1971

FOLDOUT FRAME

B/8.3

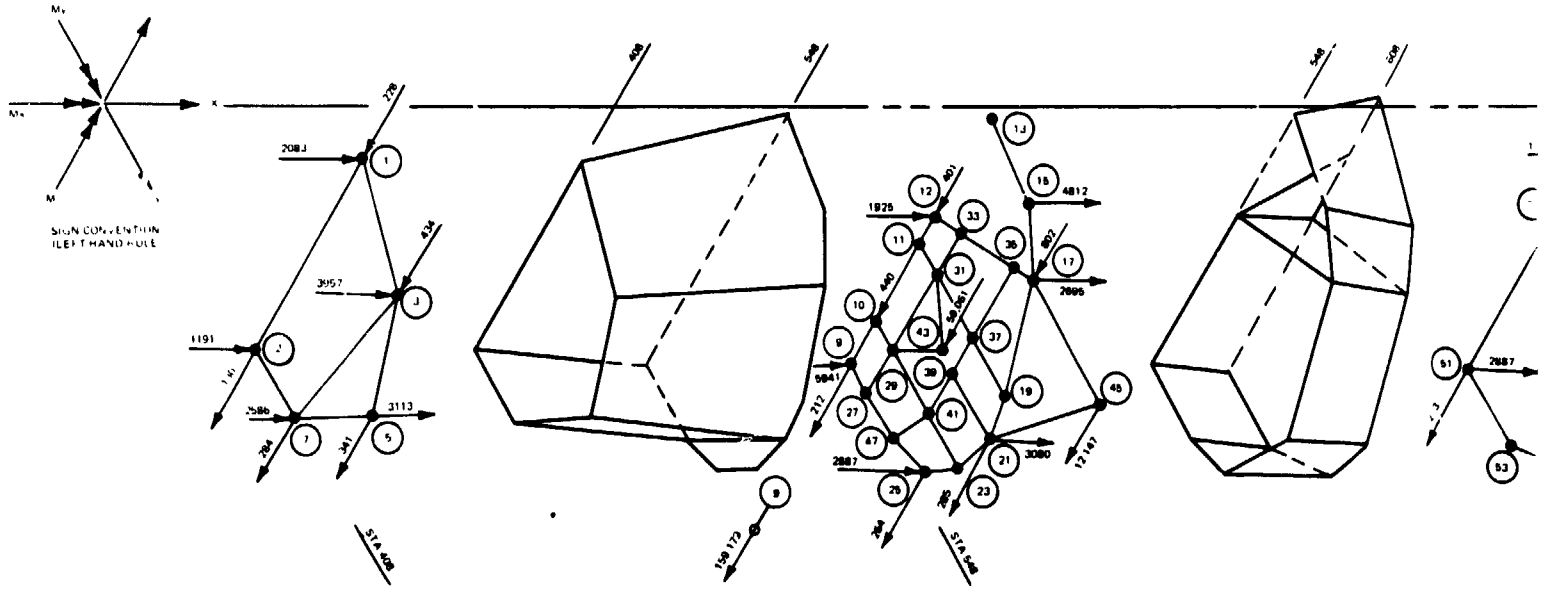

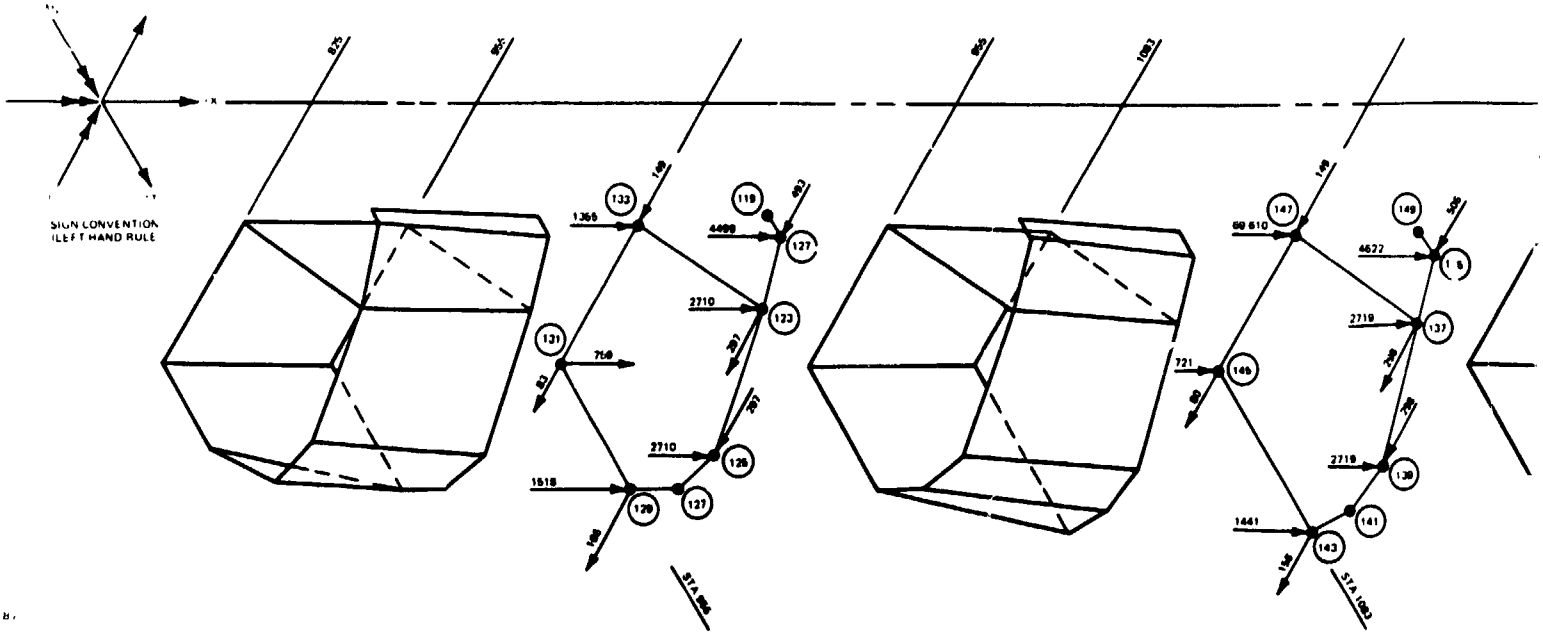

FOLDOUT FRAME 2

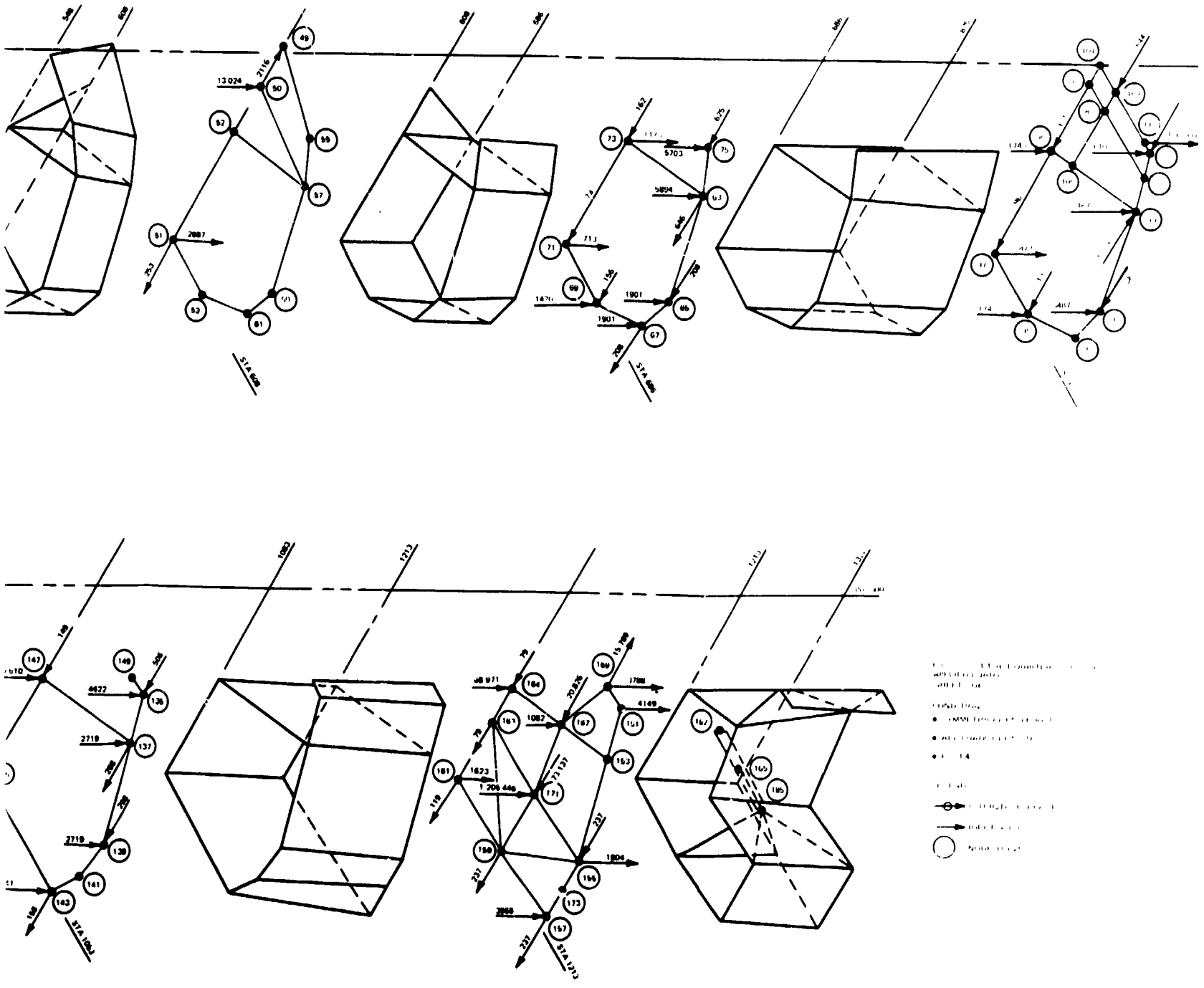

Fig. 8.3.6-21 H-3T Orbiter Fuselage Applied Loads, Symmetrical End Boost Condition (Sheet 1 of 2)

FOLDOUT FRAME |

B/8.3

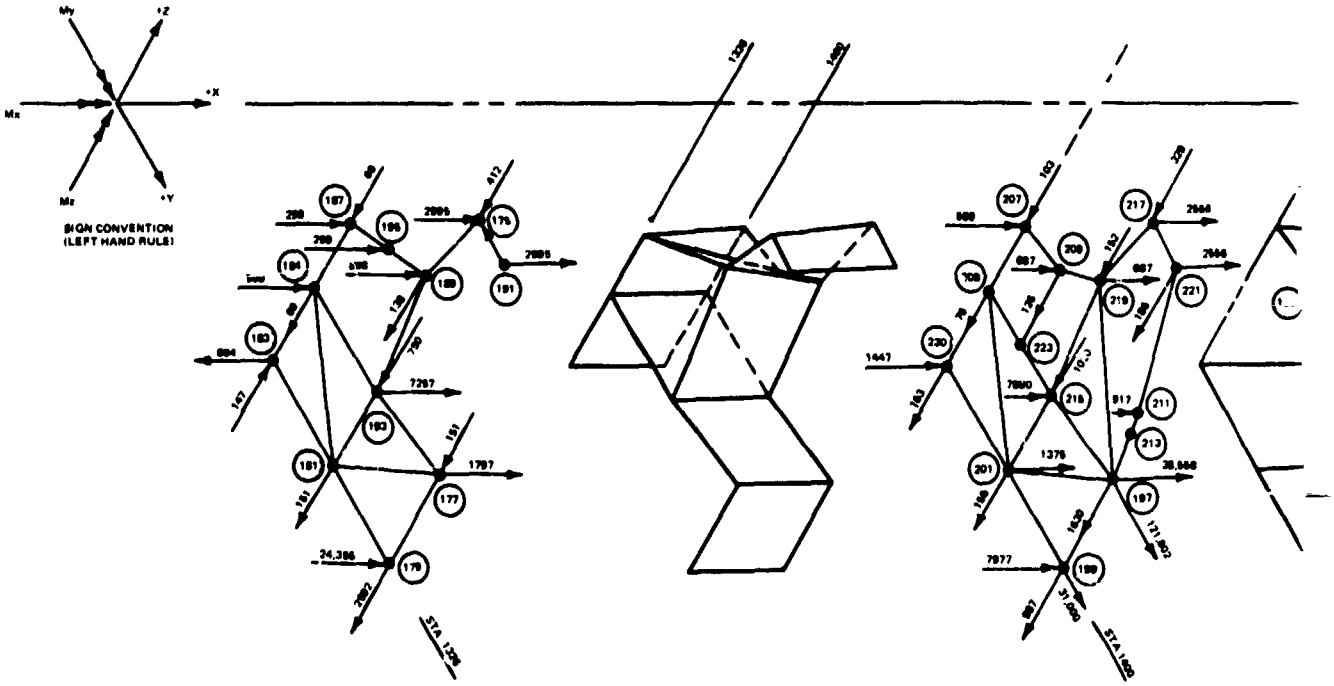

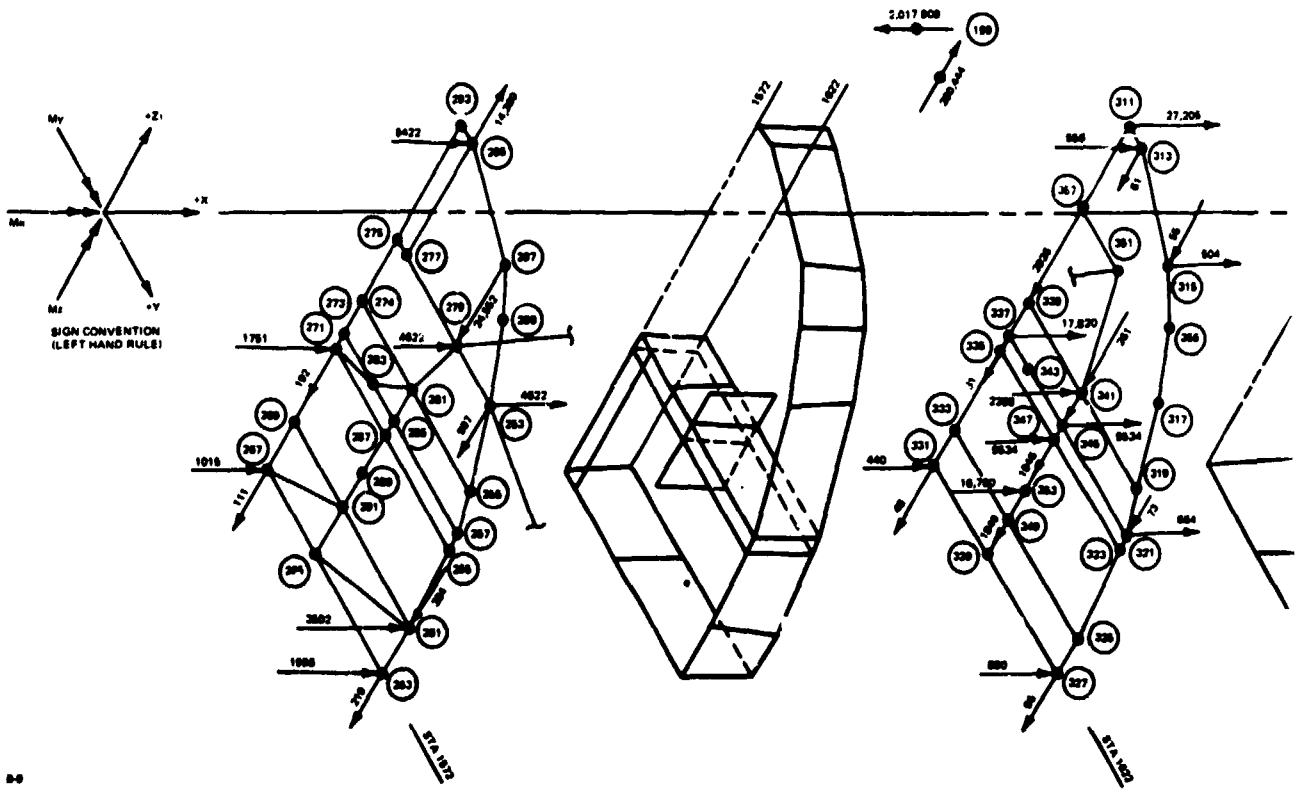

FOLDOUT FRAME 2

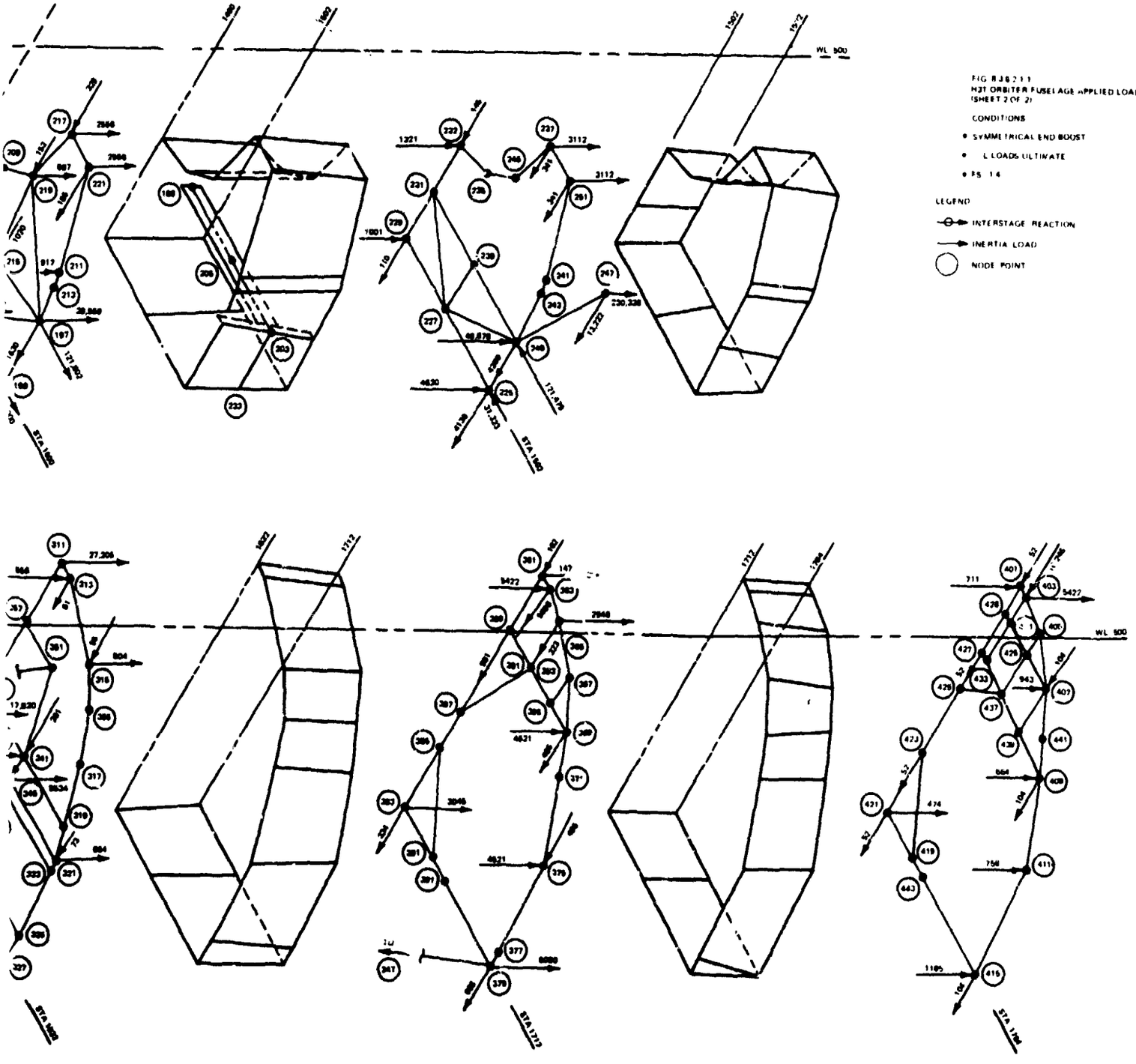

Fig. 8.3.6-21 H-3T Orbiter Fuselage Applied Loads, Symmetrical End Boost Condition (Sheet 2 of 2)

B/8.3 FOLDOUT FRAME 1

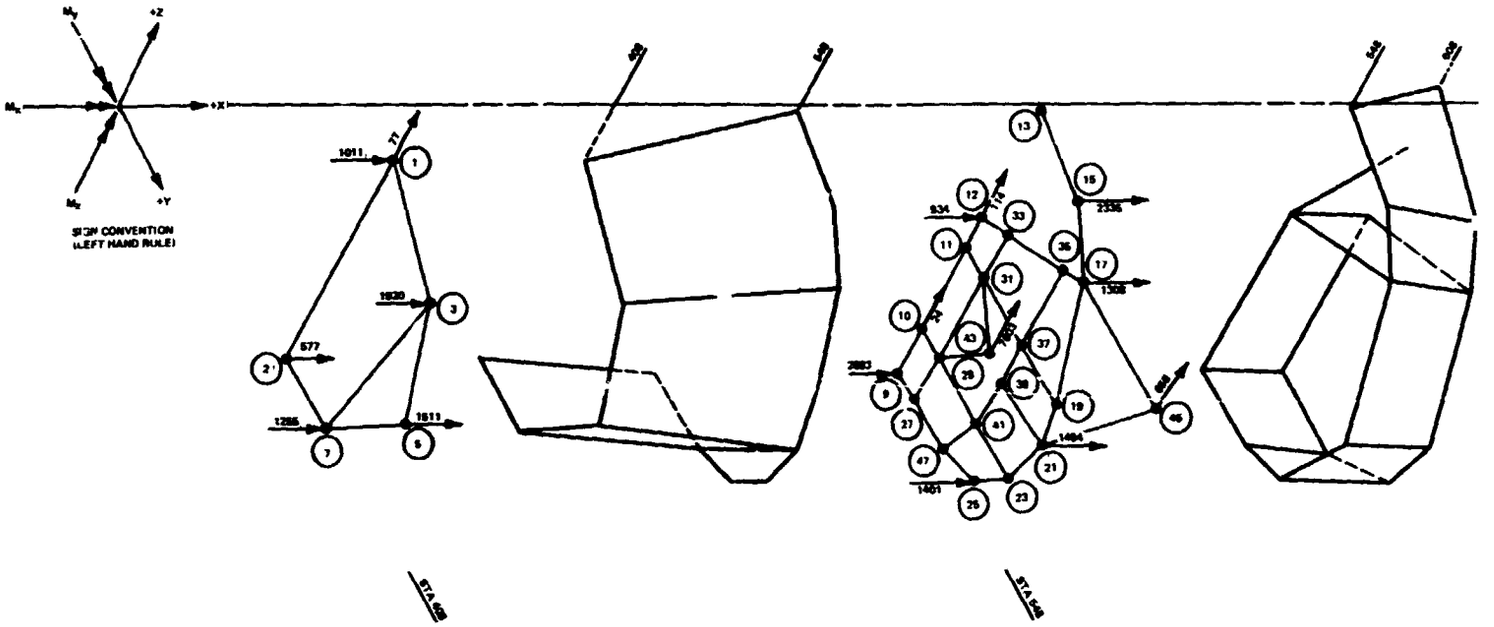

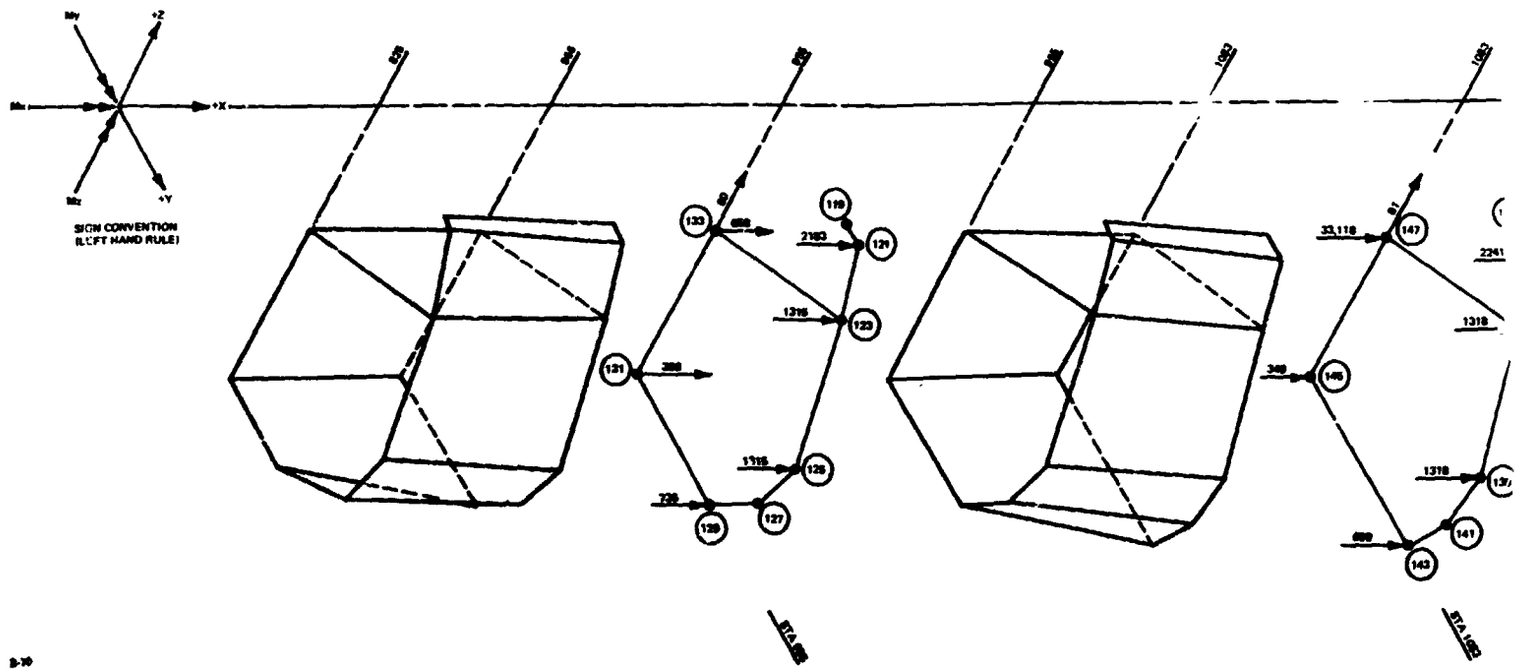

FOLDOUT FRAME 2

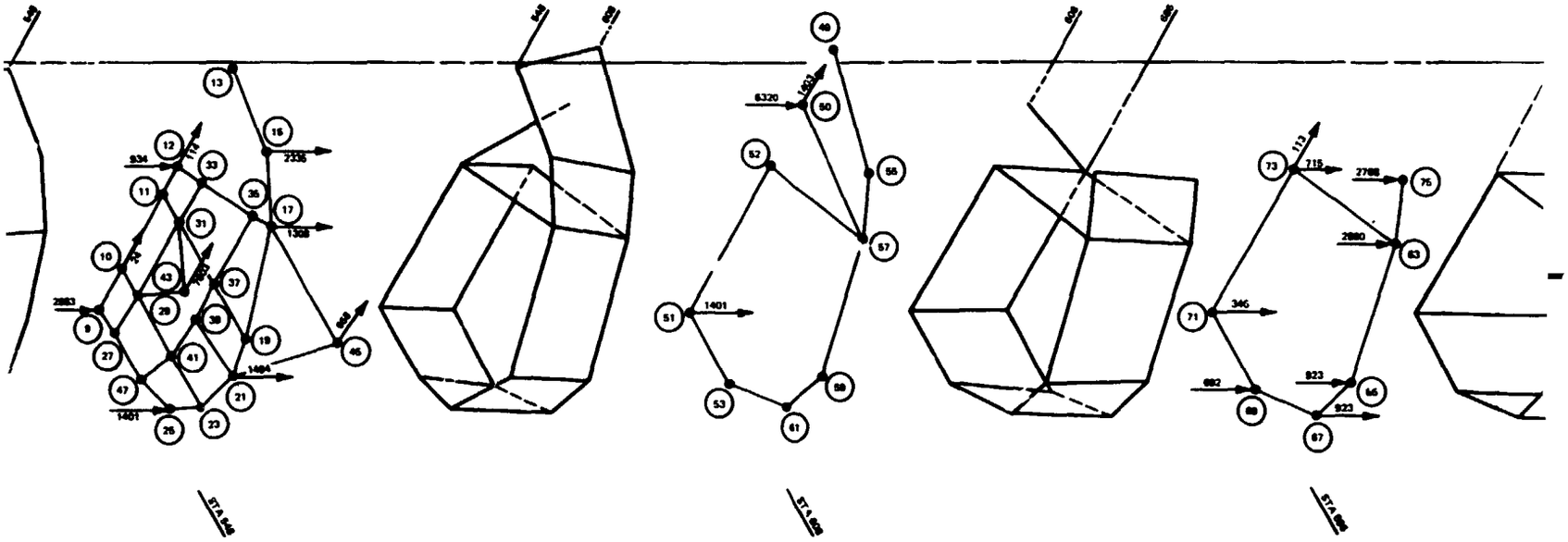

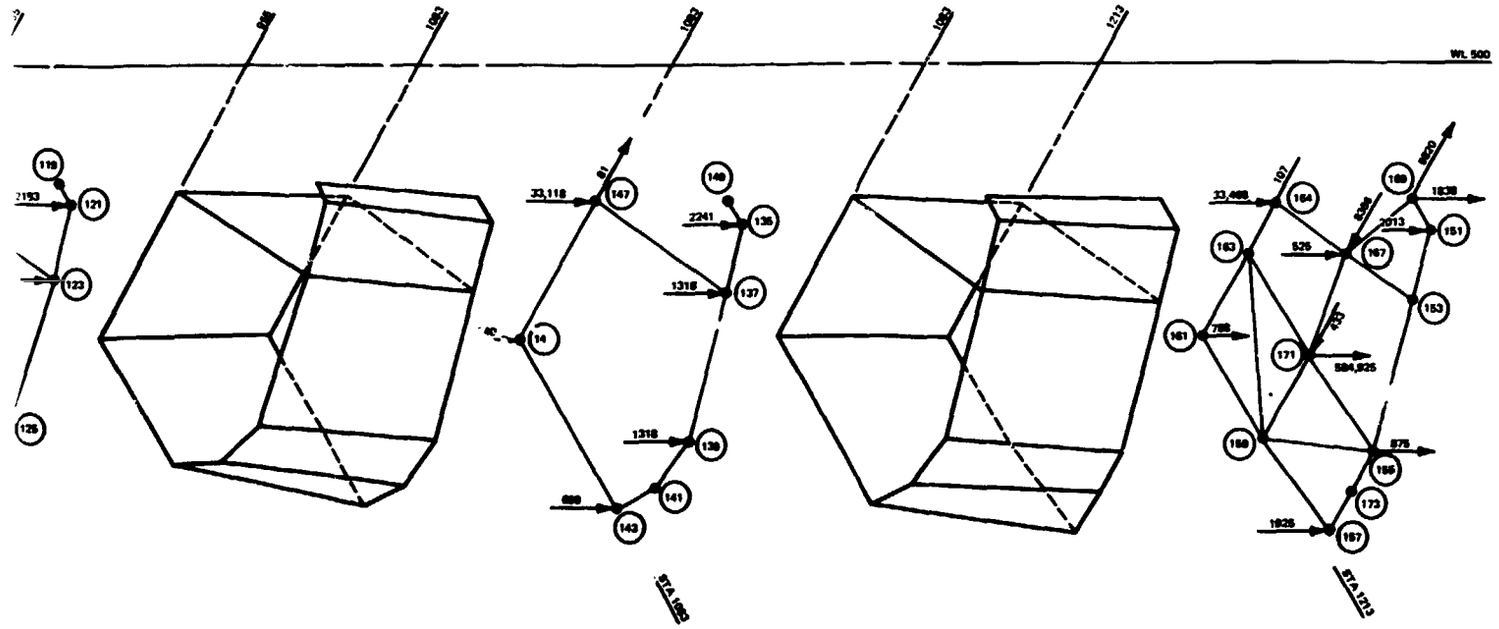

FOLDOUT FRAME 2

FOLDOUT FRAME 3

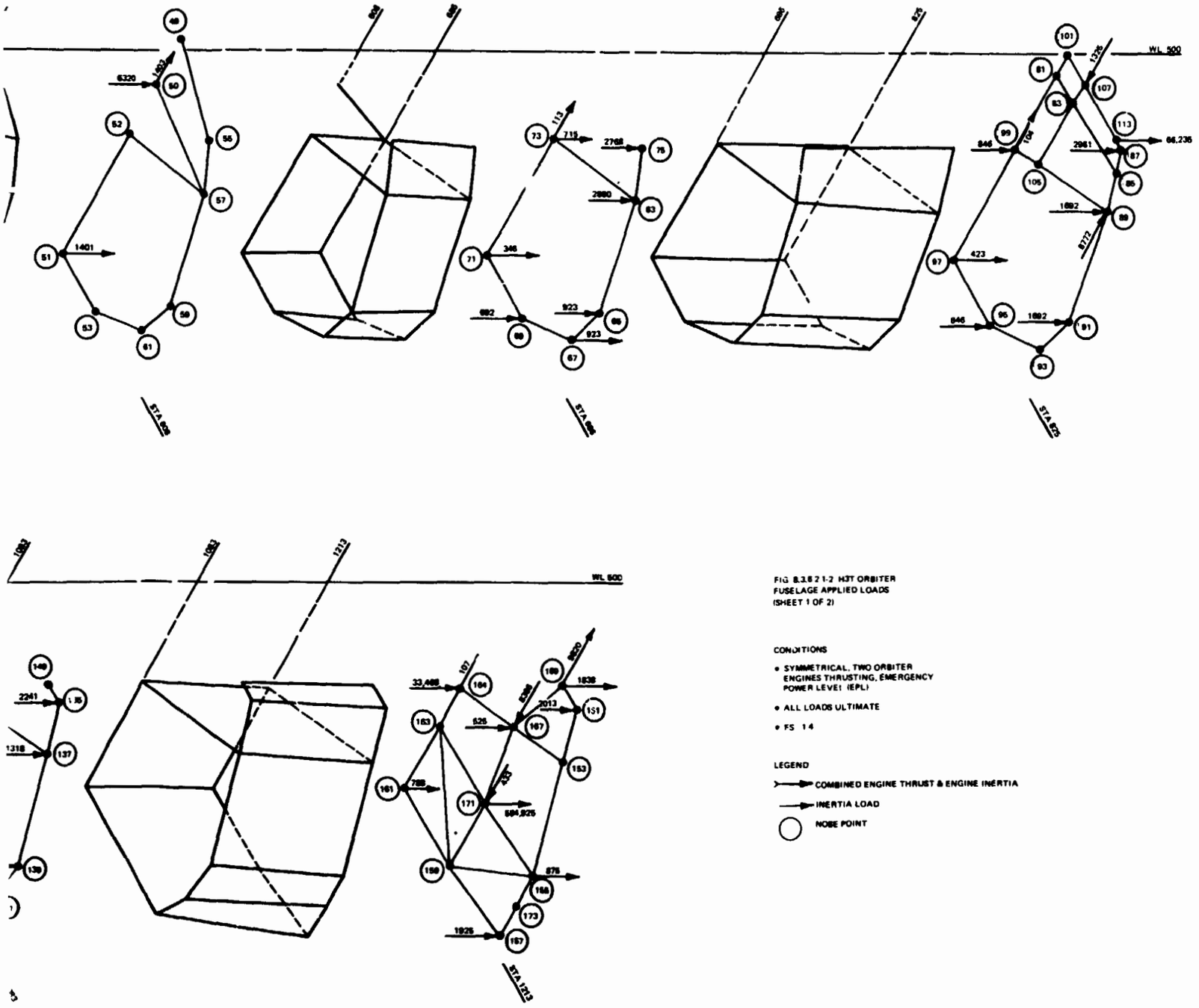

FIG 8.3.6.2.1-2 H3T ORBITER FUSELAGE APPLIED LOADS (SHEET 1 OF 2)

Fig. 8.3.6-22 H-3T Orbiter Fuselage Applied Loads, Symmetrical Orbiter Engine Thrusting Emergency Power Level (Sheet 1 of 2)

GRUMMAN BOEING

FOLDOUT FRAME

B/8.3

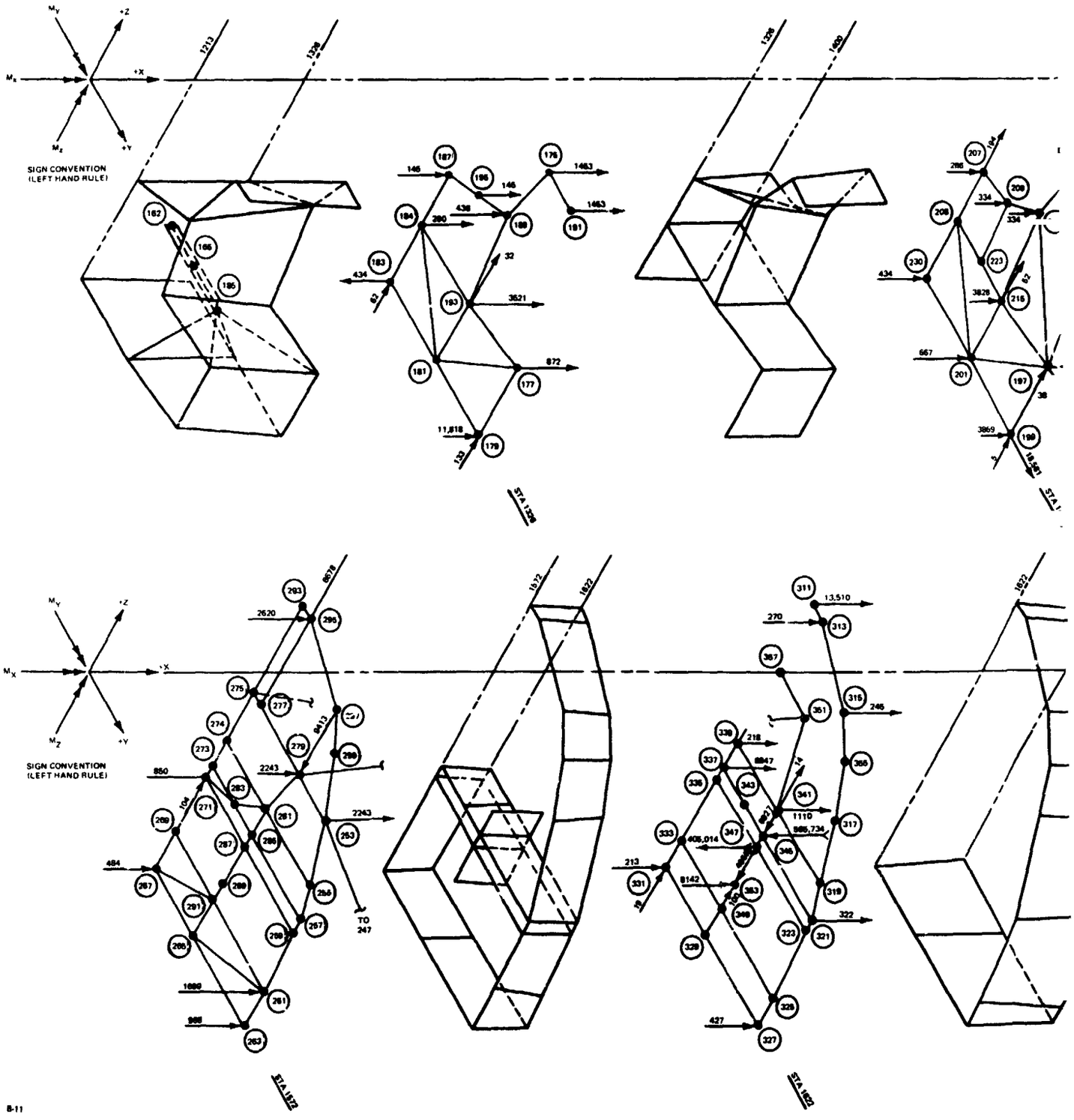

FOLDOUT FRAME 2

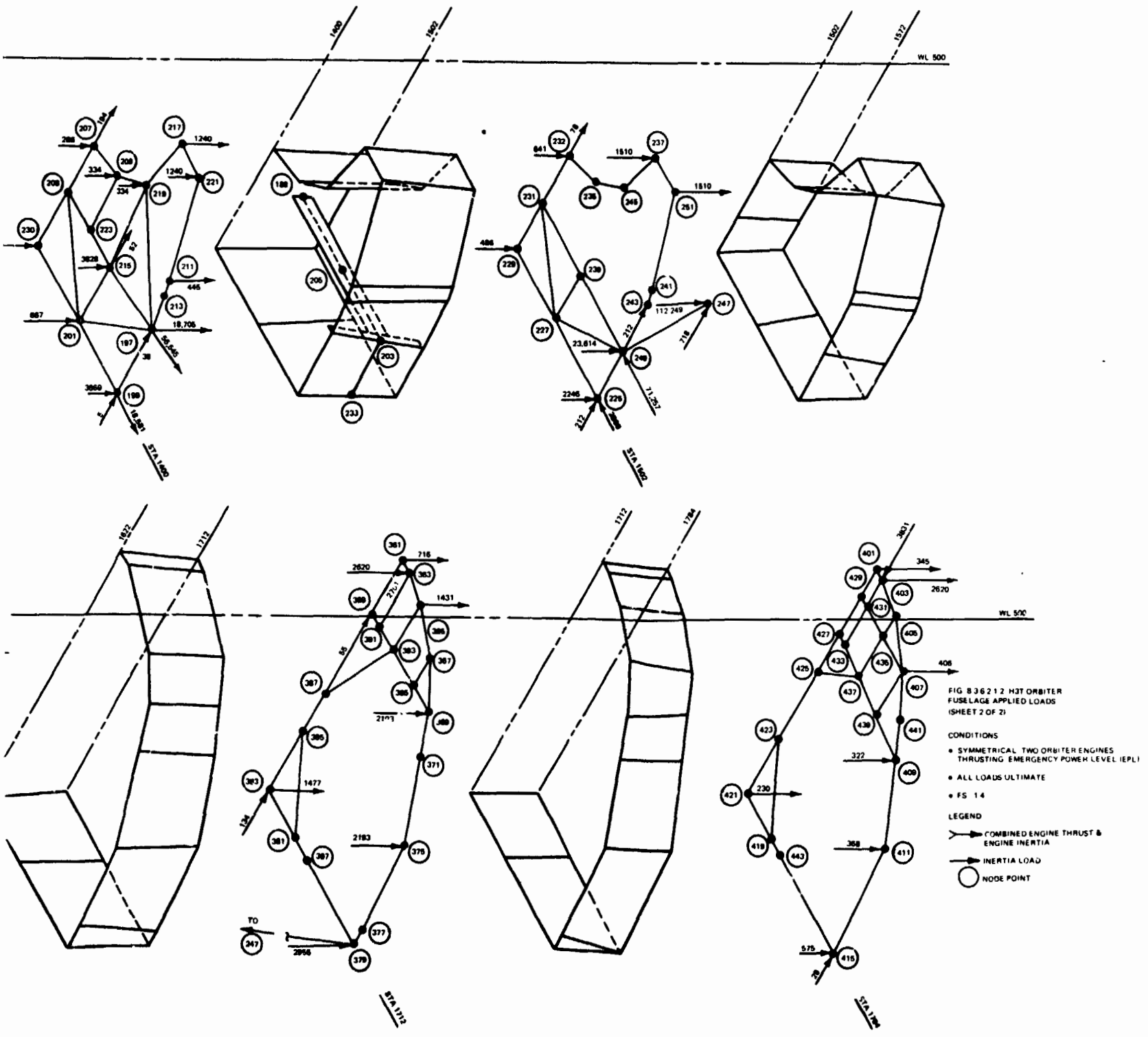

Fig. 8.3.6-22 H-3T Orbiter Fuselage Applied Loads, Symmetrical Orbiter Engine Thrusting Emergency Power Level (Sheet 2 of 2)

FOLDOUT FRAME

B/8.3

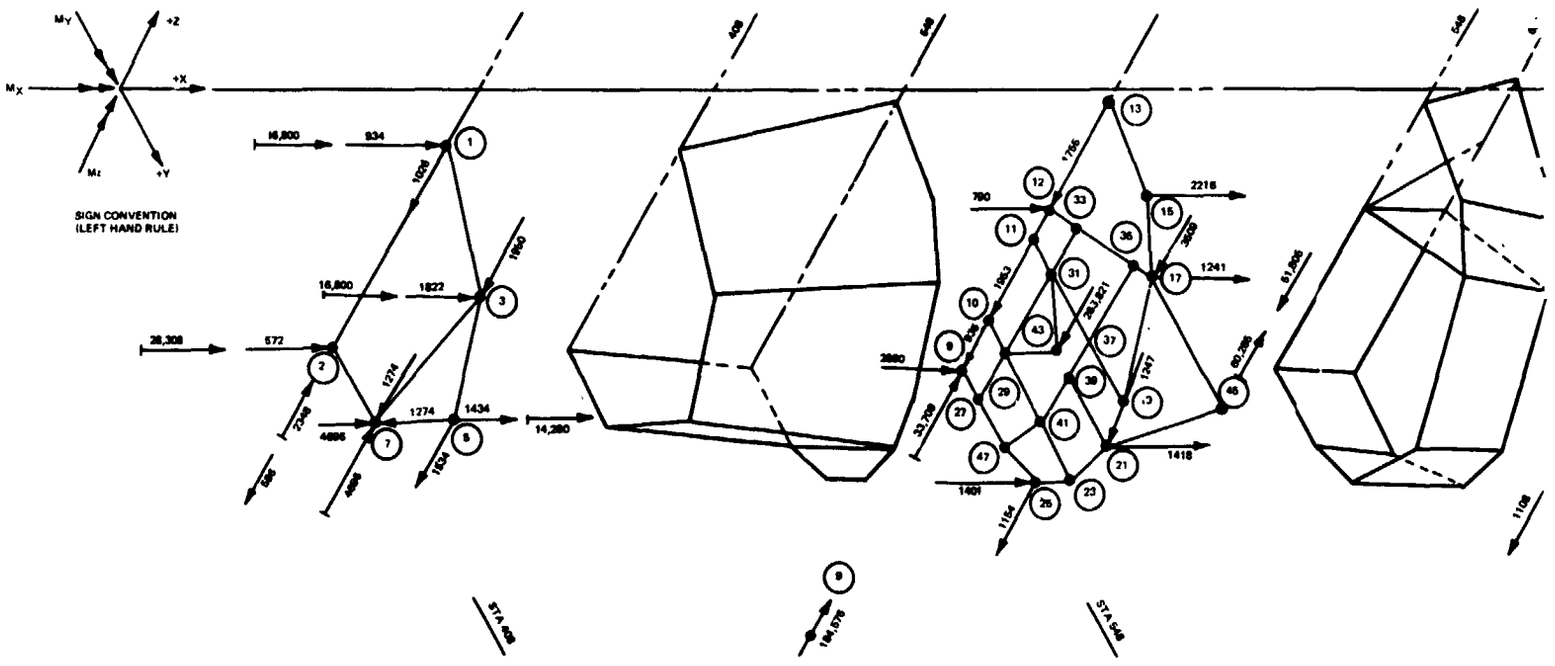

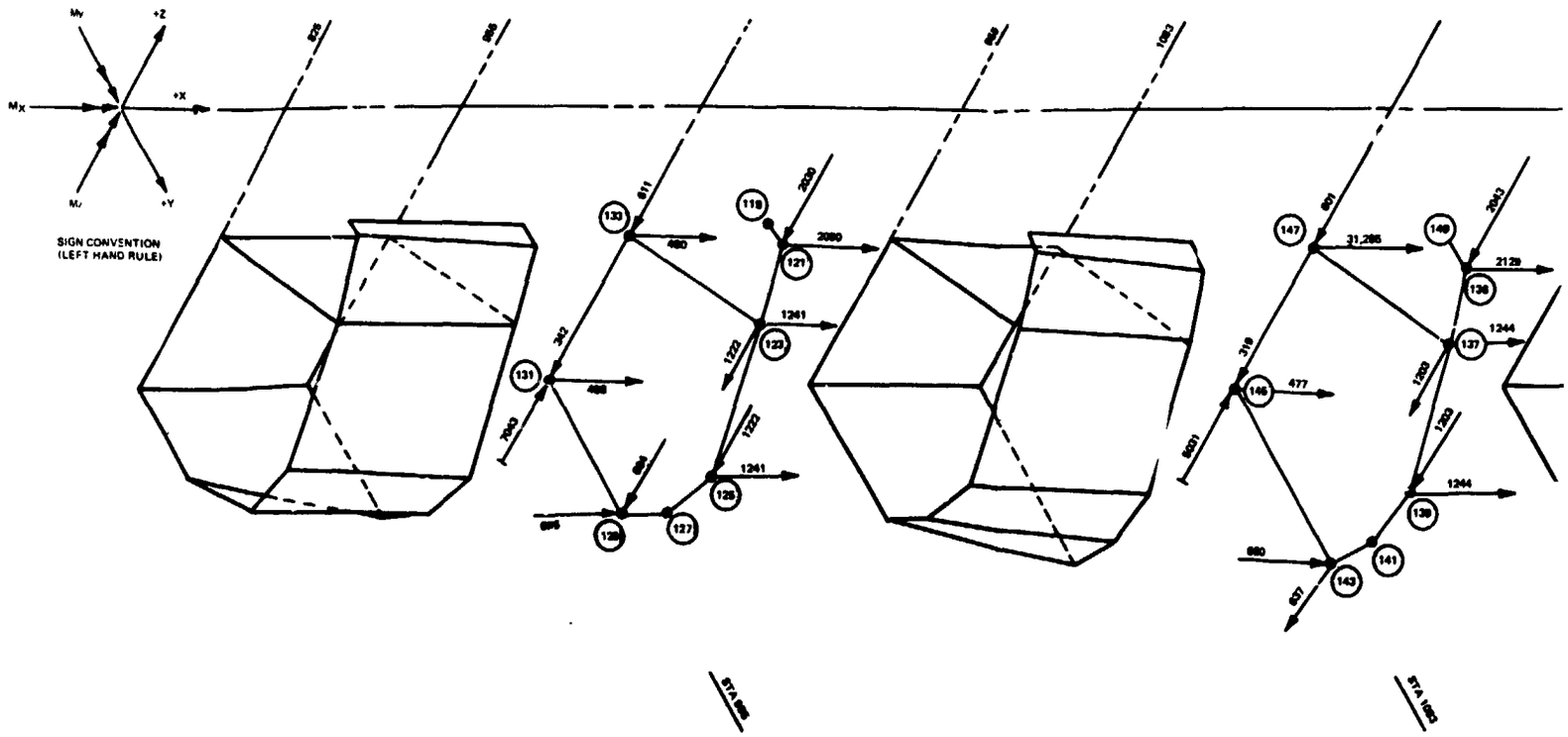

FOLDOUT FRAME 2

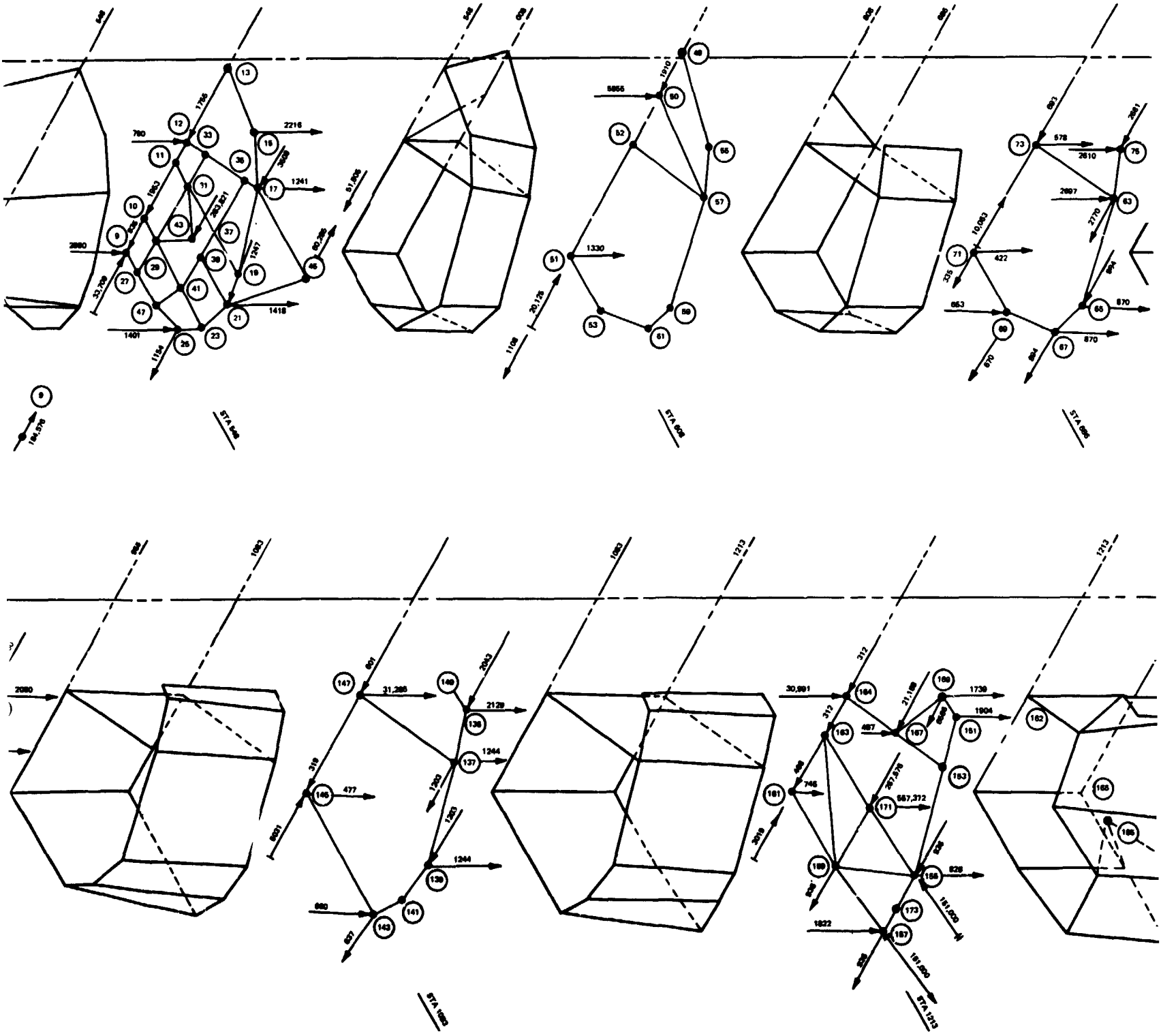

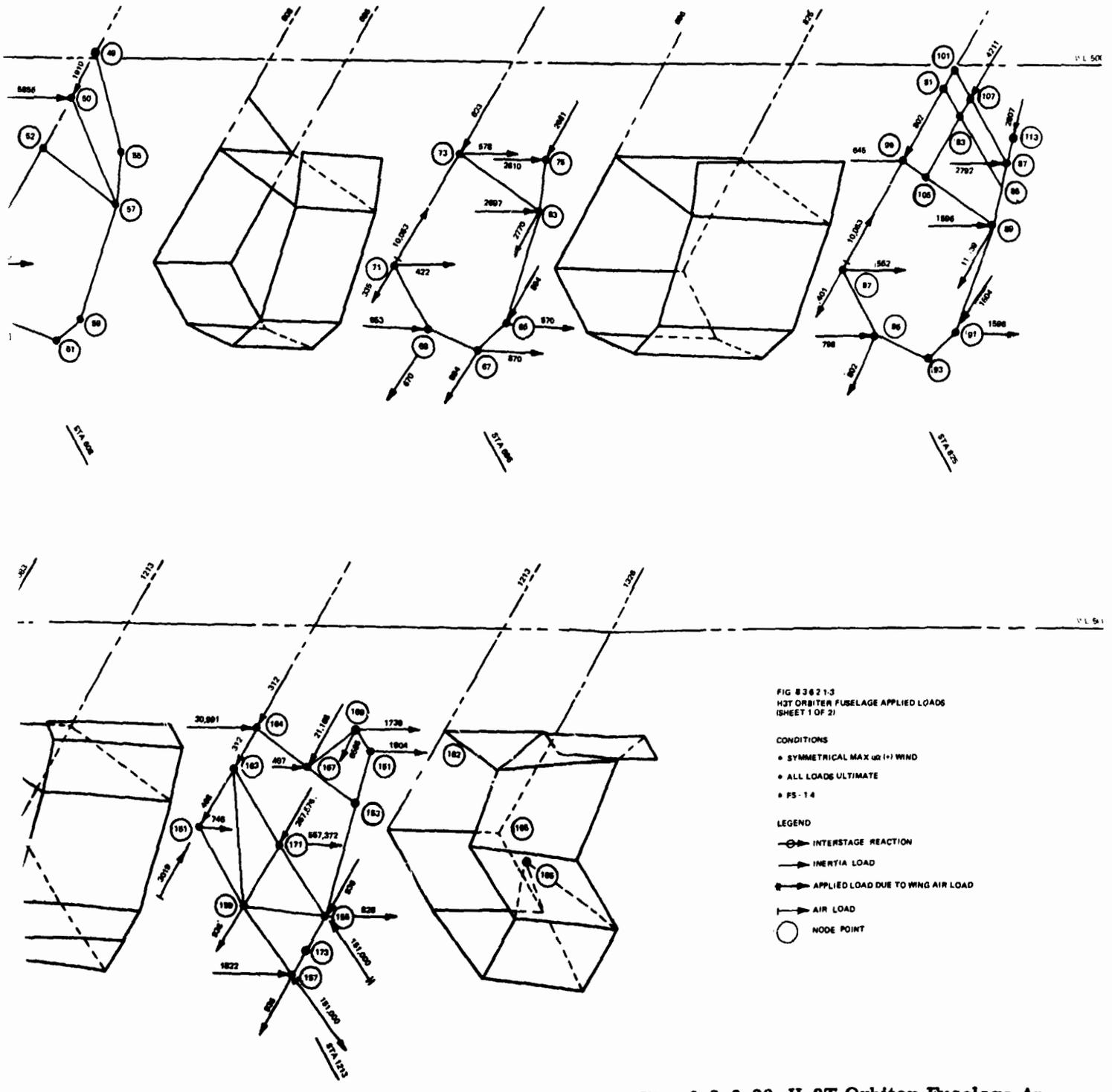

Fig. 8.3.6-23 H-3T Orbiter Fuselage Applied Loads, Symmetrical Max qα (+) Wind (Sheet 1 of 2)

FOLDOUT FRAME |

B/8.3

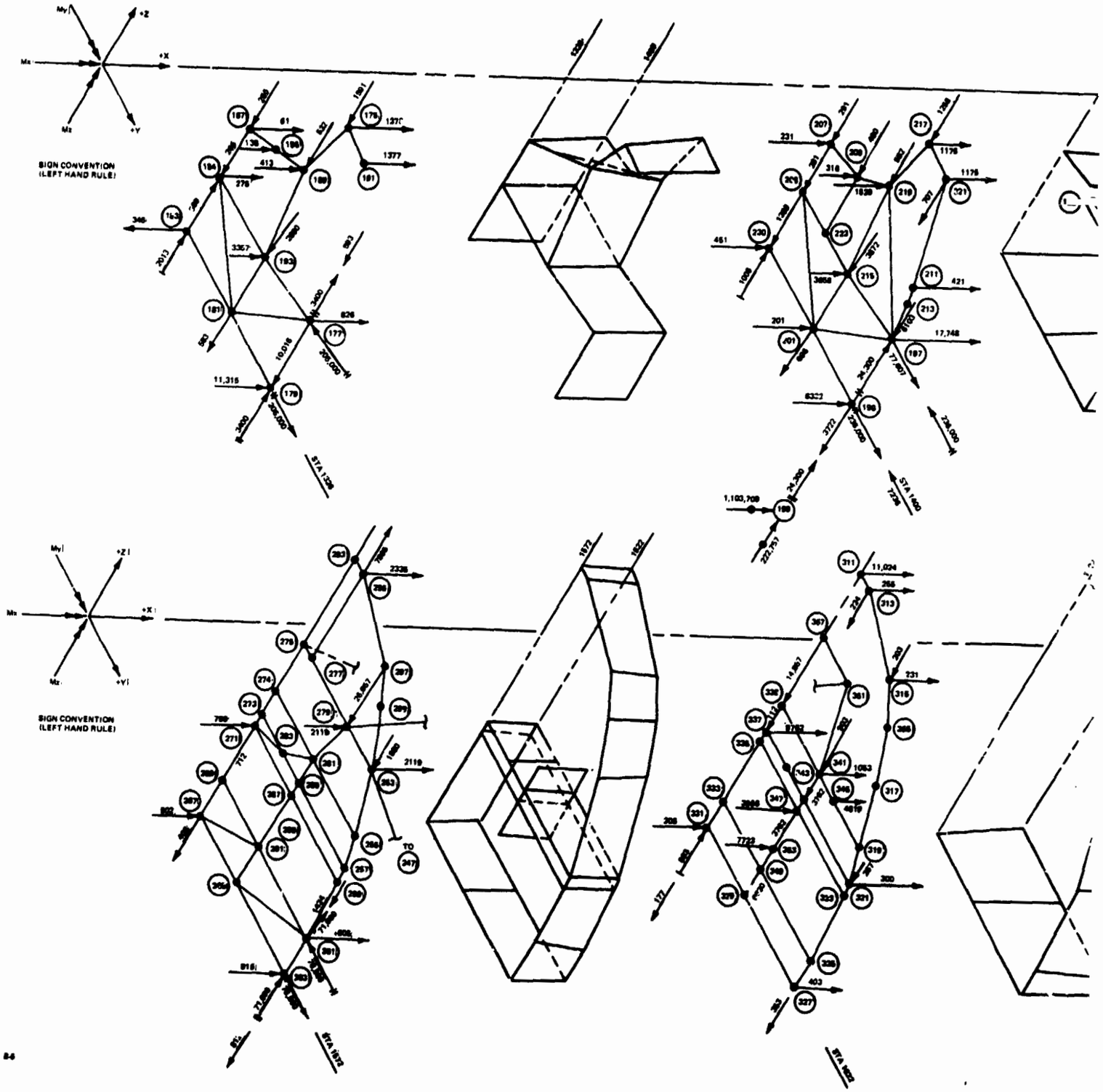

FOLDOUT FRAME 2

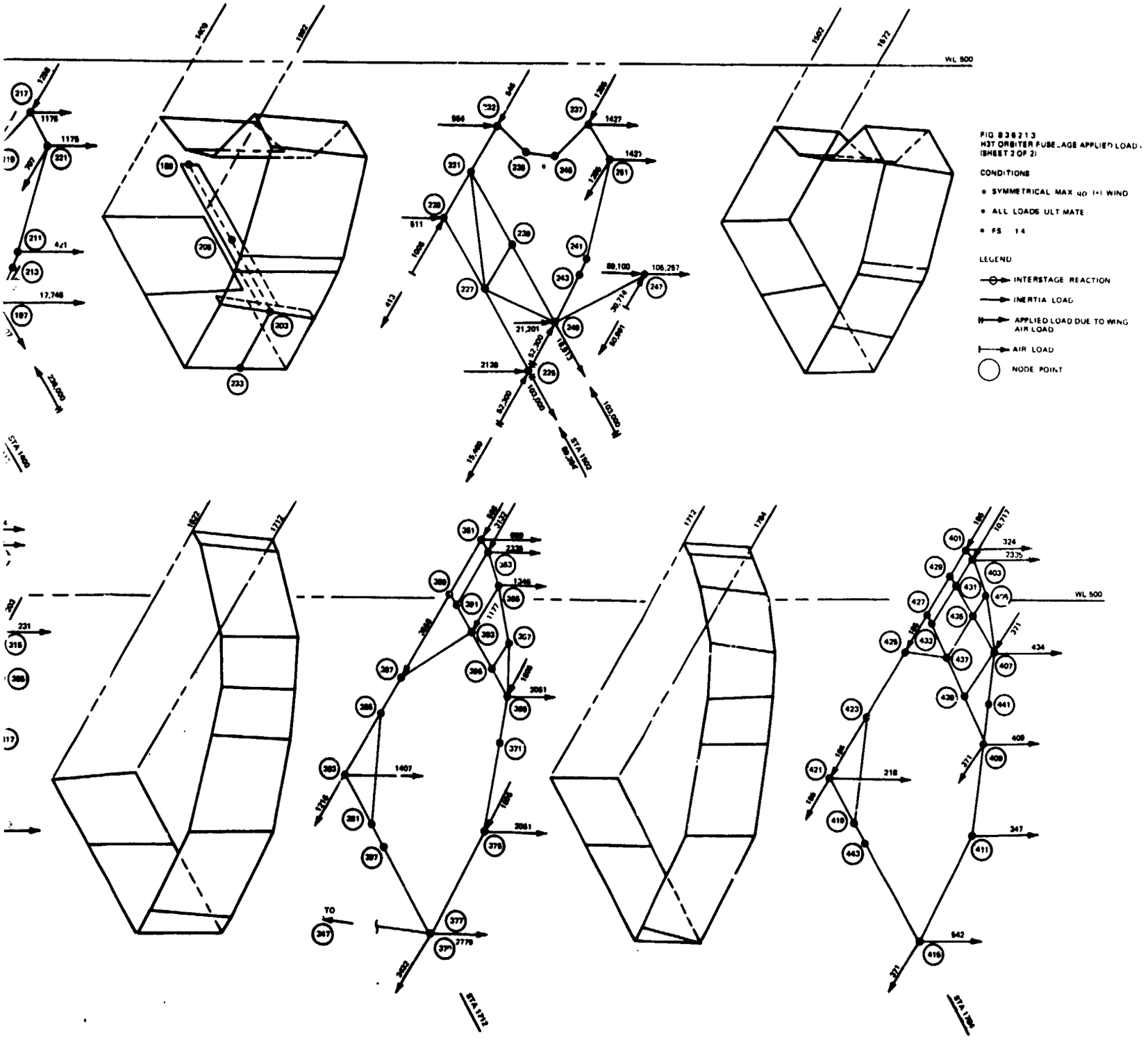

Fig. 8.3.6-23 H-3T Orbiter Fuselage Applied Loads, Symmetrical Max qα (+) Wind (Sheet 2 of 2)

FOLDOUT FRAME 1

B/8.3

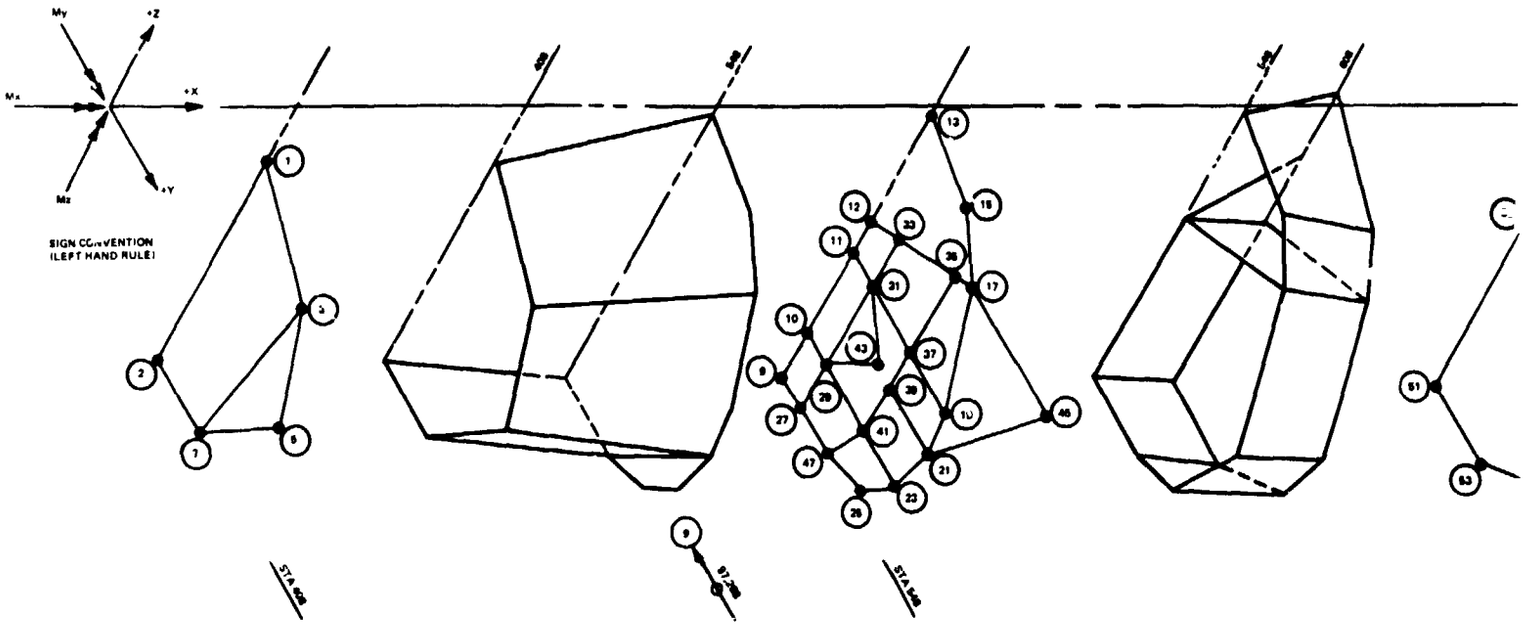

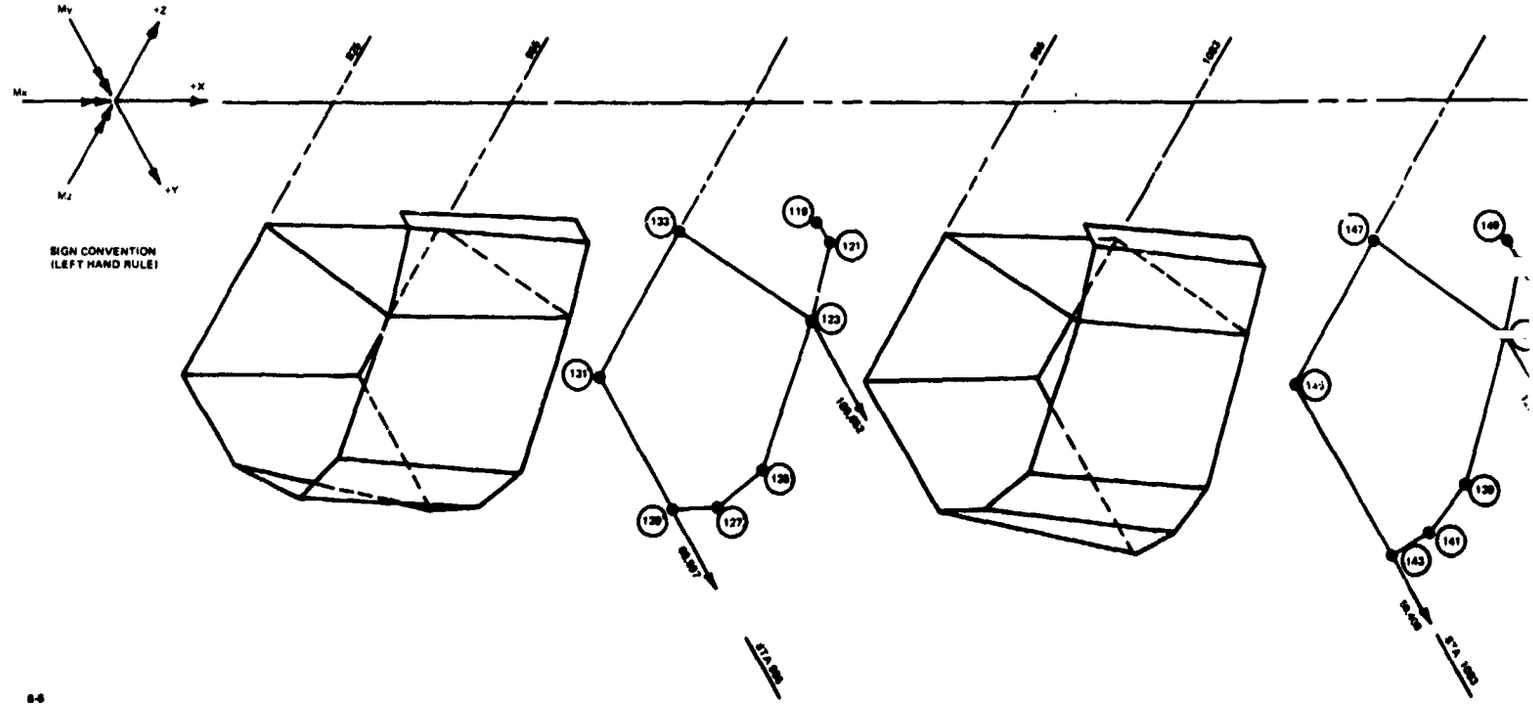

FOLDOUT FRAME 2

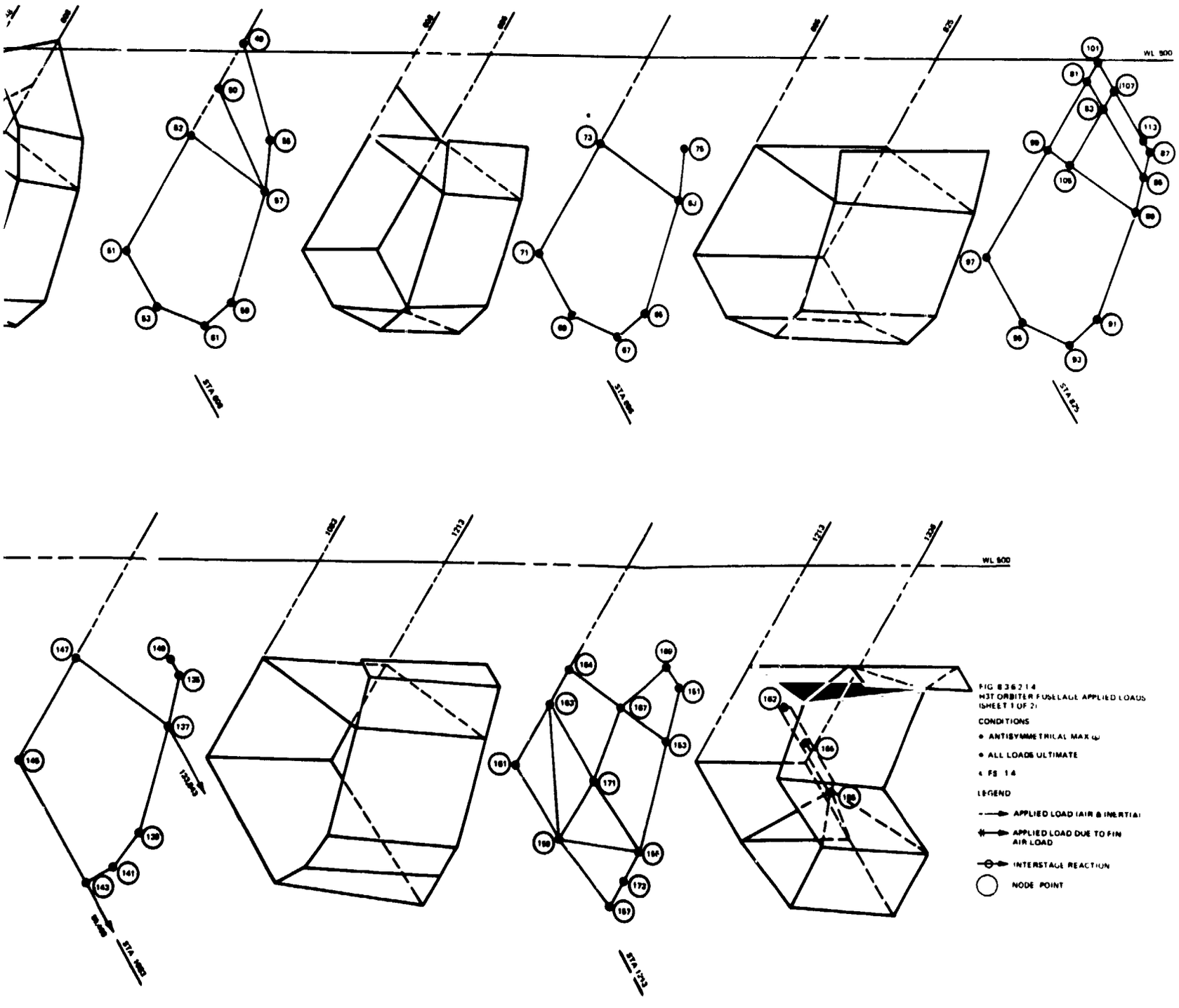

Fig. 8.3.6-24 H-3T Orbiter Fuselage Applied Loads, Antisymmetric Max $q\beta$ (Sheet 1 of 2)

FOLDOUT FRAME |

B/8.3

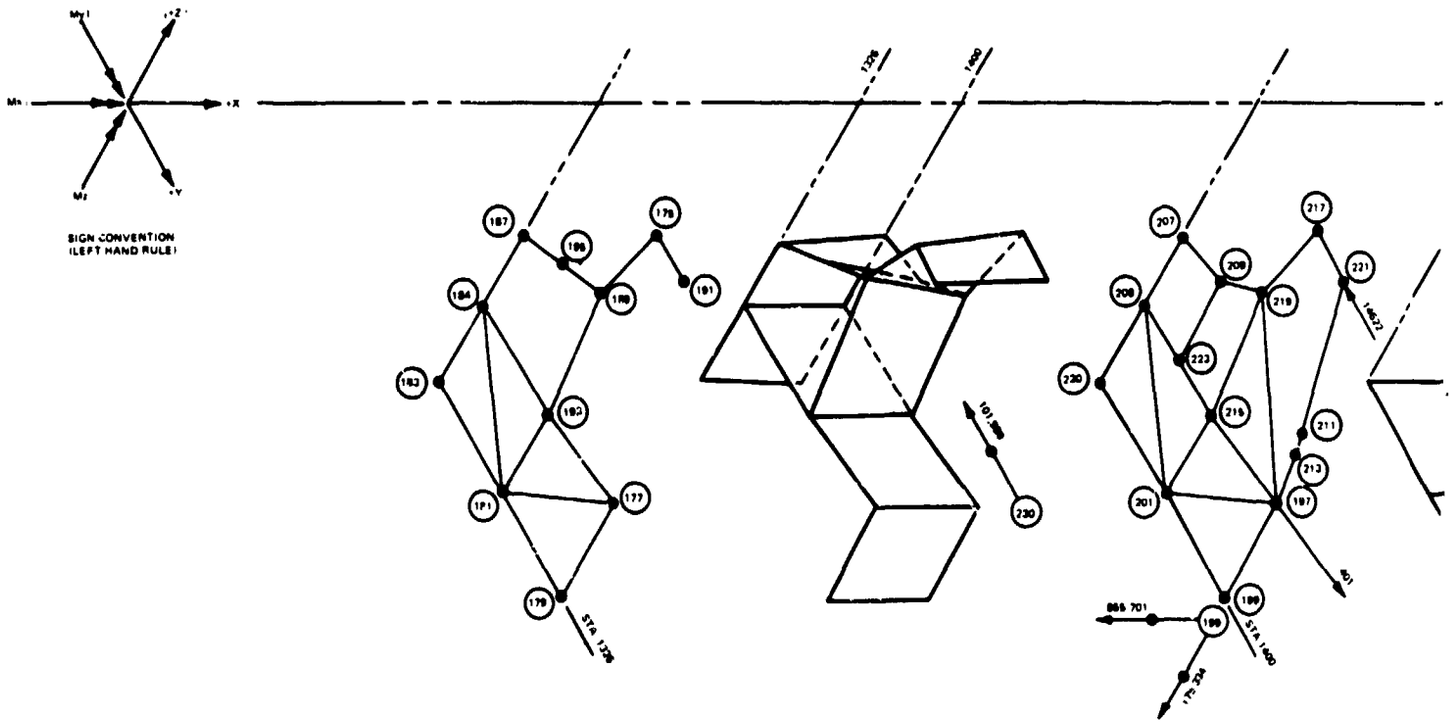

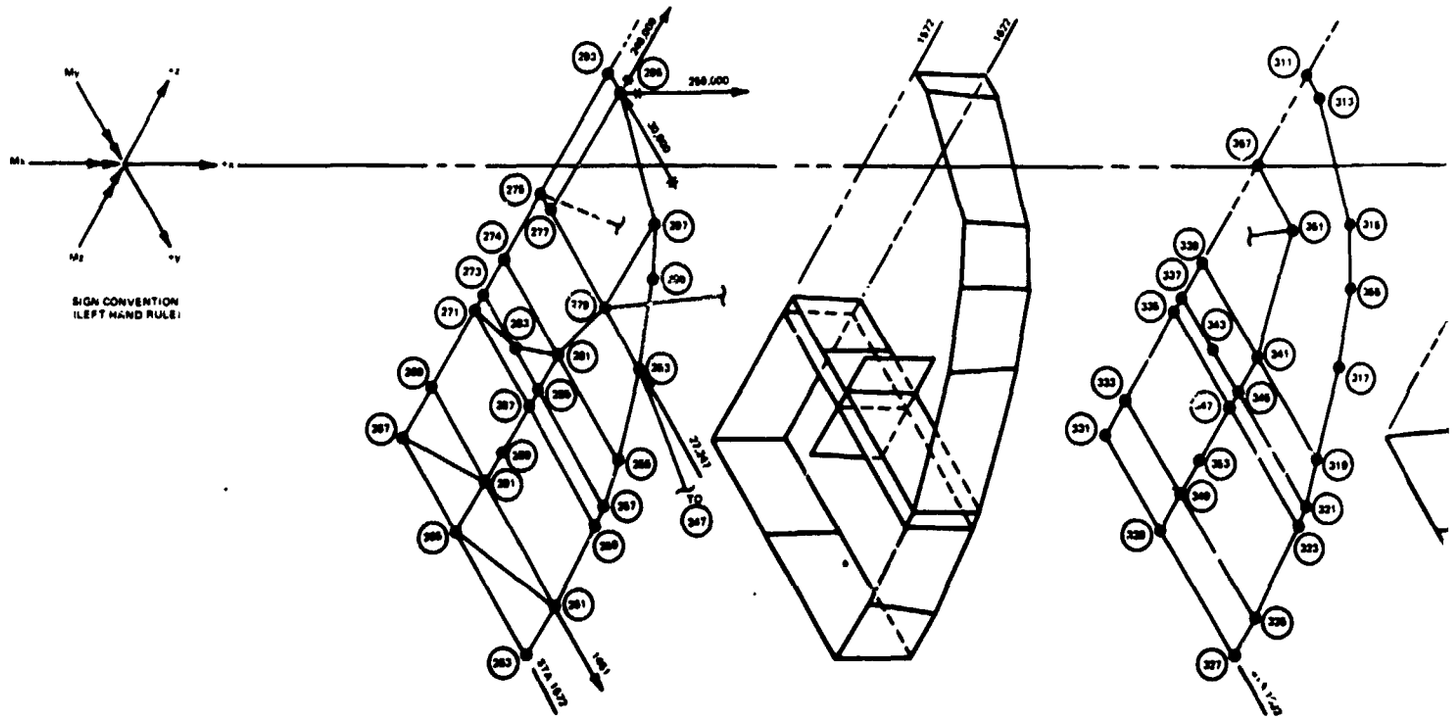

B-7

FOLDOUT FRAME 2

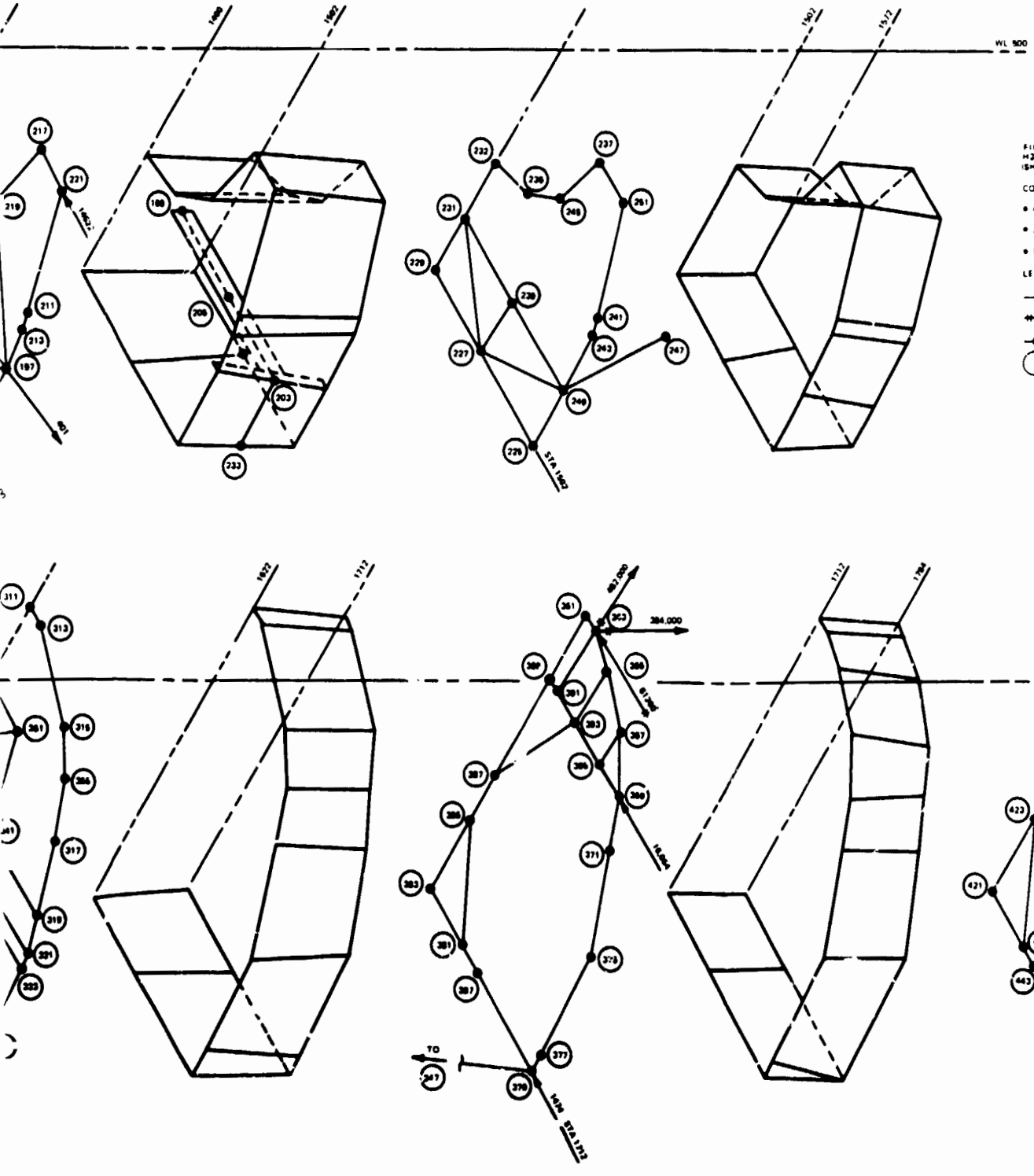

FIG 8.3.6.7.4
H3T ORBITER FUSELAGE APPLIED LOADS
(SHEET 2 OF 2)

Fig. 8.3.6-24 H-3T Orbiter Fuselage Applied Loads, Antisymmetric Max q β (Sheet 2 of 2)

GRUMMAN
BOEING

TABLE 8.3.6-7. DESIGN LOADS AND TEMPERATURES FOR H-3T MAIN PROPELLANT TANKS

Load Conditions	Inertia Limit Load Factors (Rigid Body + DMF)			System Pressure Max/Min (psig)	Max. Design Pressure (psig)	Design Temp (^{o}F)	Qty of Propel
Description	n_x	n_y	n_z				
Ground Hold	1.0	TBD	TBD	20/1	System & Hydrost	RT/ Cryog.	Empty/ Full
Lift Off	- .35+.65	0 5	±0.5	21/14	System & Hydrost	Cryog	Full
Max q	-1.6±.2	0	± 1.09±.1	31/25	System & Hydrost	Cryog	Full
Max q β	-1.6±.2	±.65±.1	0	31/25	System & Hydrost	Cryog	Full
End Boost-Booster	-3.0±.25	±0.1	±.5	31/24	System & Hydrost	Cryog	Full
End Boost-Orbiter	-3.0±.25	±0.1	±.5	31/24	System Only	LH_2: -230 LO_2: 0	Full to Empty
Subsonic Flight	±.25	±0.5	-2.5 +1.0	5/2	System Only	+250	Empty
Landing	±1.1	±0.6	-3.0	5/2	System Only	+250	Empty
Abort	TBD ←					→	TBD

The wing structure is analyzed for three critical loading conditions. For each condition the net limit load per exposed wing panel and the design center of pressure are as follows:

Condition	Limit Net Load	Center of Pressure
Max qα (+)	320,000 lb	x = 1520 Y = 407
Max qα (-)	-385,000 lb	X = 1520 Y = 407
2.5 g Pullout	178,000 lb	x = 1351 Y = 339

Recently, there has been a significant reduction in wing loads relative to those quoted above for the qα conditions. It has not been possible to incorporate the changes in

wing element sizes caused by this load relief. This deficiency is not considered detrimental to the primary objectives noted herein, but will be corrected in future iterations.

5. Sizing of Fin Structure

The fin box beam and a representative portion of the fuselage support structure were included in the math model. The fuselage structure was included to provide a better definition of the load distribution in the root area of the fin rather than treat the fin as cantilevered at the root.

The fuselage model consists of a bulkhead supporting the fin forward spar and partial ring frames supporting the remaining spars. Major fuselage longerons and side skins are included. All fuselage structure is composed of titanium bars and shear panels and was sized by hand based on an estimated preliminary load distribution at the fin root.

The entire fin box beam was sized for the Max q α air load condition using the fully stressed design (FSD) program. The total load of 218,000 lb limit was assumed to be fully reversible with a center of pressure envelope ranging from 25% to 50% chord and 30% to 50% of exposed span.

Recently, there has been a significant reduction in fin loads relative to those used for the initial sizing. It has not been possible to incorporate the change in fin element sizes caused by this load relief. This deficiency is not considered detrimental to the primary objectives noted herein.

Cover panels, rib caps, diagonals, and posts were treated as stability critical and were sized by the FSD program accordingly.

8.3.6.3.2 Description of Booster Structural Model Idealization

The fuselage, wing and tail surfaces of the booster were treated as beams with torsional and extensional flexibility in the model idealization. The major components of the booster were idealized in the following manner:

- The fuselage between the nose and the aft Y ring of the LO_2 tank was treated as a straight beam with the elastic axis located at the centerline of the tank

- The aft fuselage structure extending from the aft Y ring of the LO_2 tank and including both thrust and hold down structure, is represented by a flexibility matrix calculated from applicable structural drawings
- The wing was treated as a straight beam with its elastic axis located midway between the front and rear spars
- The horizontal tail was treated as a straight beam at the 45 percent chord line, cantilevered from the side of the fuselage
  The vertical tail was similarly idealized
- The end dome idealizations of the LH_2 and LO_2 tanks include the effect of side-wall distension caused by hydrostatic pressure in the full tanks. Their stiffnesses were simulated as axial springs
- The interstage connection for the booster is a pinned support system. The forward support is capable of transmitting vertical and lateral forces. The aft supports transmit vertical and longitudinal forces at each of two outboard supports, and a lateral force at the booster centerline. All four points are in the plane of booster W.L. 610.0. Spring stiffnesses of these points, relative to the booster structural reference axis at booster W.L. 400.0, are included in the structural idealization

Rigidity data was established for the booster wings, horizontal tail, inter-tank structure and the forward fuselage in the form of EI, GJ, and EA plots. The LH_2 and LO_2 tank rigidities are based on Boeing supplied drawings for the H3S heat sink booster. The left half of the aft fuselage was modeled in detail. Its flexibility matrix for the symmetric case incorporates, in an averaged sense, the flexibility of five left-side engine thrust points in the X and Z directions. A force transformation matrix representing an assumed rigid mechanism was used to transfer interacting forces from the wing to the fuselage beam idealizations. This transformation assumes pinned supports for the wing with rotational constraints about the Y axis at the wing root.

The structural model of the booster used 41 beam elements, six support spring stiffnesses, two end dome spring stiffnesses, and an aft fuselage flexibility matrix with 14 degrees of

freedom. The geometry of the structure was described by 66 nodes. The flexibility matrix for general unit loads has 318 degrees of freedom. The final dynamic model flexibility matrix has 76 symmetric degrees of freedom.

8.3.6.3.3 Analysis of Orbiter Structural Model

The structural analysis of the H-3T orbiter is outlined on Fig. 8.3.6-25 which is sheet number 1 of Report B36-100RP-105 to be submitted to the NASA in early July 1971. The following orbiter information will be part of the report:

- Structural arrangement drawings
- Structural model drawings
- Weights model drawings
- Airloads model drawings
- Dynamic model drawings
- Analysis flow diagram
- Model element sizes & geometry
- IBM listings of internal loads
- IBM listings of structural deflections
- Flexibility matrix for use in dynamic analyses

Certain more advanced analyses have not been performed at this stage but will be given careful attention in the future. Among these are the following:

- Evaluation of the cyclic loads caused by temperature gradients
- Evaluation of the effects (s) on stiffness which may be caused by temperature
- Incorporation of such effect (s) in the structural model and analysis thereof

The structural analysis is composed of two main efforts, the first being the analysis required to determine flexibility influence coefficients for a symmetric dynamic analysis, and the second to determine internal member loads for critical steady state flight and ground conditions. In the first analysis, only the left side of the orbiter was analyzed with

FOLDOUT FRAME 1

B/8.3

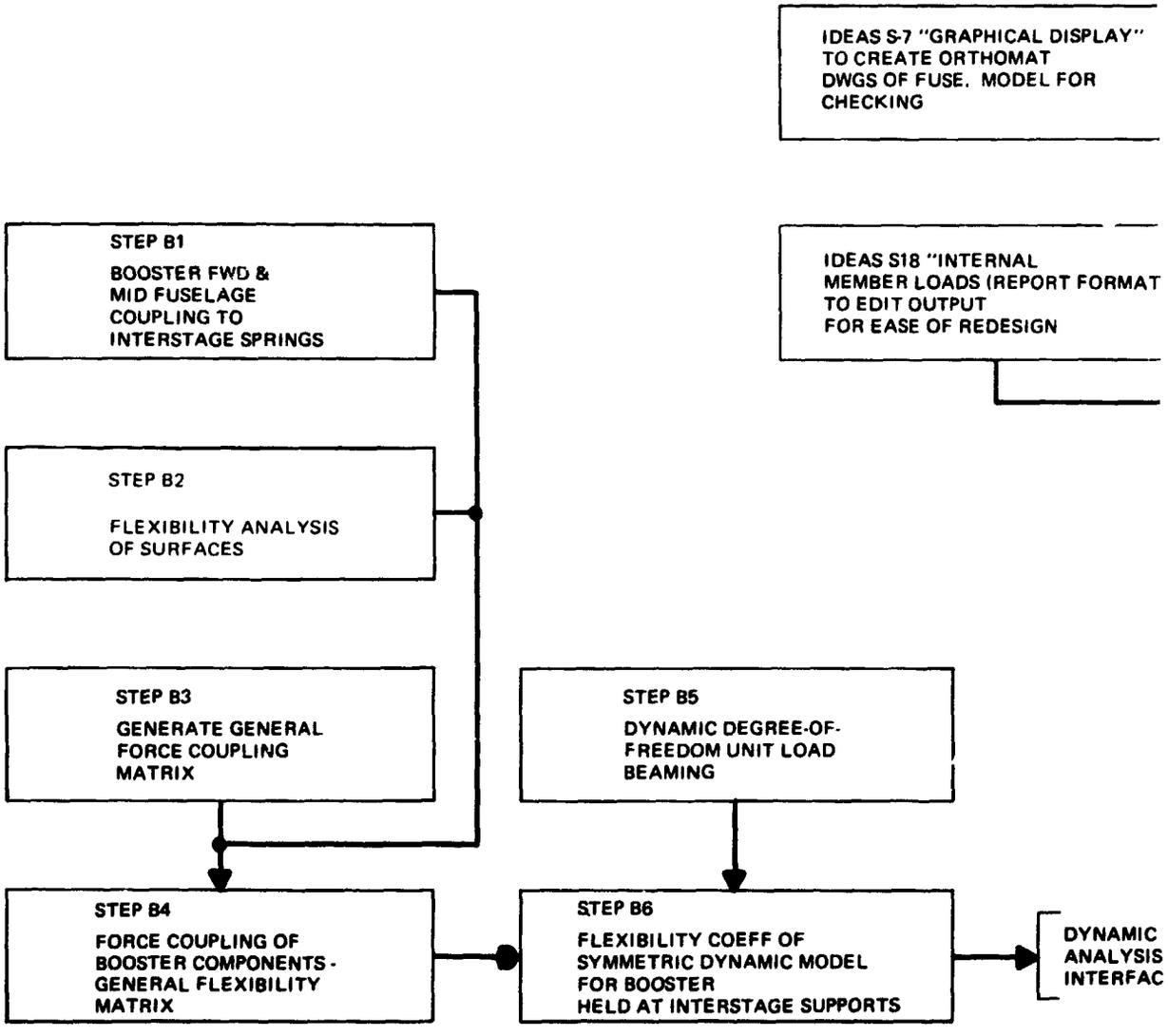

FOLDOUT FRAME 2

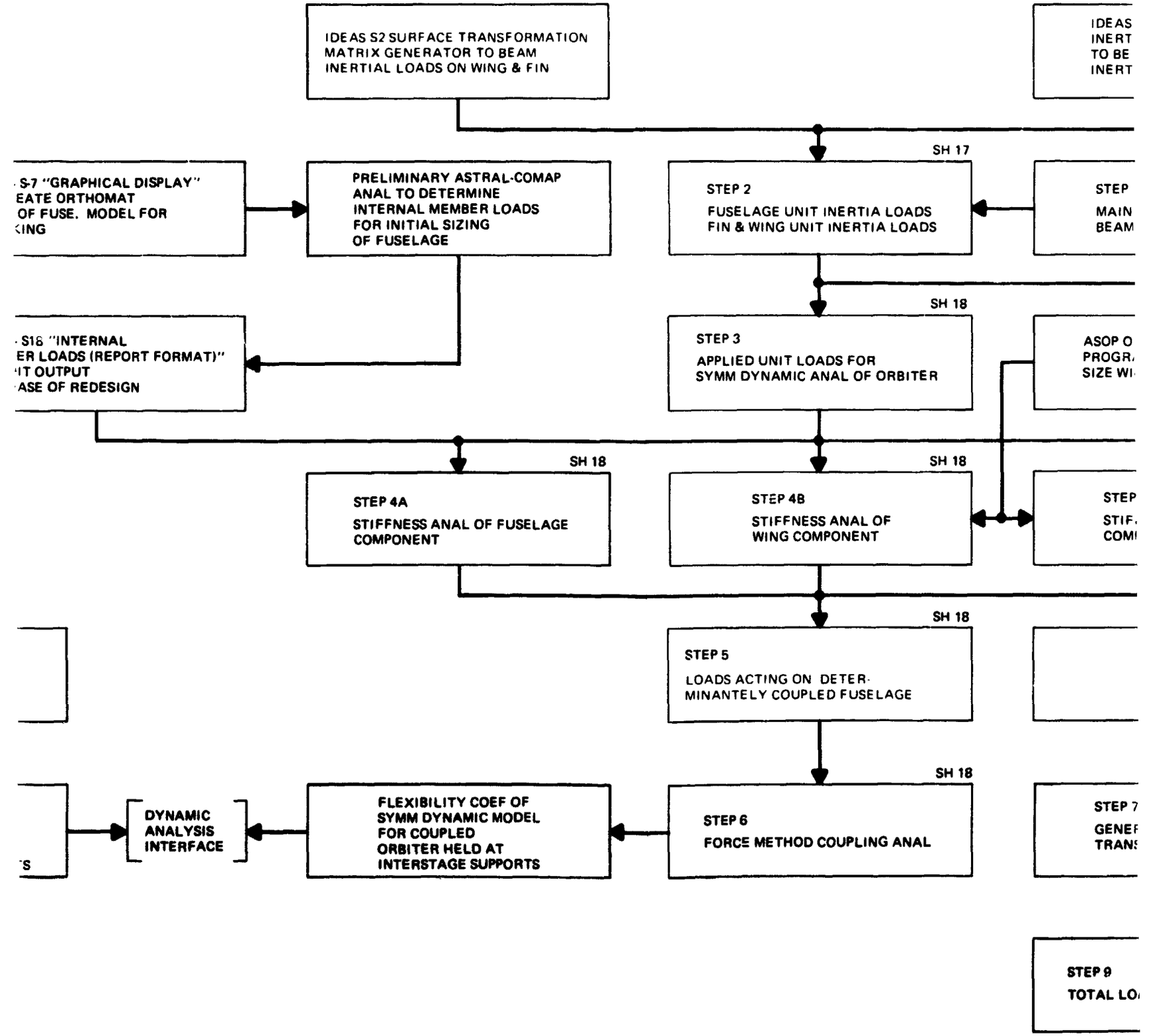

FOLDOUT FRAME 3

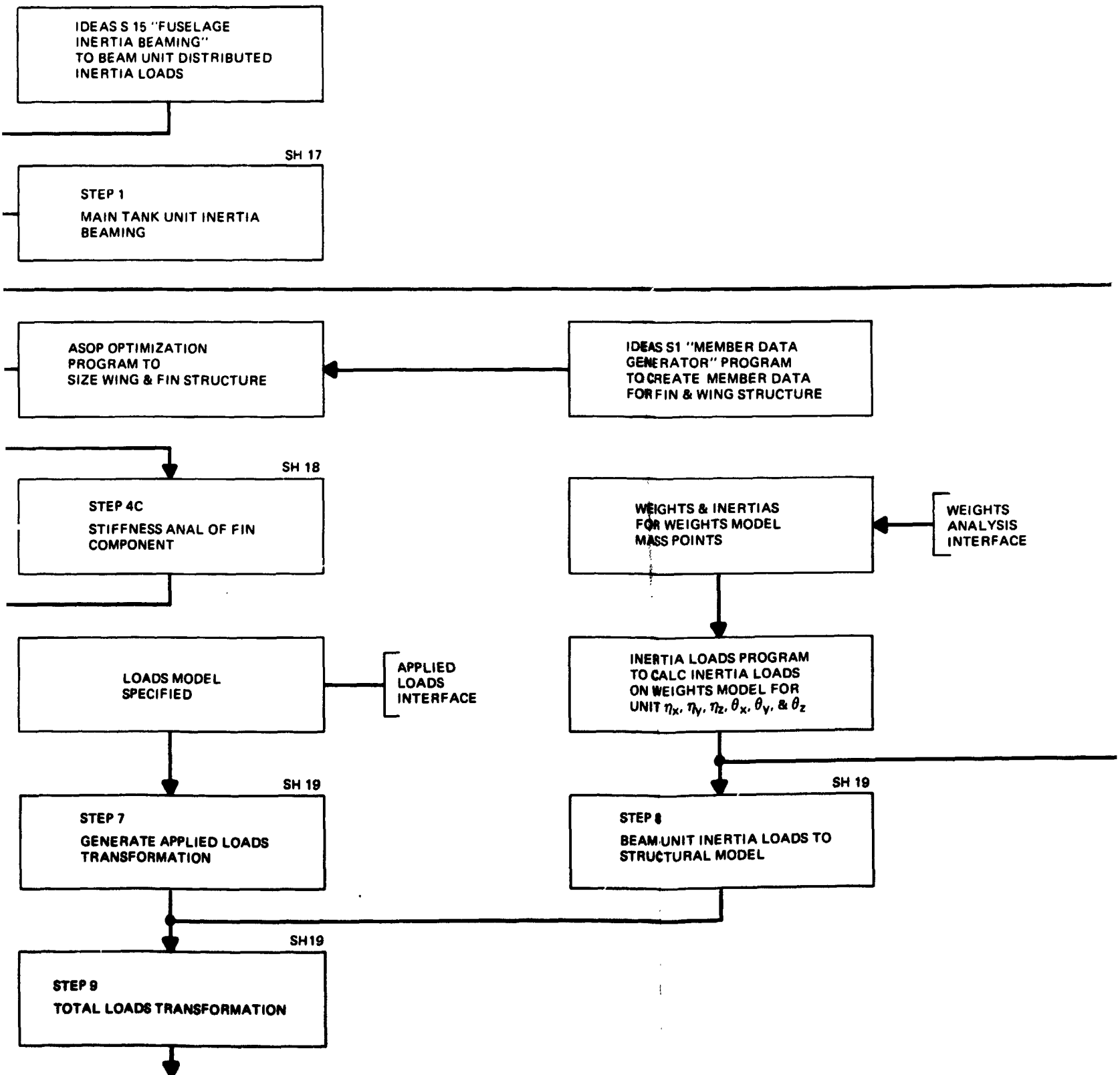

Fig. 8.3.6-25 Structural Analysis Flow (Sheet 1 of 2)

GRUMMAN BOEING

FOLDOUT FRAME 1

B/8.3

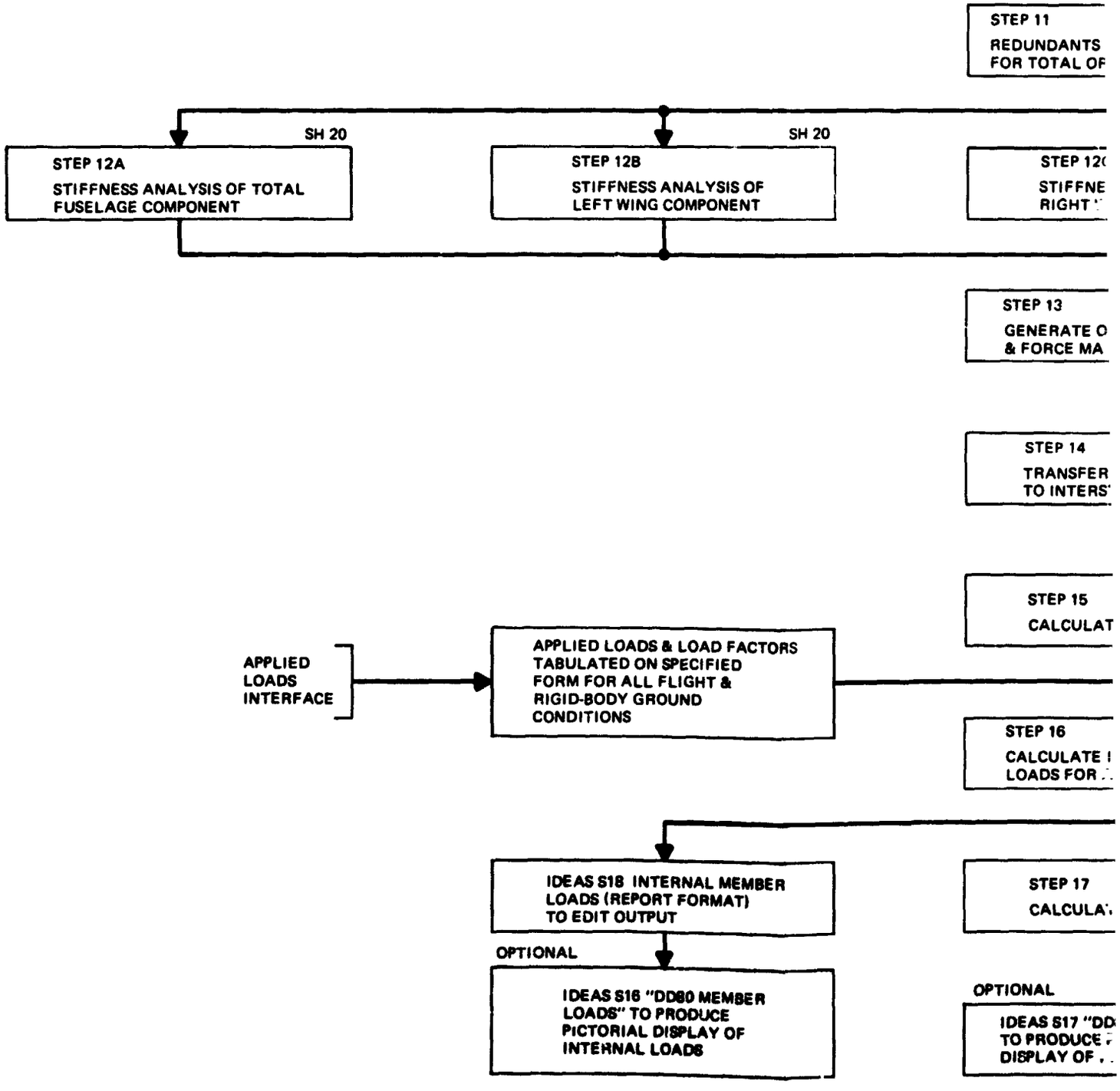

FOLDOUT FRAME 2

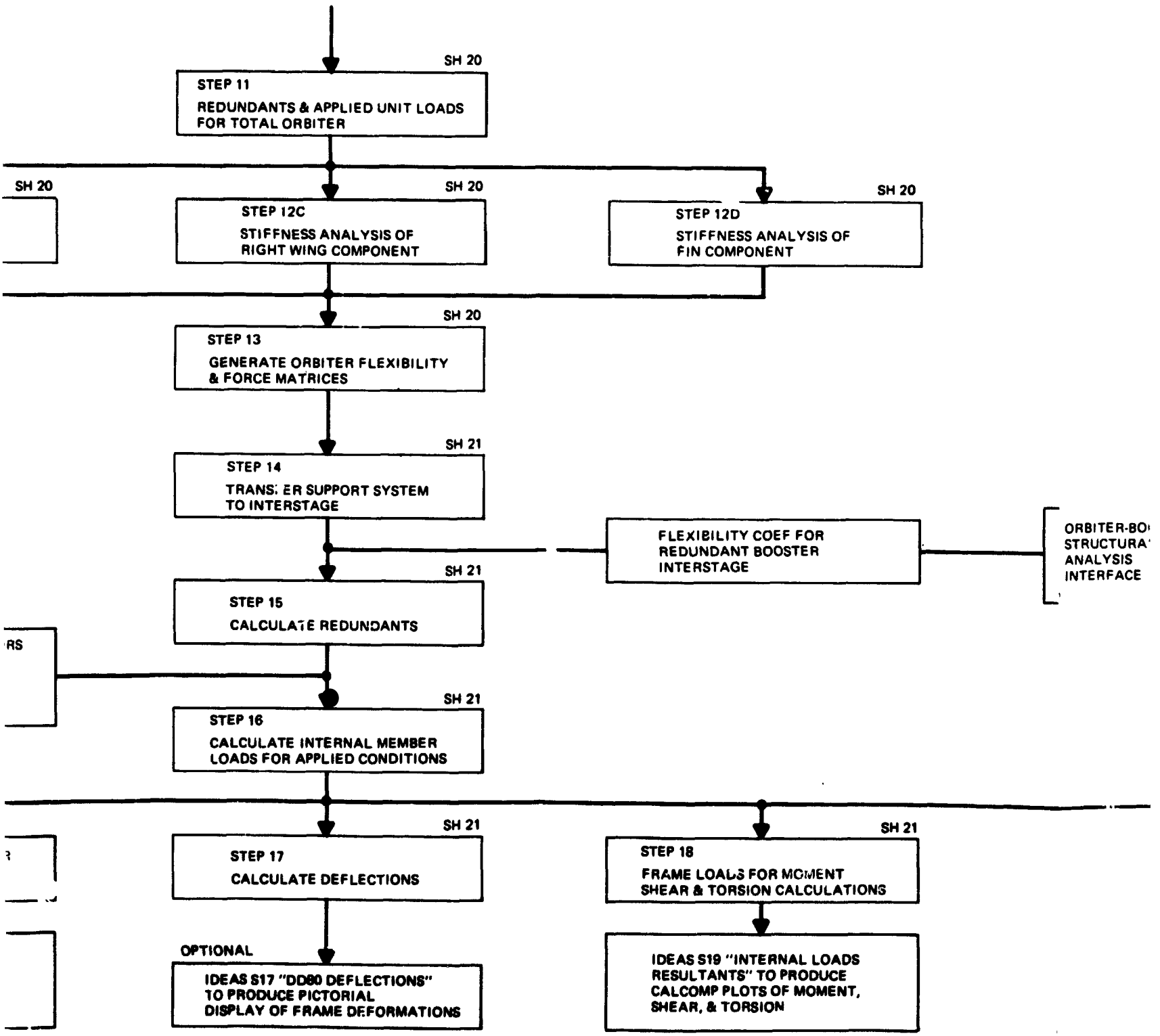

Fig. 8.

AME 2

FOLDOUT FRAME 3

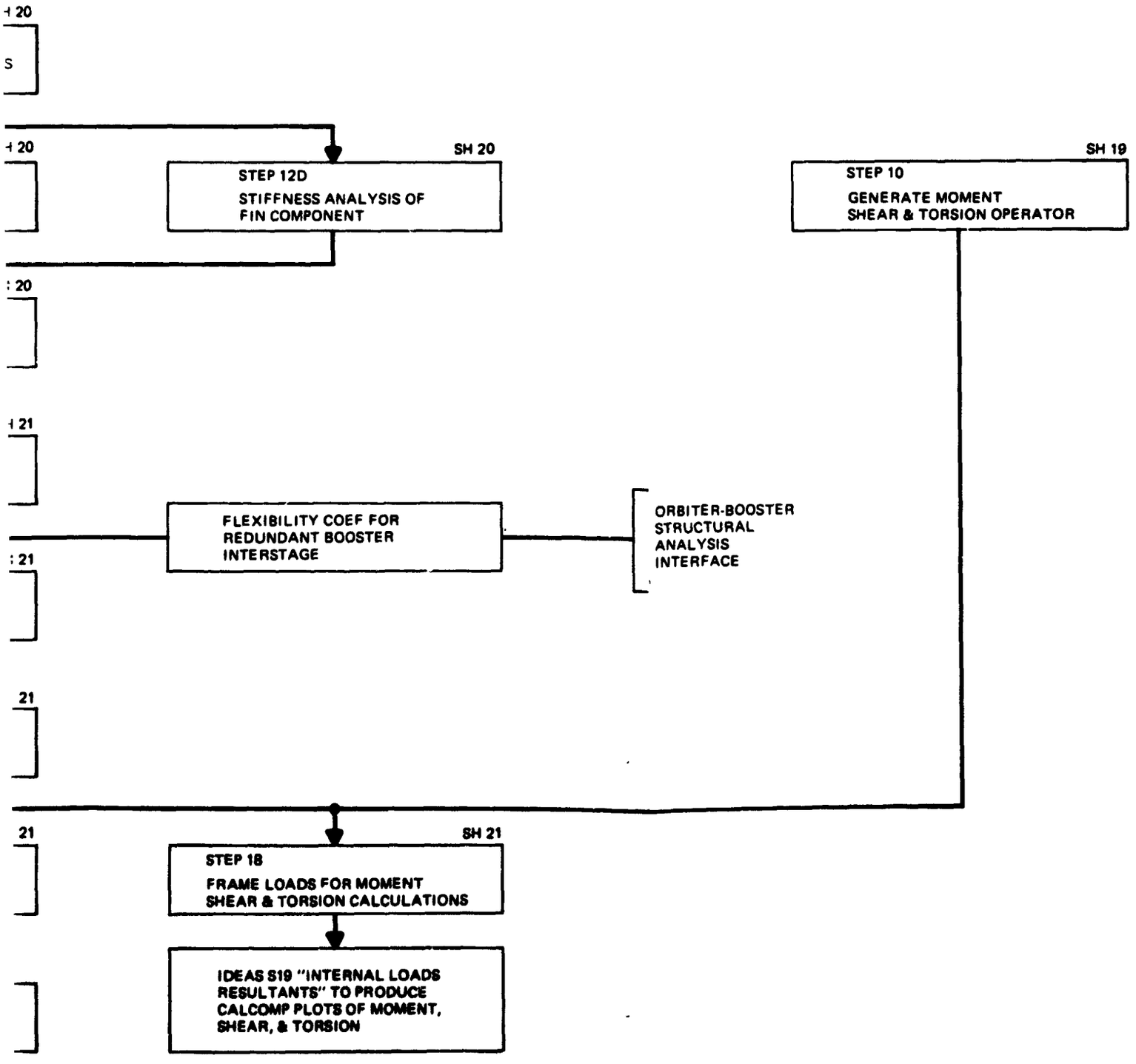

Fig. 8.3.6-25 Structural Analysis Flow (Sheet 2 of 2)

GRUMMAN BOEING

symmetry conditions imposed along the center plane. In the second analysis, the total orbiter was analyzed. This was done for the following reasons:

- The symmetric dynamic analysis was of prime concern for this study since it provides a major portion of the critical loadings. The left half of the symmetric structure was created and checked out. Subsequently, programs were used to create the right side of the model from left side data
- Analyzing the total structure for asymmetric loads requires fewer (but larger) matrix operations than would be the case if the model were separated into symmetric and anti-symmetric components.

The complete structural analysis requires the definition of four primary mathematical models which are: structural model, weight distribution model, airload/applied load distribution model, and dynamic math model.

The structural model consists of an arrangement of finite element members (bars, beams, shear panels, etc.) which are interconnected at node points. There is sufficient refinement to represent the overall structural characteristics. The H-3T Structural Model consists of certain major components and the number of elements comprising each component are given in Table 8.3.6-8.

TABLE 8.3.6-8. H-3T ORBITER STRUCTURAL MATH MODEL REPRESENTATION

Element	Fuselage (Half Structure)	LH Wing or RH Wing	Vertical Fin
Bars	359	55	294
Beams	66	-	-
Shear only - Shear Panels	175	97	56
Direct Stress - Quadrilateral Panels	-	72	124
Direct Stress - Triangular Panels	-	14	12
Nodes	211	110	202

The weights model consists of a series of lumped masses, sufficient in number to adequately represent the mass characteristics of the vehicle. The distribution of the 95 total mass points which make up the orbiter model is presented in Table 8.3.6-9. These points do not change geometrically for any given total weight condition. Weight conditions are changed by varying the value assigned to selected point masses. In the present analysis, two weight conditions have been selected to represent the full-fuel orbiter weight for a 65,000 lb payload with no air breathing engines, and the orbiter weight for the baseline landing configuration.

TABLE 8.3.6-9. H-3T ORBITER WEIGHTS MODEL MASS DISTRIBUTION

Structural Component	Number of Mass Points
Distributed Fuselage Weight	15
Left Side MPS LO_2 Tank	5
Right Side MPS LO_2 Tank	5
On Orbit LH_2 Tank, No. 1	3
On Orbit LH_2 Tank, No. 2	3
On Orbit LO_2 Tank	1
Cabin	1
Payload	1
Main Rocket Engines	2
Nose Gear	1
Main Gear	2
Left Hand LH_2 Drop Tank	6
Right Hand LH_2 Drop Tank	6
Vertical Fin	4
LH Wing Panel (Exposed)	20
RH Wing Panel (Exposed)	20

The Airload/Applied Loads Model is comprised of the 92 load points described in Table 8.3.6-10. The number of load points chosen are considered adequate to represent the airload applied loads at this stage of design.

TABLE 8.3.6-10. H-3T ORBITER AIRLOAD/APPLIED LOADS MODEL DEFINITION

Item	No. of Load Components
Fuselage lift loads at every 100-in. station	16
Fuselage side loads at every 100-in. station	16
Fuselage Drag	1
Total exposed LH wing lift acting at four discrete points	4
LH wing drag	1
Total exposed RH wing lift acting at four discrete points	4
RH wing drag	1
Total exposed vertical fin side load acting at four discrete points	4
Vertical fin drag	1
Components of load acting at the drop tank pickup points due to airloads acting on drop tanks	10
Booster - Orbiter interstage forces	7
Nose gear, LH and RH Main gear applied loads	15

The symmetric dynamic math model has 125 degrees of freedom (dof). Since, for cases of symmetric loading, the orbiter is supported determinately at the interstage pickup points, 3 dof are considered ignorable. An advantage of this choice is that it eliminates the need to statically couple the orbiter and booster for symmetric conditions. Both vehicles are coupled dynamically. The remaining dof included in the flexibility influence coefficient matrix are categorized as follows:

- Fuselage structure — 30 dof
- Major fuselage items — 24 dof
- LO_2 tank — 15 dof
- LO_2 tank fluid compressibility — 1 dog
- LH_2 tank — 18 dof

• LH_2 tank fluid compressibility	1 dof
• Left hand wing	25 dof
• Vertical fin	8 dof
	Total = 122 dof +3 ignorable dof

a. Generation of Symmetric Flexibility Influence Coefficients

Reffering to Fig. 8.3.6-25 it is seen that the symmetric flexibility influence coefficients for the dynamic model were computed through a series of matrix operations. For ease of computation, these calculations were subdivided into code steps which have physical significance.

Code steps 1 and 2 are concerned with beaming unit loads associated with the weights model to node points of the structural model. Use was made of the IDEAS S2 and S15 beaming programs in generating the pertinent transformations. The S2 program generates a transformation which converts surface loads on one grid system to a statically equivalent load system on the Structural Model. The S15 program transforms concentrated mass point loads to an equivalent load system on the fuselage structural nodes.

In step 3, unit loads for the symmetric dynamic analysis were set up and beamed to structural nodes. Since the dynamic degrees of freedom are in effect contained within the mass-point applied unit loads, the transformation developed in step 2 are simply modified by matrices which adjust the sequencing of the applied loads. In this same step, unit values of wing/fuselage and fin/fuselage redundant loads are identified.

Step 4 is subdivided into the following three separate steps:

4A - Analysis of the symmetric fuselage

4B - Analysis of the left wing

4C - Analysis of the complete fin

Applied loads for each of these component analyses are obtained from step 3. The finite element member sizes were derived as discussed in paragraphs 8.3.6.3.1 and 8.3.6.3.2.

Each of the components was analyzed by the COMAP-ASTRAL stiffness program.*

*Grumman IDEAS Manual, Vol. IIA, Section 7.

B

The outputs of these analyses are deflections of the component relative to its supports, internal member loads for the component for unit values of the redundants and applied unit dynamic loads, flexibility coefficients of the redundants and applied loads, and reactions of the component due to unit redundants and applied loads.

In step 5, the reactions to the wing and fin (applied as actions on the fuselage) were computed and lined up for use in the coupling analysis as described below in sub-paragraph b.

The components of orbiter structure are structurally coupled in step 6. (Note that the tanks are mounted in a statically determinate manner and are considered flexible structures.) The coupling was accomplished using the force method, wherein the uncoupled flexibility matrix is a block diagonal of the component flexibility matrices and the force matrix relates the component interaction forces to the redundants and applied loads. The flexibility of the determinately coupled structure was computed and the redundant interaction forces were determined. Back substitution of these redundant forces leads to the flexibility of the coupled redundant structure as held at temporary supports. Subsequently, the supports were transferred to the booster/orbiter interstage points and the flexibility matrix was modified to be used in dynamic analyses.

b. Generation of Internal Member Loads and Structural Deflections

The generation of internal member loads requires that loads on the airload/applied loads model as well as inertia forces in the weights model be transformed to the structural node points. Referring to Fig. 8.3.6-25, step 7 establishes transformation matrices which beam unit loads on the airload/applied loads model to the structural model. The unit air loads at the 100-in. stations are first beamed to the fifteen structural bulkheads. These loads are then distributed to selected nodes on the bulkheads in a fashion such as to maintain the center of pressure (CP) of the load. For the wing and fin, four assumed pressure distributions having CP's at,

- 25% chord & 35% span
- 45% chord & 50% span

- 45% chord & 35% span
- 25% chord & 50% span

are combined in the proper amounts as to represent a given flight CP. The resultant load distribution is then bridged to the structural model.

In step 8, inertia loads were developed on the structural grid as a function of unit values of n_x, n_y, n_z, $\ddot{\theta}_x$, $\ddot{\theta}_y$, $\ddot{\theta}_z$ acting at and about the orbiter center of gravity. These loads were developed in two stages. First, the inertia loads on the weights grid were calculated in terms of unit accelerations of the weights model; second, these loads were transferred to the structural model by using the transformations developed in step 2.

In step 9, the unit airload and applied load transformations from step 7 and the inertia loads transformation from step 8 were combined to form a single load transformation matrix for each of the four structural components. These transformations were checked by summing their components about the origin of the orbiter coordinates.

In step 10, a transformation matrix is developed which reduces all the fuselage applied node loads to equivalent force and moment resultants acting at the fifteen bulkhead stations. This transformation is used in step 18 to form the matrix which is used to compute moment, shear and torsion curves for the applied loading conditions.

In step 11, the unit applied loads from step 9 were combined with component redundant interaction forces to form the component applied load matrices used in steps 12A, B, C and D.

In step 12 A, B, C and D the total fuselage, left wing, right wing and fin components are analyzed respectively for the applied unit loads which were calculated in step 11. Each of these components was held in a statically determinate fashion and analyzed by the stiffness method to determine its internal member loads, structural deflections, flexibility coefficients, and reactions.

In step 13 the orbiter component flexibility and force matrices were developed by using data generated in steps 12 A, B, C and D. This was preparatory to solving for the redundant component interaction forces.

(6)

In step 14 the statically determinate orbiter support system is transferred from temporary supports to determinate interstage supports. This transformation is used in step 15 where the actual support transfer is accomplished.

In step 15 the redundant interaction forces were calculated in a series of steps. First, the redundants between the fuselage and the left wing, right wing and fin were calculated with the fuselage on temporary supports. The support system was then transferred to the determinate interstage reactions and the flexibility redundant was then added and the orbiter booster redundant (forward side force) was calculated. The redundant distributions were back substituted into the orbiter force matrix prior to determining the internal member loads discussed in step 16.

In step 16 the internal member loads as a function of unit redundants and applied unit loads that were computed in steps 12 A, B, C and D are combined with the output from step 15 to determine the final internal load distribution. In the same step the actual design conditions were substituted for the unit loads that had been used up to this point. Should need arise to study additional loading conditions it will ne necessary to only rerun step 16 for internal member loads, step 17 for deflections and step 18 for moments, shears, and torsions.

In step 17 the deflections of all structural nodes relative to the interstage points were calculated. These deflections are determined in two stages. First, the deflections of the redundant structure relative to the components' s determinate supports were evaluated, then the deflections due to the motion of these supports caused by deformation of the fuselage were added.

In step 18 the total node loads acting on the fuselage as a free body were determined and substituted into the moment shear and torsion operator developed in step 10. The output from this step consists of a matrix of net F_x, F_y, F_z, M_x, M_y, and M_z at each frame station for all loading conditions. This matrix was used as input to the IDEAS S19 program to calculate and plot moment shear and torsion curves.

8.3.6.3.4 Analysis of Booster Structural Model

The booster structure was analyzed as outlined on Fig. 8.3.6-25, which is sheet number 1 of Report B36-100RP-105 to be submitted to the NASA in early July 1971. The following booster information will be part of that report:

- Structural model drawing
- Dynamic model drawing
- Analysis flow diagram
- Computer listings of model element sizes and geometry
- Computer listings of the dynamic flexibility matrix

The booster structure was analyzed to obtain a symmetric dynamic flexibility matrix and the lateral (Y direction) flexibility of the forward interstate support point. The latter is used in the calculation of the redundant interstage loads that occur in asymmetric loading conditions when booster and orbiter are mated.

The booster was analyzed as a complete structure. It is supported at the booster-to-orbiter interstage in a statically determinate manner in cases of symmetric loadings. The symmetric flexibility matrix was obtained with reference to these points.

The flexibility matrices of the components, consisting of the fuselage, wing, horizontal and vertical tails, were obtained using the stiffness method of analysis. They were then coupled by force influence matrices.

The fuselage was separated into 3 sub-components:

- Forward fuselage
- Mid fuselage
- Aft fuselage and thrust structure

First, the flexibility matrices of the forward and mid-fuselage components were coupled with those of the interstage connectors. This resulted in the flexibility matrix of these joined sub-components, supported at the four interstage points. The flexibility matrices of the remaining structural representations were coupled to this at a later point.

The thrust point flexibility represents an averaged value for the combined thrust and supporting structure. Since it was desired to represent the symmetric flexibility of the whole booster, the flexibility matrix of this half structure was appropriately expanded to yield the full aft fuselage matrix for the symmetric case.

Tank end dome flexibilities are the inverse of calculated end dome stiffnesses.

The wing flexibility matrix was obtained with respect to a statically determinate support system at the wing root rib station. The redundant torsional moment flexibility at the left wing root is included in this flexibility matrix.

The vertical and horizontal tail flexibility matrices were obtained, assuming that their beam representations were cantilevered from the fuselage at WL 600. and BL ±220.0 respectively.

The second step consisted of generating the general force influence matrix which gives the forces applied to structural components due to the effects of:

- Loads on themselves
- Loads on other components
- Redundants

The third step consisted of coupling the component flexibility matrices by using this force influence matrix and the diagonally stacked component flexibility matrices by the usual method of redundant coupling. Although valid only for the symmetric case, this matrix represents flexibilities for six degrees of freedom at all node points. This occurs because the aft fuselage component flexibility corresponds to the symmetric case, as previously explained.

The last step was the generation and use of the load matrix corresponding to unit symmetric load cases in each of the dynamic degrees of freedom. Premultiplying the above mentioned overall flexibility matrix by the transpose of this load matrix, and then postmultiplying the product by this load matrix gave the final dynamic degree of freedom flexibility matrix of the booster for the symmetric case.

8.3.6.4 Dynamic Analysis

A symmetric dynamic mathematical model of the H-3T orbiter and booster was formulated as a lumped parameter representation of the vehicle's critical mass items. The structure's elastic properties were defined by the structural math models described in subsection 8.3.6.3. Using the Dynamic Model, vibration frequencies and mode shapes are calculated to uncouple the equations of motion so that dynamic response analysis can be efficiently performed. Dynamic responses to engine thrust oscillations are determined with the use of these modes.

8.3.6.4.1 Orbiter Dynamic Mathematical Model

The orbiter dynamic mathematical model is shown in Fig. 8.3.6-26. The total weight of the orbiter is 962,000 lb in the lift-off configuration. Combined orbiter and booster response was investigated with the orbiter in this weight configuration.

The orbiter model has 125 deg of freedom for the left half of the symmetric aircraft. The wing is represented by 25 deg of freedom to allow for use in preliminary flutter calculations in addition to the transient response analysis discussed herein. Table 8.3.6-11 summarizes these degrees of freedom.

TABLE 8.3.6-11. SYMMETRIC H-3T ORBITER DYNAMIC MATHEMATICAL MODEL (LH SIDE)

Item	Mass Point	Sym Degrees of Freedom			
		X	Y	Z	θ_y
Fuselage	15	15	0	15	
LO_2 Tank	6	6	5	5	
LH_2 Tank	7	7	6	6	
Major Items	17	11	2	12	2
Wing	20	5	0	20	
Fin	4	4	0	4	
Total	69	48	13	62	2

FOLDOUT FRAME 1

B/8.3

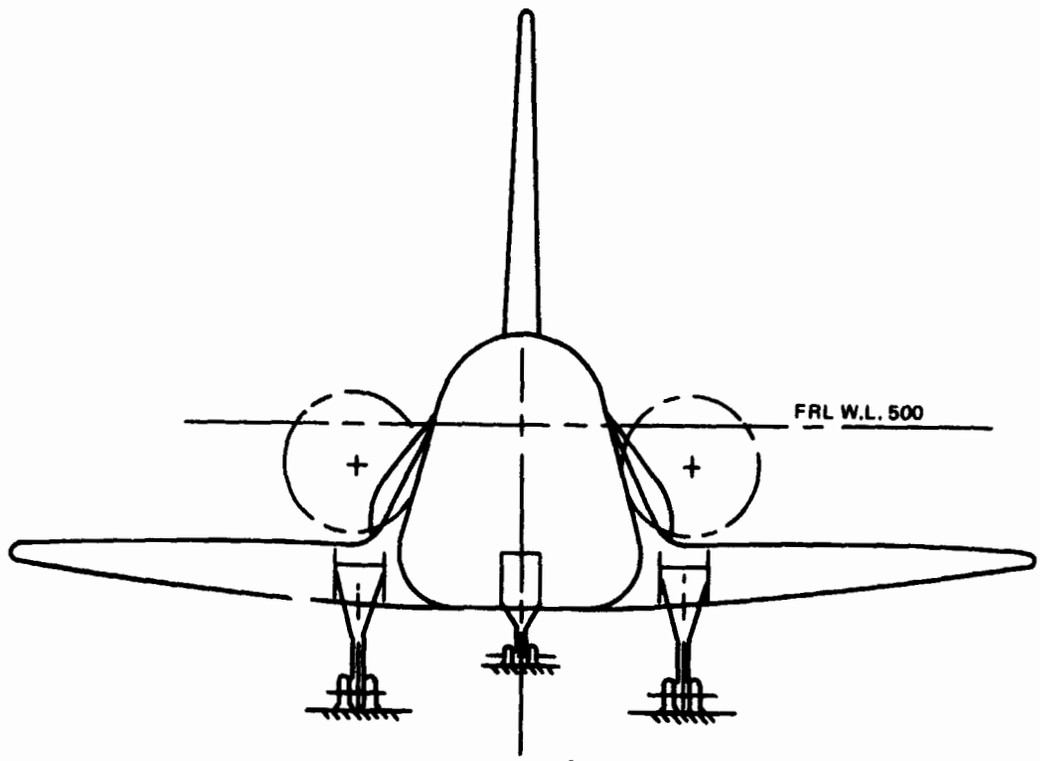

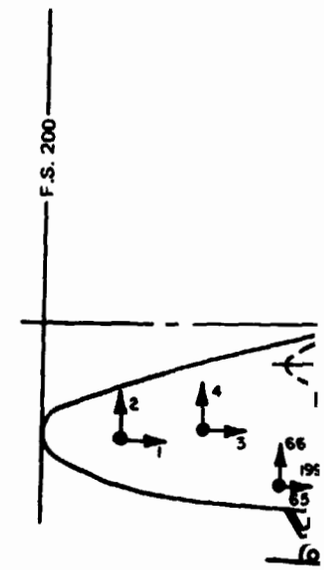

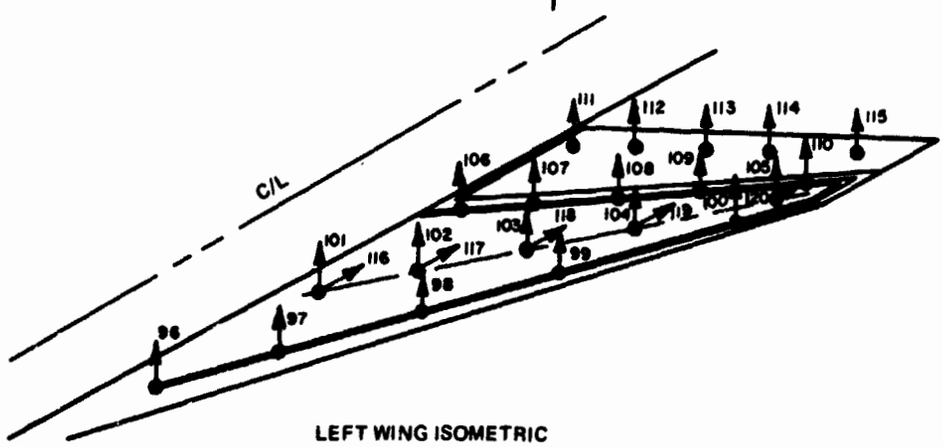

LEFT WING ISOMETRIC

FOLDOUT FRAME 2

C.8

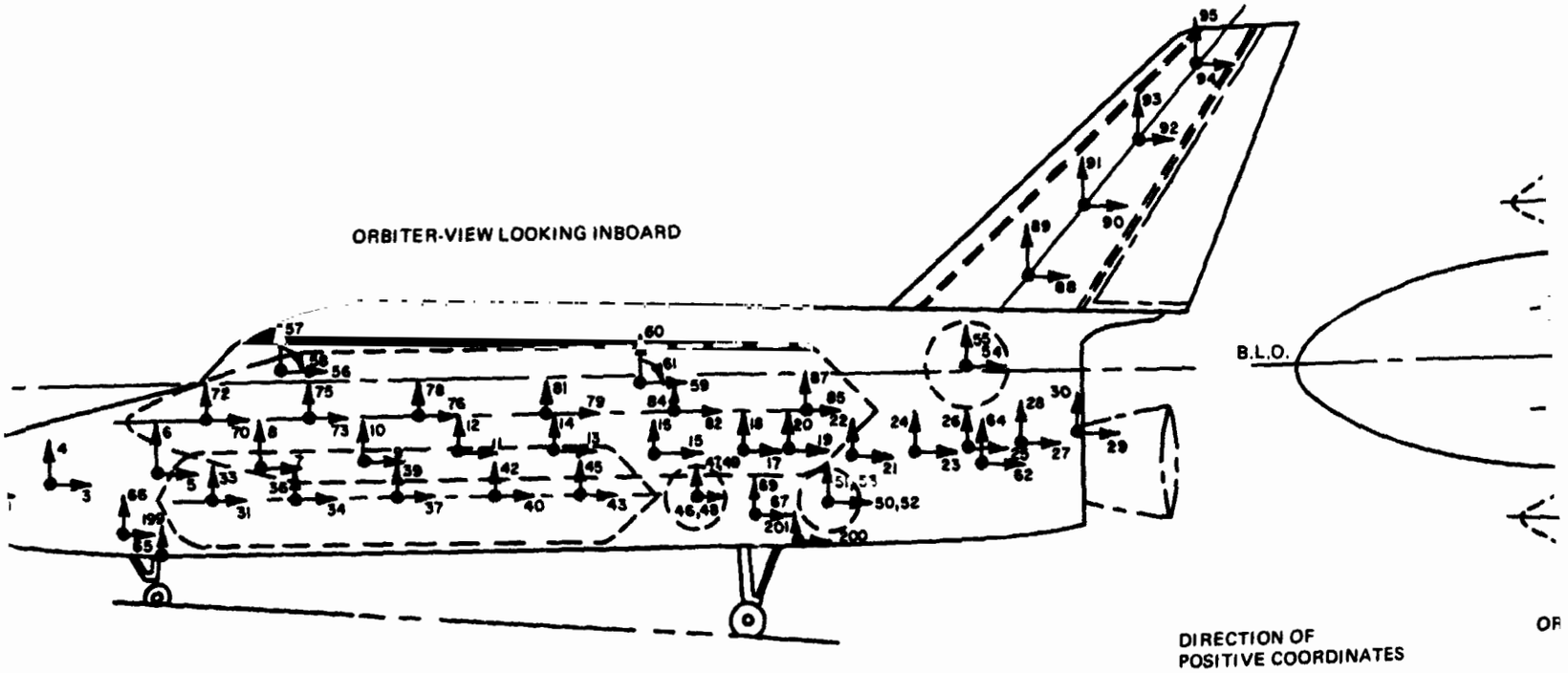

DIRECTION OF POSITIVE COORDINATES

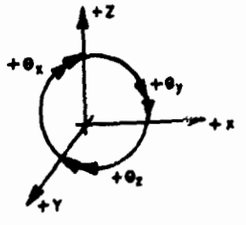

LH_2 FUEL MASSES

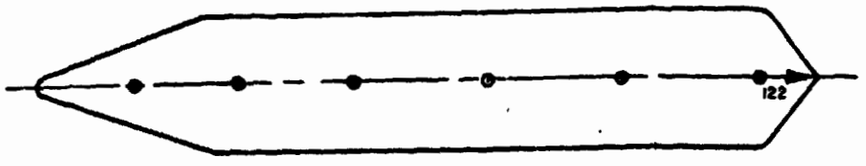

LOX FUEL MASSES

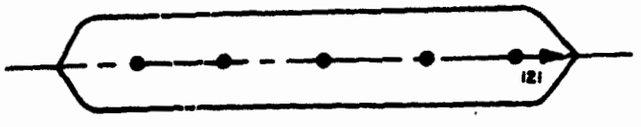

FOLDOUT FRAME 3

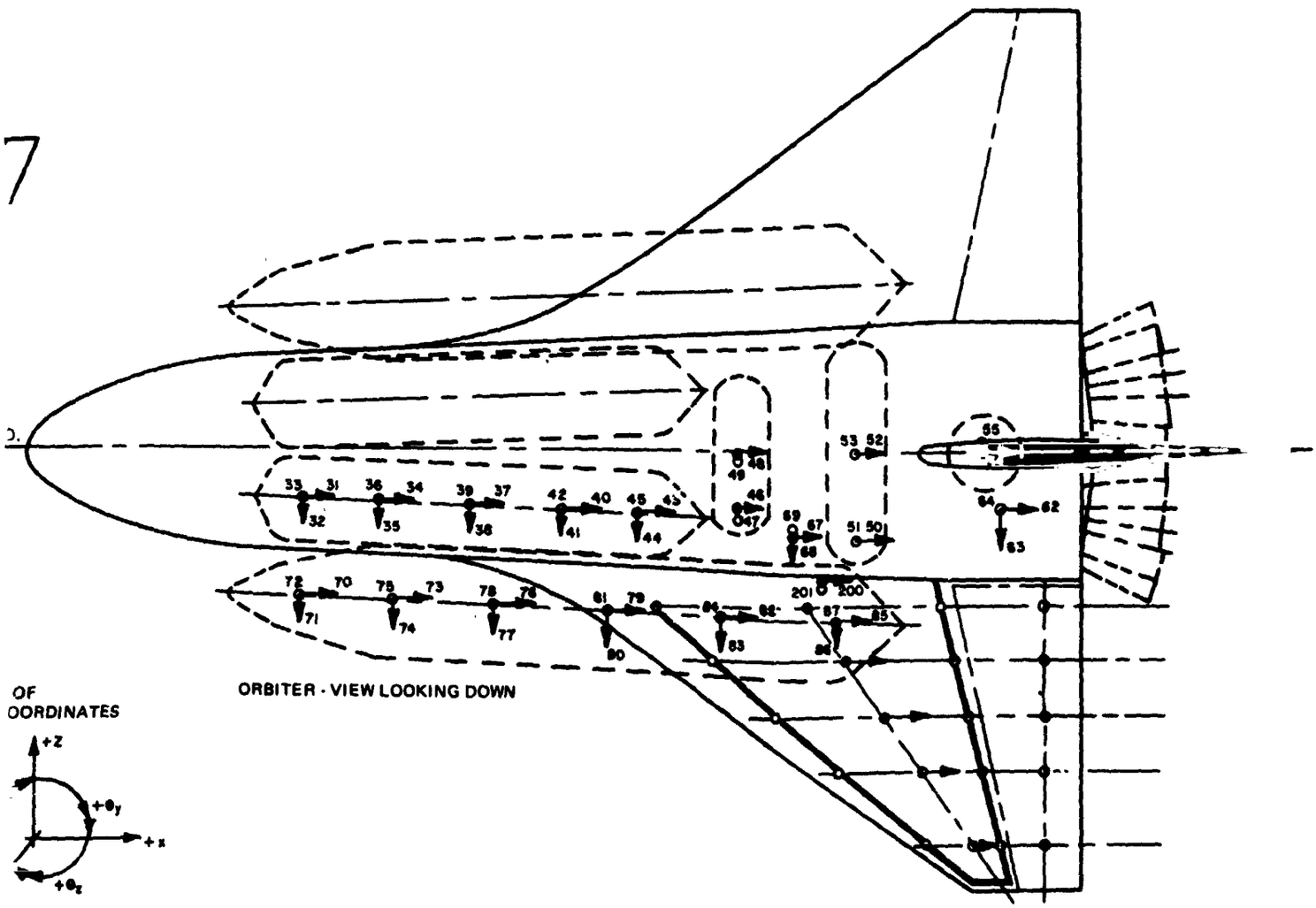

Fig. 8.3.6-26 H-3T Orbiter Dynamic Degree of Freedom Math Model (Symmetric)

8.3.6.4.2 Booster Dynamic Mathematical Model

The booster dynamic mathematical model is shown in Fig. 8.3.6-27. The booster weight is 3,400,000 lb at lift-off and 726,000 lb at booster burnout.

Symmetric booster degrees of freedom are summarized in Table 8.3.6-12. The booster model has a total of 76 deg. of freedom for the left half of the symmetric aircraft.

TABLE 8.3.6-12. H-3T DYNAMIC BOOSTER MATHEMATICAL MODEL - SYMMETRIC DEGREES OF FREEDOM (LH SIDE)

Item	Mass Points	Sym Degrees of Freedom		
		X	Z	θ_y
Fuselage	20	20	18	1
Wing	6	6	6	5
Horizontal Tail	4	4	4	4
Vertical Tail	4	4	4	
Total	34	34	32	10

8.3.6.4.3 Natural Frequencies and Mode Shapes

Symmetric frequencies and mode shapes were calculated for the combined booster and orbiter for the lift-off and booster burnout configuration. Unrestrained (free) modes were determined. Natural frequencies are summarized in Table 8.3.6-13. Plots of the mode shapes are given in Report B36-100RP-10[illegible] which will be submitted to NASA in early July, 1971.

8.3.6.4.4 Loads Due to Booster Unsteady Thrust

Using the modes and frequencies derived for the combined booster and orbiter, the response to booster engine unsteady thrust was calculated. This response was calculated for the combined vehicle for the lift-off (4,362,000 lb) and booster engine burnout (1,688,000 lb) configurations. The booster thrust acts through the combined vehicle center of gravity.

Table 8.3.6-14 shows the engine generated low frequency thrust oscillation limits.

These oscillations for 10 engines were applied sinusoidally to the booster gimbal plane and the response was calculated. Table 8.3.6-15 summarizes certain response accelerations. In addition, certain internal loads were calculated. These loads are summarized in Table 8.3.6-16. A more complete description of acceleration responses

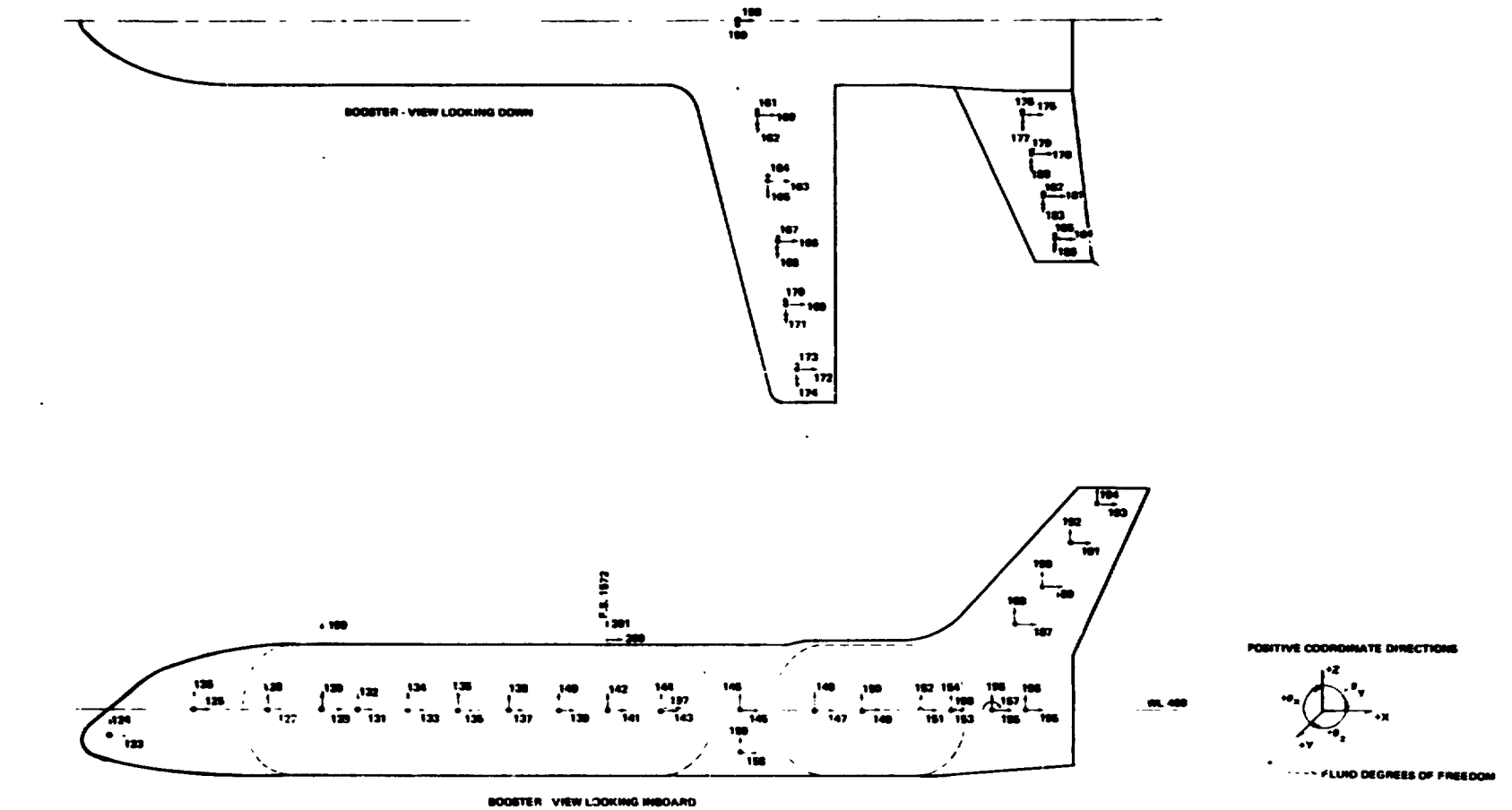

Fig. 8.3.6-27 H-3T Booster Dynamic Degree of Freedom Math Model (Symmetric)

TABLE 8.3.6-13 H-3T COMBINED ORBITER & BOOSTER
FREE-FREE NATURAL FREQUENCIES (Sheet 1 of 3)

A. Lift-off

Mode	Freq Hz	Gen Wt lb	Description
1	1.34	54,643	B LO_2 vs B H_2 & orb F&A + orb bend
2	1.56	9,206	B wing bend
3	1.63	37,976	B LOX + orb H_2 vs orb LO_2 + BH_2 F&A & orb bend
4	2.15	122,145	Orb LO_2 bend, orb LH_2 F&A & pitch vs. B LH_2 F&A, fus bend
5	2.31	179,023	Orb LO_2 lat (Y) bend
6	2.43	87,521	Orb H_2 F&A, pitch & Y vs B H_2 F&A, orb. fus. pitch
7	2.47	191,120	Orb LO_2 F&A, bend vs orb H_2 & boost H_2 F&A & bend
8	2.63	21,201	Orb H_2 F&A vert, orb wing + B stab bend (out phase)
9	2.87	38,629	Orb H_2 F&A vert, orb wing + B stab bend (in phase)
10	2.98	5,520	Orb wing bend + B stab bend (in phase)
11	3.07	6,288	Orb wing bend + B stab bend (out phase)
12	3.20	10,743	Orb orbit LO_2 & eng. vert (in phase) + B stab. bend
13	3.43	41,101	B fus vs orb LO_2 & B H_2 F&A, orb fus & wing bend
14	3.53	61,143	Orb H_2 vert, lat bend & F&A
15	3.85	15,599	B wing F&A
16	4.13	17,872	Orb orbit LO_2 & eng vert (out phase)
17	4.32	29,991	B fin, stab, orb fus vs orb wing F&A, orb fus & wing bend H_2 pitch
18	4.40	52,432	B fin, orb fus vs B stab & orb wing F&A, orb fus & wing bend H_2 pitch

TABLE 8.3.6-13 H-3T COMBINED ORBITER & BOOSTER
FREE-FREE NATURAL FREQUENCIES (Sheet 2 of 3)

Mode	Freq Hz	Gen Wt lb	Description
19	4.60	34,412	B fin, orb fus vs B stab & orb wing F&A, orb fus & wing bend H_2 pitch
20	5.39	4,281	B stab F&A bend

NOTE - B = Booster; orb = Orbiter; LO_2 = Oxygen Tank; H_2 = Hydrogen Tank; F&A = Fwd & Aft; bend = Bending; fus = Fuselage; stab = Stabilizer

B. Injection

Mode	Freq Hz	Gen Wt lbs	Description
1	1.57	15,475	Orb & B wing bend (out phase), orb fus. bend
2	1.59	21,640	Orb & B wing bend (in phase), orb fus. bend
3	2.31	176,506	Orb LO_2 lat (Y) bend
4	2.34	77,133	Orb LO_2 bend, orb fus & LH_2 pitch
5	2.60	85,321	Orb H_2 F&A, lat (Y), & pitch vs orb wing & B nose bend
6	2.75	17,585	Orb wing & B stab bend + LH_2 F&A and Z
7	2.96	11,562	Orb wing bend, LH_2 nose down pitch, aft inb'd yaw

TABLE 8.3.6-13 H-3T COMBINED ORBITER & BOOSTER
FREE-FREE NATURAL FREQUENCIES (Sheet 3 of 3)

Mode	Freq Hz	Gen Wt lb	Description
8	2.99	7,990	Orb wing bend
9	3.11	3,318	B stab bend
10	3.23	15,540	B wing & stab vs orb LO_2 F&A, orb wing & B stab bend
11	3.40	29,542	B wing & stab vert, orb fus & wing bend, orb H_2 pitch & Y bend
12	3.55	64,135	Orb H_2, lat (Y), vert bend & F&A, orb & B fin F&A
13	3.94	15,216	B wing F&A, orb & B fin, F&A
14	4.12	18,519	Orb orbit LO_2 & eng vert (out phase)
15	4.27	31,280	B wing & fin vs orb & B fus F&A
16	4.45	65,576	Orb & B pitch, orb wing bend
17	4.99	31,629	B fus bend & orb translation
18	5.39	4,241	B stab F&A bend
19	5.71	22,940	Orb fus bend, LO_2 pitch, H_2 pitch & yaw
20	6.02	41,846	Orb vs B F&A

TABLE 8.3.6-14. ENGINE-GENERATED LOW FREQUENCY THRUST OSCILLATION LIMITS (PER ENGINE)

Frequency	Allowable Thrust Variation
Hz	(0-Peak) KLBF
0 - .5	10.0
.5 - 1.5	2.0
1.5 - 25	.6

and internal loads is given Report B36-100RP-105, which will be submitted to NASA in early July 1971.

8.3.6.5 Dynamic Environment

Preliminary estimates of the high-level acoustic environment on the booster are presented in Table 8.3.6-17. This environment is considered the most significant with respect to fatigue damage of the structure, and to equipment damage or malfunction in locations forward of the main propulsion engines. Conditions creating the high-level acoustics are:

- Booster/orbiter launch
- Booster/orbiter atmospheric exit (transonic/maximum dynamic pressure)
- Captive orbiter firing of main propulsion engines
- Orbiter horizontal flight with air breathing engines

The orbiter is zoned into seven regions. The overall sound pressure levels (OA SPL) from booster engine captive firing are taken from a NASA paper*, and are considered representative of the launch condition. During launch, acoustic shadowing will exist on the underneath side of the orbiter because of its proximity to the booster. Another shadowing effect is dependent upon the booster/orbiter orientation on the launch pad with respect to the exhaust deflectors. Acoustic radiation effects between the booster and orbiter have not been estimated; attenuation of acoustic levels due to shadowing are not included in the preliminary environment.

*S.H. Guest Paper No. 14, "Space Shuttle Acoustics", Page 417, Slide No. 8, NASA TM X-2274, Vol. III - Dynamics and Aeroelasticity, April, 1971

TABLE 8.3.6-15. H-3T - MAXIMUM ACCELERATIONS (g)
DUE TO ENGINE UNSTEADY EXCITATION -
COMBINED VEHICLE (Sheet 1 of 3)

		Lift-off		Injection	
		*Accel g	Freq Hz	Accel g	Freq Hz
Orb LO_2 Tank	Fwd X	.045(.137)	1.63	.045	3.2
	Sta 622 Y	.059	11.0	.091	6.6
	Z	.195	3.4	.156	4.3
	Cent X	.045(.140)	1.63	.046	3.2
	Sta 870 Y	.052	11.0	.044	11.4
	Z	.088	1.63	.076	8.9
	Aft X	.045(.140)	1.63	.048	3.2
	Sta 1117Y	.054	11.0	.080	6.6
	Z	.189	3.4	.173	4.3
Orb LH_2 Tank	Fwd X	.093(.310)	1.34	.124	1.59
	Sta 618 Y	.346	6.1	.238	7.3
	Z	.400	6.1	.349	5.7
	Cent X	.093(.310)	1.34	.123	1.59
	Sta 1075Y	.110(.127)	3.5	.137	3.4
	Z	.326	6.1	.188	6.02
	Aft X	.092(.307)	1.34	.123	1.59
	Sta 1422Y	.390	6.1	.260	7.3
	Z	.382	4.4	.288	5.7
Orb LO_2	X	.100(.153)	4.6	.140	4.3
Orb LH_2	X	.101(.320)	4.6	.130	1.6

TABLE 8.3.6-15. H-3T - MAXIMUM ACCELERATIONS (g)
DUE TO ENGINE UNSTEADY EXCITATION -
COMBINED VEHICLE (Sheet 2 of 3)

			Lift-off		Injection	
			*Accel g	Freq Hz	Accel g	Freq Hz
Orb Fus	Nose Sta 303	X	.614	10.4	.44	6.0
		Z	1.24	6.3	.93	6.2
	Cent Sta 1084	X	.228	6.01	.194	6.0
		Z	.382	10.4	.307	9.5
	Aft End Sta 1784	X	.185(.227)	10.6	.165	11.5
		Z	.442(.550)	1.63	.396	1.59
Orb Crew Cpt		X	.805	6.1	.863	6.0
		Z	.353	4.4	.212	6.0
Orb Payload		X	.487	6.1	.370	6.0
		Z	.284	6.1	.204	6.0
Orb Wing Tip		X	.257	10.6	.209	10.6
		Z	.517	4.4	.903	3.0
Orb Fin Tip		X	.952	6.1	.982	3.2
		Z	.727(.867)	1.63	.832	3.2
Boost Fus	Fwd Sta 81	X	.221	4.6	.152	4.3
		Z	.541	4.6	.256	4.3
	LH_2 Cent Sta 1125	X	.156	4.4	.143	4.3
		Z	.053	4.6	.108	9.5

TABLE 8.3.6-15. H-3T - MAXIMUM ACCELERATIONS (g)
DUE TO ENGINE UNSTEADY EXCITATION -
COMBINED VEHICLE (Sheet 3 of 3)

			Lift-off		Injection	
			*Accel g	Freq (Hz)	Accel g	Freq Hz
Boost Fus	LO_2 Cent Sta 2325	X	.157	4.4	.149	4.3
		Z	.025	10.0	.092	4.3
	Engine Gimbal	X	.161	4.4	.157	4.3
		Z	.095	10.0	.134	5.0
Boost Wing Tip		X	.962	4.4	1.23	4.3
		Z	.486	6.1	.659	1.59
Boost Stab Tip		X	1.67	5.4	1.38	5.4
		Z	5.1	3.1	.469	3.00
Boost Fin		X	1.040	4.6	.818	4.3
		Z	.677	4.6	.582	4.3
Boost LH_2		X	.134	1.63		
Boost LO_2		X	.051(.113)	1.63		

*Values in parentheses are for 2000 lb force per engine (f <1.5 Hz)

TABLE 8.3.6-16 H-3T - MAXIMUM INTERNAL LOADS DUE TO ENGINE UNSTEADY EXCITATION - ORBITER

Reactions			Lift-off		Injection	
			Max Load (lb or in. -lb)	Freq Hz	Max Load (lb or in. -lb)	Freq Hz
LO_2 Y	Fwd React	V_y	2,143	11.0	367	14.28
	Aft React	V_y	2,226	11.0	454	14.28
	Max Bend Mom	M_z	354,419	11.0	83,979	14.28
LO_2 Z	Fwd React	V_z	2,545	4.17	716	14.28
	Aft React	V_z	5,363	4.76	876	14.28
	Max Bend Mom	M_y	977,460	4.17	162,850	14.28
LH_2 Y	Fwd React	V_y	2,544	3.52	1,686	14.28
	Aft React	V_y	2,467	3.52	567	10.99
	Max Bend Mom	M_z	735,000	3.52	222,470	14.28
LH_2 Z	Fwd React	V_z	2,270	4.76	1,100	12.98
	Aft React	V_z	2,835	4.17	795	12.44
	Max Bend Mom	M_y	709,000	4.17	146,100	12.44

TABLE 8.3.6-17 ORBITER EXTERNAL ACOUSTIC ENVIRONMENT

Zone	Booster Engines Captive Firing		Orbiter Engines Captive Firing	Air Breathing Engine Takeoff
	OA SPL*	Peak Octave	OA SPL*	OA SPL*
1. Forward Fuselage, Crew compartment, avionics	152	80-100 Hz	148	Less than 118
2. Center Body, Cargo Compartment, Avionics	152 Fwd End 156 Aft End	80-100 Hz 100-200 Hz	150 Fwd End 155 Aft End	118 Fwd End 145 Aft Top 160 Aft Side
3. Wings and Elevons	156 Fwd 160 TE	100-200 Hz 200-400 Hz	155 Fwd 159 TE	148 Aft Inboard 134 Wing Tip
4. Fin and Rudder	160	200-400 Hz	160 at Root 168 at Tip	147 at Root 129 at Tip
5. Aft Body	160	200-400 Hz	159	152
6. Main Propulsion Engines	160	200-400 Hz	168	145
7. Air Breathing Engines	154	100-200 Hz	154	-

*Overall SPL, db; Ref 2 x 10^{-5} N/M^2

It may be necessary to fire the orbiter main propulsion engines with the orbiter in a captive configuration. An estimate of the acoustic environment was generated by taking the previously referenced OA SPL curve for the twelve-engine booster firing condition and moving it forward to the orbiter main propulsion engines exit plane. For three-engine firing of the orbiter, the oscillating pressure level was reduced by a factor of $\sqrt{\frac{3}{12}} = 0.5$ in accordance with NASA prediction techniques.* This pressure magnitude reduction corresponds to a 6 db reduction in SPL; the relocated SPL curve was reduced by 6 db.

Extimated noise contours for the orbiter horizontal flight, take-off conditon, using the four air-breathing engines are indicated in Fig. 8.3.6-28. Also presented in this figure are octave band spectra of SPL for four locations along the orbiter fuselage. An estimate of the near-field noise contours is presented in Fig. 8.3.6-29. These noise contours were calculated in accordance with published noise prediction techniques.**

Acoustic environment durations, on a per-mission basis, are estimated as follows:

- Launch - 10 sec
- Transonic, Max q - 40 sec

Fluctuating pressure measurements were measured in the vicinity of the external tanks at transonic speeds from M=.6 to M=1.5 in the Ames 6x6-ft supersonic wind tunnel, ref AMES test no. 66-561 Three external tank configurations were tested on a 1/150th scale mated orbiter/booster. Pressure fluctuations were recorded at six locations by means of high frequency transducers. Results indicate RMS values of local pressure coefficient which are less than 8 percent of free stream dynamic pressure, so long as angles of attach are kept within the limits prescribed by the present control system during boost through design winds and wind shears.

*R.E. Barrett "Techniques for Predicting Localized Vibration Environments in Rocket Vehicles", NASA TN D-2158, July, 1964

**H.B. Plumblee "Near Field Noise Analysis of Aircraft Propulsion Systems with Emphasis on Prediction Techniques for Jets", TN AFFDL-TR067-43, August, 1967

FOLDOUT FRAME 1

B/8.3

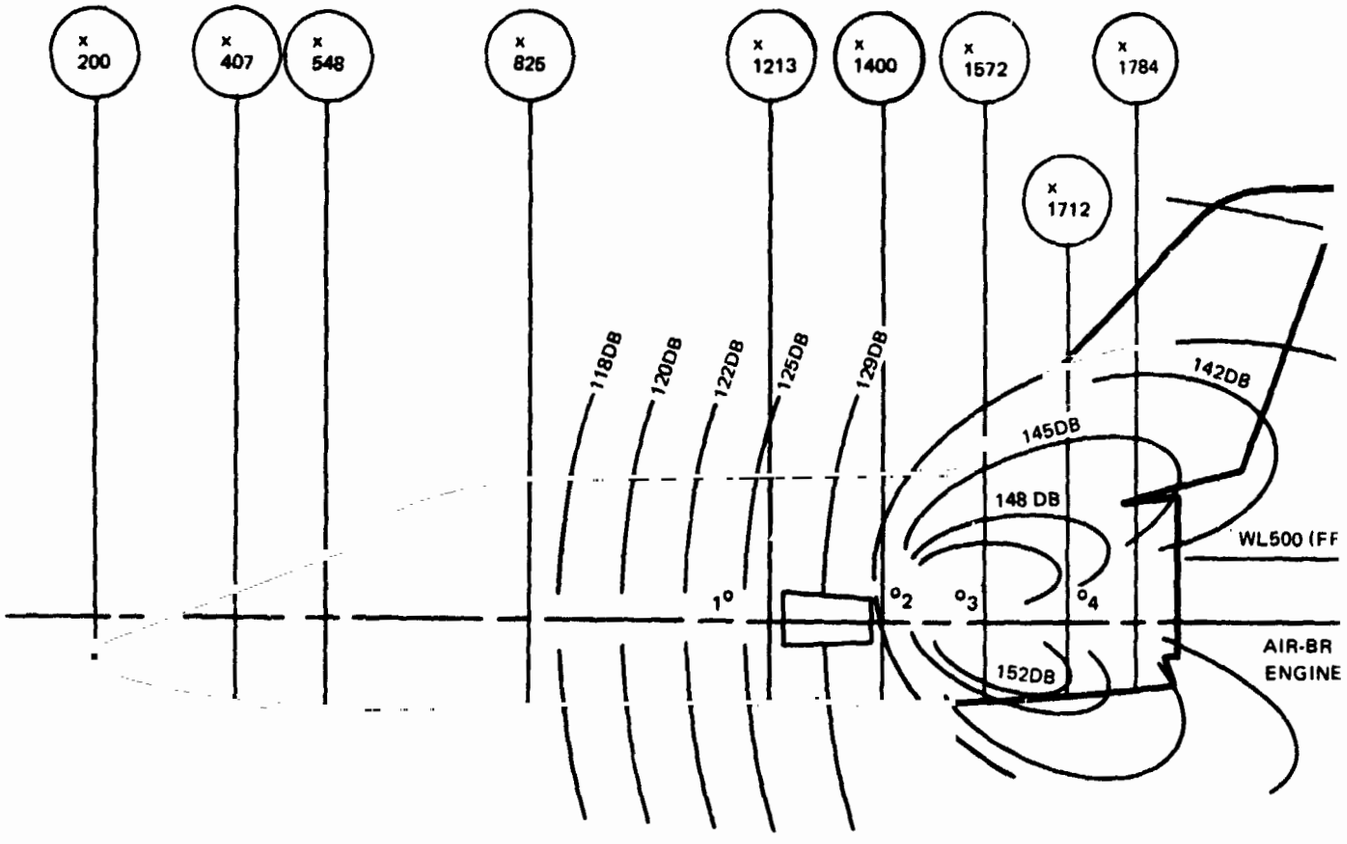

CONTOUR LINES ARE O.A. SPL, REF 2×10^{-5} N/M^2

- INCLUDES GROUND REFLECTION
- INCLUDES SURFACE REFLECTION
- INCLUDES EFFECT OF TWO ENGINES PER SIDE
- ASSUMES NO CONTRIBUTION ON FUSELAGE SIDE DUE TO OPPOSITE SIDE ENGINES
- INLET NOISE NOT INCLUDED

FOLDOUT FRAME 2

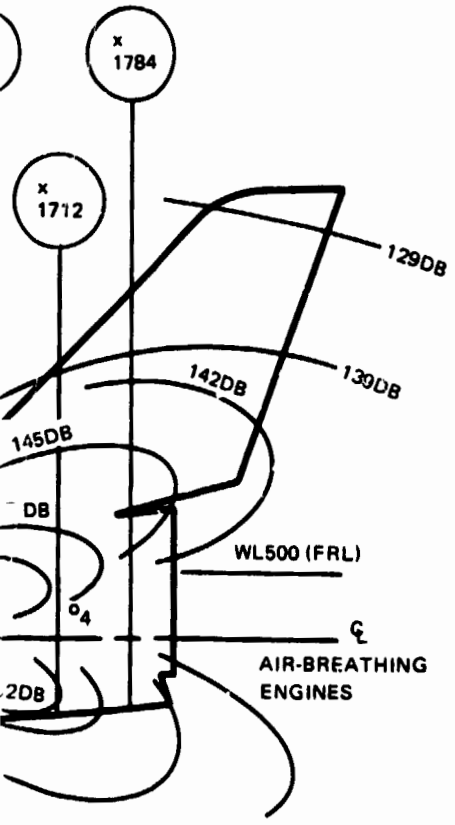

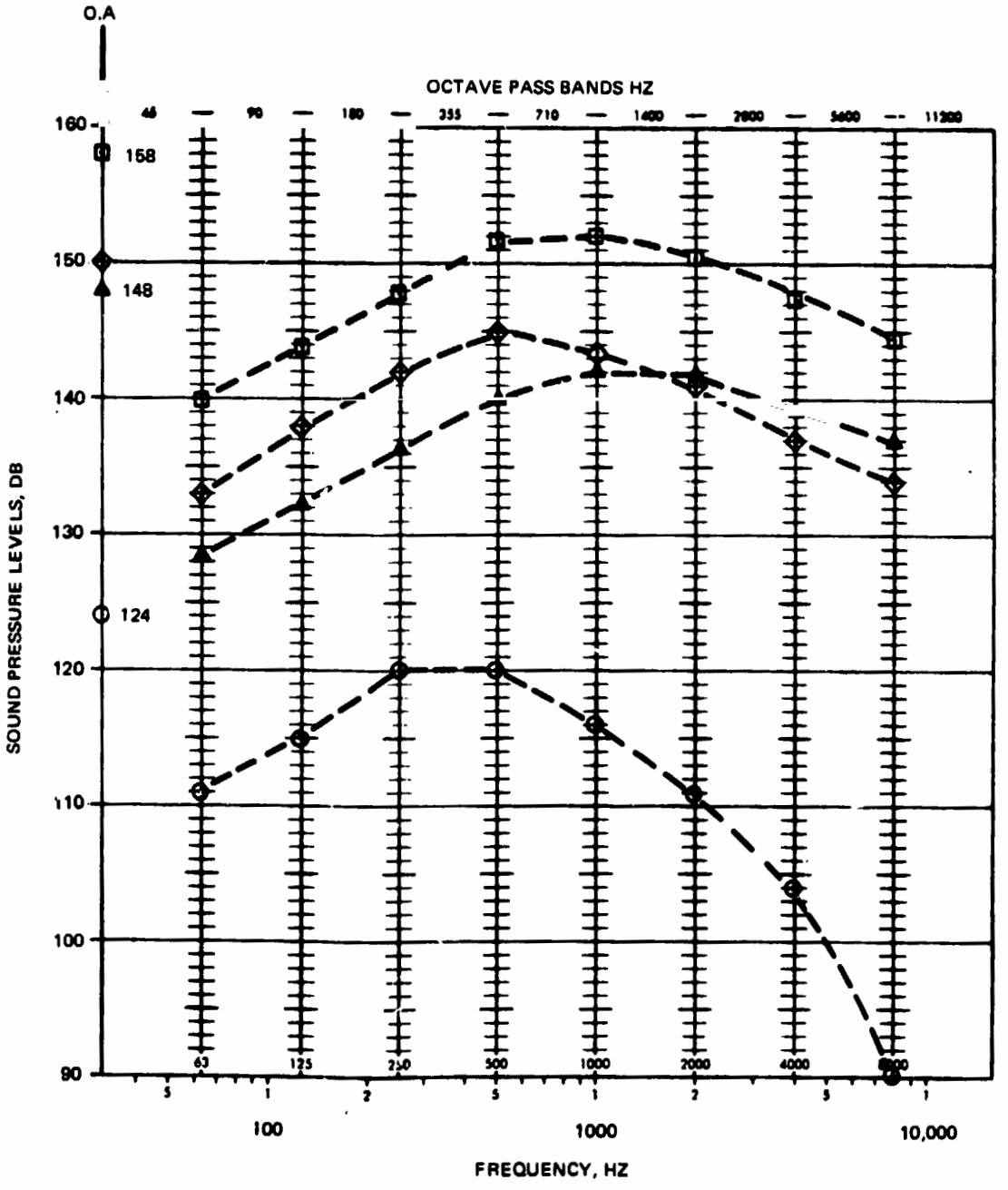

POINT NO	DISTANCE FROM ENGINE EXHAUST PLANE
○ 1	20 FEET FORWARD
△ 2	2 FEET AFT
□ 3	10 FEET AFT
◇ 4	20 FEET AFT

Fig. 8.3.6-28 Noise Contours and Spectra for Air-Breathing Engines at Maximum Static Thrust

GRUMMAN
BOEING

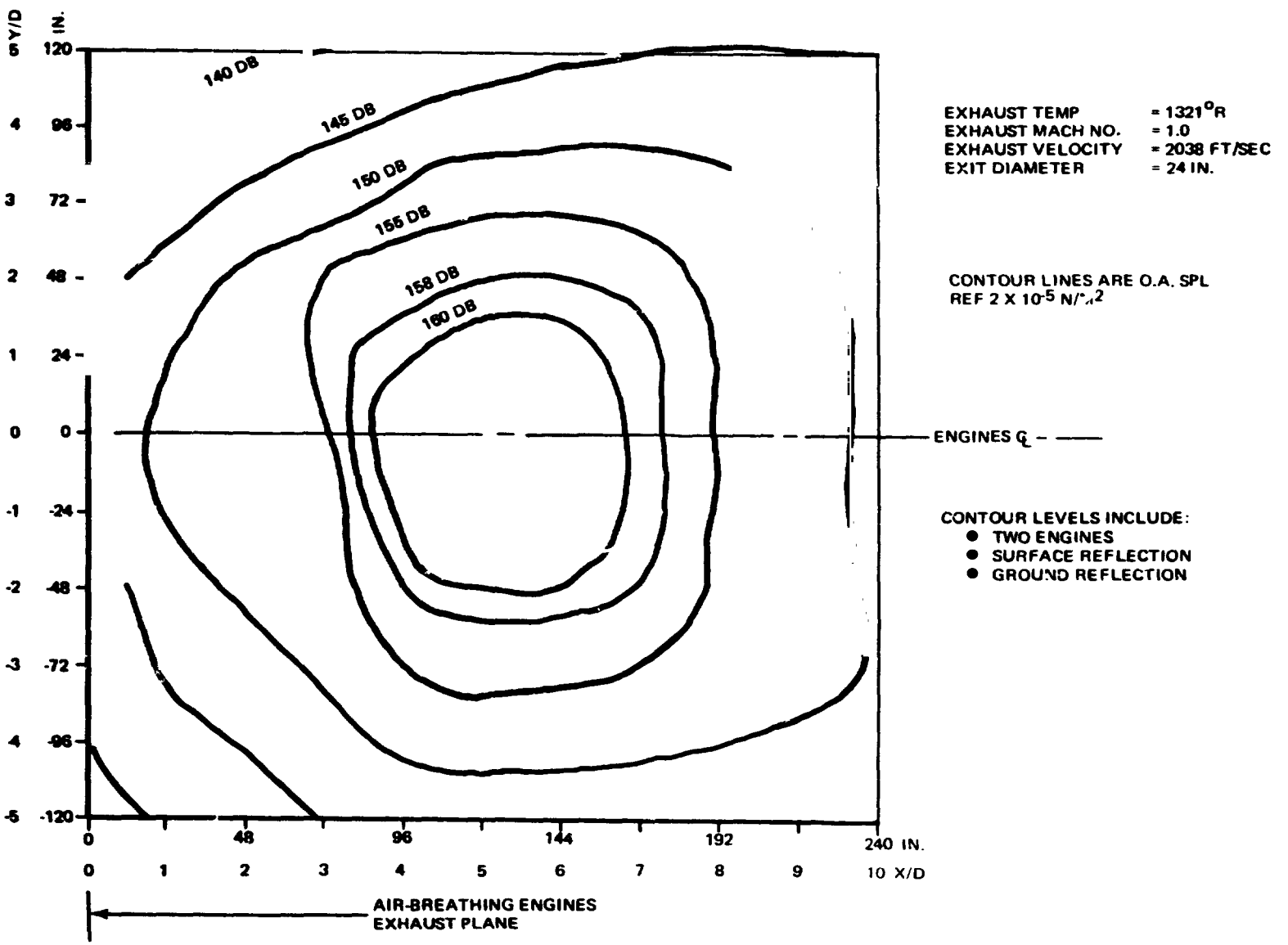

Fig. 8.3.6-29 Near Field Noise Contours For Air-breathing Engines at Maximum Static Thrust

8.3.6.6 Thermal Loads

The detailed calculation of thermal stresses involves the formulation of thermal models, the calculation of time histories of thermal model node point temperatures, and the calculation of stresses associated with temperature gradients which exist at various instants of time. It has not been possible to complete such detailed calculations for all primary structure of the H-33 orbiter. Work on a candidate design for a "hot structure" fin is in process as discussed in sub-section 8.14.23, and work will be undertaken thereafter on the "fuselage/wing carry through" region. This region is considered particularly important in that thermal stress and resulting effects on fatique life could influence a large segment of wing and fuselage primary structural arrangement. Work is also continuing to improve and integrate computer programs to enable more rapid completion and iteration of the extensive calculations required for proper optimization of structure with thermal stress taken into account. The planned organization of applicable methodology has been finalized and is presented in Fig. 8.3.6-30 and 8.3.6-31.

The flow chart shown in Fig. 8.3.6-30 summarizes the developed procedure to obtain the necessary data needed for a thermal stress analysis of the shuttle primary and secondary structure. This chart is an expansion of the thermal distributions portion of Fig. 8.3.6-31. There are four major calculation steps as follows:

Step 1 uses a trajectory analysis program (G-1) to calculate velocity, altitude and angle of attack time histories.

Step 2 uses trajectory and configuration data together with aerodynamic flow field data to predict aerodynamic heating rates. Programs for this purpose are:

- B-1-1: FPREM - Computes heating rates for laminar and turbulent flows using a modified flat plate reference enthalpy method
- B-1-2, B-1-3: STRIP, STLIN - Computes heat flux and Reynolds number using isentropic expansion and either a calculated Newtonian pressure distribution or input pressure data from test results

FOLDOUT FRAME 1

B/8.3

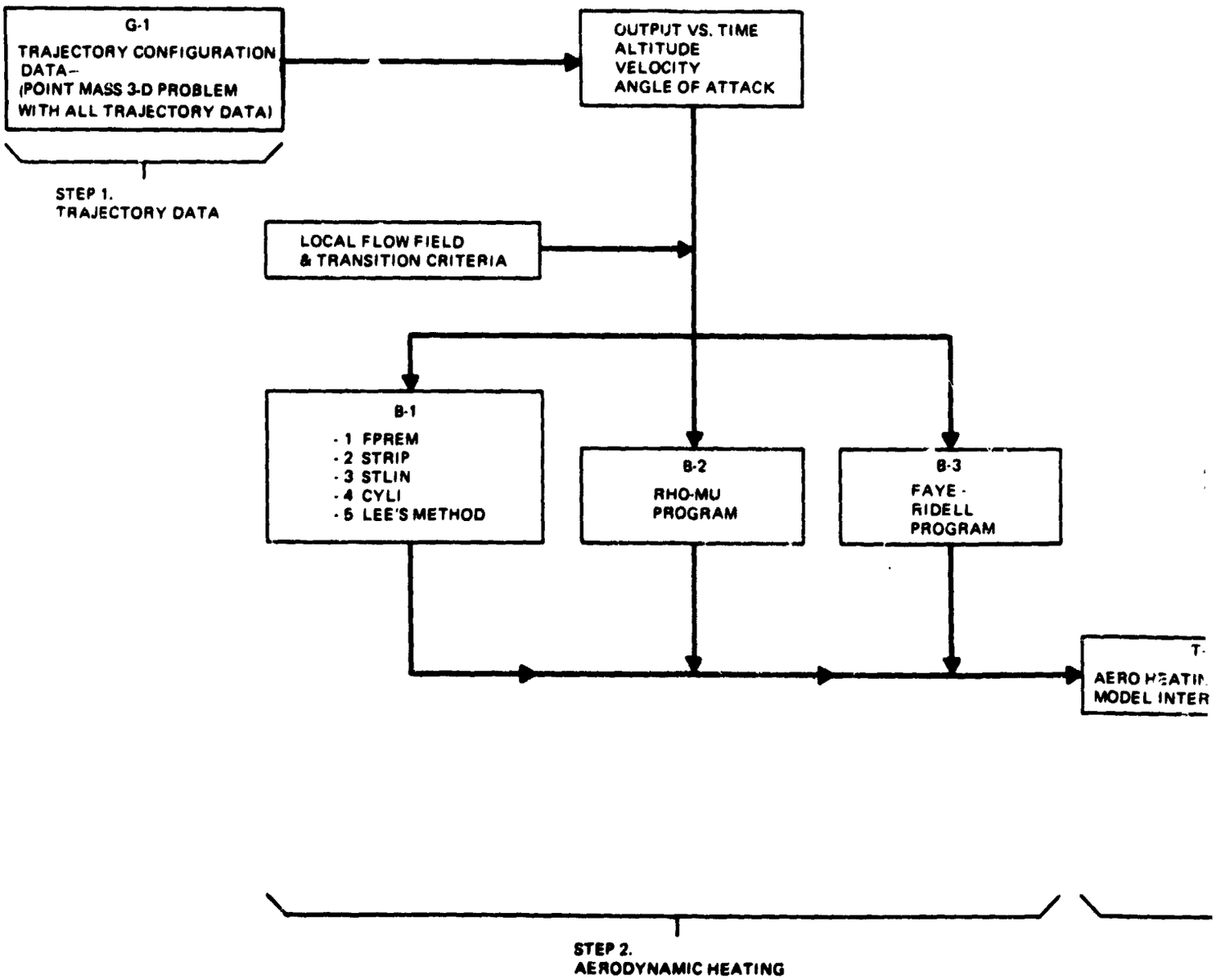

FOLDOUT FRAME 2

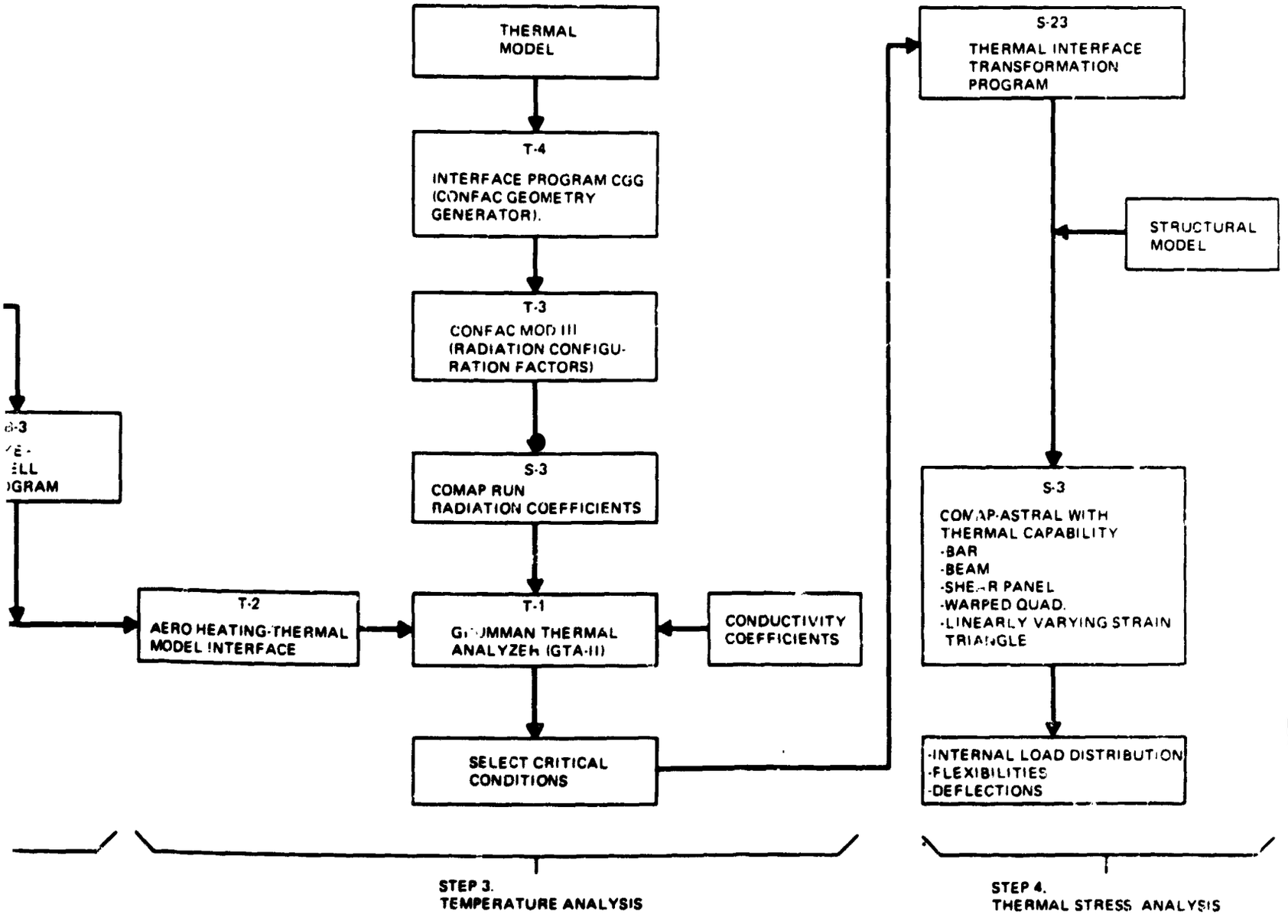

Fig. 8.3.6-30 Data Flow For Shuttle Thermal Stress Analysis

GRUMMAN BOEING

FOLDOUT FRAME

B/8.3

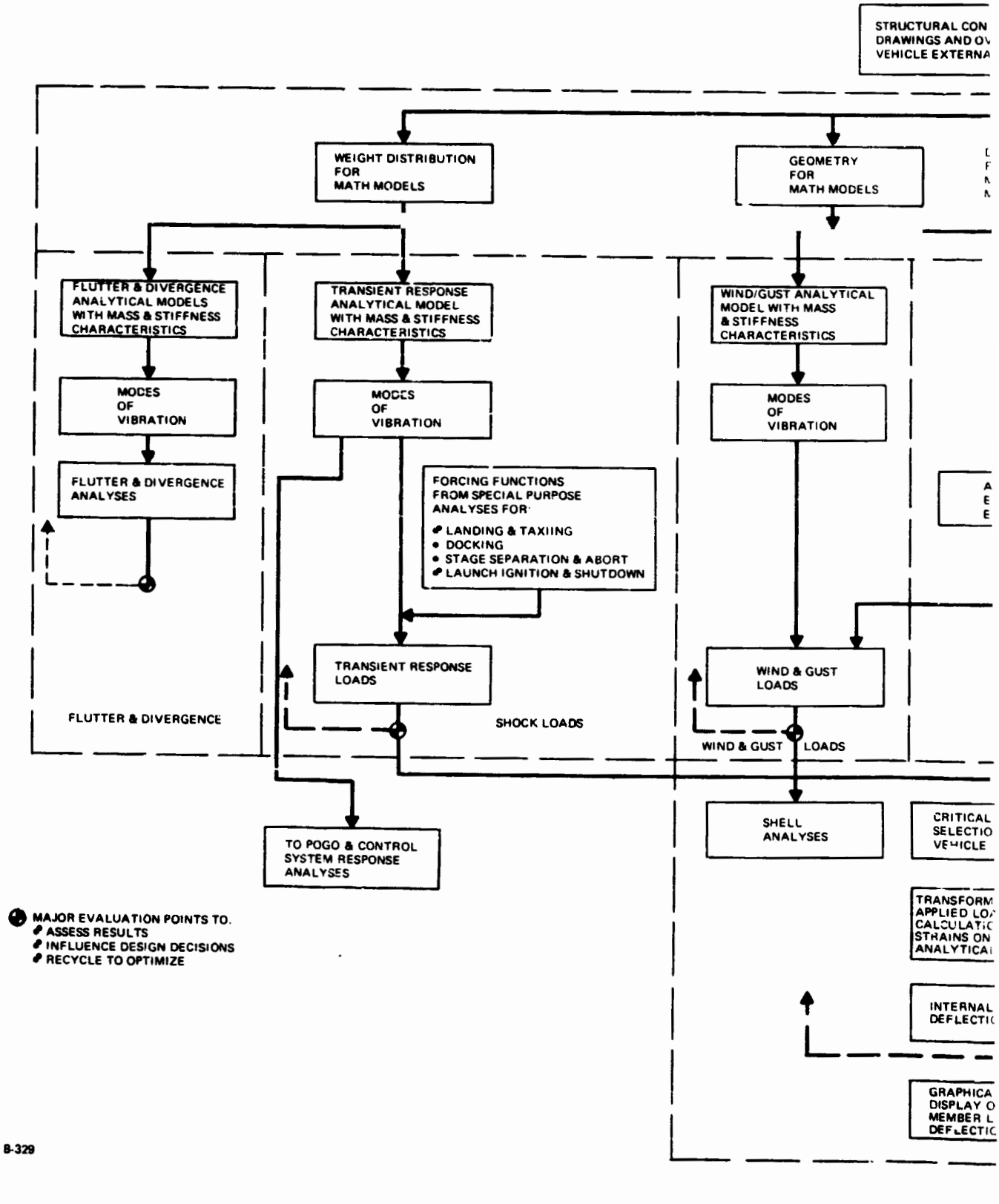

FOLDOUT FRAME 2

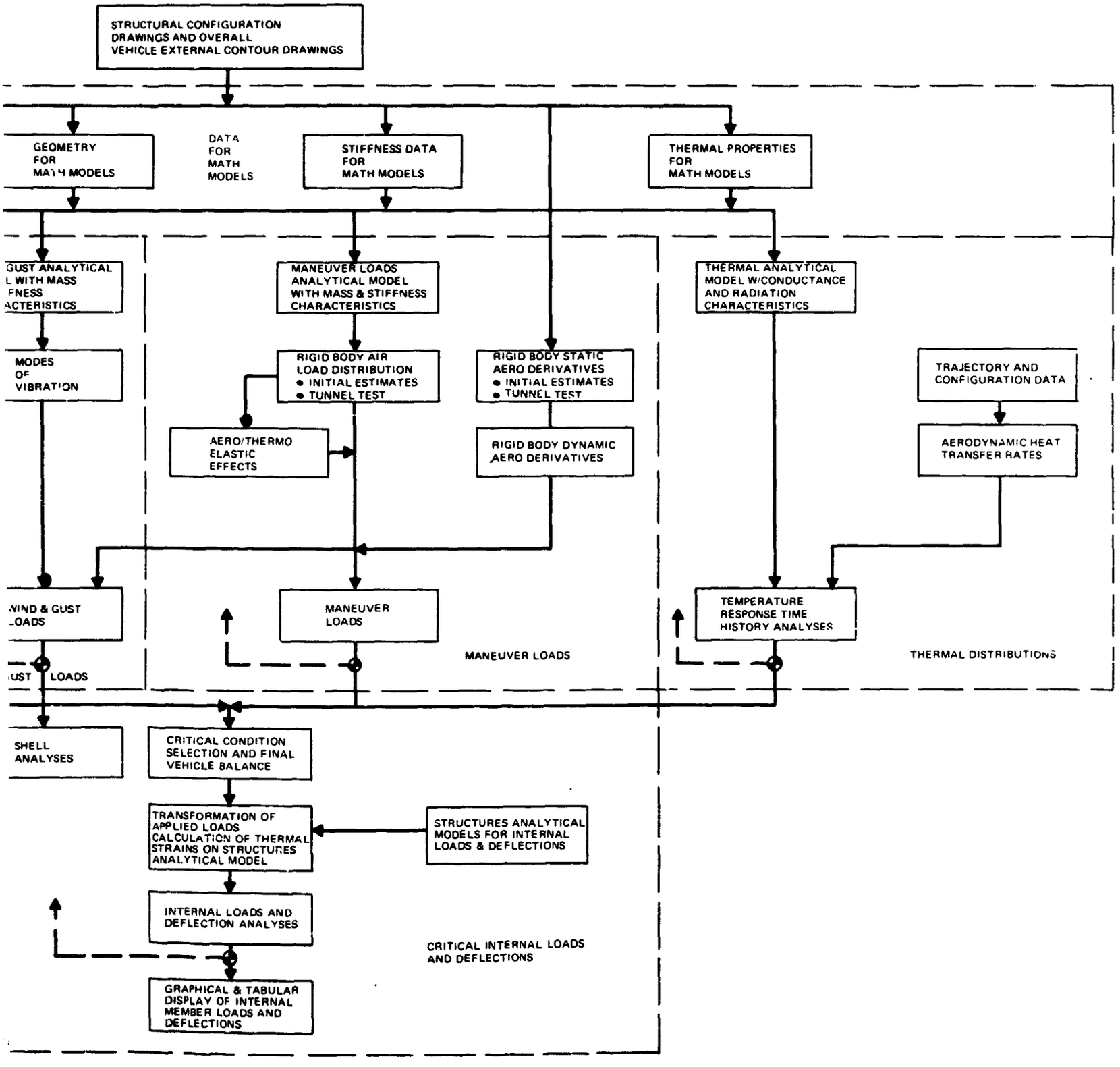

Fig. 8.3.6-31 Integrated Design and Analysis System

GRUMMAN BOEING

- B-1-4: CYCLI - Computes stagnation line heat transfer on a swept cyclinder
- B-1-5: Lee's Method - Computes the ratio of local to stagnation point heat transfer for blunt bodies
- B-2: RHO-MU - Computes aerodynamic heating effects on 3-D bodies of general shape at high angles of attack
- B-3: Faye-Riddell - Computes stagnation point heat transfer on a sphere

Step 3 transfers the aerodynamic heating rates determined in Step 2 from aerodynamic heating models to the thermal model. These heating rates are then used in conjunction with calculated radiation and conduction coefficients in a thermal network analysis to obtain temperature time histories for thermal nodes. Applicable programs are:

- T-1: Grumman Thermal Analyzer Program - Compute temperature time histories at thermal nodes using a lumped parameter network
- T-2: Aero Heating, Thermal Model Interface - Determines heating rates at thermal nodes from aerodynamic heating math models
- T-3: CONFAC MOD III - Computes radiation configuration factors for planar radiating surfaces including the effects of intervening surfaces
- T-4: CGG - Checks all input data required for T-3 and determines planar radiating surfaces for a thermal model from a finite element structural model
- S-3: COMAP - The radiative couplings or radiation coefficients required for the thermal network analysis are computed using automated matrix operations

Step 4 selects critical conditions or times by examining the output from the Thermal Analyzer (T1) Program. Temperatures of structural members for these conditions are determined by interpolation between thermal nodes on the thermal model. Induced strains corresponding to these member temperatures are utilized in a finite element structural analysis to yield internal member loads. Programs are:

D

- S-23: Thermal Interface Transformation Program - Interpolates between nodes on the thermal model to obtain temperatures and induced strains for all structural elements, and modifies finite element elastic constants as a function of temperature for the structural model
- S-3: COMAP-ASTRAL (Automated Structural Analysis) - Performs thermal stress analyses of large structures using finite element matrix methods